Active Control of Radiated Noise from a Cylindrical Shell Using External Piezoelectric Panels

by

Kyungyeol Song

Master of Science in Aerospace Engineering
Seoul National University (1998)

Bachelor of Science in Aerospace Engineering
Seoul National University (1996)

Submitted to the Department of Aeronautics and Astronautics
in partial fulfillment of the requirements for the degree of

Doctor of Philosophy

at the

MASSACHUSETTS INSTITUTE OF TECHNOLOGY

June 2002

Signature of Author .....
Department of Aeronautics and Astronautics
7 May 2002

Certified by .....
Steven R. Hall
Professor of Aeronautics and Astronautics
Thesis Supervisor

Certified by .....
Carlos E. S. Cesnik
Associate Professor of Aerospace Engineering
University of Michigan

Certified by .....
Mauro J. Atalla
United Technologies Research Center

Certified by .....
Jonathan P. How
Associate Professor of Aeronautics and Astronautics

Accepted by .....
Wallace E. Vander Velde
Professor of Aeronautics and Astronautics
Chair, Committee on Graduate Students

Active Control of Radiated Noise from a Cylindrical Shell Using External Piezoelectric Panels

by
Kyungyeol Song

Submitted to the Department of Aeronautics and Astronautics
on 7 May 2002, in partial fulfillment of the
requirements for the degree of
Doctor of Philosophy

Abstract

Control architectures and methodologies are developed for the reduction of radiated noise from a thick-walled cylindrical shell using external piezoelectric panels. The proposed approach is to cover the shell's outer surface with curved active composite panels, and to reduce the radiated noise by controlling the motion of each panel's outer surface (*i.e.*, the radiating surface), instead of the shell's outer surface. The use of external piezoelectric panels proposed in this thesis has significant advantages over the conventional approach of directly controlling the structure in reducing radiated noise from stiff structures. The reason is that the proposed approach needs much less control authority, and allows the control system to be significantly less dependent on the dynamic characteristics of the structure, than the conventional approach.

The control architecture is composed of local controllers, which are implemented for each panel to reduce its vibration level, and a global controller, which makes the shell a weak radiator by coordinating all of the panels simultaneously. For each local control, two different feedback controllers are implemented simultaneously. The first feedback controller takes the acceleration of the outer surface of each panel and uses high gain to minimize its motion. The other feedback loop, which is denoted as the *feedforward controller* in this thesis, takes acceleration on the inside surface of the panel and aims at canceling the motion of radiating surface. Several controller configurations were designed, implemented and compared, in order to find the one that is the simplest to implement, while achieving the required closed-loop performance and stability margins. After covering the surface of the cylindrical shell with active composite panels, the panel-level tonal controllers were designed and implemented on the shell vibrating in water. The controllers yielded more than 20 dB of attenuation at the target frequency in the acceleration over the radiating surface, although the actual noise level was increased under closed-loop control due to the flaws in the internal accelerometers in the panels.

For global control, a new wavenumber domain sensing method has been developed and applied to feedback controller design for active structural acoustic control. The approach is to minimize the total acoustic power radiated from vibrating structures in the wavenumber domain. We found that the method greatly simplifies the design of MIMO LQG controllers for active structural acoustic control, by reducing the effort to model the acoustic radiation from the structure, and by reducing significantly the number of transfer functions that should be identified to get a plant model. The new sensing method was numerically validated on a beam structure and a cylindrical shell with active composite panels mounted.

Thesis Supervisor: Steven R. Hall
Title: Professor of Aeronautics and Astronautics

Acknowledgments

This research would not have been possible without the support and assistance of many people. First, I would like to thank my advisor, Dr. Steven R. Hall, for his guidance and advice during my tenure as a graduate student. His profound knowledge and physical insights were invaluable and indispensable to this research. I would also like to express my deep gratitude to Dr. Mauro J. Atalla for his helpful guidance and suggestions throughout this work. Additionally, I would like to acknowledge Dr. Carlos E. S. Cesnik and Dr. Jonathan P. How for their advice, recommendations, and direction during the writing of this thesis.

I owe a great deal of thanks to Randall W. Smith at Northrop Grumman Corp., for his support, dedication, and all the water-tank experiments. I wish to thank Alan Curtis and Dan Fiore at Material Systems, Inc., and Fred Geil, Gary Rackson, Derek Prosperie, and Charles R. Kunning at Northrop Grumman Corp., for their valuable assistance. I would also like to acknowledge Paul Bauer and David C. Robertson for their support on the experiments at MIT.

I am profoundly grateful to Dr. Seung-Jo Kim at Seoul National University, for his introduction to the world of active structural acoustic control. His guidance for my master's thesis directed me to pursue my doctoral degree at MIT.

Finally, I would like to thank my parents for their love and support, and my two sisters, brother-in-law, and nephew for their love. Additionally, I would like to express my thanks to my parents-in-law, Jiwon, and Jaewon. Most importantly, I would like to thank my wife, Seongwon Moon, for her unbelievable love, understanding, and patience, and my son, Minjoon Song, for his love, smile, and high activeness.

This project was funded by the Office of Naval Research under contract number N00014-98-3-0018, with Dr. Kam W. Ng serving as technical monitor.

Contents

List of Figures

List of Tables

Nomenclature

Symbols

$\mathbf{B}$	Strain-displacement matrix
$C(s)$	Low-frequency feedthrough compensator
$C'(s)$	Low-frequency feedthrough compensator in the digital notch filter configuration
$D(s)$	DSP system dynamics (mostly time delay)
D_x, D_y	Bending stiffnesses of the unbaffled plate
E	Young's modulus (modulus of elasticity)
F	Weighting function for wavenumber components
$\widehat{F}$	Optimal weights for wavenumber components
$G(s)$	Plant transfer function
$G_{\text{power}}(s), G_{\text{pre}}(s)$	Transfer functions of a power amplifier and a pre-amplifier
G_{xy}	Transfer function from 'x' to 'y'
$\mathbf{H}$	Displacement interpolation matrix
H	Weighting function for wavenumber components of general structures
$H_1(s), H_2(s)$	Notch filter and narrow band-pass filter ($H_1(s) = 1 - H_2(s)$)
$\widehat{H}_1(s), \widehat{H}_2(s)$	Digital implementation of $H_1(s)$ and $H_2(s)$
$H_n^{(2)}(x), H_n^{(2)'}(x)$	nth Hankel function of the second kind and its first derivative
$H_n(s)$	Filter to be implemented to obtain wavenumber components from sensor measurements
$\mathbf{I}_N$	$N \times N$ identity matrix
J, J_1, J_2	Integration of the acoustic power
J_Π	Performance metric used to obtain the optimal weights for wavenumber components
$\overline{J_\Pi}$	Frequency-weighted performance metric used to obtain the optimal weights for wavenumber components
$K(s)$	Controller transfer function
$K'(s)$	Transfer function of controller that incorporates the low-frequency feedthrough compensator
$K_1(s), K_2(s)$	Feedback controller without notch filter ($K_1(s)$), and a notch filter ($K_2(s)$) (used in the digital notch filter configuration)
$K_{\text{Notch}}(s)$	Notch filter for feedback controller
$K_T(s)$	Tonal feedback controller

$K_T'(s)$	Tonal feedback controller that incorporates the low-frequency feedthrough compensator
$K_b(s)$	Feedback controller transfer function
$\overline{K}_b(s)$	Feedback controller transfer function without notch filter
$K_b'(s)$	Feedback controller that incorporates the low-frequency feedthrough compensator
$\widehat{K}_b(s), \widehat{K}_2(s)$	Digital implementation of $K_b(s)$ and $K_2(s)$ (used in the digital notch filter configuration)
$K_b^D(s), K_b^A(s)$	Digital and analog controller in the hybrid feedback control configuration
$K_b'^D(s), K_b'^A(s)$	Digital and analog controller with the low-frequency feedthrough compensator in the hybrid feedback control configuration
$K_b^H(s)$	Hybrid feedback controller
$K_f(s)$	Feedforward controller transfer function
$K_{f,1}(s), K_{f,2}(s)$	Analog and digital controller in the digital feedforward control configuration
$K_f'(s)$	Feedforward controller that incorporates the low-frequency feedthrough compensator
$K_f'^D(s)$	Digital controller with the low-frequency feedthrough compensator in the digital feedforward control configuration
L	Length of a beam, or a cylindrical shell
$L(s), H(s)$	Complementary low-pass and high-pass filter
$\mathbf{M}_p, \mathbf{C}_p, \mathbf{K}_p$	Global mass, damping and stiffness matrix of the active composite panel
$\mathbf{M}_s, \mathbf{C}_s, \mathbf{K}_s$	Global mass, damping and stiffness matrix of the cylindrical shell
N_T	Number of tonal feedback controllers implemented
N_a, N_c	Number of measurement points in the axial and circumferential direction of the cylindrical shell
N_e	Number of elements used in the finite element analysis
N_m, N_n	Number of axial and circumferential wavenumber components used to estimate the acoustic power
N_p	Number of panels mounted on the structure
N_s	1. Number of degrees of freedom in the finite element model 2. Number of measurement points in the beam structure
N_ω	Number of wavenumber components to be considered to estimate the acoustic power below an arbitrary frequency ω
$\mathbf{Q}$	Performance weight matrix for wavenumber components
$\mathbf{R}$	Radiation resistance matrix
$\mathrm{Re}(\cdot)$, $\mathrm{Im}(\cdot)$	Real and imaginary part
$S(s)$	Sensitivity transfer function
$T(s)$	Filter used to modify the plant transfer function to make the design of tonal feedback controller easier
T	Effective time delay in the digital control system
T_b	Design variable of the tonal feedback controller ($\approx 1/\omega_b$)
T_l	Latency of the digital control system
T_s	Sampling time of the digital control system
$\widehat{\mathbf{U}}$	Nodal displacements in a cylindrical shell element

$\mathbf{U}_s$	Nodal displacements of the cylindrical shell in the global coordinate
$\ddot{W}$	Wavenumber component
$\ddot{W}_d$	Wavenumber component obtained by discrete wavenumber transform
$\widehat{\ddot{W}}_d$	Estimated wavenumber component
a	Radius of a cylindrical shell or a spherical shell
b	Width of a beam structure
c	Speed of sound
g	Free-space Green's function
h	1. Thickness of the acoustic source distribution 2. Thickness of the unbaffled plate
$h_n'(x)$	First derivative of the spherical Hankel function of the first kind
k	Acoustic wavenumber
k_x	Structural wavenumber in the x direction
k_z, n	Structural wavenumber in the axial and circumferential directions in a cylindrical shell
m_p, c_p, k_p	Mass, damping and stiffness of the active composite panel
p	Acoustic pressure
q	Strength of the acoustic source distribution
t	Thickness of a cylindrical shell
u, v, w	Displacement in the axial, circumferential, and radial directions in a cylindrical shell
u_0, v_0, w_0	Displacement at the mid-surface in the axial, circumferential, and radial directions in a cylindrical shell
$\mathbf{v}$	Velocity distribution
w	Displacement variable
w_p, w_s	Displacement of the outer and inner surfaces of the panel
y_b	Acceleration of the inner surface of the panel (bottom acceleration)
y_t	Acceleration of the outer surface of the panel (top acceleration)
$\mathbf{z}, \mathbf{y}, \mathbf{u}, \mathbf{f}$	Performance, sensor output, control input, and disturbance vector
z, y, u, w	Performance, sensor output, control input, and disturbance variable
Π	Radiated acoustic power
$\widehat{\Pi}$	Estimated acoustic power
Π_d	Approximated acoustic power
$\widehat{\Phi}$	Discrete wavenumber transform matrix
Ω	Target frequency of the tonal feedback controller
α	Factor that accounts for the difference between the measured and actual acceleration of the panel
γ_{xy}, γ_{yz}, γ_{zx}	Shear strain
ε_x, ε_y, ε_z	Normal strain
ν	Poisson's ratio
ρ	Density of fluid
ρ_p	Mass per unit area of the unbaffled plate
ρ_s	Density of the shell material

σ_x, σ_y, σ_z	Normal stresses
σ_{xy}, σ_{yz}, σ_{zx}	Shear stresses
ϕ_x, ϕ_y	Rotations at the mid-surface in a cylindrical shell
χ_x, χ_y, χ_{xy}	Change of curvature, and twist of the mid-surface
ω	Angular frequency
ω_b	1. Control bandwidth of the tonal feedback controller 2. Disturbance bandwidth (or, bandwidth of interest)
ω_T	Target frequency of the tonal feedback controller
ω_p, ζ_p	Resonant frequency and damping ratio of the panel

Superscripts

$(\cdot)^H$	Hermitian transpose (complex conjugate transpose)
$(\cdot)^T$	Transpose

Abbreviations

ASAC	Active Structural Acoustic Control
DSP	Digital Signal Processing
IIR	Infinite Impulse Response
LQG	Linear Quadratic Gaussian
MIMO	Multiple-Input Multiple-Output
MSI	Material Systems Inc.
NGC	Northrop Grumman Corp.
OL,CL	Open-loop and Closed-loop
PVDF	Polyvinylidene Fluoride Polymer
PZT	Lead Zirconate Titanate
SISO	Single-Input Single-Output

Chapter 1

Introduction

Sound radiation from vibrating structures has been an important problem in many engineering applications. Some representative examples related to structurally-radiated noise include naval vessel and weapon radiation, sound transmission through aircraft fuselage panels, and noise generated by transformers, *etc.* Much research has been carried out on the development of efficient methods to reduce the noise radiated from structural vibrations. Generally, those methods can be divided into two subgroups. The first is passive methods, which try to make a quiet structure by mounting additional mass or damping treatments through mechanical redesign. The second subgroup is active methods, which reduce the structurally-radiated noise by using actuators, sensors, and control algorithms. It is widely accepted that passive techniques are not effective for the control of low-frequency sound, due to the increased weight of the passive treatments. Considerable effort has been devoted to the development of the active control techniques. Most of the structures investigated to date are flat panels and long cylinders in the case of sound radiation, and boxes and closed-cylinders in the case of interior sound control. The idea is to control structural motion that couples well with the acoustic field surrounding the structure [Fuller, 1990].

Most of the existing literature on active structural acoustic control focuses on the minimization of the radiated sound by directly controlling the dynamic behavior of the structure. This strategy is desirable when the actuators have sufficient authority over the structural behavior. This is not the case for very rigid and stiff structures, such as thick-walled metallic cylinders, which are the structures considered in this thesis. In this thesis, a method is proposed to control the radiated noise from a thick-walled stiff structure by actively isolating the motion of the structure's outer surface from the outer surface of a conformal coating mounted over the structure. The surface of the structure is covered with curved 1-3 active composite panels that contain several accelerometers attached to their outer and inner surfaces. The embedded accelerometers provide the information required for closed-loop control, while the panel's active layer provides the actuator authority. Local controllers, which consist of feedback controllers implemented as analog, digital and hybrid analog/digital circuits, *etc.*, combined with an analog and digital feedforward controller, have been designed to attenuate the outer surface's vibration for each panel. A global controller is designed to perform the high-level coordination of the local controllers.

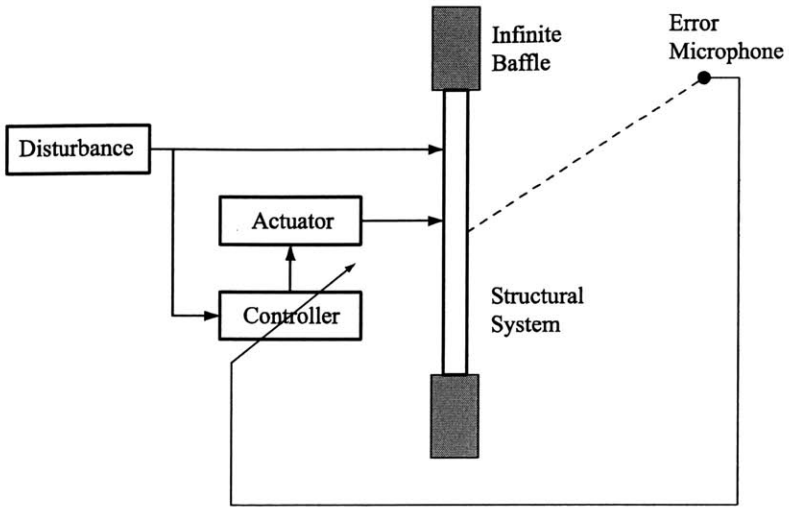

Figure 1-1: Block diagram of adaptive feedforward control algorithm.

1.1 Background and Previous Research

1.1.1 Control Algorithms

Adaptive feedforward control algorithms

Since Fuller introduced the technique of reducing the acoustic pressure radiated from vibrating structures by applying mechanical inputs directly to the structures, which is referred to as *Active Structural Acoustic Control* (ASAC) [Fuller, 1990], many researchers have developed the control algorithms to attenuate the structurally-radiated noise. Specifically, most effort has been focused on the development of efficient adaptive feedforward control algorithm. The concept can be explained using a block diagram in Figure 1-1, showing a structural system in an infinite baffle, the adaptive controller, and the disturbance signal that causes the structure to vibrate. The figure also shows the actuator, which applies the control input to the system, and the error microphone in the far field. Since the feedforward controller needs the disturbance signal as its input, we should be able to measure the disturbance signal directly, or a related signal, in order to apply the feedforward controller. In adaptive feedforward algorithms, the control inputs are computed by passing a signal which is coherent to the disturbance input through an adaptive filter, before being applied to the structure. The coefficients of the adaptive filter are updated in such a way as to minimize a quadratic cost function created from a measurable variable of the system [Vipperman, 1993]. The sum of the mean-square values of the output of sensors, such as the error microphone in Figure 1-1, is commonly used as the cost function. Representative research on the adaptive feedforward control algorithms include [Elliott, 1987], [Metcalf, 1992], [Burdisso, 1992], and [Vipperman, 1993].

Elliott *et al.* presented a generalization of the filtered x-LMS algorithm which minimizes the sum of the mean square outputs of a number of errors, each linearly related to the outputs of a number of adaptive filters [Elliott, 1987]. They showed that the algorithm can be applied to ac-

tive sound and vibration control, by using secondary sources that are suitably driven to reduce the levels of acoustic or vibrational fields. Metcalf *et al.* applied the adaptive feedforward control algorithm to reduce the sound transmitted through an elastic circular plate [Metcalf, 1992]. They used point force vibration inputs as the control input, and both the microphone in the far field and accelerometers mounted on the structure as the error sensors. After comparing the performance obtained using the microphone and the accelerometers, they concluded that the microphone resulted in much better performance than the accelerometer. Burdisso *et al.* investigated the dynamic behavior of feedforward controlled finite systems [Burdisso, 1992]. They showed that the eigenproperties of the feedforward controlled system are functions of the applied control force and error sensor locations, but are independent of the input disturbance. While Elliott *et al.* and Metcalf *et al.* considered only single and multiple sinusoidal excitations, Vipperman *et al.* developed the adaptive single-input single-output (SISO) feedforward control configurations for the active control of broadband vibration of a supported structure [Vipperman, 1993]. They modified the conventional filtered-x LMS control configuration such that the transfer function between the control input and the error output is represented by an infinite impulse response (IIR) filter. They demonstrated experimentally the attenuation of broadband structural vibration using adaptive feedforward control algorithm.

Radiation mode approach

Another important concept for active structural acoustic control approaches is *radiation mode approach*, introduced by Elliott *et al.* [Elliott, 1993]. The basic concept of the radiation mode approach is briefly reviewed. The sound power radiated by vibrating structures can be written as

$$\Pi = \mathbf{v}^H \mathbf{R} \mathbf{v} , \tag{1.1}$$

where Π is the radiated sound power, $\mathbf{v}$ is the velocity distribution, H denotes the Hermitian transpose (complex conjugate transpose), and $\mathbf{R}$ is a real symmetric positive definite matrix, which is proportional to the radiation resistance matrix [Elliott, 1993]. Since $\mathbf{R}$ is real symmetric positive definite, it has a real eigenvalue and real eigenvector decomposition of the form, given as

$$\mathbf{R} = \mathbf{Q} \mathbf{\Lambda} \mathbf{Q}^T , \tag{1.2}$$

in which $\mathbf{Q}$ is an orthogonal matrix of eigenvectors, and $\mathbf{\Lambda}$ is a diagonal matrix of eigenvalues λ_i. Elliott *et al.* termed the eigenvectors in $\mathbf{Q}$, which are the eigenvectors of radiation resistance matrix, as "radiation modes" [Elliott, 1993]. The sound power Π can thus be written by substituting Equation 1.2 in Equation 1.1, to obtain

$$\begin{aligned} \Pi &= \mathbf{v}^H \mathbf{Q} \mathbf{\Lambda} \mathbf{Q}^T \mathbf{v} \\ &= \mathbf{y}^H \mathbf{\Lambda} \mathbf{y} = \sum_{i=1}^{N} \lambda_i |y_i|^2 . \end{aligned} \tag{1.3}$$

Here, $\mathbf{y} = [y_1 \; y_2 \; \cdots y_N]^T$ is defined as $\mathbf{y} = \mathbf{Q}^T \mathbf{v}$, which is the vector of radiation modes in terms of the velocity distribution. What Equation 1.3 implies is that the radiation modes radiate acoustic power independently, *i.e.*, they are uncoupled in terms of their radiation [Elliott, 1993]. Therefore, radiation modes are velocity distributions whose radiated acoustic power is indepen-

dent of the amplitudes of the other velocity distributions. Naghshineh *et al.* proposed the same concept as the radiation mode, independently of Elliott *et al.* [Naghshineh, 1993]. They referred to the eigenvectors of the radiation impedance matrix, which was termed as the radiation mode by Elliott *et al.*, as "basis functions", and they stated that the basis functions act as "surface velocity filter". Also, they showed that the minimization of the radiated acoustic power results in a structural surface velocity filter that couples poorly to those acoustic basis functions that account for high-efficiency sound radiation.

Using this concept, Johnson *et al.* showed that when the excitation frequency is sufficiently low so that the size of structures is small compared with the acoustic wavelength, only one radiation mode has a significant radiation efficiency [Johnson, 1995]. For panels, the velocity distribution corresponding to this radiation mode is uniform across the surface of the panel, and its amplitude is proportional to the volume velocity of the structure. Specifically, they showed that volume velocity cancellation gives similar reductions in the transmitted sound power to the minimization of sound power radiation up to frequencies at which the size of the panel is about half an acoustic wavelength. Pan *et al.* demonstrated that the transmission of the sound power through a double panel partition can be reduced by the cancellation of volume velocity on either panel at low frequencies [Pan, 1998]. Cazzolato *et al.* applied this approach to the minimization of the total acoustic potential energy within a longitudinally stiffened cylinder by minimization of the amplitudes of the radiation modes [Cazzolato, 1998]. They showed that it is possible to decompose a large number of discrete surface vibration measurements into a small number of high quality error signals for an active noise control system.

Wavenumber domain approach

Since Fuller *et al.* introduced the concept of a wavenumber domain approach to the active control of radiated noise [Fuller, 1991A], there has been much research into active structural acoustic control approaches in wavenumber domain. The wavenumber domain approach is based on the fact that the acoustic pressure in the far field is entirely dependent on the corresponding wavenumber component for planar structures in an infinite baffle [Junger, 1986]. The important advantage of the wavenumber domain approach is that it eliminates the use of an error microphone in the radiation far field, which is impractical in most engineering applications, and it enables the structurally-mounted sensors to be used for active structural acoustic control. Maillard *et al.* proposed a new time domain structural sensing technique for predicting wavenumber information and applied it to a simply supported plate in order to minimize the sound radiation [Maillard, 1994A], [Maillard, 1994B]. They proposed the use of filters with an artificial time delay, to estimate the wavenumber components for the broadband disturbance. Clark *et al.* demonstrated analytically that structural acoustic control is achieved when the supersonic wavenumber components are reduced, and they investigated the possibility of implementing a cost function in the wavenumber domain [Clark, 1992A]. Scott *et al.* presented a technique to obtain the far-field radiated power from a one-dimensional structure using polyvinylidene fluoride film, which are shaped to act as low-pass wavenumber filters [Scott, 1997]. Wang presented a wavenumber domain sensing approach which applies PVDF films on a beam and defined a cost function for feedforward control as the sum of mean square values of the supersonic wavenumber components [Wang, 1998].

The research on the wavenumber domain approach mentioned in the previous paragraph

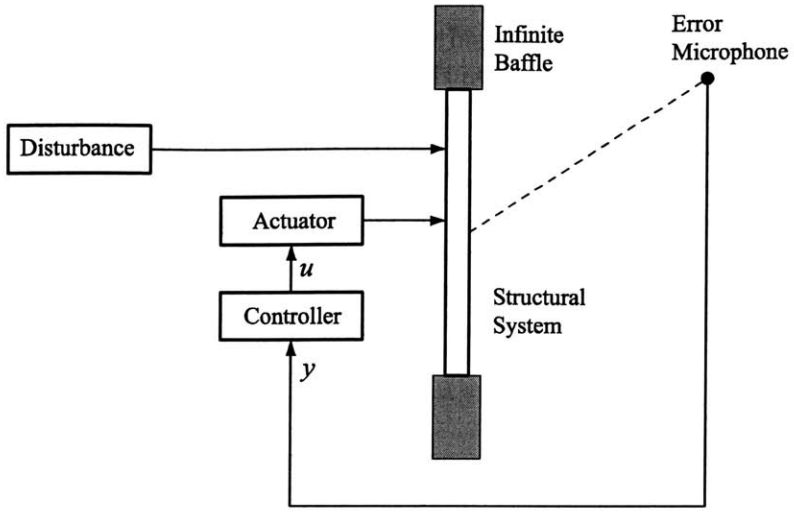

Figure 1-2: One possible way of implementing feedback control for ASAC. However, due to large phase delay in the plant transfer function, this is not easy to implement.

focused on application to feedforward control design. As will be explained in detail in Chapter 4, there has been no successful effort using the wavenumber domain approach for feedback controller design for broadband disturbance, because adding an artificial time delay, proposed by Maillard *et al.* to solve the noncausality of the filters, imposes a fundamental limitation on the achievable closed-loop performance using feedback control. Song *et al.* proposed a new wavenumber sensing method that applies the wavenumber domain approach to feedback controller design [Song, 2001]. They used the total acoustic power from a vibrating structure as the performance metric, rather than the acoustic pressure in the specific radiation direction. They showed that a state-space model can be found to estimate the magnitude of the wavenumber components that radiate the acoustic power in the controller bandwidth.

Feedback control algorithms - radiation filter

As mentioned earlier, most efforts to develop efficient control algorithms for active structural acoustic control (ASAC) have been focused on the feedforward control approaches. The preference for the feedforward control for ASAC, rather than feedback control, can be explained using Figure 1-2, which shows a block diagram of feedback control for radiation problem. Since the acoustic pressure is what we want to minimize in order to reduce structurally-radiated noise, we need a plant transfer function G_{yu} from the actuator (u) to the error microphone (y) for the feedback controller design. However, G_{yu} has a large phase delay in general, due to the traveling time of the acoustic wave from the structure to the error microphone. The time delay is proportional to the distance between the structure and the error microphone. This feature of the plant transfer function *i.e.*, the large phase delay, explains the preference for the feedforward control for ASAC. However, we know that feedforward control approach cannot be applied if we cannot measure the disturbance directly, because it needs the disturbance signal

as a control input. In that case, feedback control should be implemented.

Since the use of far-field acoustic pressure results in the large phase delay in the plant transfer functions, we should use measurements on the structure in order to implement feedback control for ASAC. One possible way to apply feedback control is to estimate the acoustic pressure using structural sensors. Griffin *et al.* presented a way to generate a state-space model to estimate the acoustic pressure using structural actuators and sensors, and applied it to suppress radiated sound in an acoustic cavity surrounded by a flexible structure [Griffin, 1999]. However, the method most widely used to design feedback control for ASAC is *radiation filter method*, proposed by Baumann *et al.* [Baumann, 1991]. The basic concept of the radiation filter method is briefly reviewed. We know that the sound power $\Pi(\omega)$ radiated by vibrating structures can be written as

$$\Pi(\omega) = \mathbf{v}^H(j\omega)\,\mathbf{R}(\omega)\,\mathbf{v}(j\omega)\ , \tag{1.4}$$

where $\mathbf{v}(j\omega)$ is the velocity distribution, and $\mathbf{R}(\omega)$ is the radiation resistance matrix. Although $\mathbf{R}(\omega)$ is not a rational matrix in general, we can approximate it to any desired accuracy by a rational matrix $\widetilde{\mathbf{R}}(\omega)$, while preserving its symmetric positive definiteness [Baumann, 1991]. Now, we can spectrally factorize $\widetilde{\mathbf{R}}(s)$ as ($\widetilde{\mathbf{R}}(\omega)$ is obtained by substituting $s = j\omega$ in $\widetilde{\mathbf{R}}(s)$)

$$\widetilde{\mathbf{R}}(s) = \mathbf{G}^T(-s)\,\mathbf{G}(s)\ , \tag{1.5}$$

where $\mathbf{G}(s)$ is a real, rational matrix that is analytic in $\mathrm{Re}(s) > 0$, which is referred to as *radiation filter* [Baumann, 1991]. Using this concept, the acoustic power can be approximated as

$$\begin{aligned}\Pi(\omega) &\approx \mathbf{v}^H(j\omega)\,\mathbf{G}^T(-j\omega)\,\mathbf{G}(j\omega)\,\mathbf{v}(j\omega) \\ &\approx \mathbf{z}^H(j\omega)\,\mathbf{z}(j\omega)\ .\end{aligned} \tag{1.6}$$

Since $\mathbf{G}(s)$ is a stable rational matrix, we can represent it as a state-space model. Therefore, we can use the approximated acoustic power, $\mathbf{z}^H(j\omega)\,\mathbf{z}(j\omega)$, as a cost function for the feedback controller design. The block diagram of feedback control using the radiation filter is shown in Figure 1-3. Baumann *et al.* used this concept to design the linear quadratic gaussian (LQG) controller to minimize the acoustic power radiated from clamped beams [Baumann, 1992]. Bingham *et al.* implemented the LQG controller including the radiation filter on the flat composite panel with embedded piezoelectric actuators and strain gauge sensors [Bingham, 1998]. Vipperman *et al.* demonstrated active structural acoustic control using multiple input/output adaptive sensoriactuators combined with radiation filters and a feedback control paradigm [Vipperman, 1999]. Gibbs *et al.* introduced a new method of reduced order modeling/design of radiation filters, termed *radiation modal expansion* [Gibbs, 2000].

As shown above, we should obtain the radiation resistance matrix $\mathbf{R}(\omega)$, analytically or experimentally, in order to apply the radiation filter method. This implies that the method is not easy to apply for a complex system, for which $\mathbf{R}(\omega)$ is difficult to obtain, although it can be easily applied to a simple structural system, such as beam or plate structures. Even if we can obtain $\mathbf{R}(\omega)$ from an analytic expression (when the structure is simple), or numerical method, such as finite element method or boundary element method (when the structure is complex), it is highly model-dependent, which means that it is not straightforward to implement experimentally the radiation filter method.

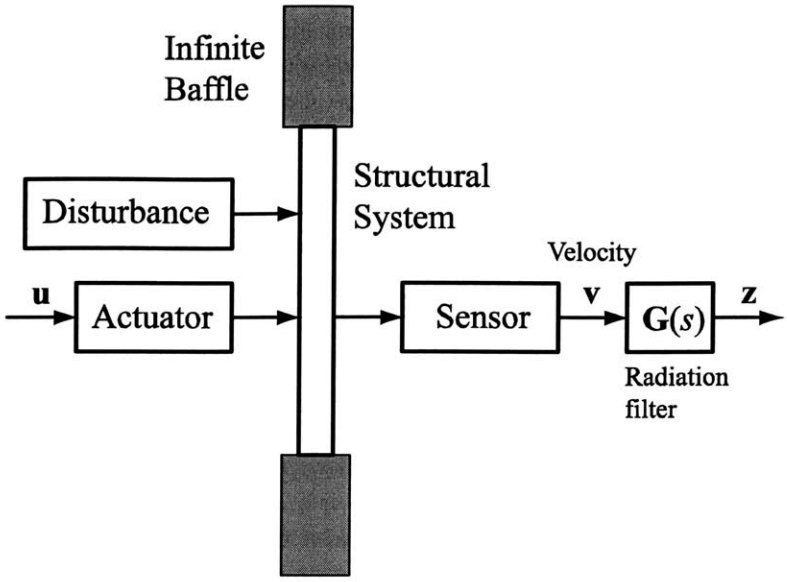

Figure 1-3: Block diagram of feedback control using the radiation filter $\mathbf{G}(s)$.

1.1.2 Actuators and Sensors

When the concept of active structural acoustic control (ASAC) was introduced in early 90's, the actuator used to implement the controller was a point force, such as a shaker [Fuller, 1990], [Mandic, 1991]. However, since Crawley *et al.* introduced the use of piezoelectric materials for active control of structures [Crawley, 1987], many techniques have been developed to perform active structural acoustic control using these materials. Dimitriadis *et al.* investigated theoretically the potential of actively controlling sound radiation from a vibrating plate using piezoelectric elements bonded to the plate surface as actuators [Dimitriadis, 1991]. Fuller *et al.* demonstrated experimentally the use of a piezoceramic actuator to control sound radiation from a vibrating rectangular thin panel [Fuller, 1991B]. Also, the possibility of using multiple piezoelectric actuators to reduce structurally-radiated noise from vibrating structures was investigated analytically [Wang, 1991] and experimentally [Clark, 1992B]. Recently, there has been much research into the use of more sophisticated actuators than simple piezoceramic patches. Johnson *et al.* investigated the use of arrays of discrete actuators, or "tiles" as they referred to them, which cancel local volume velocity by acting on local information such as local velocity or pressure, and producing a purely local reaction [Johnson, 1997]. Lane *et al.* proposed a device of collocated pressure sensors and constant volume velocity actuators, by compensating loudspeakers in order to approximate constant volume velocity behavior [Lane, 1998]. Song *et al.* used "active composite panels" that contain PZT rods embedded in a stiff polymer matrix and eight injection-molded piezoceramic accelerometers, for active structural acoustic control of a thick-walled cylindrical shell [Song, 2000]. Johnson *et al.* demonstrated the potential of an "active skin," which is a continuous covering of the vibrating portions of the structure with active, independently controllable piezoelectric, double-amplifier elements and is designed to

alter the continuous structural radiation impedance [Johnson, 2000].

As for sensors needed to design ASAC system, most research in early 90's is related to using discrete microphones located in the radiated acoustic field [Fuller, 1992], because they can directly measure the acoustic pressure, which is the performance metric to be reduced in order to control the structurally-radiated noise. However, since the use of microphones in the far field is impractical for most engineering applications, many researchers have tried to develop the way to use structurally-mounted sensors, such as piezoelectric material and accelerometers, for ASAC. Clark *et al.* have demonstrated the use of PVDF film as modal sensors in active structural acoustic control approaches applied to a simply supported plate under single frequency excitation [Clark, 1992C]. Also, they used the optimization method to determine the placement of piezoelectric actuators and PVDF sensors [Clark, 1992D]. Maillard *et al.* used accelerometers mounted on the structure and applied a time domain structural sensing technique to reduce the broadband structure-borne noise [Maillard, 1995]. Bingham *et al.* designed a flat composite panel with embedded piezoelectric actuators and strain gauge sensors to minimize the structurally radiated noise from the panel [Bingham, 1998]. Kim *et al.* designed the optimal placement of PZT actuators and the optimal electrode pattern of PVDF sensors for the control of sound field from vibrating plates in flow [Kim, 1999].

1.1.3 Experimental Work on 3-D Structures

Most of the work on ASAC systems has dealt with planar structures, such as beam or plate structures in an infinite baffle, although a few reports of experimental work on three dimensional structures can be found in the literature. Clark *et al.* achieved narrow-band active structural acoustic control on a long, thin aluminum cylinder with two rigid end-caps using piezoceramic actuators and PVDF sensors [Clark, 1994]. Maillard experimentally demonstrated broadband radiation control from a finite cylinder using piezoelectric actuators and structural acoustic sensing [Maillard, 1997]. Lane *et al.* experimentally implemented a feedback controller using spatial weighting of an array of collocated pressure sensors and constant volume velocity actuators, to attenuate the response of low frequency modes in the three dimensional aircraft fuselage section [Lane, 2000]. Savran *et al.* performed active structural acoustic control experiments on a model fuselage testbed, using collocated piezoelectric sensors and actuators [Savran, 2000].

1.2 Thesis Objectives and Overviews

The primary goal of this thesis is to develop the control architecture and methodology for the reduction of radiated noise from stiff structures by actively isolating the motion of the radiator's outer surface. The proposed approach is to cover the structure's outer surface with curved active composite panels and to reduce the radiated noise by controlling the motion of panel's outer surface. Each panel contains several embedded accelerometers mounted to the panel's outer and inner surface, allowing its use as an almost collocated sensor-actuator pair. The embedded accelerometers can sense both the motion of the panel's base and the panel's outer surface, which provide necessary information for the controller design.

The use of external piezoelectric panels proposed in this thesis has significant advantages for stiff structures over the conventional approach of directly controlling the structure. One of the important advantages is that the former needs much less control authority than the latter,

because controlling panels requires less actuation power than controlling the stiff structure. Furthermore, the approach allows the control system to be significantly less dependent on the dynamics and characteristics of the structure than directly controlling the structure, so that the control systems become robust.

The control architecture proposed in this thesis has two different levels. The first one is a local control, which is implemented for each panel to reduce its vibration level. On the other hand, the second one, which is a global controller, makes the structure a weak radiator by coordinating the large number of sensor-actuator pairs. For each local control, two different feedback controllers are designed and implemented simultaneously. The first feedback controller takes the acceleration of the outer surface of each panel and uses high gain to minimize its motion. The other feedback loop, which is denoted as the "feedforward controller" in this thesis, takes acceleration on the inside surface of the panel and commands equal and opposite panel displacement to cancel the motion of radiating surface. In order to find the local controller configuration that satisfies two conflicting requirements (good performance and easy implementation) simultaneously, several controllers, such as analog, digital, hybrid analog-digital, *etc.*, are designed, implemented and compared.

For global control, a new wavenumber sensing method is proposed and the way to apply the method to feedback controller design for active structural acoustic control is explored. The basic approach is that instead of measuring or determining the acoustic pressure at a particular radiation angle, the total acoustic power radiated from a vibrating structure is minimized in the wavenumber domain. If the required control bandwidth is finite, as all the physical problems, the target wavenumbers in the supersonic domain can be determined. Since the radiated acoustic power can be expressed as integral of the square value of wavenumber components in the supersonic region, weighted by some other factors, the wavenumber components in the supersonic domain are good candidates for the performance measure. Generally, wavenumber components are complex numbers, which makes it difficult to find directly a state-space model for estimating them. However, because it is the magnitude and not the phase of the wavenumber components that contributes to the radiated noise into the far field, it is shown that a state-space model can be found to estimate the magnitude of wavenumber components. Once we have a state-space model that can be used for active structural acoustic control, a modern controller design paradigm can be applied to minimize the acoustic power radiated from vibrating structures. The new approach enables us to systematically find a state-space model for wavenumber components in the supersonic region, and therefore makes it easy to design an optimal LQG controller. Furthermore, it is shown that the new approach can be used to reduce radiated noise from general complex structures. Several examples are used to show the effectiveness of the new wavenumber domain sensing method.

The thesis outline is organized as follows.

Chapter 2 introduces the experimental hardware, including the cylindrical shell, the active composite panels, and the signal conditioners. The geometric and dynamic characteristics of the cylindrical shell, and the features of the active composite panels are presented. The dynamic characteristics of the active composite panel are identified, and the result of testing panels is reported. Also, the modeling process of the testbed structure using the finite element method is explored.

Chapter 3 considers the local controller architecture used for each panel, which consists of two different feedback control approaches. The design methods for those controllers are presented using the numerical simulation and the experimental data. The undesirable dynamics of the active composite panel are investigated, along with their effects on the controller design and achievable closed-loop performance. Then, ways to resolve these difficulties caused by the undesirable panel dynamics are explored.

Chapter 4 is devoted to the development of a new wavenumber sensing method and its application to feedback controller design for active structural acoustic control. The theoretical basis for structural acoustics is presented, and the well-known results from radiation problem are summarized. The formulation for the new wavenumber domain sensing method and its application to the feedback controller design for ASAC is described. For mathematical convenience, the motivation and the formulation for the new wavenumber sensing method will be first explained for a beam structure, and then, the formulation for the cylindrical shell is developed. Finally, the application of the new sensing method for the general three-dimensional structures is discussed.

Chapter 5 demonstrates the wavenumber domain sensing method developed in Chapter 4 on several structural systems. The purpose of this is to numerically validate the method on the numerical model with the same order of complexity, before it is tested on a real testbed. A cantilever beam in an infinite baffle is considered first to help understand how the method is implemented on a structural system, and what the design issues are. Then, the new method is numerically validated on the main testbed in this thesis, which is the cylindrical shell with 55 active composite panels mounted.

Chapter 6 reports the results of several closed-loop experiments obtained with the local controller. The objective of this chapter is to investigate several controller configurations, such as a completely analog controller, an analog controller with digital notch, a hybrid analog/digital controller, *etc.*, and find the one for the local controller architecture that will be eventually implemented on the shell with multiple panels. The final configuration, which will be selected for the local controller architecture, should be simple and easy to implement, while its closed-loop performance is satisfactory. The basic design concepts, the motivation, the design procedure, and the implementation issues are explained for each configuration.

Chapter 7 presents the results of closed-loop experiments obtained with multiple panel-level controllers, which were designed and implemented on the cylindrical shell with 55 active composite panels mounted. The experimental setup for testing the controllers are described, and the results of identification and analysis of plant transfer functions are discussed. Then, the design process for local controllers and the corresponding closed-loop performance are reported. The results of investigating panel dynamics are presented and their effects on the closed-loop performance are explored.

Finally, Chapter 8 summarizes the results of this research. The contributions of this thesis and recommendations for future work are discussed.

Chapter 2

Testbed Description and Modeling

2.1 Introduction and Objective

The objective of this study is to develop a method of reducing the noise radiated from a thick-walled cylindrical shell in water by using an active conformal array. In this chapter, the experimental hardware, including the cylindrical shell, the active composite panels, and the signal conditioners are described. The geometric and dynamic characteristics of the cylindrical shell, and the features of the active composite panels are also discussed. The cylindrical shell with the panels mounted on its surface is used as the testbed structure in this study. Also, the signal conditioners for the panels (pre-amplifiers and power amplifiers) will be described. The dynamic characteristics of the active composite panel will be identified, and the result of testing panels will be reported. Finally, the modeling process of the testbed structure using the finite element method will be explored.

2.2 Experimental Hardware

2.2.1 Cylindrical Shell

A picture of the thick-walled cylindrical shell is shown in Figure 2-1. The shell is made of an aluminum alloy, and measures 20 inches in diameter, 32 inches in length, and 0.3 inches in thickness. It has three circumferential ribs inside the shell to add stiffness. Two circular end-caps, also made of aluminum alloy, measuring 2.25 inches in thickness, close off the end of the cylinder. The disturbance source is simulated by a shaker (Model F3/Z602WA, Wilcoxon Research, Gaithersburg, MD, USA) mounted on the inside of the shell. Figure 2-2 shows a schematic picture of the cylindrical shell showing two end caps, three ribs and the shaker inside of the shell.

In order to investigate the dynamic characteristics of the cylindrical shell, the frequency response and the structural vibration modes of the cylindrical shell were experimentally identified. Figure 2-3 shows the frequency response of the cylindrical shell obtained using the shaker inside the shell as the disturbance source. The structural response was measured with an external accelerometer (Model #352B22, PCB Piezotronics, Depew, NY) mounted on the outer surface of the shell. We see that the shell is quite stiff—the first structural resonant frequency is above 500 Hz.

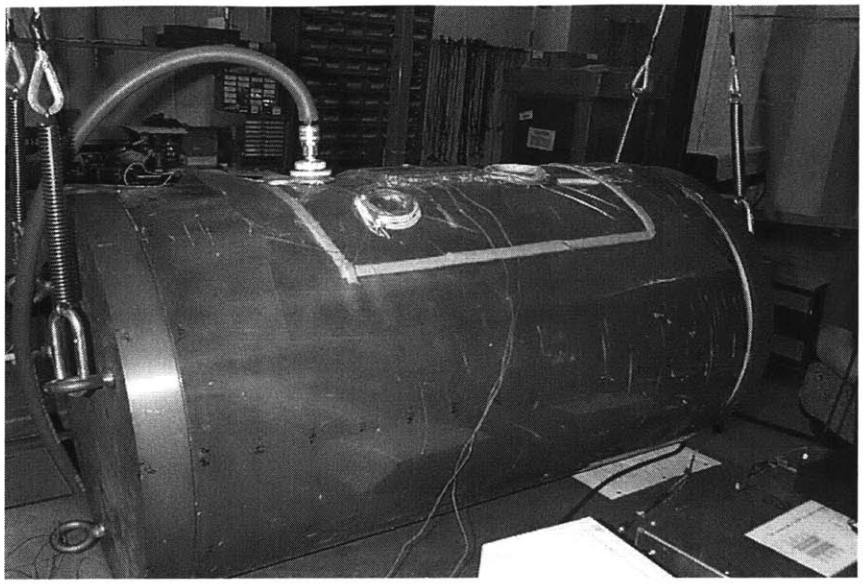

Figure 2-1: The thick-walled cylindrical shell.

Identification of the structural vibration modes of the cylindrical shell was performed with a scanning laser vibrometer. A scanning laser vibrometer measures the out-of-plane displacements at discrete points on a structure using a laser. Figure 2-4 shows the mode shape of the cylindrical shell at some resonant frequencies.

2.2.2 Active Composite Panel

The proposed approach to reduce the radiated noise from the shell employs 1-3 active composite panels manufactured by MSI (Material Systems Inc., Littleton, MA, USA) mounted on the shell's surface as a conformal array. The picture of the active composite panel is shown in Figure 2-5. The panel was designed to have the same radius of curvature as the cylindrical shell, so that it can be mounted on the surface of the shell without bending. The panel measures 6 inches on each side, so that 55 panels are needed to cover the outer surface of the cylindrical shell (5 in the axial direction, and 11 in the circumferential direction).

The active composite panels contain Lead Zirconate Titanate (PZT) rods embedded in a stiff polymer matrix, and eight injection-molded piezoceramic accelerometers attached to outer and inner circuit boards. The displacement of the panel in its thickness direction is proportional to the voltage applied to the panel actuator layer. Two groups of four accelerometers are wired in parallel, resulting in measurements of the average acceleration of each surface. This configuration results in an almost collocated sensor-actuator pair. Collocation is desirable, since it leads to well-behaved plant transfer functions that are more easily compensated than non-collocated transfer functions. Figure 2-6 shows a schematic drawing of the active composite panel, showing the embedded PZT rods and the accelerometers.

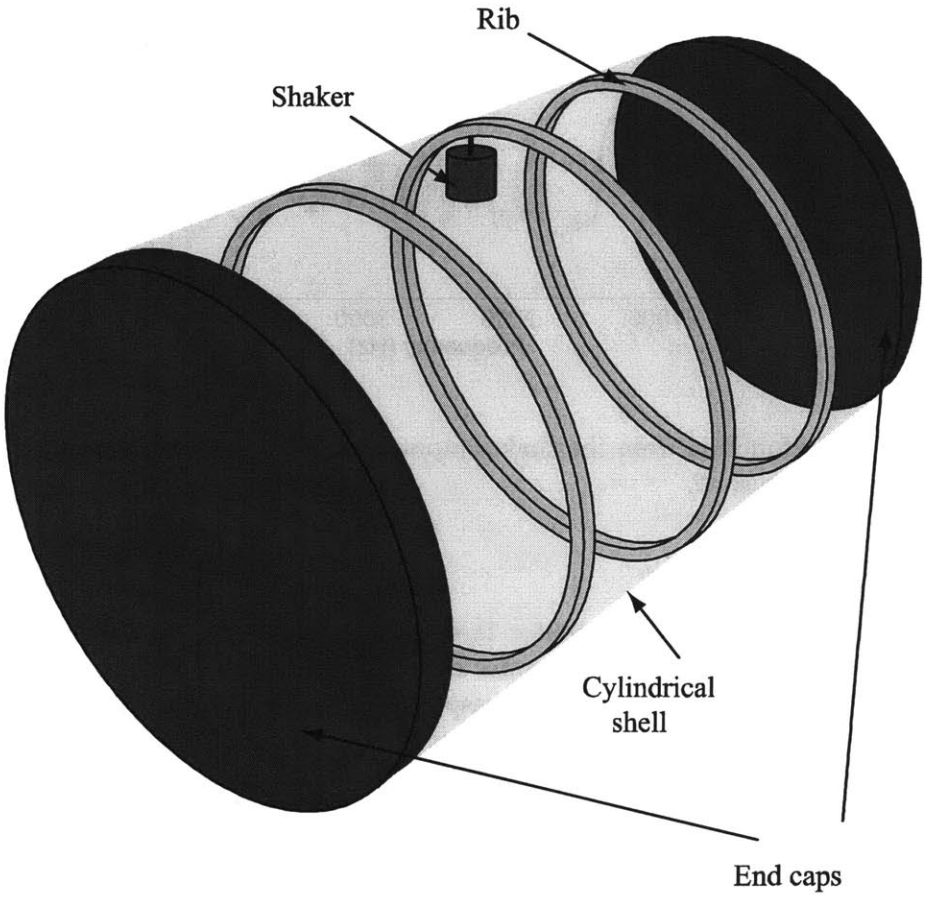

Figure 2-2: Schematic of the cylindrical shell showing two end caps, three ribs, and the shaker.

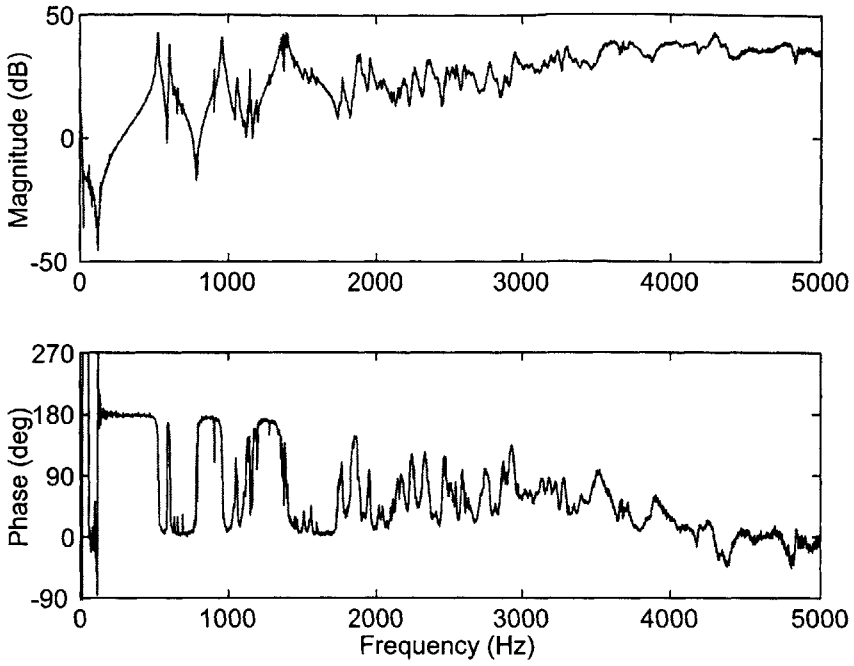

Figure 2-3: Transfer function from the shaker input to the external accelerometer mounted on the outer surface of the shell.

2.2.3 Signal Conditioners

The accelerometers and the PZT actuator layer, which are embedded in the active composite panel, need signal conditioners for proper operation. These are denoted as accelerometer pre-amplifiers and panel power amplifiers, respectively, in this study. The signal from each embedded accelerometers is conditioned and filtered by a pre-amplifier before it enters the controller, while each control signal generated at the controller is amplified further by a power amplifier so that high voltage input can be applied to the panel actuator layer. The transfer functions of both types of amplifiers are selected such that they make controller design and implementation easier. Figure 2-7 and 2-8 show the frequency responses of the pre-amplifier and the power amplifier, respectively. The pre-amplifier was chosen to be a pure gain amplifier with a gain of 34 dB, while the power amplifier was chosen to be an inverting low-pass filter with corner frequency at 188 Hz, and a DC gain of 34 dB. The gains were designed so that the saturation doesn't occur at either amplifiers, and so that the input and output voltage of the digital controller maintains a reasonable value, to minimize the quantization effect.

2.2.4 Identifying the Dynamics of the Active Composite Panel

The active composite panel plays a critical role in the control algorithms proposed in this study. Therefore, its dynamic characteristics should be identified thoroughly. In order to do so, the frequency response of the plant transfer function was measured from the voltage input of the

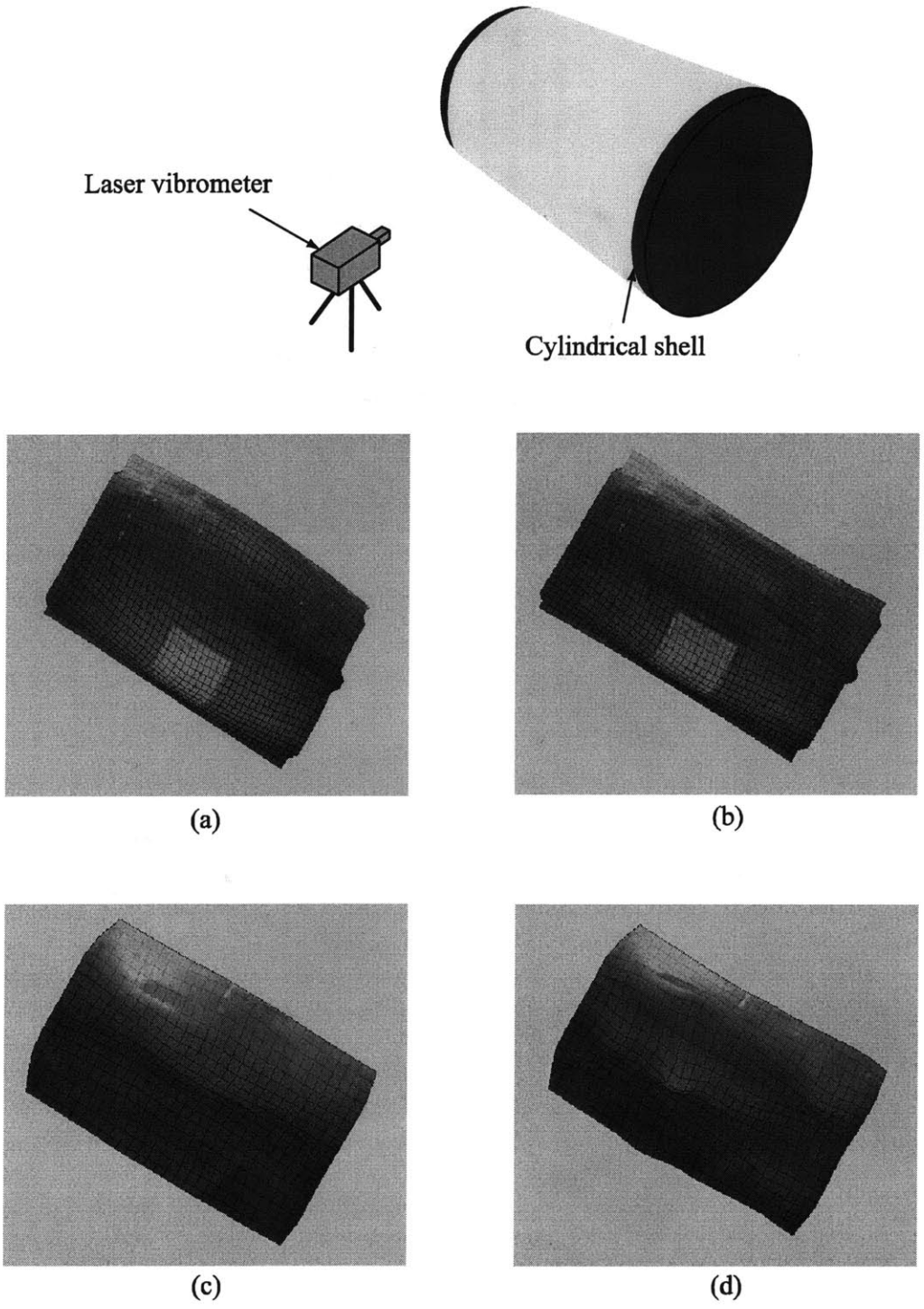

Figure 2-4: Structural mode shapes of the cylindrical shell. (a) 527 Hz, (b) 958 Hz, (c) 1368 Hz, and (d) 1960 Hz.

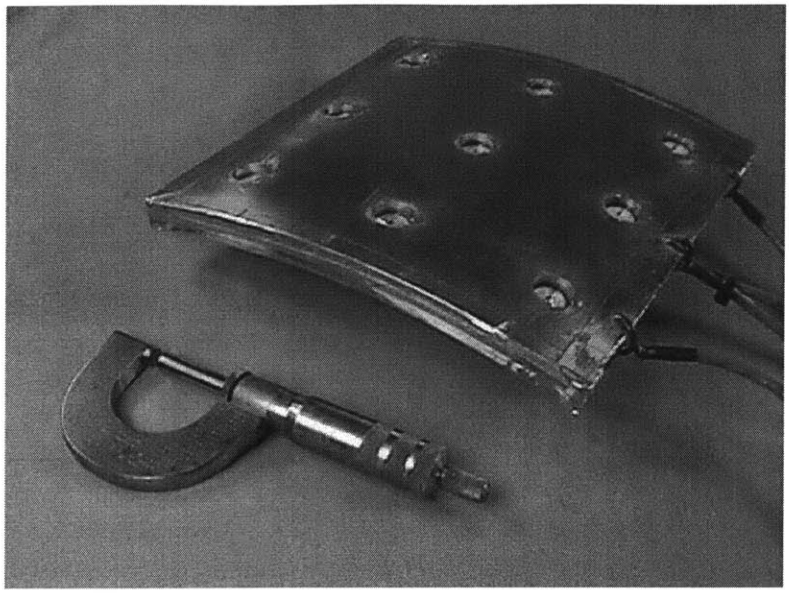

Figure 2-5: The active composite panel. (Photo courtesy of MSI)

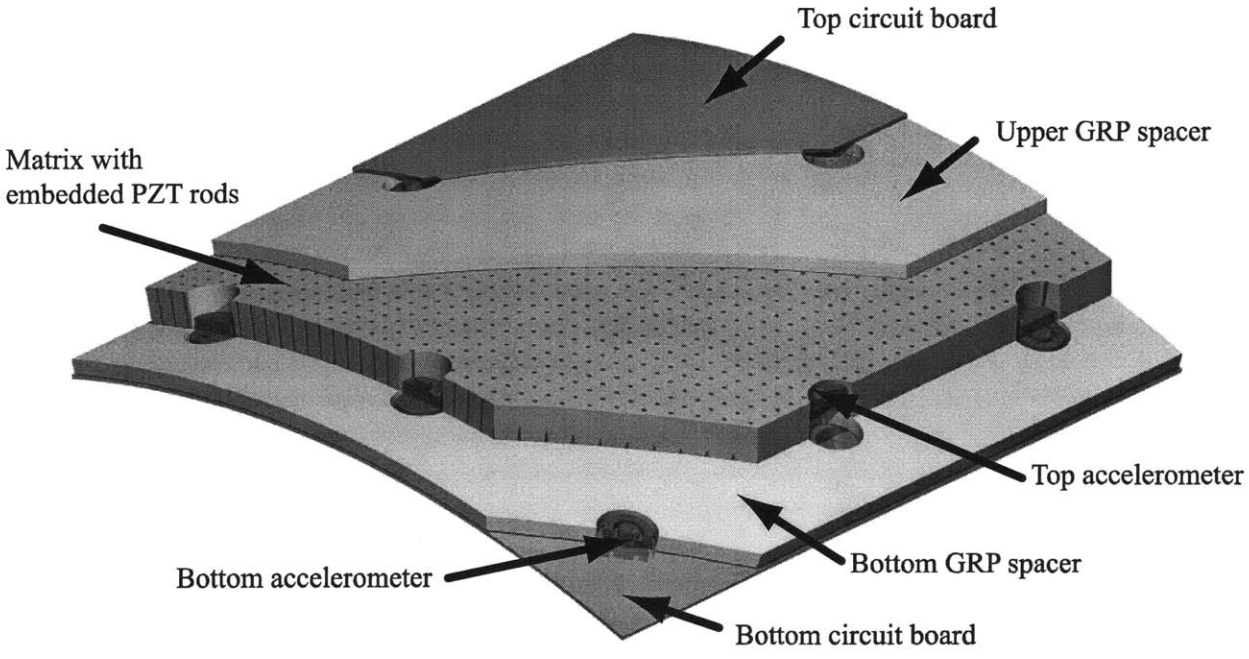

Figure 2-6: Schematic drawing of the active composite panel.

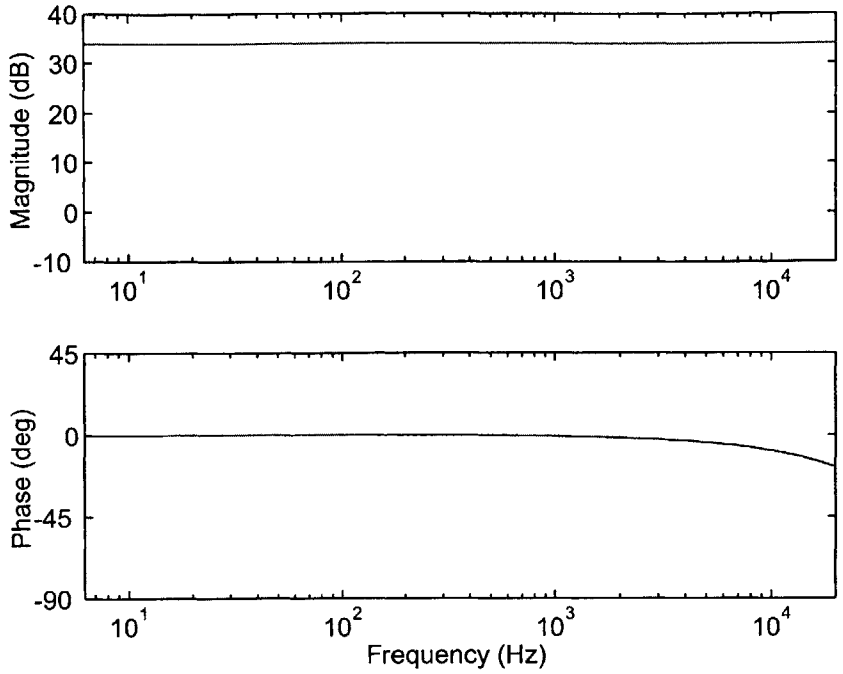

Figure 2-7: Frequency response of the pre-amplifier.

power amplifier to the output signal from the pre-amplifier, after the panel was mounted on the surface of the cylindrical shell. The power amplifier was connected to the panel actuator layer, while the pre-amplifier was connected to the accelerometer mounted on the outer surface of the panel. The result is shown in Figure 2-9. Also, the frequency response of the transfer function $\frac{ks^2}{s+188\times 2\pi}$ is shown in Figure 2-9, where k is a constant gain. The measured plant transfer function should look like the transfer function $\frac{ks^2}{s+188\times 2\pi}$, neglecting the shell modes, because

- The displacement of the panel is proportional to the voltage applied to the panel actuator layer,
- The mass of the panel is much less than that of the shell, and
- The power amplifier has a low-pass filter with corner frequency at 188 Hz.

However, Figure 2-9 shows that the two transfer functions have some differences. At low frequencies, the measured transfer function approaches a non-zero constant, rather than s^2, due to direct electrical or electromechanical feedthrough of the panel input voltage to the accelerometer. Also, at high frequencies, the resonant peak due to panel dynamics is observed. As will be shown in later chapters, these two undesirable panel dynamics make the controller design and implementation much harder. A way to compensate for those undesirable dynamics will be discussed in Chapter 3 and 6.

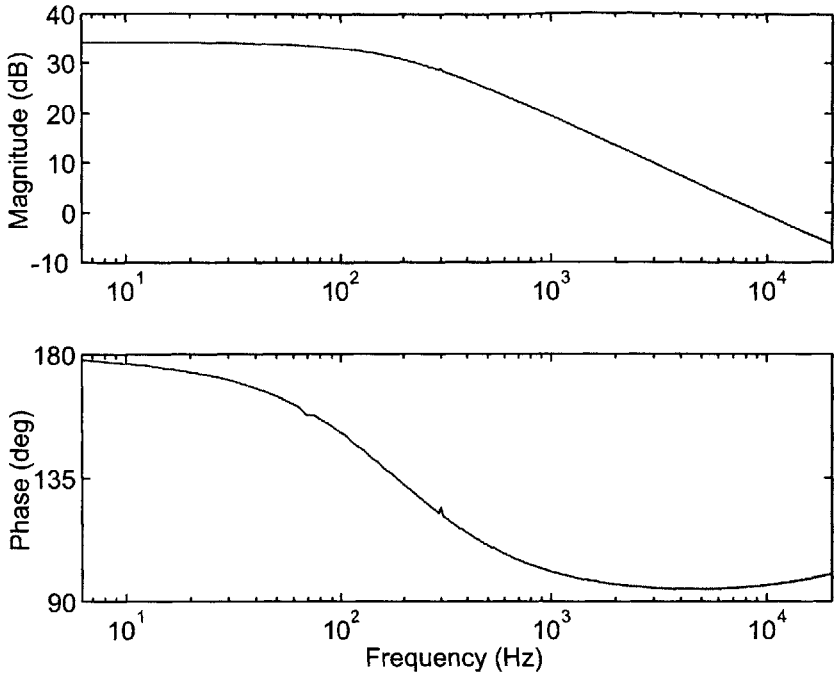

Figure 2-8: Frequency response of the power amplifier.

2.2.5 Evaluating the 55 Active Composite Panels

As mentioned earlier, 55 active composite panels were mounted on the surface of the cylindrical shell. Each panel was tested before it was rigidly mounted on the shell. In order to do that, each panel was mounted temporarily on the surface of the shell, and the frequency response of its transfer function was measured. Then, the undesirable panel dynamics (low-frequency feedthrough and high-frequency panel dynamics) were recorded for each panel. The low-frequency feedthrough was measured as a DC gain of the measured transfer function. Since the transfer function should approach s^2 at low frequencies in the ideal case, lower values of the low-frequency feedthrough are better. On the other hand, the high-frequency panel dynamics was characterized by the dominant panel resonant frequencies. Since the resonances limit the controller bandwidth, higher resonant frequencies are better. As mentioned in the previous section, these undesirable dynamics of the panel make the controller design significantly more difficult. Ideally, it would be best if all the 55 panels had the *same* degree of undesirable dynamic characteristics, so that the amount of the additional work needed to compensate for the undesirable dynamics would be minimized. The result of the test given in Table 2.1, however, is contradictory to the expectation. As can be seen from the table, each panel has different low-frequency feedthrough and dominant panel resonant frequency. The low-frequency feedthrough varies from -65.0 dB (panel 47) to -38.0 dB (panel 14), while the dominant panel resonant frequency varies from 7.2 kHz (panel 17, 18) to 15.6 kHz (panel 39, 48). Furthermore, some panels have more than 2 resonant frequencies. This result makes the controller design

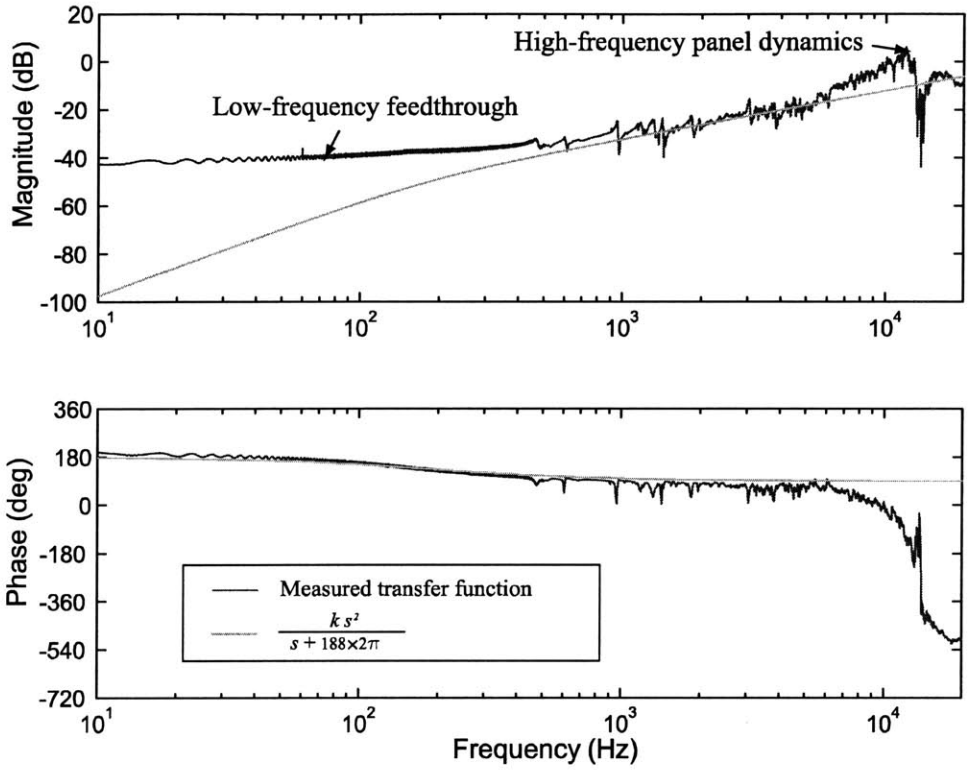

Figure 2-9: Frequency response of the plant transfer function showing the low-frequency feedthrough and the high-frequency panel dynamics.

and implementation much more involved than expected, because the controller variables must be tuned differently for each panel. The variation in panel dynamics requires the use of a digital control system, so that the controller variables can be adjusted in software, rather than in hardware.

The result of testing the panels can be used to determine where each panel should be located when they are rigidly mounted on the surface of the shell. Since the two end-caps are stiffer than the shell, the vibration level of the shell near the end-caps will be lower than the center of the shell. Therefore, better panels should be mounted on the center of the shell away from the end-caps, where most radiation occurs, while worse panels should be mounted near two end-caps, so that their effect on the closed-loop performance can be minimized.

2.3 Testbed Modeling

In this section, a process used to model the testbed is presented. The goal of the modeling is not to correlate the simulation result with the experimental result *exactly,* nor to generate the plant model needed for the synthesis of the model-based controller. Indeed, it is not feasible to model the testbed that accurately. Instead, the objective of the modeling performed in this study is to generate the mathematical model that captures the important dynamics of the real testbed, with the same order of the complexity, so that the proposed control algorithms can be validated on the model before they are experimentally implemented. The model developed in this chapter will be used to test the multi-input multi-output (MIMO) wavenumber LQG controller (Chapter 5), and the local controller architecture (Chapter 6). When the MIMO wavenumber LQG controller is numerically validated in Chapter 5, the plant model needed for the controller synthesis will be obtained using the system identification of the simulated frequency responses of the plant model developed in this chapter, not using the model directly. This approach is more realistic, because the same method of getting the plant model is applied to the LQG controller design for the real testbed.

This section is organized as follows: In Section 2.3.1, the formulation for the structural response of a finite cylindrical shell is described. The finite element method is applied for the finite cylindrical shell in Section 2.3.2. In Section 2.3.3, the modeling process for the active composite panel is described, and the coupled dynamics of the cylindrical shell and the active composite panel is derived in Section 2.3.4.

2.3.1 Structural Response of a Finite Cylindrical Shell

Basic assumptions and the geometry

A finite cylindrical shell is a sheet of elastic material which conforms to a curved surface, the mid-surface of the shell, which is closed like a hollow cylinder. The assumptions employed in the analysis of the cylindrical shell in this section are described below [Blevins, 1979].

1. The thickness of the shell is small compared to other dimensions.

2. The shell is composed of a linear, elastic, homogeneous isotropic material.

3. The deformations of the shell are small in comparison with the radius of the shell.

Table 2.1: Summary of panel characterization.

Panel No.	Low-frequency feedthrough (dB)	Dominant dynamics (kHz)	Panel No.	Low-frequency feedthrough (dB)	Dominant dynamics (kHz)
1	-51.0	12.0	29	-39.1	14.5
2	-62.0	12.0	30	-45.5	13.7
3	-43.1	12.0	31	-52.0	7.3
4	-42.7	10.2, 12.9	32	-47.4	12.6
5	-60.6	14.1	33	-45.0	11.5, 13.8
6	-55.2	14.2	34	-42.4	13.7
7	-56.9	9.1	35	-41.6	15.0
8	-52.2	12.1, 14.7	36	-39.1	11.2, 14.8
9	-46.1	15.1	37	-49.3	7.7, 14.8
10	-41.8	11.2, 14.1	38	-44.7	8.8
11	-46.0	10.8, 14.1	39	-43.2	7.7, 15.6
12	-48.8	15.0	40	-40.9	8.7, 11.9
13	-45.6	11.1, 14.2	41	-41.6	11.8, 15.0
14	-38.0	11.3, 14.1	42	-43.4	11.7, 14.2
15	-45.7	11.2, 14.1	43	-46.3	11.2, 14.8
16	-46.5	8.0, 13.9	44	-56.2	14.1
17	-43.8	7.2, 10.3, 14.5	45	-47.0	14.0
18	-49.8	7.2, 11.8	46	-41.1	15.0
19	-43.0	11.8	47	-65.0	14.7
20	-40.4	14.2	48	-44.0	7.9, 15.6
21	-43.2	15.1	49	-47.3	14.7
22	-43.6	14.4	50	-47.1	12.9
23	-48.0	10.4	51	-44.5	14.5
24	-43.0	11.7	52	-44.0	13.0
25	-46.7	11.8, 14.1	53	-40.4	15.0
26	-47.2	11.8, 15.1	54	-38.1	11.5, 15.1
27	-46.2	11.1, 13.6	55	-42.0	14.5
28	-38.8	14.8			

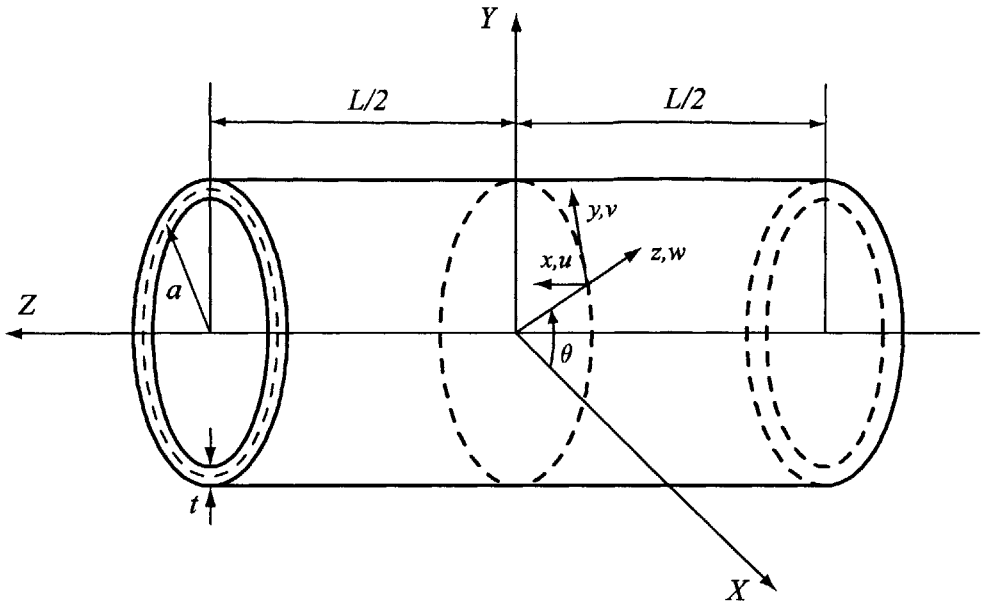

Figure 2-10: Geometry of a finite cylindrical shell.

4. Straight lines perpendicular to the mid-surface of the shell remain straight and perpendicular to the mid-surface during deformation.

5. Rotary inertia and shear deformation are neglected.

6. The transverse normal stress and the out-of-plane shear stresses are negligible.

Figure 2-10 shows the geometry of the finite cylindrical shell of length L, radius a and thickness t. The radius is measured from the center to the mid-surface of the shell. Figure 2-10 also shows the local coordinate system, (x, y, z), the global rectangular coordinate system, (X, Y, Z), and the global cylindrical coordinate system, (Z, θ). The local coordinates (x, y, z) represent the axial, circumferential, and radial directions, respectively. The displacement field is defined as (u, v, w), where u, v, and w denote the translation displacement along the axial, circumferential, and radial directions, respectively. Note that the local coordinates (x, y, z) and the global coordinates (X, Y, Z) are in different directions. The notation for the local coordinates, (x, y, z), has been conventionally adopted in the shell theory [Timoshenko, 1959], [Ashwell, 1972], and therefore it is used in this thesis.

Strain-displacement relationships

In this section, the strain-displacement relationships of the finite cylindrical shell are presented using the notation and derivation of Timoshenko [Timoshenko, 1959]. Assume an arbitrary point (x, y, z) on the cylindrical shell before deformation is displaced into the new point $(x + u, y + v, z + w)$ after the deformation. Using assumptions 4 and 5 defined in Section 2.3.1,

the displacement field (u, v, w) can be written as

$$\begin{aligned} u(x,y,z) &= u_0(x,y) + z\phi_x(x,y) \\ v(x,y,z) &= v_0(x,y) + z\phi_y(x,y) \\ w(x,y,z) &= w_0(x,y) \ , \end{aligned} \tag{2.1}$$

where (u, v, w) is the displacement field at (x, y, z), in the directions as defined in Section 2.3.1, and (u_0, v_0, w_0) is the displacement at the mid-surface in the axial, circumferential, and radial directions, respectively. ϕ_x and ϕ_y are rotations at the mid-surface about x and y, given by

$$\begin{aligned} \phi_x &= -\frac{\partial w_0}{\partial x} \\ \phi_y &= \frac{v_0}{a} - \frac{\partial w_0}{\partial y} \ . \end{aligned} \tag{2.2}$$

Combining Equation 2.1 and 2.2, the displacement field (u, v, w) at (x, y, z) can be expressed in terms of the mid-surface displacement field (u_0, v_0, w_0) as

$$\begin{aligned} u(x,y,z) &= u_0(x,y) - z\frac{\partial w_0(x,y)}{\partial x} \\ v(x,y,z) &= \left(1 + \frac{z}{a}\right) v_0(x,y) - z\frac{\partial w_0(x,y)}{\partial y} \\ w(x,y,z) &= w_0(x,y) \ . \end{aligned} \tag{2.3}$$

The strain field of the finite cylindrical shell can be expressed using assumptions 4 and 5, given as

$$\begin{aligned} \varepsilon_x &= \frac{\partial u}{\partial x} \\ \varepsilon_y &= \frac{\partial v}{\partial y} + \frac{w}{a} \\ \gamma_{xy} &= \frac{\partial u}{\partial y} + \frac{\partial v}{\partial x} \\ \varepsilon_z &= \gamma_{xz} = \gamma_{yz} = 0 \ , \end{aligned} \tag{2.4}$$

where ε and γ represent normal and shear strain, respectively. Also, the changes of curvature can be written as

$$\begin{aligned} \chi_x &= -\frac{\partial^2 w}{\partial x^2} \\ \chi_y &= \frac{1}{a}\frac{\partial v}{\partial y} - \frac{\partial^2 w}{\partial y^2} \\ \chi_{xy} &= \frac{1}{a}\frac{\partial v}{\partial x} - \frac{\partial^2 w}{\partial x \partial y} \ , \end{aligned} \tag{2.5}$$

in which χ_x and χ_y are changes of curvature, and χ_{xy} is the twist of the mid-surface.

Stress-strain relationships

Assumption 6 in Section 2.3.1 leads to

$$\sigma_z = \sigma_{xz} = \sigma_{yz} = 0 . \tag{2.6}$$

Using assumption 2 in Section 2.3.1, the non-zero stresses in the finite cylindrical shell are given by the isotropic stress-strain relationships

$$\begin{aligned} \sigma_x &= \frac{E}{1-\nu^2}(\varepsilon_x + \nu\varepsilon_y) \\ \sigma_y &= \frac{E}{1-\nu^2}(\varepsilon_y + \nu\varepsilon_x) \\ \sigma_{xy} &= \frac{E}{2(1+\nu)}\gamma_{xy} , \end{aligned} \tag{2.7}$$

where E is the modulus of elasticity, and ν is Poisson's ratio. σ_x, σ_y, and σ_z are normal stresses acting on the x, y, and z faces of the shell element, respectively, while σ_{yz}, σ_{xz}, and σ_{xy} are shear stresses acting on the x, y, and z faces of the shell element, respectively. Equation 2.7 can be also written in a matrix form as

$$\boldsymbol{\sigma} = \mathbf{C}\,\varepsilon , \tag{2.8}$$

where

$$\boldsymbol{\sigma} = \begin{bmatrix} \sigma_x \\ \sigma_y \\ \sigma_{xy} \end{bmatrix}, \varepsilon = \begin{bmatrix} \varepsilon_x \\ \varepsilon_y \\ \gamma_{xy} \end{bmatrix} ,$$

$$\mathbf{C} = \begin{bmatrix} \frac{E}{1-\nu^2} & \frac{\nu E}{1-\nu^2} & 0 \\ \frac{\nu E}{1-\nu^2} & \frac{E}{1-\nu^2} & 0 \\ 0 & 0 & \frac{E}{2(1+\nu)} \end{bmatrix} . \tag{2.9}$$

2.3.2 Finite Element Formulation

In this section, the finite element formulation for the finite cylindrical shell is presented. It begins with the equilibrium equation, given by

$$\nabla \cdot \boldsymbol{\sigma} + \mathbf{f} = \rho_s \frac{\partial^2 \mathbf{u}}{\partial t^2} , \tag{2.10}$$

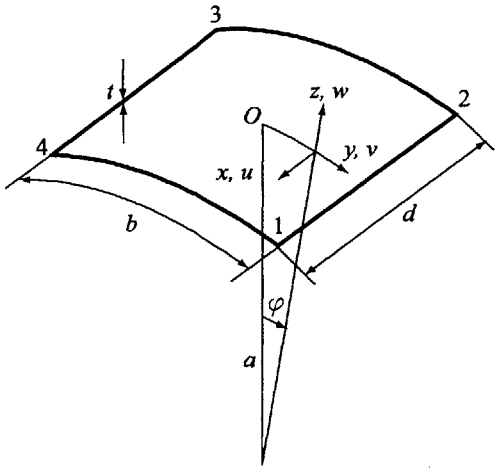

Figure 2-11: An element of the cylindrical shell.

where ρ_s is the density of the shell material, $\boldsymbol{\sigma}$ is the stress field, $\mathbf{f}$ is applied force, and $\mathbf{u}$ is the displacement field, defined as

$$\mathbf{u} = \begin{bmatrix} u \\ v \\ w \end{bmatrix} = \begin{bmatrix} u_0 + z\phi_x \\ v_0 + z\phi_y \\ w_0 \end{bmatrix} . \tag{2.11}$$

Applying the principle of virtual displacements and the divergence theorem to Equation 2.10, we obtain [Bathe, 1996]

$$\int_V \rho_s \, (\delta \mathbf{u})^T \frac{\partial^2 \mathbf{u}}{\partial t^2} \, dV \; + \; \int_V (\delta \varepsilon)^T \, \boldsymbol{\sigma} \, dV \; = \; \int_V (\delta \mathbf{u})^{\,T} \mathbf{f}_B dV \; + \; \int_S (\delta \mathbf{u})^T \, \mathbf{f}_S \, dS \, , \tag{2.12}$$

where ε is the strain field, $\mathbf{f}_B$ is body force (force per volume), $\mathbf{f}_S$ is surface force (force per area). V and S represent the volume and the surface of the cylindrical shell, respectively. Equation 2.8 can be used to eliminate $\boldsymbol{\sigma}$ from Equation 2.12, so that

$$\int_V \rho_s \, (\delta \mathbf{u})^T \frac{\partial^2 \mathbf{u}}{\partial t^2} \, dV \; + \; \int_V (\delta \varepsilon)^T \, \mathbf{C} \, \varepsilon \, dV \; = \; \int_V (\delta \mathbf{u})^{\,T} \mathbf{f}_B dV \; + \; \int_S (\delta \mathbf{u})^T \, \mathbf{f}_S \, dS \, . \tag{2.13}$$

Equation 2.13 is discretized spatially using a cylindrical shell element developed by Ashwell and Sabir [Ashwell, 1972]. The element is a four-node rectangular element having five degrees of freedom per node (three linear displacements and two rotations). Since it uses only external geometrical nodal displacements, it can be readily assembled with other structural members, and avoids the difficulties associated with internal degrees of freedom and internal nodes [Ashwell, 1972]. Figure 2-11 shows the geometry of the cylindrical shell element of a radius of curvature a, and lengths d and b in the axial and circumferential directions, respectively. Since the element has four nodes and each node has five degrees of freedom, $(u, v, w, \phi_x, \phi_y)$, the

shape function of the element contains 20 constants $c_1, c_2, ..., c_{20}$ to be determined. Using these constants, the displacement (u_0, v_0, w_0) at the mid-surface can be written as [Ashwell, 1972]

$$\begin{aligned} u_0 &= ac_2\cos\varphi + ac_4\sin\varphi + c_5 + c_7 x + \left(ac_{11} + a^3c_{19} - a^2c_{20}\right)\varphi \\ &\quad -\frac{1}{2}a^3c_{17}\varphi^2 + c_8 x\varphi - \frac{1}{6}a^3c_{19}\varphi^3 \\ v_0 &= (c_1 + c_2 x)\sin\varphi - (c_3 + c_4 x)\cos\varphi + c_6 + \left(-a^2c_{19} + ac_{20}\right)x \\ &\quad + a^2c_{16}\varphi + a^2c_{17}x\varphi + \frac{1}{2}a^2c_{18}\varphi^2 + \frac{1}{2}a^2c_{19}x\varphi^2 \\ w_0 &= -(c_1 + c_2 x)\cos\varphi - (c_3 + c_4 x)\sin\varphi + \left(ac_9 - a^2c_{16}\right) + \left(ac_{10} - a^2c_{17}\right)x \\ &\quad - a^2c_{18}\varphi - a^2c_{19}x\varphi - \frac{1}{2}c_{12}x^2 - \frac{1}{6}c_{13}x^3 - \frac{1}{2}c_{14}x^2\varphi - \frac{1}{6}c_{15}x^3\varphi\,. \end{aligned} \tag{2.14}$$

Therefore, the displacement field at the mid-surface, $\mathbf{u_0} = [u_0\ v_0\ w_0]^T$, can be expressed in terms of the constants $c_1, c_2, ..., c_{20}$, as

$$\mathbf{u_0} = \mathbf{N}_c\mathbf{c} = \begin{bmatrix} \mathbf{N}_u \\ \mathbf{N}_v \\ \mathbf{N}_w \end{bmatrix}\mathbf{c}\,, \tag{2.15}$$

where $\mathbf{c} = [c_1\ c_2\ ...\ c_{20}]^T$, and $\mathbf{N}_u$, $\mathbf{N}_v$ and $\mathbf{N}_w$ are 1×20 row vectors that represent the relationships between $\mathbf{c}$ and u_0, v_0, and w_0, respectively. Note that $\mathbf{N}_u$, $\mathbf{N}_v$ and $\mathbf{N}_w$ are functions of x and φ. This displacement field includes all rigid body displacements exactly, and satisfies the constant strain condition insofar as that condition applies to cylindrical shells [Ashwell, 1972]. The expressions for $\mathbf{N}_u$, $\mathbf{N}_v$ and $\mathbf{N}_w$ are given in Appendix A.

The next step is to express $\mathbf{c}$ in terms of the nodal displacements. Let $\left(u_k, v_k, w_k, \phi_{x,k}, \phi_{y,k}\right)$ $(k = 1, 2, 3, 4)$ be the nodal displacements at the kth node in the element. Using the definition of ϕ_x and ϕ_y in Equation 2.2, and the coordinate at the kth nodal point defined in Figure 2-11, the nodal displacement $\widehat{\mathbf{U}} = \left[u_1\, v_1\, w_1\, \phi_{x,1}\, \phi_{y,1} \cdots u_4\, v_4\, w_4\, \phi_{x,4}\, \phi_{y,4}\right]^T$ can be written in terms of $\mathbf{c}$ and the matrix of transformation from $\mathbf{c}$ to $\widehat{\mathbf{U}}$, denoted as $\mathbf{T}_{\widehat{u}c}$, as

$$\widehat{\mathbf{U}} = \mathbf{T}_{\widehat{u}c}\,\mathbf{c}\,. \tag{2.16}$$

Then, the displacement field at the mid-surface, $\mathbf{u_0}$, can be represented in terms of the nodal displacements $\widehat{\mathbf{U}}$, and the transformation matrix $\mathbf{T}_{\widehat{u}c}$, as

$$\mathbf{u_0} = \mathbf{N}_c\mathbf{c} = \mathbf{N}_c\mathbf{T}_{\widehat{u}c}^{-1}\widehat{\mathbf{U}}\,. \tag{2.17}$$

Then, using Equation 2.3 and 2.4, the displacement and strain field at (x, y, z) can be written in terms of the nodal displacements $\widehat{\mathbf{U}}$ as

$$\begin{aligned} \mathbf{u} &= \mathbf{H}\widehat{\mathbf{U}} \\ \boldsymbol{\varepsilon} &= \mathbf{B}\widehat{\mathbf{U}}\,, \end{aligned} \tag{2.18}$$

where $\mathbf{H}$ and $\mathbf{B}$ are the displacement interpolation matrix, and the strain-displacement matrix [Bathe, 1996], respectively. The procedure to derive $\mathbf{T}_{\widehat{u}c}$, $\mathbf{H}$, and $\mathbf{B}$ are explained in detail in

Appendix A.

Now, substituting Equation 2.18 into Equation 2.13, and assembling all the elements, we obtain

$$\sum_{m=1}^{N_e} \int_{V_m} \rho \mathbf{H}_m^T \mathbf{H}_m \, dV_m \, \ddot{\mathbf{U}}_s + \sum_{m=1}^{N_e} \int_{V_m} \mathbf{B}_m^T \mathbf{C} \mathbf{B}_m \, dV_m \, \mathbf{U}_s \tag{2.19}$$
$$= \sum_{m=1}^{N_e} \int_{V_m} \mathbf{H}_m^T \mathbf{f}_B dV_m + \sum_{m=1}^{N_e} \int_{S_m} \mathbf{H}_m^T \mathbf{f}_S \, dS_m \, ,$$

where N_e is the number of elements used in the finite element analysis, the subscript m represents mth element, $\mathbf{U}_s$ is the nodal displacements of the shell in the global coordinate, and $\mathbf{H}_m$ and $\mathbf{B}_m$ are the displacement interpolation matrix, and the strain-displacement matrix evaluated at the mth element, respectively. Equation 2.19 can be expressed in a matrix form as

$$\mathbf{M}_s \ddot{\mathbf{U}}_s + \mathbf{K}_s \mathbf{U}_s = \mathbf{F}_B + \mathbf{F}_S \, , \tag{2.20}$$

where $\mathbf{M}_s$ and $\mathbf{K}_s$ are the global mass and stiffness matrix for the cylindrical shell, given by

$$\mathbf{M}_s = \sum_{m=1}^{N_e} \int_{V_m} \rho \mathbf{H}_m^T \mathbf{H}_m \, dV_m \tag{2.21}$$
$$\mathbf{K}_s = \sum_{m=1}^{N_e} \int_{V_m} \mathbf{B}_m^T \mathbf{C} \mathbf{B}_m \, dV_m \, ,$$

and $\mathbf{F}_B$ and $\mathbf{F}_S$ are the body and surface force vectors, given as

$$\mathbf{F}_B = \sum_{m=1}^{N_e} \int_{V_m} \mathbf{H}_m^T \mathbf{f}_B dV_m \tag{2.22}$$
$$\mathbf{F}_S = \sum_{m=1}^{N_e} \int_{S_m} \mathbf{H}_m^T \mathbf{f}_S \, dS_m \, .$$

Figure 2-12 shows the finite element mesh of the cylindrical shell used in this study. Considering the fact that 55 panels will be mounted on the shell (5 in the axial direction and 11 in the circumferential direction), 10 and 22 elements were chosen in the axial and circumferential directions, respectively. Therefore, the finite element model of the shell has 220 elements, and 1100 degrees of freedom. Figure 2-12 also shows the locations of the panels to be mounted, marked as "•".

The two end-caps were not considered in the finite element model of the cylindrical shell developed here. Strictly speaking, the two end-caps are circular plate structures, and therefore, plate elements should be used if they are to be modeled. However, since the two end-caps are much stiffer than the cylindrical shell, the radial displacements at the two end-caps are much smaller than others, and can be neglected. Therefore, the effect of the two end-caps can be properly modeled using the simply-supported or clamped boundary conditions at the

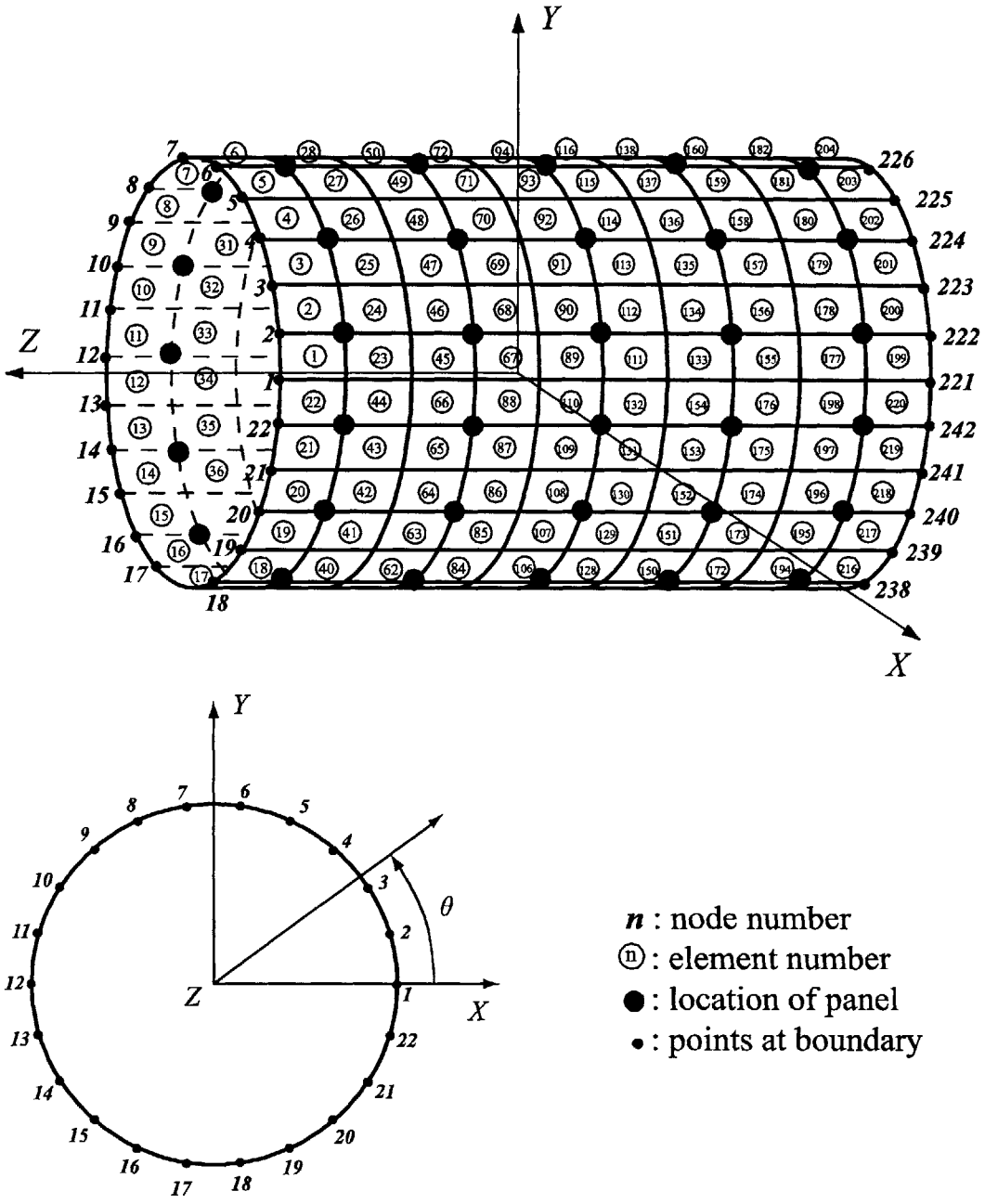

Figure 2-12: Finite elements used for the analysis of the finite cylindrical shell in this study. 10 elements in the axial direction and 22 elements in the circumferential direction are used.

Table 2.2: Boundary conditions applied to the cylindrical shell.

Node no.	Boundary condition	Node no.	Boundary condition
1	Clamped	221	Clamped
2	Clamped	222	Clamped
3	Clamped	223	Clamped
4	Clamped	224	Clamped
5	Simply-supported	225	Clamped
6	Simply-supported	226	Clamped
7	Simply-supported	227	Clamped
8	Simply-supported	228	Clamped
9	Simply-supported	229	Clamped
10	Simply-supported	230	Simply-supported
11	Simply-supported	231	Simply-supported
12	Simply-supported	232	Simply-supported
13	Simply-supported	233	Simply-supported
14	Simply-supported	234	Simply-supported
15	Simply-supported	235	Clamped
16	Simply-supported	236	Clamped
17	Simply-supported	237	Clamped
18	Simply-supported	238	Clamped
19	Simply-supported	239	Clamped
20	Simply-supported	240	Clamped
21	Simply-supported	241	Clamped
22	Simply-supported	242	Clamped

boundaries of the shell, given by

$$\begin{aligned} \text{Simply-supported:} \quad & u = v = w = 0 \\ \text{Clamped:} \quad & u = v = w = \phi_x = 0 \,. \end{aligned} \tag{2.23}$$

Table 2.2 shows the boundary conditions applied to the cylindrical shell. The node numbers at the boundary of the shell are given in Figure 2-12. The reason for the irregular application of the boundary conditions, instead of applying the same boundary condition at each boundary of the shell, is to make the model more realistic. That is, if the same boundary conditions were applied at each boundary, the modeled shell structure would be exactly symmetric with respect to the axial direction, which would make the model over-simplified. In that case, the wavenumber sensing method developed in Chapter 4 would be equivalent to the implementation of *modal sensor* [Lee, 1990], which would be unrealistic. In order to avoid this ideal over-simplified case and generate the realistic model, two boundary conditions (simply-supported and clamped) were irregularly applied.

The frequency response of the cylindrical shell modeled using the finite elements in Figure 2-12, with the boundary condition in Table 2.2, is shown in Figure 2-13. It is the counterpart of the frequency response of the real cylindrical shell obtained experimentally in Figure 2-3. The

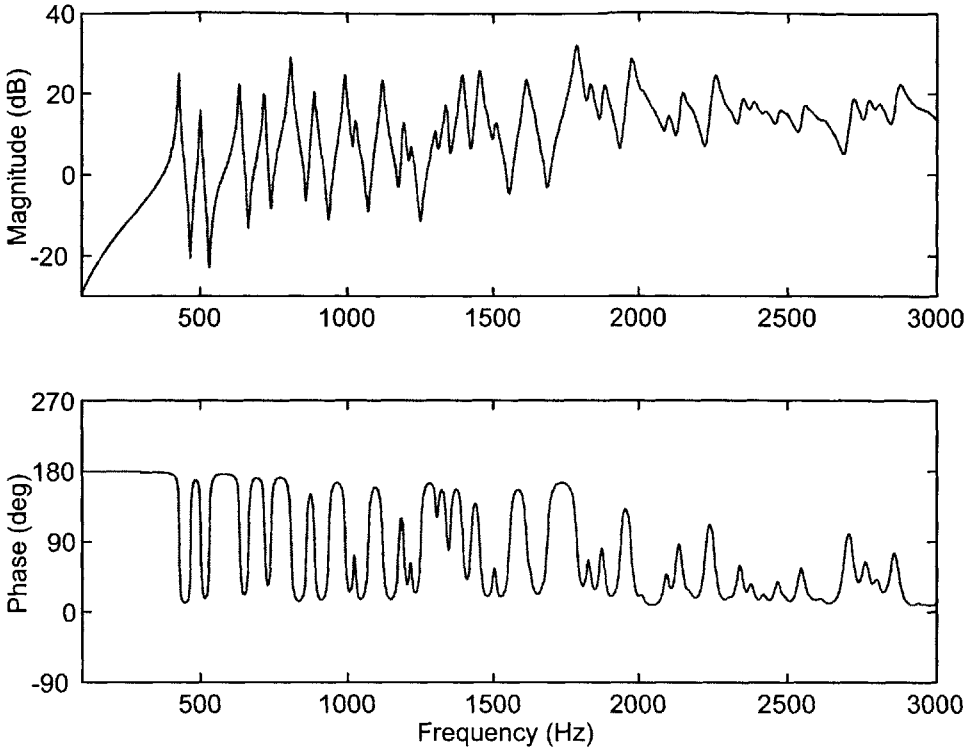

Figure 2-13: Frequency response of the cylindrical shell modeled using the finite element method.

shaker was modeled as a point force acting at the same location as the shaker. The masses of the shaker and the accelerometer were neglected. We see that the model captures the important dynamics of the real cylindrical shell, with the same order of the complexity.

2.3.3 Modeling of an Active Composite Panel

The active composite panel is a very complex structure itself: it is a curved shell structure with PZT rods embedded in a stiff polymer matrix and eight injection-molded piezoceramic accelerometers attached to outer and inner surfaces of the panel. It would be very hard to model the panel in detail. As mentioned earlier, the motivation for the modeling in this study is not to correlate the simulation result with the experimental result *exactly,* but to generate the mathematical model that captures representative dynamics of the real testbed, with the same order of the complexity, such that the proposed control algorithms can be validated on the model before they are experimentally implemented. Therefore, the modeling of the panel in detail, which considers the effect of the curved structure, PZT rods, a stiff polymer matrix, injection-molded piezoceramic accelerometers, circuit boards, *etc.*, will not be pursued in this thesis. Instead, only the representative dynamics of the panel will be considered.

The function of the active composite panel is to measure the accelerations of its top and

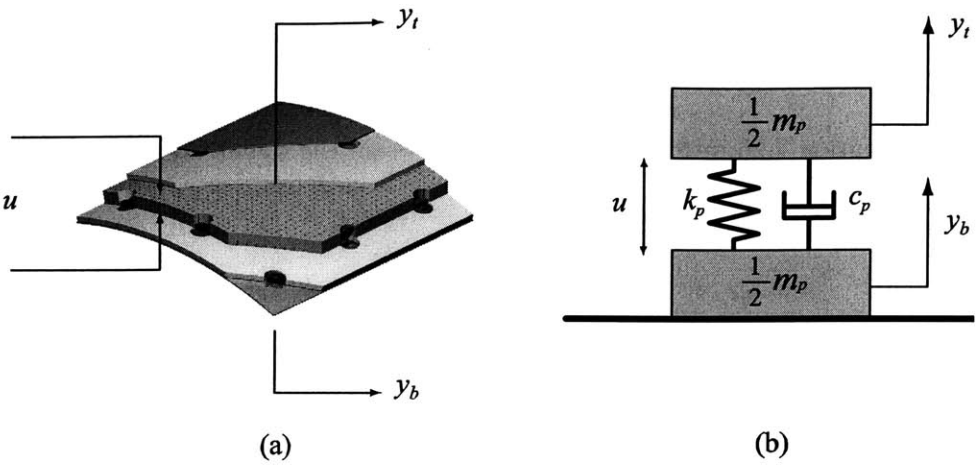

Figure 2-14: The schematic picture of the active composite panel (a) and its simplified model (b).

bottom surfaces, and to generate the displacement proportional to the applied voltage in its thickness direction. Since the panel is rigidly mounted on the cylindrical shell, which is much stiffer than the panel, its bending or torsion modes can be neglected. The only dominant mode of the panel is the extension mode in its thickness direction. Therefore, the panel can be modeled as a system with two masses connected with a spring and a damper, as shown in Figure 2-14. The mass of the panel, m_p, is chosen to be that of the real panel, while the stiffness of the panel, k_p, is selected such that the natural frequency of the panel model is similar to the measured value.

2.3.4 Coupled Dynamics of the Shell and the Panel

Once we have completed the modeling of the cylindrical shell and the active composite panels, the coupled dynamics of the shell and the panels should be considered when the panels are rigidly mounted on the shell. Figure 2-15 shows the force diagram of the shell and the kth panel. It also shows the disturbance f, control input to the kth panel, u_k, the displacement of the kth panel, $w_{p,k}$, the radial displacement of the shell on which the kth panel is mounted, $w_{s,k}$, the internal force between the shell and the lower part of the panel, e_k, and the internal force between the lower and upper part of the panel, d_k. Note that the upper and lower parts make one active composite panel (Figure 2-14). As shown in Figure 2-15, we can consider the dynamics of the shell and the panel independently, if the internal forces d_k and e_k are considered. Using the force diagram in Figure 2-15, the dynamics of the kth panel can be written as

$$\begin{aligned} \text{Upper part:} \quad & \tfrac{1}{2}m_p\ddot{w}_{p,k} = u_k + d_k \\ \text{Lower part:} \quad & \tfrac{1}{2}m_p\ddot{w}_{s,k} = -u_k - d_k + e_k \,, \end{aligned} \tag{2.24}$$

where m_p is the mass of the panel. Since d_k is produced by the force at the spring and the damper of the panel, it is given by

$$d_k = k_p(w_{s,k} - w_{p,k}) + c_p(\dot{w}_{s,k} - \dot{w}_{p,k}) . \tag{2.25}$$

Substituting Equation 2.25 into Equation 2.24, we obtain the dynamics of the kth panel as

$$\begin{aligned} \text{Upper part:} \quad & \tfrac{1}{2}m_p\ddot{w}_{p,k} + c_p\dot{w}_{p,k} + k_p w_{p,k} = c_p\dot{w}_{s,k} + k_p w_{s,k} + u_k \\ \text{Lower part:} \quad & \tfrac{1}{2}m_p\ddot{w}_{s,k} + c_p\dot{w}_{s,k} + k_p w_{s,k} = c_p\dot{w}_{p,k} + k_p w_{p,k} - u_k + e_k . \end{aligned} \tag{2.26}$$

Considering all the panels mounted on the shell (assuming N_p panels are used), the dynamics of the panels can be written in a matrix form as

$$\begin{aligned} \text{Upper part:} \quad & \frac{1}{2}\mathbf{M}_p\ddot{\mathbf{w}}_p + \mathbf{C}_p\dot{\mathbf{w}}_p + \mathbf{K}_p\mathbf{w}_p = \mathbf{C}_p\dot{\mathbf{w}}_s + \mathbf{K}_p\mathbf{w}_s + \mathbf{u} \\ \text{Lower part:} \quad & \frac{1}{2}\mathbf{M}_p\ddot{\mathbf{w}}_s + \mathbf{C}_p\dot{\mathbf{w}}_s + \mathbf{K}_p\mathbf{w}_s = \mathbf{C}_p\dot{\mathbf{w}}_p + \mathbf{K}_p\mathbf{w}_p - \mathbf{u} + \mathbf{e} , \end{aligned} \tag{2.27}$$

where $\mathbf{w}_p = \begin{bmatrix} w_{p,1} & w_{p,2} & \cdots & w_{p,N_p} \end{bmatrix}^T$ is a column vector of the N_p panel displacements, $\mathbf{w}_s = \begin{bmatrix} w_{s,1} & w_{s,2} & \cdots & w_{s,N_p} \end{bmatrix}^T$ is a column vector of the radial displacement of the shell on which panels are mounted, $\mathbf{u} = \begin{bmatrix} u_1 & u_2 & \cdots & u_{N_p} \end{bmatrix}^T$ is a column vector of the control input to the panels, and $\mathbf{e} = \begin{bmatrix} e_1 & e_2 & \cdots & e_{N_p} \end{bmatrix}^T$ is a column vector of the internal force between the shell and the lower part of the panels. Also, $\mathbf{M}_p$, $\mathbf{C}_p$, and $\mathbf{K}_p$ are $N_p \times N_p$ matrices of the panel's mass, damping, and stiffness, respectively, defined as

$$\mathbf{M}_p = \begin{bmatrix} m_p & 0 & 0 & \cdots & 0 & 0 \\ 0 & m_p & 0 & \cdots & 0 & 0 \\ 0 & 0 & \ddots & & \vdots & \vdots \\ \vdots & & & \ddots & 0 & 0 \\ 0 & 0 & \cdots & 0 & m_p & 0 \\ 0 & 0 & \cdots & 0 & 0 & m_p \end{bmatrix}, \quad \mathbf{C}_p = \begin{bmatrix} c_p & 0 & 0 & \cdots & 0 & 0 \\ 0 & c_p & 0 & \cdots & 0 & 0 \\ 0 & 0 & \ddots & & \vdots & \vdots \\ \vdots & & & \ddots & 0 & 0 \\ 0 & 0 & \cdots & 0 & c_p & 0 \\ 0 & 0 & \cdots & 0 & 0 & c_p \end{bmatrix}$$

$$\mathbf{K}_p = \begin{bmatrix} k_p & 0 & 0 & \cdots & 0 & 0 \\ 0 & k_p & 0 & \cdots & 0 & 0 \\ 0 & 0 & \ddots & & \vdots & \vdots \\ \vdots & & & \ddots & 0 & 0 \\ 0 & 0 & \cdots & 0 & k_p & 0 \\ 0 & 0 & \cdots & 0 & 0 & k_p \end{bmatrix} . \tag{2.28}$$

Now, the dynamics of the cylindrical shell is described using the finite element model developed in Section 2.3.2. Let $\mathbf{U}_s$ be a $N_s \times 1$ column vector of the nodal displacements of the shell in the global coordinate, defined in Equation 2.19, where N_s is the number of degrees of freedom in the finite element model. Note that $\mathbf{U}_s$ contains not only $\mathbf{w}_s$, the radial displace-

ment of the shell on which panels are mounted, but also other degrees of freedom, such as linear displacements in the axial and circumferential directions, and rotations for each node. Given $\mathbf{U}_s$, $\mathbf{w}_s$ can be extracted from $\mathbf{U}_s$ using

$$\mathbf{w}_s = \mathbf{T_{wu}}\mathbf{U}_s \,, \tag{2.29}$$

where $\mathbf{T_{wu}}$ is a $N_p \times N_s$ matrix that picks up the degrees of freedom corresponding to $\mathbf{w}_s$ from $\mathbf{U}_s$, defined as

$$\mathbf{T_{wu}}(m,n) = \begin{cases} 1, \text{ if } \mathbf{w}_s(m) = \mathbf{U}_s(n) \\ 0, \text{ otherwise} \end{cases} \,, \quad m = 1,2,...,N_p \,,\ n = 1,2,...,N_s \,. \tag{2.30}$$

Therefore, using the matrix $\mathbf{T_{wu}}$ and the finite element method developed in Section 2.3.2, the dynamic equation of the cylindrical shell can be written as

$$\mathbf{M}_s\ddot{\mathbf{U}}_s + \mathbf{C}_s\dot{\mathbf{U}}_s + \mathbf{K}_s\mathbf{U}_s = \mathbf{B}_f f - \mathbf{T}_{\mathbf{wu}}^T\mathbf{e} \,, \tag{2.31}$$

where $\mathbf{M}_s$ and $\mathbf{K}_s$ are the global mass and stiffness matrix for the cylindrical shell defined in Equation 2.21, $\mathbf{C}_s$ is the damping matrix for the cylindrical shell, which was obtained using the modal damping here, and $\mathbf{B}_f$ is a column vector representing the location where the disturbance acts. Using Equation 2.27, $\mathbf{e}$ is given by

$$\mathbf{e} = \frac{1}{2}\mathbf{M}_p\ddot{\mathbf{w}}_s + \mathbf{C}_p\dot{\mathbf{w}}_s + \mathbf{K}_p\mathbf{w}_s - \mathbf{C}_p\dot{\mathbf{w}}_p - \mathbf{K}_p\mathbf{w}_p + \mathbf{u} \,. \tag{2.32}$$

Also, using the relationships between $\mathbf{w}_s$ and $\mathbf{U}_s$ in Equation 2.29, $\mathbf{e}$ can be written as

$$\mathbf{e} = \frac{1}{2}\mathbf{M}_p\mathbf{T_{wu}}\ddot{\mathbf{U}}_s + \mathbf{C}_p\mathbf{T_{wu}}\dot{\mathbf{U}}_s + \mathbf{K}_p\mathbf{T_{wu}}\mathbf{U}_s - \mathbf{C}_p\dot{\mathbf{w}}_p - \mathbf{K}_p\mathbf{w}_p + \mathbf{u} \,. \tag{2.33}$$

Substituting $\mathbf{e}$ in Equation 2.33 into Equation 2.31, we obtain the dynamic equation of the cylindrical shell as

$$\begin{aligned} &\left(\mathbf{M}_s + \tfrac{1}{2}\mathbf{T}_{\mathbf{wu}}^T\mathbf{M}_p\mathbf{T_{wu}}\right)\ddot{\mathbf{U}}_s + \left(\mathbf{C}_s + \mathbf{T}_{\mathbf{wu}}^T\mathbf{C}_p\mathbf{T_{wu}}\right)\dot{\mathbf{U}}_s + \left(\mathbf{K}_s + \mathbf{T}_{\mathbf{wu}}^T\mathbf{K}_p\mathbf{T_{wu}}\right)\mathbf{U}_s \\ &= \mathbf{B}_f f - \mathbf{T}_{\mathbf{wu}}^T\mathbf{u} + \mathbf{T}_{\mathbf{wu}}^T\left(\mathbf{K}_p\mathbf{w}_p + \mathbf{C}_p\dot{\mathbf{w}}_p\right) \,. \end{aligned} \tag{2.34}$$

Combining Equation 2.27 and Equation 2.34, we obtain the coupled dynamic equation of the shell and the panels, given by

$$\begin{aligned} &\begin{bmatrix} \left(\mathbf{M}_s + \frac{1}{2}\mathbf{T}_{\mathbf{wu}}^T\mathbf{M}_p\mathbf{T_{wu}}\right) & \mathbf{0} \\ \mathbf{0} & \frac{1}{2}\mathbf{M}_p \end{bmatrix}\begin{Bmatrix} \ddot{\mathbf{U}}_s \\ \ddot{\mathbf{w}}_p \end{Bmatrix} + \begin{bmatrix} \left(\mathbf{C}_s + \mathbf{T}_{\mathbf{wu}}^T\mathbf{C}_p\mathbf{T_{wu}}\right) & -\mathbf{T}_{\mathbf{wu}}^T\mathbf{C}_p \\ -\mathbf{C}_p\mathbf{T_{wu}} & \mathbf{C}_p \end{bmatrix}\begin{Bmatrix} \dot{\mathbf{U}}_s \\ \dot{\mathbf{w}}_p \end{Bmatrix} \\ &+ \begin{bmatrix} \left(\mathbf{K}_s + \mathbf{T}_{\mathbf{wu}}^T\mathbf{K}_p\mathbf{T_{wu}}\right) & -\mathbf{T}_{\mathbf{wu}}^T\mathbf{K}_p \\ -\mathbf{K}_p\mathbf{T_{wu}} & \mathbf{K}_p \end{bmatrix}\begin{Bmatrix} \mathbf{U}_s \\ \mathbf{w}_p \end{Bmatrix} = \begin{bmatrix} \mathbf{B}_f \\ \mathbf{0} \end{bmatrix} f + \begin{bmatrix} -\mathbf{T}_{\mathbf{wu}}^T \\ \mathbf{I}_{N_p} \end{bmatrix}\mathbf{u} \,. \end{aligned} \tag{2.35}$$

Here, $\mathbf{I}_{N_p}$ is an $N_p \times N_p$ identity matrix. The model developed in this section will be used to test the wavenumber domain feedback control algorithms in Chapter 4–5, and the local controller

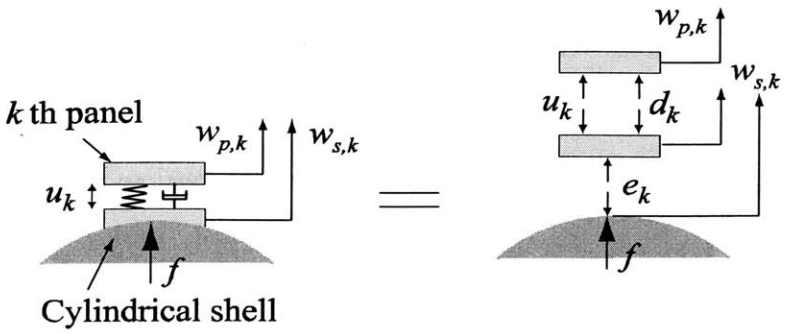

Figure 2-15: Force diagram of the cylindrical shell with the active composite panels mounted.

architecture in Chapter 6.

2.4 Summary

In this chapter, the experimental hardware used in this study, including the thick-walled cylindrical shell, and the active composite panels, was presented. They constitute the testbed structure, where the proposed control algorithms will be implemented in later chapters. The signal conditioners for the panels, which are the pre-amplifier and the power amplifier, were also described.

Furthermore, the modeling process for the cylindrical shell and the active composite panels was explored. The objective of the modeling performed in this chapter is to generate a mathematical model of the plant that captures the representative dynamics of the real testbed, not to correlate exactly the experimental data with the simulation. The finite element method was used to model the dynamics of the cylindrical shell. Simply-supported and clamped boundary conditions were irregularly applied to produce an effect similar to that produced by the end-caps, given the fact that they are much stiffer than the shell. The active composite panel was modeled as a mass-spring-damper system, noting that only the extension mode in its thickness direction is important in this study. Finally, their coupled dynamics were found after completing the modeling of the shell and the panel.

Chapter 3

Local Control Architecture

3.1 Introduction and Objective

This chapter considers the local controller architecture used for each panel. The goal of the local controllers is to reduce the vibration level of each panel's outer surface (the radiating surface) by actively isolating the panel motion from the cylinder's surface. In the chapter, two different feedback control approaches are discussed. The design methods for those controllers are presented using the model developed in Chapter 2, and the experimental data. The undesirable dynamics of the active composite panel are shown, and the implication in the feedback controller design will be examined. Finally, methods to resolve the difficulties caused by the undesirable panel dynamics will be explored.

3.2 Local Controller Architecture

Figure 3-1 shows the cylindrical shell with one active composite panel mounted on its surface. The shell has two end-caps, three ribs, and one shaker mounted inside of the shell. The shaker is used to produce a broadband disturbance. More information about the shell and the active composite panel can be found in Chapter 2.

The standard control system representation is shown in Figure 3-2, showing the disturbances w, performance z, input u, and measurement y. The (matrix) transfer function of the system is G, and the feedback control law is K. For the problem discussed in this chapter, the disturbance w is the voltage input to the shaker installed inside the shell. The performance variable z is the acceleration of the outer surface of the active composite panel mounted directly above the shaker, and the control input u is the voltage input to the panel actuator layer. There are two possible measurements y for the problem considered in this chapter: the top accelerometer measurement, which measures the performance z directly; and the bottom accelerometer measurement, which measures the effect of the disturbance on the panel.

Two possible approaches for reducing the performance variable are investigated. In the feedback control approach (Figure 3-3), the top accelerometer measurement is fed back to the actuator layer of the panel. Because the measurement y directly senses the performance z in the feedback approach, the disturbance attenuation at frequency ω is directly proportional to

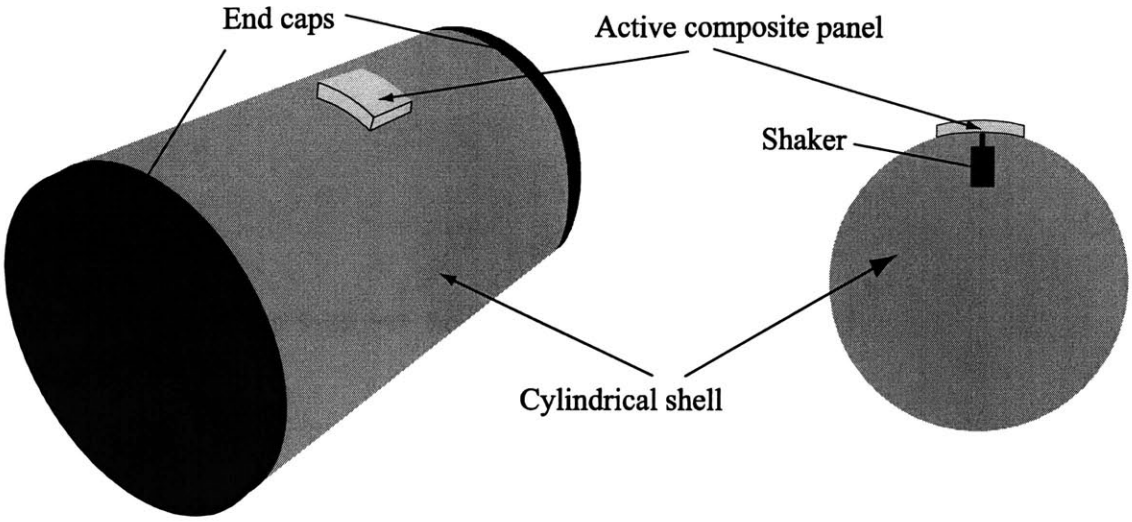

Figure 3-1: The cylindrical shell with one active composite panel mounted on its surface.

the sensitivity transfer function, given by

$$S(j\omega) = \frac{1}{1 + G(j\omega) K(j\omega)} . \tag{3.1}$$

Thus, the performance of the system is improved by large controller gains.

The other approach considered is to measure the acceleration of the inner surface of the panel (*i.e.*, the outer surface of the shell), and feed that signal back to the panel. Since the panel is mounted on the outer surface of the shell, this approach is equivalent to feeding back the acceleration of the outer surface of the shell back to the panel. Because the mass of each panel is small compared to that of the shell, the control signal has little effect on the dynamics of the shell, and therefore $G_{yu}(s)$ is small. However, the control signal directly affects the

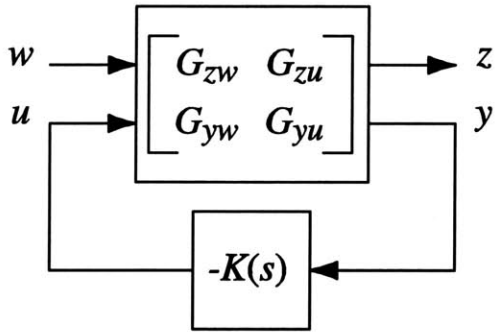

Figure 3-2: Standard control system representation.

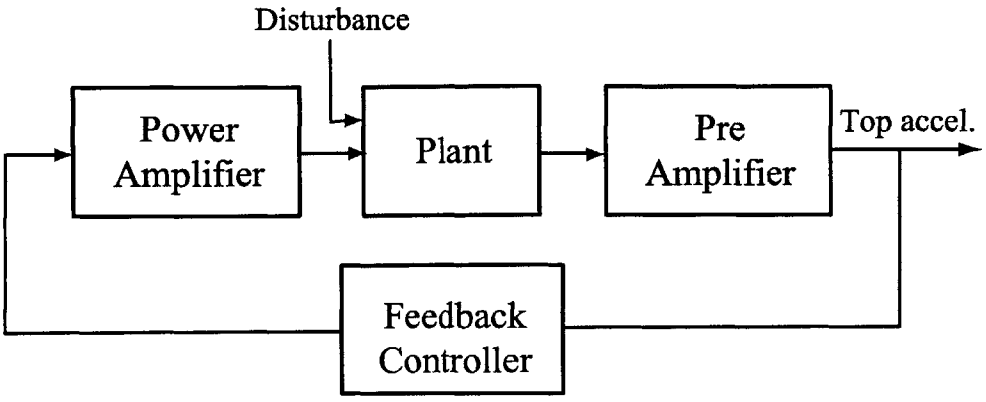

Figure 3-3: Generic feedback control block digram.

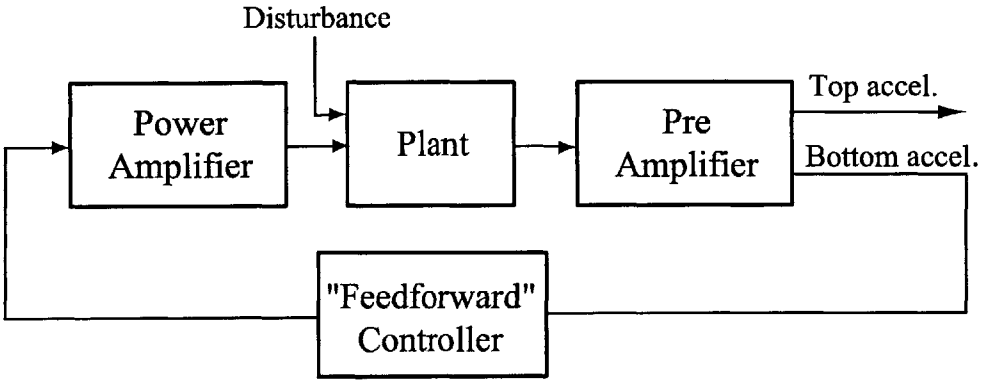

Figure 3-4: Generic feedforward control block diagram.

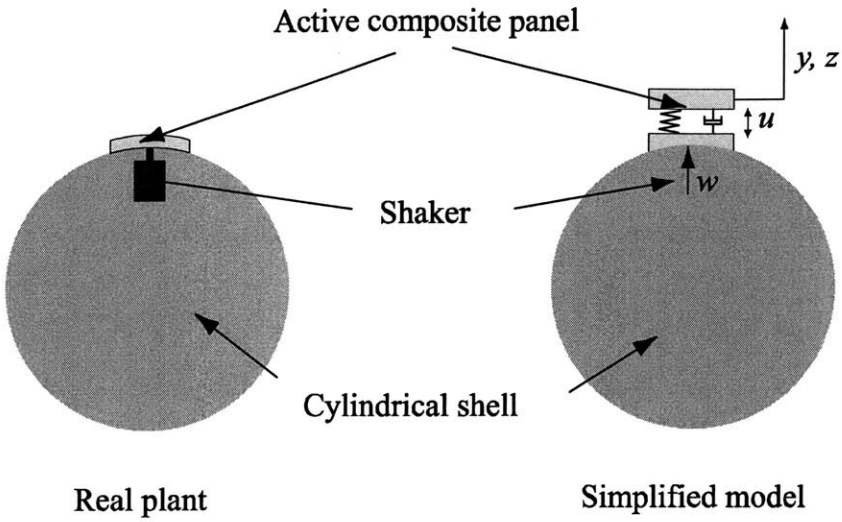

Figure 3-5: The cylindrical shell with one active panel mounted on its surface and its simplified model for feedback control design.

panel displacement, so the transfer function G_{zu} is significant. As a result, high controller gains don't guarantee high performance — indeed, a high-gain controller would be counterproductive. Instead, the best performance is achieved by choosing the feedback gain $K(s)$ to produce a displacement equal and opposite to the shell displacement. This is denoted as "feedforward" control in this thesis, because the measurement depends strongly on the disturbance, although it is not a true feedforward controller in a conventional sense. The block diagram representing feedforward controller is shown in Figure 3-4.

In fact, these two approaches (feedback and feedforward) are complementary, and can be applied simultaneously. Because there is little interaction between the two controllers, the net attenuation is approximately equal to the product of the attenuations of the two controllers. (If expressed in decibels, the attenuation is the sum of the attenuations of the two controllers.)

3.3 Design of Compensators

3.3.1 Feedback Compensation

In this section, the design of the feedback control loop shape is described. As mentioned in Section 3.2, the basic approach of feedback control is to apply large control gain, while maintaining the closed-loop stability, such that the sensitivity transfer function defined in Equation 3.1 is as small as possible in the control bandwidth. The displacement of the active composite panel is directly proportional to the voltage applied to the panel, at least below the first resonance of the panel, which is near 12 kHz. Furthermore, because the mass of the panel is much smaller than that of the shell ($< 1\%$), most of the panel displacement occurs at the outer surface. Therefore, the transfer functions from panel excitation (u) to acceleration of the outer surface

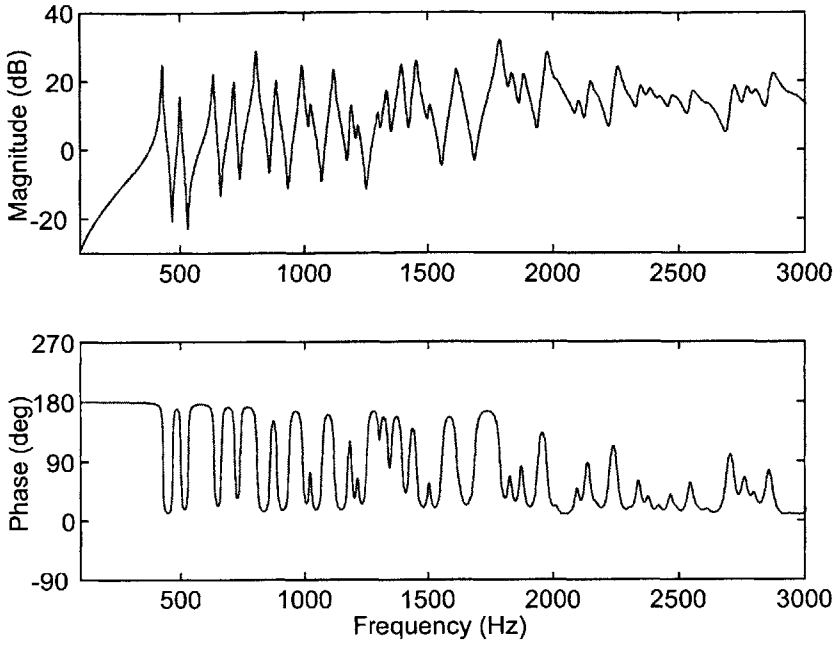

Figure 3-6: Frequency response of $G_{zw}(s)$ obtained using the model developed in Chapter 2.

of the panel (z) should be proportional to s^2. Then, as mentioned in Chapter 2, the active composite panel can be modeled as a mass-spring-damper system with a natural frequency of 12 kHz. Figure 3-5 shows the shell with one active panel mounted on its surface, and its simplified model for feedback control design. It also shows the disturbance (w), control input (u), and sensor output (y). The shaker is modeled as a point force acting on the shell. The mass of the shaker is neglected, because it is much smaller than that of the shell. If the active composite panel doesn't have its own dynamics, the sensor output (y) is the same as the performance output (z) in feedback control design setup.

Figure 3-6 and 3-7 show the frequency responses of $G_{zw}(s)$ and $G_{zu}(s)$ obtained using the model developed in Chapter 2, respectively. We can see that the transfer function $G_{zu}(s)$ has a slope of 40 dB/decade below 188 Hz, and 20 dB/decade above 188 Hz. Recalling that the plant has a low-pass filter at 188 Hz in the power amplifier, this behavior is as expected. Also, note that $G_{zu}(s)$ in Figure 3-7 is typical of a collocated structural transfer function. This results in plant transfer functions that are more easily compensated than non-collocated transfer functions.

The proposed feedback controller to achieve this goal is shown in Figure 3-8. It has two low-pass filters at 200 Hz and 20,000 Hz, with a reasonable gain. The low-pass filter at 200 Hz behaves as an integrator, while the one at 20,000 Hz provides roll-off at high frequency. Remembering that the power-amplifier has a low-pass filter at 188 Hz, the feedback controller basically integrates the signal from the accelerometer twice to get a displacement, multiplies it by the gain to reduce the sensitivity transfer function, and provides roll-off at high frequency to avoid the effect of high-frequency noise or unmodeled dynamics. The resulting loop transfer

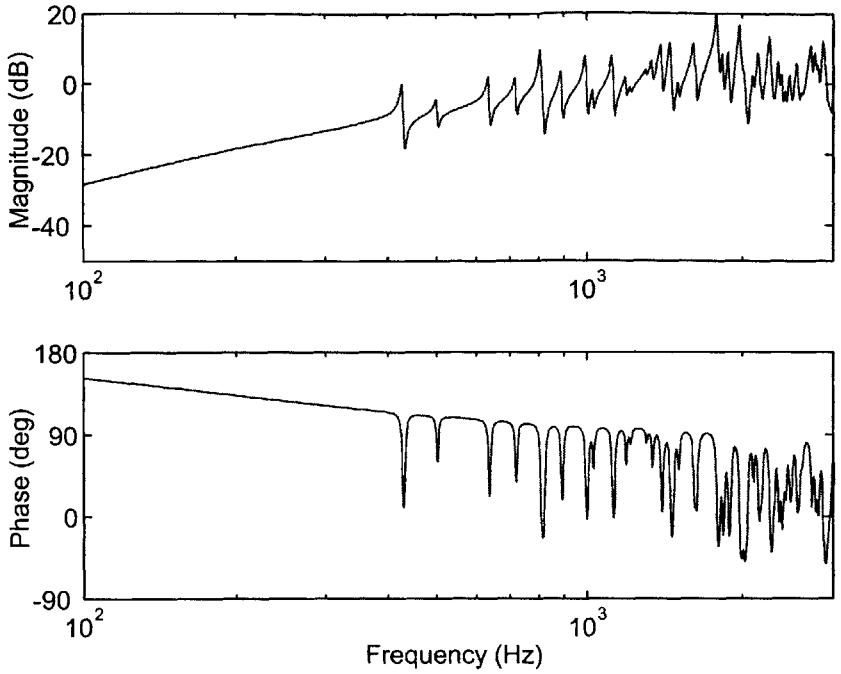

Figure 3-7: Frequency response of $G_{zu}(s)$ obtained using the model developed in Chapter 2.

function using this controller is shown in Figure 3-9. The loop transfer function has a gain of around 10–20 dB below 2 kHz, and good phase margin.

The result of simulating models looks promising, and seems to imply that the feedback controller design is straightforward and easy to apply. The experimental data, however, shows that it is not so easy as expected, primarily due to undesirable panel dynamics. The features of the undesirable panel dynamics were briefly mentioned in Chapter 2. In this chapter, they are investigated more thoroughly. Figure 3-10 shows the plant transfer functions $G_{yu}(s)$, as measured experimentally by the accelerometers embedded in the active panel; and $G_{zu}(s)$, as measured by an external accelerometer (Model #352B22, PCB Piezotronics, Depew, NY). The transfer function $G_{zu}(s)$ behaves as expected. From about 50 Hz to 100 Hz, the transfer function has a slope of about 40 dB/decade, corresponding to a transfer function $G_{zu}(s) \sim s^2$. Below 50 Hz, the acceleration signal is very small, and the low signal-to-noise ratio prevents an accurate identification of the transfer function. Above 188 Hz, the slope of the transfer function decreases to about 20 dB/decade, because the plant includes a power amplifier for the panel actuator with a low-pass filter at 188 Hz. In the frequency range 500–10,000 Hz, there are also numerous small peaks, due to shell modes. The peaks are small, because each resonant pole in the transfer function is nearly cancelled by a zero, due to the low controllability of the shell modes by the panel actuator. Finally, at 12 kHz, a significant resonant peak is seen, which is due to the panel dynamics.

Also in Figure 3-10 is the transfer function G_{yu}. Ideally, the transfer function G_{yu} would be identical to G_{zu}, indicating that the embedded accelerometers are accurately measuring

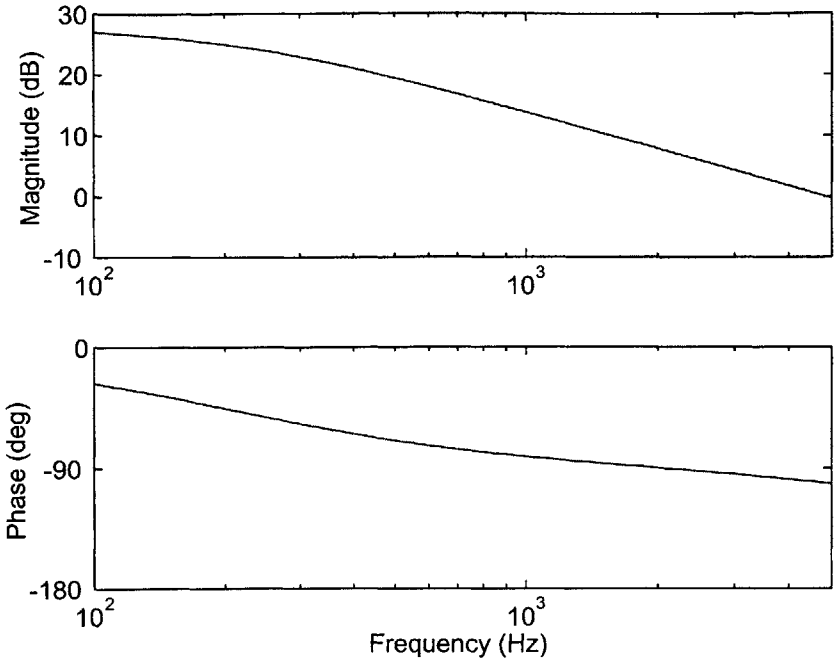

Figure 3-8: Frequency response of feedback controller for the model.

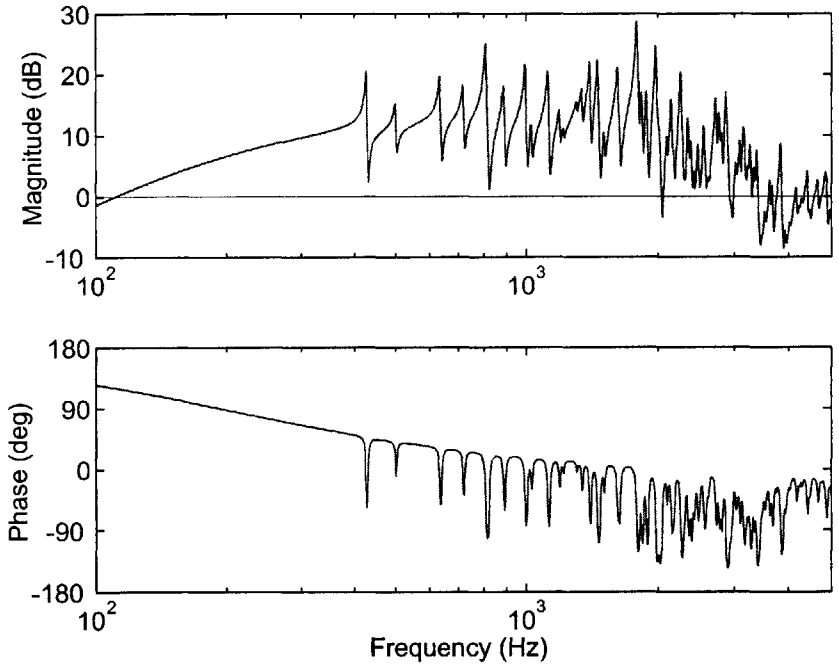

Figure 3-9: The loop transfer function for feedback control.

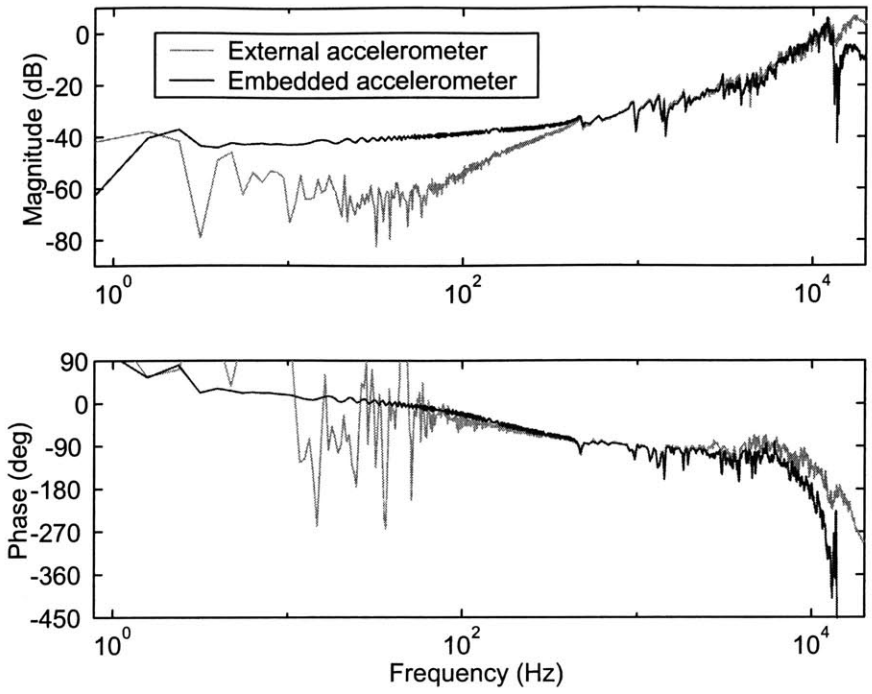

Figure 3-10: Plant transfer function for feedback control.

the acceleration of the radiating surface. Unfortunately, the two transfer functions show some discrepancies. At high frequencies (above 12 kHz), the two transfer functions are significantly different, most likely due to participation of the embedded accelerometers in the modal behavior of the panel. This discrepancy is not too serious, since the bandwidth of the controller will be well below 12 kHz anyway. The more serious problem is the discrepancy below 500 Hz, which is inside the bandwidth interest. This discrepancy appears to be due to direct electrical or electromechanical feedthrough of the panel input voltage to the accelerometer. The low-frequency feedthrough critically limits the achievable closed-loop performance. In order to achieve satisfactory performance, it is necessary to compensate for the feedthrough effect.

The low frequency feedthrough can be cancelled, at least approximately, by adding a low-pass filter to the plant. The transfer function G_{zu} can be approximated below the resonant frequency of the panel as a double differentiator s^2 times a low-pass filter at 188 Hz, given as

$$G_{zu} = k\frac{s^2}{s + 2\pi \times 188}, \tag{3.2}$$

where k is a constant gain, and small peaks due to shell modes are neglected. On the other hand, the transfer function G_{yu} can be approximated as

$$G_{yu} = k\frac{s^2 - c^2}{s + 2\pi \times 188}, \tag{3.3}$$

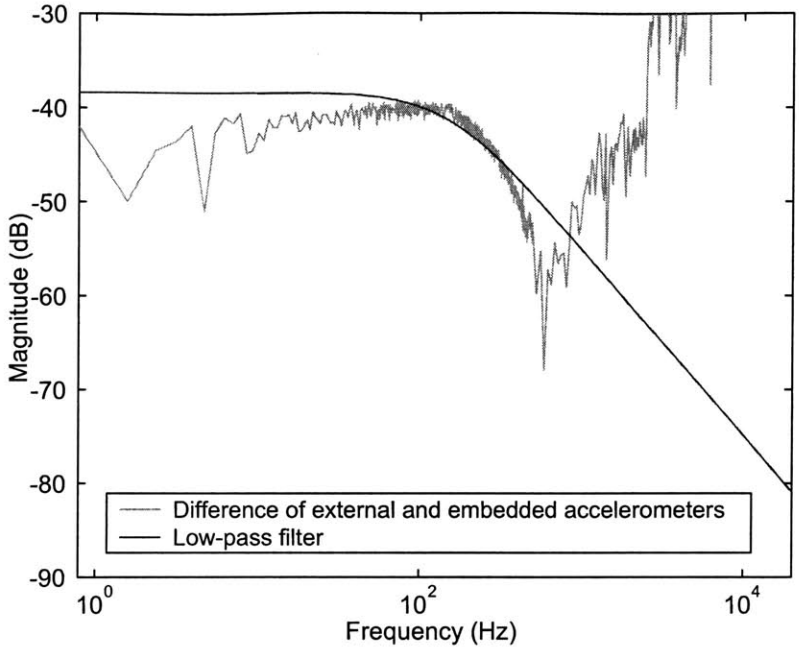

Figure 3-11: Difference in the transfer functions of the embedded and external accelerometers. The low-pass filter transfer function is an approximate fit to the actual difference.

where c^2 corresponds to the low-frequency feedthrough. The negative sign is needed before c^2, because imaginary zeros are not found in the low-frequency in G_{yu}. Therefore, in order to extract G_{zu} from the measurement of G_{yu}, a low-pass filter $C(s)$ should be designed and implemented, given by

$$C(s) = \frac{k\,c^2}{s + 2\pi \times 188}\,. \tag{3.4}$$

Then, G_{zu} can be obtained by adding $C(s)$ to G_{yu}. Figure 3-11 shows the difference between the acceleration measured by the external accelerometer and the embedded ones ($G_{zu} - G_{yu}$), and the low-pass filter that (approximately) matches the difference ($C(s)$). The result of adding the low-pass filter to the plant is shown in Figure 3-12. It can be seen that the low frequency feedthrough is significantly reduced, and the compensated plant transfer function is a much better match to the performance transfer function. This will significantly improve the closed-loop performance in the frequency range below 500 Hz.

The feedback control law can be determined from the requirements on the attenuation of radiated noise. For example, in order to achieve better than 10 dB of reduction in the range 250–2000 Hz, the loop gain must be greater than 10 dB over this range. In order for the system to be stable, the loop must roll off at high frequencies, with a slope of about –20 dB/decade. It is also necessary for the loop shape to roll off at low frequencies. If it did not, the control loop would try to control the large, low-frequency motion of the shell that occurs in the laboratory when the shell swings or bounces on its suspension. Therefore, in addition to the low-pass filter associated with the power amplifier, two additional low-pass filters are needed to give the

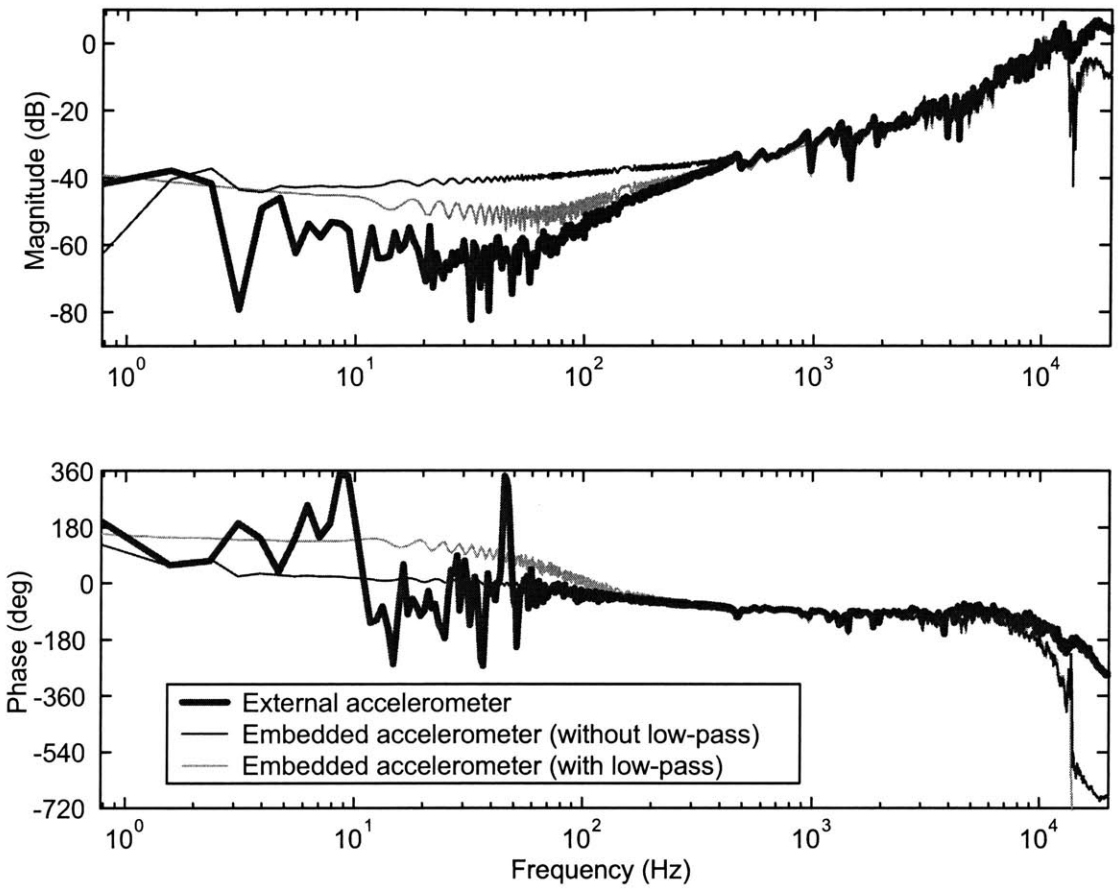

Figure 3-12: Plant transfer function as measured by the embedded and external accelerometers, and by the embedded accelerometers with compensation.

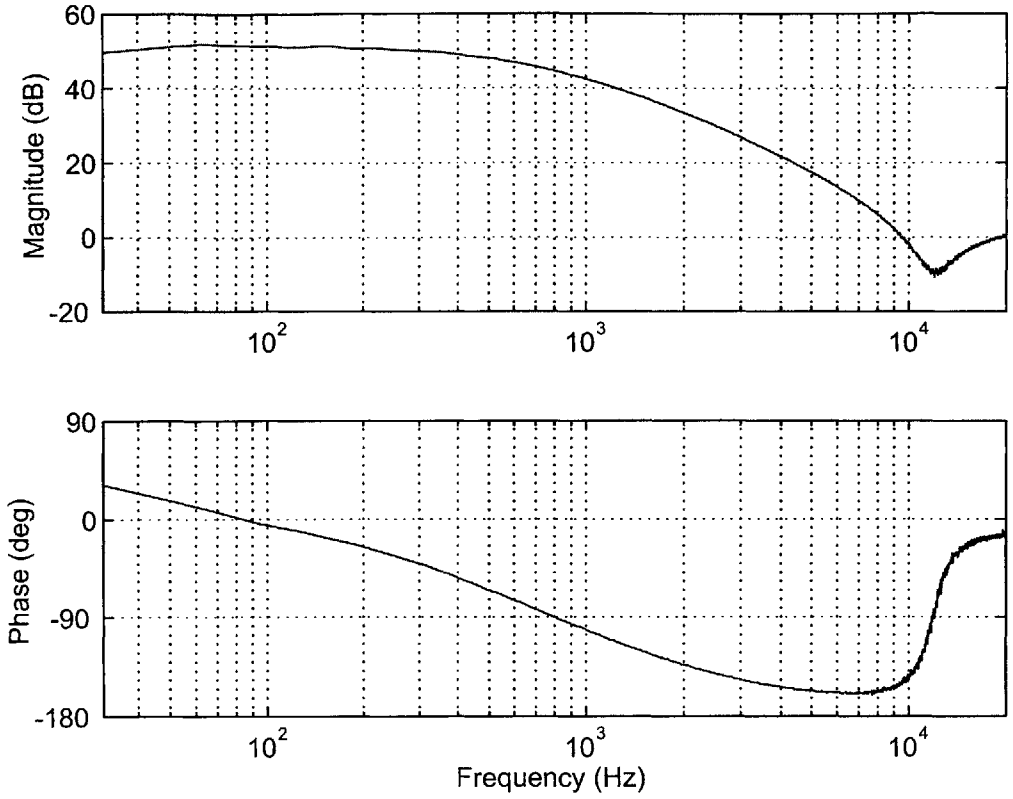

Figure 3-13: Feedback controller frequency response function.

correct roll-off at high frequencies. Also, a high-pass filter is required to ensure that the loop rolls off at low frequencies with a slope of 20 dB/decade. Finally, there must be compensation for the high-frequency panel dynamics, which can cause instability. The way to compensate for the high-frequency panel dynamics will be explored in detail in Chapter 6.

Figure 3-13 shows the basic feedback controller transfer function used in this study. The feedback compensator has a low-pass filter with a pole at 600 Hz, another low-pass filter at 1000 Hz, and a high-pass filter at 14 Hz. The controller transfer function in Figure 3-13 doesn't have a low-pass filter at 188 Hz, which is included in the plant. In addition, there is a notch filter at about 12 kHz, which is tuned to the panel resonance. Figure 3-14 and 3-15 show the frequency response and Nyquist plot of the resulting loop transfer function. As can be seen from the figures, the loop shape achieves the desired goals. The loop gain is greater than 10 dB between 250 Hz and 2000 Hz. At the lower crossover frequency of 70 Hz, the phase margin is close to 90 deg. (Note that for a low-frequency crossover, the phase margin is the difference between the loop phase and +180 deg). At the higher frequency, the phase margin is lower, but adequate. For some of the implementations described in Chapter 6, it was necessary to reduce the loop gain somewhat, in order to keep the phase margin at acceptable levels, and prevent instabilities.

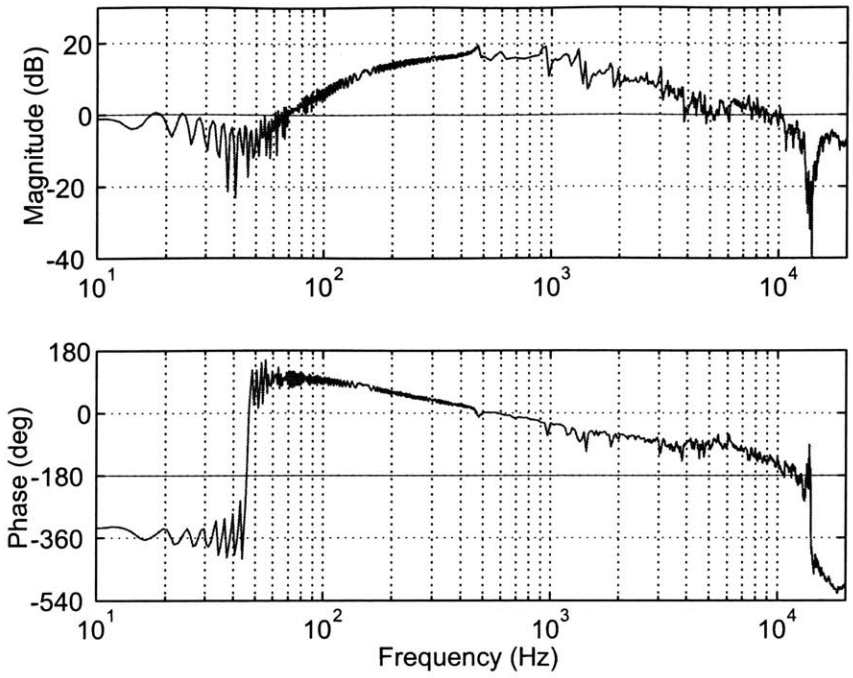

Figure 3-14: Loop transfer function of the feedback controller.

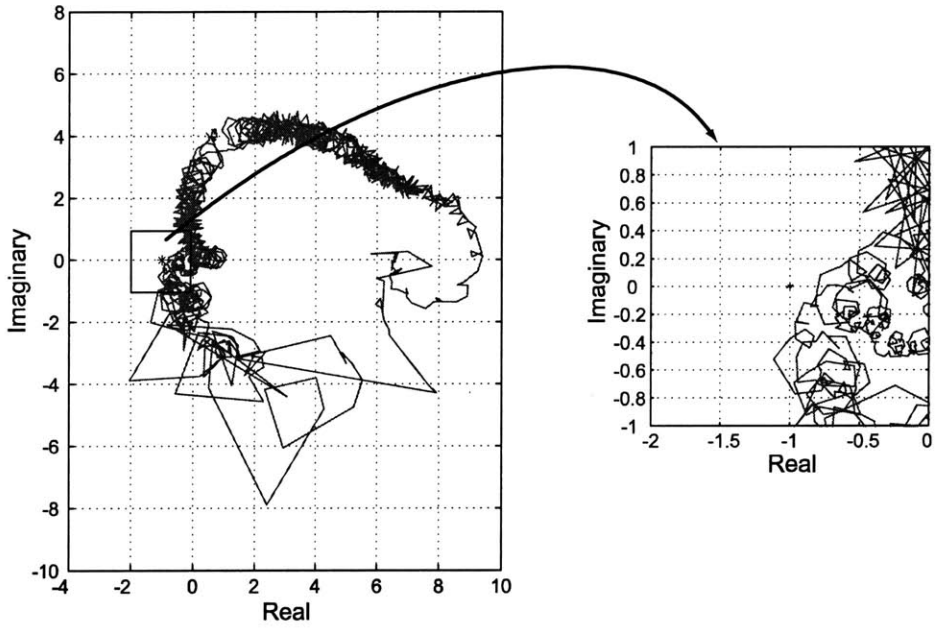

Figure 3-15: Nyquist plot of the loop transfer function for feedback control. "$*$" represents the critical point -1.

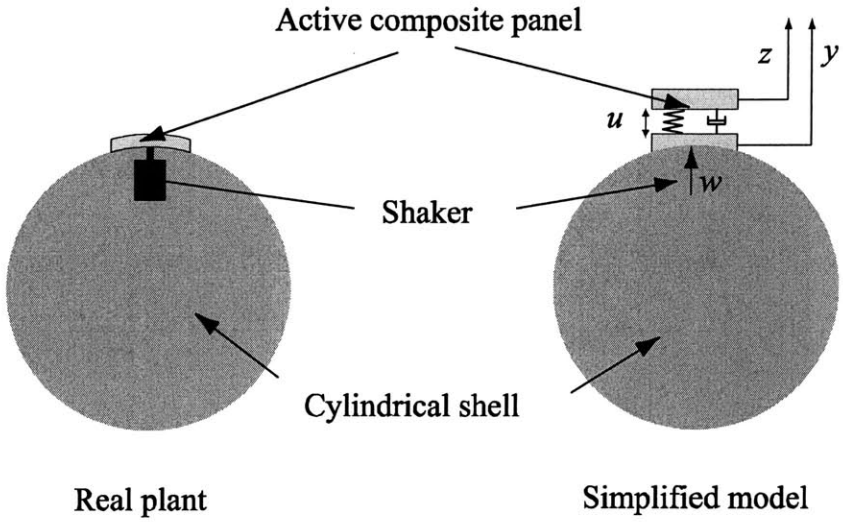

Figure 3-16: The cylindrical shell with one active panel mounted on its surface and its simplified model for feedforward control design.

3.3.2 Feedforward Compensation

In some ways, the problem of feedforward compensation is more straightforward than feedback compensation. When the bottom accelerometer is used as the measurement, the coupling between the applied control and the measurement, G_{yu}, is small, so that for moderate control signals, there is no risk of instability. Figure 3-16 shows the cylindrical shell with one active composite panel mounted on its surface, and its simplified model for feedforward control design. It also shows the disturbance (w), control input (u), and sensor output (y), and performance output (z).

Figure 3-17 shows the frequency response of $G_{zw}(s)$ and $G_{yw}(s)$, while Figure 3-18 shows the frequency response of $G_{zu}(s)$ and $G_{yu}(s)$. They are obtained using the model developed in Chapter 2. It can be seen that $G_{zw}(s)$ and $G_{yw}(s)$ are indistinguishable below the resonant peak at 12 kHz of the panel (the resonance is not shown in the Figure 3-17). This implies that the inner surface of the panel moves about the same as the outer surface of the shell, under the influence of a disturbance, below the resonance of the panel. Figure 3-18 says that $G_{yu}(s)$ is smaller than $G_{zu}(s)$, below 2 kHz, primarily because the mass of the active composite panel is much smaller than that of the shell. These two features of the plant transfer functions ($G_{yw} \approx G_{zw}$, and G_{yu} is small) have critical advantages in feedforward controller design, as shown below.

In contrast to feedback control, the goal of feedforward control is to choose the control gain so that the performance output (z) is cancelled. From the standard control system representation in Figure 3-2, the performance output (z) and the sensor output (y) can be written as

$$\begin{aligned} z &= G_{zw}w + G_{zu}u \\ y &= G_{yw}w + G_{yu}u\,. \end{aligned} \tag{3.5}$$

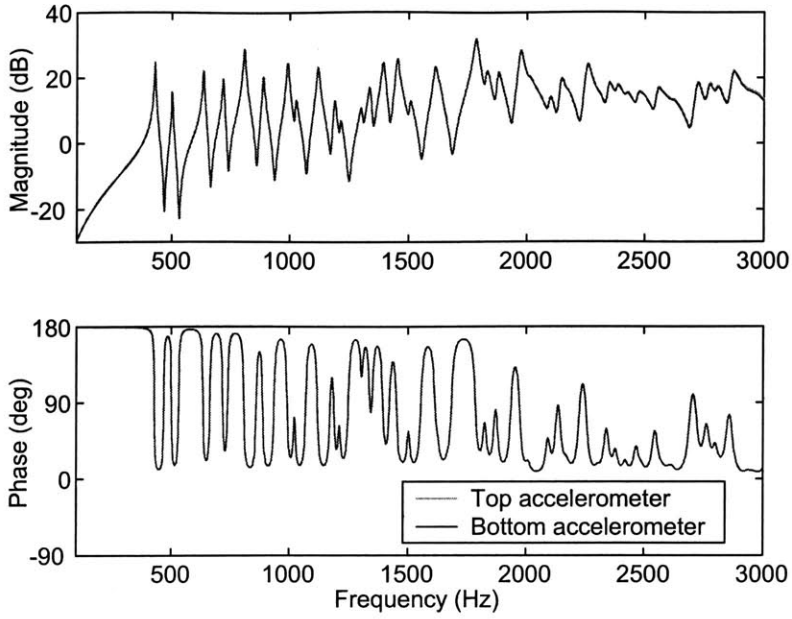

Figure 3-17: Frequency response of $G_{zw}(s)$ and $G_{yw}(s)$ obtained using the model developed in Chapter 2.

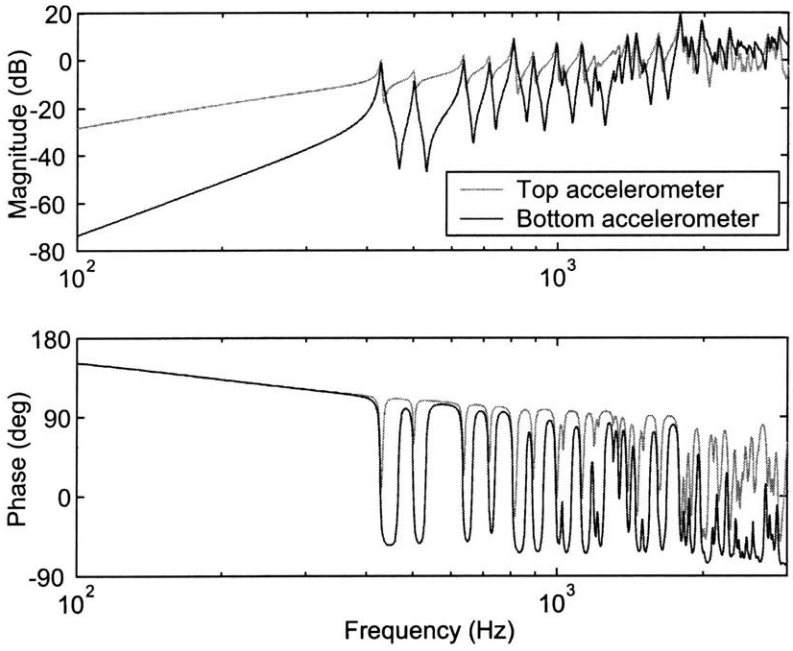

Figure 3-18: Frequency response of $G_{zu}(s)$ and $G_{yu}(s)$ obtained using the model developed in Chapter 2.

The feedforward controller $K_f(s)$ can be implemented as

$$u = K_f\, y\,. \tag{3.6}$$

Using this controller, the closed-loop performance output (z) can be written as

$$\begin{aligned} z &= G_{zw}w + G_{zu}K_f\, y \\ &= \left[\frac{G_{zw} + K_f\,(G_{zu}G_{yw} - G_{zw}G_{yu})}{1 - K_f\,G_{yu}}\right] w\,. \end{aligned} \tag{3.7}$$

Therefore, we can see that z is *exactly* cancelled when $K_f(s)$ is selected such that

$$K_f = -\frac{G_{zw}}{G_{zu}G_{yw} - G_{zw}G_{yu}}\,, \tag{3.8}$$

provided that the closed-loop system is stable.

The desired control law $K_f(s)$ in Equation 3.8 can be simplified further using the fact that G_{yu} is small, and $G_{yw} \approx G_{zw}$. Therefore,

$$K_f \approx -\frac{1}{G_{zu}}\,. \tag{3.9}$$

But $G_{zu} \sim s^2$. So, the appropriate control law is for $K_f(s)$ to be a double integrator with appropriate gain. Figure 3-19 shows the frequency response function of the feedforward controller $K_f(s)$ obtained using Equation 3.8 and 3.9 in the same figure. They are so similar that it is not possible to see the difference. The frequency response function shown in Figure 3-19 is not a double integrator ($1/s^2$), but a double integrator multiplied by a polynomial function ($s + 188 \times 2\pi$), which comes from the inverse of the low-pass filter in the power amplifier. The resulting loop transfer function $K_f(s)\,G_{yu}(s)$ for feedforward controller is shown in Figure 3-20. In contrast to feedback control, the loop gain for feedforward control is small, as expected. Most resonant peaks are around the 0 dB line, although some peaks cross the 10 dB line. Also, from Figure 3-20, we can see that the closed-loop system using the feedforward controller $K_f(s)$ from Equation 3.9 is stable. Therefore, the feedforward controller shown in Figure 3-19 *exactly* cancels the performance output (z). However, this cannot happen in a real world, because G_{yw} is not exactly equal to G_{zw}, and there is no guarantee that feedforward controller obtained using Equation 3.8 will stabilize the closed-loop system. Also, as a practical matter, it is better for $K_f(s)$ to be a low-pass filter with two poles, instead of a double integrator, since the match is important only above 250 Hz, and indeed there is not enough control authority to cancel low-frequency motion. Therefore, the design approach to feedforward controller is to find a stabilizing $K_f(s)$ such that it is as close as possible to the one defined in Equation 3.8.

Figure 3-21 and 3-22 show the frequency response of $G_{zw}(s)$, $G_{yw}(s)$ and $G_{zu}(s)$, $G_{yu}(s)$, respectively, as measured experimentally by the accelerometers embedded in the active composite panel. We can see that $G_{zw}(s)$ and $G_{yw}(s)$ are very similar below 2 kHz, although they begin to diverge from each other above 3 kHz. Also, Figure 3-22 says that $G_{yu}(s)$ is very small, compared to $G_{zu}(s)$, below 2 kHz. Since the two features of plant transfer functions for feedforward control, which were assumed before, are valid below 2kHz, it is expected that the feedforward controller will achieve reasonable closed-loop performance below this frequency.

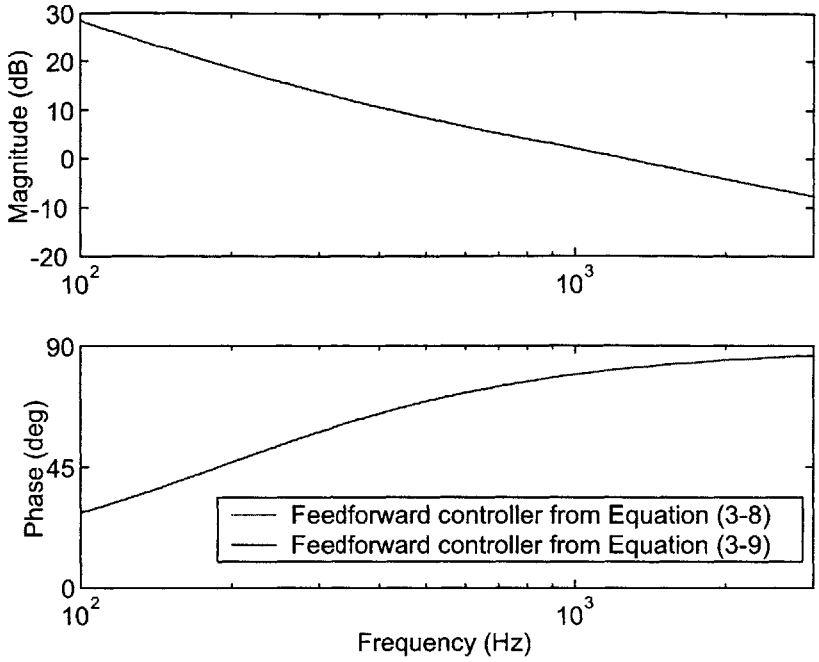

Figure 3-19: Feedforward controller $K_f(s)$ obtained using Equation 3.8 and 3.9.

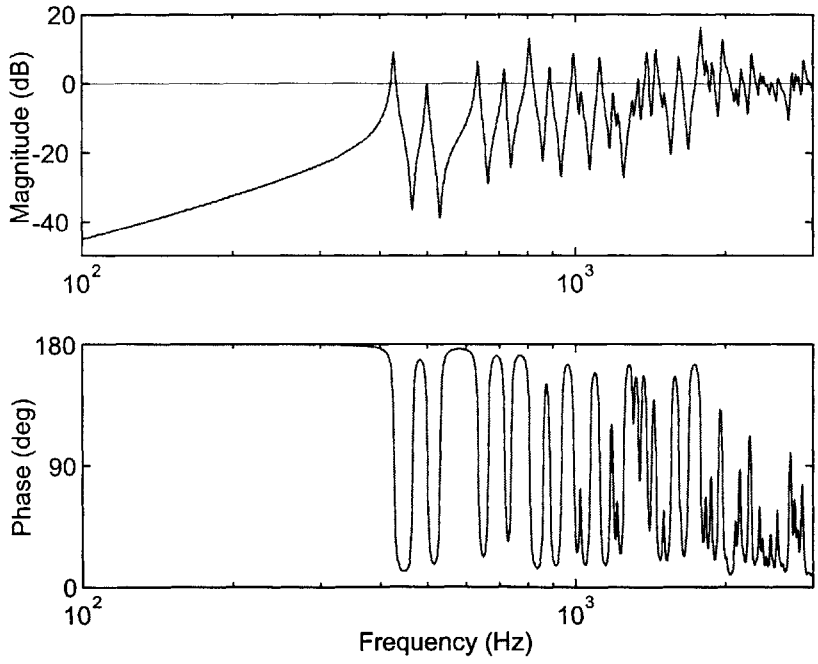

Figure 3-20: Frequency response function of the loop transfer function for feedforward control.

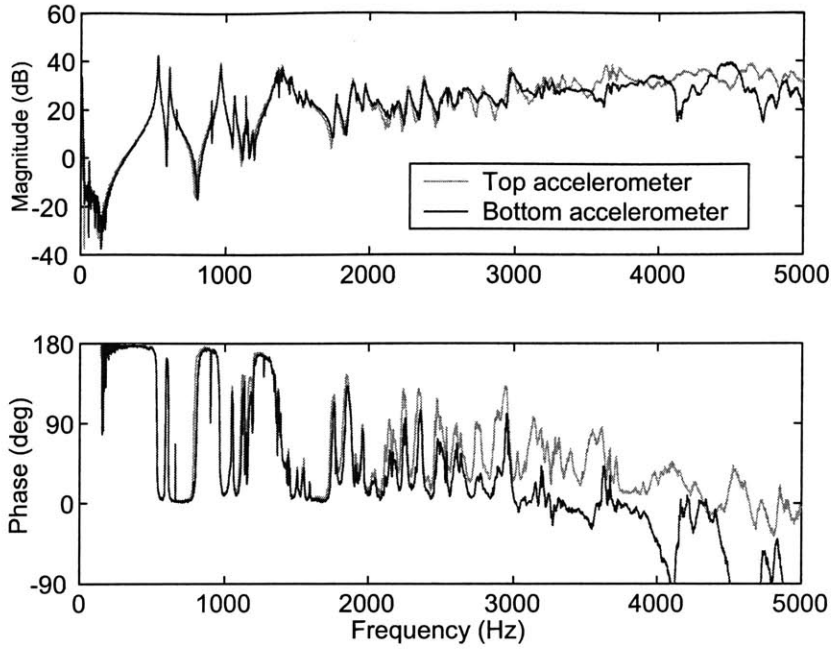

Figure 3-21: Frequency response functions of $G_{zw}(s)$ and $G_{yw}(s)$.

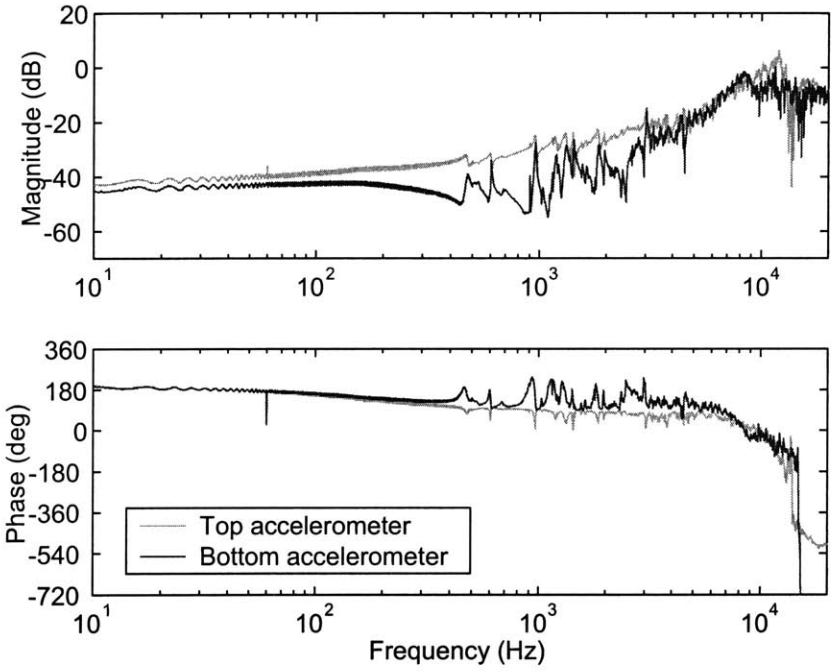

Figure 3-22: Frequency response functions of $G_{zu}(s)$ and $G_{yu}(s)$.

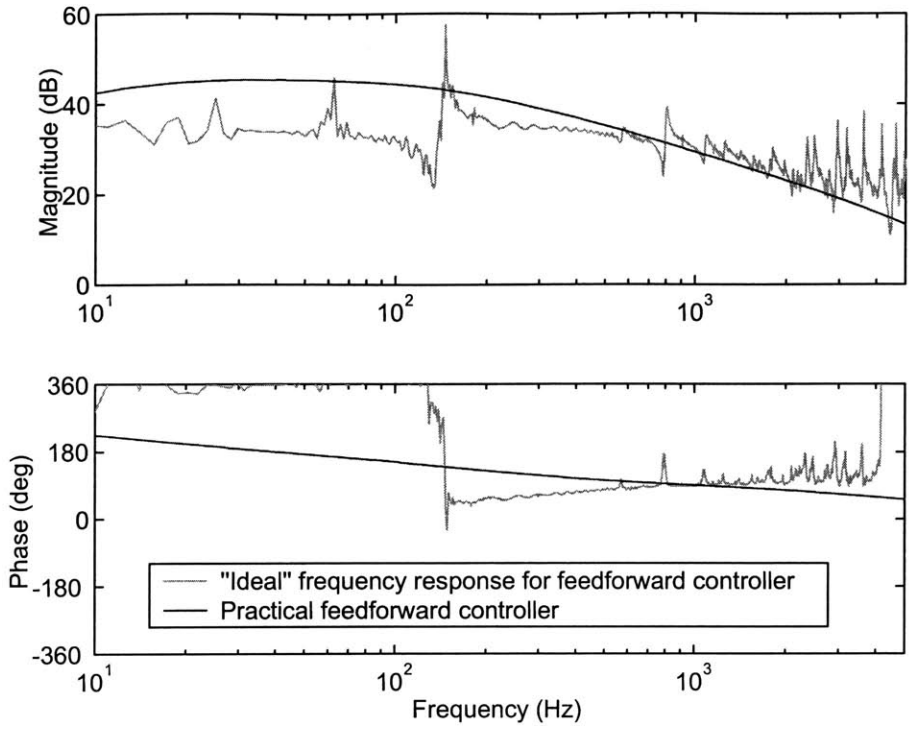

Figure 3-23: Frequency response of the ideal feedforward controller and its best fit $K_f(s)$.

Figure 3-23 shows the frequency response of the ideal feedforward controller, as defined in Equation 3.8, and its best fit $K_f(s)$, which is denoted as "practical feedforward controller" in the figure. $K_f(s)$ has one pole at 150 Hz, which functions as a double integrator, combined with the low-pass filter in the power amplifier. In addition, one low-pass filter pole was added at 6000 Hz to add roll-off, which prevents instability due to high-frequency modes of the shell. Finally, $K_f(s)$ has a high-pass filter at 11 Hz to avoid DC saturation. Because of the pole location of $K_f(s)$, the best matching of transfer functions (and therefore the best attenuation) will occur between 500 Hz and 2000 Hz. The resulting loop transfer function is shown in Figure 3-24 (frequency response), and 3-25 (Nyquist plot), respectively. We can see that the closed-loop system is almost gain-stabilized, because most resonant peaks are below 0 dB, although a few peaks cross the 0 dB line.

3.3.3 Low-frequency Feedthrough Compensator

In Section 3.3.1, we saw that the low-frequency feedthrough can be approximately cancelled by adding a low-pass filter to the plant. Feedback and feedforward controllers were designed on the plant improved by adding the low-pass filter. The block diagram for the closed-loop system with both feedback and feedforward controller is shown in Figure 3-26. In the block diagram shown in the figure, the "accelerometer compensator," which is the low-pass filter added to the plant, is considered as a part of the plant. However, we can incorporate the accelerometer

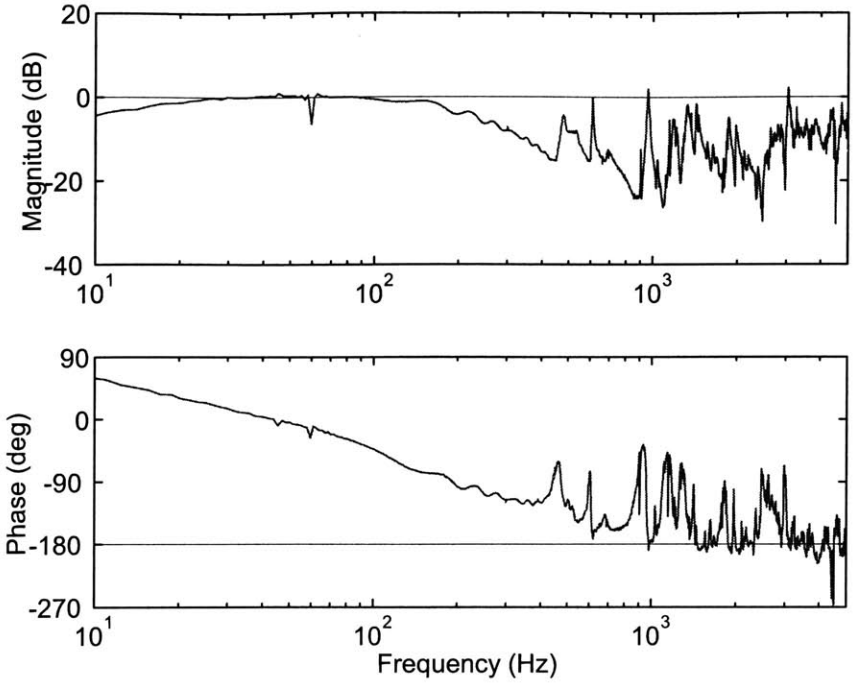

Figure 3-24: Frequency response of loop transfer function for feedforward control.

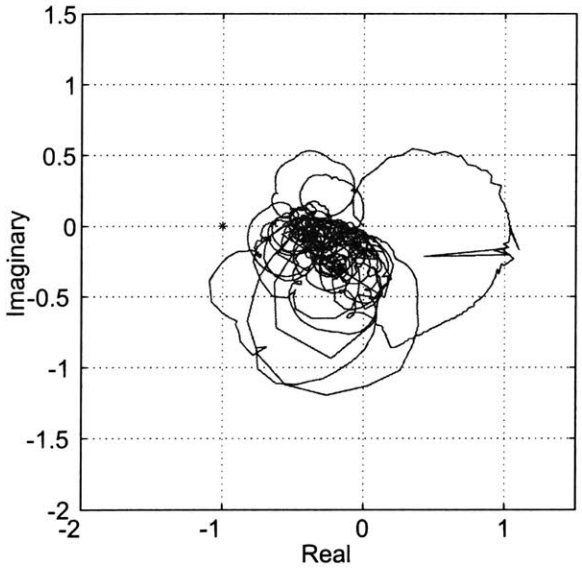

Figure 3-25: Nyquist plot of loop transfer function for feedforward control. "*" represents the critical point -1.

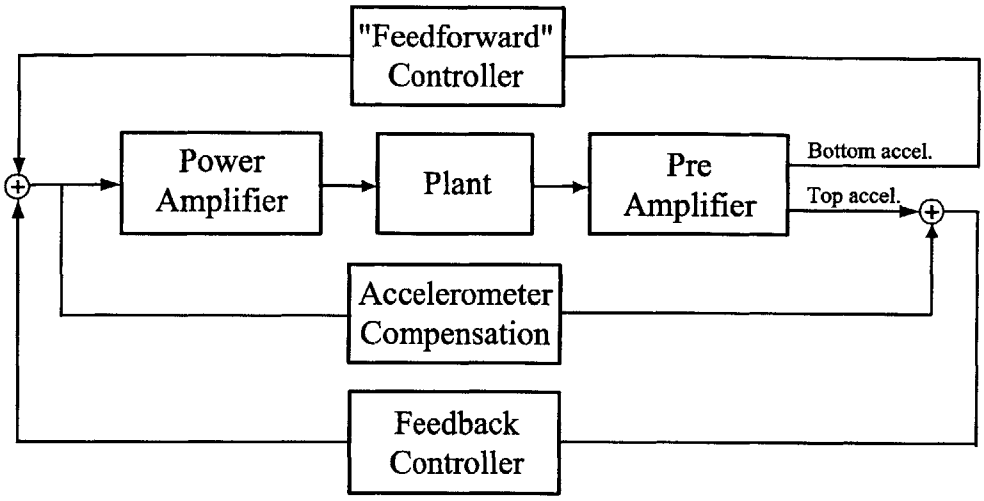

Figure 3-26: Block diagram for the closed-loop system.

compensator into the feedback and feedforward controller as follows.

In the block diagram shown in Figure 3-27, $K_b(s)$, $K_f(s)$, and $C(s)$ are the feedback controller, feedforward controller, and accelerometer compensator, respectively. In addition, u, y_t, and y_b are the controller input, top accelerometer measurement, and bottom accelerometer measurement, respectively. The performance output z is also shown in the figure. Using the first block diagram in Figure 3-27, the relation between u, y_t, and y_b can be written as

$$u = K_f(s)\, y_b + K_b(s)\,[y_t + C(s)u] \ . \tag{3.10}$$

Therefore, u can be expressed in terms of y_t, and y_b, given by

$$u = \frac{K_f(s)}{1 - C(s)\, K_b(s)}\, y_b + \frac{K_b(s)}{1 - C(s)\, K_b(s)}\, y_t \ . \tag{3.11}$$

Also, using the second block diagram in Figure 3-27, u can be expressed in terms of y_t, and y_b as

$$u = K_f'(s)\, y_b + K_b'(s)\, y_t \ , \tag{3.12}$$

where $K_b'(s)$, and $K_f'(s)$ are the equivalent feedback and feedforward controllers that incorporate the accelerometer compensator, respectively. Using Equation 3.11 and 3.12, we can find the expression for $K_b'(s)$, and $K_f'(s)$ as

$$\begin{aligned} K_f' &= \frac{K_f(s)}{1 - C(s)\, K_b(s)} \\ K_b' &= \frac{K_b(s)}{1 - C(s)\, K_b(s)} \ . \end{aligned} \tag{3.13}$$

Figure 3-28 shows the block diagram for feedback controller $K_b'(s)$ and feedforward controller

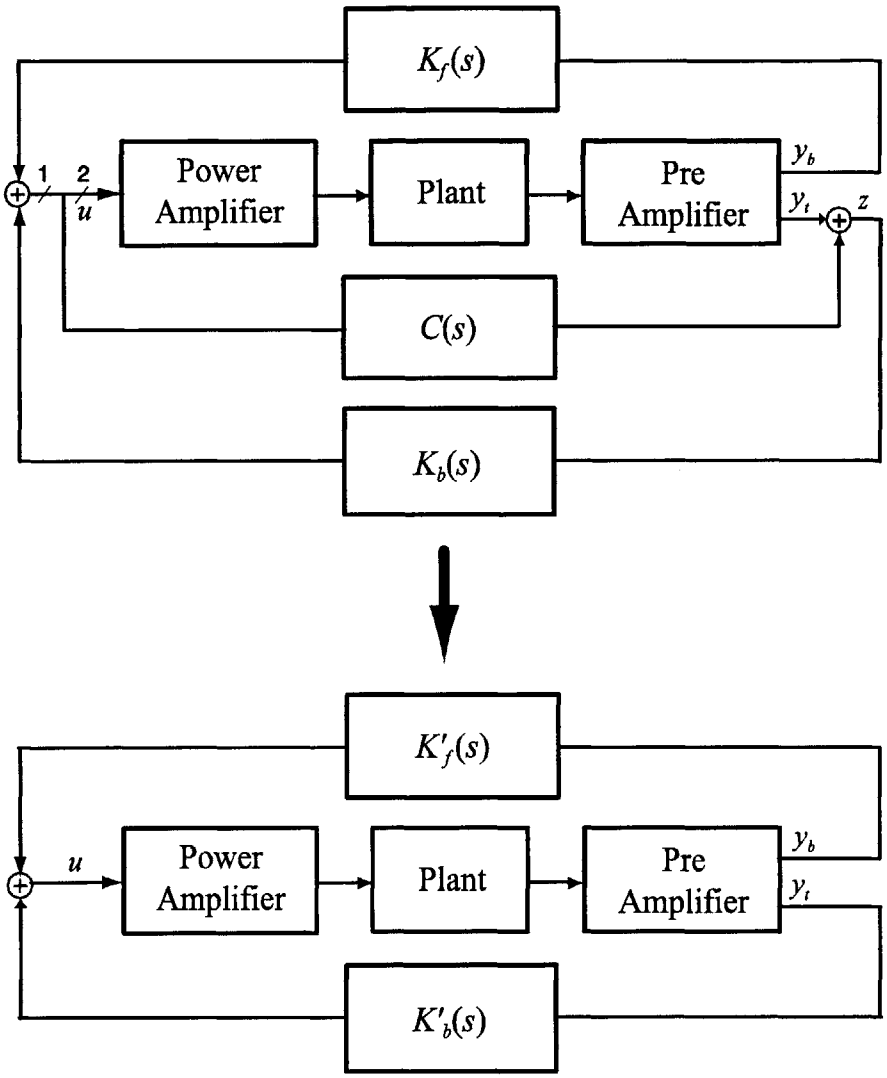

Figure 3-27: Equivalent block diagram for the closed-loop system.

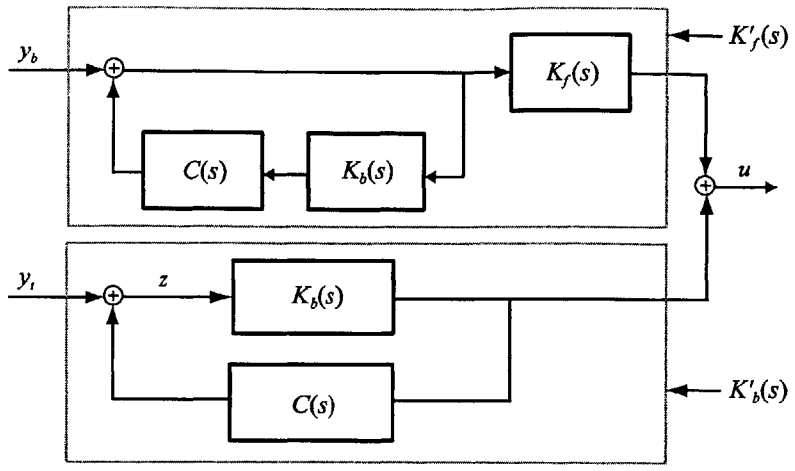

Figure 3-28: Block diagram for feedback and feedforward controller.

$K'_f(s)$. It also shows the relation between $\left(K'_b(s), K'_f(s)\right)$ and $(K_b(s), K_f(s))$; $K'_b(s)$ is a feedback connection of $K_b(s)$ and $C(s)$, while $K'_f(s)$ is $K_f(s)$ multiplied by the feedback connection of $K_b(s)$ and $C(s)$. Let N_b, N_f, and N_c be the number of states needed to implement $K_b(s)$, $K_f(s)$, and $C(s)$, respectively. Then, N'_b and N'_f , which are the numbers of states needed to implement $K'_b(s)$, and $K'_f(s)$, respectively, can be written as

$$\begin{aligned} N'_b &= N_b + N_c \\ N'_f &= N_b + N_c + N_f \,. \end{aligned} \tag{3.14}$$

Therefore, because of the accelerometer compensation to compensate for the undesirable low-frequency dynamics of the active composite panel, the total number of states needed to implement the feedback and feedforward controller is increased by $N_b + 2N_c$ for each panel. If N_p panels are used to cover the surface of the cylindrical shell, the increased number of states is $N_p\,(N_b + 2N_c)$. For example, if $N_p = 55$ (55 panels will be mounted on the shell, eventually), $N_c = 1$, and $N_b = 3$ (typical numbers of states to implement $C(s)$, and $K_b(s)$), then the increased number of states becomes 275. This fact shows how the undesirable panel dynamics makes controller implementation harder, although it can be efficiently compensated for.

It should be remembered that the real performance z to be reduced is not y_t, but $y_t + C(s)\,u$. Therefore, it is better to design $K_b(s)$ and $K_f(s)$ first, based on the plant modified by adding $C(s)$, rather than designing $K'_b(s)$ and $K'_f(s)$ directly. After designing $K_b(s)$ and $K_f(s)$, $K'_b(s)$ and $K'_f(s)$ can be found using Equation 3.13. This approach will be used in Chapter 6, where several feedback and feedforward controllers will be designed and implemented. The controller transfer functions shown in Figure 3-13 and 3-23 are $K_b(s)$ and $K_f(s)$, respectively, not $K'_b(s)$ and $K'_f(s)$. Also, the loop transfer function shown in Figure 3-14 for feedback controller, and the loop transfer function shown in Figure 3-24 for feedforward controller are $(G_{y_t u}(s) + C(s))\,K_b(s)$ and $G_{y_b u}(s)\,K_f(s)$, which are obtained by cutting the loop at "1" in the first block diagram in Figure 3-27, respectively. Here, $G_{y_t u}(s)$ and $G_{y_b u}(s)$ are plant

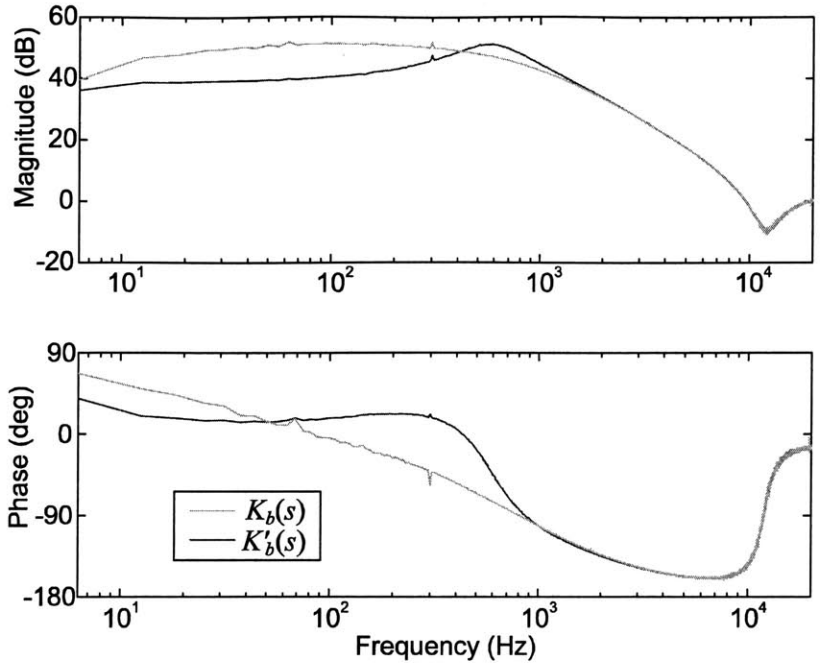

Figure 3-29: Frequency response of feedback controller.

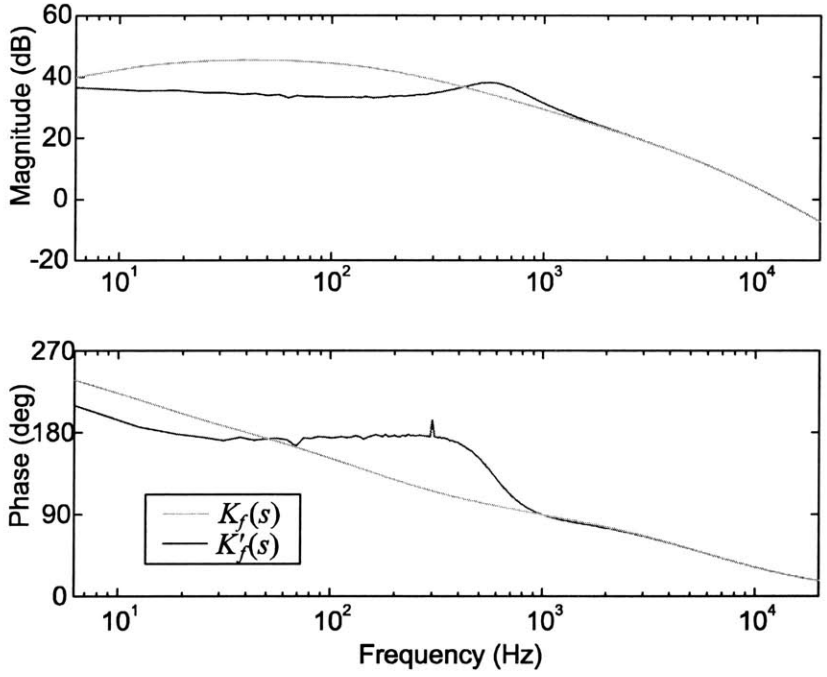

Figure 3-30: Frequency response of feedforward controller.

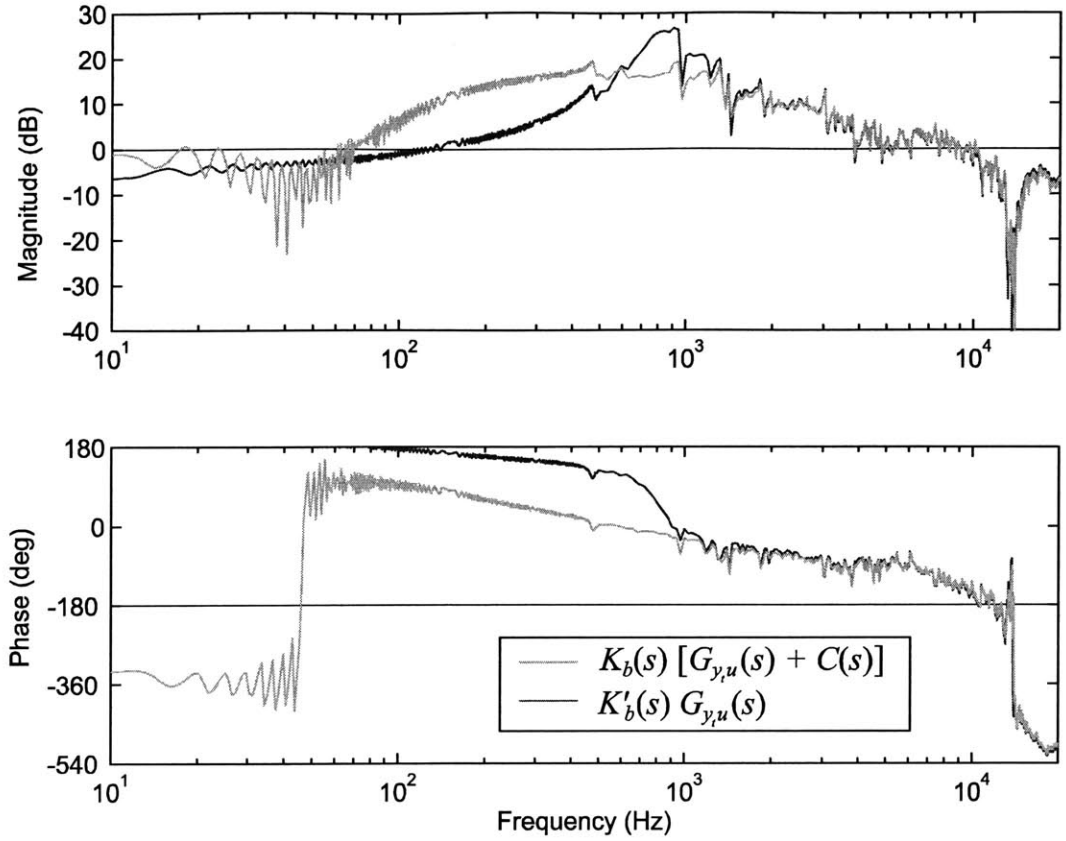

Figure 3-31: Frequency response of loop transfer function for feedback control.

transfer functions from u to y_t and y_b, with power and pre-amplifier included. Figure 3-29 shows the frequency response of $K'_b(s)$, overplotted with $K_b(s)$, while Figure 3-30 shows the frequency response of $K'_f(s)$, overplotted with $K_f(s)$. The resulting loop transfer function $K'_b(s)\,G_{y_t u}(s)$ for feedback control, which is obtained by cutting the loop at "2" in the first block diagram in Figure 3-27, is shown in Figure 3-31, overplotted with $(G_{y_t u}(s) + C(s))\,K_b(s)$. The feedforward controller $K'_f(s)$ should not be used without the feedback controller $K'_b(s)$, because $K'_f(s)$ was derived based on the assumption that the feedback controller is closed. Therefore, the loop transfer function for feedforward control $G_{y_b u}(s)\,K'_f(s)$ doesn't give any meaningful information about the closed-loop system.

3.4 Summary

In this chapter, the design method for local controller architecture was described. The goal of local controller was introduced, and two different feedback control approaches to implement local controllers were explained. The first feedback control approach takes the output of the accelerometers embedded on the outer surface of the panel, which makes the measurement y

directly sense the performance output z, and feeds it back to the panel actuator layer such that the motion of the radiating surface is reduced. On the other hand, the second feedback control approach measures the motion of the surface of the shell, and feeds it back to the panel actuator layer. This approach was denoted as "feedforward," because the measurement strongly depends on the disturbance, although it is not a true feedforward controller.

Design methods for feedback and feedforward controllers, to guarantee high performance and stability, and to compensate for undesirable plant dynamics, were also investigated. The two approaches were first validated on the model developed in Chapter 2. The result of simulating the approaches looks promising and straightforward to implement. However, it turned out that two undesirable panel dynamics, which are low-frequency feedthrough below 500 Hz and high-frequency panel resonance at 12 kHz, critically limit the achievable closed-loop performance. A way to compensate for the undesirable panel dynamics was explored. Modified feedback and feedforward control approaches that efficiently eliminate the effect of panel dynamics were introduced.

In the next chapter, the wavenumber domain feedback controller design methodology, which will be used as a global control architecture, will be presented.

Chapter 4

Global Control Architecture

4.1 Introduction and Objective

During last decade, considerable effort has been devoted to the development and use of structure-mounted sensors, such as accelerometers and piezoelectric ceramics and polymers, for active structural acoustic control (ASAC) [Clark, 1992C], [Maillard, 1997]. Structure-mounted sensors are attractive because they replace error microphones placed in the radiated far field, which is an impractical approach in many applications [Fuller, 1991A].

One of the challenges in using structure-mounted sensors for ASAC is how to extract information about the acoustic response (*i.e.*, acoustic pressure) from the measurement of structural response (*i.e.*, acceleration or strain). Wavenumber domain approaches have been proposed to address this problem [Fuller, 1991A], [Maillard, 1997]. The wavenumber domain approaches are based on the fact that the acoustic pressure in the far field can be entirely described by the corresponding wavenumber components for simple structures such as beams and plates in a infinite baffles [Fahy, 1985]. The first wavenumber-based approach was developed by Fuller and Burdisso [Fuller, 1991A]. They applied this approach numerically to a 2-D baffled simply-supported beam excited by a disturbance at a tonal frequency. By designing a feedforward controller that reduces the target wavenumber component, they showed that the acoustic pressure at the corresponding radiation angle can be reduced. Maillard proposed a new time domain structural sensing technique for predicting wavenumber information and applied it to infinite baffled structural systems in order to reduce the acoustic pressure in the far field [Maillard, 1997]. Scott *et al.* presented a technique to obtain the far-field acoustic power radiated from a one-dimensional structure using PVDF film sensors as low-pass wavenumber filters [Scott, 1997]. Wang presented a wavenumber domain sensing approach using polyvinylidene fluoride (PVDF) films on a beam, and designed feedforward control by defining a cost function as the sum of mean square values of the supersonic wavenumber components [Wang, 1998].

Wavenumber domain approaches can be easily implemented to control a tonal noise disturbance at a single frequency because the target wavenumber is constant. For a broadband disturbance, however, this is not so straightforward, because the target wavenumbers are not constant, but a function of the characteristics of the disturbance spectrum. Filters can be implemented to estimate wavenumber components in the case of broadband disturbance. Maillard proposed the use of filters with an artificial time delay in order to overcome a noncausality problem, so that the wavenumber components for the broadband disturbance can be estimated

[Maillard, 1997]. He showed that, when used in a feedforward control approach, a filter with an artificial time delay yields the same control performance as the filter without delay. However, time delays impose a fundamental limitation on the achievable closed-loop performance using feedback control. So far there has been no successful effort using the wavenumber domain approach for feedback controller design.

Another critical issue in using structure-mounted sensors for ASAC is the selection of control algorithms. Most effort on the control algorithms for ASAC has been focused on the development of efficient feedforward control methods, primarily because the acoustic pressure in general cannot be used as feedback control input, due to the large phase delay in the plant transfer functions. However, the use of structure-mounted sensors has allowed the application of feedback control approach for broadband ASAC. One of the methods used most widely to design feedback control for ASAC is the *radiation filter method*, proposed by Baumann *et al.*[Baumann, 1991]. They approximated the radiation resistance matrix using a rational matrix (radiation filter), which can be implemented by a state-space model, and used the radiation filter as a cost function for a model-based feedback controller. Baumann *et al.* used this concept to design the linear quadratic gaussian (LQG) controller to minimize the acoustic power radiated from clamped beams [Baumann, 1992]. Bingham *et al.* implemented the LQG controller to reduce the sound radiation from a flat composite panel using the radiation filter [Bingham, 1998]. Gibbs *et al.* proposed a method of reduced order modeling/design of radiation filters, termed *radiation modal expansion* [Gibbs, 2000].

The success of applying this method depends on the accuracy of the radiation resistance matrix that can be achieved for the plant, analytically or experimentally. This implies that the method may not be easy to apply for a complex system, for which the radiation resistance matrix is difficult to obtain, although it can be easily applied to a simple structural system, such as beam or plate structures. Even if we can obtain the matrix from an analytic expression (when the structure is simple), or numerical method, such as finite element method or boundary element method (when the structure is complex), it is highly model-dependent, which means that it is not straightforward to implement the radiation filter method experimentally.

In this chapter, a new wavenumber sensing method and its application to feedback controller design for active structural acoustic control is proposed. The approach taken is to minimize the total acoustic power radiated from a vibrating structure in the wavenumber domain, instead of measuring or determining the acoustic pressure at a particular radiation angle. The radiated acoustic power can be expressed as an weighted integral of the square value of the wavenumber components in the supersonic region, in which the structural wavenumber is less than the acoustic wavenumber, so the wavenumber components in the supersonic domain are good candidates for the performance measure. The target wavenumbers in the supersonic domain can be determined when the bandwidth of the disturbance spectrum is known. In general, wavenumber components are complex numbers, complicating their estimation by means of a state-space model. However, because it is the magnitude and not the phase of the wavenumber components that contributes to the radiated noise into the far field, it is shown that a state-space model that estimates the magnitudes of wavenumber components can be found. Once such a state-space model is available, a modern controller design paradigm can be applied to minimize the acoustic power radiated from vibrating structures. This new approach enables the systematic development of state-space models for wavenumber components in the supersonic region, and therefore enables the design of optimal LQG controllers for radiated noise control.

This chapter is organized as follows: Section 4.2 presents the theoretical basis for structural acoustics. Well-known results from the structural acoustic radiation problem will be summarized for later reference. In Section 4.3, the formulation for the new wavenumber domain sensing method and its application to the feedback controller design for ASAC is described. For mathematical convenience, the motivation and the formulation for the new wavenumber sensing method will be first explained for a beam structure in Section 4.3.1. Then, in Section 4.3.2, the formulation for the cylindrical shell is developed. The process of LQG controller design using the new sensing method is also described. Finally, in Section 4.3.3, the application of the new sensing method for the general three-dimensional structures will be discussed.

4.2 Basic Theory of Sound Radiation

In this section, the basic steps to formulate the structural acoustic problem used throughout this chapter are presented. First, the Helmholtz integral equation will be introduced to obtain a representation of the arbitrary acoustic field in terms of surface accelerations and surface pressures. Then, the procedure of reducing it to Rayleigh's formula for planar radiators, as well as the formulation of the acoustic pressure for the infinite baffled cylindrical shell will be described. Finally, the radiated acoustic power, which is used as performance metric in this new approach, will be derived.

4.2.1 The Helmholtz Integral Equation

Figure 4-1 shows the geometry of a generic three-dimensional structure excited by a harmonic force $e^{-j\omega t}$ inside a volume V bounded by surfaces S_0 and S_1, where the inner surface S_0 coincides with the geometry of the structure. The normal displacement and acceleration of the structure are denoted as w and $\ddot{w}$ in the figure, respectively. In the interior of the volume V, the acoustic pressure $p(\mathbf{r},t)$ at field point $\mathbf{r}$ satisfies the wave Equation [Pierce, 1981]

$$\nabla^2 p \;=\; \frac{1}{c^2}\frac{\partial^2 p}{\partial t^2}\,, \tag{4.1}$$

where ∇^2 is the Laplace operator and c is speed of sound in the fluid. For steady-state conditions with a harmonic disturbance $e^{-j\omega t}$, the acoustic pressure $p(\mathbf{r},t)$ can be represented as

$$p(\mathbf{r},t) \;=\; p(\mathbf{r})\,e^{-j\omega t}\,. \tag{4.2}$$

Substituting Equation 4.2 into Equation 4.1 yields the Helmholtz equation [Junger, 1986]

$$\left(\nabla^2 + k^2\right) p \;=\; 0\,, \tag{4.3}$$

where k is the acoustic wavenumber, defined by $k = \omega/c$, and ω is the excitation frequency. The solution of Equation 4.3 is subject to the boundary conditions over the radiating surface S_0

$$(\nabla p)\cdot\mathbf{n} \;=\; -\rho\ddot{w}\,, \tag{4.4}$$

in which $\mathbf{n}$ is the outward normal unit vector at $\mathbf{r}_0$, $\ddot{w}$ is the normal acceleration of the radiator at S_0, and ρ is the density of the fluid. Equation 4.4 is obtained by applying Euler's equation

$\nabla p = -\rho \dot{\mathbf{v}}$ at S_0, where $\mathbf{v}$ is the velocity field, and states that the pressure gradient normal to the radiating surface must be equal to the normal acceleration of the radiator times the fluid density.

The solution of Equation 4.3 is also subject to the boundary condition over the surface S_1. Assuming the outer boundary surface S_1 is located at infinity ($|\mathbf{R}_1| \rightarrow \infty$), the acoustic field p should satisfy the Sommerfeld radiation condition [Junger, 1986], given by

$$\lim_{|\mathbf{R}_1| \rightarrow \infty} |\mathbf{R}_1| \left[jkp(\mathbf{R}_1) - \frac{\partial p(\mathbf{R}_1)}{\partial |\mathbf{R}_1|} \right] = 0 . \tag{4.5}$$

The Sommerfeld radiation condition (Equation 4.5) assumes that the medium surrounding the radiator is unbounded, and that no reflection occurs on the surface S_1. Using the two boundary conditions given in Equations 4.4 and 4.5, the acoustic pressure $p(\mathbf{r})$ at field point $\mathbf{r}$ can be expressed in terms of the surface pressure $p(\mathbf{r}_0)$ and the out-of-plane acceleration field $\ddot{w}(\mathbf{r}_0)$,

$$p(\mathbf{r}) = -\varepsilon \int_{S_0} \left[p(\mathbf{r}_0) \left(\nabla g(|\mathbf{r} - \mathbf{r}_0|) \right) \cdot \mathbf{n} + \rho \ddot{w}(\mathbf{r}_0)\, g(|\mathbf{r} - \mathbf{r}_0|) \right] dS_0 , \tag{4.6}$$

where ε is defined as

$$\varepsilon = \begin{cases} 0 \text{ for } \mathbf{r} \text{ not in } V \\ 1 \text{ for } \mathbf{r} \text{ in } V \\ 2 \text{ for } \mathbf{r} \text{ on } S_0 \text{ or } S_1 \end{cases} , \tag{4.7}$$

and $g(|\mathbf{r} - \mathbf{r}_0|)$ is the free-space Green's function, given by

$$g(|\mathbf{r} - \mathbf{r}_0|) = -\frac{e^{jk|\mathbf{r} - \mathbf{r}_0|}}{4\pi |\mathbf{r} - \mathbf{r}_0|} . \tag{4.8}$$

The free-space Green's function satisfies the inhomogeneous Helmholtz equation,

$$\left(\nabla^2 + k^2 \right) g(|\mathbf{r} - \mathbf{r}_0|) = \delta(\mathbf{r} - \mathbf{r}_0) , \tag{4.9}$$

subject to the Sommerfeld radiation condition [Junger, 1986],

$$\lim_{|\mathbf{r} - \mathbf{r}_0| \rightarrow \infty} |\mathbf{r} - \mathbf{r}_0| \left[jkg(|\mathbf{r} - \mathbf{r}_0|) - \frac{\partial g(|\mathbf{r} - \mathbf{r}_0|)}{\partial |\mathbf{r} - \mathbf{r}_0|} \right] = 0 , \tag{4.10}$$

which is used to ensure that the wave is traveling outward. Here, $\delta(\mathbf{r} - \mathbf{r}_0)$ is the three-dimensional Dirac delta function. Physically, the free-space Green's function $g(|\mathbf{r} - \mathbf{r}_0|)$ represents the acoustic pressure at $\mathbf{r}$ generated by a unit point source at $\mathbf{r}_0$.

The resulting expression in Equation 4.6 is known as the *Helmholtz Integral Equation*, and is used to construct a pressure field in space from the information on the acceleration and pressure field over a surface of the structure.

4.2.2 Rayleigh's Formula for Planar Radiators

As mentioned in Section 4.2.1, both the acceleration and pressure field over the surface of a structure are needed to obtain the acoustic pressure in the medium. Only the acceleration

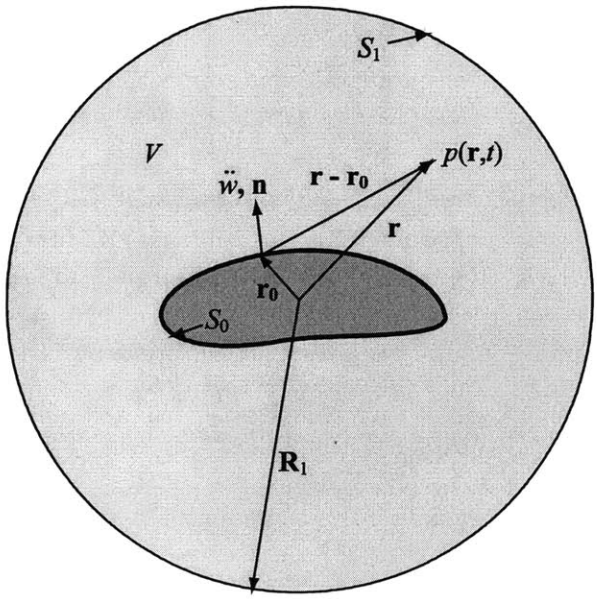

Figure 4-1: Geometry of radiation problem of the general 3-D structure.

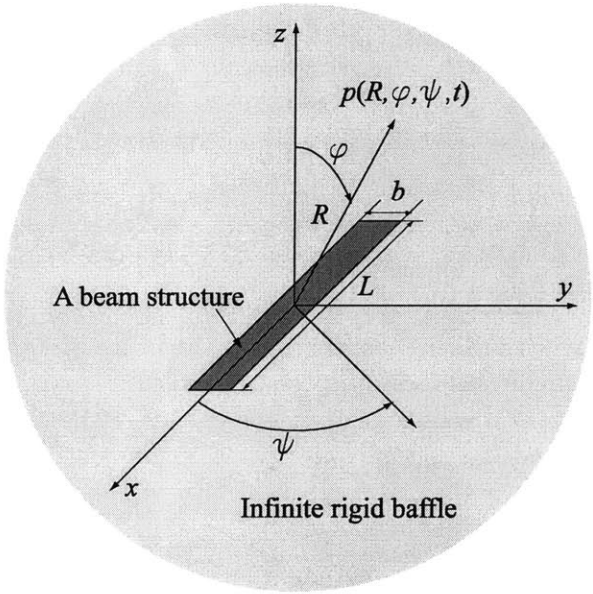

Figure 4-2: Infinite baffled beam structure.

field would be needed if a Green's function $G(\mathbf{r}, \mathbf{r}_0)$ satisfying Neumann's boundary conditions, given by

$$(\nabla G(\mathbf{r}, \mathbf{r}_0)) \cdot \mathbf{n} = 0 , \tag{4.11}$$

could be found. Then, the Helmholtz integral equation in Equation 4.6 would be reduced to a simple integral representation

$$p(\mathbf{r}) = -\rho \int_{S_0} G(\mathbf{r}, \mathbf{r}_0) \ddot{w}(\mathbf{r}_0) \, dS_0 . \tag{4.12}$$

An infinite planar radiator (Figure 4-2) is one of the problems in which a Green's function that satisfies Neumann's boundary conditions in Equation 4.11 can be found. The desired Green's function for an infinite planar radiator is given by [Junger, 1986]

$$G(\mathbf{r}, \mathbf{r}_0) = 2g(|\mathbf{r} - \mathbf{r}_0|) = -\frac{e^{jk|\mathbf{r}-\mathbf{r}_0|}}{2\pi |\mathbf{r} - \mathbf{r}_0|} . \tag{4.13}$$

Therefore, for an infinite planar radiator, the Helmholtz integral equation reduces to

$$p(\mathbf{r}) = \frac{\rho}{2\pi} \int_{S_0} \frac{e^{jk|\mathbf{r}-\mathbf{r}_0|}}{|\mathbf{r} - \mathbf{r}_0|} \ddot{w}(\mathbf{r}_0) \, dS_0 . \tag{4.14}$$

Equation 4.14 states that for planar radiators the acoustic pressure $p(\mathbf{r})$ at field point $\mathbf{r}$ can be solely determined in terms of the out-of-plane acceleration field $\ddot{w}(\mathbf{r}_0)$; the acoustic pressure at the radiating surface is not needed to calculate $p(\mathbf{r})$. Equation 4.14 can be further simplified if $|\mathbf{r}| \gg |\mathbf{r}_0|$. In that case, the resulting equation is called *Rayleigh's formula for planar radiators*, and is given by [Junger, 1986]

$$p(\mathbf{r}) = \frac{\rho}{2\pi |\mathbf{r}|} \int_{S_0} e^{jk|\mathbf{r}-\mathbf{r}_0|} \ddot{w}(\mathbf{r}_0) \, dS_0 . \tag{4.15}$$

Physically, Rayleigh's formula means that a planar source located in an infinite baffle is equivalent to a distribution of point sources.

4.2.3 Cylindrical Radiator

An infinite baffled cylindrical shell is another case in which a Green's function that satisfies the Neumann boundary conditions in Equation 4.11 can be found. Figure 4-3 shows a finite cylindrical shell of length L and radius a in an infinite baffle. Using the simplified Helmholtz integral in Equation 4.12, the acoustic pressure $p(r, \varphi, z)$ in the cylindrical coordinate can be written as

$$p(r, \varphi, z) = -\rho \int_{-L/2}^{L/2} \int_0^{2\pi} G(r, \varphi, z \,;\, a, \varphi_0, z_0) \ddot{w}(\varphi_0, z_0) \, a \, d\varphi_0 dz_0 , \tag{4.16}$$

where (a, φ_0, z_0) is the cylindrical coordinate on the surface of the cylindrical shell, $\ddot{w}(\varphi_0, z_0)$ is the acceleration field at the surface on the radial direction, and $G(r, \varphi, z \,;\, a, \varphi_0, z_0)$ is the Green's function that satisfies the Neumann boundary conditions for the infinite baffled cylin-

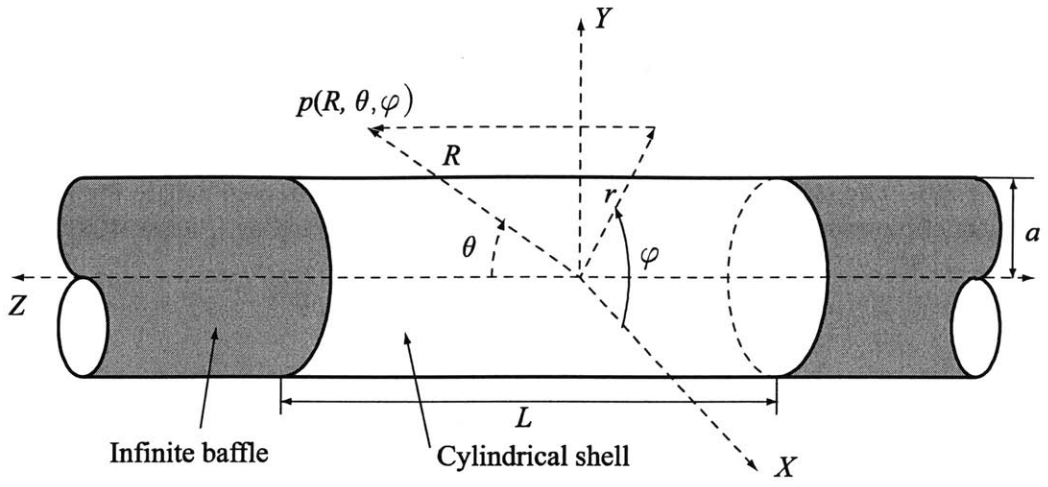

Figure 4-3: Infinite baffled cylindrical shell.

drical shell. The desired Green's function for an infinite baffled cylindrical shell is given by [Maillard, 1997]

$$G\left(r,\varphi,z\,;\,a,\varphi_0,z_0\right) \;=\; \frac{1}{4\pi^2}\sum_{n=0}^{\infty}\frac{2}{\varepsilon_n}\cos\left[n\left(\varphi-\varphi_0\right)\right]\int_{-\infty}^{+\infty} q_n\left(\beta\right)e^{-j\gamma(z-z_0)}d\gamma\;, \tag{4.17}$$

where

$$q_n\left(\beta\right) \;=\; \frac{H_n^{(2)}\left(\beta r\right)}{\beta a H_n^{(2)'}\left(\beta a\right)};\beta \;=\; \sqrt{(k^2-\gamma^2)};\varepsilon_n \;=\; \begin{cases} 2, & n=0 \\ 1, & n>0 \end{cases} \tag{4.18}$$

Here, the functions $H_n^{(2)}\left(x\right)$ and $H_n^{(2)'}\left(x\right)$ denote the nth Hankel function of the second kind and its first derivative, respectively. For far-field radiation, this expression can be further simplified to [Maillard, 1997]

$$G\left(R,\theta,\varphi\,;\,a,\varphi_0,z_0\right) \;\approx\; \frac{e^{-jk(R-z_0\cos\theta)}}{\pi^2 akR\sin\theta}\sum_{n=0}^{\infty}\frac{j^{n+1}}{\varepsilon_n}\frac{\cos\left[n\left(\varphi-\varphi_0\right)\right]}{H_n^{(2)'}\left(ka\sin\theta\right)}\;. \tag{4.19}$$

The next step is to write the acoustic pressure in the far field for the infinite baffled cylindrical shell by substituting Equation 4.19 into Equation 4.16, to yield [Junger, 1986]

$$\begin{aligned} p\left(R,\theta,\varphi\right) \;=\; & -\frac{\rho e^{-jkR}}{\pi^2 kR\sin\theta}\sum_{n=0}^{\infty}\frac{j^{n+1}}{\varepsilon_n H_n^{(2)'}\left(ka\sin\theta\right)} \\ & \times\int_0^{2\pi}\int_{-L/2}^{+L/2}\ddot{w}\left(\varphi_0,z_0\right)\cos\left[n\left(\varphi-\varphi_0\right)\right]e^{jkz_0\cos\theta}d\varphi_0 dz_0\;. \end{aligned} \tag{4.20}$$

4.2.4 Acoustic Power

In general, two acoustic variables are used as performance metrics for active structural acoustic control (ASAC). The first one is the acoustic pressure, which can be obtained by means of the Helmholtz integral equation for the generic three-dimensional structure (Equation 4.6), or the Rayleigh's formula for planar radiators (Equation 4.15) and cylindrical shell structures (Equation 4.20). The other acoustic variable used as the performance metric for ASAC is the radiated acoustic power. The radiated acoustic power Π is defined as [Pierce, 1981]

$$\Pi = \int_S \mathbf{I} \cdot \mathbf{n}\, dS = \int_S (p\mathbf{v}) \cdot \mathbf{n}\, dS\,, \tag{4.21}$$

where $\mathbf{I} = p\mathbf{v}$ is the acoustic intensity, S is a surface enclosing the acoustic source, p and $\mathbf{v}$ are the acoustic pressure and velocity on the surface S, and $\mathbf{n}$ is the unit normal vector pointing out of the volume containing the source. Note that the radiated acoustic power averaged over all time is independent of the surface S over which integration is performed, as long as S encloses the acoustic source, due to the energy conservation in an inviscid acoustic medium. The acoustic intensity over a large sphere of radius R concentric with the source is given by $\frac{|p(R,\varphi,\psi,t)|^2}{2\rho c}$ and, consequently, the acoustic power can be described by

$$\Pi = \int_0^{2\pi} \int_0^{\pi} \frac{|p(R,\varphi,\psi)|^2}{2\rho c} R^2 \sin\varphi\, d\varphi\, d\psi\,, \quad kR \gg 1\,. \tag{4.22}$$

Here, the acoustic pressure p is expressed in terms of spherical coordinates (R,φ,ψ). Throughout this chapter, the acoustic power Π will be used as the performance metric for ASAC.

4.3 Wavenumber Domain Feedback Controller Design

In this section, the formulation for the new wavenumber domain sensing method and its application to the feedback controller design for ASAC is described using an infinite baffled beam and an infinite baffled cylinder as examples.

4.3.1 Beam Structures

Figure 4-2 shows an infinite baffled beam structure of length L and width b, excited by a harmonic force of angular frequency ω. The acoustic pressure $p(R,\varphi,\psi=0,t)$ in the far-field in Figure 4-2 can be found by substituting $|\mathbf{r}| = R$, $|\mathbf{r}-\mathbf{r}_0| \approx R - x\sin\varphi$, and $\int_{S_0} \cdots dS_0 = b\int_{-L/2}^{L/2} \cdots dx$ in Rayleigh's formula for planar radiators (Equation 4.15). The result is

$$p(R,\varphi,\psi=0,t) = \left[\frac{\rho b}{2\pi R}\int_{-L/2}^{L/2} e^{jk(R-x\sin\varphi)}\, \ddot{w}(x)\, dx\right] e^{-j\omega t}\,. \tag{4.23}$$

Note that the structural waves travel solely along the x direction, because the beam structure in Figure 4-2 assumes a constant response along the y direction.

The acoustic pressure in the far-field can also be described as a function of the wavenumber transform of the beam's surface motion. The wavenumber transform in the continuous domain

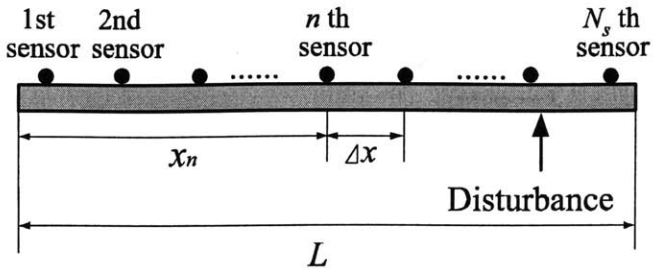

Figure 4-4: Location of evenly distributed sensors mounted on an infinite baffled beam.

of a quantity, in this case the beam's out-of-plane acceleration, is the spatial Fourier transform of that quantity, given by

$$\ddot{W}(k_x) = \int_{-L/2}^{L/2} \ddot{w}(x)\, e^{-jk_x x}\, dx\,. \tag{4.24}$$

In the expression above, k_x is the structural wavenumber along the beam (x direction) and $\ddot{W}(k_x)$ is the wavenumber component corresponding to the acceleration field $\ddot{w}(x)$. Using the wavenumber transform, $p(R,\varphi,\psi=0,t)$ in Equation 4.23 can be written as

$$p(R,\varphi,\psi=0,t) = \frac{\rho b e^{jkR}}{2\pi R}\ddot{W}(k\sin\varphi)\, e^{-j\omega t}\,, \tag{4.25}$$

where $\ddot{W}(k\sin\varphi)$ is the wavenumber component obtained by substituting $k_x = k\sin\varphi$ in Equation 4.24.

For the practical implementation, the discrete wavenumber transform would be preferred to the continuous one because the continuous acceleration field $\ddot{w}(x)$ is often not available. The discrete wavenumber transform corresponding to Equation 4.24 is defined using the discrete Fourier transform,

$$\ddot{W}_d(k_x) = \Delta x \sum_{n=1}^{N_s} \ddot{w}(x_n)\, e^{-jk_x x_n}, \tag{4.26}$$

where x_n is the location of the nth measurement point, Δx is the spacing between measurement points, N_s is the number of measurement points, and $\ddot{W}_d(k_x)$ is the wavenumber component corresponding to the acceleration field $\ddot{w}(x_n)$, $n = 1...N_s$ (Figure 4-4). Also, Δx and x_n are defined as

$$\begin{aligned} \Delta x &= \frac{L}{N_s}\,, \\ x_n &= -\frac{L}{2} + \frac{\Delta x}{2}(2n-1)\,,\ n = 1,2,...,N_s\,. \end{aligned} \tag{4.27}$$

Using the discrete wavenumber transform, the acoustic pressure $p(R,\varphi,\psi=0,t)$ is approximated as

$$p(R,\varphi,\psi=0,t) \approx \frac{\rho b e^{jkR}}{2\pi R}\ddot{W}_d(k\sin\varphi)\, e^{-j\omega t}\,. \tag{4.28}$$

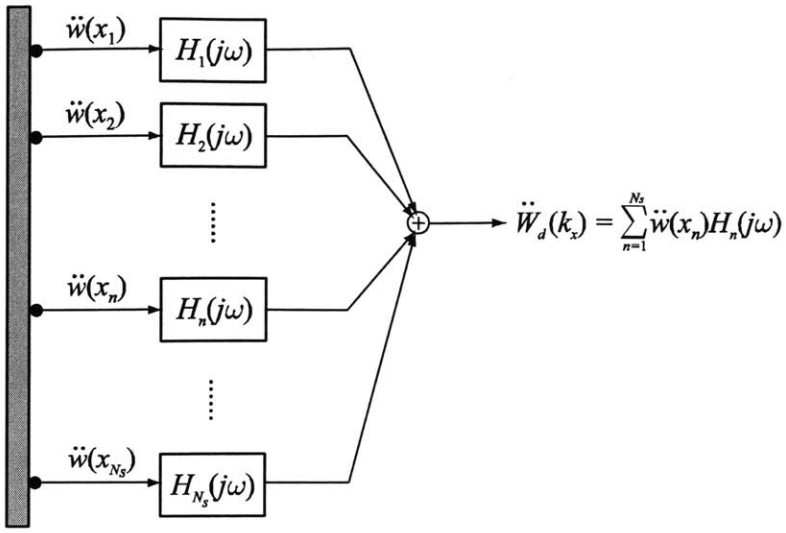

Figure 4-5: Estimating wavenumber components using $H_n(j\omega)$.

Equations 4.25 and 4.28 imply that the far field acoustic pressure in the direction $(\varphi, \psi = 0)$ is completely determined by the corresponding wavenumber component $\ddot{W}(k \sin\varphi)$. It enables structure-mounted sensors, such as accelerometers or piezoelectric ceramics, to be used for ASAC, since one can extract information about the acoustic pressure $p(R, \varphi, \psi = 0, t)$ from the structural response $\ddot{W}(k \sin\varphi)$. Fuller and Burdisso showed numerically that this method can be used for the design of feedforward controllers to reject the noise due to tonal disturbances [Fuller, 1991A]. Also, this approach can be implemented without any difficulty for feedback controller design to reject a tonal disturbance, since the target wavenumber $k_x = (\omega/c) \sin\varphi$ is constant, and one can weight each sensor output signal such that the weighted sum approximates the target wavenumber component $\ddot{W}_d(k \sin\varphi)$.

However, it is difficult to apply this method to the rejection of broadband disturbances, because the target wavenumber $k_x = (\omega/c) \sin\varphi$ is no longer a constant, but a function of the disturbance spectrum. Therefore, the set of wavenumber component to be minimized is written as

$$\begin{aligned} \ddot{W}_d(k_x) &= \Delta x \sum_{n=1}^{N_s} \ddot{w}(x_n)\, e^{-jk_x x_n} = \Delta x \sum_{n=1}^{N_s} \ddot{w}(x_n)\, e^{-jx_n(\omega/c)\sin\varphi} \\ &\triangleq \sum_{n=1}^{N_s} \ddot{w}(x_n)\, H_n(j\omega)\ , \end{aligned} \tag{4.29}$$

where $H_n(j\omega)$ is a filter that is implemented to obtain the wavenumber component $\ddot{W}_d(k_x)$ from sensor measurements. The filter $H_n(j\omega)$ is given by

$$H_n(j\omega) = \Delta x\, e^{-jx_n(\omega/c)\sin\varphi}\ , \tag{4.30}$$

and the procedure to estimate the wavenumber component $\ddot{W}_d(k_x)$ using a filter $H_n(j\omega)$ is shown in Figure 4-5. We see that $H_n(j\omega)$ cannot be implemented if $x_n \sin\varphi$ is less than 0, because it becomes noncausal. Mailard modified $H_n(j\omega)$ by adding a time delay to render it causal [Maillard, 1997]. He showed that the modified filter yields the same control performance as the original filter without delay, when used in a feedforward control approach. However, this technique cannot be applied for feedback control design since time delays impose a fundamental limitation on the achievable closed-loop performance of feedback controllers.

The new wavenumber domain sensing method proposed in this chapter combines the wavenumber domain approach with a feedback control architecture. The basic idea is to use the radiated acoustic power as the performance metric, instead of the acoustic pressure in a specific radiation angle. The radiated acoustic power Π from a vibrating beam structure can be written in terms of the wavenumber transform as [Fahy, 1985]

$$\Pi(\omega) = \frac{\rho k c}{4\pi\omega^2} \int_{-k}^{k} \frac{\left|\ddot{W}(k_x)\right|^2}{\sqrt{k^2 - k_x^2}}\, dk_x \,. \tag{4.31}$$

The physical meaning of Equation 4.31 is presented through an example of an infinitely baffled, simply-supported beam of length L. Assume that the acceleration distribution $\ddot{w}(x)$ is

$$\ddot{w}(x,t) = \begin{cases} \overline{w} \sin\left(\dfrac{n\pi}{L}\right) e^{-j\omega t}, & 0 < x < L,\ n \text{ is an integer} \\ 0, & \text{otherwise} \end{cases} \tag{4.32}$$

The wavenumber transform of $\ddot{w}(x,t)$, computed by using Equation 4.24, is given by [Fahy, 1985]

$$\ddot{W}(k_x) = \int_0^L \ddot{w}(x)\, e^{-jk_x x}\, dx = \overline{w} \frac{\left(\dfrac{n\pi}{L}\right)\left[(-1)^n e^{-jk_x L} - 1\right]}{\left[k_x^2 - \left(\dfrac{n\pi}{L}\right)^2\right]} \,. \tag{4.33}$$

The magnitude squared of $\ddot{W}(k_x)$, $\left|\ddot{W}(k_x)\right|^2$, is plotted in Figure 4-6 for the case $n = 8$. As expected, $\left|\ddot{W}(k_x)\right|^2$ reaches its maximum when k_x is equal to the dominant structural wavenumber, which is $\dfrac{n\pi}{L}$. If the beam were infinitely long without any boundary, the wavenumber transform would be zero everywhere, except at $k_x = \pm\dfrac{n\pi}{L}$. Since the beam structure considered in this example is bounded, its wavenumber spectrum has non-zero values almost everywhere, although its maximum value occurs at $k_x = \pm\dfrac{n\pi}{L}$.

Figure 4-6 also shows the acoustic wavenumber $k = \omega/c$ for an arbitrarily given frequency ω. What Equation 4.31 implies is that, at this given frequency, only *supersonic* wavenumber components satisfying the condition $k_x \leq k$ can radiate sound energy, and that *subsonic* wavenumber components ($k_x \geq k$) simply create near field disturbance of the fluid and don't contribute to the radiated sound power [Fahy, 1985]. This result means that in order to reduce the radiated noise from vibrating beam structures, the supersonic wavenumber components should be reduced. This represents the fundamental difference between vibration control, which tries to reduce *all* the wavenumber components, and structural acoustic control, which tries to

reduce only *supersonic* wavenumber components.

As mentioned earlier, the discrete wavenumber transform $\ddot{W}_d(k_x)$ would be preferred for the practical implementation over the continuous wavenumber transform. In that case, the acoustic power $\Pi(\omega)$ can be approximated using the discrete wavenumber transform, given by

$$\Pi(\omega) \approx \frac{\rho k c}{4\pi\omega^2} \int_{-k}^{k} \frac{\left|\ddot{W}_d(k_x)\right|^2}{\sqrt{k^2 - k_x^2}} dk_x \ . \tag{4.34}$$

Equation 4.34 is obtained by replacing $\ddot{W}(k_x)$ in Equation 4.31 by its discrete counterpart, $\ddot{W}_d(k_x)$. The next step is to implement the integration operation in a real-time. One obvious way is to approximate the integration by a summation, resulting in

$$\Pi_d(\omega) = \frac{\rho k c}{4\pi\omega^2} \sum_{m=1}^{N_\omega} \frac{\left|\ddot{W}_d(k_m)\right|^2}{\epsilon_m \sqrt{k^2 - k_m^2}} \Delta k_m \ , \tag{4.35}$$

where each k_m is a discrete wavenumber that can be obtained from Equation 4.26 using N_s sensors, and Δk_m is the spacing of the discrete wavenumbers (or wavenumber resolution), respectively. They are written as

$$\begin{aligned} k_m &= \left(\frac{2\pi}{\Delta x}\right) \frac{m-1}{N_s} \ (m = 1, 2, ..., N_\omega) \ , \\ \Delta k_m &= \frac{2\pi}{N_s \Delta x} = \frac{2\pi}{L} \ . \end{aligned} \tag{4.36}$$

Also, ϵ_m is defined as

$$\epsilon_m = \begin{cases} 1, & m = 1 \\ \\ \dfrac{1}{2}, & m > 1 \end{cases} \ . \tag{4.37}$$

The discrete wavenumber k_m is selected such that $\ddot{W}_d(k_m)$ and $\ddot{w}(x_n)$ represent a discrete wavenumber transform pair (neglecting a normalization constant). Also, N_ω is the maximum integer that satisfies

$$k_{N_\omega} = \left(\frac{2\pi}{\Delta x}\right) \frac{N_\omega - 1}{N_s} \leq k = \frac{\omega}{c} \ . \tag{4.38}$$

Note that N_ω is a function of the excitation frequency ω. The magnitude squared of $\ddot{W}_d(k_m)$, $\left|\ddot{W}_d(k_m)\right|^2$, is overplotted with $\left|\ddot{W}(k_m)\right|^2$ in Figure 4-7 when the length L is 30 inches, the number of sensors N_s is 20, and n is 8 for the acceleration field in Equation 4.32.

As shown in Figure 4-6, the continuous wavenumber magnitude squared, $\left|\ddot{W}(k_x)\right|^2$, is non-zero almost everywhere, although its main peak occurs at $k_x = \pm\frac{n\pi}{L}$. Therefore, no matter how many sensors are used, spatial aliasing cannot be avoided. However, its effect will be reduced significantly if the spatial sampling wavenumber, $k_s = 2\pi N_s/L$, is greater than twice the dominant structural wavenumber of interest in the control bandwidth. This condition can

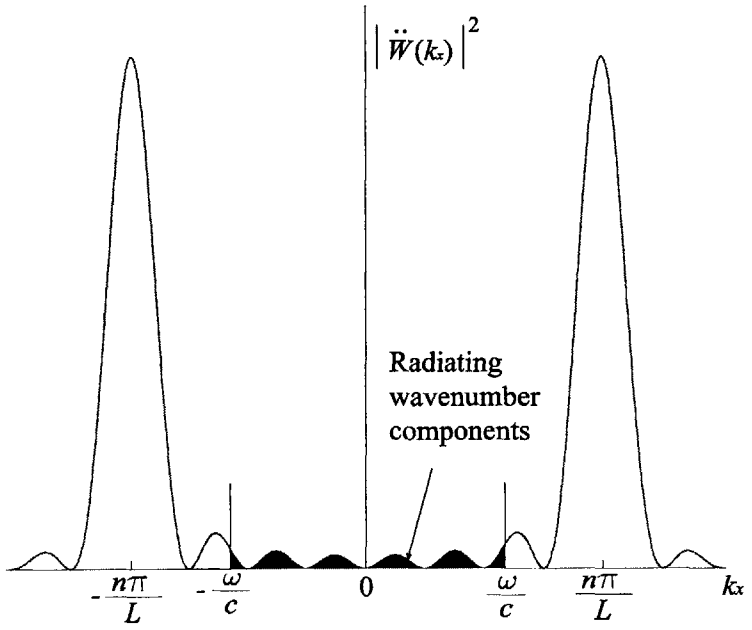

Figure 4-6: The squared wavenumber magnitude of the acceleration field, highlighting the radiating wavenumber components [Fahy, 1985].

be applied to the acceleration field in Equation 4.32, given as

$$k_s = \frac{2\pi N_s}{L} > 2 \times \frac{n\pi}{L} . \tag{4.39}$$

This condition is equivalent to the Sampling Theorem in the time domain [Oppenheim, 1997]. The condition in Equation 4.39 can be simplified to

$$N_s > n , \tag{4.40}$$

where n is the index of the highest mode of interest in the control bandwidth. Therefore, in order to minimize the effect of the spatial aliasing, the number of sensors, N_s, should be greater than the index of the highest mode of interest in the control bandwidth.

As mentioned earlier, Equation 4.31 states that only *supersonic* wavenumber components contribute to sound power radiation. Therefore, the goal of reducing structurally-radiated noise can be achieved by developing a control system that minimizes the supersonic wavenumber components. However, the approximate acoustic power in Equation 4.35 cannot be used as the performance metric for feedback control in a real-time implementation because the number of wavenumber components to be considered, N_ω, is a function of the excitation frequency ω. This difficulty can be overcome when the control bandwidth is finite, which is the case for all the physical problems. Let the control bandwidth be ω_b, that is, the controller is intended to reduce the radiated noise below the frequency ω_b. Then, the estimated radiated acoustic power

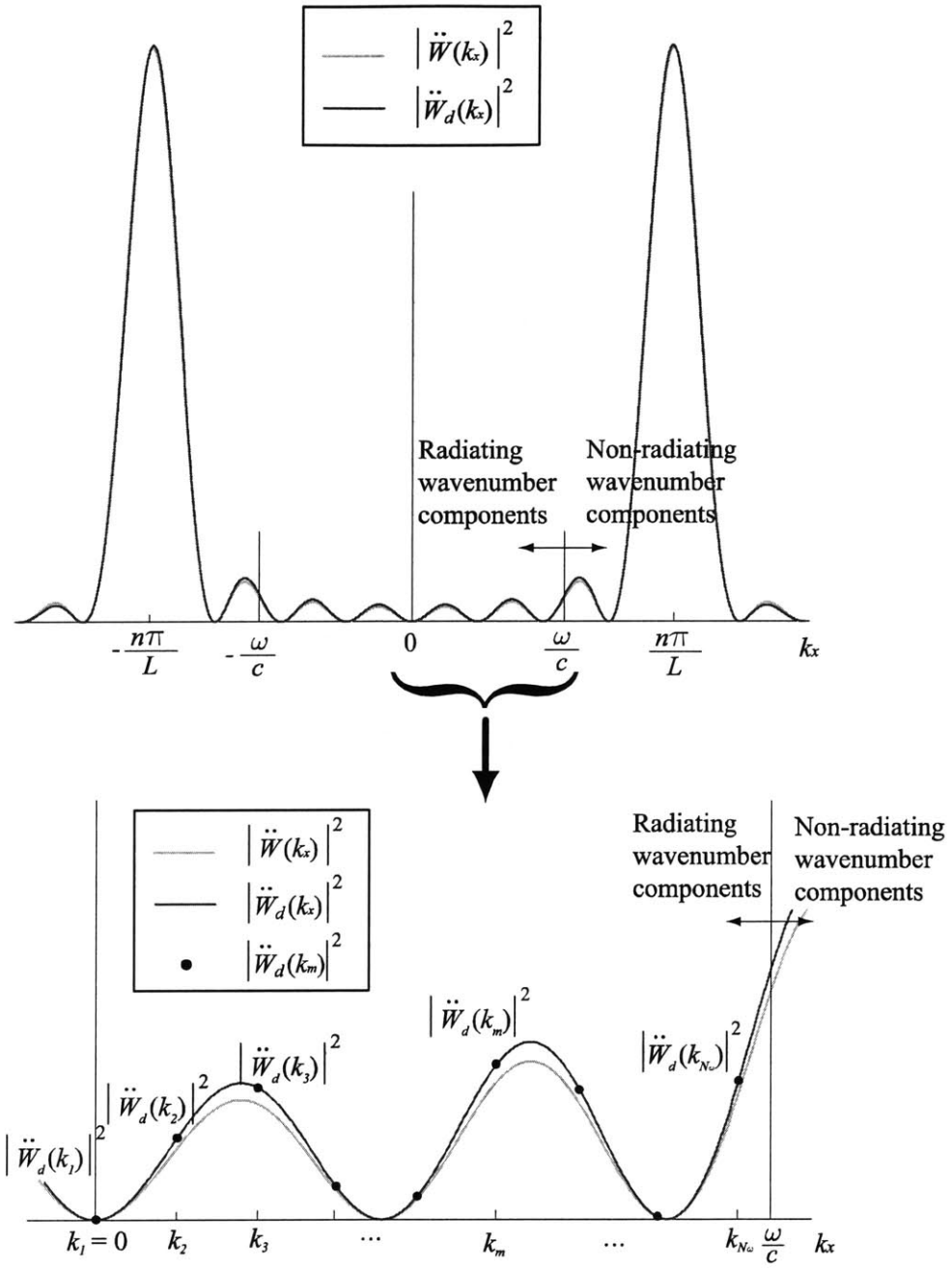

Figure 4-7: The continuous and discrete wavenumber magnitude squared of the acceleration field.

$\widehat{\Pi}(\omega)$ is defined as

$$\widehat{\Pi}(\omega) \triangleq \frac{\rho kc}{4\pi\omega^2} \sum_{m=1}^{N_m} \frac{\left|\ddot{W}_d(k_m)\right|^2}{\epsilon_m \sqrt{k^2 - k_m^2}} \Delta k_m = \sum_{m=1}^{N_m} F(k_m) \left|\ddot{W}_d(k_m)\right|^2 , \tag{4.41}$$

where k_m is the discrete wavenumber obtained from Equation 4.26 using N_s sensors, given as

$$k_m = \left(\frac{2\pi}{\Delta x}\right) \frac{m-1}{N_s} \quad (m = 1, 2, ..., N_m) , \tag{4.42}$$

and N_m is the maximum integer that satisfies

$$k_{N_m} = \left(\frac{2\pi}{\Delta x}\right) \frac{N_m - 1}{N_s} \leq \frac{\omega_b}{c} . \tag{4.43}$$

Note that $\widehat{\Pi}(\omega)$ is obtained from $\Pi_d(\omega)$ by replacing N_ω, which is a function of the excitation frequency ω, by N_m, which is constant. In Equation 4.41, $F(k_m)$ is a weighting function for the wavenumber component $\ddot{W}_d(k_m)$, defined as

$$F(k_m) \triangleq \begin{cases} \dfrac{\rho kc}{4\pi\omega^2} \dfrac{\Delta k_m}{\epsilon_m \sqrt{k^2 - k_m^2}}, & k_m \leq k = \dfrac{\omega}{c} \\ 0, & k_m \geq k = \dfrac{\omega}{c} \end{cases} \tag{4.44}$$

From Equation 4.35 and Equation 4.41, we can see that $\Pi_d(\omega) \leq \widehat{\Pi}(\omega)$ in the control bandwidth ($\omega \leq \omega_b$), since a larger number of wavenumber components are considered in $\widehat{\Pi}(\omega)$. Therefore, if a control system is developed to minimize $\widehat{\Pi}(\omega)$, then $\Pi_d(\omega)$ will also be minimized in the control bandwidth. Since $\Pi_d(\omega)$ is the best approximate measure of the acoustic power when using N_s sensors, the goal of reducing structurally-radiated noise will be achieved if we minimize $\widehat{\Pi}(\omega)$. Furthermore, the feedback control system minimizing $\widehat{\Pi}(\omega)$ can be implemented in real-time without any difficulty because N_m, which is the number of wavenumber components to be considered, is constant and independent of the excitation frequency ω.

As shown above, $F(k_m)$ is a function of the excitation frequency ω. However, an optimal constant weight $\widehat{F}(k_m)$ can be computed such that the difference between $\Pi(\omega)$, the actual acoustic power, and $\widehat{\Pi}(\omega)$, the estimated acoustic power, is minimized. The performance metric to be minimized in order to obtain the optimal constant weight, J_Π, is defined as

$$J_\Pi = \sum_{i=1}^{N} \left|\Pi(\omega_i) - \widehat{\Pi}(\omega_i)\right|^2 = \sum_{i=1}^{N} \left|\Pi(\omega_i) - \sum_{m=1}^{N_m} F(k_m) \left|\ddot{W}_d(k_m)\right|^2\right|^2 . \tag{4.45}$$

Here, ω_i is the frequency at which the acoustic power is computed, and N is the total number of frequency points. Also, J_Π can be written in matrix form as

$$J_\Pi = (\mathbf{b} - \mathbf{A}\mathbf{x})^T (\mathbf{b} - \mathbf{A}\mathbf{x}) , \tag{4.46}$$

where $\mathbf{b}$, $\mathbf{A}$, and $\mathbf{x}$ are defined as

$$\mathbf{b} = \begin{bmatrix} \Pi(\omega_1) \\ \Pi(\omega_2) \\ \vdots \\ \Pi(\omega_N) \end{bmatrix}, \quad \mathbf{x} = \begin{bmatrix} \widehat{F}(k_1) \\ \widehat{F}(k_2) \\ \vdots \\ \widehat{F}(k_{N_m}) \end{bmatrix}, \tag{4.47}$$

$$\mathbf{A} = \begin{bmatrix} \left|\ddot{W}_d(k_1,\omega_1)\right|^2 & \left|\ddot{W}_d(k_2,\omega_1)\right|^2 & \cdots & \left|\ddot{W}_d(k_{N_m},\omega_1)\right|^2 \\ \left|\ddot{W}_d(k_1,\omega_2)\right|^2 & \left|\ddot{W}_d(k_2,\omega_2)\right|^2 & \cdots & \left|\ddot{W}_d(k_{N_m},\omega_2)\right|^2 \\ \vdots & \vdots & \ddots & \vdots \\ \left|\ddot{W}_d(k_1,\omega_N)\right|^2 & \left|\ddot{W}_d(k_2,\omega_N)\right|^2 & \cdots & \left|\ddot{W}_d(k_{N_m},\omega_N)\right|^2 \end{bmatrix}.$$

The solution $\mathbf{x}$ that minimizes J_Π in Equation 4.46,

$$\mathbf{x} = \left(\mathbf{A}^T\mathbf{A}\right)^{-1}\mathbf{A}^T\mathbf{b}\,, \tag{4.48}$$

represents the set of constant optimal weights $\widehat{F}(k_m)$ [Strang, 1986].

Generally, the acoustic power is an increasing function of the excitation frequency ω, because the acoustic pressure is proportional to ω^2. Therefore, the optimization in Equation 4.45 may achieve its goal by reducing J_Π in the high frequency beyond the bandwidth of interest, where $\Pi(\omega)$ is dominant. In order to avoid this effect, a frequency weighting function for J_Π can be used so that the difference between the actual and the estimated acoustic power is minimized in the bandwidth of interest. The new frequency weighted performance metric, $\overline{J_\Pi}$, is written as

$$\overline{J_\Pi} = \sum_{i=1}^{N} |H(j\omega_i)|^2 \left|\Pi(\omega_i) - \widehat{\Pi}(\omega_i)\right|^2 = (\mathbf{Wb} - \mathbf{WAx})^T(\mathbf{Wb} - \mathbf{WAx})\,, \tag{4.49}$$

where $H(j\omega)$ is the frequency weighting function for the performance metric, and $\mathbf{W}$ is a diagonal matrix of $|H(j\omega)|$ evaluated at discrete frequencies, given by

$$\mathbf{W} = \begin{bmatrix} |H(j\omega_1)| & 0 & \cdots & 0 \\ 0 & |H(j\omega_2)| & \cdots & 0 \\ \vdots & \vdots & \ddots & \vdots \\ 0 & 0 & \cdots & |H(j\omega_N)| \end{bmatrix}. \tag{4.50}$$

The optimal constant weights for the wavenumber components, $\widehat{F}(k_m)$, that minimizes $\overline{J_\Pi}$ in Equation 4.49 can be expressed in matrix form as

$$\mathbf{x} = \begin{bmatrix} \widehat{F}(k_1) \\ \widehat{F}(k_2) \\ \vdots \\ \widehat{F}(k_{N_m}) \end{bmatrix} = \left(\mathbf{A}^T\mathbf{W}^T\mathbf{WA}\right)^{-1}\mathbf{A}^T\mathbf{W}^T\mathbf{Wb}\,. \tag{4.51}$$

Once the set of optimal constant weights is found, one can estimate the acoustic power from a vibrating structure and use it as the performance metric in an optimal LQG controller design. It should be noted that one should obtain the actual acoustic power, $\Pi(\omega)$, by measurements or simulation, to find the optimal constant weight; the optimal constant weights cannot be found with insufficient information on $\Pi(\omega)$. This may occur for complex structures, or when few measurements of the acoustic pressure in the far field are available. In those cases, the weights can be used as design knobs, so that the resulting closed-loop response is satisfactory.

Next, the procedure to estimate $\ddot{W}_d(k_m)$ from sensor measurements $\ddot{w}(x_n)$ is presented. From Equation 4.26, $\ddot{W}_d(k_m)$ can be written as

$$\ddot{W}_d(k_m) = \Delta x \sum_{n=1}^{N_s} \ddot{w}(x_n)\, e^{-jk_m x_n} = \left[\phi_m^1\ \phi_m^2\ \cdots\ \phi_m^{N_s}\right] \left\{ \begin{array}{c} \ddot{w}(x_1) \\ \ddot{w}(x_2) \\ \vdots \\ \ddot{w}(x_{N_s}) \end{array} \right\} \triangleq \Phi_m \ddot{\mathbf{w}}\,, \tag{4.52}$$

where

$$\Phi_m = \left[\phi_m^1\ \phi_m^2\ \cdots\ \phi_m^{N_s}\right];\ \phi_m^n = \Delta x\, e^{-jk_m x_n};\ \ddot{\mathbf{w}} = \left\{\ddot{w}(x_1)\ \ddot{w}(x_2)\ \cdots\ \ddot{w}(x_{N_s})\right\}^T\,. \tag{4.53}$$

In general, Φ_m is a complex vector, which cannot be used in a state-space formulation. However, from Equation 4.41, it can be observed that it is the magnitude of the wavenumber component that is needed in order to estimate the acoustic power. Using this fact, $\widehat{\ddot{W}}_d(k_m)$ can be computed such that $\left|\ddot{W}_d(k_m)\right| = \left|\widehat{\ddot{W}}_d(k_m)\right|$, yielding

$$\begin{aligned} \widehat{\ddot{W}}_d(k_m) &= \left\{ \begin{array}{ll} \left[\begin{array}{cccc} \mathrm{Re}\left(\phi_m^1\right) & \mathrm{Re}\left(\phi_m^2\right) & \cdots & \mathrm{Re}\left(\phi_m^{N_s}\right) \\ \mathrm{Im}\left(\phi_m^1\right) & \mathrm{Im}\left(\phi_m^2\right) & \cdots & \mathrm{Im}\left(\phi_m^{N_s}\right) \end{array} \right] \left\{ \begin{array}{c} \ddot{w}(x_1) \\ \ddot{w}(x_2) \\ \vdots \\ \ddot{w}(x_{N_s}) \end{array} \right\}, & \text{if } \phi_m^n \text{ is complex} \\ \left[\phi_m^1\ \phi_m^2\ \cdots\ \phi_m^{N_s}\right] \left\{ \begin{array}{c} \ddot{w}(x_1) \\ \ddot{w}(x_2) \\ \vdots \\ \ddot{w}(x_{N_s}) \end{array} \right\}, & \text{if } \phi_m^n \text{ is real} \end{array} \right. \\ &\triangleq \widehat{\Phi}_m \ddot{\mathbf{w}}\,. \end{aligned} \tag{4.54}$$

Now, assume a state-space model for the plant is available either by finite element modeling or experimental system identification, given by

$$\begin{aligned} \dot{\mathbf{x}} &= \mathbf{A}\mathbf{x} + \mathbf{B_1}\mathbf{f} + \mathbf{B_2}\mathbf{u} \\ \mathbf{y} &= \mathbf{C}\mathbf{x} \end{aligned} \tag{4.55}$$

where $\mathbf{x}$ is the state vector, $\mathbf{f}$ is the disturbance, and $\mathbf{u}$ is the control input. Also, $\mathbf{y}$ is the sensor output, defined as

$$\mathbf{y} = \ddot{\mathbf{w}} = \left\{\ddot{w}(x_1)\ \ddot{w}(x_2)\ \cdots\ \ddot{w}(x_{N_s})\right\}^T\,. \tag{4.56}$$

Using Equation 4.55, the performance metric $\mathbf{z}$ can be defined as

$$\mathbf{z} = \begin{bmatrix} q_1 \widehat{\ddot{W}}_d(k_1) \\ q_2 \widehat{\ddot{W}}_d(k_2) \\ \vdots \\ q_{N_m} \widehat{\ddot{W}}_d(k_{N_m}) \end{bmatrix} = \begin{bmatrix} q_1 & 0 & & \cdots & & 0 \\ 0 & q_2 & & & & \\ & & q_2 & & & \\ \vdots & & & \ddots & & \vdots \\ & & & & q_{N_m} & 0 \\ 0 & & & \cdots & 0 & q_{N_m} \end{bmatrix} \begin{bmatrix} \widehat{\Phi}_1 \\ \widehat{\Phi}_2 \\ \vdots \\ \widehat{\Phi}_{N_m} \end{bmatrix} \mathbf{y} = \mathbf{Q}\widehat{\Phi}\mathbf{C}\mathbf{x}\,, \quad (4.57)$$

where q_m is the weight for $\widehat{\ddot{W}}_d(k_m)$, and $\mathbf{Q}$ and $\widehat{\Phi}$ are defined as

$$\mathbf{Q} = \begin{bmatrix} q_1 & 0 & & \cdots & & 0 \\ 0 & q_2 & & & & \\ & & q_2 & & & \\ \vdots & & & \ddots & & \vdots \\ & & & & q_{N_m} & 0 \\ 0 & & & \cdots & 0 & q_{N_m} \end{bmatrix}, \quad \widehat{\mathbf{\Phi}} = \begin{bmatrix} \widehat{\Phi}_1 \\ \widehat{\Phi}_2 \\ \vdots \\ \widehat{\Phi}_{N_m} \end{bmatrix}. \quad (4.58)$$

Note that $\widehat{\Phi}$ is in general a $2N_m - 1$ by N_s matrix, because $\widehat{\Phi}_1$ is a real row vector ($k_1 = 0$), while $\widehat{\Phi}_m$ ($m \neq 1$) is a 2 by 1 matrix. From Equation 4.57, we see that

$$\|\mathbf{z}\|_2^2 = \sum_{m=1}^{N_m} q_m^2 \left|\widehat{\ddot{W}}_d(k_m)\right|^2 \quad (4.59)$$

is the estimated acoustic power $\widehat{\Pi}$ if $q_m = \sqrt{\widehat{F}(k_m)}$ is used. Since a state-space model to estimate the acoustic power is now available, one can use a modern control design paradigm, such as H_2, H_∞, LQG, *etc.*, to minimize the acoustic power radiated from vibrating structures. If we cannot find the optimal constant weight $\widehat{F}(k_m)$, primarily due to the insufficient information on the actual acoustic power Π, we can use q_m as design knobs, as mentioned earlier, so that the resulting closed-loop performance is satisfactory.

Figure 4-8 shows the block diagram of a wavenumber domain LQG controller. The sensor output $\mathbf{y}$ is processed at the discrete wavenumber transform matrix, $\widehat{\mathbf{\Phi}}$, followed by the performance weighting matrix, $\mathbf{Q}$. The performance variable in the LQG controller is $\mathbf{z} = \mathbf{Q}\widehat{\mathbf{\Phi}}\mathbf{y}$, whose magnitude square is the estimated acoustic power $\widehat{\Pi}$. Minimizing radiated acoustic power is achieved by minimizing the performance variable.

As shown above, by using the new wavenumber domain sensing method, we can generate a state-space model to estimate the radiated acoustic power, and we can apply a modern control design method to the model such that the acoustic power is minimized. One of the advantages of the new sensing method is that it doesn't require additional modeling process to determine the acoustic power from sensor measurements. Thus, there is a significant difference between this approach and the radiation filter method [Baumann, 1991], which needs the radiation filter to be modeled from an analytic expression (when the structure is simple), or a numerical method such as finite element or boundary element methods (when the structure is complex). Another important advantage of the new sensing method is that the number of transfer functions needed

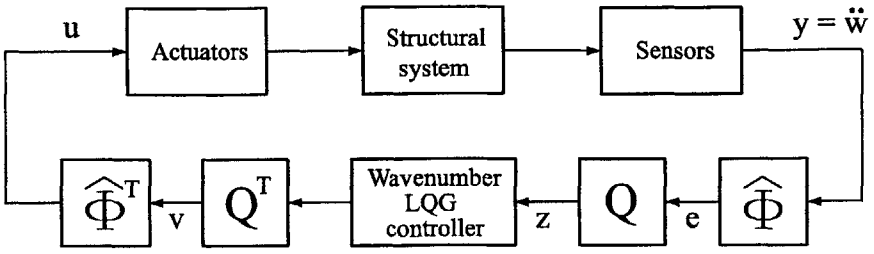

Figure 4-8: Block diagram of the wavenumber LQG controller implementation.

to be identified to get a plant model for controller design is much reduced. When N_m (the number of supersonic wavenumber components in the control bandwidth) is less than N_s (the number of sensors), one needs only to perform the system identification on the transfer matrix from $\mathbf{v}$ to $\mathbf{e}$ ($(2N_m-1)\times(2N_m-1)$ matrix), not from $\mathbf{u}$ to $\mathbf{y}$ ($N_s \times N_s$ matrix) in Figure 4-8, using the wavenumber sensing method. By doing that, the number of transfer functions that should be identified is significantly reduced from N_s^2 (from $\mathbf{u}$ to $\mathbf{y}$) to $(2N_m-1)^2$ (from $\mathbf{v}$ to $\mathbf{e}$). In the next chapter, numerical examples of a beam structure with 10 sensor-actuator pairs are presented ($N_s = 10$). As shown in the next chapter, it was found that considering three wavenumber components was enough to reduce the radiated noise from the vibrating beam structure in the examples ($N_m = 3$). Therefore, in this case, the number of transfer functions that should be identified is significantly reduced from 100 $\left(= N_s^2\right)$ to 25 $\left(= (2N_m-1)^2\right)$.

4.3.2 Cylindrical Shell

In this section, the formulation of the new wavenumber domain sensing method is developed for a cylindrical shell, such as the finite cylindrical shell of length L and radius a in an infinite baffle shown in Figure 4-3. The continuous wavenumber transform of the acceleration is written as a two-dimensional Fourier transform

$$\ddot{W}(k_\varphi, k_z) = \frac{1}{2\pi}\int_{-L/2}^{+L/2}\int_0^{2\pi} \ddot{w}(\varphi, z)\, e^{-jk_\varphi\varphi} e^{-jk_z z}\, d\varphi\, dz\,, \tag{4.60}$$

where $\ddot{w}(\varphi, z)$ is the acceleration field of the cylindrical shell in the radial direction, $\ddot{W}(k_\varphi, k_z)$ is the wavenumber component corresponding to the acceleration field $\ddot{w}(\varphi, z)$, and k_φ and k_z are the circumferential and axial wavenumbers, respectively. Note that k_φ is an integer, since $\ddot{w}(\varphi, z) = \ddot{w}(\varphi + 2\pi, z)$, and therefore $k_\varphi = n$ will be used from this point forward. As in Section 4.3.1, using the discrete Fourier transform, the discrete wavenumber transform is written as

$$\ddot{W}_d(n, k_z) = \frac{1}{2\pi}\Delta\varphi\Delta z \sum_{l=1}^{N_c}\sum_{s=1}^{N_a} \ddot{w}(\varphi_l, z_s)\, e^{-jn\varphi_l} e^{-jk_z z_s}\,, \tag{4.61}$$

where z_s, Δz, and N_a are the sth location, the spacing, and the number of measurement points in the axial direction, while φ_l, $\Delta\varphi$, and N_c, are the lth location, the spacing, and the

number of measurement points in the circumferential direction, respectively. These are shown in Figure 4-9, and are written as

$$\begin{aligned} \Delta z &= \frac{L}{N_a},\ z_s = -\frac{L}{2} + \frac{\Delta z}{2}(2s-1) \\ \Delta\varphi &= \frac{2\pi}{N_c},\ \varphi_l = \frac{\pi}{N_c} + \Delta\varphi(l-1)\ . \end{aligned} \tag{4.62}$$

Using the wavenumber transform $\ddot{W}(n,k_z)$, the acoustic pressure in the far field for the baffled cylindrical shell can be rewritten as [Song, 2001]

$$p(R,\theta,\varphi) = -\frac{\rho e^{-jkR}}{\pi kR\sin\theta}\sum_{n=-\infty}^{\infty}\frac{j^{|n|+1}}{H_{|n|}^{(2)'}(ka\sin\theta)}\ddot{W}(n,-k\cos\theta)\,e^{jn\varphi}\ , \tag{4.63}$$

where $H_n^{(2)'}(x)$ denotes the first derivative of the nth Hankel function of the second kind, and $\ddot{W}(n,-k\cos\theta)$ is wavenumber component obtained by substituting $k_z = -k\cos\theta$ in Equation 4.60. As in Section 4.3.1, the discrete wavenumber transform in Equation 4.61 would be preferred for the practical implementation, and to that end the acoustic pressure $p(R,\theta,\varphi)$ is approximated using the discrete wavenumber transform,

$$p(R,\theta,\varphi) \approx -\frac{\rho e^{-jkR}}{\pi kR\sin\theta}\sum_{n=-\infty}^{\infty}\frac{j^{|n|+1}}{H_{|n|}^{(2)'}(ka\sin\theta)}\ddot{W}_d(n,-k\cos\theta)\,e^{jn\varphi}\ . \tag{4.64}$$

It can be observed from Equations 4.63 and 4.64 that the far field acoustic pressure in the direction (θ,φ) is determined by the corresponding wavenumber component in the axial direction $k_z = -k\cos\theta$, and by *all* the circumferential wavenumber components. This indicates that, compared to the planar radiator, it is less clear which wavenumber components to be controlled in order to reduce the structurally-radiated noise for the cylindrical radiator. However, as shown in Figure 4-10, the weighting function $j^{n+1}/H_n^{(2)'}(ka\sin\theta)$ of the wavenumber component $\ddot{W}(n,-k\cos\theta)$ decreases very fast as n increases. Therefore, the fact that *all* the circumferential wavenumber components contribute to the sound power radiation will not cause any difficulty for real implementation, since only a small number is responsible for most of the acoustic power.

As mentioned earlier, it is difficult to use the acoustic pressure as the performance metric for feedback control of a broad-band disturbance. The new wavenumber domain sensing method proposed in this chapter combines the wavenumber domain approach with a feedback control architecture, by using the radiated acoustic power as the performance metric, instead of the acoustic pressure in the specific radiation angle. Using the wavenumber transform, the radiated acoustic power Π from a vibrating cylindrical shell can be written as [Song, 2001]

$$\Pi(\omega) = \frac{\rho ck}{\pi\omega^2}\sum_{n=-\infty}^{\infty}\int_{-k}^{k}\frac{\left|\ddot{W}(n,k\cos\theta)\right|^2}{\left|H_{|n|}^{(2)'}\left(a\sqrt{k^2-k_z^2}\right)\right|^2(k^2-k_z^2)}dk_z\ . \tag{4.65}$$

Following the same procedure used in Section 4.3.1, the acoustic power in Equation 4.65 can

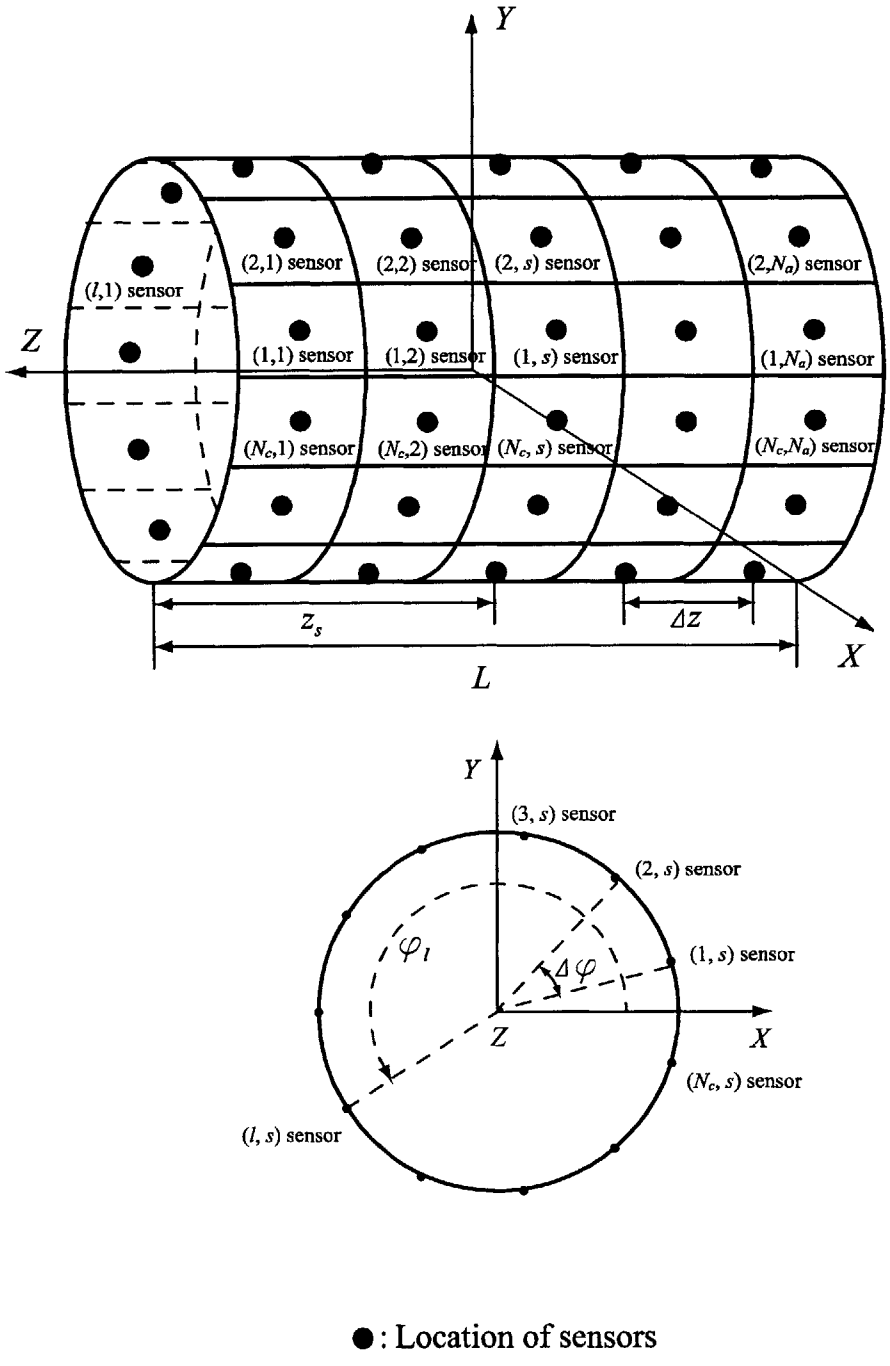

Figure 4-9: Location of measurement points distributed over the cylindrical shell.

be approximated using the discrete wavenumber transform,

$$\Pi_d(\omega) = \frac{2\rho ck}{\pi\omega^2} \sum_{n=0}^{N_n-1} \sum_{m=1}^{N_\omega} \frac{\left|\ddot{W}_d(n,k_m)\right|^2}{\varepsilon_n \epsilon_m \left|H_n^{(2)'}\left(a\sqrt{k^2-k_m^2}\right)\right|^2 (k^2-k_m^2)} \Delta k_m \,. \tag{4.66}$$

In Equation 4.66, k_m is discrete wavenumber in the axial direction, which can be obtained from Equation 4.61 using N_a sensors in the axial direction, and Δk_m is the spacing of the discrete wavenumbers (or wavenumber resolution), respectively. These quantities are written as

$$\Delta k_m = \frac{2\pi}{N_a \Delta z} = \frac{2\pi}{L}, \; k_m = \left(\frac{2\pi}{\Delta z}\right) \frac{m-1}{N_a} \;\; (m = 1, 2, ..., N_\omega) \,. \tag{4.67}$$

Also, N_ω is the maximum integer satisfying

$$k_{N_\omega} = \left(\frac{2\pi}{\Delta z}\right) \frac{N_\omega - 1}{N_a} \;\leq\; k = \frac{\omega}{c} \,, \tag{4.68}$$

and N_n is the number of circumferential wavenumber components considered in the approximation of $\Pi(\omega)$. Equation 4.65 says that all the circumferential wavenumber components contribute to the sound power radiation, while only supersonic axial wavenumber components do. As pointed in Section 4.3.1, the approximate acoustic power in Equation 4.66 cannot be used as the performance metric for feedback control in a real-time implementation, because the number of wavenumber components to be considered, N_ω, is a function of the excitation frequency ω. Therefore, the new sensing method proposed in this chapter uses the *estimated* acoustic power (Equation 4.69), as the performance metric for feedback control implementation, given by

$$\begin{aligned} \widehat{\Pi}(\omega) &= \frac{2\rho ck}{\pi\omega^2} \sum_{n=0}^{N_n-1} \sum_{m=1}^{N_m} \frac{\left|\ddot{W}_d(n,k_m)\right|^2}{\varepsilon_n \epsilon_m \left|H_n^{(2)'}\left(a\sqrt{k^2-k_m^2}\right)\right|^2 (k^2-k_m^2)} \Delta k_m \\ &= \sum_{n=0}^{N_n-1} \sum_{m=1}^{N_m} F(n,k_m) \left|\ddot{W}_d(n,k_m)\right|^2 \,. \end{aligned} \tag{4.69}$$

In the expression above, k_m is discrete wavenumber in the axial direction, which can be obtained from Equation 4.61 using N_a sensors in the axial direction, as

$$k_m = \left(\frac{2\pi}{\Delta z}\right) \frac{m-1}{N_a} \;\; (m = 1, 2, ..., N_m) \,, \tag{4.70}$$

and N_m is the maximum integer that satisfies

$$k_{N_m} = \left(\frac{2\pi}{\Delta z}\right) \frac{N_m - 1}{N_a} \;\leq\; \frac{\omega_b}{c} \,. \tag{4.71}$$

Here, ω_b is the bandwidth of interest. Note that $\widehat{\Pi}(\omega)$ is obtained from $\Pi_d(\omega)$ by replacing N_ω,

which is a function of the excitation frequency ω, by N_m, which is constant. In Equation 4.69, $F(n,k_m)$ is a weighting function for the wavenumber component $\ddot{W}_d(n,k_m)$, defined as

$$F(n,k_m) = \begin{cases} \dfrac{2\rho ck}{\pi\omega^2} \dfrac{\Delta k_m}{\varepsilon_n \epsilon_m \left| H_n^{(2)'}\left(a\sqrt{k^2-k_m^2}\right)\right|^2 (k^2-k_m^2)} , & k_m \le k = \dfrac{\omega}{c} \\ 0 , & k_m \ge k = \dfrac{\omega}{c} \end{cases} \tag{4.72}$$

Although $F(n,k_m)$ is a function of excitation frequency ω, we can find the optimal constant weight $\widehat{F}(n,k_m)$, as shown earlier, such that the difference between $\Pi(\omega)$, the actual acoustic power, and $\widehat{\Pi}(\omega)$, the estimated acoustic power, is minimized.

The next step is to generate a state-space model to estimate the supersonic wavenumber components and the radiated acoustic power in the control bandwidth, to augment a state space model for the acceleration field. Basically, the approach similar to the one in the previous section is adopted here. A state-space model for the plant is given by

$$\begin{aligned} \dot{\mathbf{x}} &= \mathbf{A}\mathbf{x} + \mathbf{B_1}\mathbf{f} + \mathbf{B_2}\mathbf{u} \\ \mathbf{y} &= \mathbf{C}\mathbf{x} . \end{aligned} \tag{4.73}$$

In the state-space model above $\mathbf{x}$ is a state vector, $\mathbf{f}$ is the disturbance vector, and $\mathbf{u}$ is control input vector. Also, $\mathbf{y}$ is a vector of sensor outputs, defined as

$$\mathbf{y} = \ddot{\mathbf{w}} = \left\{ \ddot{w}(\varphi_1, z_1)\ \ddot{w}(\varphi_2, z_1) \cdots \ddot{w}\left(\varphi_{N_c}, z_1\right) \cdots \ddot{w}\left(\varphi_{N_c}, z_{N_a}\right) \right\}^T . \tag{4.74}$$

The discrete wavenumber transform $\ddot{W}_d(n,k_m)$ can be obtained from sensor measurements $\ddot{w}(\varphi_l, z_s)$ using Equation 4.61,

$$\begin{aligned} \ddot{W}_d(n,k_m) &= \frac{1}{2\pi}\Delta\varphi\Delta z \sum_{l=1}^{N_c}\sum_{s=1}^{N_a} \ddot{w}(\varphi_l, z_s)\, e^{-jn\varphi_l} e^{-jk_m z_s} \\ &= \left[\phi_{n,m}^{(1,1)}\ \phi_{n,m}^{(2,1)} \cdots \phi_{n,m}^{(N_c,1)} \cdots \phi_{n,m}^{(N_c,N_a)}\right] \begin{Bmatrix} \ddot{w}(\varphi_1, z_1) \\ \ddot{w}(\varphi_2, z_1) \\ \vdots \\ \ddot{w}\left(\varphi_{N_c}, z_1\right) \\ \vdots \\ \ddot{w}\left(\varphi_{N_c}, z_{N_a}\right) \end{Bmatrix} \\ &= \Phi_{n,m}\ddot{\mathbf{w}} , \end{aligned} \tag{4.75}$$

where

$$\begin{aligned} \Phi_{n,m} &= \left[\phi_{n,m}^{(1,1)}\ \phi_{n,m}^{(2,1)} \cdots \phi_{n,m}^{(N_c,1)} \cdots \phi_{n,m}^{(N_c,N_a)}\right] \\ \phi_{n,m}^{(l,s)} &= \frac{1}{2\pi}\Delta\varphi\Delta z\, e^{-jn\varphi_l} e^{-jk_m z_s} . \end{aligned} \tag{4.76}$$

Since $\Phi_{n,m}$ is a complex vector in general, it cannot be easily used in a state-space formulation

meant for real-time implementation. However, observing from Equation 4.69 that it is the magnitude of the wavenumber component that determines the acoustic power, $\widehat{\ddot{W}}_d(k_m)$ can be computed such that $\left|\ddot{W}_d(n,k_m)\right| = \left|\widehat{\ddot{W}}_d(n,k_m)\right|$ is satisfied. The solution to this problem is given as

$$\widehat{\ddot{W}}_d(n,k_m) = \begin{cases} \begin{bmatrix} \mathrm{Re}\left(\phi_{n,m}^{(1,1)}\right) & \mathrm{Re}\left(\phi_{n,m}^{(2,1)}\right) & \cdots & \mathrm{Re}\left(\phi_{n,m}^{(N_c,1)}\right) & \cdots & \mathrm{Re}\left(\phi_{n,m}^{(N_c,N_a)}\right) \\ \mathrm{Im}\left(\phi_{n,m}^{(1,1)}\right) & \mathrm{Im}\left(\phi_{n,m}^{(2,1)}\right) & \cdots & \mathrm{Im}\left(\phi_{n,m}^{(N_c,1)}\right) & \cdots & \mathrm{Im}\left(\phi_{n,m}^{(N_c,N_a)}\right) \end{bmatrix} \\ \qquad \times \begin{Bmatrix} \ddot{w}(\varphi_1,z_1) \\ \ddot{w}(\varphi_2,z_1) \\ \vdots \\ \ddot{w}(\varphi_{N_c},z_1) \\ \vdots \\ \ddot{w}(\varphi_{N_c},z_{N_a}) \end{Bmatrix}, & \text{if } \phi_{n,m}^{(l,s)} \text{ is complex} \\ \begin{bmatrix} \phi_{n,m}^{(1,1)} & \phi_{n,m}^{(2,1)} & \cdots & \phi_{n,m}^{(N_c,1)} & \cdots & \phi_{n,m}^{(N_c,N_a)} \end{bmatrix} \begin{Bmatrix} \ddot{w}(\varphi_1,z_1) \\ \ddot{w}(\varphi_2,z_1) \\ \vdots \\ \ddot{w}(\varphi_{N_c},z_1) \\ \vdots \\ \ddot{w}(\varphi_{N_c},z_{N_a}) \end{Bmatrix}, & \text{if } \phi_{n,m}^{(l,s)} \text{ is real} \end{cases} \tag{4.77}$$

$$= \widehat{\Phi}_{n,m}\ddot{\mathbf{w}}.$$

Now, the performance metric to be minimized in the wavenumber LQG controller can be defined as

$$\mathbf{z} = \begin{bmatrix} q_{0,1}\widehat{\ddot{W}}_d(0,k_1) \\ q_{0,2}\widehat{\ddot{W}}_d(0,k_2) \\ \vdots \\ q_{0,N_m}\widehat{\ddot{W}}_d(0,k_{N_m}) \\ \vdots \\ q_{N_n-1,N_m}\widehat{\ddot{W}}_d(N_n-1,k_{N_m}) \end{bmatrix} \tag{4.78}$$

$$= \begin{bmatrix} q_{0,1} & 0 & \cdots & & 0 \\ 0 & q_{0,2} & & & \\ & & q_{0,2} & & \\ \vdots & & \ddots & & \vdots \\ & & & q_{N_n-1,N_m} & 0 \\ 0 & & \cdots & 0 & q_{N_n-1,N_m} \end{bmatrix} \begin{bmatrix} \widehat{\Phi}_{0,1} \\ \widehat{\Phi}_{0,2} \\ \vdots \\ \widehat{\Phi}_{0,N_m} \\ \vdots \\ \widehat{\Phi}_{N_n-1,N_m} \end{bmatrix} \mathbf{y}$$

$$= \mathbf{Q}\widehat{\mathbf{\Phi}}\mathbf{C}\mathbf{x},$$

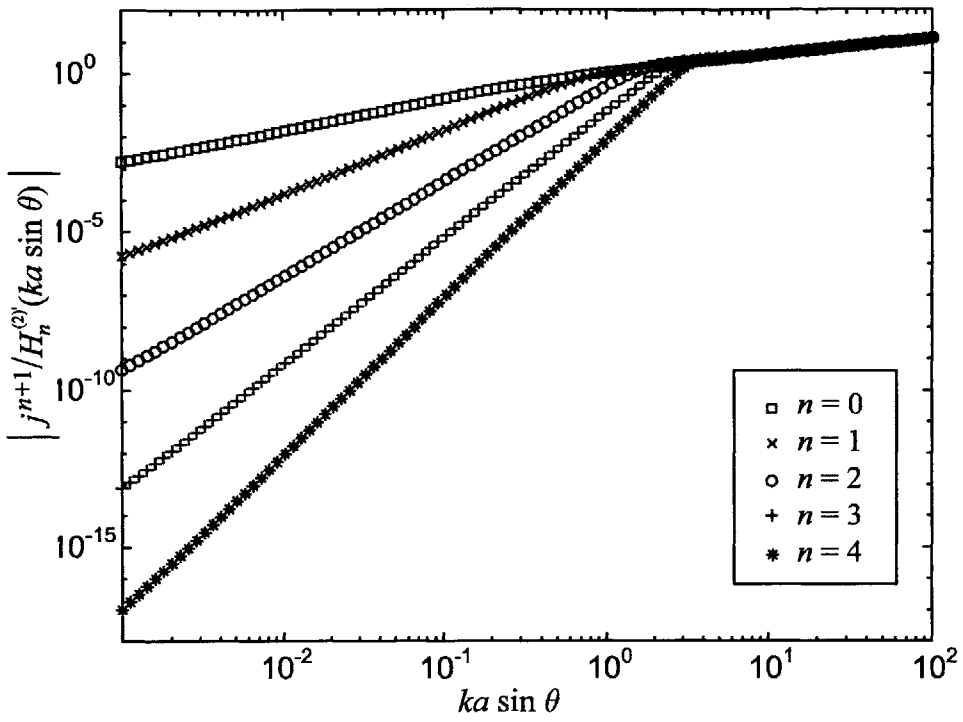

Figure 4-10: Magnitude of $j^{n+1} / H_n^{(2)'}(ka \sin\theta)$.

where $q_{n,m}$ is the weight for $\widehat{\ddot{W}}_d(n, k_m)$, and $\mathbf{Q}$ and $\widehat{\mathbf{\Phi}}$ are defined as

$$\mathbf{Q} = \begin{bmatrix} q_{0,1} & 0 & \cdots & & 0 \\ 0 & q_{0,2} & & & \\ & & q_{0,2} & & \\ \vdots & & & \ddots & \vdots \\ & & & q_{N_n-1,N_m} & 0 \\ 0 & & \cdots & 0 & q_{N_n-1,N_m} \end{bmatrix}, \quad \widehat{\mathbf{\Phi}} = \begin{bmatrix} \widehat{\Phi}_{0,1} \\ \widehat{\Phi}_{0,2} \\ \vdots \\ \widehat{\Phi}_{0,N_m} \\ \vdots \\ \widehat{\Phi}_{N_n-1,N_m} \end{bmatrix}. \tag{4.79}$$

Here, $\widehat{\Phi}$ is in general a $2N_nN_m - 1$ by N_cN_a matrix because $\widehat{\Phi}_{0,1}$ is a real row vector ($k_1 = 0$), while $\widehat{\Phi}_{n,m}$ ($n \neq 0$, or $m \neq 1$) is a 2 by 1 matrix. It is simple to verify that $\|\mathbf{z}\|_2^2$ is the estimated acoustic power $\widehat{\Pi}$ when $q_{n,m} = \sqrt{\widehat{F}(n, k_m)}$ is used. The existence of a state-space model that estimates the acoustic power in the control bandwidth allows the use of modern control design methods such that the acoustic power radiated from vibrating structures can be controlled and minimized. As mentioned earlier, when the optimal $\widehat{F}(n, k_m)$ cannot be easily computed, $q_{n,m}$ can be used as a design knob so that the resulting closed-loop response is satisfactory.

4.3.3 Application to the General 3-D Structures

In this chapter, the formulation of the new wavenumber domain sensing method for active structural acoustic control has been developed for the infinite baffled beam structure (Section 4.3.1), and the infinite baffled cylindrical shell (Section 4.3.2). For those structures, we can find a state-space model to estimate the supersonic wavenumber components, and therefore the radiated acoustic power, such that the structurally-radiated noise is reduced. The formulation is based on the fact that only supersonic wavenumber components contribute to the radiated sound power for the infinite baffled planar structures and the infinite baffled cylindrical shell.

However, for general three-dimensional structures, there are no simple relationships between the supersonic wavenumber components and the radiated acoustic power. For example, for spherical structures, all the wavenumber components radiate acoustic power in the far field, as will be shown later in this section. Therefore, it may appear that the new wavenumber domain sensing method developed in this chapter does not apply to those structures.

Still, the wavenumber sensing method has significant advantages for active structural acoustic control of the complex structures, because the weights for the wavenumber components in general decrease very rapidly as the wavenumber increases. In this section, the application of the new wavenumber sensing method to the complex structures will be discussed. First, the principle of wave superposition will be introduced. Using this principle, we can compute the acoustic fields of arbitrarily shaped radiator by replacing it with an array of simple acoustic sources, such as spherical radiators and unbaffled planar structures. Then, the relationships between the wavenumber transform and the acoustic pressure radiated from spherical radiators and unbaffled planar structures will be investigated. Finally, it will be discussed how those results can be used to apply the new wavenumber sensing method to the complex structures.

The principle of wave superposition

The principle of wave superposition is based on the idea that the acoustic field of a complex radiator can be constructed as a superposition of fields generated by an array of simple acoustic sources enclosed within the radiator [Koopmann, 1989]. The basic concept can be explained using the diagram in Figure 4-11, which shows a complex radiator S_0. We want to compute the acoustic field $p(\mathbf{r})$, given the acceleration field $\ddot{w}(\mathbf{r}_0)$ over the radiating surface S_0. The acoustic pressure $p(\mathbf{r})$ can be obtained using the Helmholtz integral equation, given by

$$p(\mathbf{r}) = -\int_{S_0} \left[p(\mathbf{r}_0) \left(\nabla g(|\mathbf{r}-\mathbf{r}_0|) \right) \cdot \mathbf{n}_0 + \rho \ddot{w}(\mathbf{r}_0)\, g(|\mathbf{r}-\mathbf{r}_0|) \right] dS \,, \tag{4.80}$$

where $g(|\mathbf{r}-\mathbf{r}_0|)$ is the free-space Green's function defined in Equation 4.8, ρ is fluid density, and $\mathbf{n}_0$ is the outward normal unit vector at $\mathbf{r}_0$. Koopmann *et al.* [Koopmann, 1989] showed that $p(\mathbf{r})$ can also be computed using a continuous source distribution that produces the same acoustic field, given by

$$p(\mathbf{r}) = -j\rho\omega \int_V q(\mathbf{r}_1)\, g(|\mathbf{r}-\mathbf{r}_1|)\, dV \,, \tag{4.81}$$

where ω is the angular frequency of the harmonic vibration of the radiating surface S_0 enclosing the volume V of the radiator, and $q(\mathbf{r}_1)$ is the strength of the source distribution evaluated at $\mathbf{r}_1$ inside V. They showed that the principle of wave superposition in Equation 4.81 is equivalent

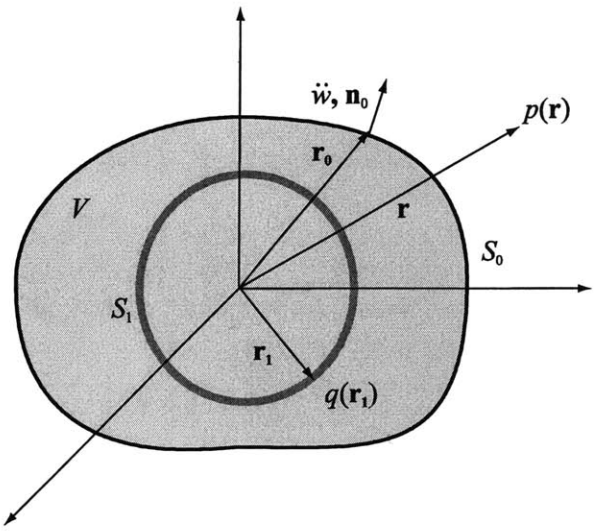

Figure 4-11: The diagram of the fictitious source sphere S_1 inside of a complex radiator S_0.

to the Helmholtz integral equation in Equation 4.80, if $q(\mathbf{r}_1)$ is selected so that

$$\ddot{w}(\mathbf{r}_0) = j\omega \int_V q(\mathbf{r}_1) \left(\nabla g(|\mathbf{r}_0 - \mathbf{r}_1|)\right) \cdot \mathbf{n}_0 \, dV \tag{4.82}$$

is satisfied.

Since there is no restriction on the location of $q(\mathbf{r}_1)$, it can be placed anywhere inside of the radiating surface S_0 [Koopmann, 1989]. Therefore, for convenience, we can assume that the source distribution has the form of a spherical shell for general thick radiators, and a planar shell for general thin radiators. Here, "thick radiators" mean radiators in which all three dimensions have the same order of magnitude, while "thin radiators" mean radiators in which one of the dimension is much smaller than the other two. In any case, the sources can be assumed to be distributed over the surface, which results in

$$\ddot{w}(\mathbf{r}_0) = j\omega \int_{S_1} q(\mathbf{r}_1) \left(\nabla g(|\mathbf{r}_0 - \mathbf{r}_1|)\right) \cdot \mathbf{n}_0 \, h \, dS \, . \tag{4.83}$$

Here, S_1 is the surface over which the sources $q(\mathbf{r}_1)$ are distributed, and h is the thickness of the surface. If the acceleration field $\ddot{w}(\mathbf{r}_0)$ on S_0 is given, the strength of sources $q(\mathbf{r}_1)$ can be obtained using Equation 4.83.

Now, the relationships between the acoustic pressure and the wavenumber transform are investigated. The wavenumber transforms of $q(\mathbf{r}_1)$ and $\ddot{w}(\mathbf{r}_0)$ are given by

$$\begin{aligned} Q(k_{\xi_1}, k_{\eta_1}) &= \int_{S_1} q(\boldsymbol{\xi}_1, \eta_1) \, e^{-jk_{\xi_1}\xi_1} e^{-jk_{\eta_1}\eta_1} \, d\boldsymbol{\xi}_1 d\eta_1 \\ \ddot{W}(k_{\xi_0}, k_{\eta_0}) &= \int_{S_0} \ddot{w}(\boldsymbol{\xi}_0, \eta_0) \, e^{-jk_{\xi_0}\xi_0} e^{-jk_{\eta_0}\eta_0} \, d\boldsymbol{\xi}_0 d\eta_0 \, , \end{aligned} \tag{4.84}$$

where $(\boldsymbol{\xi}_0, \eta_0)$ and $(\boldsymbol{\xi}_1, \eta_1)$ are tangential orthogonal coordinates on the surface of S_0 and S_1, respectively, and k_χ is the wavenumber in the χ direction ($\chi = \boldsymbol{\xi}_0,\ \eta_0,\ \boldsymbol{\xi}_1,\ \eta_1$). The integration $\int_{S_1} \cdots d\boldsymbol{\xi}_1 d\eta_1$ means that it is performed for $(\boldsymbol{\xi}_1, \eta_1) \in S_1$. Note that $\mathbf{r}_1 = \mathbf{r}_1(\boldsymbol{\xi}_1, \eta_1)$, and $\mathbf{r}_0 = \mathbf{r}_0(\boldsymbol{\xi}_0, \eta_0)$. Using the inverse Fourier transform, $q(\boldsymbol{\xi}_1, \eta_1)$ and $\ddot{w}(\boldsymbol{\xi}_0, \eta_0)$ can be represented in terms of $Q\left(k_{\xi_1}, k_{\eta_1}\right)$ and $\ddot{W}\left(k_{\xi_0}, k_{\eta_0}\right)$, given by

$$
\begin{aligned}
q(\boldsymbol{\xi}_1, \eta_1) &= \frac{1}{(2\pi)^2} \int_{-\infty}^{+\infty} \int_{-\infty}^{+\infty} Q\left(k_{\xi_1}, k_{\eta_1}\right) e^{jk_{\xi_1}\boldsymbol{\xi}_1} e^{jk_{\eta_1}\eta_1}\, dk_{\xi_1} dk_{\eta_1} \qquad (4.85)\\
\ddot{w}(\boldsymbol{\xi}_0, \eta_0) &= \frac{1}{(2\pi)^2} \int_{-\infty}^{+\infty} \int_{-\infty}^{+\infty} \ddot{W}\left(k_{\xi_0}, k_{\eta_0}\right) e^{jk_{\xi_0}\boldsymbol{\xi}_0} e^{jk_{\eta_0}\eta_0}\, dk_{\xi_0} dk_{\eta_0}\ .
\end{aligned}
$$

Substituting Equation 4.83 in Equation 4.84, and using Equation 4.85, $\ddot{W}\left(k_{\xi_0}, k_{\eta_0}\right)$ can be expressed in terms of $Q\left(k_{\xi_1}, k_{\eta_1}\right)$, given by

$$
\ddot{W}\left(k_{\xi_0}, k_{\eta_0}\right) = \int_{-\infty}^{+\infty} \int_{-\infty}^{+\infty} G\left(k_{\xi_0}, k_{\eta_0}; k_{\xi_1}, k_{\eta_1}\right) Q\left(k_{\xi_1}, k_{\eta_1}\right)\, dk_{\xi_1} dk_{\eta_1}\ , \qquad (4.86)
$$

in which $G\left(k_{\xi_0}, k_{\eta_0}; k_{\xi_1}, k_{\eta_1}\right)$ is defined as

$$
G\left(k_{\xi_0}, k_{\eta_0}; k_{\xi_1}, k_{\eta_1}\right) = \frac{jh\omega}{(2\pi)^2} \int_{S_0} \left[\int_{S_1} \left(\nabla g\left(|\mathbf{r}_0 - \mathbf{r}_1|\right)\right) \cdot \mathbf{n}_0\, e^{-jk_{\xi_0}\boldsymbol{\xi}_0} e^{-jk_{\eta_0}\eta_0}\, e^{jk_{\xi_1}\boldsymbol{\xi}_1} e^{jk_{\eta_1}\eta_1}\, dS \right] d\boldsymbol{\xi}_0 d\eta_0\ . \qquad (4.87)
$$

Here, we can evaluate $\left(\nabla g\left(|\mathbf{r}_0 - \mathbf{r}_1|\right)\right) \cdot \mathbf{n}_0$ using the definition of a free space Green's function in Equation 4.8, given by

$$
\left(\nabla g\left(|\mathbf{r}_0 - \mathbf{r}_1|\right)\right) \cdot \mathbf{n}_0 = -\frac{1}{4\pi} \frac{e^{jk|\mathbf{r}_0 - \mathbf{r}_1|}}{|\mathbf{r}_0 - \mathbf{r}_1|} \left(jk\,|\mathbf{r}_0 - \mathbf{r}_1| - 1\right) \cos\phi_0\ , \qquad (4.88)
$$

where ϕ_0 is the angle between $\mathbf{r}_0 - \mathbf{r}_1$ and $\mathbf{n}_0$. Also, we can write $d\boldsymbol{\xi}_0 d\eta_0$ as $A_0(\boldsymbol{\xi}_0, \eta_0)\, dS(\mathbf{r}_0)$, for a function $A_0(\boldsymbol{\xi}_0, \eta_0)$ that depends on the chosen orthogonal coordinate. Using these results, $G\left(k_{\xi_0}, k_{\eta_0}; k_{\xi_1}, k_{\eta_1}\right)$ in Equation 4.87 can be rewritten as

$$
\begin{aligned}
G\left(k_{\xi_0}, k_{\eta_0}; k_{\xi_1}, k_{\eta_1}\right) = -\frac{jh\omega}{16\pi^3} \int_{S_0} \int_{S_1} &\left(jk\,|\mathbf{r}_0 - \mathbf{r}_1| - 1\right) \cos\phi_0 A_0(\boldsymbol{\xi}_0, \eta_0) \qquad (4.89)\\
&\times \frac{e^{jk|\mathbf{r}_0 - \mathbf{r}_1|}}{|\mathbf{r}_0 - \mathbf{r}_1|} e^{-jk_{\xi_0}\boldsymbol{\xi}_0} e^{-jk_{\eta_0}\eta_0}\, e^{jk_{\xi_1}\boldsymbol{\xi}_1} e^{jk_{\eta_1}\eta_1}\, dS_1 dS_0\ .
\end{aligned}
$$

Now, the acoustic pressure $p(\mathbf{r})$ can be written in terms of the wavenumber components $Q\left(k_{\xi_1}, k_{\eta_1}\right)$, by substituting $q(\boldsymbol{\xi}_1, \eta_1)$ given in Equation 4.85 into Equation 4.81, so that

$$
p(\mathbf{r}) = \int_{-\infty}^{+\infty} \int_{-\infty}^{+\infty} F\left(\mathbf{r}, k_{\xi_1}, k_{\eta_1}\right) Q\left(k_{\xi_1}, k_{\eta_1}\right)\, dk_{\xi_1} dk_{\eta_1}\ , \qquad (4.90)
$$

where $F\left(\mathbf{r}, k_{\xi_1}, k_{\eta_1}\right)$ is the weighting function for the wavenumber component $Q\left(k_{\xi_1}, k_{\eta_1}\right)$, given

as

$$F\left(\mathbf{r}, k_{\xi_1}, k_{\eta_1}\right) = \frac{j\rho h\omega}{16\pi^3} \int_{S_1} \frac{e^{jk|\mathbf{r}-\mathbf{r}_1|}}{|\mathbf{r}-\mathbf{r}_1|} e^{jk_{\xi_1}\xi_1} e^{jk_{\eta_1}\eta_1} dS \,. \tag{4.91}$$

Here, the free space Green's function $g\left(|\mathbf{r}-\mathbf{r}_1|\right) = -\frac{e^{jk|\mathbf{r}-\mathbf{r}_1|}}{4\pi|\mathbf{r}-\mathbf{r}_1|}$ defined in Equation 4.8 was used.

Equation 4.90 has an important meaning. It implies that the acoustic pressure from any complex three-dimensional structure can be computed from the wavenumber components of a fictitious source distribution, such as sphere radiators or planar radiators. If it turns out that $\left|F\left(\mathbf{r}, k_{\xi_1}, k_{\eta_1}\right)\right|$ decreases very rapidly as k_{ξ_1} and k_{η_1} increase for those simple source distributions, we need only to consider a few wavenumber components to estimate the acoustic pressure or acoustic power, although it is generally true that all the wavenumber components contribute to sound radiation for complex three-dimensional structures. Then, the wavenumber domain sensing method developed in this chapter can be applied for any complex three-dimensional structures. It will be shown later in this section that the proposed assumption, which is that $\left|F\left(\mathbf{r}, k_{\xi_1}, k_{\eta_1}\right)\right|$ decreases very rapidly as k_{ξ_1} and k_{η_1} increase for the sphere radiators or planar radiators, is generally true.

It remains to find how to relate the acoustic pressure $p\left(\mathbf{r}\right)$ with the wavenumber transform of the surface acceleration $\ddot{w}\left(\mathbf{r}_0\right)$, because what we can measure directly is $\ddot{w}\left(\mathbf{r}_0\right)$, not $q\left(\mathbf{r}_1\right)$, and we can apply the wavenumber transform to $\ddot{w}\left(\mathbf{r}_0\right)$ in real-time. From the Helmholtz integral equation given in Equation 4.6, we know that the acoustic pressure at any point $p\left(\mathbf{r}\right)$ in the medium can be expressed in terms of the acceleration and pressure field over a surface of the structure, $\ddot{w}\left(\mathbf{r}_0\right)$ and $p\left(\mathbf{r}_0\right)$, respectively. Since it implies that the acoustic pressure on the surface of the structure can be written in terms of the acceleration field on the surface $\left(\mathbf{r} = \mathbf{r}_0\right)$, we can conclude that the acoustic pressure at any point $p\left(\mathbf{r}\right)$ can be represented in terms of the surface acceleration field only. This becomes possible by substituting the surface pressure expressed in terms of the surface acceleration into the Helmholtz integral equation, although the closed-form solution will not be easy to obtain. Using these facts, we see that $p\left(\mathbf{r}\right)$ can be represented in terms of $\ddot{W}\left(k_{\xi_0}, k_{\eta_0}\right)$ defined in Equation 4.84, as

$$p\left(\mathbf{r}\right) = \int_{-\infty}^{+\infty} \int_{-\infty}^{+\infty} H\left(\mathbf{r}, k_{\xi_0}, k_{\eta_0}\right) \ddot{W}\left(k_{\xi_0}, k_{\eta_0}\right) \, dk_{\xi_0} dk_{\eta_0} \,, \tag{4.92}$$

where $H\left(\mathbf{r}, k_{\xi_0}, k_{\eta_0}\right)$ is the weighting function for the wavenumber component $\ddot{W}\left(k_{\xi_0}, k_{\eta_0}\right)$ of the general structures, yet to be determined. We hope that $\left|H\left(\mathbf{r}, k_{\xi_0}, k_{\eta_0}\right)\right|$ decreases rapidly as k_{ξ_0} and k_{η_0} increase, so that the wavenumber domain sensing method can be applied. Substituting Equation 4.86 into Equation 4.92, we can find the relation between $F\left(\mathbf{r}, k_{\xi_1}, k_{\eta_1}\right)$ and $H\left(\mathbf{r}, k_{\xi_0}, k_{\eta_0}\right)$, given as

$$F\left(\mathbf{r}, k_{\xi_1}, k_{\eta_1}\right) = \int_{-\infty}^{+\infty} \int_{-\infty}^{+\infty} G\left(k_{\xi_0}, k_{\eta_0}; k_{\xi_1}, k_{\eta_1}\right) H\left(\mathbf{r}, k_{\xi_0}, k_{\eta_0}\right) dk_{\xi_0} dk_{\eta_0} \,. \tag{4.93}$$

This expression has the form of a two-dimensional convolution. We can see that $\left|H\left(\mathbf{r}, k_{\xi_0}, k_{\eta_0}\right)\right|$ decreases rapidly as k_{ξ_0} and k_{η_0} increase, if $\left|F\left(\mathbf{r}, k_{\xi_1}, k_{\eta_1}\right)\right|$ and $\left|G\left(k_{\xi_0}, k_{\eta_0}; k_{\xi_1}, k_{\eta_1}\right)\right|$ decrease rapidly as k_{ξ_0}, k_{η_0} and k_{ξ_1}, k_{η_1} increase. As mentioned earlier, it will be shown later that $F\left(\mathbf{r}, k_{\xi_1}, k_{\eta_1}\right)$ behaves as we want, for the spherical or planar radiators. Furthermore, comparing

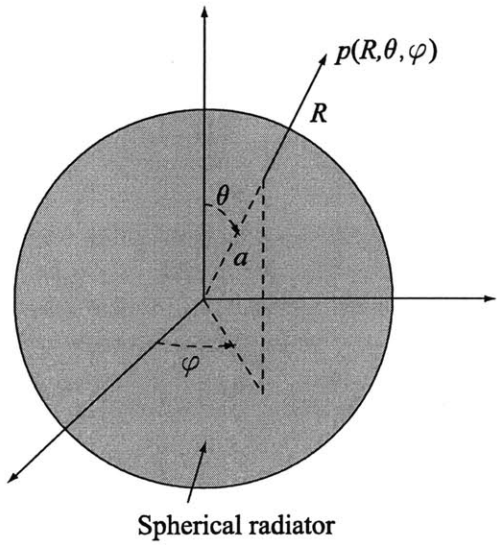

Figure 4-12: A spherical radiator with a radius a.

$F\left(\mathbf{r}, k_{\xi_1}, k_{\eta_1}\right)$ in Equation 4.91 with $G\left(k_{\xi_0}, k_{\eta_0}; k_{\xi_1}, k_{\eta_1}\right)$ in Equation 4.89, we can see that $G\left(k_{\xi_0}, k_{\eta_0}; k_{\xi_1}, k_{\eta_1}\right)$ decrease rapidly as k_{ξ_0}, k_{η_0} and k_{ξ_1}, k_{η_1} increase, if $F\left(\mathbf{r}, k_{\xi_1}, k_{\eta_1}\right)$ does, because they have the same dependence on the wavenumbers k_{ξ_0}, k_{η_0} and k_{ξ_1}, k_{η_1}. Therefore, we can conclude that $\left|H\left(\mathbf{r}, k_{\xi_0}, k_{\eta_0}\right)\right|$ decreases rapidly as k_{ξ_0} and k_{η_0} increase for general three-dimensional structures, and that we can apply the new wavenumber sensing method for those structures, in addition to the infinite baffled planar structures or cylindrical shell.

In the next sections, the relationships between the wavenumber transform and the acoustic pressure radiated from spherical radiators and unbaffled planar structures will be investigated.

Spherical radiators

Figure 4-12 shows a spherical radiator with a radius a. For the sphere, the acceleration $\ddot{w}\left(\theta, \varphi\right)$ is represented as a double series in Legendre functions of the polar angle (or latitude) θ, and in cosines of the circumferential angle (or longitude) φ, given by [Junger, 1986]

$$\ddot{w}\left(\theta, \varphi\right) = \sum_{n=0}^{\infty} \sum_{m=0}^{n} \ddot{W}_{mn} P_n^m \left(\cos\theta\right) \cos m\varphi \ , \tag{4.94}$$

where, $P_n^m\left(\eta\right)$ is defined as

$$P_n^m\left(\eta\right) = \begin{cases} P_n\left(\eta\right) \ , & m = 0 \\ \left(1-\eta^2\right)^{m/2} \dfrac{d^m P_n\left(\eta\right)}{d\eta^m} \ , & m \geq 1 \end{cases} \ . \tag{4.95}$$

Here, $P_n\left(\eta\right)$ is the Legendre polynomial, and $P_n^m\left(\eta\right)$ $\left(m \geq 1\right)$ are the associated Legendre functions. Using the orthogonality relations of $P_n^m\left(\eta\right)$ and $\cos m\varphi$, $\ddot{W}_{mn}$ can be computed from

$\ddot{w}(\theta,\varphi)$, given by [Junger, 1986]

$$\ddot{W}_{mn} = \frac{-1}{N_{mn}} \int_0^{2\pi} \left[\int_0^{\pi} P_n^m(\cos\theta)\, \ddot{w}(\theta,\varphi) \sin\theta\, d\theta \right] \cos m\varphi\, d\varphi \,, \tag{4.96}$$

where N_{mn} is the normalization factor, given as

$$N_{mn} = \begin{cases} \dfrac{4\pi}{2n+1} \dfrac{(n+m)!}{(n-m)!} \,, & m = 0 \\ \\ \dfrac{2\pi}{2n+1} \dfrac{(n+m)!}{(n-m)!} \,, & m \geq 1 \end{cases} . \tag{4.97}$$

Using $\ddot{W}_{mn}$, the acoustic pressure $p(R,\theta,\varphi)$ in the far field can be written as [Junger, 1986]

$$p(R,\theta,\varphi) = \frac{\rho e^{jkR}}{k^2 R} \sum_{n=0}^{\infty} \sum_{m=0}^{n} \frac{(-j)^{n-1}}{h_n'(ka)} \ddot{W}_{mn} P_n^m(\cos\theta) \cos m\varphi \,, \; kR \gg n^2 + 1 \,, \tag{4.98}$$

where $h_n'(x)$ denotes the first derivative of the spherical Hankel function of the first kind. Note that Equation 4.98 doesn't show the relation between the wavenumber transform and the acoustic pressure; $\ddot{W}_{mn}$ is *not* the wavenumber transform of $\ddot{w}(\theta,\varphi)$ adopted in this thesis. The wavenumber transform of $\ddot{w}(\theta,\varphi)$ can be defined as

$$\ddot{W}(r,s) = \frac{1}{4\pi^2} \int_0^{2\pi} \int_0^{2\pi} \ddot{w}(\theta,\varphi)\, e^{-jr\theta} e^{-js\varphi} d\theta d\varphi \,. \tag{4.99}$$

Since $\ddot{w}(\theta,\varphi) = \ddot{w}(\theta,\varphi+2\pi)$ and $\ddot{w}(\theta,\varphi) = \ddot{w}(\theta+2\pi,\varphi)$, $\ddot{w}(\theta,\varphi)$ can be represented using $\ddot{W}(r,s)$, given by

$$\ddot{w}(\theta,\varphi) = \sum_{r=-\infty}^{\infty} \sum_{s=-\infty}^{\infty} \ddot{W}(r,s)\, e^{jr\theta} e^{js\varphi} \,. \tag{4.100}$$

Substituting Equation 4.100 in Equation 4.96, we can express $\ddot{W}_{mn}$ in terms of $\ddot{W}(r,s)$, as

$$\ddot{W}_{mn} = \sum_{r=-\infty}^{\infty} \sum_{s=-\infty}^{\infty} A_{mnrs} \ddot{W}(r,s) \,, \tag{4.101}$$

where

$$A_{mnrs} = \frac{-1}{N_{mn}} \int_0^{2\pi} \int_0^{\pi} P_n^m(\cos\theta) \sin\theta \cos m\varphi\, e^{jr\theta} e^{js\varphi}\, d\theta d\varphi \,. \tag{4.102}$$

Now, substituting Equation 4.101 in Equation 4.98, we can represent the acoustic pressure $p(R,\theta,\varphi)$ in terms of the wavenumber transform of $\ddot{w}(\theta,\varphi)$, as

$$p(R,\theta,\varphi) = \frac{\rho e^{jkR}}{k^2 R} \sum_{r=-\infty}^{\infty} \sum_{s=-\infty}^{\infty} F(r,s)\, \ddot{W}(r,s) \,, \tag{4.103}$$

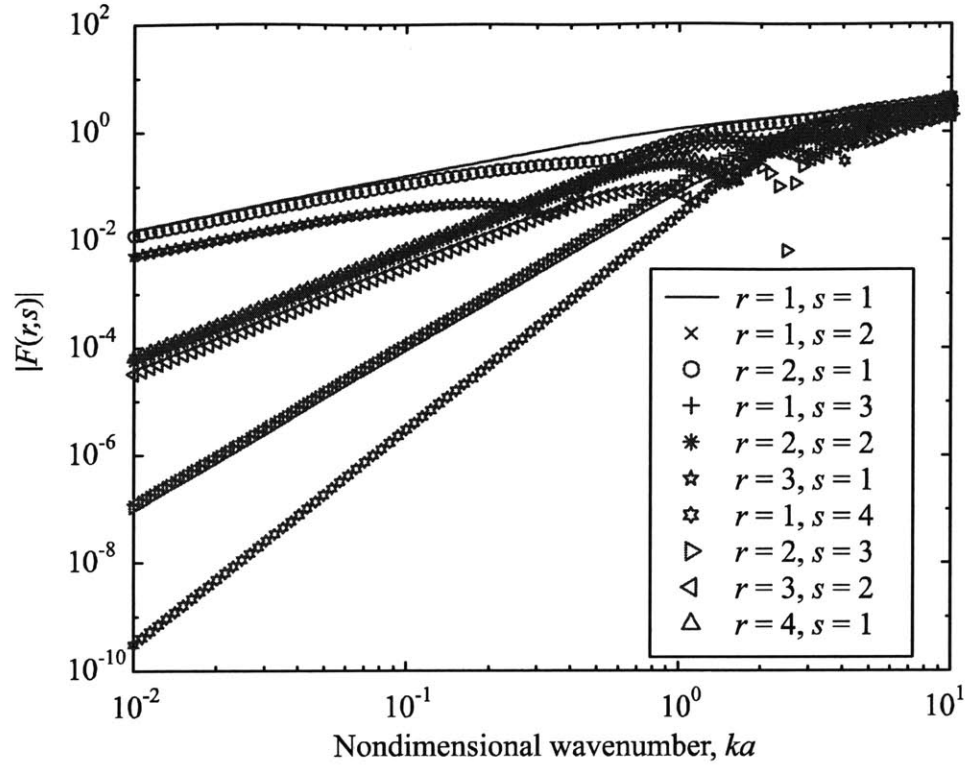

Figure 4-13: Magnitude of the weighting function $F(r,s)$ for θ=45° and φ=60°.

where $F(r,s)$ is the weighting function for the wavenumber components $\ddot{W}(r,s)$,

$$F(r,s) = \sum_{n=0}^{\infty}\sum_{m=0}^{n} \frac{(-j)^{n-1}}{h_n'(ka)} A_{mnrs} P_n^m(\cos\theta)\cos m\varphi \,. \tag{4.104}$$

The magnitudes of $F(r,s)$ for θ=45° and φ=60° are shown in Figure 4-13. As can be seen from Equation 4.103, all the wavenumber components radiate acoustic power for a spherical radiator. However, Figure 4-13 shows that the magnitudes of $F(r,s)$ decrease very fast as r and s increase, and that only a few wavenumber components dominate the radiated acoustic power for $ka \leq 1$. Therefore, we can still apply the wavenumber sensing method proposed in this chapter for the spherical radiators, by considering a few dominant wavenumber components.

Unbaffled planar radiators

An unbaffled planar radiator excited by a harmonic driving force of angular frequency ω is shown in Figure 4-14. The plate has length of a in the X direction, and b in the Y direction. The mass per unit area of the plate is denoted as ρ_p, and its thickness as h. Assuming the plate is orthotropic and the out-of-plane displacement has the form of $w(x,y,t)$=$w(x,y)\,e^{-j\omega t}$, the

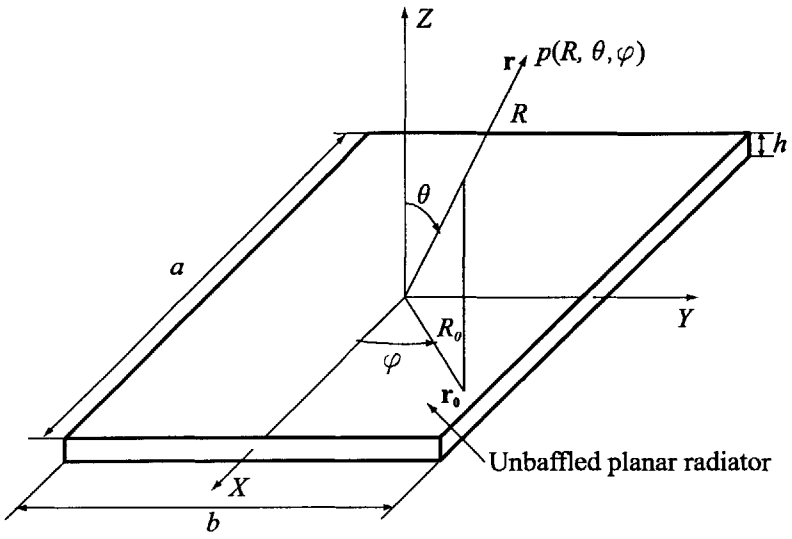

Figure 4-14: Geometry of an unbaffled planar radiator.

equation of motion is given by

$$D_x \frac{\partial^4 w(x,y)}{\partial x^4} + 2\sqrt{D_x D_y} \frac{\partial^4 w(x,y)}{\partial x^2 \partial y^2} + D_y \frac{\partial^4 w(x,y)}{\partial y^4} - \rho_p \omega^2 w(x,y) = f(x,y) + \Delta p(x,y) \ , \tag{4.105}$$

where D_x and D_y are the bending stiffnesses in the two orthogonal directions, X and Y, respectively, and $f(x,y)$ is the disturbance. $\Delta p(x,y)$ is the difference of the acoustic surface pressure (pressure jump over the plate), given by

$$\Delta p(x,y) = p^-(x,y) - p^+(x,y) \ , \tag{4.106}$$

where $p^-(x,y)$ and $p^+(x,y)$ are the surface pressures on the negative and positive side of the plate, respectively.

For an unbaffled planar radiator, the acoustic pressure $p(R,\theta,\varphi)$ is governed by [Atalla, 1996]

$$p(R,\theta,\varphi) = -\int_{-b/2}^{+b/2} \int_{-a/2}^{+a/2} \Delta p(x,y) \left(\nabla g(|\mathbf{r} - \mathbf{r}_0|)\right) \cdot \mathbf{n}_0 \, dxdy \ , \tag{4.107}$$

where $\mathbf{n}_0$ is the outward unit normal vector to the plate, $\mathbf{r} = (R\sin\theta\cos\varphi, R\sin\theta\sin\varphi, R\cos\theta)$, and $\mathbf{r}_0 = (R_0\cos\varphi, R_0\sin\varphi, 0)$. Note that the acoustic pressure $p(R,\theta,\varphi)$ is represented in spherical coordinates, while the surface pressure and the out-of-plane displacement are represented in rectangular coordinates, because it helps show the relationship between the wavenumber transform and the acoustic field.

In Equation 4.107, $(\nabla g(|\mathbf{r}-\mathbf{r}_0|)) \cdot \mathbf{n}_0$ is given by

$$(\nabla g(|\mathbf{r}-\mathbf{r}_0|)) \cdot \mathbf{n}_0 = -\frac{1}{4\pi}\frac{e^{jk|\mathbf{r}-\mathbf{r}_0|}}{|\mathbf{r}-\mathbf{r}_0|}(jk|\mathbf{r}-\mathbf{r}_0|-1)\cos\phi\,, \tag{4.108}$$

where ϕ is angle between $\mathbf{r}-\mathbf{r}_0$ and $\mathbf{n}_0$. Using the inner product of $\mathbf{r}-\mathbf{r}_0$ and $\mathbf{n}_0$, $\cos\phi$ can be expressed as

$$\cos\phi = \frac{R\cos\theta}{|\mathbf{r}-\mathbf{r}_0|}\,. \tag{4.109}$$

Since we are interested in the far field acoustic power, $|\mathbf{r}-\mathbf{r}_0|$ and $\cos\phi$ reduce to

$$\begin{aligned} |\mathbf{r}-\mathbf{r}_0| &\approx R - x\sin\theta\cos\varphi - y\sin\theta\sin\varphi \\ \cos\phi &\approx \cos\theta\,, \end{aligned} \tag{4.110}$$

for $R \gg a, b$. Then, the acoustic pressure $p(R,\theta,\varphi)$ in Equation 4.107 reduces to using the far field approximation, given by

$$p(R,\theta,\varphi) \approx \frac{e^{jkR}}{4\pi R}(jkR-1)\cos\theta\int_{-b/2}^{+b/2}\int_{-a/2}^{+a/2}\Delta p(x,y)\,e^{-jkx\sin\theta\cos\varphi}e^{-jky\sin\theta\sin\varphi}dxdy\,. \tag{4.111}$$

Substituting Equation 4.105 in Equation 4.111, the far field acoustic pressure $p(R,\theta,\varphi)$ can be represented in terms of the out-of-plane displacement of the plate, so that

$$\begin{aligned} p(R,\theta,\varphi) \approx\ & \frac{e^{jkR}}{4\pi R}(jkR-1)\cos\theta\int_{-b/2}^{+b/2}\int_{-a/2}^{+a/2} \\ & \times\left[D_x\frac{\partial^4 w(x,y)}{\partial x^4} + 2\sqrt{D_xD_y}\frac{\partial^4 w(x,y)}{\partial x^2\partial y^2} + D_y\frac{\partial^4 w(x,y)}{\partial y^4} - \rho_p\omega^2 w(x,y) - f(x,y)\right] \\ & \times e^{-jkx\sin\theta\cos\varphi}e^{-jky\sin\theta\sin\varphi}dxdy\,. \end{aligned} \tag{4.112}$$

Now, the relationships between the acoustic pressure and the wavenumber transform are investigated. The wavenumber transforms of $w(x,y)$ and $f(x,y)$ are defined as

$$\begin{aligned} W(k_x,k_y) &= \int_{-b/2}^{+b/2}\int_{-a/2}^{+a/2} w(x,y)\,e^{-jk_xx}e^{-jk_yy}dxdy \\ F(k_x,k_y) &= \int_{-b/2}^{+b/2}\int_{-a/2}^{+a/2} f(x,y)\,e^{-jk_xx}e^{-jk_yy}dxdy\,. \end{aligned} \tag{4.113}$$

Using the property of the wavenumber transform,

$$\begin{aligned} &\int_{-b/2}^{+b/2}\int_{-a/2}^{+a/2}\left[D_x\frac{\partial^4 w(x,y)}{\partial x^4} + 2\sqrt{D_xD_y}\frac{\partial^4 w(x,y)}{\partial x^2\partial y^2} + D_y\frac{\partial^4 w(x,y)}{\partial y^4}\right]e^{-jk_xx}e^{-jk_yy}dxdy \\ &= \left(\sqrt{D_x}k_x^2 + \sqrt{D_y}k_y^2\right)^2 W(k_x,k_y)\,, \end{aligned} \tag{4.114}$$

the far field acoustic pressure $p(R,\theta,\varphi)$ can be represented using the wavenumber component

$W(k_x, k_y)$ by substituting $k_x = k\sin\theta\cos\varphi$, and $k_y = k\sin\theta\sin\varphi$, so that

$$\begin{aligned} & p(R,\theta,\varphi) \\ & = \frac{e^{jkR}}{4\pi R}(jkR-1)\cos\theta\left\{\left[\sqrt{D_x}(k\sin\theta\cos\varphi)^2+\sqrt{D_y}(k\sin\theta\sin\varphi)^2\right]^2-\rho_p\omega^2\right\} \\ & \quad \times W(k\sin\theta\cos\varphi, k\sin\theta\sin\varphi) - F(k\sin\theta\cos\varphi, k\sin\theta\sin\varphi)\frac{e^{jkR}}{4\pi R}(jkR-1)\cos\theta\,. \end{aligned} \tag{4.115}$$

Therefore, $p(R,\theta,\varphi)$ is given by

$$p(R,\theta,\varphi) = C_1 W(k\sin\theta\cos\varphi, k\sin\theta\sin\varphi) - C_2 F(k\sin\theta\cos\varphi, k\sin\theta\sin\varphi)\,, \tag{4.116}$$

where

$$\begin{aligned} C_1 &= \frac{e^{jkR}}{4\pi R}(jkR-1)\cos\theta\left\{\left[\sqrt{D_x}(k\sin\theta\cos\varphi)^2+\sqrt{D_y}(k\sin\theta\sin\varphi)^2\right]^2-\rho_p\omega^2\right\} \\ C_2 &= \frac{e^{jkR}}{4\pi R}(jkR-1)\cos\theta\,. \end{aligned} \tag{4.117}$$

What Equation 4.116 implies is that the far field acoustic pressure in the direction (θ,φ) is completely determined by the corresponding wavenumber component $W(k\sin\theta\cos\varphi, k\sin\theta\sin\varphi)$ for the unbaffled planar radiator, as for the infinite baffled planar radiator. The difference between the two cases is that for the unbaffled planar radiator, the wavenumber transform of the disturbance, $F(k\sin\theta\cos\varphi, k\sin\theta\sin\varphi)$, appears in the expression for the far field acoustic pressure. However, it doesn't matter, because we don't have the authority to change the disturbance, anyway. What is important in Equation 4.116 is that the acoustic pressure, and therefore acoustic power, from the unbaffled planar radiator can be reduced by controlling the corresponding wavenumber components.

Application of the wavenumber sensing method to the general 3-D structures

In this section, we have shown the following:

1. Any complex radiator can be replaced by a simple acoustic source distribution, such as a spherical radiator, or an unbaffled planar radiator.

2. The wavenumber sensing method proposed in this chapter can be applied to the general complex structures, if it can be applied to the spherical or planar radiators.

3. For the spherical radiator, only a few dominant wavenumber components dominate in the radiation of acoustic power. Therefore, we can apply the wavenumber sensing method for the spherical radiators, by considering a few dominant wavenumber components.

4. For the unbaffled planar radiators, the far field acoustic pressure in the radiation direction is completely determined by the corresponding wavenumber component. Therefore, all the results in Section 4.3.1 can be applied to this structure. We can apply the wavenumber sensing method for the unbaffled planar radiators by considering the supersonic wavenumber components.

Combining the results 1–4, we can conclude that the new wavenumber domain sensing method and its use as feedback controller design can be applied for any complex structures.

4.4 Summary

In this chapter, a new wavenumber domain sensing method and its application to the LQG feedback ASAC problem has been reported. In this new sensing method, the total acoustic power radiated from vibrating structures is minimized in the wavenumber domain. Given the control bandwidth, a state-space model can be found to estimate the magnitude of supersonic wavenumber components. An LQG controller is designed on the state-space model to minimize the estimated acoustic power.

One of the significant advantages of the method proposed in this chapter is that it doesn't need any modeling process to estimate the acoustic power from sensor measurements, once we have a state-space model for those measurements. As shown in the previous sections, the discrete wavenumber transform matrix, $\widehat{\mathbf{\Phi}}$, where sensor measurements are processed, is obtained from the definition of wavenumber transform, not from the structural acoustic models. As for the performance weights in matrix $\mathbf{Q}$, we can select them such that the difference between the actual and estimated acoustic power is minimized, if we have enough information on the actual acoustic power. If we cannot get the actual acoustic power due to the insufficient measurements or complexity of the plant, we can still use the performance weights in matrix $\mathbf{Q}$ as design knobs for optimal controller design. The results of numerical examples in the next chapter show that the closed-loop performance is not very sensitive to the performance weights, so an accurate acoustic model is not required to achieve the acceptable performance.

Another significant advantage of the new sensing method is that it makes the controller design easier by reducing the number of transfer functions that need to be identified. As shown in Section 4.3.1, the method reduces the size of transfer function matrix to be identified from (the number of sensors)^2 to the order of (the number of wavenumber components to be considered)^2. These advantages are critical when the structure is complex enough that we may not be able to apply, say, the finite element method and, therefore, we need to perform system identification to get a plant model.

In the next chapter, the new sensing method will be numerically validated on a beam structure with 10 active composite panels, and a thick-walled cylindrical shell with 55 active composite panels mounted on its surface.

Chapter 5

Numerical Examples of Wavenumber Domain Feedback Control

5.1 Introduction and Objective

This chapter demonstrates the wavenumber domain sensing method developed in the previous chapter on structural systems. The purpose of this is to numerically validate the method on the numerical model with the same order of complexity, before it is tested on a real testbed. The theoretical basis for the wavenumber domain sensing method is briefly reviewed for completeness in Section 5.2. In Section 5.3, a cantilever beam in an infinite baffle is considered first as a numerical example for its simplicity. Finally, in Section 5.4, the method will be numerically validated on the main testbed in this thesis, which is the cylindrical shell.

5.2 Wavenumber Domain Feedback Controller Design

In the wavenumber domain feedback control approach, the acoustic power from vibrating structures is chosen as a performance metric, and control systems are designed to estimate and minimize the acoustic power expressed in the wavenumber domain. This approach is based on the fact that only *supersonic* wavenumber components radiate acoustic power for infinitely baffled planar or cylindrical structures [Junger, 1986], and the acoustic power can be estimated in real time with good accuracy within a certain bandwidth of interest. A block diagram showing how the approach is implemented is shown in Figure 5-1. The output signal, $\mathbf{y}$, of sensors mounted on structures, such as accelerometers, is multiplied by the *discrete wavenumber transform matrix* $\widehat{\Phi}$, which is derived from the definition of the discrete wavenumber transform, *i.e.*, discrete Fourier transform in the spatial domain, not from material properties or dynamic characteristics of the structure. Therefore, no process of structural acoustic modeling is required to compute $\widehat{\Phi}$. The output of the multiplication of $\mathbf{y}$ by $\widehat{\Phi}$, which is denoted as $\mathbf{e}$ in Figure 5-1, is then multiplied by a diagonal weighting matrix $\mathbf{Q}$ to generate the performance metric $\mathbf{z}$. Each diagonal element in $\mathbf{Q}$ is a weight for the corresponding wavenumber component, selected such that the 2-norm of $\mathbf{z}$ squared, $\|\mathbf{z}\|_2^2$, approximates the actual acoustic power radiated from the vibrating structure. One way to compute the diagonal elements in $\mathbf{Q}$ is by calculating optimal weights that minimize the difference between the actual acoustic power Π and the estimated

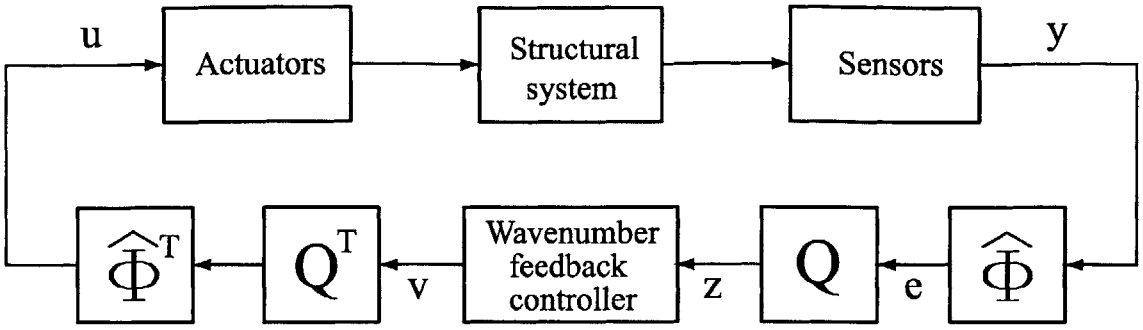

Figure 5-1: Block diagram of the wavenumber feedback controller implementation.

acoustic power $\widehat{\Pi}$. In other words, the optimal weights minimize

$$\overline{J_\Pi} = \sum_{i=1}^{N} |H(j\omega_i)|^2 \left|\Pi(\omega_i) - \widehat{\Pi}(\omega_i)\right|^2 = \sum_{i=1}^{N} |H(j\omega_i)|^2 \left|\Pi(\omega_i) - \|\mathbf{z}(\omega_i)\|_2^2\right|^2. \tag{5.1}$$

Here, $H(j\omega)$ is a frequency weighting function for the performance metric, ω_i is the frequency at which the acoustic power is computed, and N is the total number of frequency points. The expression above assumes the availability of the actual acoustic power Π through simulation or measurements. If the actual acoustic power is not available, the diagonal weighting matrix $\mathbf{Q}$ can be used as design knobs in the controller design process, as in the linear quadratic regulator (LQR) controller design. The iterative procedure of finding $\mathbf{Q}$, which occurs when the actual acoustic power cannot be obtained, is not an unstructured blind trial-and-error approach, but rather is a structured and systematic one. The rationale is that the acoustic power is dominated by only a few wavenumber components in most engineering applications, and one only needs to find the weights for those radiating wavenumber components (determined by $\widehat{\Phi}$) during the controller design.

It should be noted that the wavenumber domain feedback control approach significantly simplifies the feedback controller design for active structural acoustic control, because the approach reduces the effort required to model the acoustic radiation from the structure. As mentioned earlier, no modeling process is required to find $\widehat{\Phi}$, and $\mathbf{Q}$ can be obtained by a structured iterative procedure. Therefore, if one has a model from $\mathbf{u}$ to $\mathbf{y}$, *i.e.*, a model for the structure, then the acoustic power can be estimated using $\widehat{\Phi}$ and $\mathbf{Q}$, which can be obtained without detailed acoustic modeling. Furthermore, the approach simplifies the controller design by reducing the number of transfer functions that need to be computed or identified. Figure 5-1 indicates that transfer functions from $\mathbf{v}$ to $\mathbf{z}$, not from $\mathbf{u}$ to $\mathbf{y}$, are needed in order to design controllers. Generally, the size of vectors $\mathbf{v}$ or $\mathbf{z}$, *i.e.*, the number of wavenumber components considered, is much smaller than that of vectors $\mathbf{u}$ or $\mathbf{y}$, *i.e.*, the number of sensors or actuators. These advantages make the approach a useful tool to design feedback control systems to reduce the radiated noise from vibrating structures.

5.3 Beam Structures

5.3.1 Problem Statement

The new wavenumber domain sensing method is tested numerically on an infinite baffled cantilever beam with ten active composite panels. The schematic of the beam structure with panels is shown in Figure 5-2, showing the disturbance and the sensor measurements $\ddot{\mathbf{w}}_p = [\ddot{w}_1\, \ddot{w}_2 \cdots \ddot{w}_{10}]^T$. The disturbance was modeled as a point force acting at the point shown in Figure 5-2, with a bandwidth below 1000 Hz. It is assumed that the beam is vibrating in air. The beam has a length of 1 m, a width of 0.05 m, and a thickness of 0.05 m, with a Young's modulus of 70 GPa, and density of 2700 kg/m^3. The beam structure was modeled using the finite element method, while the active composite panel was modeled as a mass-spring-damper system, as described in Chapter 2. The equation of motion for the beam structure with panels is written as

$$\begin{bmatrix} (\mathbf{M}_s + \frac{1}{2}\mathbf{T}_{\mathbf{wu}}^T \mathbf{M}_p \mathbf{T}_{\mathbf{wu}}) & \mathbf{0} \\ \mathbf{0} & \frac{1}{2}\mathbf{M}_p \end{bmatrix} \begin{Bmatrix} \ddot{\mathbf{U}}_s \\ \ddot{\mathbf{w}}_p \end{Bmatrix} + \begin{bmatrix} (\mathbf{C}_s + \mathbf{T}_{\mathbf{wu}}^T \mathbf{C}_p \mathbf{T}_{\mathbf{wu}}) & -\mathbf{T}_{\mathbf{wu}}^T \mathbf{C}_p \\ -\mathbf{C}_p \mathbf{T}_{\mathbf{wu}} & \mathbf{C}_p \end{bmatrix} \begin{Bmatrix} \dot{\mathbf{U}}_s \\ \dot{\mathbf{w}}_p \end{Bmatrix} \tag{5.2}$$

$$+ \begin{bmatrix} (\mathbf{K}_s + \mathbf{T}_{\mathbf{wu}}^T \mathbf{K}_p \mathbf{T}_{\mathbf{wu}}) & -\mathbf{T}_{\mathbf{wu}}^T \mathbf{K}_p \\ -\mathbf{K}_p \mathbf{T}_{\mathbf{wu}} & \mathbf{K}_p \end{bmatrix} \begin{Bmatrix} \mathbf{U}_s \\ \mathbf{w}_p \end{Bmatrix} = \begin{bmatrix} \mathbf{B}_f \\ \mathbf{0} \end{bmatrix} f + \begin{bmatrix} -\mathbf{T}_{\mathbf{wu}}^T \\ \mathbf{I}_{N_p} \end{bmatrix} \mathbf{u}\,.$$

Equation 5.2 has the same form as given in Equation 2.35 in Chapter 2 for the cylindrical shell with panels, except that the global mass, damping, and stiffness matrix, $\mathbf{M}_s$, $\mathbf{C}_s$, $\mathbf{K}_s$, should be computed on the beam structure. The procedure to obtain those matrices is described in detail in most textbooks on finite element methods, such as [Bathe, 1996].

Once we have the acceleration measurements, $\ddot{\mathbf{w}}_p = [\ddot{w}_1\, \ddot{w}_2 \cdots \ddot{w}_{10}]^T$, we can compute the radiated acoustic power $\Pi(\omega)$ from the vibrating beam as

$$\Pi(\omega) \;=\; \dot{\mathbf{w}}_p^H(j\omega)\, \mathbf{R}(j\omega)\, \dot{\mathbf{w}}_p(j\omega)\;, \tag{5.3}$$

where $\dot{\mathbf{w}}_p(j\omega)$ is a 10×1 vector of velocity, obtained by integrating $\ddot{\mathbf{w}}_p$, and $\mathbf{R}(j\omega)$ is a 10×10 radiation resistance matrix for the beam structure, given by [Elliott, 1993]

$$\mathbf{R}(j\omega) \;=\; \frac{\rho S^2 \omega^2}{4\pi c} \begin{bmatrix} 1 & \frac{\sin(kr_{1,2})}{kr_{1,2}} & \cdots & \frac{\sin(kr_{1,10})}{kr_{1,10}} \\ \frac{\sin(kr_{2,1})}{kr_{2,1}} & 1 & & \\ \vdots & & \ddots & \frac{\sin(kr_{9,10})}{kr_{9,10}} \\ \frac{\sin(kr_{10,1})}{kr_{10,1}} & & \frac{\sin(kr_{10,9})}{kr_{10,9}} & 1 \end{bmatrix}. \tag{5.4}$$

Here, ω is the excitation frequency, ρ is the density of air, S is the area of the discretized radiator on which each measurement is taken, c is the speed of sound in air, k is the acoustic wavenumber, and $r_{m,n}$ is the distance between the center of mth and nth velocity locations. Equation 5.3 and Equation 5.4 are used to compute the open-loop and closed-loop acoustic power for the beam structure.

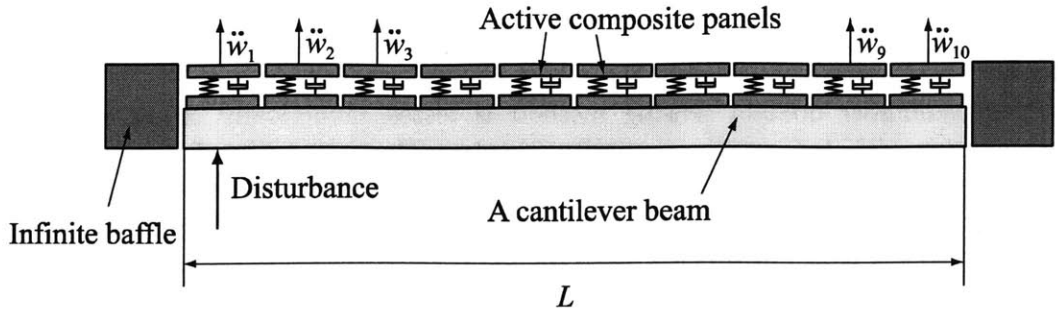

Figure 5-2: An infinite baffled cantilever beam with 10 panels mounted. The thickness of each panel is exaggerated.

In this example, the model in Equation 5.2 is used only for evaluating the open-loop and closed-loop frequency responses. The model needed for controller synthesis is obtained using system identification. By doing that, we can assume the frequency responses from the model are the measured data from the real structures. This approach makes the controller design more realistic, because it is very often the case that we should identify the plant model from measured transfer functions, especially for complex structures.

5.3.2 Design Issues

In order to design LQG controller using the new wavenumber sensing approach, two design issues should be considered. The first one is how many wavenumber components to be used; the other is how to select the weight for each wavenumber component. In this section, these two design issues will be discussed.

Number of wavenumber components

First, we determine how many wavenumber components are needed. Recall that only supersonic wavenumber components contribute to the sound power radiation for the beam structures in an infinite baffle, so we can determine N_m, the number of wavenumber components needed in the controller design. Using the information

$$\begin{aligned} \omega_b &= \text{control bandwidth} = 2\pi \times 1000 \text{ (rad/s)} \\ c &= \text{speed of sound in air} = 343 \text{ m/s} \\ N_s &= \text{number of sensors} = 10 \\ L &= \text{length of the beam} = 1 \text{ m} \\ \Delta x &= \text{the spacing of the sensors} = 0.1 \text{ m } (= L/N_s) \ , \end{aligned}$$

and the condition of the supersonic wavenumber components,

$$k_m = \left(\frac{2\pi}{\Delta x}\right)\frac{m-1}{N_s} \leq \frac{\omega_b}{c} \ (m = 1, 2, ..., N_m) \ , \tag{5.5}$$

we can see that $N_m = 3$ should be enough.

Weighting functions

As shown in the previous chapter, the estimated acoustic power from vibrating beams can be written as

$$\widehat{\Pi}(\omega) = \sum_{m=1}^{N_m} F(k_m, \omega) \left| \ddot{W}_d(k_m, \omega) \right|^2 , \tag{5.6}$$

where $\ddot{W}_d(k_m, \omega)$ is the discrete wavenumber transform of the acceleration field $\ddot{\mathbf{w}}_p = [\ddot{w}_1\, \ddot{w}_2 \cdots \ddot{w}_{10}]^T$, given as

$$\ddot{W}_d(k_m, \omega) = \Delta x \sum_{n=1}^{10} \ddot{w}_n(j\omega)\, e^{-jk_m x_n} . \tag{5.7}$$

The frequency weighting function, $F(k_m, \omega)$, which is defined in Equation 5.6, is a function of excitation frequency, ω. However, as mentioned in Chapter 4, we can find the optimal constant weight, $\widehat{F}(k_m)$, such that the difference between $\Pi(\omega)$, the actual acoustic power, and $\widehat{\Pi}(\omega)$, the estimated acoustic power, is minimized. Once we find the optimal constant weight, we can estimate the acoustic power from vibrating structures and use it as the performance metric in the optimal LQG controller design. Here, it should be noted that we should know the actual acoustic power, $\Pi(\omega)$, by measurements or simulation, to find the optimal weights. If we don't have enough information on $\Pi(\omega)$, we cannot find the optimal weights. This may occur, especially for the general complex structures, if we don't have enough measurements for acoustic pressure in the far field. In that case, the weight can be used as a design knob, as mentioned in Chapter 4, so that the resulting closed-loop response is satisfactory.

5.3.3 Estimation of the Acoustic Power

In this section, the effect of the number of wavenumber components and the weighting functions on the accuracy of estimated acoustic power is discussed. First, the results of estimating the acoustic power are presented, with the optimal weights obtained using the method in Chapter 4. Then, the effects of non-optimal weights on the estimation of the acoustic power are investigated.

Case 1 : Optimal weights

Figure 5-3 through 5-6 show the actual acoustic power, $\Pi(\omega)$, and the estimated acoustic power, $\widehat{\Pi}(\omega)$, as the number of wavenumber components increases. Two butterworth filters, with corner frequency at 100 Hz, are used as a frequency-weighting function for the performance metric $\overline{J_\Pi}$. Here, it is assumed that we have enough measurements of the acoustic pressure in the far field, so that the actual acoustic power can be computed. In that case, we can find the optimal weights using the method given in Chapter 4. The optimal weights for each wavenumber components are given in Table 5.1, showing N_m, the number of wavenumber components, and $\widehat{F}(k_m)$, the optimal weights. Note that the weights in Table 5.1 are normalized with respect to $\widehat{F}(k_1)$, the weight for the first wavenumber component.

Figure 5-3 shows that the first wavenumber component ($\ddot{W}_d(k_1)$) can capture the actual acoustic power up to the second mode (~400 Hz); it begins to diverge from the actual acoustic

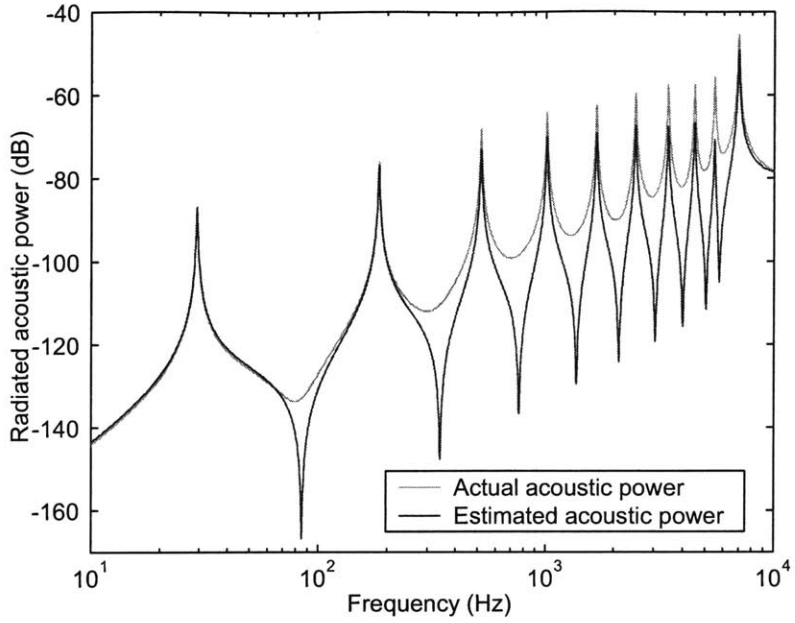

Figure 5-3: Actual and estimated acoustic power obtained using one wavenumber component.

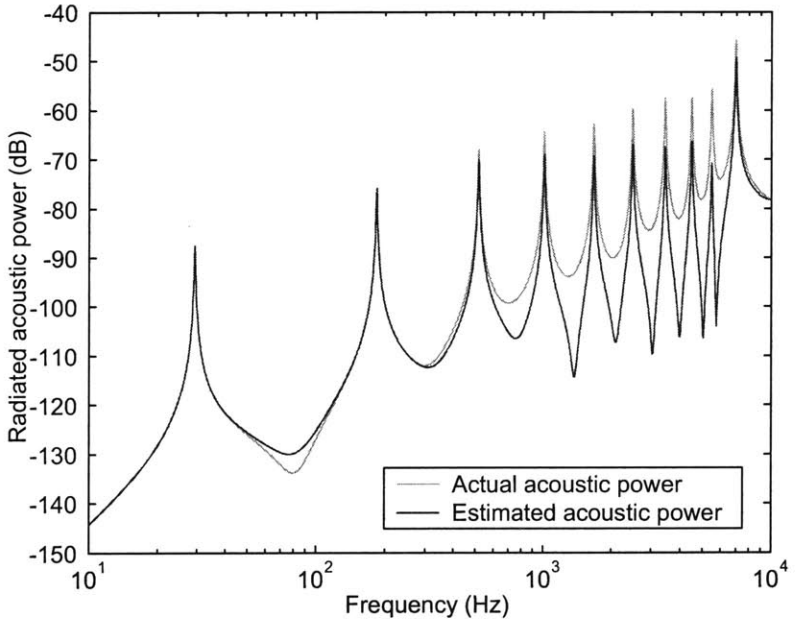

Figure 5-4: Actual and estimated acoustic power obtained using two wavenumber components with optimal weights.

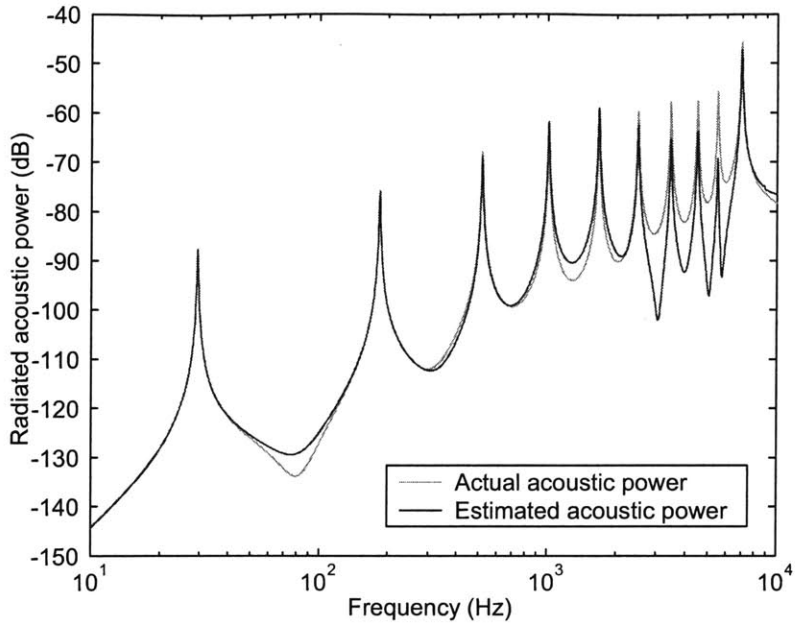

Figure 5-5: Actual and estimated acoustic power obtained using three wavenumber components with optimal weights.

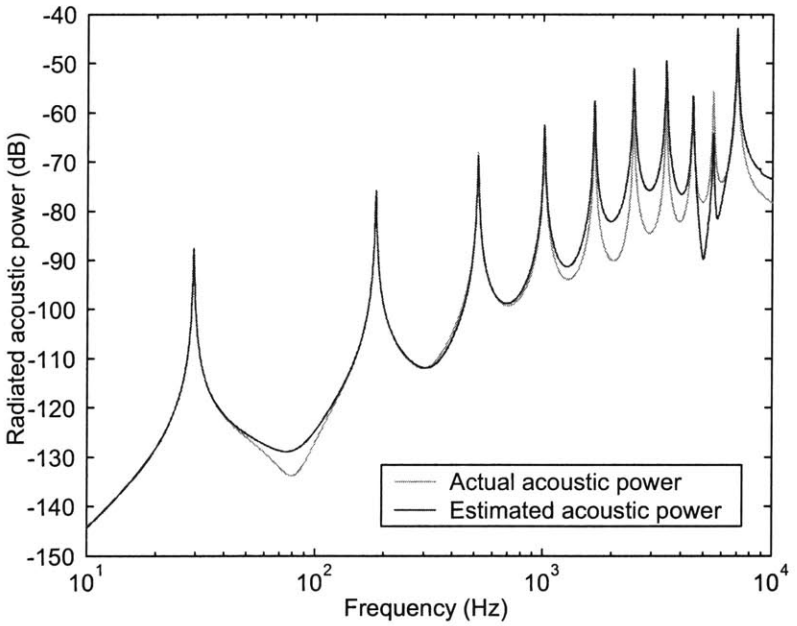

Figure 5-6: Actual and estimated acoustic power obtained using four wavenumber components with optimal weights.

Table 5.1: The optimal weights.

N_m	$\widehat{F}(k_1)$	$\widehat{F}(k_2)$	$\widehat{F}(k_3)$	$\widehat{F}(k_4)$
1	1.0000			
2	1.0000	0.2628		
3	1.0000	0.2227	0.7140	
4	1.0000	0.1717	0.5177	0.2191

power above that frequency. Since $k_1 = 0$, using the first wavenumber component only (*i.e.*, the zero wavenumber component only) to estimate and reduce the acoustic power is equivalent to the volume velocity cancellation method [Johnson, 1995]. Figure 5-3 implies that if the required bandwidth of the system were around 400 Hz, it would be enough to sense and reduce the first wavenumber component, *i.e.*, the zero wavenumber component, to reduce the structurally-radiated noise. On the other hand, it can be seen from Figure 5-4 that the first two wavenumber components ($\ddot{W}_d(k_1)$, $\ddot{W}_d(k_2)$) are needed to estimate the acoustic power with enough accuracy up to the third mode (~800 Hz).

Figure 5-5 shows the actual acoustic power and its estimated acoustic power obtained using three wavenumber components. We concluded in Section 5.3.2 that three wavenumber components are required in order to estimate the acoustic power up to 1 kHz. Figure 5-5 supports this conclusion. Furthermore, we can see that the first three wavenumber components can approximate the actual acoustic power up to 2 kHz, not just 1 kHz, in Figure 5-5. Since the LQG controller tries to minimize the estimated acoustic power obtained using a state-space model below 2 kHz, and since the estimated acoustic power is similar to the actual acoustic power in the same frequency range, it is expected that the LQG controller considering three wavenumber components will reduce the actual acoustic power below 2 kHz.

Finally, the result of estimating the acoustic power with four wavenumber components is shown in Figure 5-5. It is true that they can approximate the actual acoustic power with enough accuracy up to 3–4 kHz. However, it is a waste of control energy to use four wavenumber components when the required control bandwidth is 1 kHz, because three wavenumber components turned out to be enough to estimate the acoustic power up to 1 kHz. Using more wavenumber components than required doesn't guarantee a good closed-loop performance, especially when the control energy is finite, because the control energy is wasted unnecessarily.

Figure 5-7 shows the effect of the number of wavenumber components on the performance metric $\overline{J_\Pi}$, which was defined in Equation 5.1. Here, $\overline{J_\Pi}$ was calculated up to 1 kHz for each case, which is the required control bandwidth. It is observed that there is not much difference between $N_m = 3$, and $N_m = 4$, compared with other cases. Again, this supports the conclusion that $N_m = 3$ is enough to reduce the structurally-radiated noise up to 1 kHz.

Case 2 : Non-optimal weights

In this case, it is assumed that we don't have enough measurements of the acoustic pressure in the far field, so that the actual acoustic power cannot be computed. Since we cannot find the optimal weights in that case, we should select the weights in an *ad hoc* manner. As mentioned earlier, we can use the weights as a design knob in the LQG controller design.

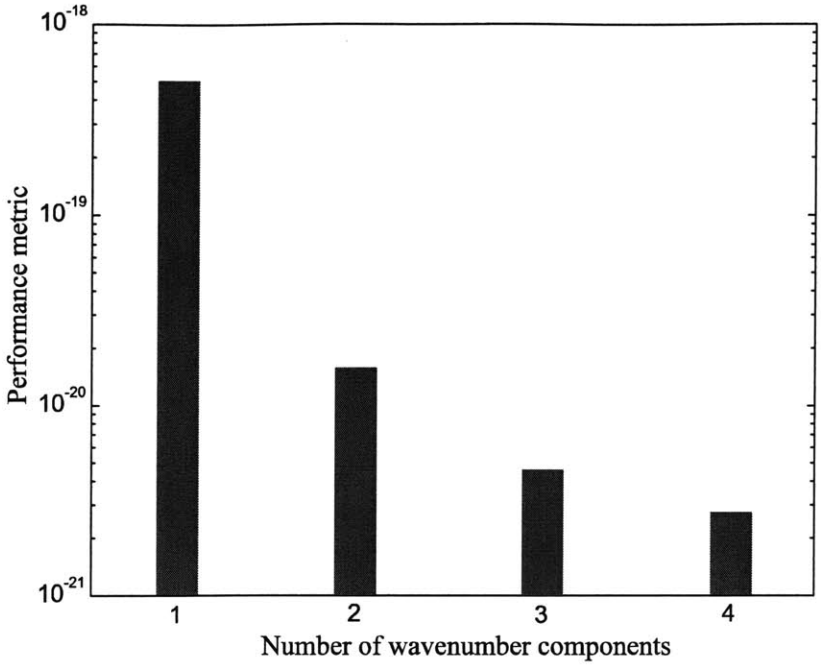

Figure 5-7: The effect of the number of wavenumber components on the performance metric.

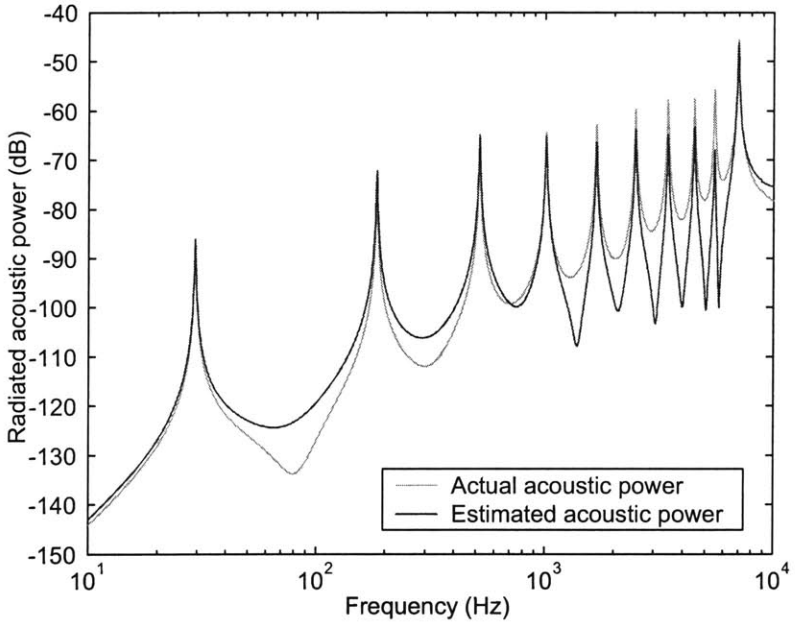

Figure 5-8: Actual and estimated acoustic power obtained using two wavenumber components with non-optimal weights.

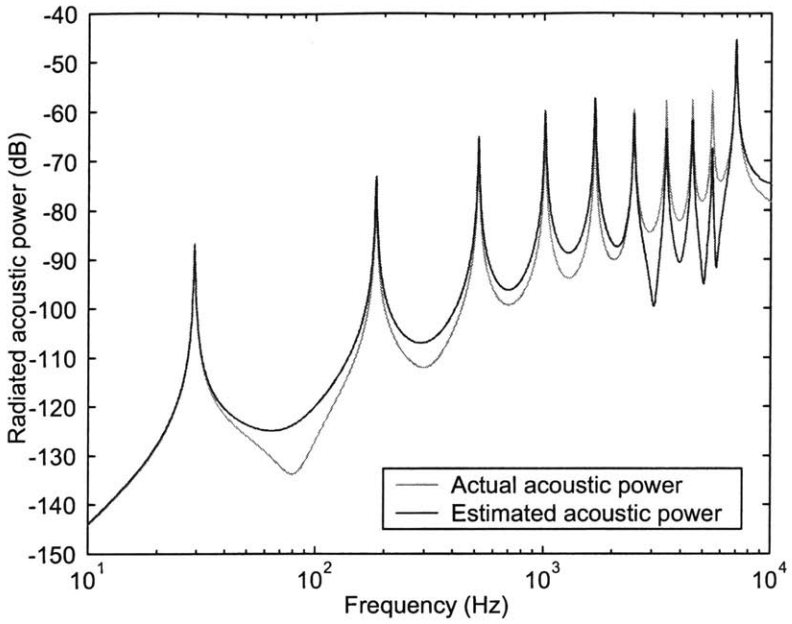

Figure 5-9: Actual and estimated acoustic power obtained using three wavenumber components with non-optimal weights.

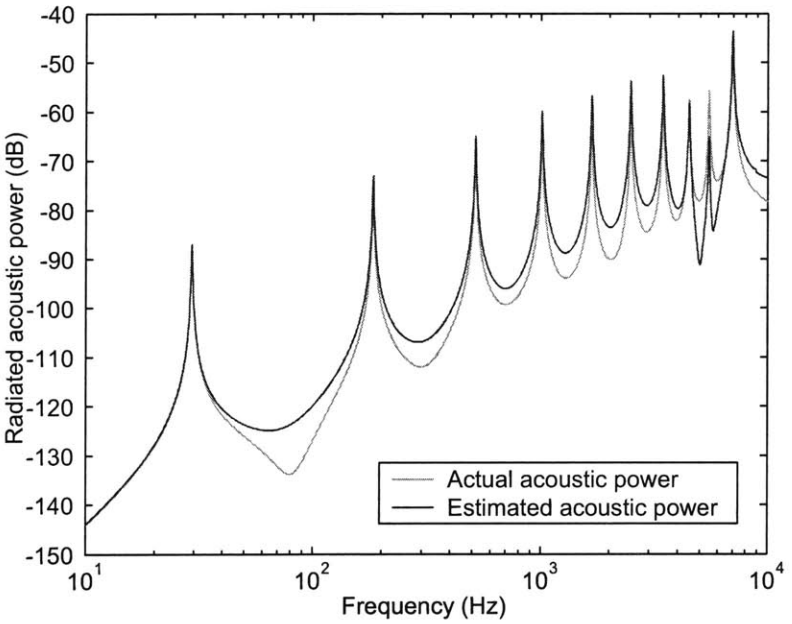

Figure 5-10: Actual and estimated acoustic power obtained using four wavenumber components with non-optimal weights.

Table 5.2: The weights selected in an ad-hoc manner.

N_m	$\widehat{F}(k_1)$	$\widehat{F}(k_2)$	$\widehat{F}(k_3)$	$\widehat{F}(k_4)$
1	1.0000			
2	1.0000	1.0000		
3	1.0000	1.0000	1.0000	
4	1.0000	1.0000	1.0000	1.0000

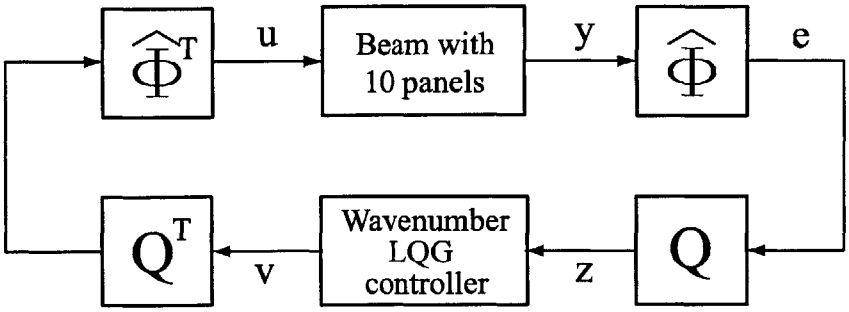

Figure 5-11: Block diagram of the LQG controller implementation for the cantilever beam with 10 panels mounted.

Figure 5-8 through 5-10 show the actual acoustic power, $\Pi(\omega)$, and the estimated acoustic power, $\widehat{\Pi}(\omega)$, as the number of wavenumber components increases. The weights for each wavenumber components are given in Table 5.2, which shows that the same weights are used for each wavenumber component in all cases. This is a good initial guess to determine the weights, when we don't know what acoustic power looks like in advance. From the figures, it can be seen that the weights selected in an *ad hoc* manner produce very similar results to the optimally-selected weights. Therefore, it is expected that the closed-loop performance using the weights selected in an *ad hoc* manner will be comparable with that obtained using the optimal weights. The insensitiveness of the achievable closed-loop performance to the availability of the acoustic power is an important advantage of the wavenumber domain sensing method, because it means that the method can be applied even when we cannot measure or compute the acoustic power, which is the case for most complex structural systems.

5.3.4 LQG Controller Design

As mentioned earlier, the model for the plant obtained using finite elements is used only for evaluating the open-loop and closed-loop frequency responses. The model needed for controller synthesis is obtained using system identification. Figure 5-11 shows the block diagram of the LQG controller designed in the wavenumber domain. The output measurements from the accelerometers embedded in the panels, collected in a single vector as $\mathbf{y} = \ddot{\mathbf{w}}_p = [\ddot{w}_1\, \ddot{w}_2 \cdots \ddot{w}_{10}]^T$, are multiplied by the discrete wavenumber transform matrix $\widehat{\Phi}^T = \left[\widehat{\Phi}_1^T\, \widehat{\Phi}_2^T \cdots \widehat{\Phi}_{N_m}^T\right]$, defined

in Equation 4.57, such that the output of the matrix becomes

$$\mathbf{e} = \widehat{\Phi}\mathbf{y} = \begin{bmatrix} \widehat{\ddot{W}}_d(k_1) \\ \widehat{\ddot{W}}_d(k_2) \\ \vdots \\ \widehat{\ddot{W}}_d(k_{N_m}) \end{bmatrix}. \tag{5.8}$$

Also, the weighting matrix $\mathbf{Q}$ in Figure 5-11 is defined as

$$\mathbf{Q} = \begin{bmatrix} \sqrt{\widehat{F}(k_1)} & 0 & \cdots & 0 \\ 0 & \sqrt{\widehat{F}(k_2)} & & \\ & & \sqrt{\widehat{F}(k_2)} & \\ \vdots & & \ddots & \vdots \\ & & & \sqrt{\widehat{F}(k_{N_m})} \quad 0 \\ 0 & & \cdots & 0 \quad \sqrt{\widehat{F}(k_{N_m})} \end{bmatrix}, \tag{5.9}$$

so that the 2-norm of its output, denoted as $\mathbf{z}$ in Figure 5-11,

$$\mathbf{z} = \begin{bmatrix} \sqrt{\widehat{F}(k_1)}\widehat{\ddot{W}}_d(k_1) \\ \sqrt{\widehat{F}(k_2)}\widehat{\ddot{W}}_d(k_2) \\ \vdots \\ \sqrt{\widehat{F}(k_{N_m})}\widehat{\ddot{W}}_d(k_{N_m}) \end{bmatrix}, \tag{5.10}$$

becomes the estimated acoustic power $\widehat{\Pi}(\omega)$, given as

$$\widehat{\Pi}(\omega) = \|\mathbf{z}\|_2^2 = \sum_{m=1}^{N_m} \widehat{F}(k_m) \left|\ddot{W}_d(k_m)\right|^2. \tag{5.11}$$

Using the wavenumber sensing method developed in this thesis, we need only to do the system identification on the transfer matrix from $\mathbf{v}$ to $\mathbf{e}$ or $\mathbf{z}$, not from $\mathbf{u}$ to $\mathbf{y}$. By doing that, the number of transfer functions that should be identified is significantly reduced from 100 (from $\mathbf{u}$ to $\mathbf{y}$) to $(2N_m - 1)^2$ (from $\mathbf{v}$ to $\mathbf{e}$ or $\mathbf{z}$), if N_m is less than 10. In the previous section, it was shown that $N_m = 3$ would be enough to estimate the acoustic power within the required bandwidth, and therefore, the number of transfer functions that should be identified is reduced to 25 in this case.

Once we have a state-space model, we can design the LQG controller to minimize the estimated acoustic power.

5.3.5 Closed-loop Results

In this section, the results of several closed-loop simulations are reported. Both the effects of the number of wavenumber components, N_m, and the weights for each wavenumber component, $\widehat{F}(k_m)$, on the closed-loop performance are discussed.

The closed-loop responses obtained using optimal weights and non-optimal weights are shown in Figure 5-12 through Figure 5-18, as N_m increases, with ratios of open-loop response to closed-loop response for each case. Note that negative and positive ratios indicate attenuation and amplification of the disturbance, respectively. The optimal weights are obtained such that they minimize the performance metric $\overline{J_\Pi}$ defined in Equation 5.1, while the non-optimal weights are selected such that the resulting closed-loop response is acceptable. The same weights as used in the previous section are adopted here in both cases; they are given in Table 5.1 and Table 5.2, respectively. Also, in order to compare the performance of each control loop, two performance indices J_1 and J_2 are defined as

$$J_1 = \int_0^{2\pi\times 1000\,(\mathrm{rad/s})} \Pi(\omega)\, d\omega\,, \tag{5.12}$$

$$J_2 = \int_0^{2\pi\times 2000\,(\mathrm{rad/s})} \Pi(\omega)\, d\omega\,.$$

Here, J_1 and J_2 represent the integration of the acoustic power below 1000 Hz and 2000 Hz, respectively. The two performance indices are summarized in Table 5.3 for each control loop. The performance in the table represents the ratio of the open-loop to the closed-loop performance index. Figure 5-19 and Figure 5-20 show the effect of N_m and $\widehat{F}(k_m)$ on the performance index J_1 and J_2 of the closed-loop system.

If we compare the results in Figure 5-12 through Figure 5-15, we can see how the number of wavenumber components N_m affects the closed-loop performance. From Figure 5-12, we see that 25 dB of attenuation is achieved at 29 Hz (first mode), and 15 dB of reduction is achieved at 184 Hz (second mode) by minimizing the first wavenumber component $\widehat{\ddot{W}}_d(k_1)$. This was expected from the result of comparing the actual acoustic power with the estimated one in Figure 5-3. Using the first two wavenumber components ($\widehat{\ddot{W}}_d(k_1)$, $\widehat{\ddot{W}}_d(k_2)$), the effective control bandwidth increases up to around 800 Hz; more than 20 dB of reduction at the first two modes (29 Hz and 184 Hz), and 10 dB of reduction at the third mode (516 Hz) is achieved. This trend continues when $N_m = 3$ and $N_m = 4$. For both cases, almost 20 dB of attenuation is achieved at each mode up to 2 kHz.

The initial conclusion we might get from the figures is that the closed-loop performance improves as N_m increases. However, Table 5.3 and Figure 5-19 imply that higher N_m doesn't guarantee better performance, if the control energy is finite and N_m is unnecessarily higher than needed. For example, if the required control bandwidth is 1 kHz, $N_m = 3$ gives better performance than $N_m = 4$. $N_m = 3$ was chosen in Section 5.3.2 as the number of wavenumber components to be considered in order to reduce the structurally-radiated noise up to 1 kHz. If $N_m = 4$ is chosen, the finite control energy is consumed unnecessarily to reduce the wavenumber component $\widehat{\ddot{W}}_d(k_4)$, which doesn't radiate acoustic power below 1 kHz. Note that the structural wavenumber k_4 is greater than the acoustic wavenumber below 1 kHz (Equation 5.5). If the required bandwidth is set to be 2 kHz, however, it is natural that $N_m = 4$ gives better

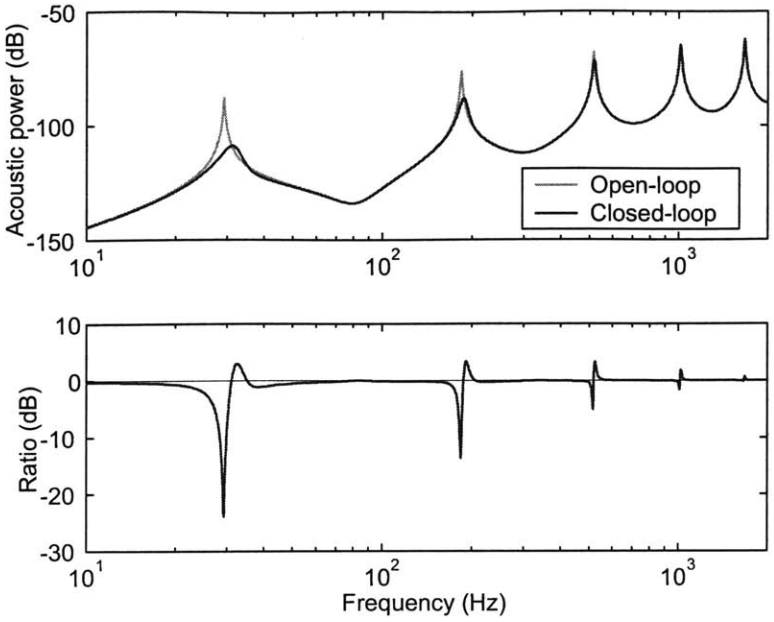

Figure 5-12: Closed-loop performance obtained using one wavenumber component with optimal weight.

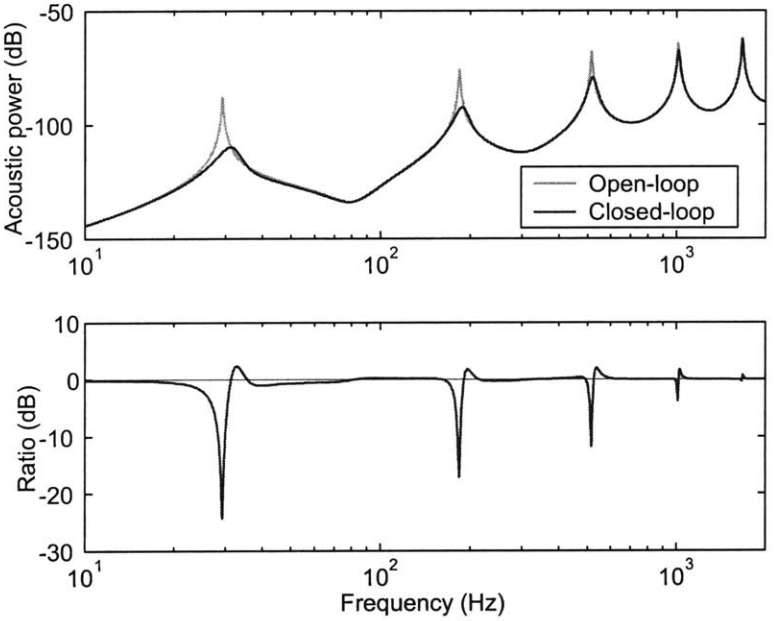

Figure 5-13: Closed-loop performance obtained using two wavenumber components with optimal weights.

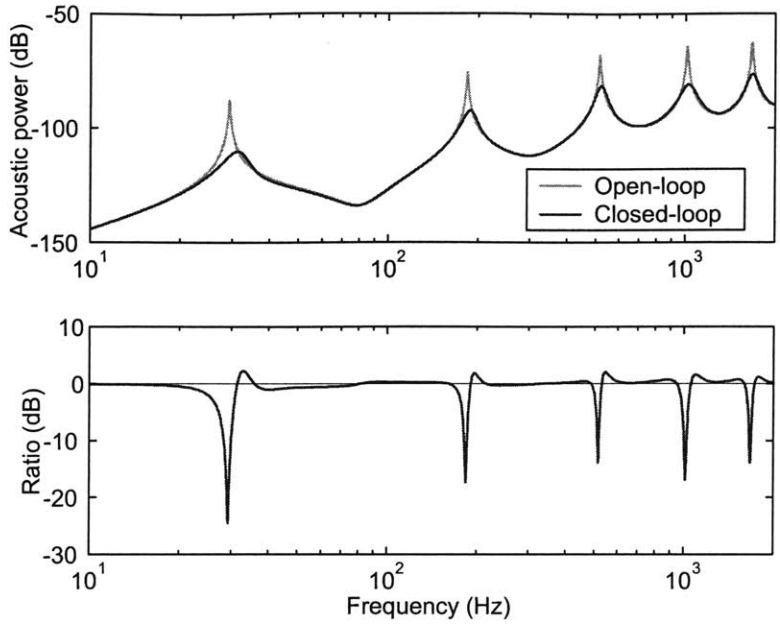

Figure 5-14: Closed-loop performance obtained using three wavenumber components with optimal weights.

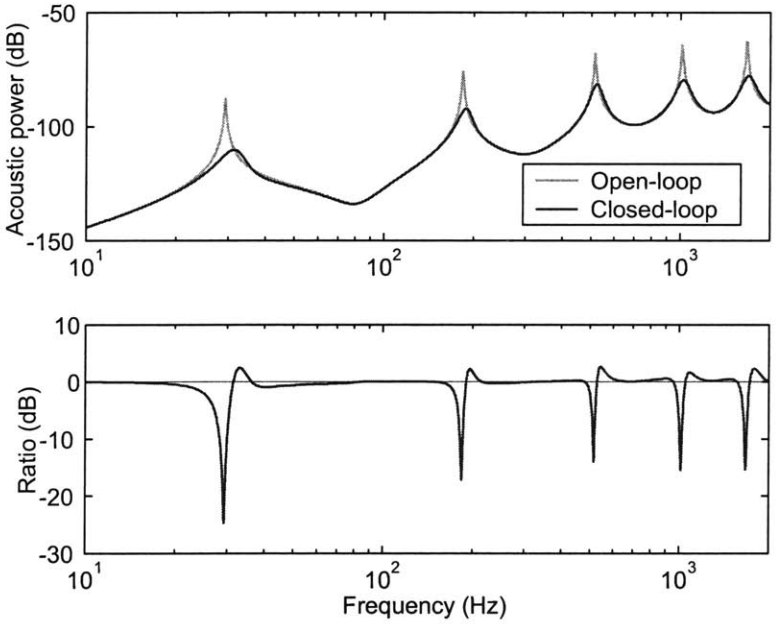

Figure 5-15: Closed-loop performance obtained using four wavenumber components with optimal weights.

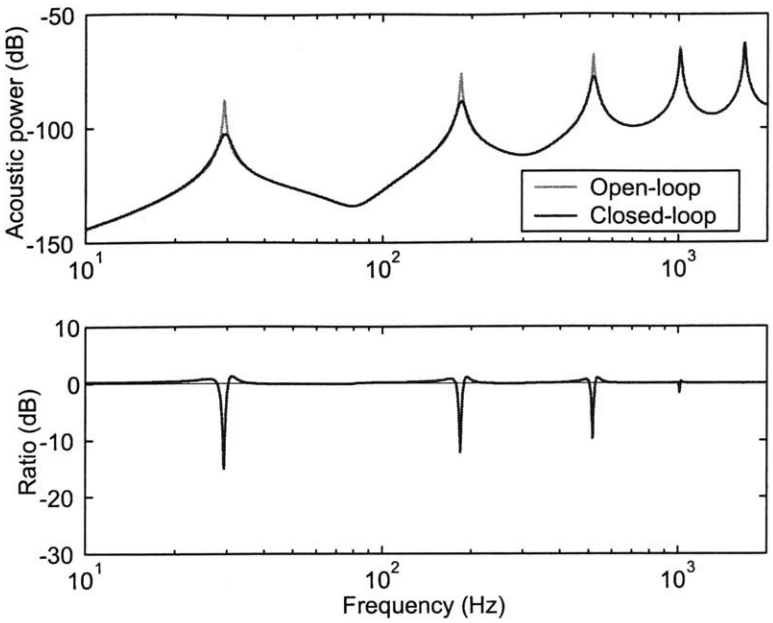

Figure 5-16: Closed-loop performance obtained using two wavenumber components with non-optimal weights.

performance than $N_m = 3$ (Figure 5-20), because $\widehat{\ddot{W}}_d(k_4)$ becomes a radiating wavenumber component above 1 kHz. This fact shows how important the choice of N_m is to yield the satisfactory closed-loop performance, given the required bandwidth and the finite control energy.

The effect of the weights for each wavenumber component, $\widehat{F}(k_m)$, can be found by comparing the closed-loop performance in Figure 5-13 with Figure 5-16, Figure 5-14 with 5-17, and Figure 5-15 with 5-18, respectively. Also, each closed-loop performance can be compared easily using Figure 5-19 and Figure 5-20. It is observed that the closed-loop performance obtained using the optimal weights is a little better than that obtained using the non-optimal weights, but their difference is not significant. This shows that non-optimal weights selected in an *ad hoc* manner result in the closed-loop performance that is very similar to the performance obtained using optimal weights. Therefore, the new wavenumber domain sensing method can be used without any difficulty, even when the acoustic power cannot be obtained during the controller design.

5.4 Cylindrical Shell

5.4.1 Problem Statement

In this section, the result of applying the new wavenumber domain sensing method on an infinite baffled cylindrical shell is reported. The shell is covered with 55 active composite panels, five in the axial direction and eleven in the circumferential direction (Figure 5-21). It is assumed that the shell is vibrating in water, thereby radiating acoustic power. The shell has a length of

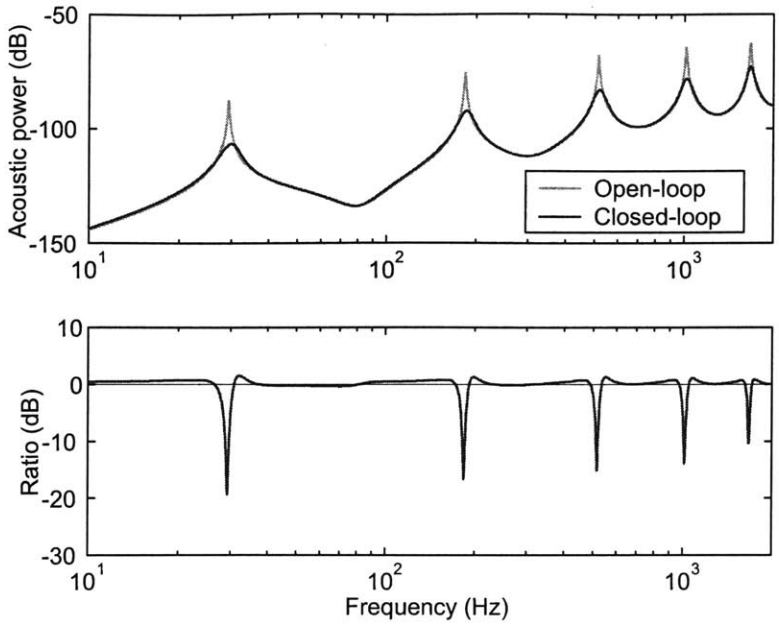

Figure 5-17: Closed-loop performance obtained using three wavenumber components with non-optimal weights.

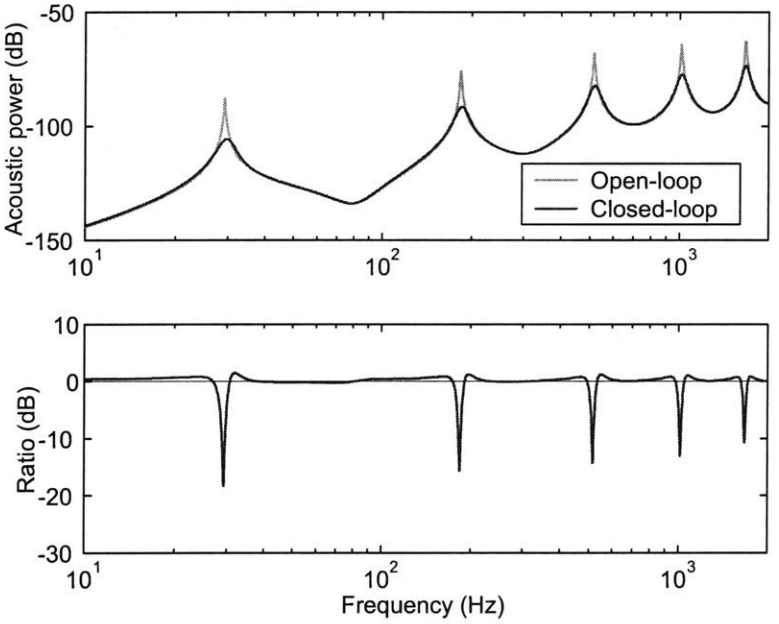

Figure 5-18: Closed-loop performance obtained using four wavenumber components with non-optimal weights.

Table 5.3: The performance index for each control loop.

	J_1	Performance	J_2	Performance
Open loop	2.12×10^{-6}	1.00 (0.0 dB)	2.28×10^{-5}	1.00 (0.0 dB)
Optimal weights, $N_m = 1$	1.72×10^{-6}	1.23 (0.9 dB)	2.30×10^{-5}	0.99 (-0.0 dB)
Optimal weights, $N_m = 2$	1.14×10^{-6}	1.87 (2.7 dB)	2.08×10^{-5}	1.09 (0.4 dB)
Non-optimal weights, $N_m = 2$	1.27×10^{-6}	1.67 (2.2 dB)	2.12×10^{-5}	1.08 (0.3 dB)
Optimal weights, $N_m = 3$	6.71×10^{-7}	3.16 (5.0 dB)	4.91×10^{-6}	4.63 (6.7 dB)
Non-optimal weights, $N_m = 3$	7.53×10^{-7}	2.82 (4.5 dB)	6.91×10^{-6}	3.29 (5.2 dB)
Optimal weights, $N_m = 4$	7.30×10^{-7}	2.91 (4.6 dB)	4.77×10^{-6}	4.77 (6.8 dB)
Non-optimal weights, $N_m = 4$	8.21×10^{-7}	2.59 (4.1 dB)	6.87×10^{-6}	3.31 (5.2 dB)

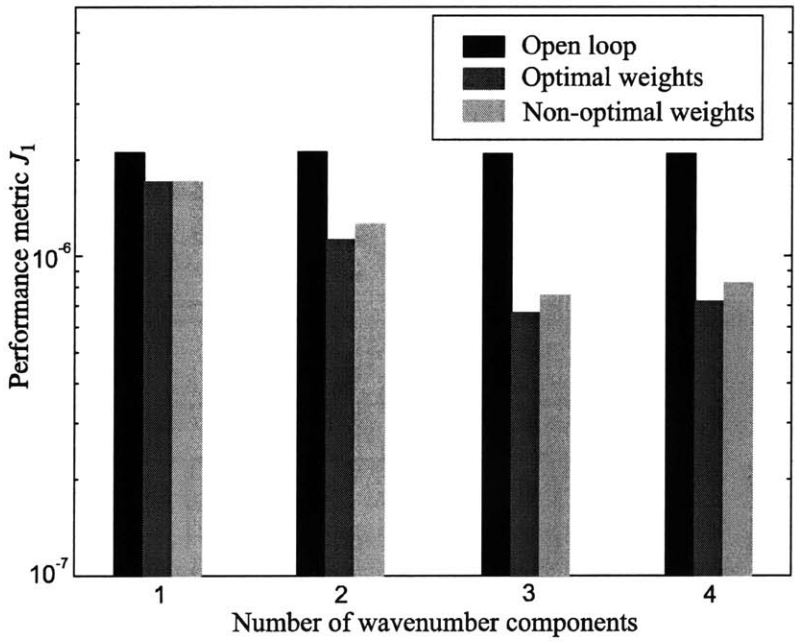

Figure 5-19: The performance index J_1 of the open-loop and closed-loop system.

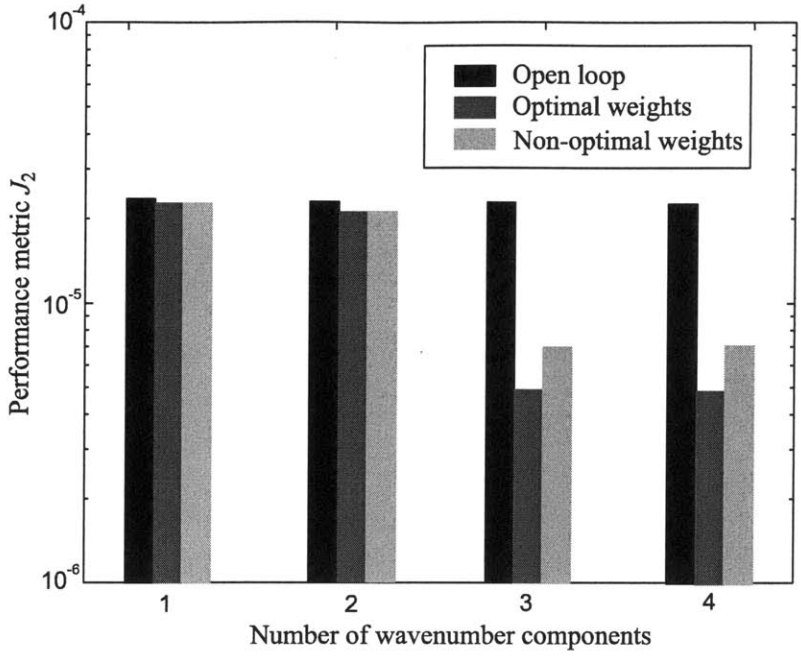

Figure 5-20: The performance index J_2 of the open-loop and closed-loop system.

32 inches, a diameter of 20 inches, a thickness of 0.3 inches, with a Young's modulus of 70 GPa, and density of 2700 kg/m^3. The geometry of the shell modeled in this section is the same as that of the real testbed cylindrical shell.

The disturbance was modeled as a point force acting at the point shown in Figure 5-21, with a bandwidth below 1200 Hz. The shell was modeled using the finite element method, while the panel was modeled as a mass-spring-damper system. The modeling procedure for the shell and the panel is given in detail in Chapter 2. Finally, the acoustic responses, such as the acoustic pressure and the acoustic power, were obtained by using the analytic expressions in Equation 4.20 and Equation 4.22 in Chapter 4.

As in the previous section, the model developed for the shell and the panels is not used to get a plant model for controller synthesis. The model is used only for computing the open-loop and closed-loop frequency responses.

5.4.2 Design Issues

Two main design issues for applying the new wavenumber sensing method, which are to determine the number of wavenumber components and select the weights for each wavenumber component, are discussed in this section.

Number of wavenumber components

For an infinite baffled cylindrical shell, only supersonic wavenumber components contribute to the sound power radiation in the axial direction, while all the wavenumber components radiate

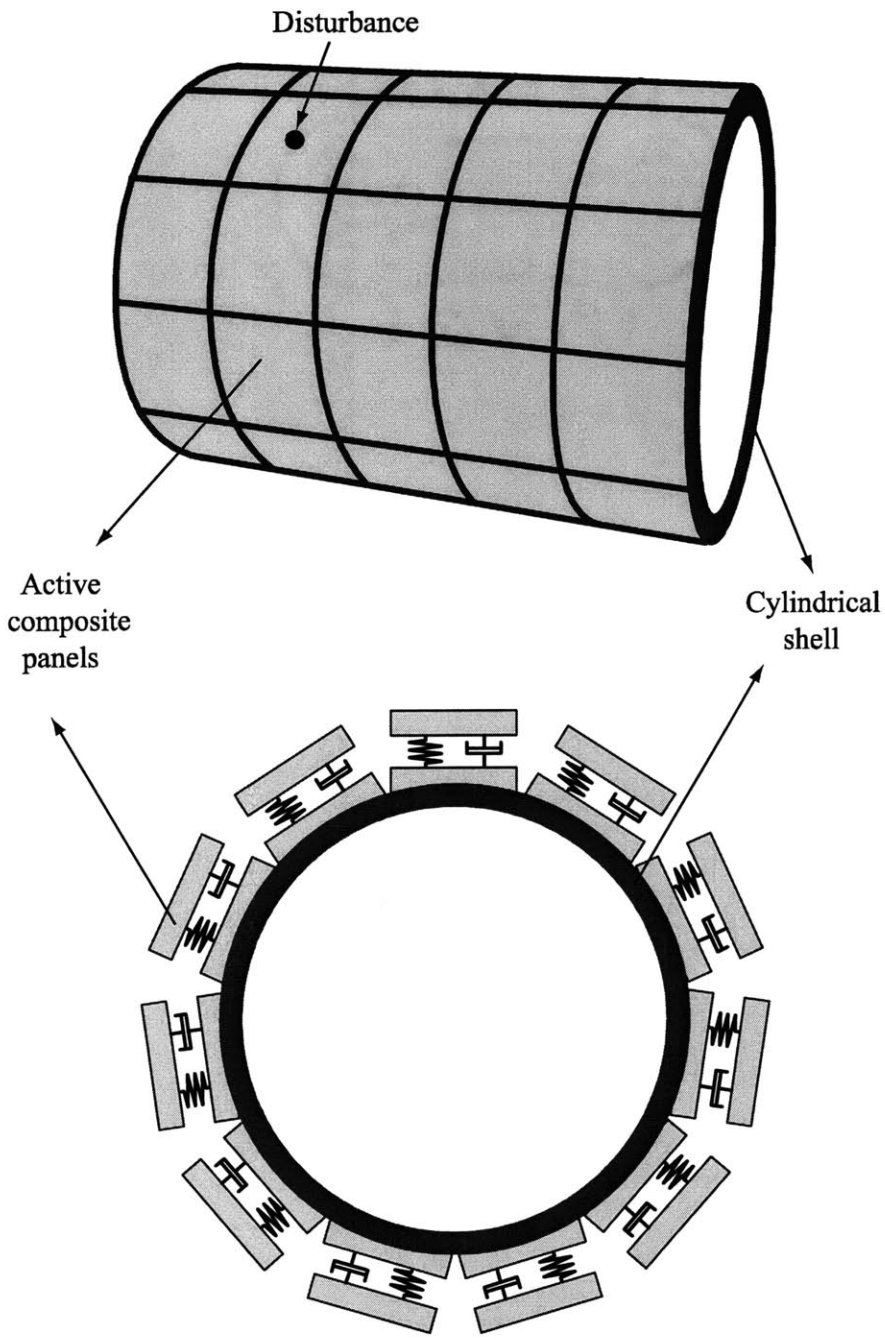

Figure 5-21: Cylindrical shell with 55 panels mounted. The thickness of each panel is exaggerated.

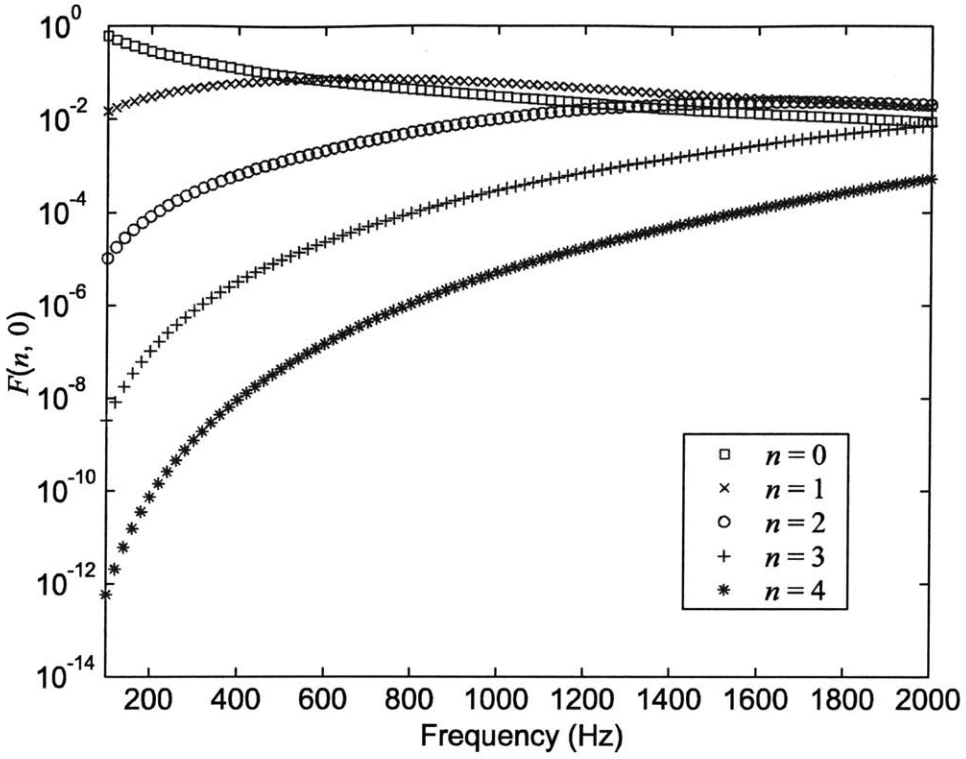

Figure 5-22: Weighting function $F(n,0)$ for the circumferential wavenumber components $\ddot{W}_d(n,0)$. The axial wavenumber, k_m, is set to be 0 (the first wavenumber component).

the acoustic power in the circumferential direction. Therefore, we should determine the number of wavenumber components to be considered in both directions based on different criterion. In the axial direction, we can determine N_m, the number of axial wavenumber components needed in the controller design, using the fact that only supersonic axial wavenumber components radiate acoustic power. Given the information,

$$\begin{aligned}
\omega_b &= \text{control bandwidth} = 2\pi \times 1200 \text{ (rad/s)} \\
c &= \text{speed of sound in water} = 1500 \text{ m/s} \\
N_a &= \text{number of sensors in the axial direction} = 5 \\
L &= \text{length of cylindrical shell} = 32 \text{ inches} \\
\Delta z &= \text{the spacing of the sensors in the axial direction} = 6.4 \text{ inches } (= L/N_a) \ ,
\end{aligned}$$

and the condition of the supersonic wavenumber components,

$$\begin{aligned}
k_m &= \left(\frac{2\pi}{\Delta z}\right)\frac{m-1}{N_a} \\
&\leq \frac{\omega_b}{c} \ (m = 1, 2, ..., N_m) \ ,
\end{aligned} \tag{5.13}$$

we see that $N_m = 1$ should be enough. On the other hand, since all the circumferential wavenumber components contribute to the sound power radiation, there is no decisive way to determine N_n, the number of circumferential wavenumber components needed in the controller design. N_n is determined in an *ad hoc* way, based on the mode shape in the control bandwidth and the weighting function for the radiating wavenumber components. As shown in the previous chapter, the estimated acoustic power from a vibrating cylindrical shell in an infinite baffle can be written as

$$\widehat{\Pi}(\omega) = \sum_{n=0}^{N_n-1} \sum_{m=1}^{N_m} F(n,k_m) \left| \ddot{W}_d(n,k_m) \right|^2 , \tag{5.14}$$

where $\ddot{W}_d(n,k_m)$ is the discrete wavenumber transform of the acceleration field $\ddot{w}(\varphi_l, z_s)$, given as

$$\ddot{W}_d(n,k_z) = \frac{1}{2\pi} \Delta\varphi \Delta z \sum_{l=1}^{11} \sum_{s=1}^{5} \ddot{w}(\varphi_l, z_s)\, e^{-jn\varphi_l} e^{-jk_z z_s} . \tag{5.15}$$

The expressions for $\Delta\varphi$, Δz, φ_l, and z_s are given in Equation 4.62 in Chapter 4. Also, the frequency weighting function $F(n,k_m)$ in Equation 5.14 is given by

$$F(n,k_m) = \begin{cases} \dfrac{2\rho c k}{\pi\omega^2} \dfrac{\Delta k_m}{\varepsilon_n \epsilon_m \left| H_n^{(2)\prime}\left(a\sqrt{k^2-k_m^2}\right)\right|^2 (k^2-k_m^2)} , & k_m \le k = \dfrac{\omega}{c} \\ 0 , & k_m \ge k = \dfrac{\omega}{c} \end{cases} \tag{5.16}$$

Figure 5-22 shows the weighting function $F(n,k_m)$ when k_m is set to be 0, which is the first wavenumber in the axial direction. It can be seen that the first three or four wavenumber components in the circumferential direction (n = 0–2 or 3) will be enough to estimate the acoustic power within the required bandwidth of 1.2 kHz, and therefore, an LQG controller minimizing the first three or four circumferential wavenumber components will reduce the estimated acoustic power within that frequency range.

Weighting functions

As shown in Figure 5-22, the frequency weighting function $F(n,k_m)$ is a function of excitation frequency ω. However, using the method in Chapter 4, we can find the optimal constant weight, $\widehat{F}(n,k_m)$, such that the difference between the actual and the estimated acoustic power is minimized, if we have information about the actual acoustic power from measurements or simulation. If we cannot compute the optimal weights, primarily because we don't have enough measurements to compute the acoustic power, we can use the weights as a design knob in the controller design process.

5.4.3 Estimation of the Acoustic Power

The results of estimating the acoustic power radiated from the cylindrical shell using the new wavenumber domain sensing method are presented in this section. Figure 5-23 through 5-26 show the actual acoustic power, $\Pi(\omega)$, and the estimated acoustic power, $\widehat{\Pi}(\omega)$, obtained using the optimal weights as the number of circumferential wavenumber components N_n increases.

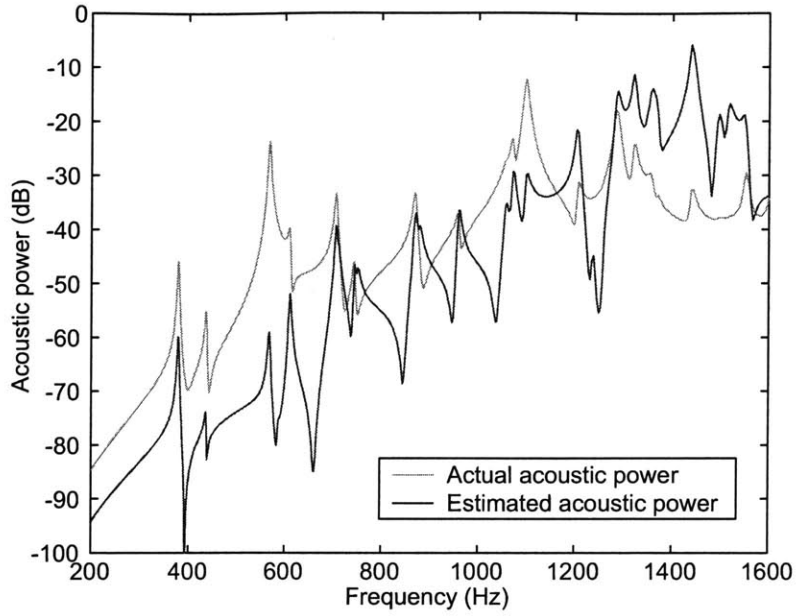

Figure 5-23: Actual and estimated acoustic power obtained using one circumferential wavenumber component with optimal weight.

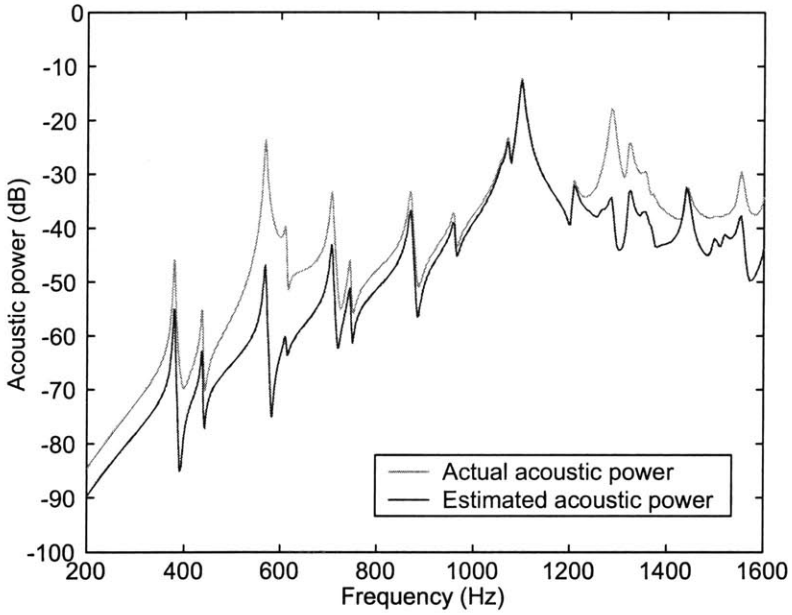

Figure 5-24: Actual and estimated acoustic power obtained using two circumferential wavenumber components with optimal weights.

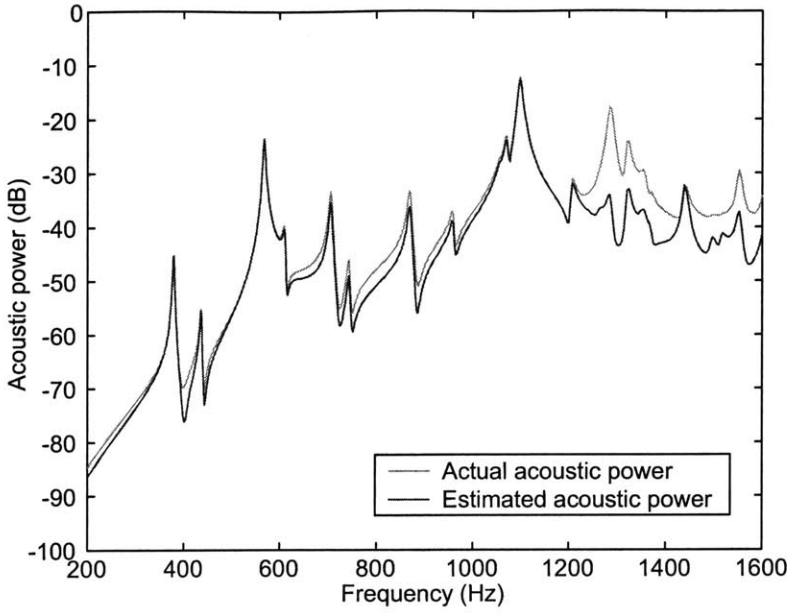

Figure 5-25: Actual and estimated acoustic power obtained using three circumferential wavenumber components with optimal weights.

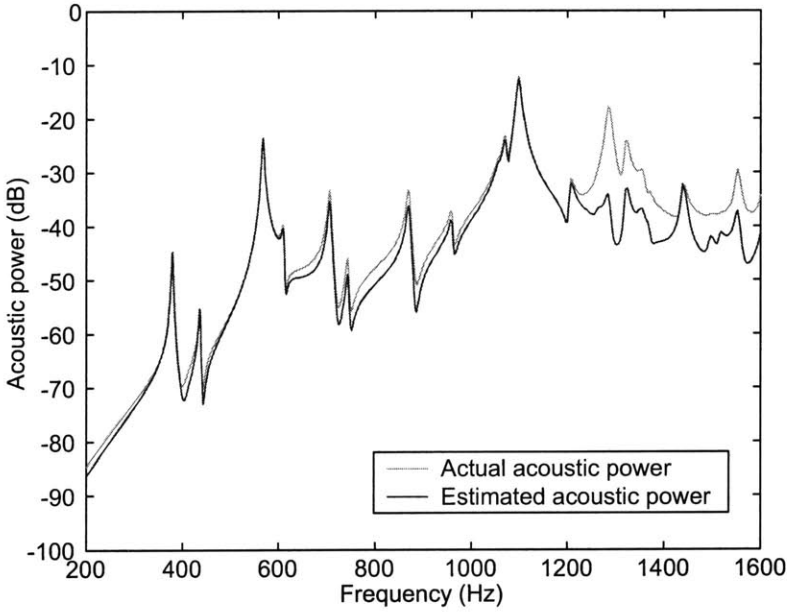

Figure 5-26: Actual and estimated acoustic power obtained using four circumferential wavenumber components with optimal weights.

Table 5.4: The optimal weights.

N_n	$\widehat{F}(0,0)$	$\widehat{F}(1,0)$	$\widehat{F}(2,0)$	$\widehat{F}(3,0)$
1	1.00×10^{0}			
2	1.00×10^{0}	1.42×10^{0}		
3	1.00×10^{0}	1.42×10^{0}	7.62×10^{-2}	
4	1.00×10^{0}	1.42×10^{0}	7.62×10^{-2}	1.24×10^{-4}

Here, the number of axial wavenumber component, N_m, is set to be 1. Two butterworth filters with corner frequency at 10 Hz are used as a frequency function to compute the optimal weights and the performance metric $\overline{J_\Pi}$. The optimal weights for each wavenumber components are given in Table 5.4, showing N_n, the number of circumferential wavenumber components, and $\widehat{F}(n,0)$, the optimal weight. Note that the weights in Table 5.4 are normalized with respect to $\widehat{F}(0,0)$, the weight for the first wavenumber component. Also, the axial wavenumber k_m is set to be 0, because only the first axial wavenumber component is considered.

Figure 5-23 shows that estimating the acoustic power using the first wavenumber component only is not a good approach in this application. The first wavenumber component alone cannot capture the actual acoustic power within the required control bandwidth. Therefore, reducing the first wavenumber component, or the volume velocity cancellation method, will not help reduce the acoustic power radiated from the cylindrical shell considered in this example.

Figure 5-24 indicates that the most dominant peak around 1100 Hz within the control bandwidth can be estimated using the first two wavenumber components in the circumferential direction. However, they cannot estimate the acoustic power at other frequency ranges. On the other hand, it can be seen from Figure 5-25 and Figure 5-26 that the acoustic power can be estimated with enough accuracy up to 1.2 kHz using the first three or four wavenumber components. This observation supports the conclusion in Section 5.4.2. Since LQG controller minimizes the estimated acoustic power, and since it can be made similar to the actual acoustic power in the required bandwidth, it is expected that LQG controller will reduce the actual acoustic power using three wavenumber components in the circumferential direction. It is difficult to see the difference between Figure 5-25 ($N_n = 3$) and Figure 5-26 ($N_n = 4$). This observation implies that there is no reason to use four wavenumber components. As will be shown in the next section, considering three wavenumber components gives a little better closed-loop performance in terms of the total acoustic power in the control bandwidth than considering four wavenumber components.

Figure 5-27 shows the performance metric $\overline{J_\Pi}$ used to select the optimal weights. $\overline{J_\Pi}$ was computed up to the required control bandwidth, which is 1.2 kHz. It can be seen from the figure that the performance metric for $N_n = 3$ is a little smaller than for $N_n = 4$, although their difference is negligible.

If we cannot compute the optimal weights for each wavenumber component, we should select the weights in an *ad hoc* manner, such that the resulting closed-loop performance is acceptable. Figure 5-28 through 5-30 show the actual and estimated acoustic power obtained using the weights selected in an *ad hoc* manner. The weights for each wavenumber components are given in Table 5.5. As in the case for the optimal weights, the number of axial wavenumber component, N_m, is set to be 1. From the figures, we can see that the resulting estimated

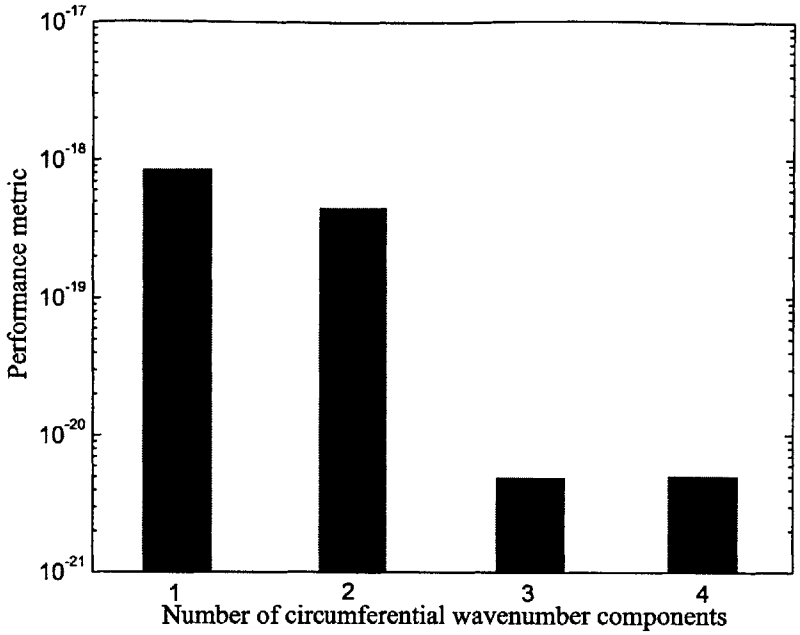

Figure 5-27: The effect of the number of circumferential wavenumber components on the performance metric.

Table 5.5: The weights selected in an ad-hoc manner.

N_n	$\widehat{F}(0,0)$	$\widehat{F}(1,0)$	$\widehat{F}(2,0)$	$\widehat{F}(3,0)$
1	1.0000			
2	1.0000	1.0000		
3	1.0000	1.0000	1.0000	
4	1.0000	1.0000	0.25	0.0225

acoustic power obtained using the non-optimal weights are very similar to those obtained using the optimally-selected weights. This observation implies that non-optimal weights, if properly selected by iteration, will result in the closed-loop performance that is comparable with the performance obtained using optimal weights. This is one of the important advantages of the new wavenumber domain sensing method developed in this study.

5.4.4 Closed-loop Results

This section presents the results of applying the wavenumber domain LQG controller design to the cylindrical shell. The closed-loop responses obtained using optimal weights and non-optimal weights are shown from Figure 5-31 to Figure 5-37, as N_n varies from 1 to 4, with ratios of open-loop response to closed-loop response for each case. In all cases, $N_m = 1$ is considered. Note that negative and positive ratios indicate attenuation and amplification of the disturbance,

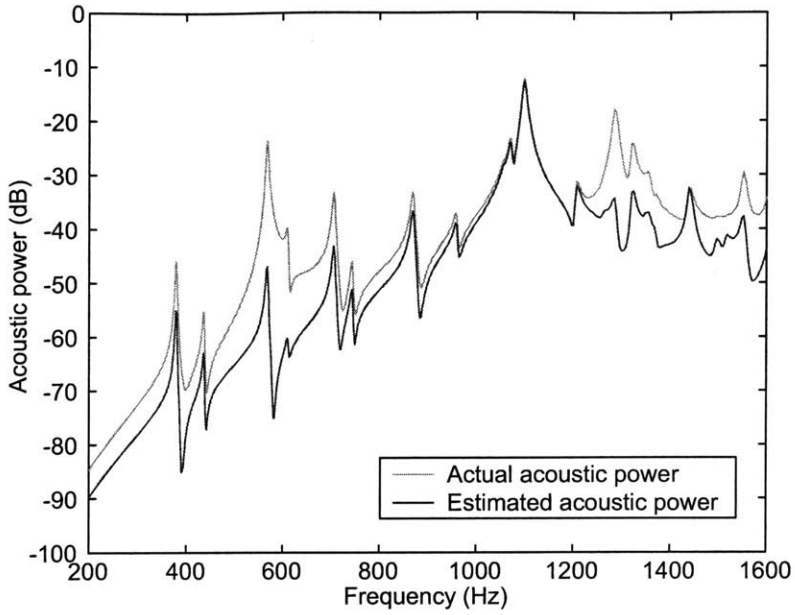

Figure 5-28: Actual and estimated acoustic power obtained using two circumferential wavenumber components with non-optimal weights.

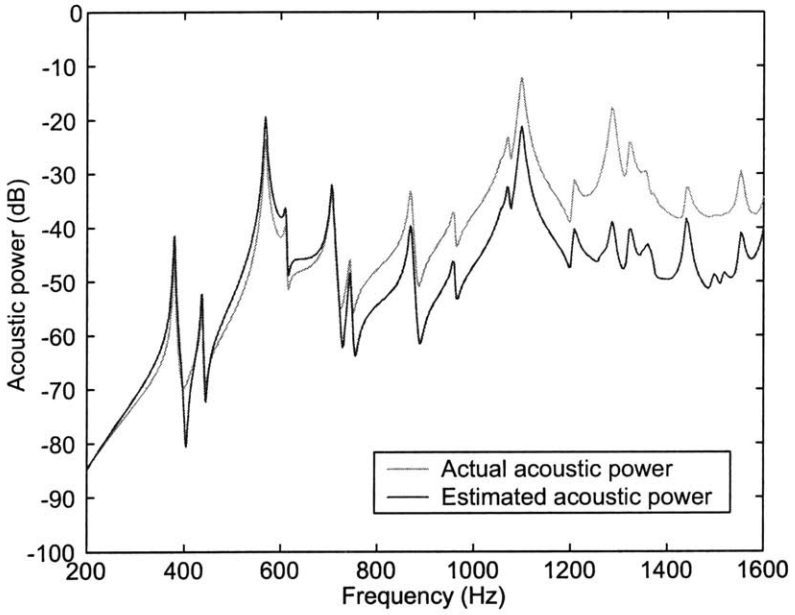

Figure 5-29: Actual and estimated acoustic power obtained using three circumferential wavenumber components with non-optimal weights.

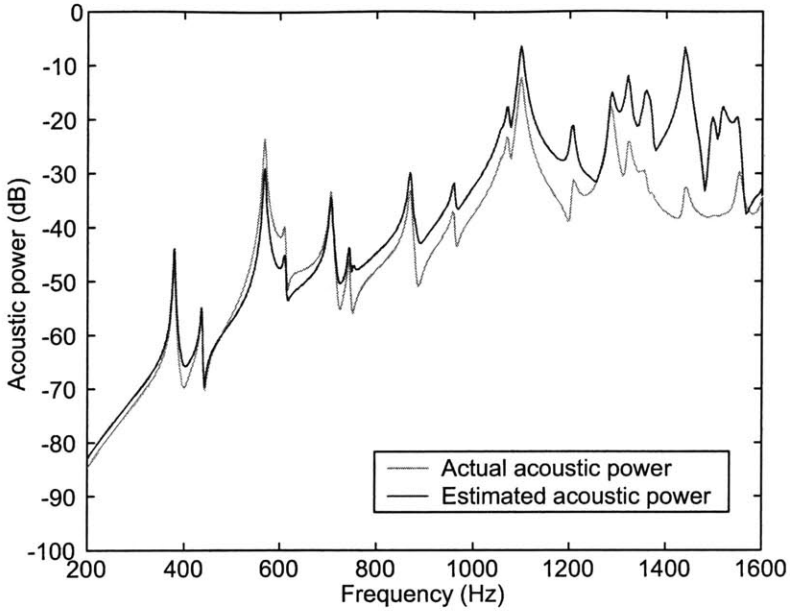

Figure 5-30: Actual and estimated acoustic power obtained using four circumferential wavenumber components with non-optimal weights.

respectively. The optimal and non-optimal weights used to estimate the acoustic power and design LQG controller are given in Table 5.4 and Table 5.5, respectively. The performance metric J is defined as the integration of the acoustic power in the control bandwidth, to measure the closed-loop performance and to compare the performance of each control loop, given as

$$J = \int_0^{2\pi \times 1200\,(\mathrm{rad/s})} \Pi(\omega)\, d\omega \,. \tag{5.17}$$

The performance index is summarized in Table 5.6 for each control loop. The performance in the table represents the ratio of the open-loop to the closed-loop performance index. Figure 5-38 shows the effect of N_n and $\widehat{F}(n,0)$ on the performance index J of the closed-loop system.

As expected in the previous section, using only the zero wavenumber component doesn't yield any closed-loop performance at all (Figure 5-31). The volume velocity cancellation method, which is equivalent to reducing the zero wavenumber component to reduce structurally-radiated noise, doesn't work in this example, because the dominant resonant frequencies are too high for the method to be applied. Considering the first two circumferential wavenumbers (n = 0 and 1) results in better closed-loop performance (Figure 5-32). We can reduce the acoustic power at the most dominant peak around 1100 Hz, although we cannot reduce the acoustic power at other frequency ranges, using the first two circumferential wavenumber components.

Figure 5-33 and Figure 5-34 show that most dominant peaks in the acoustic power are reduced by considering three or four wavenumber components (N_n = 3 or 4) with optimal weights. In both cases, we see that 20 dB of attenuation is achieved at 600 and 1100 Hz, and

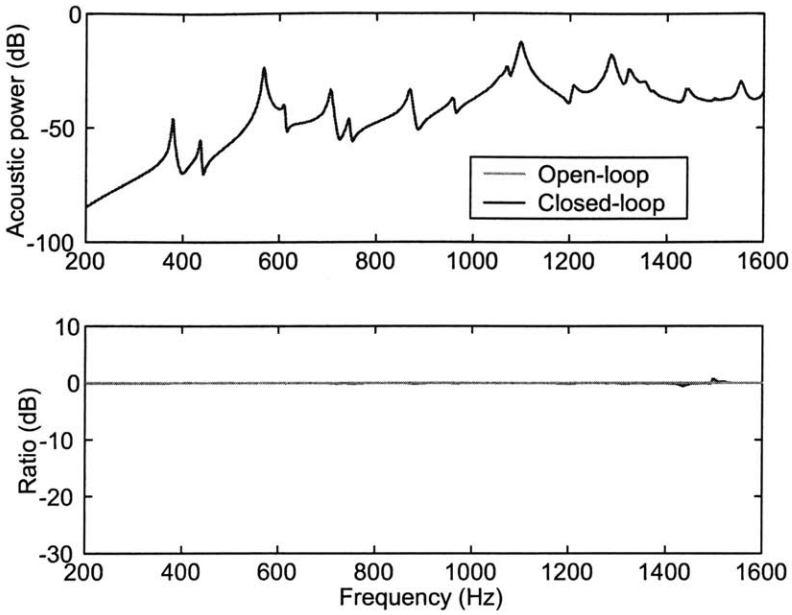

Figure 5-31: Closed-loop performance obtained using one circumferential wavenumber component with optimal weight.

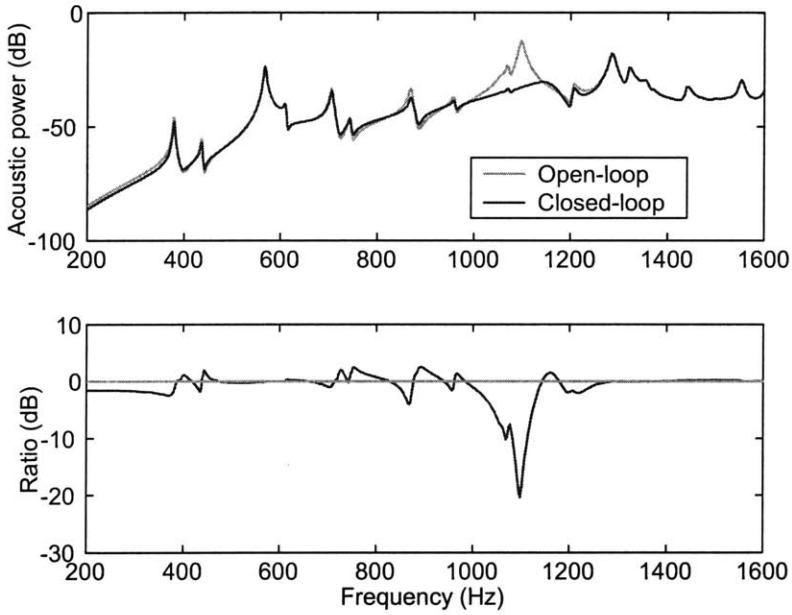

Figure 5-32: Closed-loop performance obtained using two circumferential wavenumber components with optimal weights.

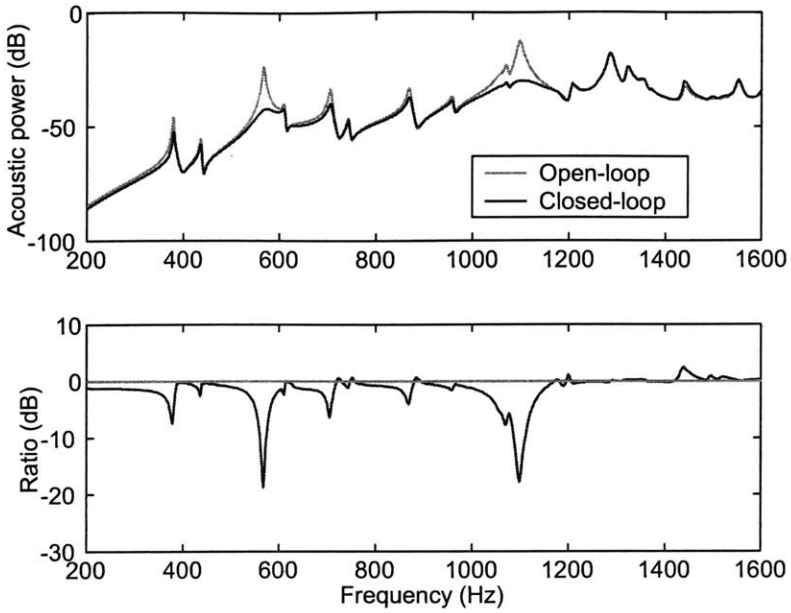

Figure 5-33: Closed-loop performance obtained using three circumferential wavenumber components with optimal weights.

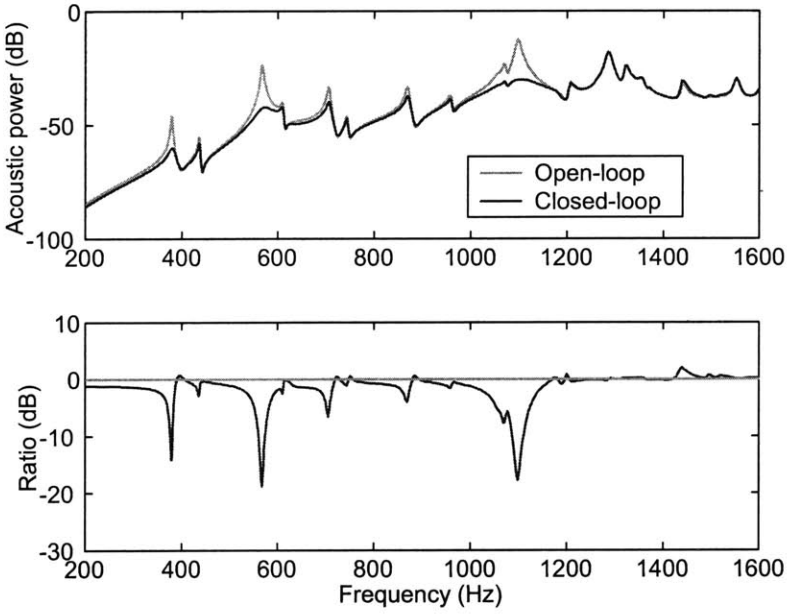

Figure 5-34: Closed-loop performance obtained using four circumferential wavenumber components with optimal weights.

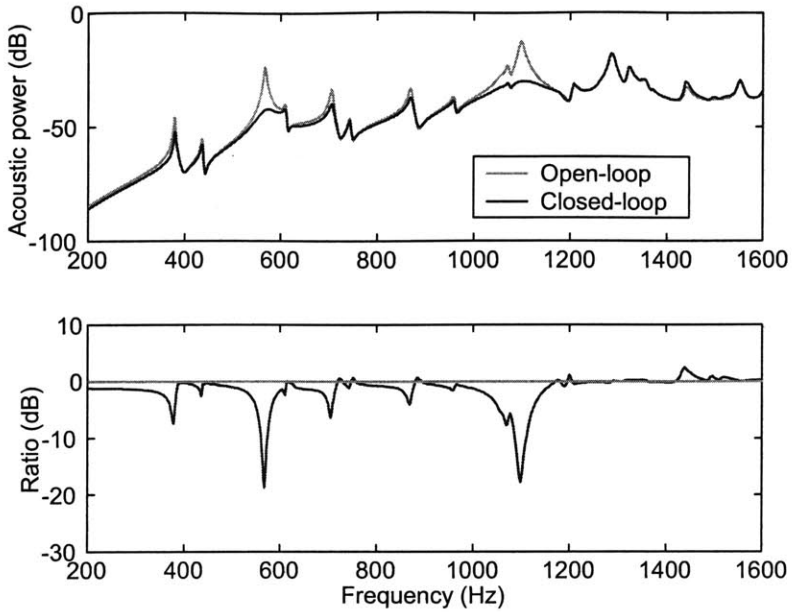

Figure 5-33: Closed-loop performance obtained using three circumferential wavenumber components with optimal weights.

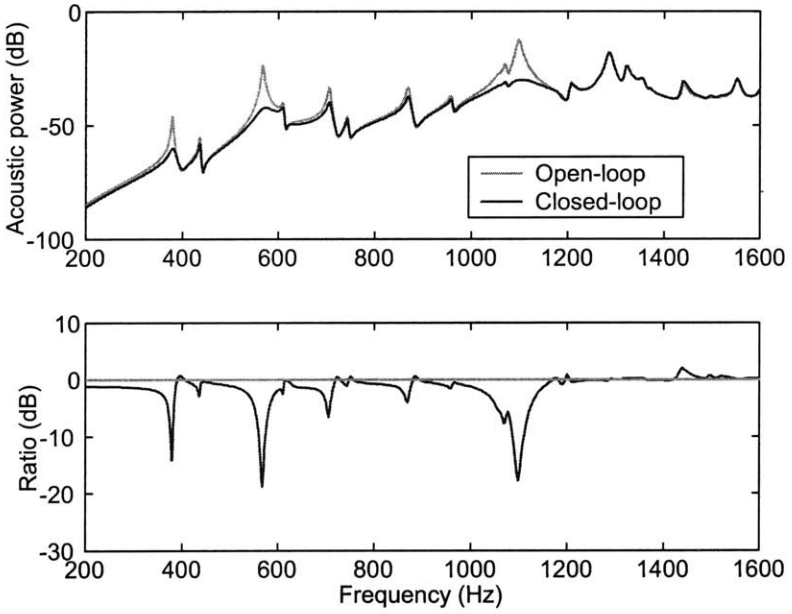

Figure 5-34: Closed-loop performance obtained using four circumferential wavenumber components with optimal weights.

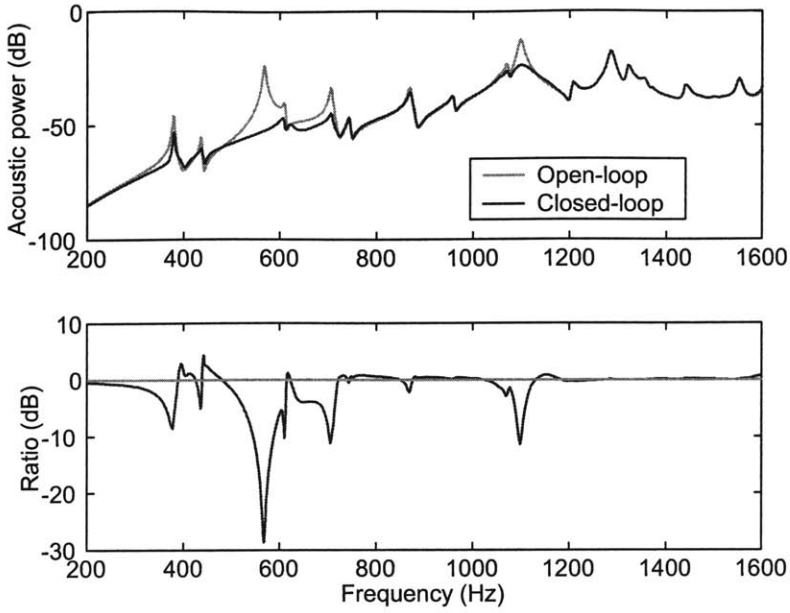

Figure 5-36: Closed-loop performance obtained using three circumferential wavenumber components with non-optimal weights.

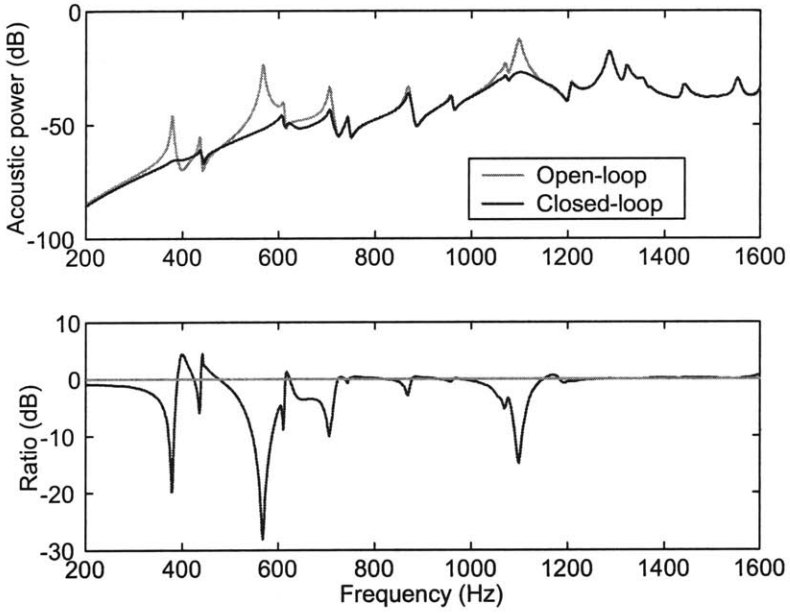

Figure 5-37: Closed-loop performance obtained using four circumferential wavenumber components with non-optimal weights.

Table 5.6: The performance index for each control loop.

	J	Performance
Open loop	1.0122	
Optimal weights, $N_n = 1$	1.0122	1.00 (0.0 dB)
Optimal weights, $N_n = 2$	0.14373	7.04 (8.5 dB)
Non-optimal weights, $N_n = 2$	0.14373	7.04 (8.5 dB)
Optimal weights, $N_n = 3$	0.12287	8.24 (9.2 dB)
Non-optimal weights, $N_n = 3$	0.29473	3.43 (5.4 dB)
Optimal weights, $N_n = 4$	0.12296	8.23 (9.2 dB)
Non-optimal weights, $N_n = 4$	0.18623	5.43 (7.3 dB)

better performance than optimal weights. However, Table 5.6 indicates that the closed-loop performance obtained using optimal weights is better than that obtained using non-optimal weights, in terms of the performance metric J ($J = 0.12296$ for optimal weights, and $J = 0.18623$ for non-optimal weights). The rationale used in the previous paragraph applies to this case in the same way. LQG controller using optimal weights tries to minimize the H_2 norm of the system by putting more weight on the peak at 1100 Hz, while the LQG controller using non-optimal weights achieves its goal by putting more weight on the peak at 400 Hz. Note that the peak at 1100 Hz is much more dominant than the peak at 400 Hz in the bandwidth of interest.

However, as in the example of beam structures, this example also shows that non-optimal weights selected in an *ad hoc* manner result in the closed-loop performance that is comparable with the performance obtained using optimal weights. Note that the iterative procedure of finding weights is very common in any optimal controller design. Also, it should be stressed that finding weights by iteration in the new wavenumber domain sensing method can be done in a systematic way, because the acoustic power depends on only a first few wavenumber components in most engineering applications. Therefore, the new wavenumber domain sensing method developed in this study can be applied without any difficulty, even when the acoustic power is not available during the feedback controller design.

5.4.5 Effect of Time-delay in the Digital Control System

This section investigates the effect of time delay in the digital control system on the achievable closed-loop performance, and explores the way to compensate for it. The motivation for this is that the wavenumber domain LQG control algorithm should be implemented digitally, due to its multi-input multi-output (MIMO) features, although the simulation results shown throughout this chapter assume that it is implemented in analog.

One of the problems in implementing digital control system is the effective time delay. Assuming the zero-order-hold method is used during the sampling process, and the latency of the digital control system can be as large as the sampling time, the effective time delay T in the digital control system is given by

$$T = \frac{3}{2} T_s \,, \tag{5.18}$$

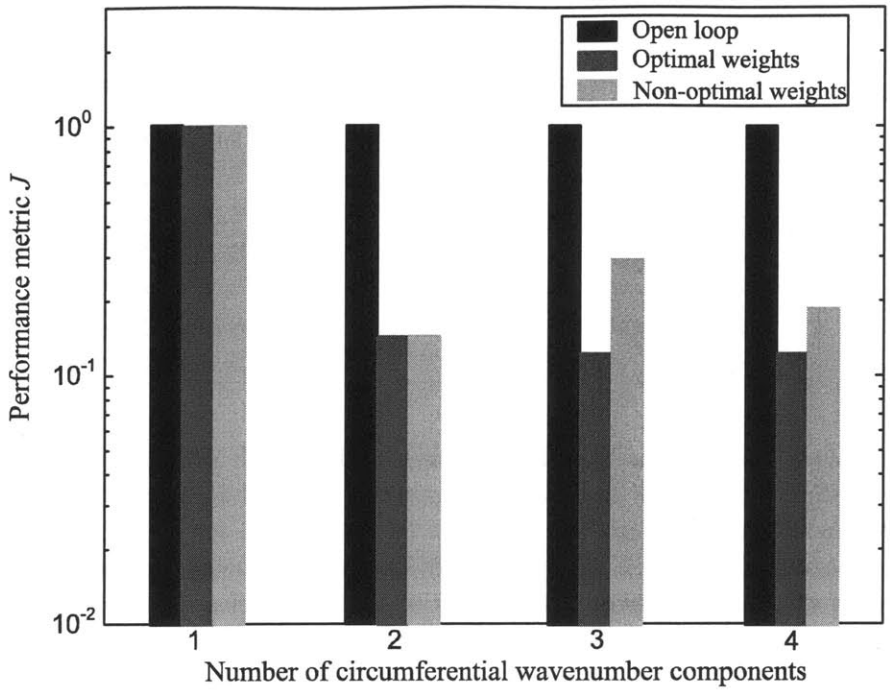

Figure 5-38: The performance metric J of the open-loop and closed-loop system.

where T_s is the sampling time of the digital control system. Therefore, if controllers are designed in the continuous domain without considering the effective time delay, and then implemented digitally, the achievable closed-loop performance would be worse than the expected performance. In an extreme case, the closed-loop system may be unstable if the effective time delay is large enough.

In order to see how the effective time delay degrades the closed-loop performance, the same wavenumber domain LQG controller as in the previous section (which considers four circumferential wavenumber components with optimal weights) was applied to the plant with the effective time delay, and its performance was compared with the case without time delay. Figure 5-39 shows the block diagram of the LQG controller designed on the plant without considering the effective time delay. The sampling frequency (sampling time) of the digital control system was assumed to be 20 kHz (50 μs). The effective time delay e^{-Ts} is approximated using the first order Pade approximation [Lewis, 1992], given as

$$e^{-Ts} \approx \frac{1 - \frac{T}{2}s}{1 + \frac{T}{2}s} . \tag{5.19}$$

As mentioned above, the LQG controller in Figure 5-39 is the same one as in the previous section. It considers one axial wavenumber component and four circumferential wavenumber

Table 5.7: The performance index for each control loop.

	J	Performance
Open loop	1.0122	
Case I	0.12296	8.23 (9.2 dB)
Case II	0.17373	5.83 (7.7 dB)
Case III	0.14812	6.83 (8.3 dB)

components, with the optimal weights given in Table 5.4. The difference between the current setup in Figure 5-39 and the one in the previous section is that the LQG controller is applied to the plant with the time delay. Figure 5-40 and 5-41 compare the characteristic loci [Maciejowski, 1989] of two cases. The first case in Figure 5-40, where the LQG controller is applied to the system without time delay, shows the typical feature of LQG control system; most of dominant dynamics are bounded in phase between -90° and 90°, with small peaks inside the unit circle centered at the critical point -1 due to spill-over. On the other hand, the second case in Figure 5-41, where the same LQG controller is applied to the system with time delay, shows that there is a phase shift in the clockwise direction, *i.e.* phase delay, due to the effective time delay. The effect of time delay is not so serious in this example; most dominant peaks are still away from the unit circle at -1, and their phase margins are large enough. Nevertheless, the closed-loop performance of the second case is a little worse than that of the first case, as can be observed from Figure 5-42 and 5-43, which show the closed-loop performances of two cases. They are very similar to each other below 1 kHz, but the closed-loop performance of the second case begins to degrade above that frequency. The performance metrics J defined in Equation 5.17 for both cases are given in Table 5.7. In the table, Case I represents the system on which the LQG controller is applied without time delay, while Case II represents the system on which the LQG controller is applied with time delay.

In the third case, denoted as Case III in Table 5.7, LQG controller is designed on the plant assuming it has a time-delay. A block diagram in Figure 5-44 shows its design setup. Since the plant on which LQG controller is designed includes the time delay (it is represented as the first Pade approximation in Figure 5-44), the LQG controller knows how to compensate for it. The resulting characteristic loci and closed-loop performance are given in Figure 5-45 and Figure 5-46, respectively. It can be seen that the phase delay in the plant is effectively recovered by the LQG controller for most dominant peaks. Also, the closed-loop performance in Figure 5-46 is very similar to that in Figure 5-42. Table 5.7 indicates that the performance metric J of Case III is a little larger than that of Case I, but lower than Case II. This shows that if it is not too significant, the effective time delay in the digital control system can be compensated for by the LQG controller.

5.5 Summary

In this chapter, the new wavenumber domain sensing method proposed in the previous chapter was numerically validated on finite beams and cylinders in an infinite baffle. The finite element method and analytic expressions were used to model the structural and acoustic responses,

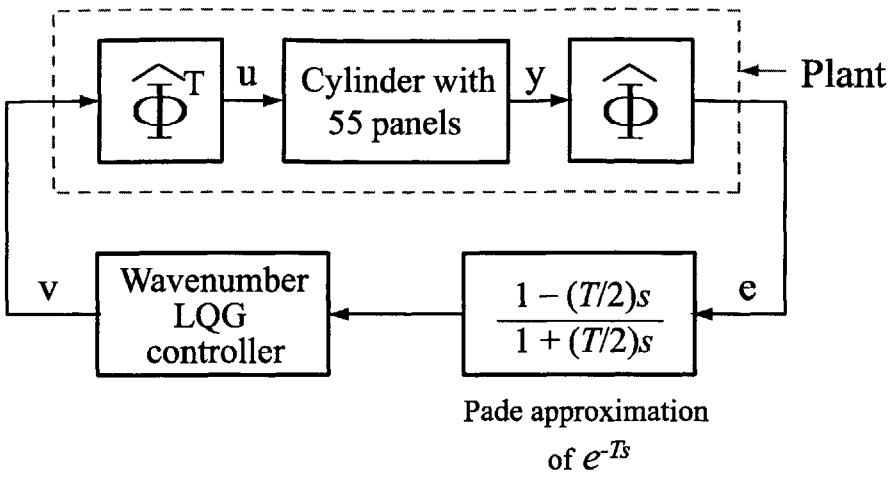

Figure 5-39: Block diagram of wavenumber domain LQG controller designed on the plant without considering the effective time delay.

respectively, and to compute the open-loop and closed-loop behavior of the system. Once frequency responses were computed for the structural system from the model, the plant model needed to design LQG controller was obtained by doing system identification on those computed frequency responses. No acoustic model was included in the LQG controller designed to reduce the acoustic power from vibrating structures.

The results show that only first a few wavenumber components were enough to estimate and reduce the acoustic power in the reasonable bandwidth of interest, while considering only the first wavenumber component, *i.e.* volume velocity cancellation, couldn't yield a good closed-loop performance in the case of a finite cylinder considered in this paper. Also, the examples demonstrate that the closed-loop performance is still satisfactory in spite of the unavailability of the acoustic power for the controller design. In other words, the weights selected in an *ad-hoc* way, not using the actual acoustic power, yielded the closed-loop performance similar to the weights selected optimally using the actual acoustic power. This has a critical implication in the control system design for active structural acoustic control, because it is not easy to compute or measure the acoustic power for most engineering systems, and therefore use it in the controller design.

In addition to making the acoustic modeling unnecessary to design controllers, the new wavenumber domain sensing method significantly simplifies the controller design by reducing the transfer functions to be considered from 100 ($=10^2$) to 25 ($=(2N_m-1)^2$, N_m=3) in the case of beam structures, and from 3025 ($=55^2$) to 25 ($=(2N_n-1)^2$, N_n=3) in the case of cylindrical shells. Note that designing LQG controllers for 55 inputs and 55 outputs is probably not feasible, although it is for 5 inputs and 5 outputs. This advantage again makes the method a useful tool to design feedback controllers for reducing the radiated noise from structures.

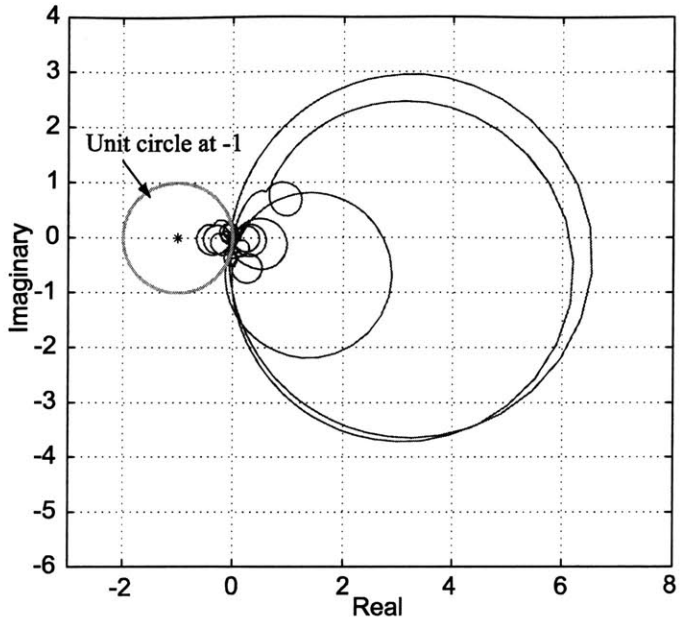

Figure 5-40: The characteristic loci of loop transfer matrix for the LQG controller implemented in analog.

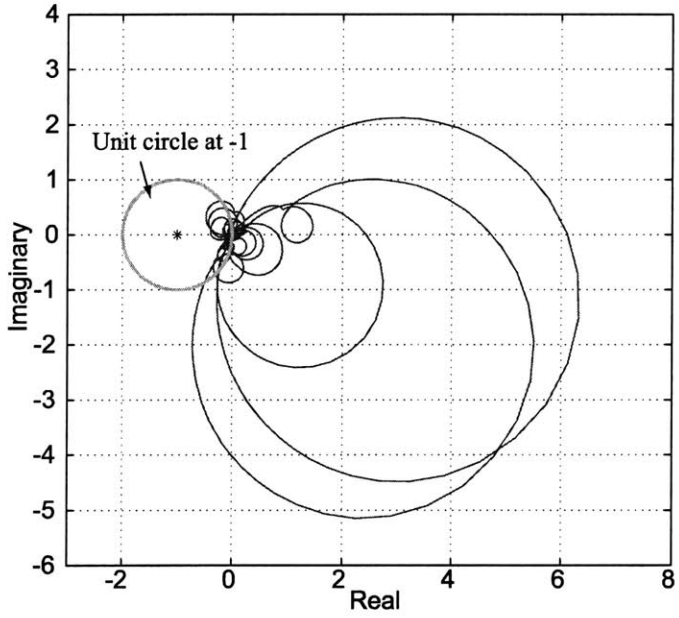

Figure 5-41: The characteristic loci of loop transfer matrix for the LQG controller designed on the plant without considering the effective time delay, but with time delay present.

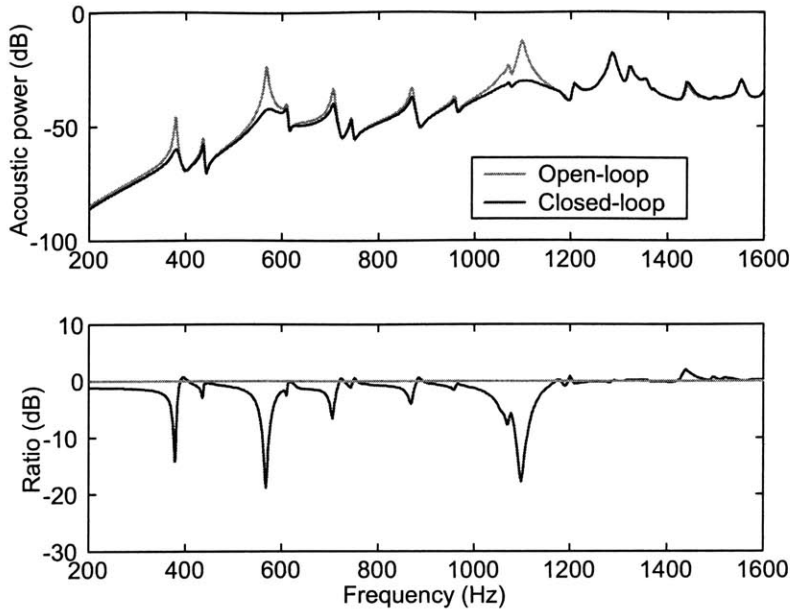

Figure 5-42: Closed-loop performance obtained using four circumferential wavenumber components with optimal weights.

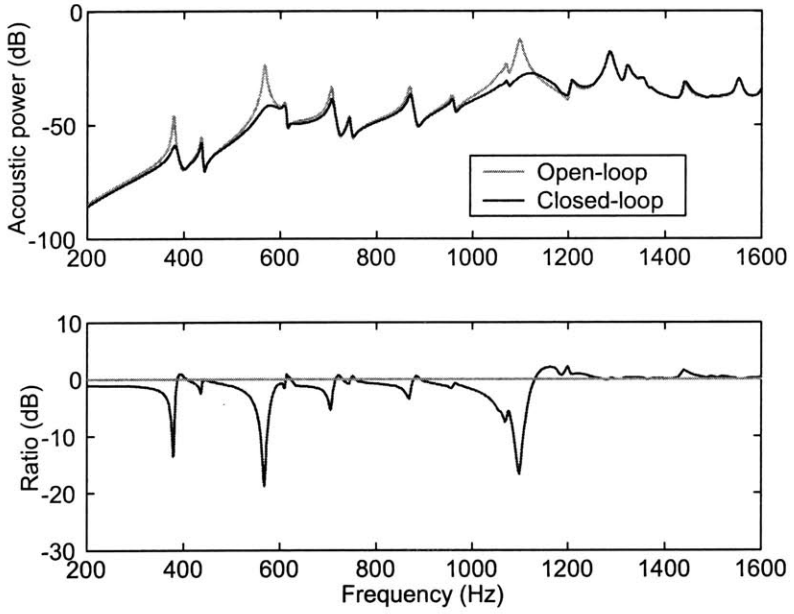

Figure 5-43: Closed-loop performance obtained using LQG controller designed on the plant without time delay, but with time delay present.

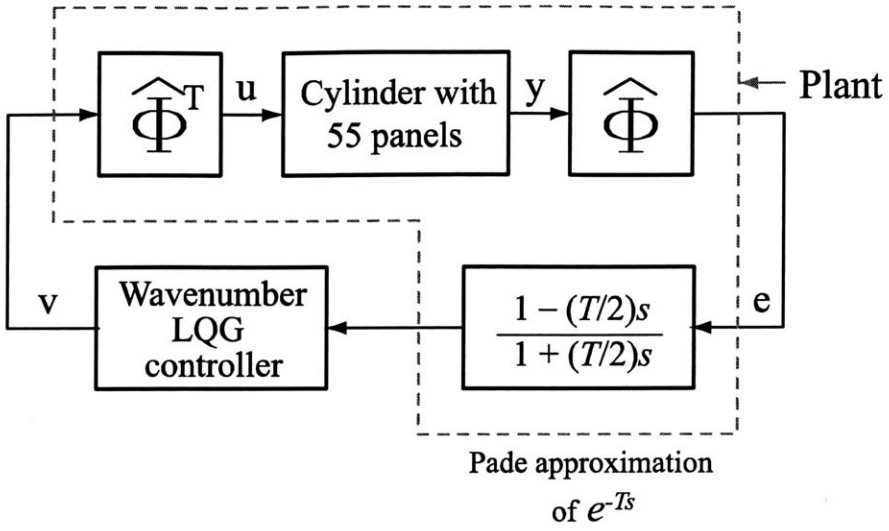

Figure 5-44: Block diagram of wavenumber domain LQG controller designed on the plant considering the effective time delay.

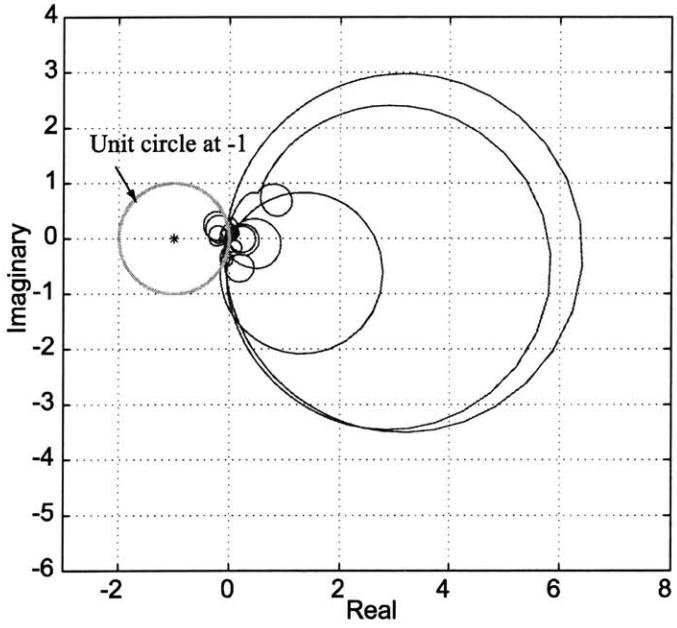

Figure 5-45: The characteristic loci of loop transfer matrix for the LQG controller designed on the plant considering the effective time delay.

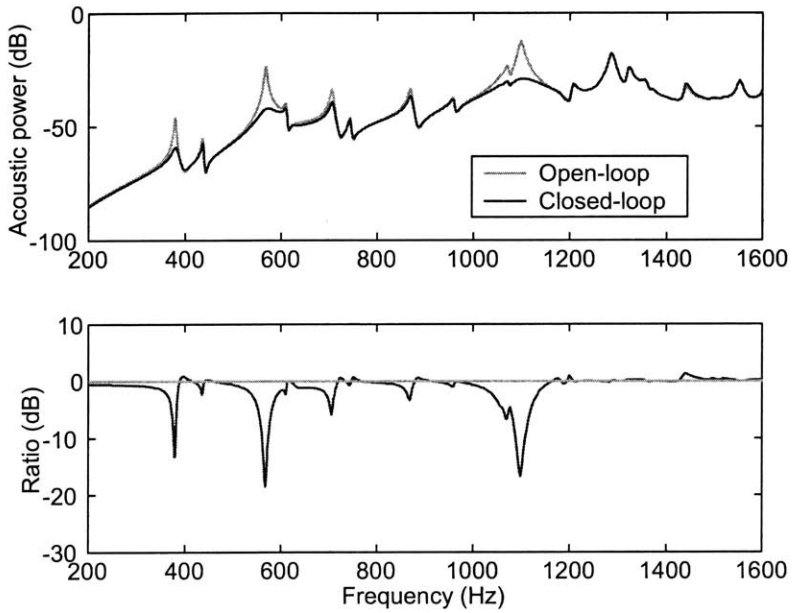

Figure 5-46: Closed-loop performance obtained using LQG controller designed on the plant considering the effective time delay.

Chapter 6

Local Controller Closed-loop Experimental Results

6.1 Introduction and Objective

In this chapter, the results of several closed-loop experiments obtained with local controllers are reported. Ultimately, much of the control functions for the multi-input multi-output (MIMO) controller will be implemented digitally. Digital control systems have many advantages, such as flexibility of use, ease of programming, and high reliability. However, it is not feasible to implement the MIMO controllers completely with digital electronics, because at the bandwidth required (up to 10 kHz), the effective time delays are too large. Nevertheless, it is obvious that a digital controller is required for MIMO control, to allow changes in the control law to be implemented in software, rather than hardware. One way to solve this problem may be to design a hybrid analog/digital controller, with the digital controller used to control the global behavior of the conformal array, and a hybrid analog/digital controller used for local, panel-level control. In this configuration, a hybrid analog/digital subsystem is acted on frequencies above 1 kHz, where the added phase lag from the digital controller becomes large, and a digital subsystem is acted on frequencies below 1 kHz, coordinating all the panels that cover the outer surface of the shell.

The objective of this chapter is to investigate the controller configurations, and find the one that will be used eventually for the local controller architecture. All of the control configurations considered in this chapter have the form of the feedback and feedforward controllers proposed in Chapter 3. Different configurations are distinguished by the relative amount of analog and digital components used to implement each configuration. Requirements that controllers should satisfy include acceptable closed-loop performance, enough stability margins, and the easiness in implementation. The one selected for the local controller architecture should be the simplest to implement, while achieving the required closed-loop performance and stability margins.

In the sections below, eight controllers are discussed, and the experimental results for those controllers are shown. The eight controllers are (1) A completely analog controller; (2) An analog controller with the notch filter implemented digitally; (3) A hybrid digital/analog feedback and analog feedforward controller; (4) A hybrid analog/digital feedback with digital notch filter; (5) A hybrid digital/analog feedback and digital feedforward controller; (6) A digital

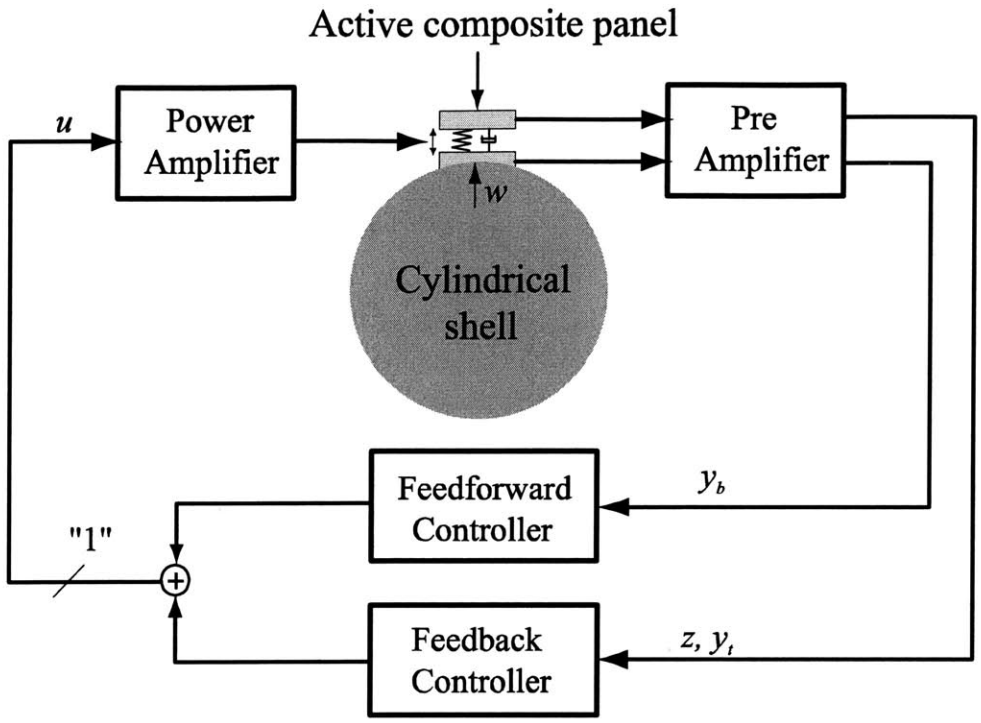

Figure 6-1: Block diagram for feedback and feedforward controller on the model of the cylindrical shell with one active composite panel. "1" represents the point which is cut to find the loop transfer function in Figures 6-9 and 6-10.

feedback and digital feedforward controller; (7) A digital tonal feedback controller; and (8) A hybrid analog/digital feedback and digital linear quadratic gaussian (LQG) controller. The analog controller establishes a benchmark against which the other controllers can be compared. Before presenting the experimental results, the feedback and feedforward controller, which were explored in Chapter 3, will be designed and implemented on the model developed in Chapter 2, and the closed-loop results will be presented.

6.2 Simulating Controllers on the Model

Figure 6-1 shows the block diagram for the feedback and feedforward controller on the model of the cylindrical shell with one active composite panel, which was developed in Chapter 2. It also shows the disturbance w, control input u, the acceleration of the panel y_t, and the acceleration of the shell y_b. The performance output z is the same as y_t in this example. The cylindrical shell was modeled using the finite element method, while the active composite panel was modeled using a mass-spring-damper system. The pre-amplifier and power amplifier were modeled as a gain of unity and a low-pass filter at 188 Hz, respectively. The open-loop plant transfer functions from (w, u) to (y_t, y_b) are shown in Figure 6-2.

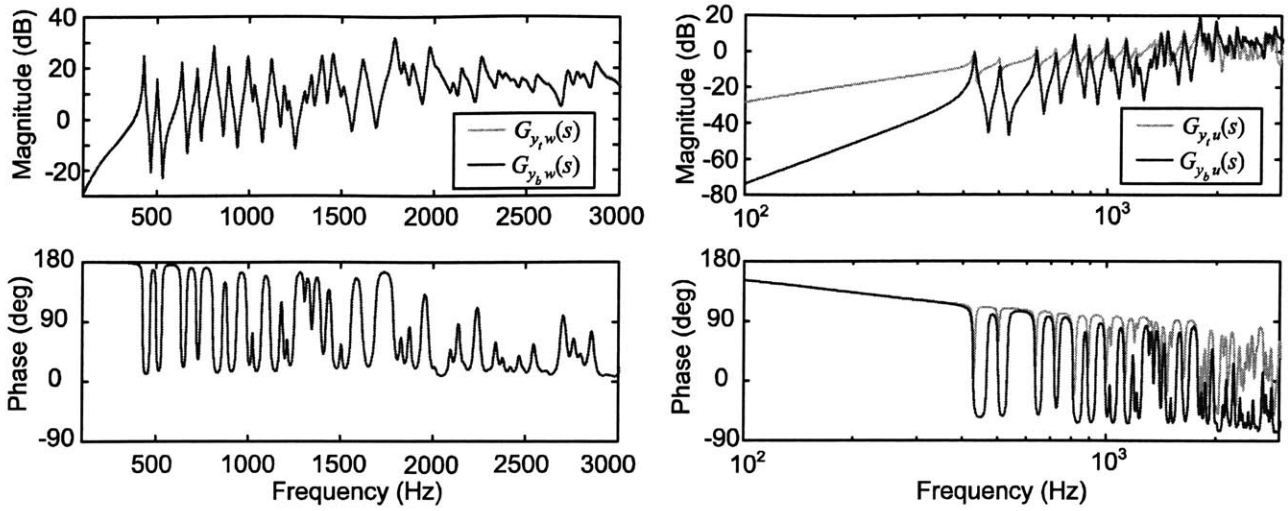

Figure 6-2: Plant transfer functions from (w,u) to (y_t, y_b) using the model.

The feedback controller for this plant was proposed as two low-pass filters at 200 Hz and 20,000 Hz in Chapter 3. The low-pass filter at 200 Hz, combined with the low-pass filter in the power amplifier, functions as a double integrator, while the filter at 20,000 Hz provides a roll-off at high frequency. The frequency responses of the feedback controller and its loop transfer function are shown in Figure 6-3.

The closed-loop performance using feedback controller is shown in Figure 6-4, with a ratio of open-loop transfer function to closed-loop transfer function. It can be seen that more than 15 dB of attenuation is achieved between 200–2000 Hz. This result is as expected, because the loop gain shown in Figure 6-3 is more than 15 dB in this frequency range.

Figure 6-5 shows the frequency response of the feedforward controller proposed in Chapter 3, and its loop transfer function. It should be noted that the loop transfer function of the feedforward controller doesn't give any information on the closed-loop performance, because the feedforward controller measures the acceleration of the shell (y_b), not the acceleration of the panel (z). It was shown in Chapter 3 that the feedforward controller shown in Figure 6-5 *exactly* cancels the performance output z, because the controller in the figure is almost the same as the one that cancels the performance output z perfectly, which was given in Equation 3.8. Since this cannot happen in a real world, it is assumed in this section that there is uncertainty in the feedforward loop, as shown in Figure 6-6. In Figure 6-6, k and φ represent gain and phase uncertainty in the feedforward loop, respectively. For example, $k = 0.7$ corresponds to a 30% gain mismatch, and $\varphi = 10°$ corresponds to additional phase delay of 10° in the loop. Figure 6-7 shows the closed-loop performance using the feedforward controller when there is gain uncertainty ($\varphi = 0°$). It can be seen that the achievable closed-loop performance using the feedforward controller is about 10 dB of reduction, when the loop has 30% of gain uncertainty. It becomes worse, as expected, when the gain uncertainty is increased; the achievable closed-loop performance is reduced to about 5 dB of reduction when the loop has 50% of gain uncertainty. However, the gain uncertainty is not a serious problem in the controller implemen-

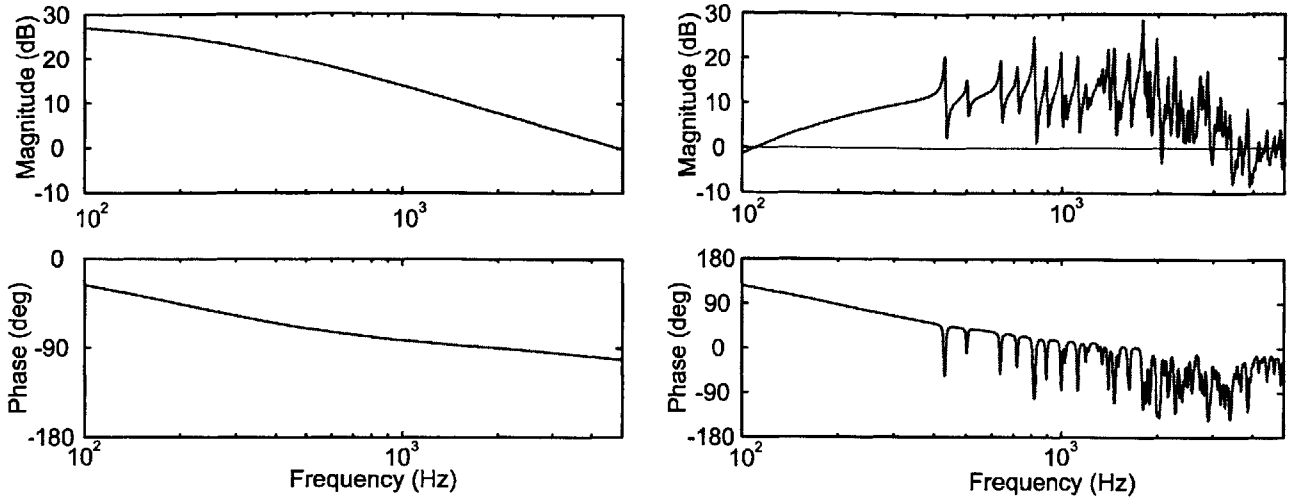

Figure 6-3: Frequency response of (a) the feedback controller, and (b) the loop transfer function.

tation, because we can reduce it to less than 10% in the controller bandwidth, in general, by careful design of the feedforward controller. The more serious problem is phase uncertainty in the loop. Figure 6-8 shows the closed-loop performance using the feedforward controller when there is phase uncertainty ($k = 1$). It can be seen that the achievable closed-loop performance using the feedforward controller is about 15 dB of reduction when the loop has phase delay of 10°, with the amplification of disturbance about 20 dB at some frequencies. When there is an additional phase delay of 20° in the loop, the performance becomes much worse; at most resonant peaks, the disturbance is amplified by more than 10 dB. Recalling that a phase delay of 10–20° can easily happen in the real implementation, especially in the digital control loop, this fact implies that we should try to reduce the phase delay within the control bandwidth when designing feedforward controller. If the phase delay is inevitable in the feedforward loop, the gain should be reduced in that region, so that its effect on the closed-loop performance is minimized. It is true that we should try to reduce the phase delay in feedback controller design, too. However, the feedback control is not as sensitive to phase delay, in contrast to feedforward control, as long as the closed loop is stable.

In fact, as mentioned in Chapter 3, the feedback and feedforward approaches are complementary, and they can be applied simultaneously, because there is little interaction between the two controllers. From the block diagram in Figure 6-1, the performance output z, and the acceleration of the shell y_b can be written as

$$\begin{aligned} z &= y_t = G_{y_t w} w + G_{y_t u} u \\ y_b &= G_{y_b w} w + G_{y_b u} u \,. \end{aligned} \tag{6.1}$$

The feedback control $K_b(s)$ and the feedforward control $K_f(s)$ can be applied simultaneously,

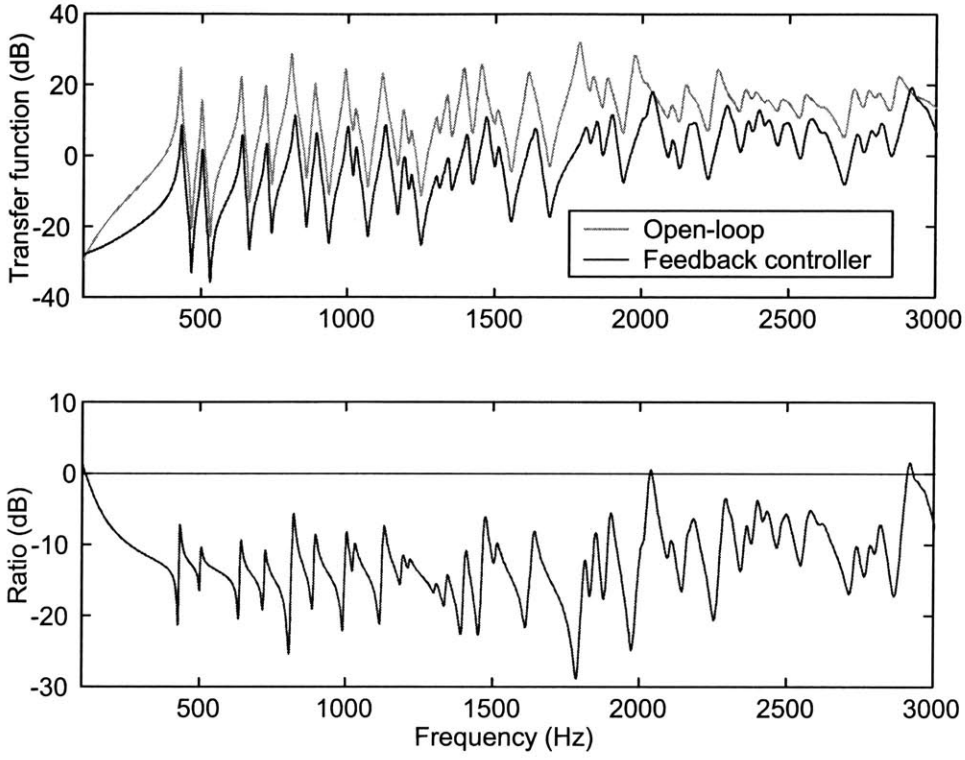

Figure 6-4: Closed-loop performance using feedback controller. "Ratio" represents the ratio of the open-loop response to the closed-loop response. Negative ratios indicate attenuation; positive ratios indicate amplification.

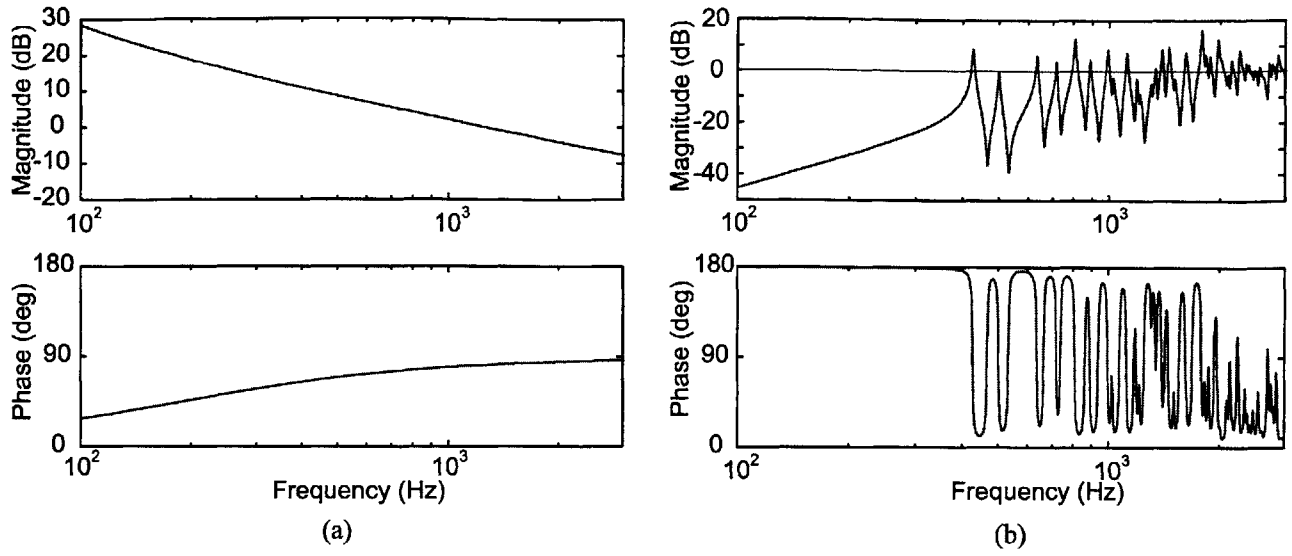

Figure 6-5: Frequency response of (a) the feedforward controller, and (b) the loop transfer function.

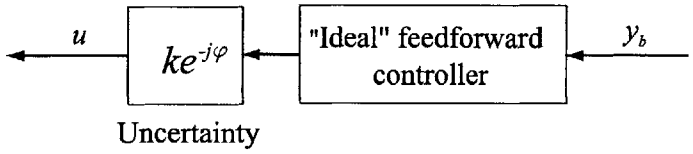

Figure 6-6: Uncertainty in feedforward loop.

so that the control law is

$$u = K_b\, y_t + K_f\, y_b\,. \tag{6.2}$$

Using this controller, the closed-loop performance output z can be written as

$$z = y_t = G_{y_t w} w + G_{y_t u}\,(K_b\, y_t + K_f\, y_b)\,. \tag{6.3}$$

Substituting $y_b = G_{y_b w} w + G_{y_b u}\,(K_b\, y_t + K_f\, y_b)$ into Equation 6.3 yields

$$z = y_t = \frac{G_{y_t w} + K_f\,(G_{y_t u} G_{y_b w} - G_{y_b u} G_{y_t w})}{1 - K_f G_{y_b u} - K_b G_{y_t u}}\,. \tag{6.4}$$

The corresponding loop transfer function is $-K_f G_{y_b u} - K_b G_{y_t u}$, which is obtained by cutting the loop at "1" in Figure 6-1. The frequency response and Nyquist plot of the loop transfer function are shown in Figure 6-9, and 6-10, respectively. Here, the feedback controller $K_b\,(s)$ is defined in Figure 6-3, while the feedforward controller $K_f\,(s)$ is $0.8\,e^{-j20^\circ}$ (20% gain uncertainty, and 20° phase delay) times the ideal feedforward controller shown in Figure 6-5. The

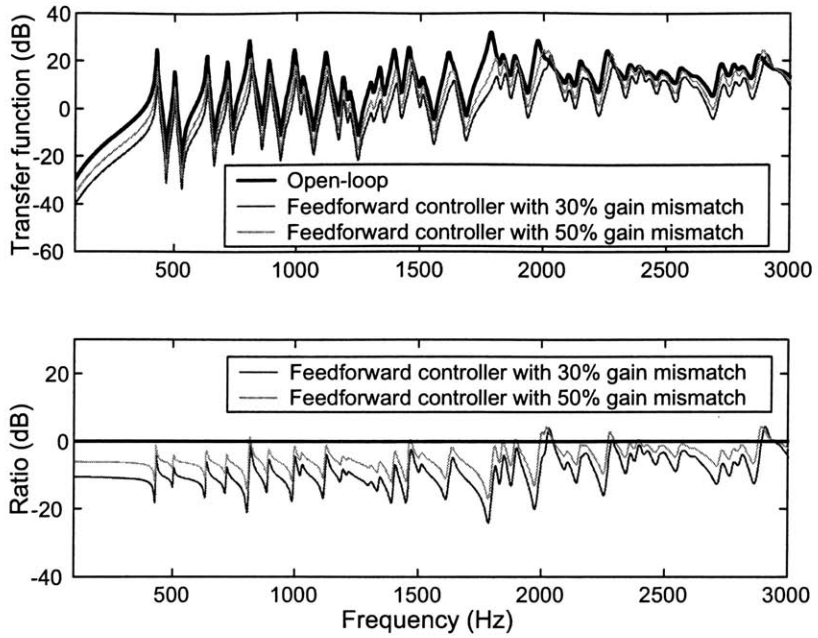

Figure 6-7: Closed-loop performance using feedforward controller when there is gain uncertainty in the loop.

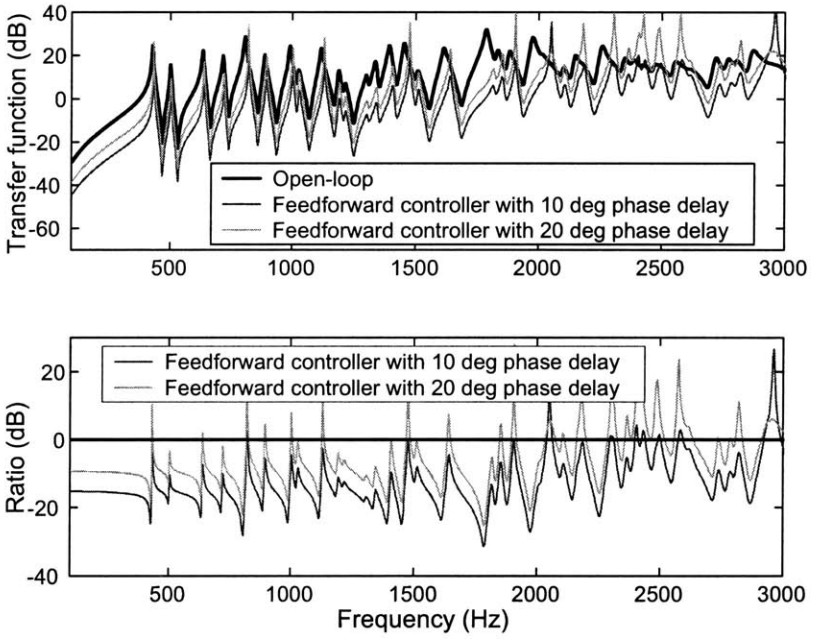

Figure 6-8: Closed-loop performance using feedforward controller when there is phase uncertainty in the loop.

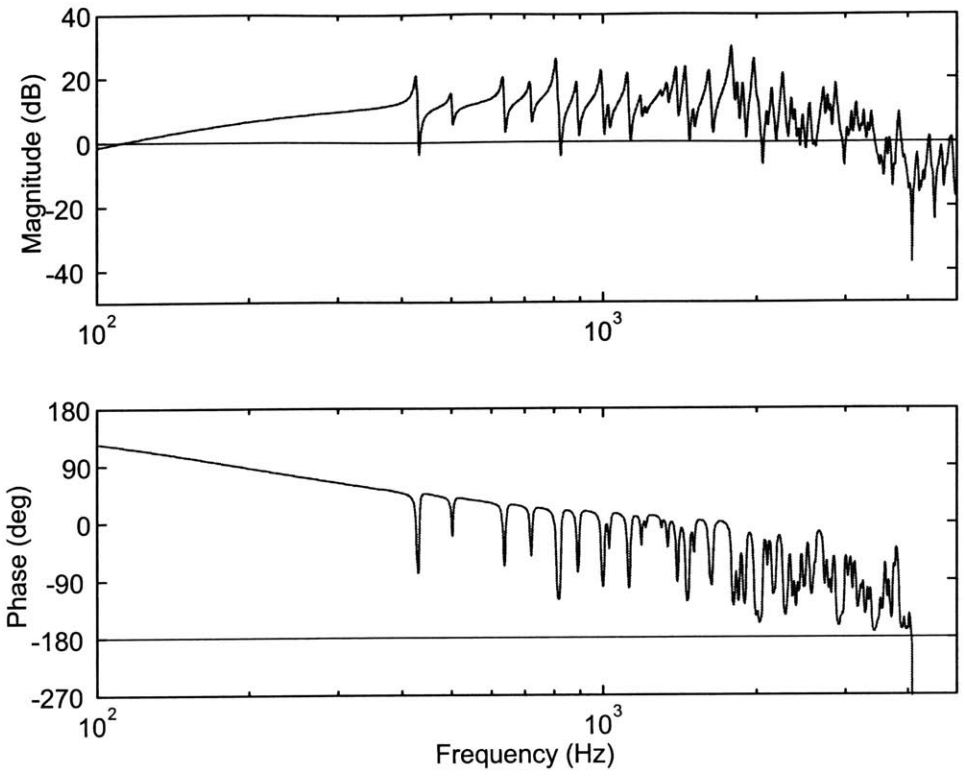

Figure 6-9: Frequency response of loop transfer function $-K_f G_{y_b u} - K_b G_{y_t u}$.

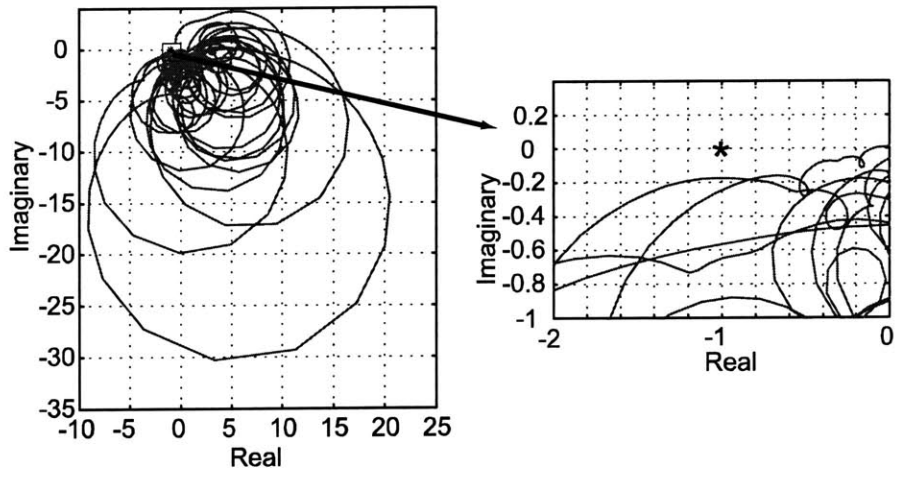

Figure 6-10: Nyquist plot of loop transfer function $-K_f G_{y_b u} - K_b G_{y_t u}$.

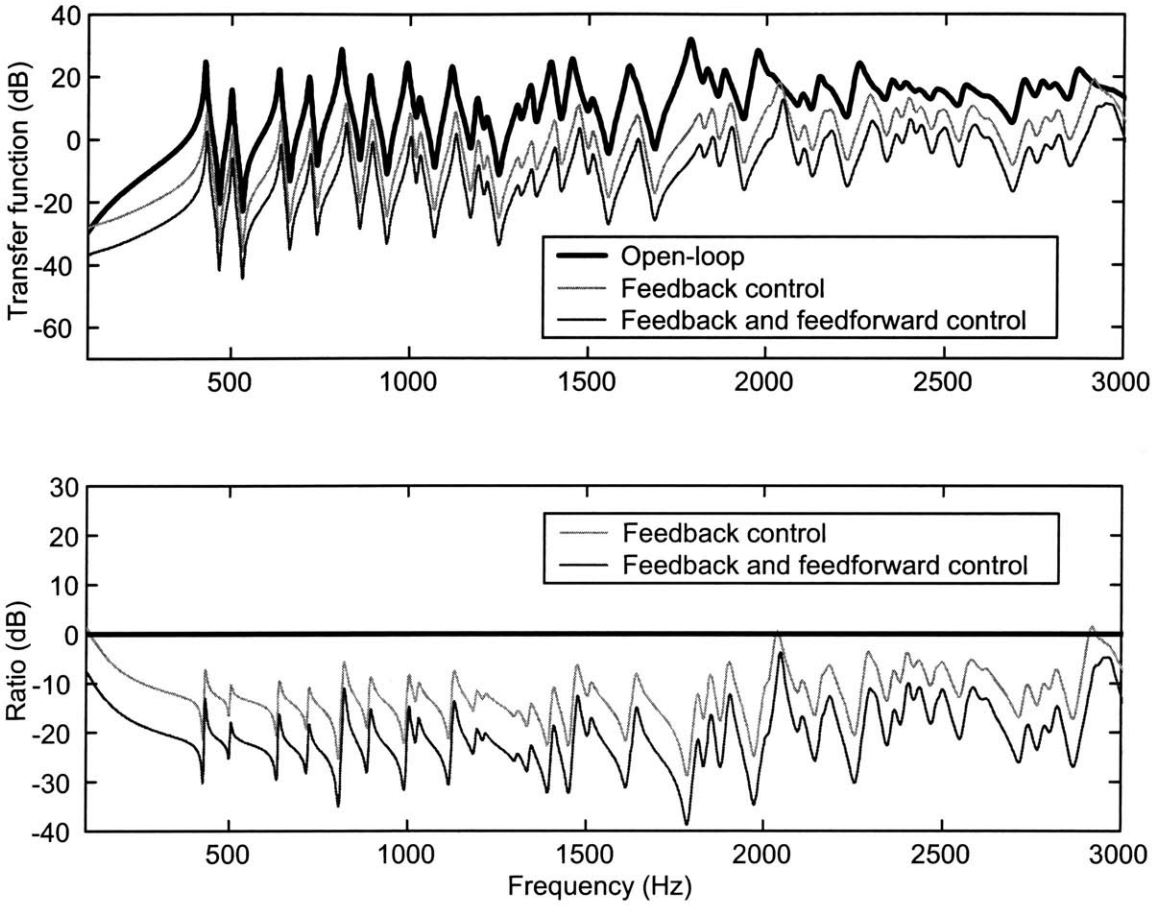

Figure 6-11: Closed-loop performance using feedback and feedforward controller simultaneously. "Ratio" represents the ratio of the open-loop response to the closed-loop response. Negative ratios indicate attenuation; positive ratios indicate amplification.

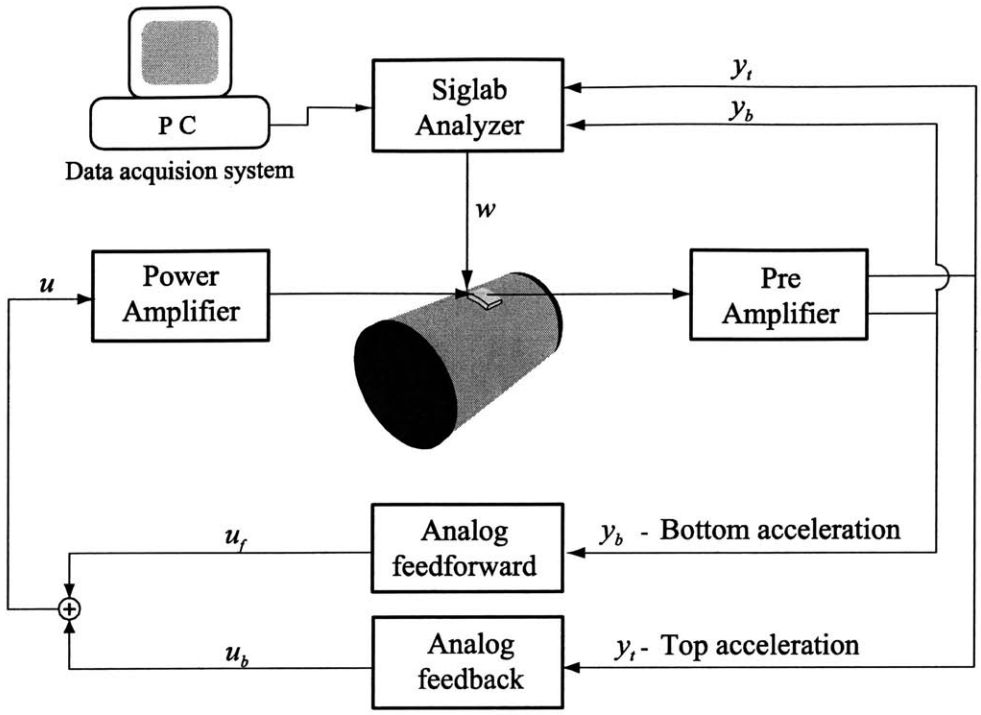

Figure 6-12: Block diagram of the analog-only controller implementation.

corresponding closed-loop performance is shown in Figure 6-11. Using the feedback and feedforward controller at the same time, more than 20 dB of attenuation is achieved over most of the range of interest (200–2000 Hz). This attenuation is approximately equal to the product of the attenuations of the feedback and feedforward controllers. In the following sections, it will be seen that the promising results of simulating controllers on the model will be applied to the experimental implementation.

6.3 Analog Controller

The first controller implemented is an analog-only controller; both feedback and feedforward controllers, including the low-frequency feedthrough compensator, are implemented using the analog circuits. It is true that it is unfeasible to implement *all* the controllers needed with analog electronics. The motivation for the analog-only approach is to evaluate the proposed feedback and feedforward control approaches on the real system. Also, the analog controller establishes a benchmark against which the other controllers can be compared.

Figure 6-12 shows the block diagram of the analog-only control approach. It has the cylindrical shell with one active composite panel mounted on its surface, which is used as the testbed. The Siglab analyzer connected to the personal computer makes up the data acquisition system; the open-loop and closed-loop frequency response functions are measured using Siglab analyzer. It is also used to generate the broadband disturbance to the testbed. The signals

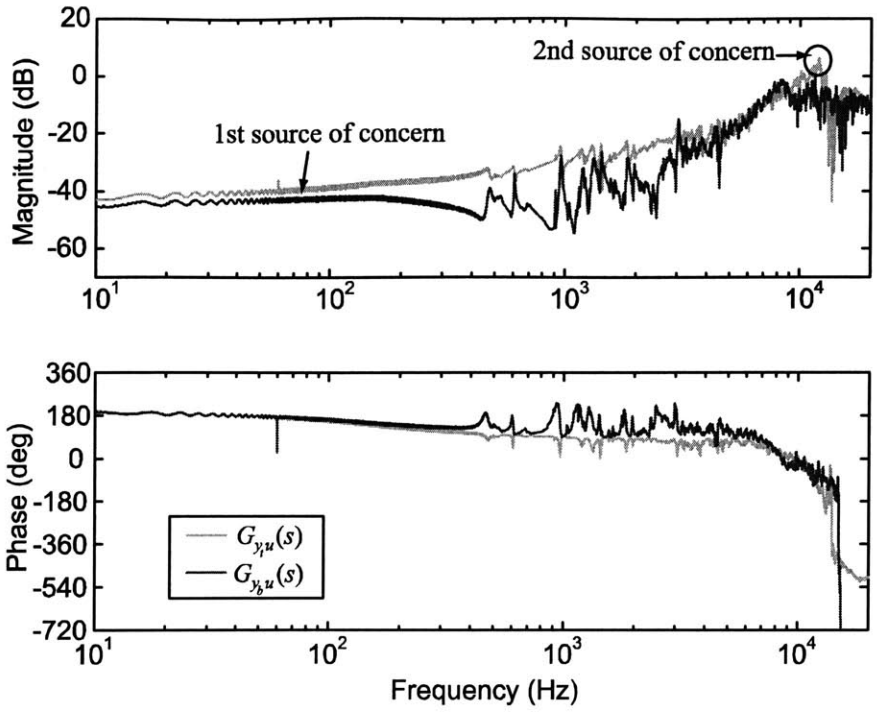

Figure 6-13: Frequency response function of plant transfer functions.

from the accelerometers mounted on the top and bottom surface of the active composite panel are processed at the pre-amplifier, which is a pure gain amplifier. The control input is further amplified at the power amplifier, which has a low-pass filter at 188 Hz. The characteristics of both pre-amplifier and power amplifier are explained in Chapter 2. The broadband disturbance is applied to the testbed using a shaker mounted inside the shell.

Figure 6-12 also shows the signals from the top and bottom accelerometers mounted on the panel that are processed at the pre-amplifier (y_t and y_b, respectively), output from the feedback and feedforward controllers (u_b and u_f, respectively), disturbance w, and control input u. The plant transfer functions from u to (y_t, y_b) are shown in Figure 6-13.

As mentioned in Chapter 3, there are two undesirable features in the plant transfer functions, which are related with the dynamics of the active composite panel. The first source of concern is the low-frequency feedthrough below 500 Hz, due to direct electrical or electromechanical problem in the panel. The second problem is the resonant peak with large phase delay at 12 kHz, due to participation of the embedded accelerometers in the modal behavior of the panel. It was proposed in Chapter 3 that the low-frequency feedthrough can be efficiently cancelled by adding a low-pass filter to the plant transfer function. In this chapter, the way to compensate for the high-frequency panel dynamics problem will be explored.

In Chapter 3, the transfer function $G_{y_t u}$ from u to y_t was approximated below the resonant frequency of the panel as a double differentiation with low-frequency feedthrough times a low-pass filter at 188 Hz. If the resonant peak of the panel dynamics at 12 kHz is also considered,

$G_{y_t u}$ can be approximated as

$$G_{y_t u}(s) = k\frac{s^2 - c^2}{(s + 2\pi \times 188)} \cdot \frac{\omega_p^2}{s^2 + 2\zeta_p \omega_p s + \omega_p^2}, \tag{6.5}$$

where k is a constant gain, c^2 is the low-frequency feedthrough, ω_p is the resonant frequency at 12 kHz, and ζ_p is the corresponding damping ratio. Figure 6-14 shows the frequency response function of the measured $G_{y_t u}(s)$, and its approximation defined in Equation 6.5, when ω_p is $2\pi \times 12{,}000$ (rad/sec), and ζ_p is 0.1. It can be seen that the approximate $G_{y_t u}(s)$ is a good match to the measured $G_{y_t u}(s)$, at least up to about 10 kHz. The difference in phase between the approximate and the measured $G_{y_t u}(s)$ around 10 kHz will not cause any problem, because the resonant pole around that frequency in the measured $G_{y_t u}(s)$ will be canceled out by notch filter, and therefore, will not affect the control system. Now, the proposed feedback controller $K_b(s)$ is given by

$$\begin{aligned} K_b(s) &= g_b \frac{s}{s + 2\pi \times 14} \cdot \frac{1}{(s + 2\pi \times 600)(s + 2\pi \times 1000)} \cdot \frac{s^2 + 2\zeta_p \omega_p s + \omega_p^2}{\omega_p^2} \\ &= \overline{K}_b(s)\, K_{\text{Notch}}(s), \end{aligned} \tag{6.6}$$

where

$$\begin{aligned} \overline{K}_b(s) &= g_b \frac{s}{s + 2\pi \times 14} \cdot \frac{1}{(s + 2\pi \times 600)(s + 2\pi \times 1000)}, \\ K_{\text{Notch}}(s) &= \frac{s^2 + 2\zeta_p \omega_p s + \omega_p^2}{\omega_p^2}. \end{aligned} \tag{6.7}$$

It should be noted that $K_b(s)$ is feedback controller for $G_{y_t u}$ with the low-frequency feedthrough compensator $C(s)$ added, *i.e.*, $[G_{y_t u}(s) + C(s)]$, not for $G_{y_t u}$ itself. As can be seen from Equation 6.6, $K_b(s)$ has a high-pass filter at 14 Hz to avoid DC saturation, and two low-pass filters at 600 and 1000 Hz to make a good loop shape, with a gain g_b. It also has a *notch filter* $K_{\text{Notch}}(s)$ at the frequency ω_p. $K_{\text{Notch}}(s)$ cannot be implemented alone because it is not proper. However, it can be implemented with $\overline{K}_b(s)$, since $K_b(s) = \overline{K}_b(s)\, K_{\text{Notch}}(s)$ is proper. If the values of ω_p and ζ_p determined in Equation 6.5 are used in the notch filter, $K_{\text{Notch}}(s)$ cancels the resonant peak due to panel dynamics at 12 kHz, so that the loop transfer function $K_b(s)\,[G_{y_t u}(s) + C(s)]$ doesn't have the resonant peak at 12 kHz. Figure 6-15 shows the frequency response of the feedback controller $K_b(s)$ and the loop transfer function $K_b(s)\,[G_{y_t u}(s) + C(s)]$. We can see that the resonant peak at 12 kHz is effectively cancelled by the notch filter in the loop transfer function.

The feedforward controller $K_f(s)$ has a high-pass filter at 11 Hz to eliminate DC saturation at the analog circuit, and two low-pass filters at 150 Hz and 6000 Hz with a gain g_f, given by

$$K_f(s) = g_f \frac{s}{s + 2\pi \times 11} \cdot \frac{1}{(s + 2\pi \times 150)(s + 2\pi \times 6000)}. \tag{6.8}$$

$K_f(s)$ is selected so that it is stabilizing, and it is as close as possible to the frequency response that cancels the performance output exactly shown in Equation 3.8. Also, it is better for

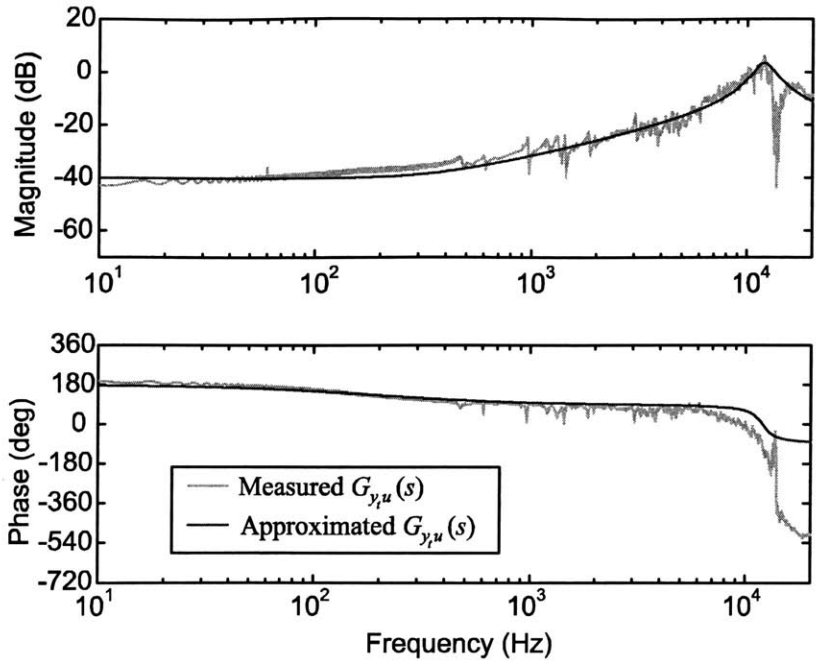

Figure 6-14: Frequency response of measured $G_{y_t u}(s)$ and its approximation.

$K_f(s)$ to be a low-pass filter, rather than a pure integrator, because there is not enough control authority to cancel the low-frequency motion of the shell. Figure 6-16 shows the frequency response of the feedforward controller $K_f(s)$ and the loop transfer function $K_f(s)\, G_{y_b u}(s)$.

After designing $K_b(s)$ and $K_f(s)$ based on the modified plant transfer functions by adding the low-frequency feedthrough compensator $C(s)$, the equivalent controllers $K_b'(s)$ and $K_f'(s)$ are given by

$$\begin{aligned} K_f'(s) &= \frac{K_f(s)}{1 - C(s)\, K_b(s)} \\ K_b'(s) &= \frac{K_b(s)}{1 - C(s)\, K_b(s)} \,. \end{aligned} \tag{6.9}$$

Here, $K_f'(s)$ can be simplified by replacing $K_b(s)$ with $\overline{K}_b(s)$, so that

$$K_f'(s) = \frac{K_f(s)}{1 - C(s)\, \overline{K}_b(s)} \,, \tag{6.10}$$

because $K_b(s) \approx \overline{K}_b(s)$ below the resonant frequency at 12 kHz, and the effect of $C(s)$ is important only at low frequency range. This has a significant advantage in the implementation of the feedforward controller, because the notch filter is the most difficult component to build in the analog electronics. Also, the number of states needed to implement the feedforward controller is reduced by 2 for each panel, if it is implemented digitally.

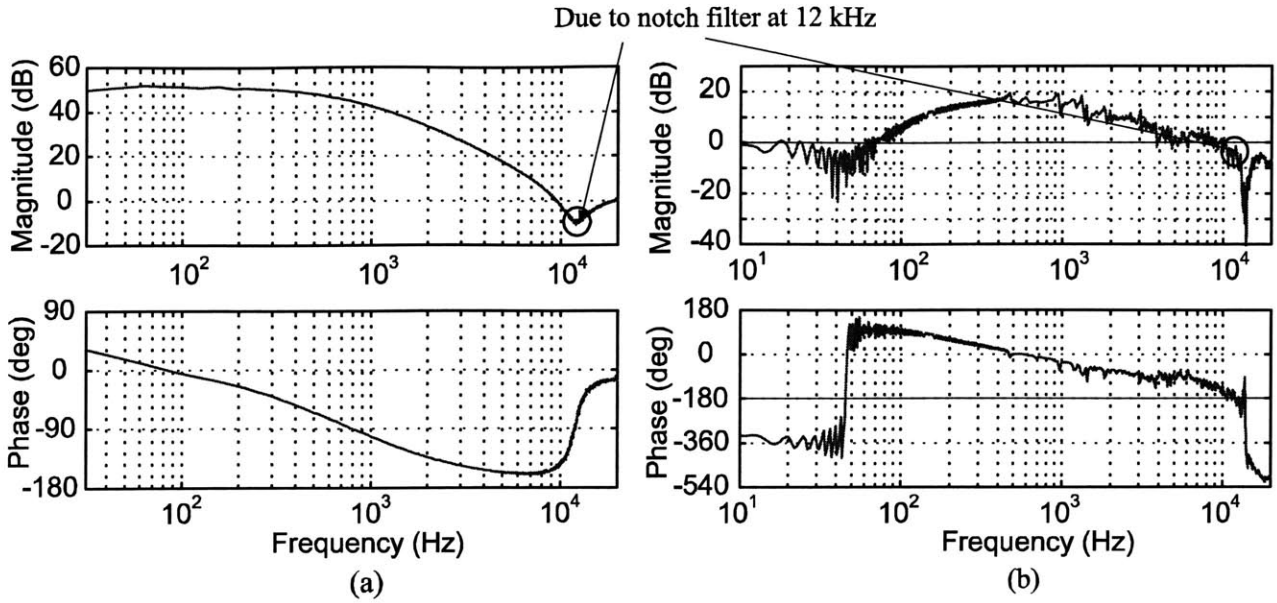

Figure 6-15: Frequency response of (a) the feedback controller $K_b(s)$, and (b) the loop transfer function $K_b(s)\,[G_{y_t u}(s) + C(s)]$.

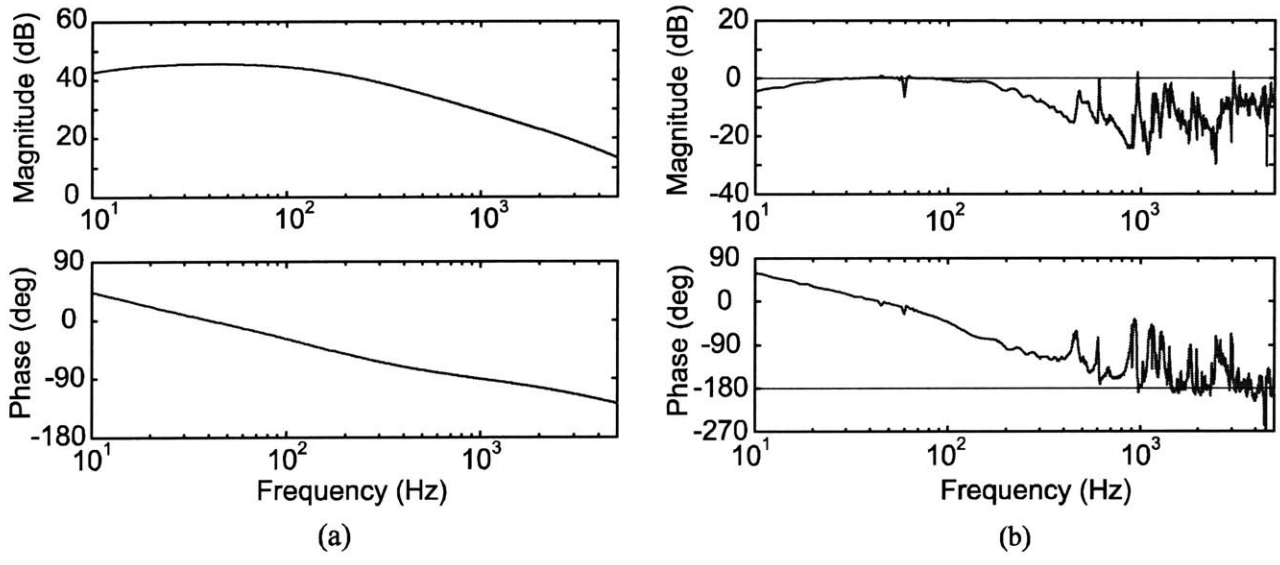

Figure 6-16: Frequency response of (a) feedforward controller $K_f(s)$, and (b) loop transfer function $K_f(s)\,G_{y_b u}(s)$.

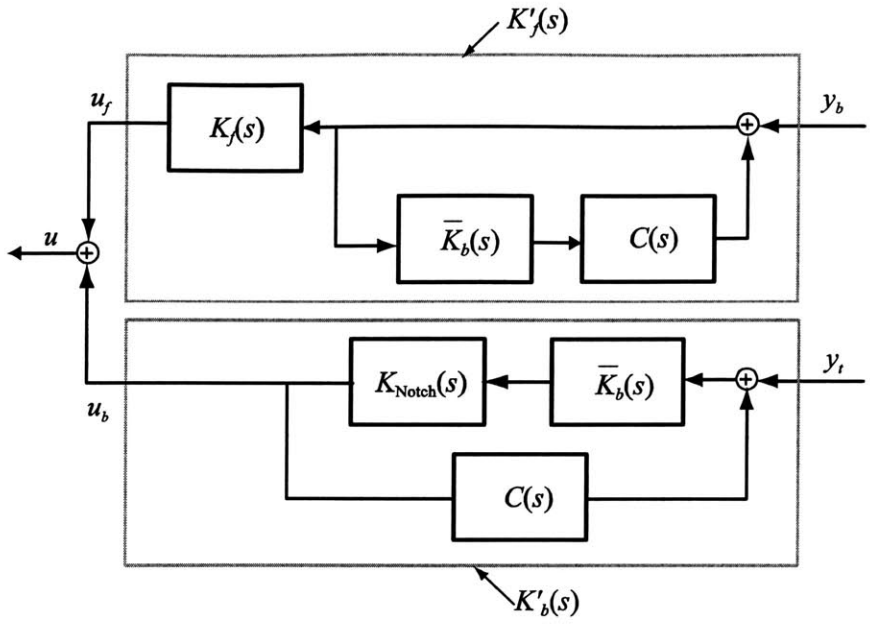

Figure 6-17: Block diagram for the analog feedback and feedforward controller.

The block diagram for the analog feedback and feedforward controller is shown in Figure 6-17. The resulting closed-loop performance using this controller is shown in Figure 6-18, with and without the feedforward control. The disturbance spectrum is broadband up to 5 kHz. With only feedback control, more than 10 dB of attenuation is achieved over most of the range of interest, 200–2000 Hz. The few spots where the attenuation is less than 10 dB occur at frequencies where there is a zero in the disturbance to performance transfer function, so that the performance there is less critical. With feedforward control added, more than 15 dB reduction is achieved between 250 Hz and 1800 Hz. In the narrower frequency range 500–1000 Hz (where the performance is most important), more than 20 dB of reduction is obtained, with attenuation as high as 30 dB for the peaks of the performance transfer function.

The analog circuits for both feedback and feedforward controller are shown in Appendix C.

6.4 Analog Controller with Digital Notch Filter

6.4.1 The Concept of a Digital Notch Filter

The implementation of the analog notch filter is critical to the closed-loop performance of the system; without the notch, the loop gain or controller bandwidth must be reduced considerably to guarantee stability, and the resulting performance is unacceptable. Of course, to succeed, the notch must be carefully tuned to the resonance of the panel. However, as shown in Chapter 2, each panel has different resonant frequency. It is impractical to design and implement different analog notch filters with different target frequencies for all the panels. Therefore, it is desirable

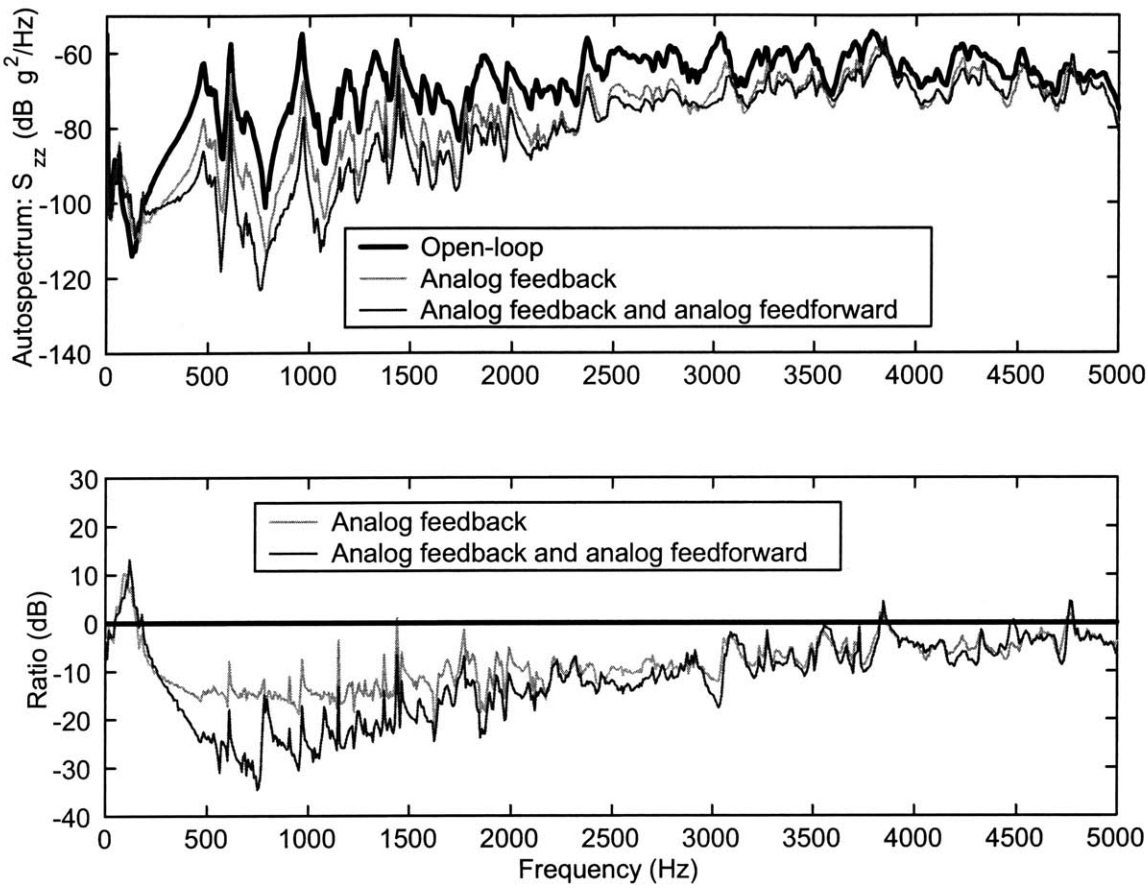

Figure 6-18: Closed-loop performance of the analog-only controller design. "Ratio" represents the ratio of the open-loop response to the closed-loop response. Negative ratios indicate attenuation; positive ratios indicate amplification.

to implement the notch filter digitally, so that the tuning is more easily accomplished in software. However, the digital notch filter cannot be implemented directly, because the frequency to be notched out is relatively high (12 kHz), compared with the maximum achievable sampling frequency (40 kHz) of the DSP system used in this study (DS2003, DS2103, DS1003, dSPACE Inc., Northville, MI). The resulting phase delay would be unacceptable.

The basic idea of implementing digital notch filter is described as follows. It is observed that the notch filter to be designed $H_1(s)$ is decomposed as

$$H_1(s) = 1 - H_2(s) , \tag{6.11}$$

where $H_2(s)$ is a narrow bandpass filter, with peak resonance $H_2(\omega_p) = 1$ at the desired notch frequency ω_p. The filter $H_2(s)$ is implemented digitally; however, the feedthrough term (the "1" in Equation 6.11) is implemented as an analog circuit. Because the magnitude and phase of $H_2(s)$ are important only in a narrow frequency range around ω_p, the effect of delay in the digital controller is less important. More precisely, the implementation of $H_2(s)$ is designed so that the phase delay at ω_p is taken into account. The transfer function implemented in $H_2(s)$ is [Song, 2000]

$$\widehat{H}_2(s) = \frac{cs + d}{s^2 + 2\zeta\omega_p s + \omega_p^2} \cdot D(s) , \tag{6.12}$$

where $D(s)$ represents the DSP system dynamics (mostly time delay), ζ is the damping ratio of the resonant bandpass, and c and d are chosen so that the best match with the desired analog notch filter is achieved.

An example of designing a digital notch filter is given to illuminate its concept. Assume we want to implement a notch filter $H_1(s)$, given as

$$H_1(s) = \frac{s^2 + 2\zeta_1\omega_p s + \omega_p^2}{s^2 + 2\zeta_2\omega_p s + \omega_p^2} , \tag{6.13}$$

where ω_p is the frequency to be notched out, and ζ_1 and ζ_2 are damping ratios of the notch filter. The frequency response of $H_1(s)$ is shown in Figure 6-19(a), when $\omega_p = 2\pi\times 10{,}000$ (rad/s), $\zeta_1 = 0.03$, and $\zeta_2 = 0.3$, respectively. Now, as shown in Equation 6.11, $H_1(s)$ can be decomposed as

$$\begin{aligned} H_1(s) &= \frac{s^2 + 2\zeta_1\omega_p s + \omega_p^2}{s^2 + 2\zeta_2\omega_p s + \omega_p^2} \\ &= 1 - \frac{as + b}{s^2 + 2\zeta_2\omega_p s + \omega_p^2} \\ &= 1 - H_2(s) , \end{aligned} \tag{6.14}$$

where

$$\begin{aligned} H_2(s) &= \frac{as + b}{s^2 + 2\zeta_2\omega_p s + \omega_p^2} \\ a &= 2\zeta_2\omega_p - 2\zeta_1\omega_p \\ b &= 0 . \end{aligned} \tag{6.15}$$

Figure 6-19 shows the relation between $H_1(s)$ and $H_2(s)$. As mentioned above, the narrow bandpass filter $H_2(s)$ is implemented digitally, while the feedthrough term "1" is implemented in analog. It is not feasible to implement directly $H_1(s)$ digitally for a high notch frequency ω_p, due to the phase delay in the digital control system. However, it is feasible to implement $H_2(s)$ digitally, because the effect of $H_2(s)$ is negligible, compared with the feedthrough term "1", except around the notch frequency ω_p; $H_2(s)$ is important only around ω_p. Therefore, if the width of the frequency range to be notched out ($\Delta\omega_p$ in Figure 6-19) is reasonably small compared to the sampling frequency, regardless of ω_p itself, $H_2(s)$ can be efficiently implemented digitally so that the resulting $H_1(s)$ is similar to what it is supposed to be. The digital implementation of $H_2(s)$ (defined as $\widehat{H}_2(s)$ above) is given by

$$\widehat{H}_2(s) = \frac{cs + d}{s^2 + 2\zeta_2\omega_p s + \omega_p^2} \cdot D(s) . \tag{6.16}$$

Generally, the dynamics of the DSP system $D(s)$ can be replaced with the time delay transfer function e^{-Ts} with effective time delay T. Let T_s and T_l be the sampling time and the latency (time required to perform the digital calculation) of the DSP system, respectively. Then, assuming the zero-order-hold method is used during the sampling process, the effective time delay T in $D(s)$ is given by

$$T = \frac{T_s}{2} + T_l . \tag{6.17}$$

Very frequently, the latency T_l can be as large as the sampling time T_s, depending on the required digital calculation. In that case, the effective time delay is

$$T = 1.5T_s . \tag{6.18}$$

Therefore, given the sampling time T_s, $\widehat{H}_2(s)$ can be written as

$$\widehat{H}_2(s) = \frac{cs + d}{s^2 + 2\zeta_2\omega_p s + \omega_p^2} \cdot e^{-\frac{3T_s}{2}s} . \tag{6.19}$$

The real constants c and d are selected so that they satisfy the following relation

$$\widehat{H}_2(j\omega) = H_2(j\omega) \quad \text{at } \omega = \omega_p . \tag{6.20}$$

The resulting digital implementation of the notch filter $H_1(s)$, which is denoted as $\widehat{H}_1(s)$, is given by

$$\widehat{H}_1(s) = 1 - \widehat{H}_2(s) . \tag{6.21}$$

Note that only $\frac{cs+d}{s^2+2\zeta_2\omega_p s+\omega_p^2}$ should be actually implemented for $\widehat{H}_2(s)$. The time delay component $e^{-\frac{3T_s}{2}s}$ is necessary only to compute the parameters c and d using Equation 6.20.

Figures 6-20 through 6-23 show the frequency response of $H_2(s)$, $\widehat{H}_2(s)$, $H_1(s)$, and $\widehat{H}_1(s)$ with various sampling times. It can be seen that even the sampling frequency of 12.5 kHz (sampling time of 80 μs) produces a reasonably good notch filter at 10 kHz, although the width of the frequency range to be notched out is reduced, and a difference in the gain at low-frequency is observed. These discrepancies can be improved by tuning the damping ratio and the notch frequency, as shown in the next section.

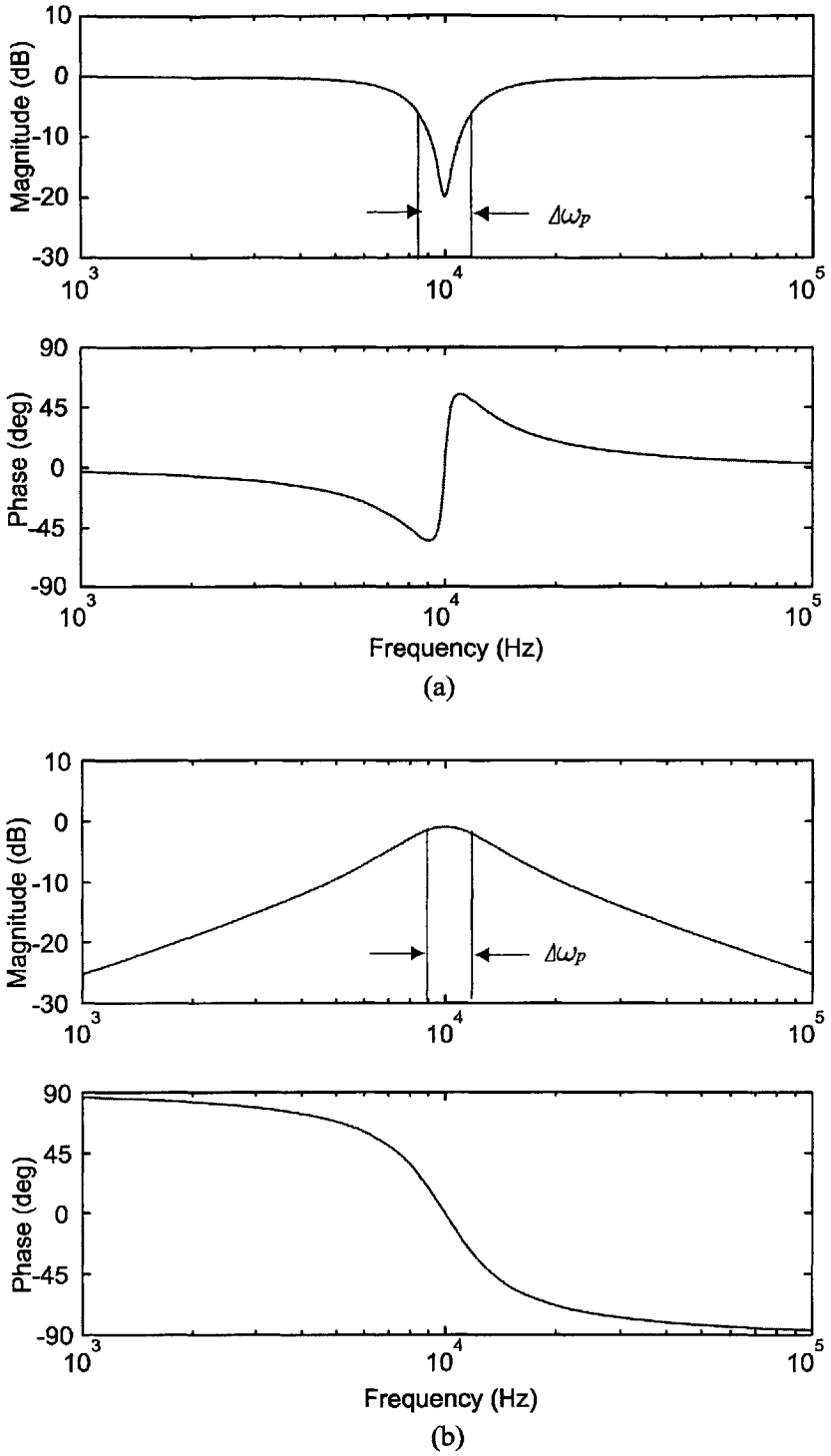

Figure 6-19: Frequency response of (a) $H_1(s)$, and (b) $H_2(s)$. Note $H_1(s) = 1 - H_2(s)$.

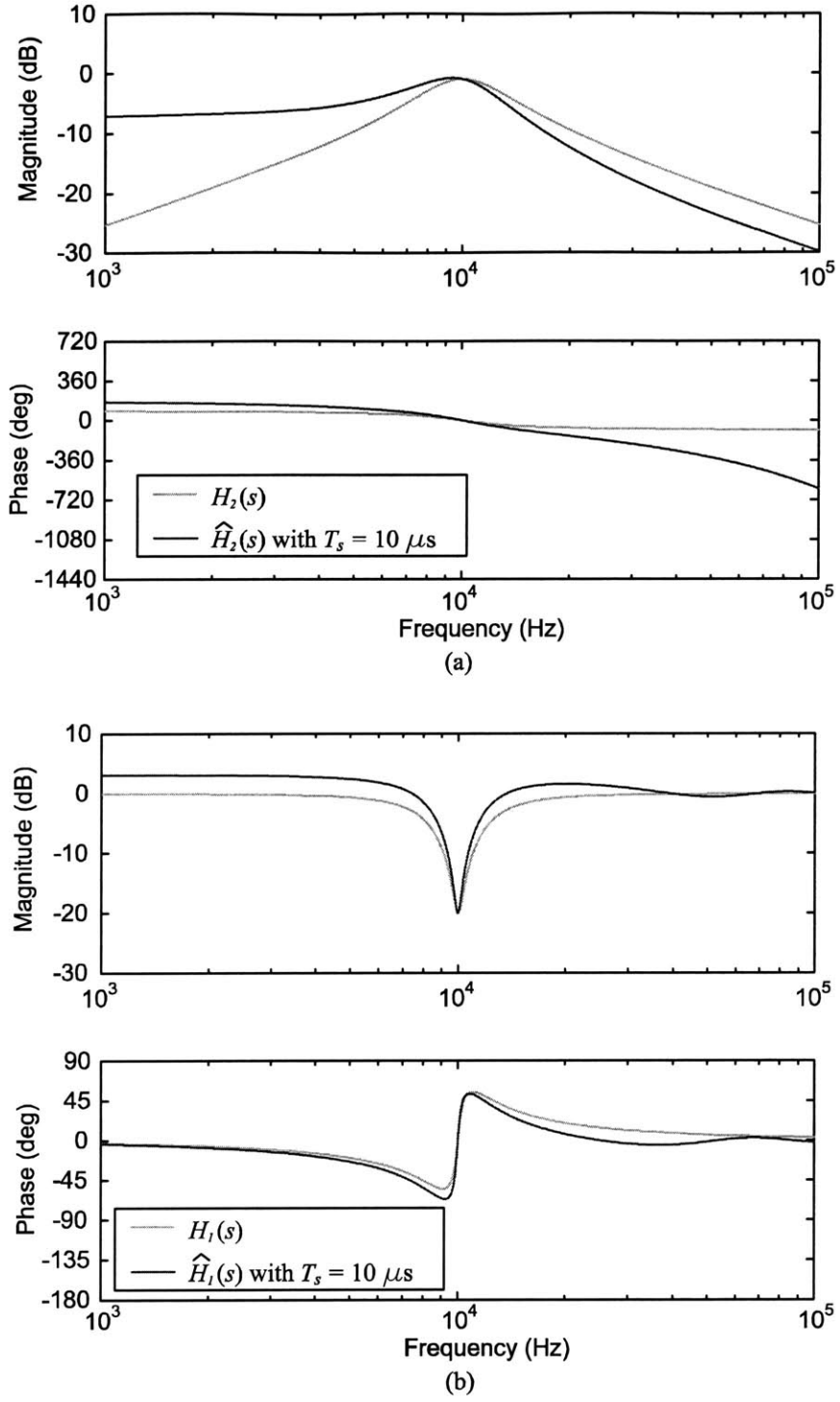

Figure 6-20: Frequency response of (a) $H_2(s)$ and $\widehat{H}_2(s)$, and (b) $H_1(s)$ and $\widehat{H}_1(s)$, when the sampling time $T_s = 10\,\mu s$. (The sampling frequency is 100 kHz.)

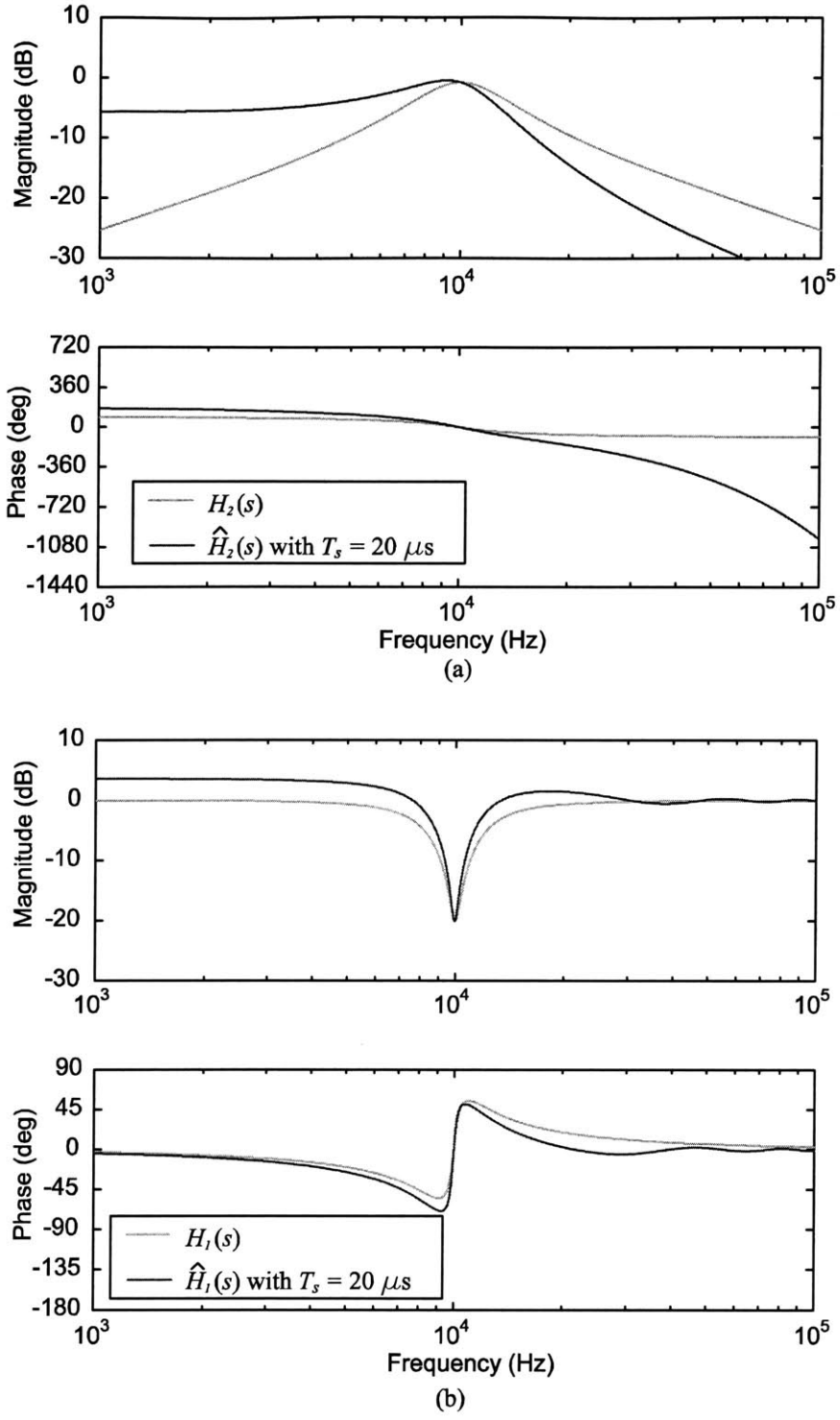

Figure 6-21: Frequency response of (a) $H_2(s)$ and $\widehat{H}_2(s)$, and (b) $H_1(s)$ and $\widehat{H}_1(s)$, when the sampling time $T_s = 20\,\mu s$. (The sampling frequency is 50 kHz.)

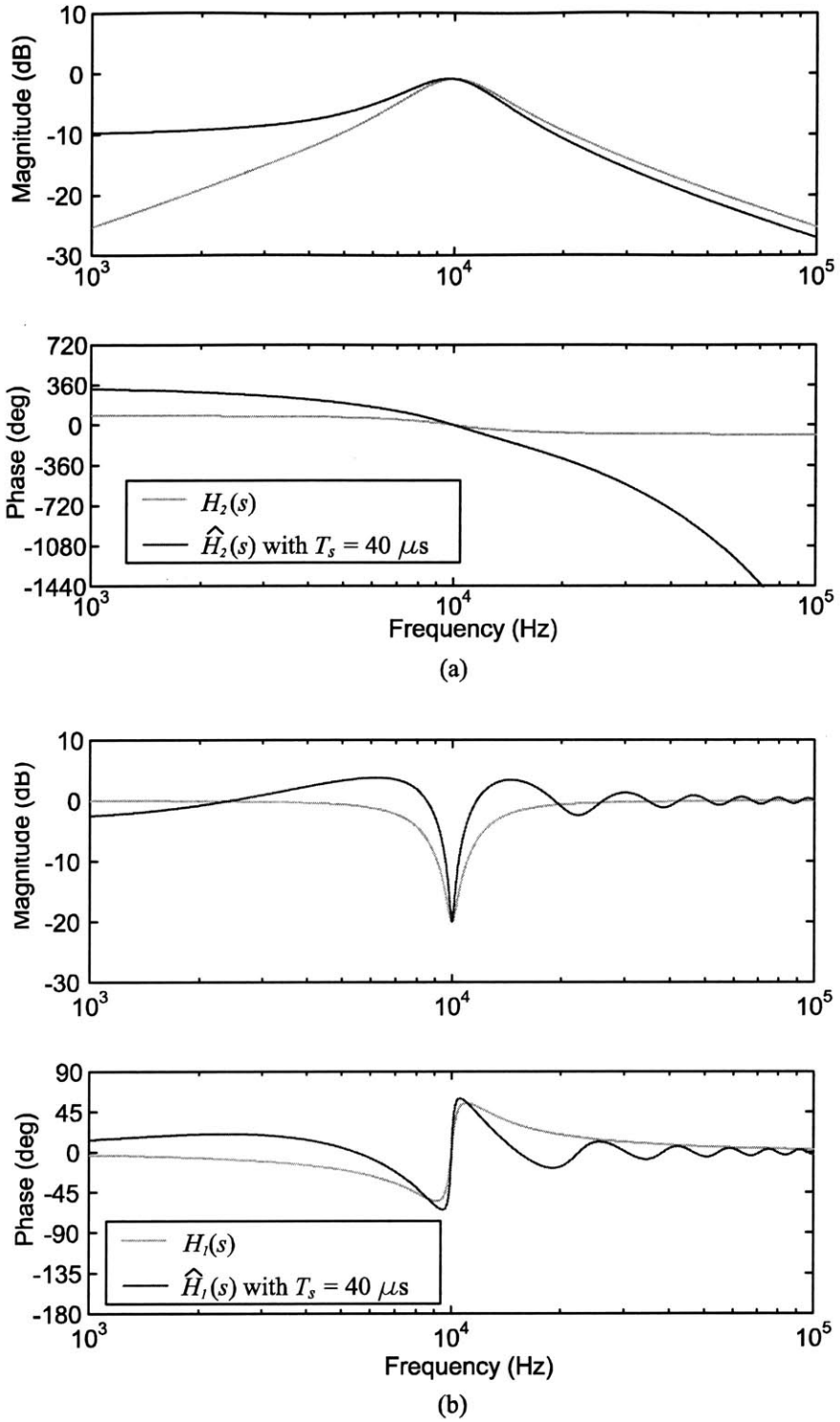

Figure 6-22: Frequency response of (a) $H_2(s)$ and $\widehat{H}_2(s)$, and (b) $H_1(s)$ and $\widehat{H}_1(s)$, when the sampling time $T_s = 40\,\mu s$. (The sampling frequency is 25 kHz.)

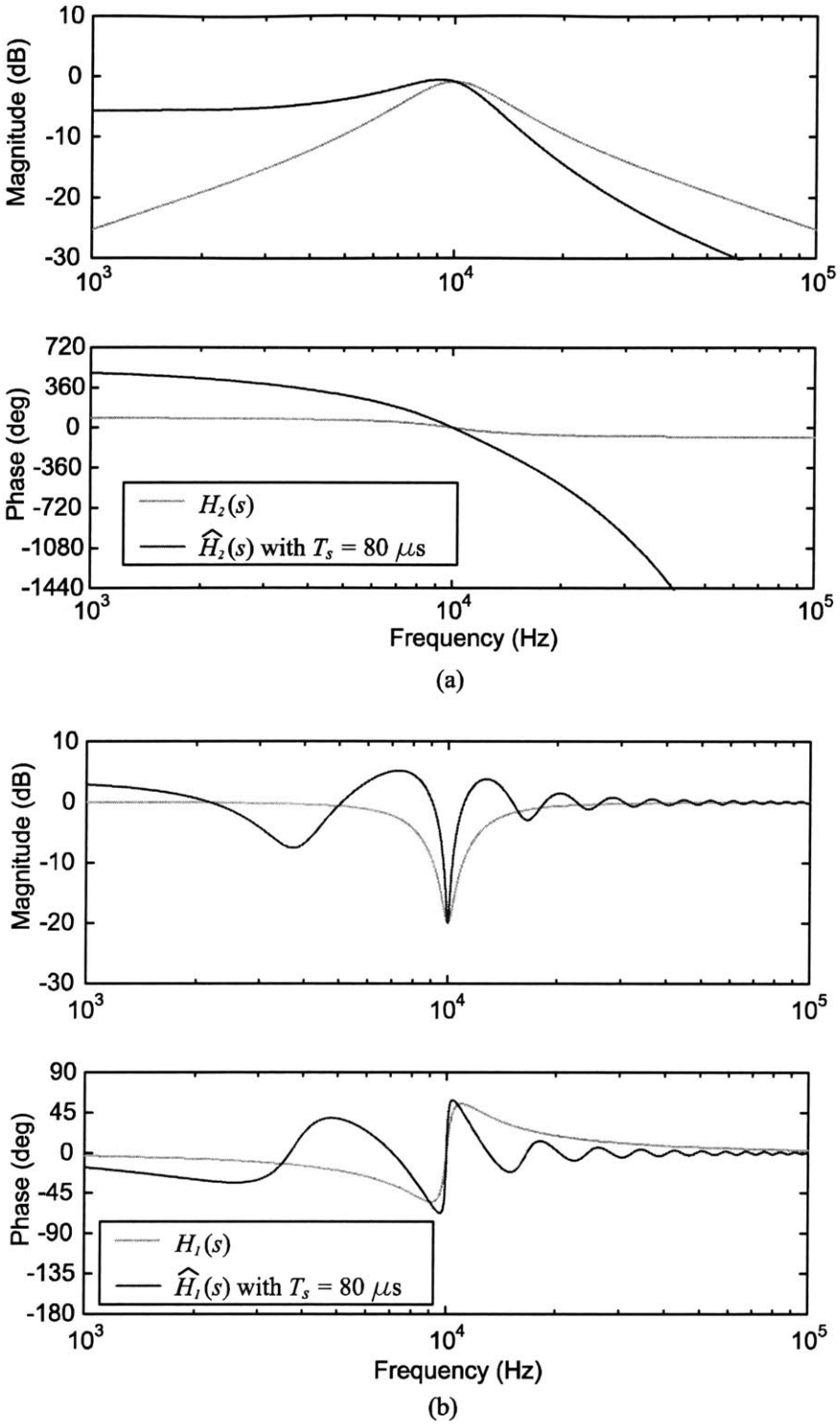

Figure 6-23: Frequency response of (a) $H_2(s)$ and $\widehat{H}_2(s)$, and (b) $H_1(s)$ and $\widehat{H}_1(s)$, when the sampling time $T_s = 80\,\mu s$. (The sampling frequency is 12.5 kHz.)

6.4.2 Design of the Digital Notch Filter

In this section, the design process for the digital notch filter is presented. The feedback controller $K_b(s)$ to be implemented is shown in Equation 6.22, given by

$$K_b(s) = g_b \cdot \frac{s}{s+2\pi\times 14} \cdot \frac{\left(\frac{s}{\omega_p}\right)^2 + \frac{2\zeta_p s}{\omega_p} + 1}{(s+2\pi\times 600)(s+2\pi\times 1000)} . \tag{6.22}$$

We can decompose $K_b(s)$ as

$$\begin{aligned} K_b(s) &= g_b \cdot \frac{s}{s+2\pi\times 14} \cdot \frac{\left(\frac{s}{\omega_p'}+1\right)^2}{(s+2\pi\times 600)(s+2\pi\times 1000)} \cdot \frac{\left(\frac{s}{\omega_p}\right)^2 + \frac{2\zeta_p s}{\omega_p} + 1}{\left(\frac{s}{\omega_p'}+1\right)^2} \\ &= K_1(s)\left[1 - K_2(s)\right] , \end{aligned} \tag{6.23}$$

where

$$\begin{aligned} K_1(s) &= g_b \cdot \frac{s}{s+2\pi\times 14} \cdot \frac{\left(\frac{s}{\omega_p'}+1\right)^2}{(s+2\pi\times 600)(s+2\pi\times 1000)} , \\ K_2(s) &= 1 - \frac{\left(\frac{s}{\omega_p}\right)^2 + \frac{2\zeta_p s}{\omega_p} + 1}{\left(\frac{s}{\omega_p'}+1\right)^2} . \end{aligned} \tag{6.24}$$

Here, ω_p' is a design variable for digital notch filter. The natural choice for ω_p' would be $\omega_p' = \omega_p$, so that $K_2(s)$ has zero magnitude at DC and infinitely high frequency. However, this may cause a difference in the gain at low-frequency, as shown in Section 6.4.1. Now, the digital implementation of $K_2(s)$, denoted as $\widehat{K}_2(s)$, can be written as

$$\widehat{K}_2(s) = \frac{cs+d}{\left(\frac{s}{\omega_p'}+1\right)^2} \cdot e^{-\frac{3T_s}{2}s} . \tag{6.25}$$

As in Section 6.4.1, the real constants c and d are selected such that they satisfy

$$\widehat{K}_2(j\omega_p) = K_2(j\omega_p) . \tag{6.26}$$

Also, the resulting digital implementation of the feedback controller $K_b(s)$, which is denoted as $\widehat{K}_b(s)$, is given by

$$\widehat{K}_b(s) = K_1(s)\left[1 - \widehat{K}_2(s)\right] . \tag{6.27}$$

The block diagram of $\widehat{K}_b(s)$ is shown in Figure 6-24.

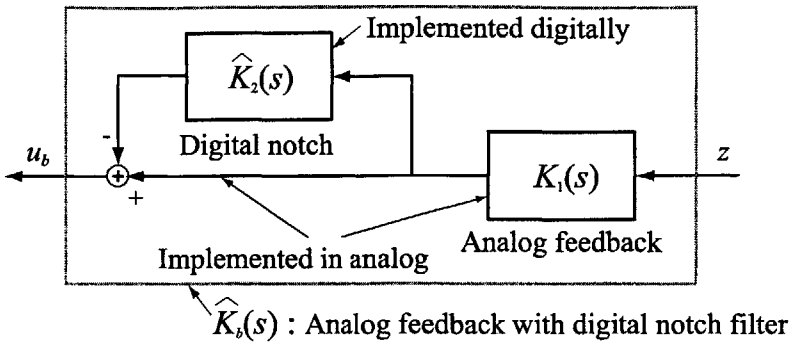

Figure 6-24: Block diagram of the analog feedback controller with a digital notch filter.

The design process for the digital notch filter can be summarized as follows:

1. Assume ω_p' ($\omega_p' = \omega_p$ may be a good initial guess).
2. Determine c and d such that Equation 6.26 is satisfied.
3. Implement $\widehat{K}_2(s)$ digitally without expected time delay component $e^{-\frac{3T_s}{2}s}$. Here, the Tustin method [Franklin, 1998] may be used to transform the controller designed in the continuous domain into the digital controller.
4. Measure the frequency response of $\widehat{K}_b(s)$ and compare it with that of $K_b(s)$.

Generally, the resulting $\widehat{K}_b(s)$ is a good match to $K_b(s)$ around the notch frequency ω_p. However, there may be a discrepancy of the gain at low frequency. This can be reduced by changing the total gain of $\widehat{K}_b(s)$. If that is not acceptable, ω_p' should be adjusted until the acceptable digital notch filter is acquired. Therefore, the design process becomes iterative in that case.

Figure 6-25 shows the frequency response of feedback controller using analog and digital notch filter ($K_b(s)$, and $\widehat{K}_b(s)$, respectively), with a sampling frequency of 40 kHz. It can be seen that $\widehat{K}_b(s)$ has a notch filter at 12 kHz, as expected, although it has higher gain than $K_b(s)$ at low frequency. If this is not acceptable, ω_p' should be adjusted (sometimes, the damping ratio ζ_p and the real constants c and d selected using the condition in Equation 6.26 may need to be adjusted, too) until the resulting $\widehat{K}_b(s)$ is similar enough to $K_b(s)$. Figure 6-26 shows the frequency response of a new $\widehat{K}_b(s)$ with $\omega_p' = 2\pi \times 15{,}000$ (rad/sec), after a few iterations, with a sampling frequency of 40 kHz. We can see that $\widehat{K}_b(s)$ is *exactly* the same as $K_b(s)$ below 5 kHz, and it also has a notch filter at 12 kHz that is very similar to $K_b(s)$. The resulting loop transfer function is shown in Figure 6-27 (frequency response), and 6-28 (Nyquist plot).

Next, our approach for incorporating the low-frequency feedthrough compensator $C(s)$ in the controller is described. Figure 6-29 shows block diagrams of two possible ways to combine $C(s)$ in the feedback controller. The configuration in (a) is what should be implemented to generate the equivalent feedback controller. However, the configuration in (b) may be preferred

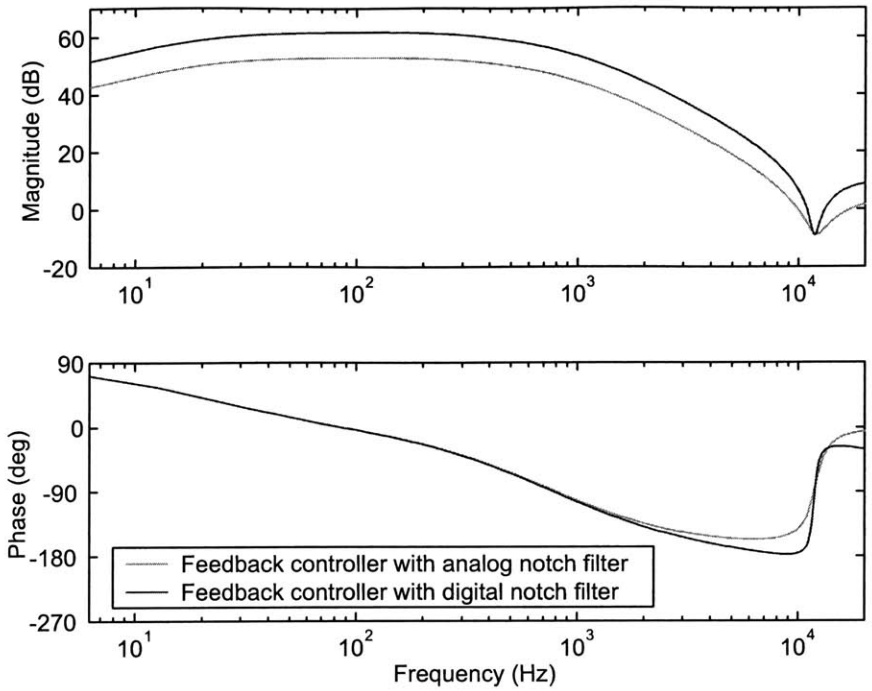

Figure 6-25: Frequency response of the feedback controller with analog and digital notch filters using initial guess of $\omega_p' = \omega_p = 2\pi \times 12{,}000$ (rad/sec).

because it is easier to implement than (a). In order for both of them to generate the same control output u_b, $C'(s)$ should be selected so that

$$C'(s) = C(s)\left[1 - \widehat{K}_2(s)\right] \tag{6.28}$$

is satisfied. However, since the effect of $\widehat{K}_2(s)$ is important only around the notch frequency ω_p, where $C(s)$ is negligible, $C'(s)$ can be replaced with $C(s)$ without causing any problem.

Figure 6-30 shows the block diagram of the analog controller with digital notch filter. The basic set-up is the same as shown in Figure 6-12. It has the cylindrical shell with one active composite panel mounted on its surface, the pre-amplifier and power amplifier to process the signal of the panel. There is a shaker mounted inside the shell, which applies the broadband disturbance to the testbed. The Siglab analyzer is used to measure the open-loop and closed-loop frequency response functions, and to generate the broadband disturbance up to 5 kHz. The digital notch filter algorithm is implemented in a dSpace digital controller with a sampling frequency of 40 kHz.

The block diagram of the equivalent feedback and feedforward controller $K_b'(s)$ and $K_f'(s)$ is shown in Figure 6-31. For $K_f'(s)$, the same feedforward controller $K_f(s)$ is used as the one designed in Section 6.3., with the feedback controller $K_1(s)$ defined in Equation 6.24. Also, instead of $K_1(s)$, the feedback controller $\overline{K}_b(s)$ defined in Equation 6.7 can be used in the

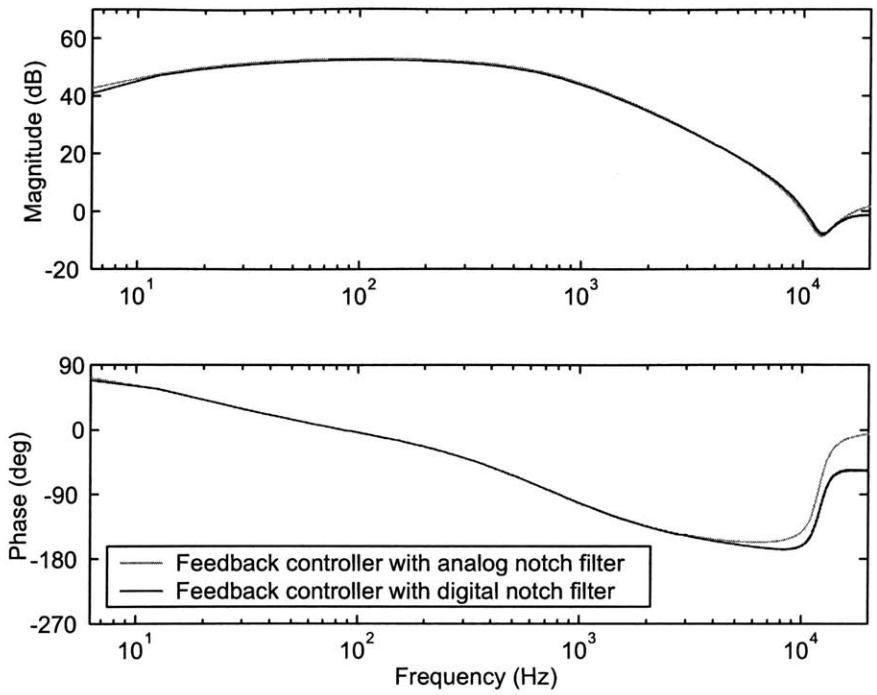

Figure 6-26: Frequency response of the feedback controller with analog and digital notch filters. $\omega_p' = 2\pi \times 15{,}000$ (rad/sec).

feedforward block diagram, because their difference is negligible in the control bandwidth. For $K_b'(s)$, the configuration of (b) in Figure 6-29 is used. The resulting closed-loop performance using this controller is shown in Figure 6-32, with and without the feedforward control. The disturbance spectrum is broadband up to 5 kHz. The result is almost indistinguishable from that obtained using the analog controller. However, this controller configuration enables us to change the frequency to be notched out easily, so that it is now feasible to implement notch filters with different target frequencies for each panel.

The circuits for analog components used in this controller configuration are shown in Appendix D.

6.5 Hybrid Analog/Digital Feedback and Analog Feedforward Controller

In this section, a hybrid analog/digital feedback and analog feedforward controller is implemented. In the hybrid analog/digital feedback configuration, part of the feedback control law is implemented digitally. Figure 6-33 shows the block diagram of the hybrid feedback and analog feedforward controller. The main new features of this configuration are the complementary high-pass and low-pass filters, which control the bands in which the analog and digital control laws act. The low-pass filter consists of a second order Butterworth low-pass filter with a corner

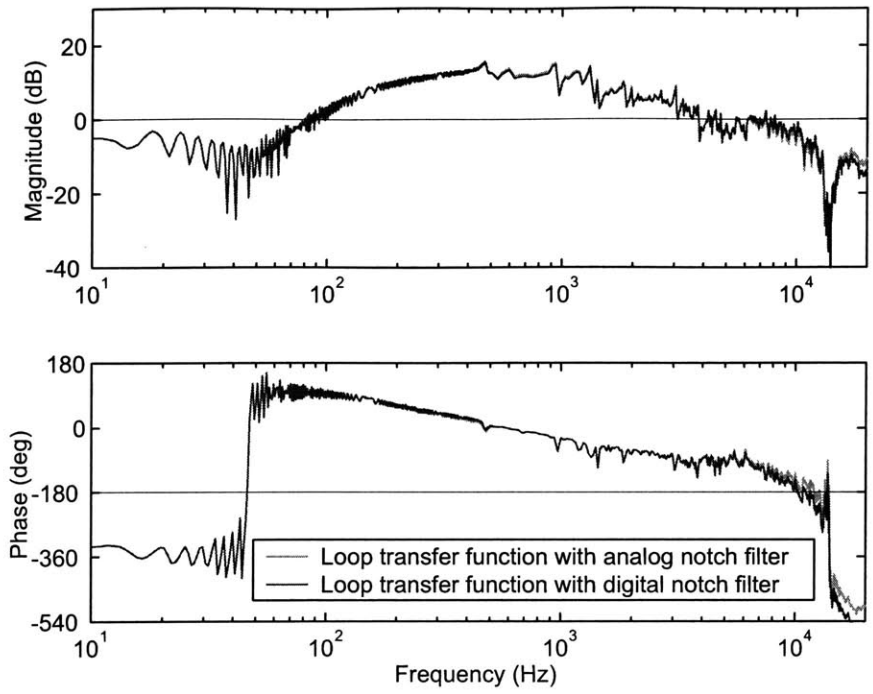

Figure 6-27: Frequency response of loop transfer function for the feedback control with analog and digital notch filters.

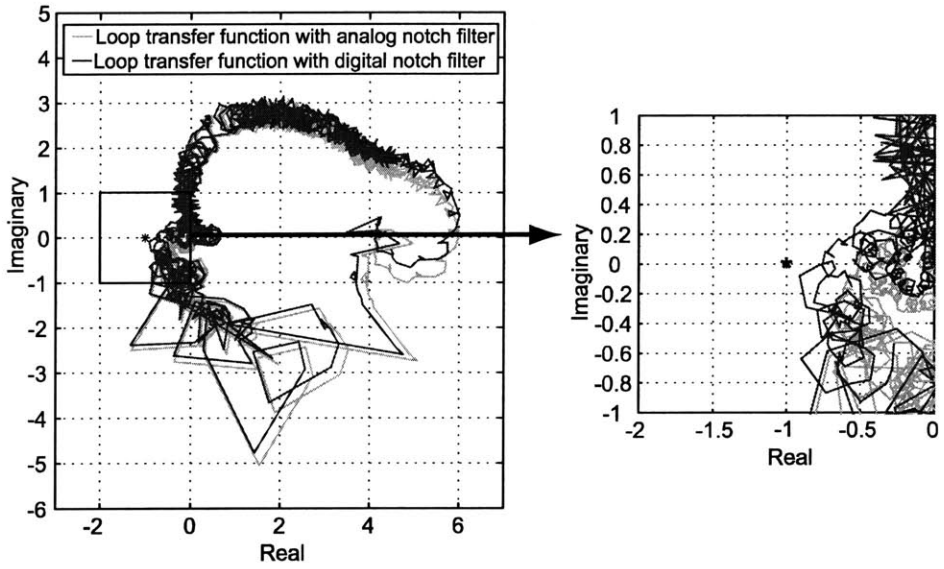

Figure 6-28: Nyquist plot of loop transfer function for the feedback control with analog and digital notch filters.

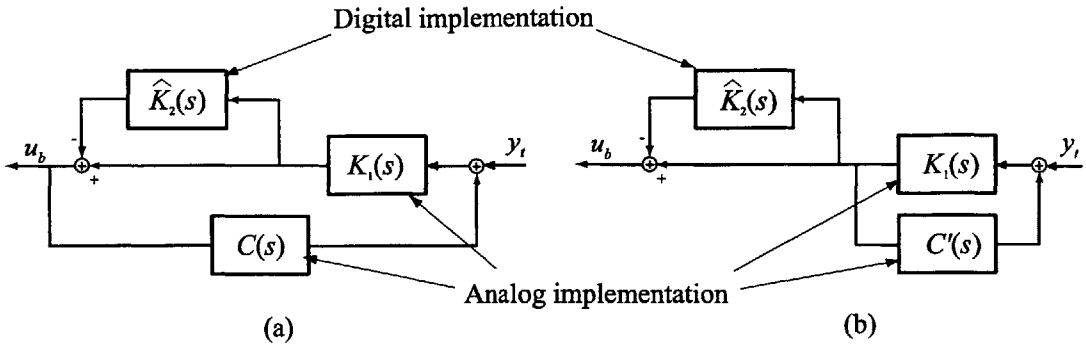

Figure 6-29: Two possible ways to incorporate the low-frequency feedthrough compensator $C(s)$ in the feedback controller.

frequency of 1 kHz [Ghausi, 1981]. On the other hand, the high-pass filter is implemented such that it is *complementary* to the low-pass filter, so that its sum with the low-pass filter becomes unity. Of necessity, the complementary filters are implemented in analog. Figures 6-34 and 6-35 show the frequency response of the complementary filters. The analog circuits for these filters are shown in Appendix E.

The block diagram of the hybrid feedback controller without the low-frequency feedthrough compensator $C(s)$ is shown in Figure 6-36. The digital control law $K_b^D(s)$ implements the low-pass filters at 600 Hz and 1000 Hz, and the high-pass filter at 14 Hz, which were previously implemented in analog. However, the notch filter was not implemented digitally, since its main effect is well above 1 kHz. The analog controller $K_b^A(s)$ was the same as implemented in the analog controller in Section 6.3, including the notch filter. More specifically, they are given by

$$\begin{aligned} K_b^D(s) &= g_b \cdot \frac{s}{s+2\pi\times 14} \cdot \frac{1}{(s+2\pi\times 600)(s+2\pi\times 1000)} \\ K_b^A(s) &= g_b \cdot \frac{\left(\frac{s}{\omega_p}\right)^2 + \frac{2\zeta_p s}{\omega_p} + 1}{(s+2\pi\times 600)(s+2\pi\times 1000)} . \end{aligned} \tag{6.29}$$

The analog controller $K_b^A(s)$ doesn't have the high-pass filter at 14 Hz, because its input is already processed by the complementary high-pass filter. The second-order Butterworth low-pass filter $L(s)$ and its complementary high-pass filter $H(s)$ can be written as (for Butterworth filter at 1 kHz, $\zeta_l = 0.707$, $\omega_l = 2\pi\times 1000$ (rad/sec))

$$\begin{aligned} L(s) &= \frac{\omega_l^2}{s^2 + 2\zeta_l\omega_l s + \omega_l^2} , \\ H(s) &= 1 - L(s) \\ &= \frac{s^2 + 2\zeta_l\omega_l s}{s^2 + 2\zeta_l\omega_l s + \omega_l^2} . \end{aligned} \tag{6.30}$$

Using $K_b^D(s)$, $K_b^A(s)$, $L(s)$, and $H(s)$ in Figure 6-36, the hybrid feedback controller $K_b^H(s)$ is

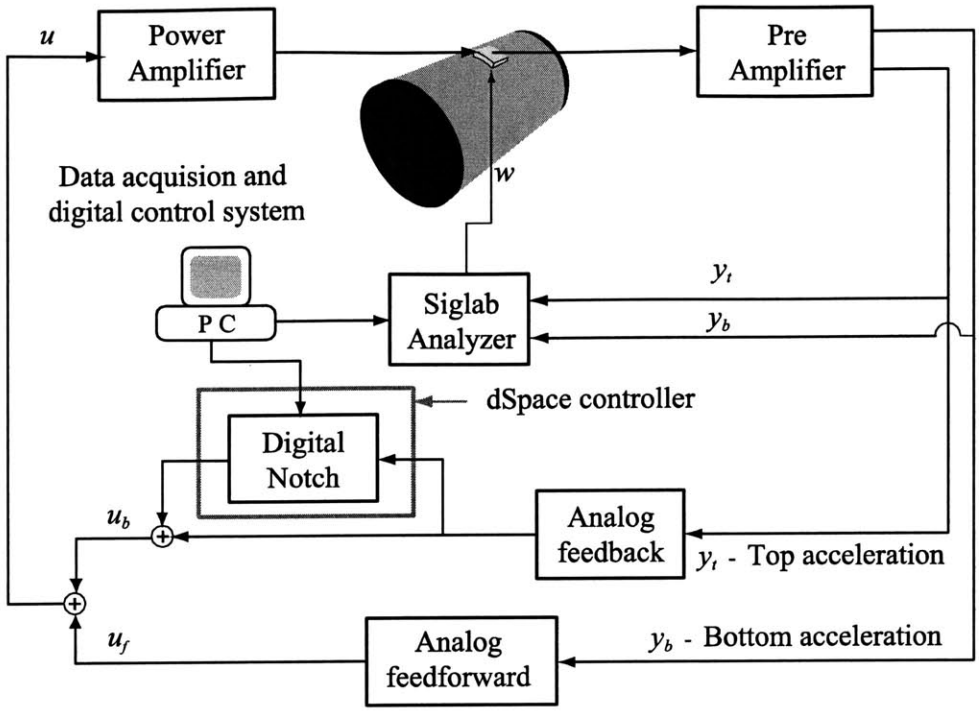

Figure 6-30: Block diagram of the analog controller with the digital notch filter.

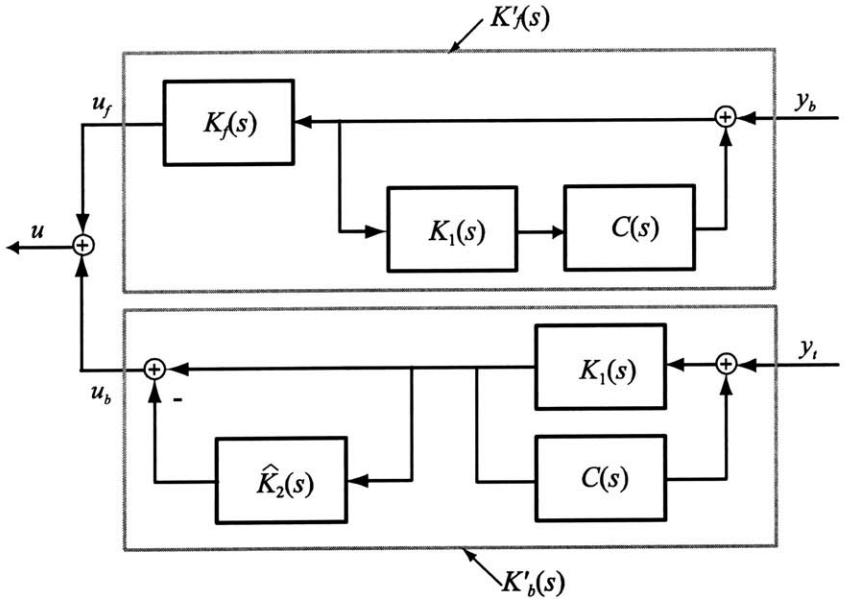

Figure 6-31: Block diagram for the analog controller with the digital notch filter.

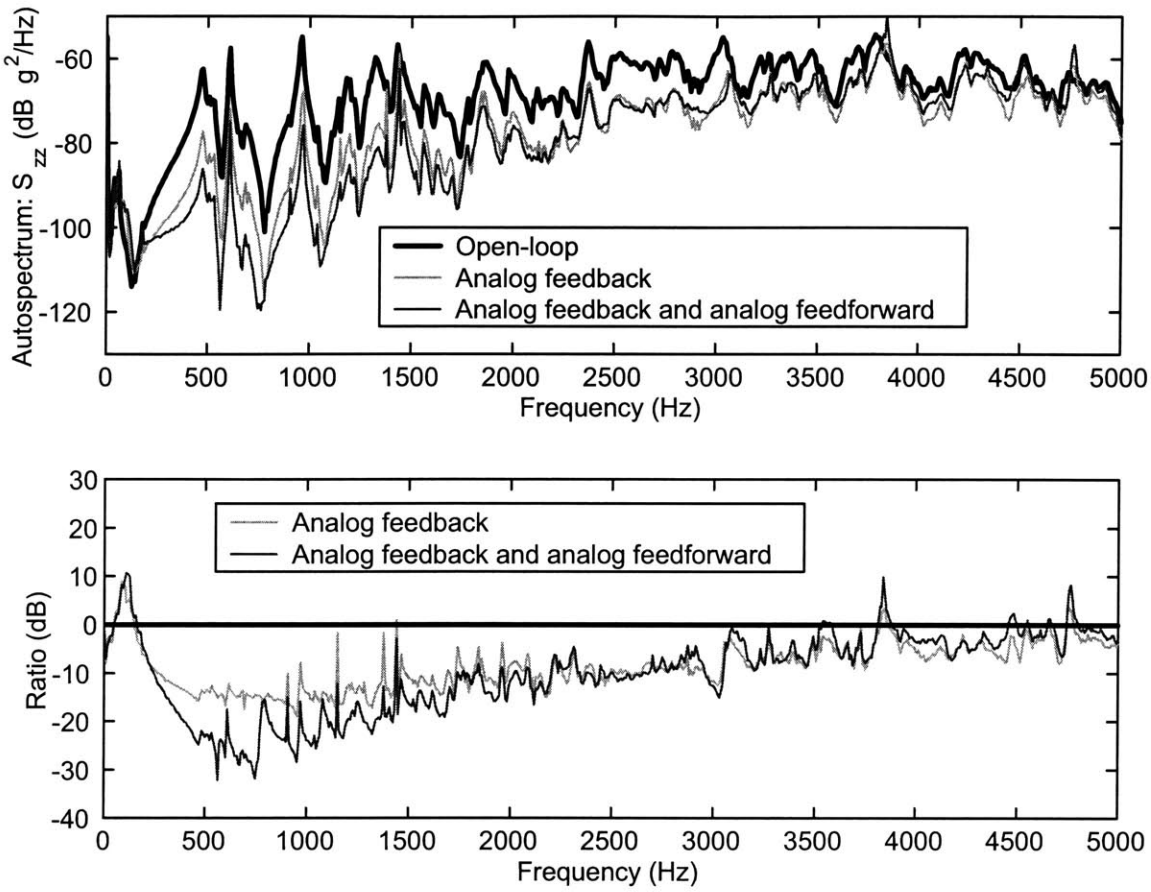

Figure 6-32: Closed-loop performance obtained with the analog controller with digital notch filter. "Ratio" represents the ratio of the open-loop response to the closed-loop response. Negative ratios indicate attenuation; positive ratios indicate amplification.

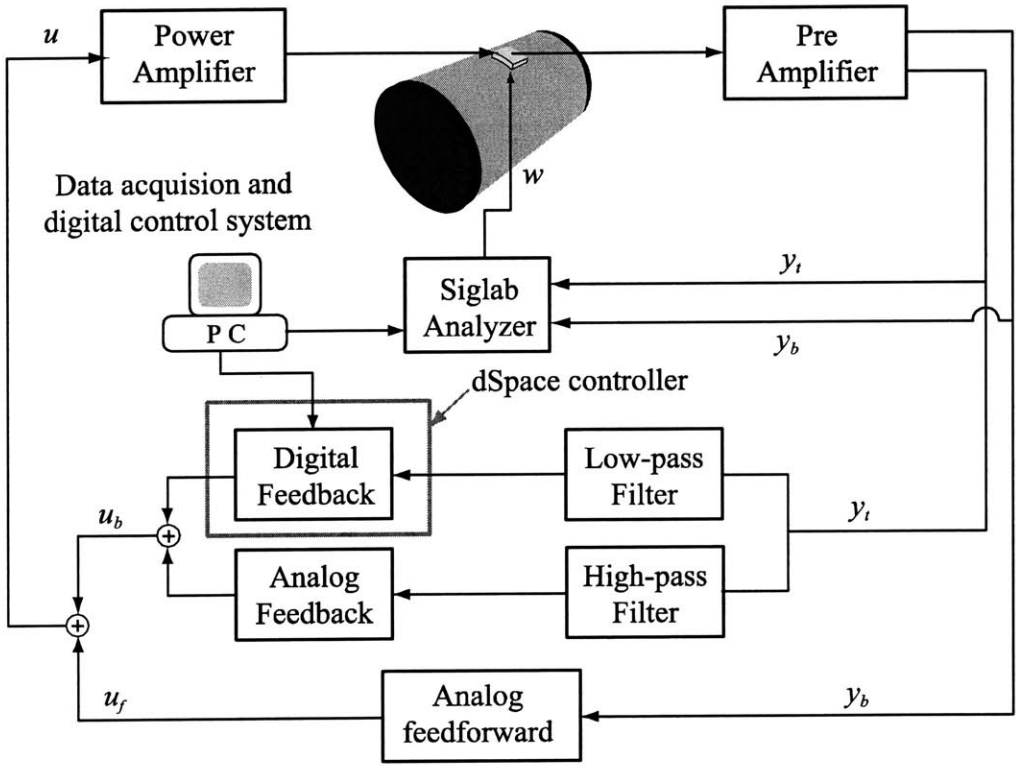

Figure 6-33: Block diagram of the hybrid feedback and analog feedforward controller.

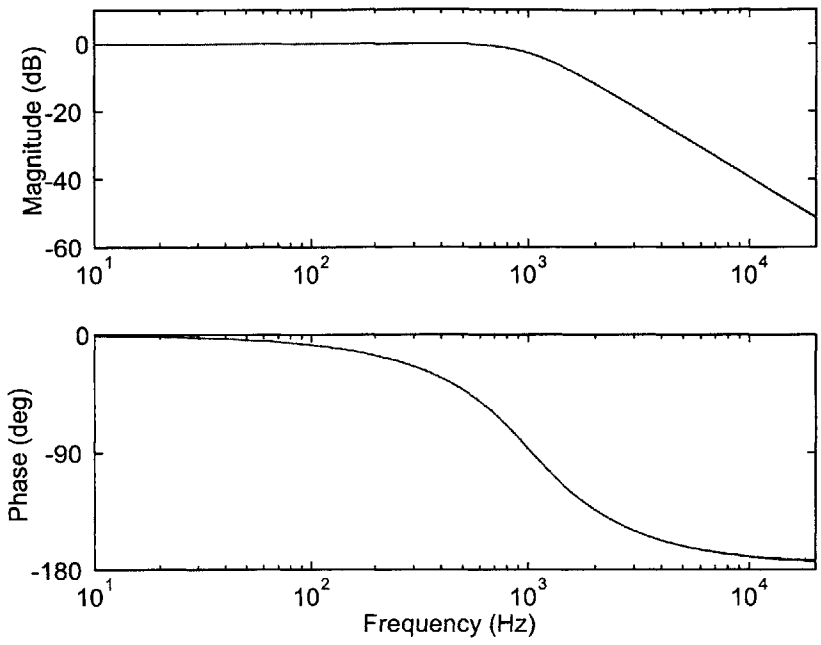

Figure 6-34: Frequency response of a second order Butterworth low-pass filter at 1 kHz.

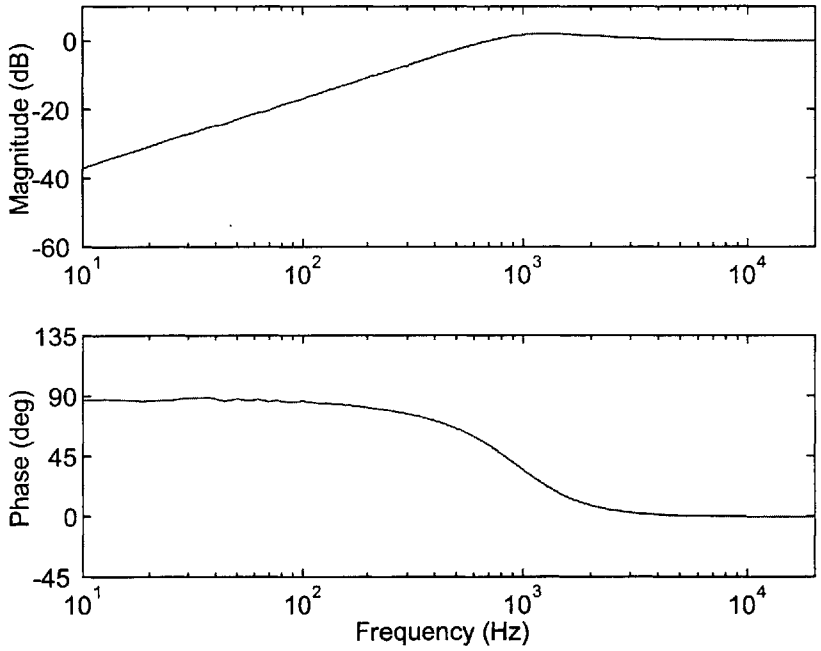

Figure 6-35: Frequency response of the complementary high-pass filter.

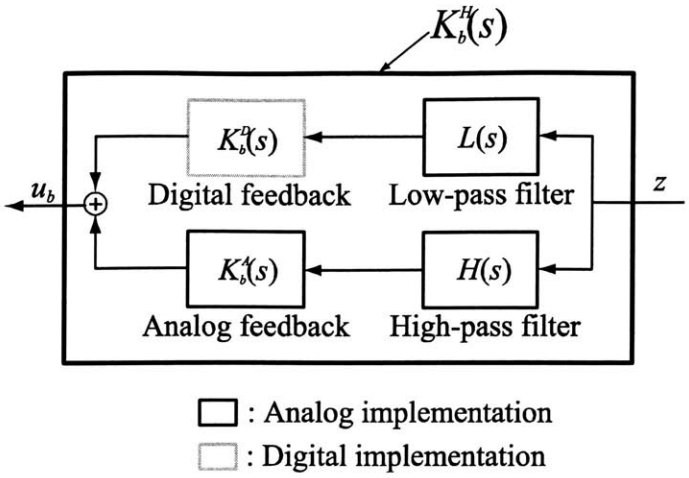

Figure 6-36: Block diagram of the hybrid feedback controller without the low-frequency feedthrough compensator.

given by

$$K_b^H(s) = K_b^D(s)\,L(s) + K_b^A(s)\,H(s)\,. \tag{6.31}$$

Figure 6-37 compares the hybrid feedback controller $K_b^H(s)$ with its counterpart analog feedback controller $K_b(s)$. The digital controller $K_b^D(s)$ is implemented with a sampling frequency of 40 kHz. They are very similar, although a small discrepancy is observed around 1 kHz, where the complementary filters act. The effect of the time delay in the digital component on the controller transfer function is negligible, especially at high frequency, due to the complementary low-pass filter.

After designing $K_b^H(s)$ and $K_f(s)$ based on the plant transfer function that has been modified by adding $C(s)$ (the same feedforward controller $K_f(s)$ is used as the one in Section 6.3), the feedback and feedforward controller that incorporate $C(s)$ can be obtained using the block diagram in Figure 6-38. The relation between u, y_t, and y_b can be written using the first block diagram (a) in Figure 6-38 as

$$u = K_f(s)y_b + \left[K_b^D(s)\,L(s) + K_b^A(s)\,H(s)\right]\left[y_t + C(s)u\right]\,. \tag{6.32}$$

Therefore, u can be written in terms of y_t and y_b as

$$\begin{aligned} u = {} & \frac{K_f(s)}{1 - C(s)\left[K_b^D(s)\,L(s) + K_b^A(s)\,H(s)\right]}y_b \\ & + \frac{K_b^D(s)\,L(s) + K_b^A(s)\,H(s)}{1 - C(s)\left[K_b^D(s)\,L(s) + K_b^A(s)\,H(s)\right]}y_t\,. \end{aligned} \tag{6.33}$$

Since $u = K_f'(s)\,y_b + \left[K_b'^D(s)\,L(s) + K_b'^A(s)\,H(s)\right]y_t$ from the second block diagram (b) in

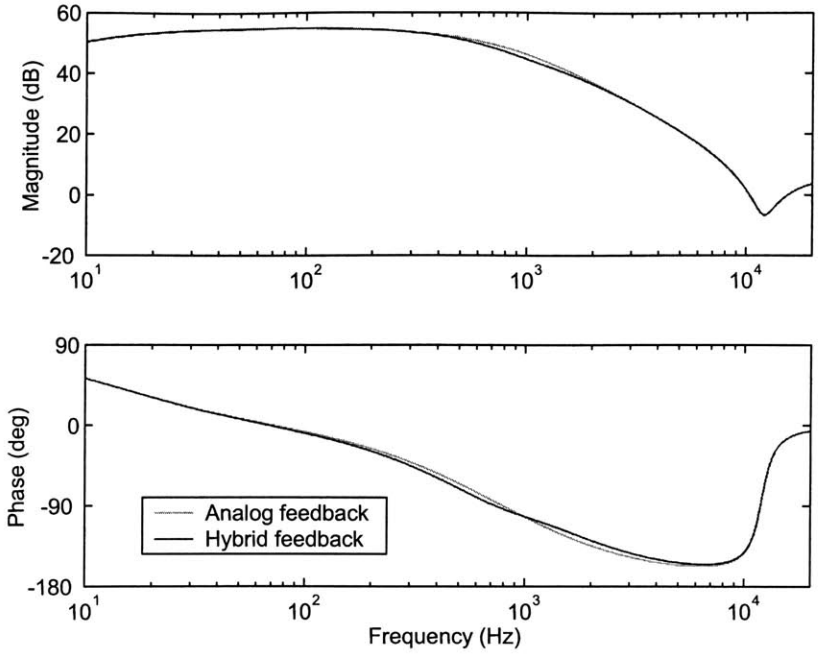

Figure 6-37: Frequency response of the analog feedback controller $K_b(s)$ and the hybrid feedback controller $K_b^H(s)$.

Figure 6-38, the controllers incorporating $C(s)$ can be written as

$$\begin{aligned} K_f'(s) &= \frac{K_f(s)}{1 - C(s)\left[K_b^D(s)\,L(s) + K_b^A(s)\,H(s)\right]}, \\ K_b'^D(s) &= \frac{K_b^D(s)}{1 - C(s)\left[K_b^D(s)\,L(s) + K_b^A(s)\,H(s)\right]}, \\ K_b'^A(s) &= \frac{K_b^A(s)}{1 - C(s)\left[K_b^D(s)\,L(s) + K_b^A(s)\,H(s)\right]}. \end{aligned} \tag{6.34}$$

However, using the fact that $K_b^A(s) \approx \left[K_b^D(s)\,L(s) + K_b^A(s)\,H(s)\right]$, $C(s)$ is important only at low frequency, $K_b^A(s)\,H(s)$ is negligible at low frequency, and $L(s)$ is unity at low frequency, the controllers in Equation 6.34 can be simplified further as

$$\begin{aligned} K_f'(s) &= \frac{K_f(s)}{1 - C(s)K_b^D(s)}, \\ K_b'^D(s) &= \frac{K_b^D(s)}{1 - C(s)K_b^D(s)}, \\ K_b'^A(s) &= \frac{K_b^A(s)}{1 - C(s)K_b^A(s)}. \end{aligned} \tag{6.35}$$

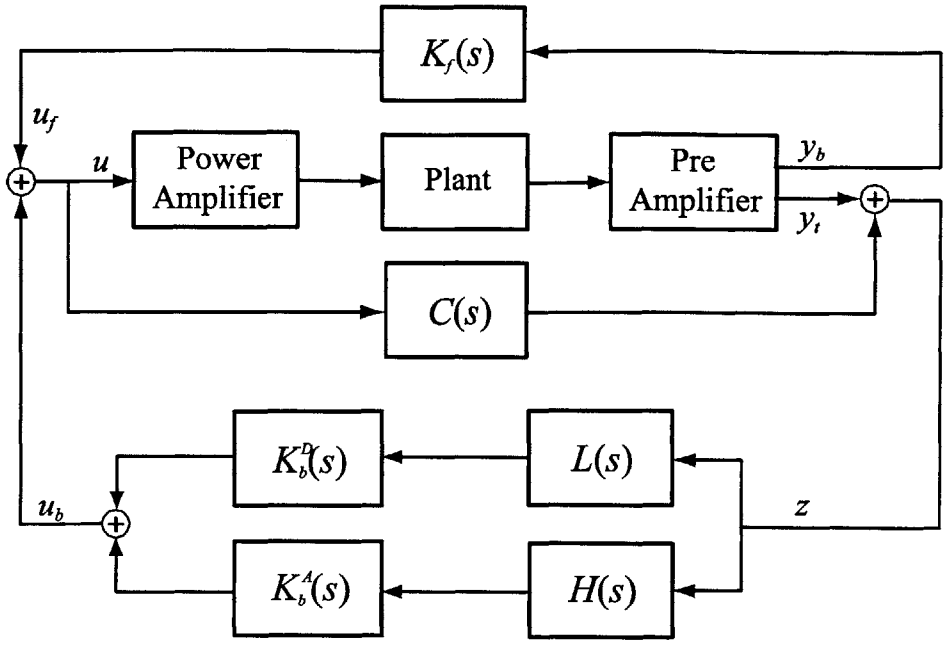

(a)

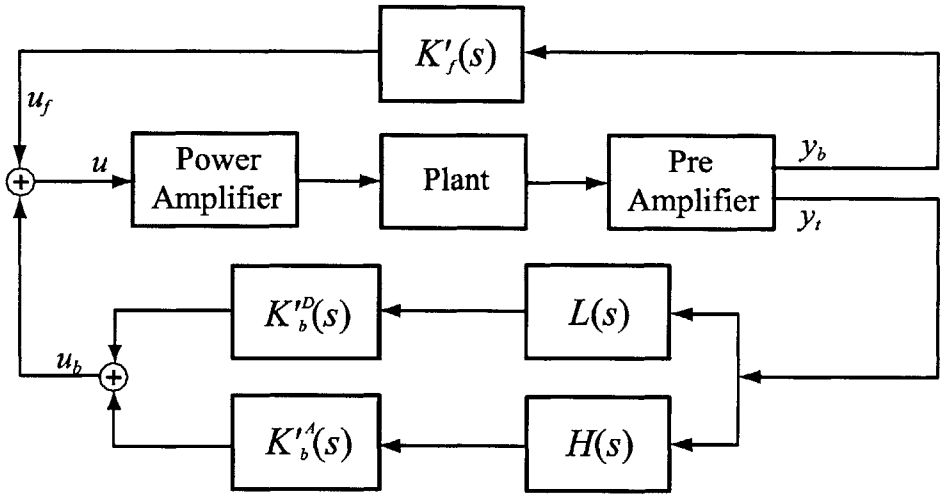

(b)

Figure 6-38: Equivalent block diagram of the closed-loop system using the hybrid feedback and analog feedforward controller. (a) $C(s)$ is considered as a part of the plant. (b) $C(s)$ is incorporated into the controllers.

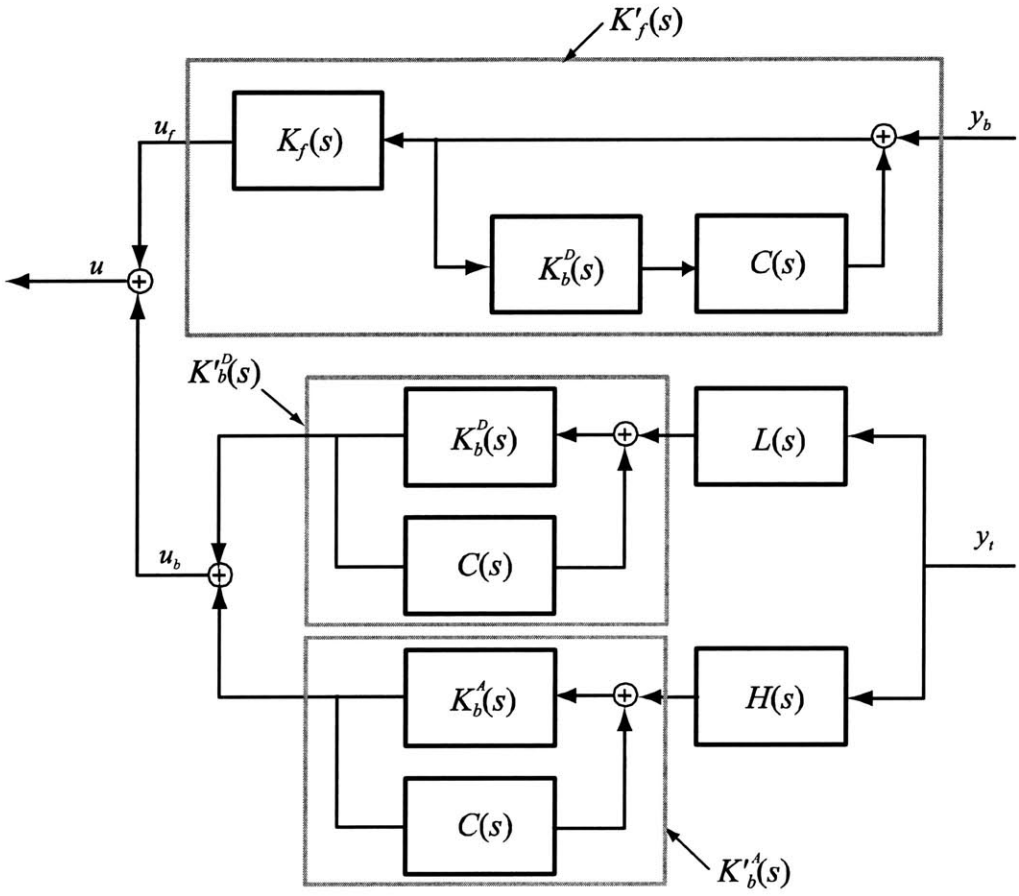

Figure 6-39: Block diagram of the hybrid feedback and analog feedforward controller.

The resulting controller configuration is shown in Figure 6-39. This approximation significantly reduces the analog components and the size of the digital computation. The closed-loop performance using this controller is shown in Figure 6-40, with and without the feedforward control. The disturbance spectrum is broadband up to 5 kHz. The digital feedback controller is implemented in a dSpace digital controller with a sampling frequency of 40 kHz. It was necessary to reduce the feedback control gain slightly (by 1.4 dB), in order to maintain a stable feedback loop. The result is very similar to that obtained using the analog controller. The performance is slightly worse, reflecting the slightly lower feedback gain, as well as a slightly lower signal-to-noise ratio, due to digital quantization. In any event, we are still achieving better than 10 dB of attenuation over the band 200–2000 Hz.

The circuits for analog components used in this controller configuration are shown in Appendix E.

6.6 Hybrid Analog/Digital Feedback and Digital Notch Filter

In this section, the concept of the hybrid analog/digital feedback control and the digital notch filter approach are combined. Figure 6-41 shows the block diagram of this controller configuration. As in the hybrid feedback and analog feedforward control approach in Section 6.5, the complementary filters are used to control the bands in which the analog and digital control laws act. The new feature of this configuration is that the analog feedback controller is decomposed again as the analog and digital component, so that the frequency to be notched out can be adjusted in software, as in Section 6.4. The design processes of the digital feedback control law and the digital notch filter are the same as in Section 6.5, and 6.4, respectively. The resulting controller configuration is shown in Figure 6-42. The same $L(s)$, $H(s)$, $K_b^D(s)$, $K_1(s)$, $\widehat{K}_2(s)$, $K_b'^D(s)$, and $K_b'^A(s)$ are implemented as in Section 6.5, and 6.4. The closed-loop performance using this controller is shown in Figure 6-43. The disturbance spectrum is broadband up to 5 kHz. The digital feedback controller and the digital notch filter are implemented in a dSpace digital controller with a sampling frequency of 33 kHz. It was necessary to reduce the sampling frequency due to the increased amount of calculation in the DSP system. Using the feedback controller, we achieve 10 dB of attenuation below 1 kHz, and 5 dB of attenuation up to 3 kHz in this configuration.

6.7 Hybrid Analog/Digital Feedback and Digital Feedforward Controller

A hybrid analog/digital feedback and digital feedforward controller is implemented in this section. The hybrid feedback controller implemented here is the same as the one shown in Section 6.5. In this configuration, the feedforward controller is implemented digitally. Figure 6-44 shows the block diagram of the hybrid analog/digital feedback and digital feedforward controller. The new feature of this configuration is that the feedforward controller, which has been implemented in analog until now, is decomposed into analog and digital parts in series.

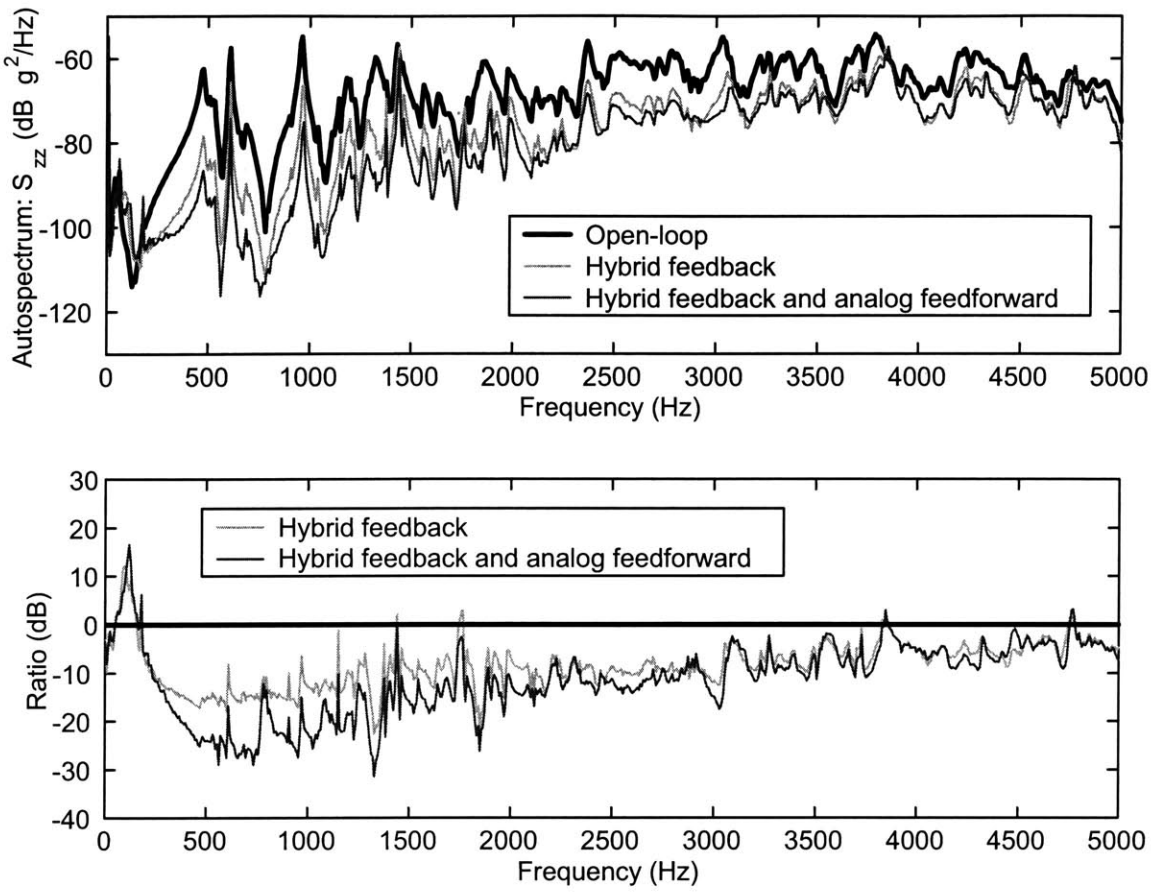

Figure 6-40: Closed-loop performance obtained with the hybrid feedback and analog feedforward controller. "Ratio" represents the ratio of the open-loop response to the closed-loop response. Negative ratios indicate attenuation; positive ratios indicate amplification.

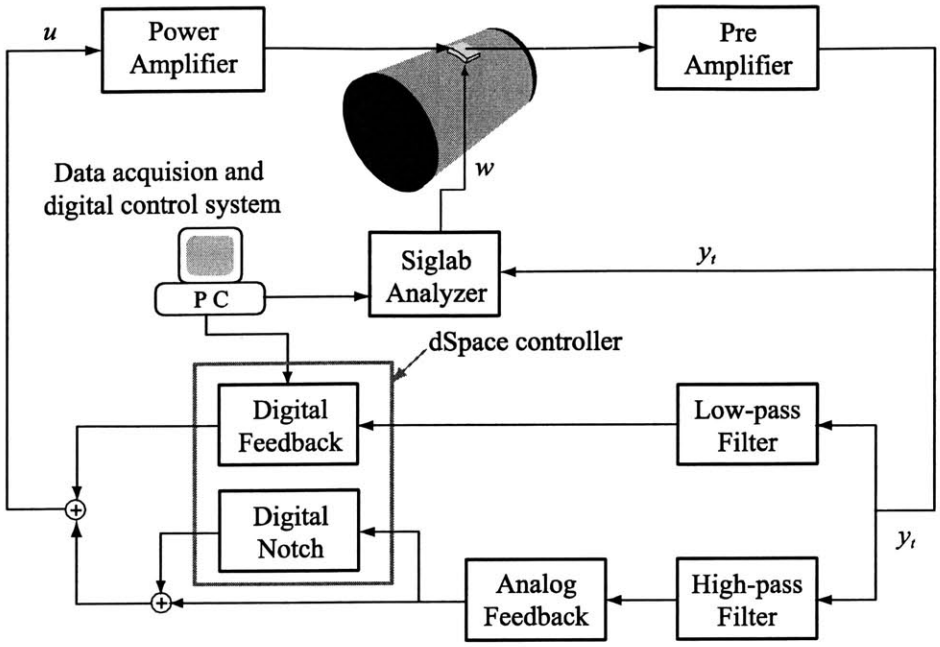

Figure 6-41: Block diagram of the hybrid feedback control and digital notch filter approach.

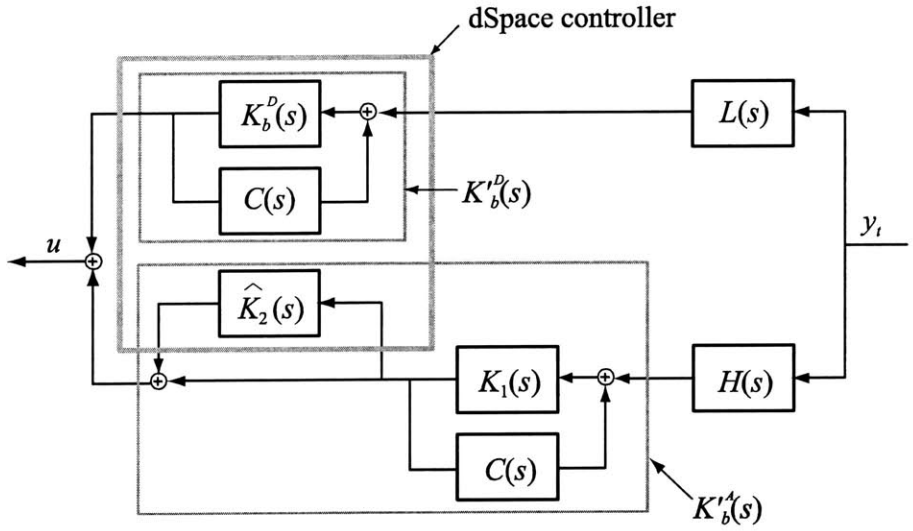

Figure 6-42: Block diagram of the hybrid feedback controller and the digital notch filter.

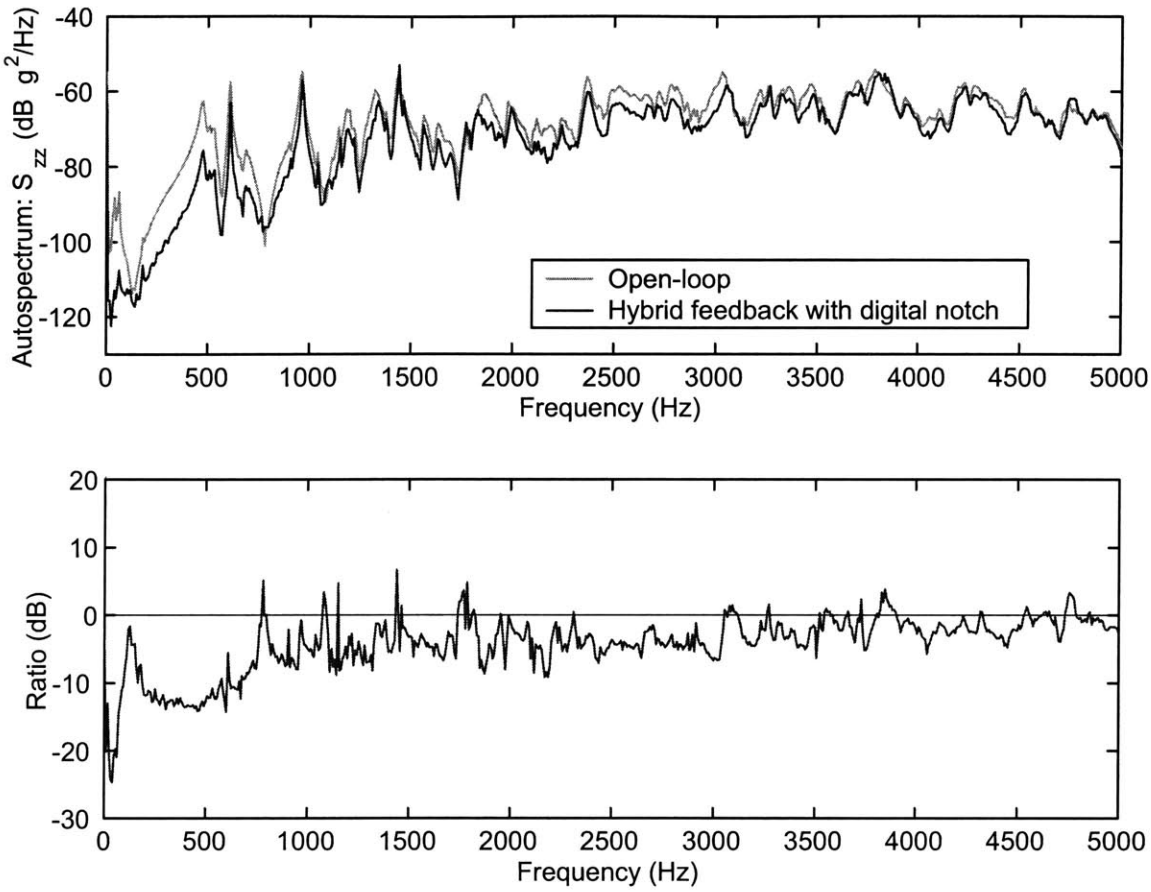

Figure 6-43: Closed-loop performance obtained with the hybrid feedback and digital notch filter approach. "Ratio" represents the ratio of the open-loop response to the closed-loop response. Negative ratios indicate attenuation; positive ratios indicate amplification.

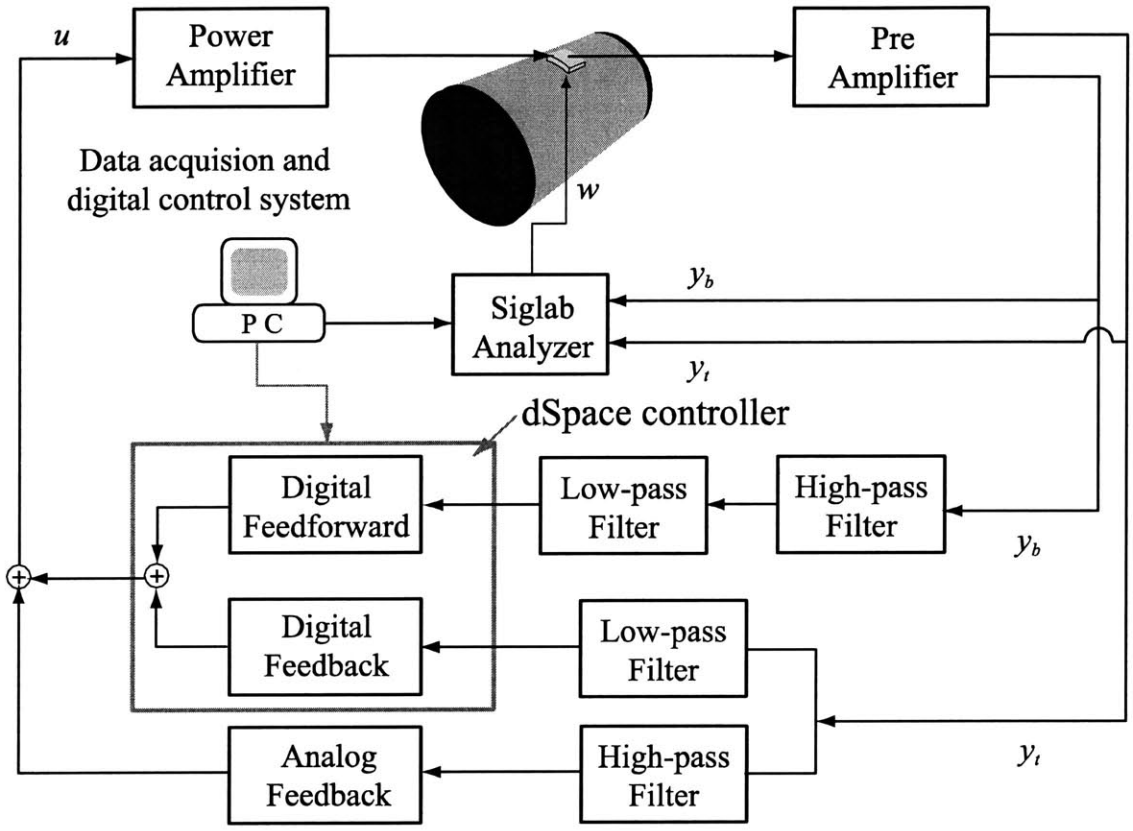

Figure 6-44: Block diagram of the hybrid feedback and digital feedforward control approach.

The analog feedforward controller $K_f(s)$ implemented in Section 6.3 is given by

$$\begin{aligned} K_f(s) &= g_f \frac{s}{s + 2\pi \times 11} \cdot \frac{1}{(s + 2\pi \times 150)} \cdot \frac{1}{(s + 2\pi \times 4000)} \\ &= K_{f,1}(s)\, K_{f,2}(s) \ , \end{aligned} \tag{6.36}$$

where

$$\begin{aligned} K_{f,1}(s) &= g_{f,1} \frac{s}{s + 2\pi \times 11} \cdot \frac{1}{(s + 2\pi \times 150)} \\ K_{f,2}(s) &= g_{f,2} \frac{1}{(s + 2\pi \times 4000)} \ . \end{aligned} \tag{6.37}$$

Here, the feedforward gain g_f is decomposed into $g_{f,1}$ and $g_{f,2}$, which are the constant gains of $K_{f,1}(s)$, and $K_{f,2}(s)$ ($g_{f,1}g_{f,2} = g_f$). $g_{f,1}$ and $g_{f,2}$ are chosen such that the quantization effect is minimized, and the signal is not saturated at each block. The resulting equivalent analog feedforward controller $K_f'(s)$, which combines the low-frequency feedthrough compensator $C(s)$, is given by

$$K_f'(s) = \frac{K_f(s)}{1 - C(s)K_b^D(s)} \ . \tag{6.38}$$

The block diagram of the analog feedforward controller configuration is shown in Figure 6-45. Now, the feedforward controller $K_f'(s)$ is decomposed as

$$\begin{aligned} K_f'(s) &= \frac{K_{f,1}(s)\, K_{f,2}(s)}{1 - C(s)K_b^D(s)} \\ &= \frac{K_{f,2}(s)}{1 - C(s)K_b^D(s)} K_{f,1}(s) \\ &= K_f'^D(s)\, K_{f,1}(s) \ , \end{aligned} \tag{6.39}$$

where

$$K_f'^D(s) = \frac{K_{f,2}(s)}{1 - C(s)K_b^D(s)} \ . \tag{6.40}$$

The idea of digital feedforward approach is that $K_f'^D(s)$ is implemented digitally, while $K_{f,1}(s)$ is implemented in analog (Figure 6-46). By doing so, the analog component $K_{f,1}(s)$, which has a high-pass filter at 11 Hz and a low-pass filter at 150 Hz, can be combined within the pre-amplifier, and the design variable for the feedforward controller, such as a corner frequency in $K_{f,2}(s)$, can be adjusted in software. Furthermore, $C(s)$ and $K_b^D(s)$, which should be implemented in analog for analog feedforward control approach, can be implemented digitally. This reduces considerably the amount of work needed to implement the feedforward controller. The configuration for the hybrid feedback control and digital feedforward control approach is shown in Figure 6-47. In order to implement this controller, we need two input channels and one output channel of the DSP board for each panel. The resulting closed-loop performance using this controller configuration is shown in Figure 6-48. The disturbance spectrum is broadband up to 5 kHz. The digital feedback and feedforward controller are implemented in a dSpace digital controller with a sampling frequency of 30 kHz. The sampling frequency is reduced,

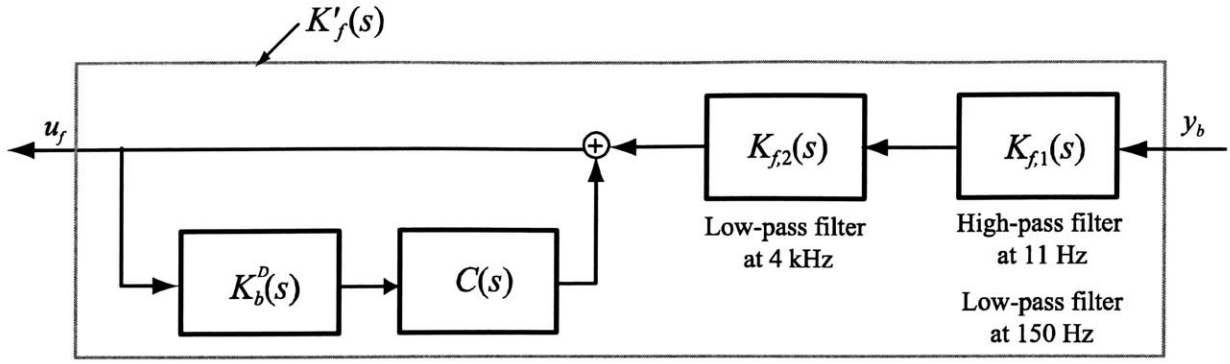

Figure 6-45: Block diagram of the analog feedforward controller.

compared with the case of hybrid feedback and analog feedforward control (40 kHz), due to the increased amount of calculation in the DSP system. The closed-loop performance obtained using this controller is very similar to that obtained using the analog feedback/feedforward controller. The performance is slightly worse, however, likely due to slightly lower signal-to-noise ratio caused by quantization. Nevertheless, we are still achieving better than 10 dB of attenuation over the band 200–2000 Hz.

6.8 Digital Feedback and Digital Feedforward Controller

In this section, the feedback controller is also implemented digitally. Figure 6-49 shows the block diagram of digital feedback and digital feedforward controller. For the feedforward controller, the same analog electronics (a high-pass filter at 11 Hz and a low-pass filter at 150 Hz) are used as the ones shown in Section 6.7. For the feedback control, however, the complementary filters implemented in Section 6.7 are not needed in this configuration, because the analog feedback control is not used. A low-pass filter for the digital feedback controller is a second-order Butterworth low-pass filter with corner frequency at 2 kHz, instead of 1 kHz used for the hybrid feedback configuration. The block diagram of the digital feedback controller without the low-frequency feedthrough compensator $C(s)$ is shown in Figure 6-50. The digital control law $K_b^D(s)$ implements the low-pass filter at 500 Hz, and the high-pass filter at 20 Hz, given as

$$K_b^D(s) = g_b \cdot \frac{s}{s + 2\pi \times 20} \cdot \frac{1}{s + 2\pi \times 500} \,. \tag{6.41}$$

It is different from the digital feedback controller implemented in Section 6.7, which has the low-pass filters at 600 Hz and 1000 Hz, and the high-pass filter at 14 Hz. Also, a notch filter to cancel the undesirable dynamics of the panel around 12 kHz is not needed in this configuration, because the second-order Butterworth low-pass filter at 2 kHz, which is denoted as $L(s)$ in Figure 6-50, given as

$$L(s) = \frac{\omega_l^2}{s^2 + 2\zeta_l\omega_l s + \omega_l^2} \,, \tag{6.42}$$

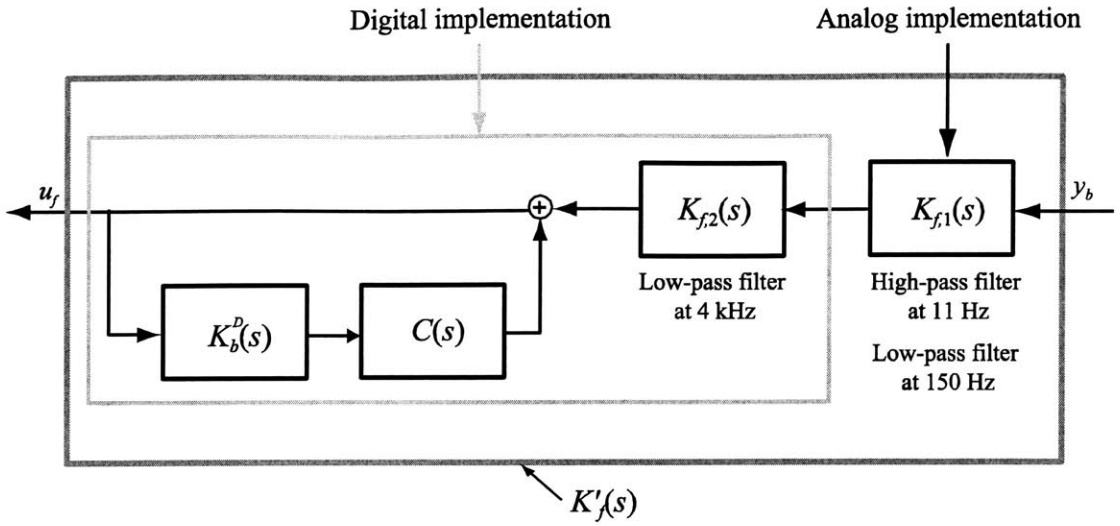

Figure 6-46: Block diagram of the digital feedforward controller.

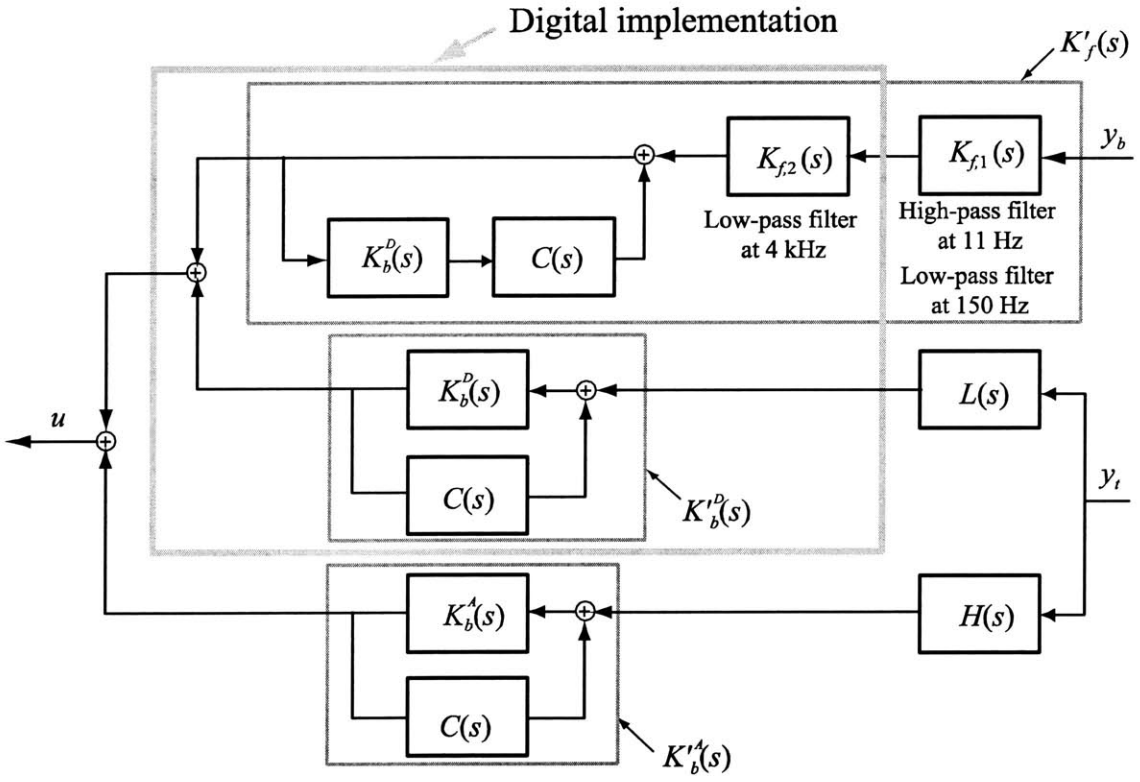

Figure 6-47: Block diagram of the hybrid feedback and digital feedforward control approach.

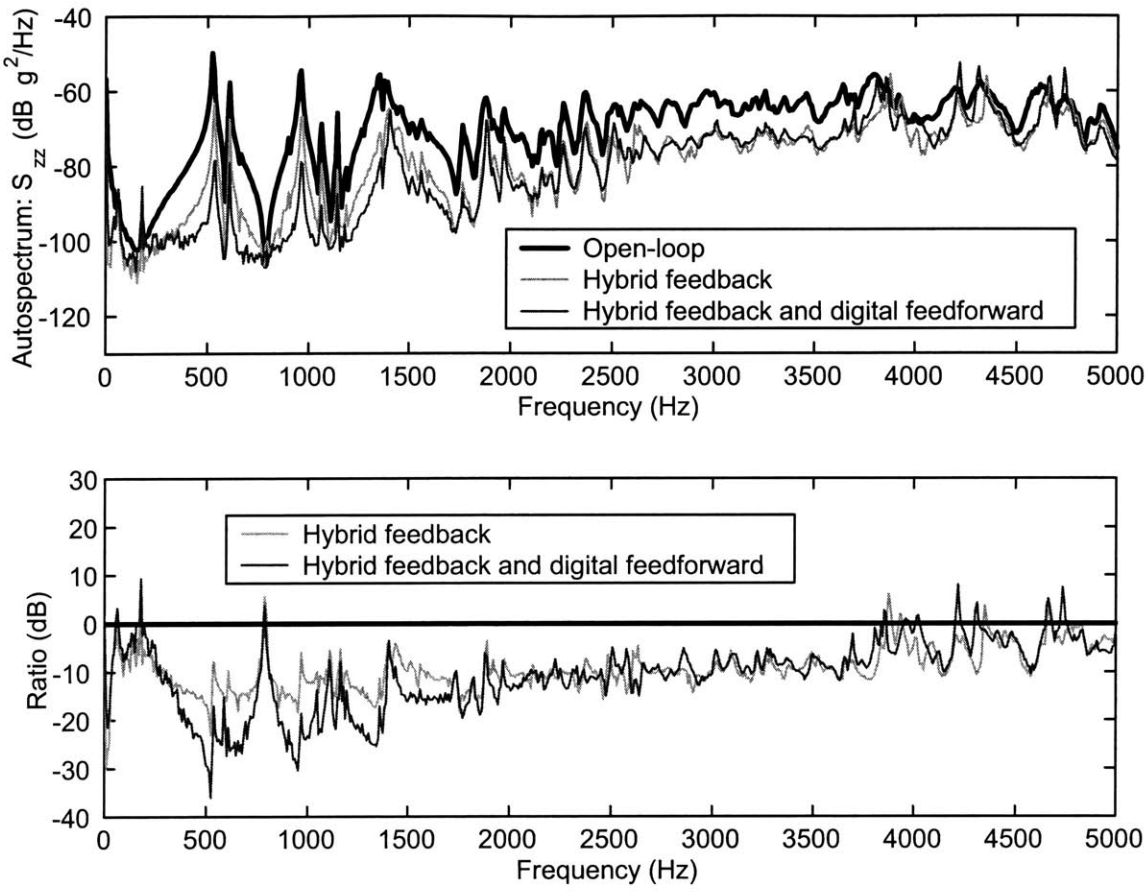

Figure 6-48: Closed-loop performance obtained with the hybrid feedback and digital feedforward controller. "Ratio" represents the ratio of the open-loop response to the closed-loop response. Negative ratios indicate attenuation; positive ratios indicate amplification.

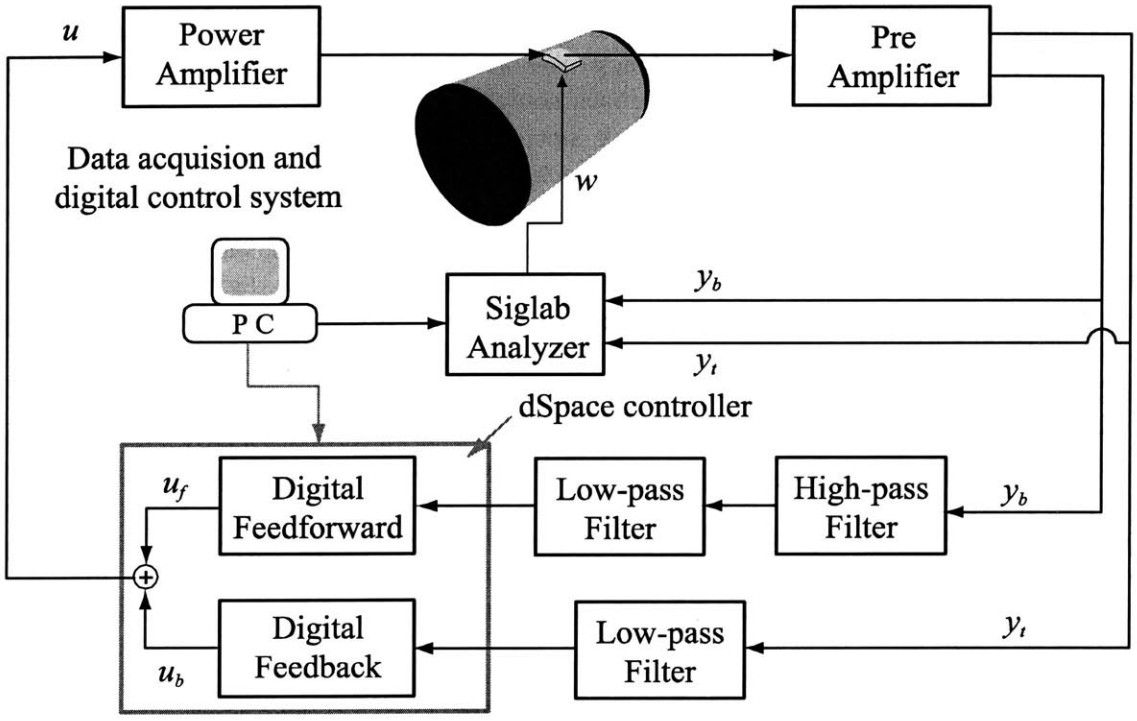

Figure 6-49: Block diagram of the digital feedback and feedforward control approach.

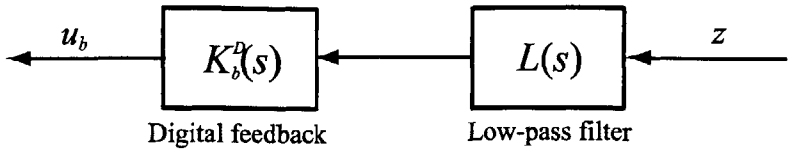

Figure 6-50: Block diagram of the digital feedback controller without the low-frequency feedthrough compensator..

gives enough roll-off at high frequency. However, since the complementary analog feedback controller is not used simultaneously, the phase delay caused by digital component is not recovered in this configuration. Therefore, the feedback controller gain had to be reduced by 50% to avoid instability, compared with the hybrid feedback controller gain.

Figure 6-51 compares the digital feedback controller $K_b^D(s)\,L(s)$ with its counterpart analog feedback controller $K_b(s)$. The digital feedback controller is implemented with a sampling frequency of 33 kHz. It has a similar shape to the analog feedback up to 1 kHz; they have almost the same phase, with different gains due to the reduced gain in the digital feedback control, in this frequency range. However, above 1 kHz, the phase delay in the digital feedback control is significant, compared with the analog feedback control, because the complementary analog feedback controller is not used simultaneously. The phase delay caused by digital component is not recovered in this configuration. The time delay in the digital component critically limits the achievable closed-loop performance using the digital feedback control. The resulting loop transfer function is shown in Figure 6-52 (frequency response), and 6-53 (Nyquist plot).

After designing $K_b^D(s)$ and $K_f(s)$ based on the plant transfer function modified by adding $C(s)$ (the same feedforward controller $K_f(s)$ is used as the one in Section 6.3), the feedback and feedforward controller that incorporate $C(s)$, which are denoted as $K_b^{\prime D}(s)$ and $K_f^{'}(s)$, respectively, can be obtained using the same way in Section 6.5 from the block diagram in Figure 6-54, given as

$$\begin{aligned} K_f^{'}(s) &= \frac{K_f(s)}{1 - C(s)K_b^D(s)\,L(s)}, \\ K_b^{\prime D}(s) &= \frac{K_b^D(s)}{1 - C(s)K_b^D(s)\,L(s)}. \end{aligned} \tag{6.43}$$

Since $C(s)$ is important only at low frequency, and $L(s)$ is unity at low frequency, the controllers in Equation 6.43 can be simplified further as

$$\begin{aligned} K_f^{'}(s) &= \frac{K_f(s)}{1 - C(s)K_b^D(s)}, \\ K_b^{\prime D}(s) &= \frac{K_b^D(s)}{1 - C(s)K_b^D(s)}. \end{aligned} \tag{6.44}$$

Now, using the same approach as in Section 6.7, the feedforward controller $K_f^{'}(s)$ can be

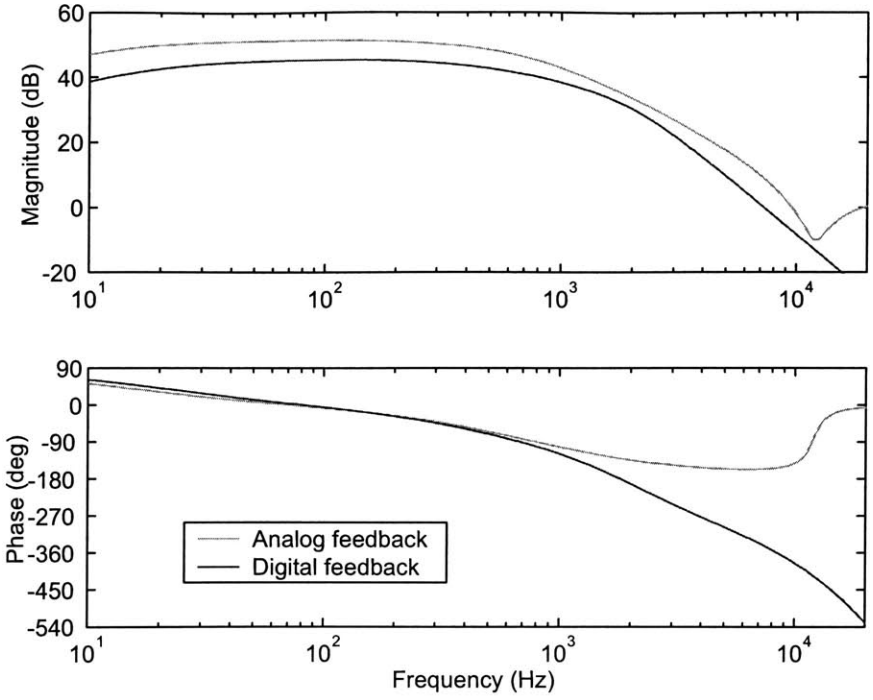

Figure 6-51: Frequency response of the analog feedback and digital feedback controller.

decomposed as

$$\begin{aligned} K_f^{'}(s) &= \frac{K_{f,1}(s)\,K_{f,2}(s)}{1 - C(s)K_b^D(s)} \\ &= \frac{K_{f,2}(s)}{1 - C(s)K_b^D(s)} K_{f,1}(s) \\ &= K_f^{\prime D}(s)\,K_{f,1}(s)\ , \end{aligned} \tag{6.45}$$

where

$$K_f^{\prime D}(s) = \frac{K_{f,2}(s)}{1 - C(s)K_b^D(s)}\ . \tag{6.46}$$

As in Section 6.7, $K_f^{\prime D}(s)$ is implemented digitally, while $K_{f,1}(s)$ is implemented in analog. Figure 6-55 shows the resulting block diagram of the digital feedback and digital feedforward control approach. The closed-loop performance obtained with this controller is shown in Figure 6-56, with and without the feedforward control. The disturbance spectrum is broadband up to 5 kHz. The digital feedback and feedforward controller are implemented in a dSpace digital controller with a sampling frequency of 33 kHz. As expected, the performance is much worse than that obtained using the analog feedback or the hybrid feedback controller, reflecting the much lower feedback gain. Furthermore, the effect of disturbance is amplified above 2 kHz, likely due to unrecoverable phase delay caused by the sampling effect. It is found that if we

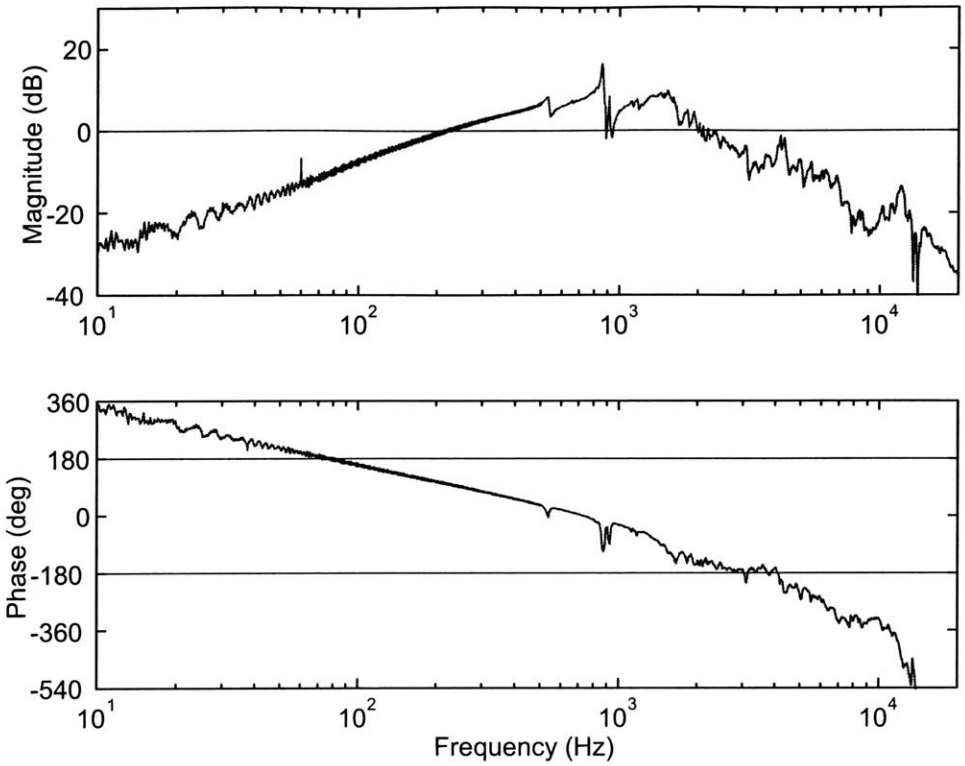

Figure 6-52: Frequency response of loop transfer function for the digital feedback control.

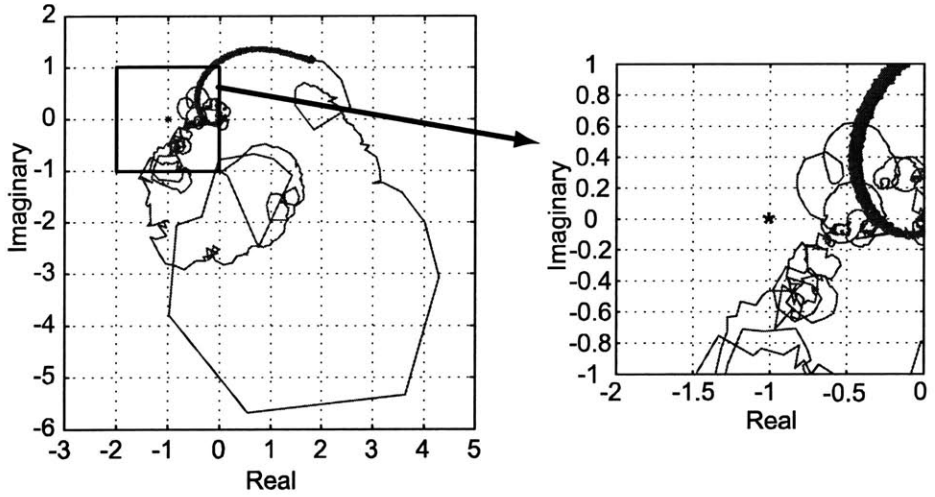

Figure 6-53: Nyquist plot of loop transfer function for the digital feedback control.

want better performance (attenuation) below 2 kHz, we have to accept worse performance (amplification) above 2 kHz. The digital feedforward controller provided additional improvement of performance, especially between 500 and 1300 Hz. However, the effect of disturbance is still amplified above 2 kHz.

As mentioned above, it is true that the performance of digital feedback and digital feedforward controller is much worse than other configurations given in the previous sections. However, if the disturbance doesn't have much energy above 2 kHz, this configuration may be a good solution, since controller variables can be adjusted in software, and more than 10 dB of attenuation is achieved between 200 and 2000 Hz anyway.

6.9 Digital Tonal Feedback Controller

6.9.1 The Concept of Tonal Feedback Controller

The digital tonal feedback control approach is introduced in this section. It can be very efficiently used to reduce several discrete harmonics in the disturbance spectrum. The important advantage of this approach is that it can be used for the reduction of harmonics at high frequencies, provided that the width of the frequency range to be controlled is small enough. It is the width of the frequency range, not the frequency itself, that limits the achievable closed-loop performance using this control approach. Therefore, the tonal feedback controller can be easily implemented digitally, no matter how high the target frequency may be, if the width of the frequency range to be reduced is relatively small compared to the sampling frequency.

Figure 6-57 shows the disturbance spectrum used in this section. Most of the disturbance energy is concentrated below 1 kHz. It also has three discrete harmonics at 300, 600, and 900 Hz. The objective of the digital tonal feedback control implemented in this section is to reduce these three harmonics.

Figure 6-58 shows a block diagram for the tonal feedback controller. Assuming we can measure the performance variable to be reduced directly, the loop transfer function using the feedback controller $K_T(s)$, which is given by $G_{yu}(s)K_T(s)$, gives information about the achievable closed-loop performance. Define the tonal feedback controller $K_T(s)$ as

$$K_T(s) = \frac{2}{T_b} \cdot \frac{as + b\omega_T}{s^2 + \omega_T^2}, \tag{6.47}$$

where ω_T is the target frequency, *i.e.*, the frequency of discrete harmonics in the disturbance to be reduced. The parameters in the controller are determined such that the control system has enough stability margins and controller bandwidth of ω_b at the target frequency $s = j\omega_T$. The controller parameters are given as [Hall, 1989]

$$\begin{aligned} a &= \mathrm{Re}\left\{\frac{1}{G_{yu}(j\omega_T)}\right\} \\ b &= -\mathrm{Im}\left\{\frac{1}{G_{yu}(j\omega_T)}\right\} \\ T_b &\approx \frac{1}{\omega_b}. \end{aligned} \tag{6.48}$$

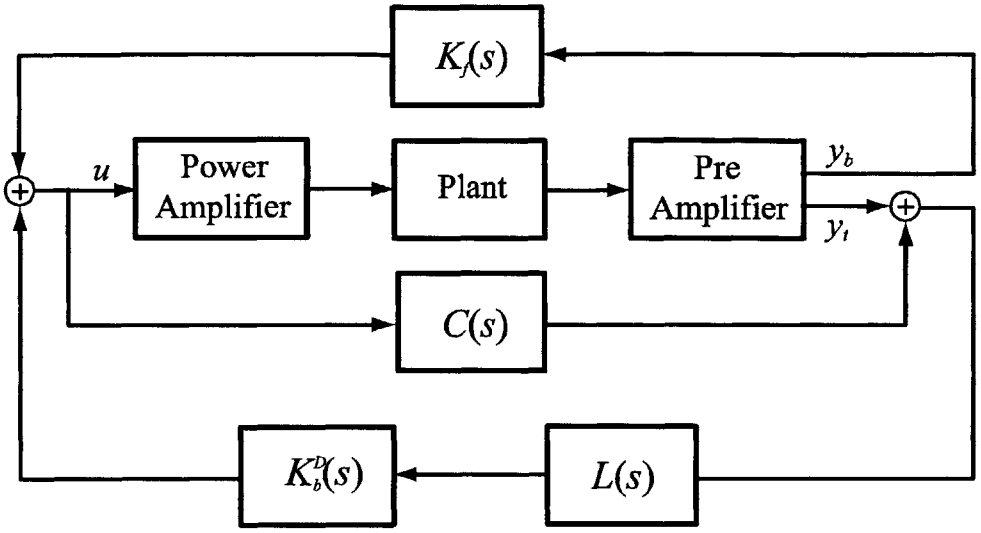

(a)

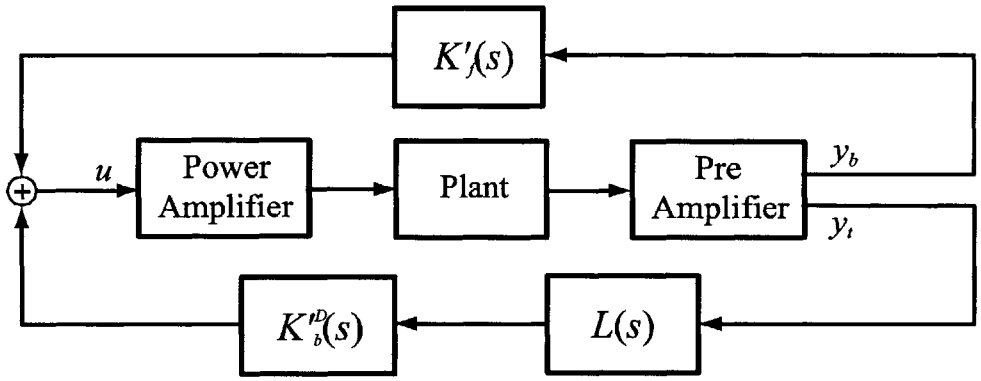

(b)

Figure 6-54: Equivalent block diagram of the closed-loop system using the digital feedback and digital feedforward controller. (a) $C(s)$ is considered as a part of the plant. (b) $C(s)$ is incorporated into the controllers.

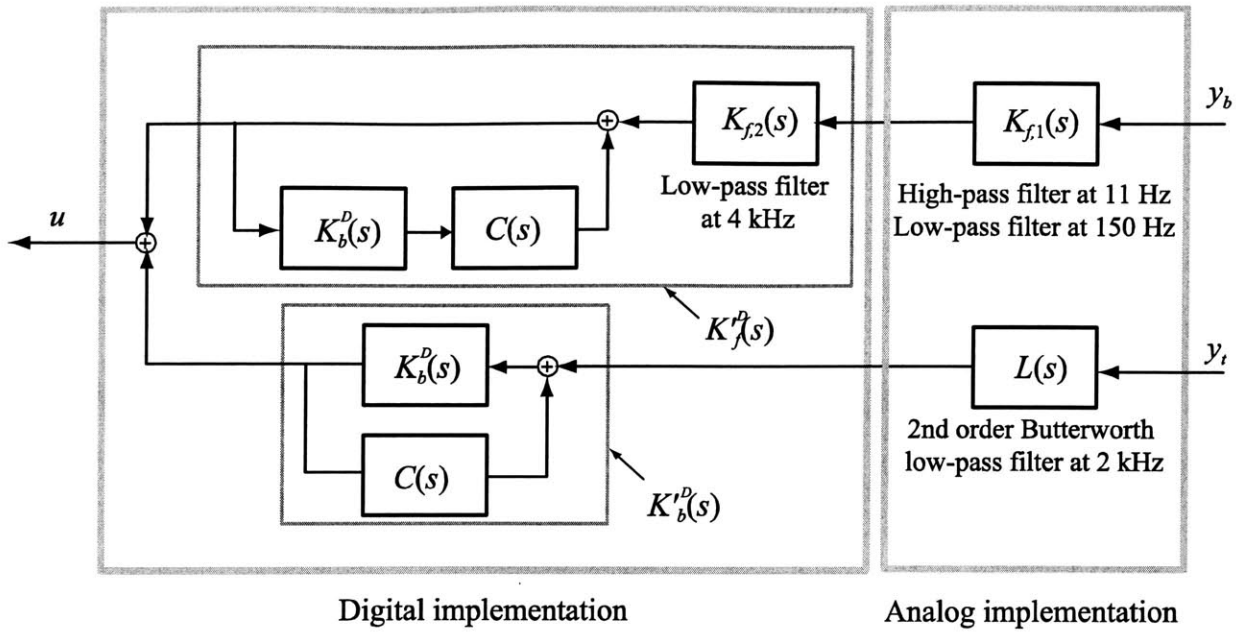

Figure 6-55: Block diagram of the digital feedback and digital feedforward control approach.

The amplification or attenuation of the disturbance by the closed-loop system is determined by the sensitivity transfer function $S(s)$, given as

$$S(s) = \frac{z}{d} = \frac{1}{1 + G_{yu}(s)K_T(s)} . \tag{6.49}$$

If the tonal feedback controller $K_T(s)$ in Equation 6.48 is used, $S(s)$ has a zero magnitude at the frequency $s = j\omega_T$, and therefore the controller should completely eliminate vibration at that frequency. Figure 6-59 shows one example of the typical loop transfer function obtained with the tonal feedback controller. It can be seen that the loop transfer function has a high gain at the target frequency of 300 Hz, and enough phase margins ($\sim 90°$).

If the tonal feedback controller is implemented digitally, the effect of time delay in the digital control systems should be considered when determining a and b. This can be done by including the time delay e^{-sT_d}, where T_d is the time delay in the digital control systems, in the plant and computing a and b by replacing $G_{yu}(s)$ with $G_{yu}(s)e^{-sT_d}$ in Equation 6.48.

We can also implement several tonal feedback controllers simultaneously, given as

$$K_T(s) = \sum_{n=1}^{N_T} \frac{2}{T_{b,n}} \frac{a_n s + b_n \omega_{T,n}}{s^2 + \omega_{T,n}^2} , \tag{6.50}$$

where $\omega_{T,n}$ is the nth target frequency, N_T is the number of controllers to be designed, and a_n, b_n and $T_{b,n}$ are design variables for nth tonal feedback controller. Theoretically, controllers should be designed by closing the loop sequentially to ensure that each control loop satisfies the

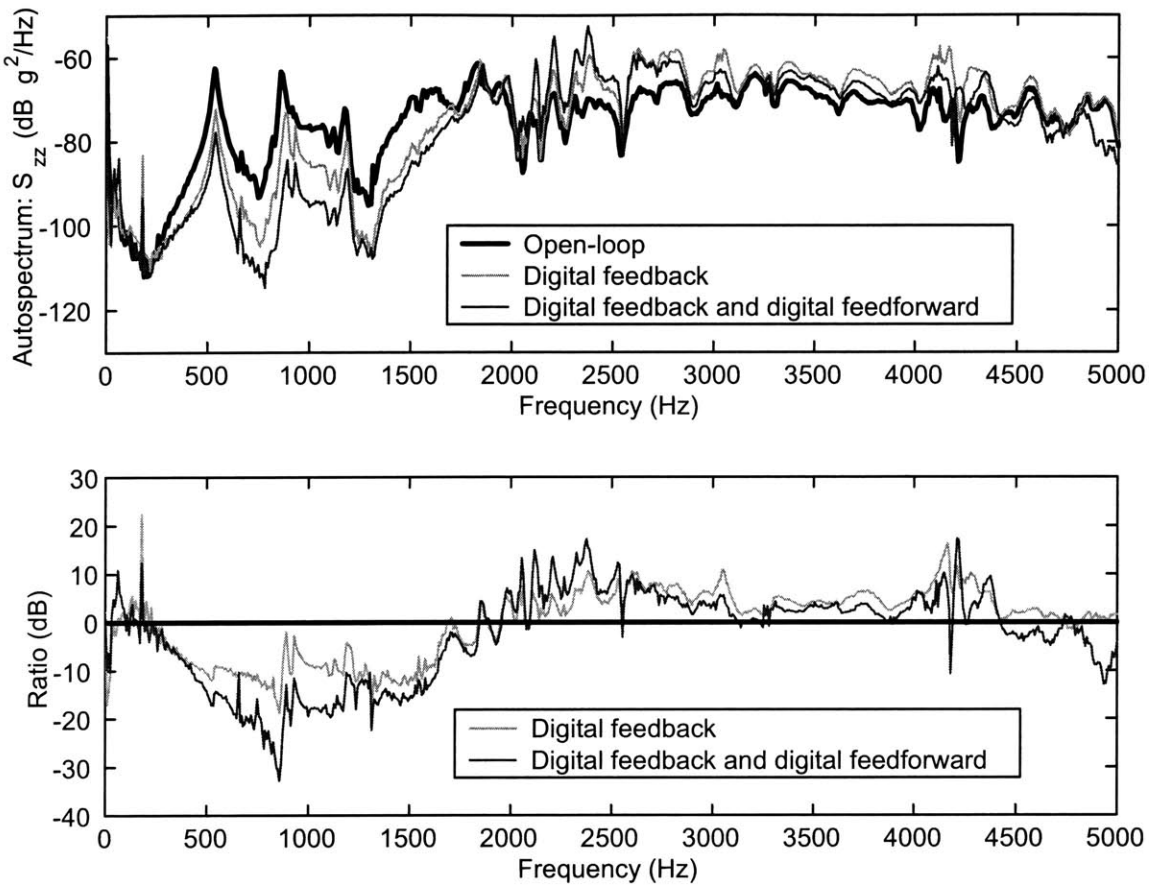

Figure 6-56: Closed-loop performance obtained with the digital feedback and feedforward controller. "Ratio" represents the ratio of the open-loop response to the closed-loop response. Negative ratios indicate attenuation; positive ratios indicate amplification.

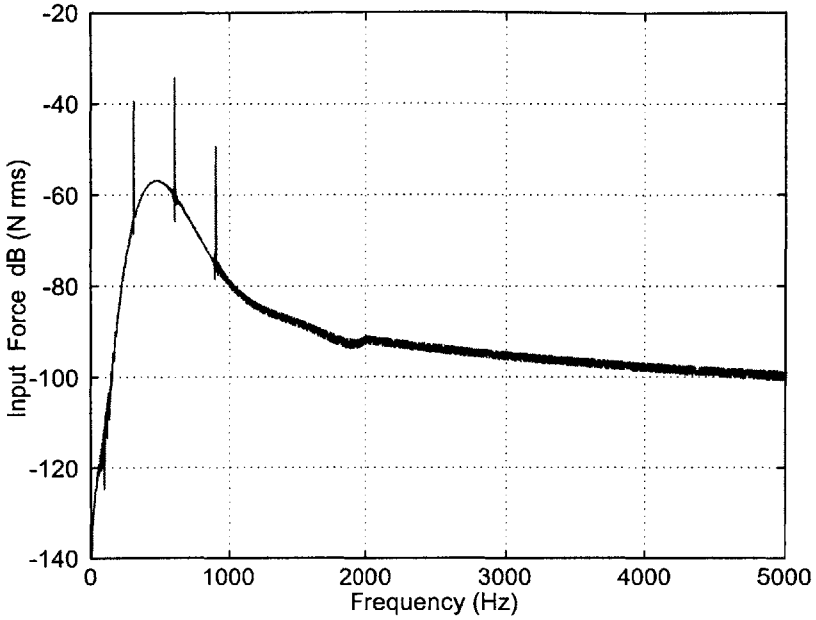

Figure 6-57: Disturbance spectrum.

design requirements. However, we may design each controller independently and close all the loops simultaneously, if the difference between the adjacent target frequencies $|\omega_{T,n+1} - \omega_{T,n}|$ is large, compared to the bandwidth of the nth tonal feedback controller. The rationale is that the nth tonal feedback controller, $\frac{2}{T_{b,n}} \frac{a_n s + b_n \omega_{T,n}}{s^2 + \omega_{T,n}^2}$, is dominant only around $\omega = \omega_{T,n}$, and is negligible elsewhere in that case.

6.9.2 Implementation of the Digital Tonal Feedback Controller

In this section, three digital tonal feedback controllers are designed and implemented on the cylindrical shell with one active composite panel mounted, to reduce the three discrete harmonics in the disturbance spectrum (Figure 6-57). The block diagram of this approach is shown in Figure 6-60. It can be seen that no analog electronics is used, except the pre-amplifier and power amplifier. The output from the accelerometer mounted on the top surface of the panel, which is denoted as y in the figure, is processed first by $T(s)$. It modifies the plant transfer function $G_{yu}(s)$, so that it becomes easier to design the tonal feedback controller by yielding a good loop shape. Figure 6-61 shows the frequency response of $G_{yu}(s)$ in (a), and $G_{yu}(s)T(s)$ in (b). Here, $T(s)$ has a high-pass filter at 100 Hz, and low-pass filters at 100 Hz, 3 kHz, and 5 kHz. Before adding $T(s)$, the plant transfer function $G_{yu}(s)$ rolls up in the high frequency and shows a resonant peak around 10 kHz, which will limit the closed-loop performance by limiting the gain of the controller. However, by augmenting the plant by $T(s)$, the transfer function yields a better loop shape, so that the tonal feedback controllers can produce better closed-loop performance.

Three tonal feedback controllers at 300, 600, and 900 Hz were designed by closing the loop

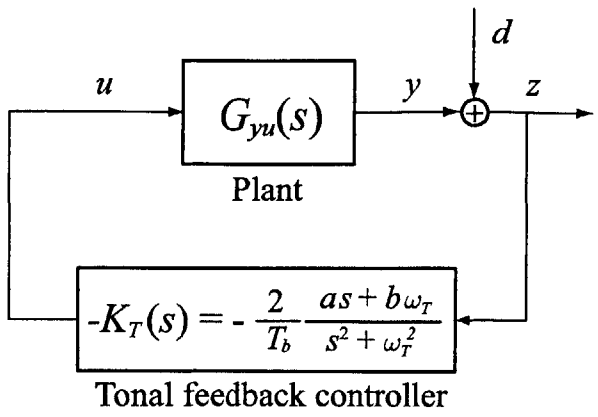

Figure 6-58: Block diagram of the tonal feedback controller.

sequentially to improve the stability and performance of the control system. It should be noted that $G_{yu}(s)$ in Equation 6.48 should be replaced by $G_{yu}(s)T(s)$ when computing the controller parameters. The resulting controller is shown in Figure 6-62. It is implemented digitally with a sampling frequency of 25 kHz. The effect of time delay in the digital component is considered in the design of the controllers. The loop transfer function using this controller is shown in Figure 6-63 (frequency response), and 6-64 (Nyquist plot). It can be seen that the closed-loop system is stable, and the loop transfer function has high gains at 300, 600, and 900 Hz, and enough phase margins. The closed-loop performance is shown in Figure 6-65. The same disturbance spectrum in Figure 6-57 is used to compare the open-loop and the closed-loop autospectrum. We can see that better than 20 dB of attenuation is achieved at 600 and 900 Hz. Also, 15 dB of reduction is achieved at 300 Hz.

6.9.3 Effect of the Low-frequency Feedthrough

Throughout this chapter, we have seen that the low-frequency feedthrough in the plant transfer function makes controller implementation much harder and more complicated, although solutions for these problems have been proposed and the resulting closed-loop performance has been very promising. The digital tonal feedback control approach is also affected by the low-frequency feedthrough. The basic condition for applying the tonal feedback controller is that the sensor used in the control system should be able to measure the performance variable z to be reduced. However, this condition is not satisfied here, because the signal from the embedded accelerometers in the panel is corrupted by the low-frequency feedthrough. If the target frequency is away from the range corrupted by the low-frequency feedthrough, its effect can be neglected, and we can design the tonal feedback controller as described earlier. However, if the bandwidth of interest is inside the range affected by the low-frequency feedthrough, it should be compensated before the controller is designed. In this section, it will be shown how the low-frequency feedthrough degrades the closed-loop performance, and what we can do to compensate for it.

Figure 6-66 shows the frequency response of plant transfer functions $G_{zu}(s)$ and $G_{yu}(s)$.

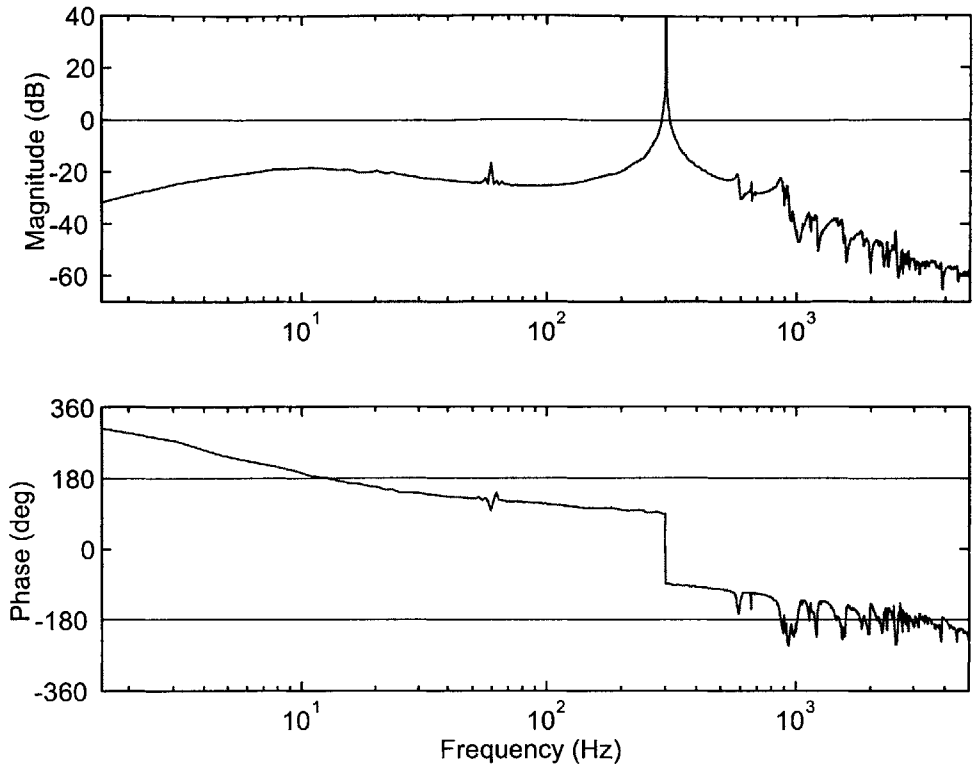

Figure 6-59: Frequency response of loop transfer function using the tonal feedback controller.

The discrepancy between those two transfer functions, which corresponds to the low-frequency feedthrough effect, can be observed in the figure. As shown in Chapter 3, $G_{zu}(s)$ may be obtained from the measurement of $G_{yu}(s)$ by adding the low-frequency feedthrough compensator $C(s)$. Now, the tonal feedback controller will be designed and implemented to reduce the discrete harmonics at 300 Hz. First, the effect of the low-frequency feedthrough will be neglected, and the controller will be designed based on $G_{yu}(s)$, not on $G_{zu}(s)$, using the condition in Equation 6.48. The corresponding loop transfer function $G_{yu}(s)T(s)K_T(s)$ is shown in Figure 6-67. Note that the loop transfer function $G_{yu}(s)T(s)K_T(s)$ provides the information about the closed-loop response in terms of the sensor output y. As expected, it has a high gain at 300 Hz and enough phase margins. The closed-loop autospectrum $S_{yy}(s)$ obtained using this controller is shown in Figure 6-68. The disturbance spectrum in Figure 6-57 is used to compare the open-loop and the closed-loop autospectrum. We can see that better than 30 dB of attenuation is achieved at 300 Hz in the sensor output y. However, this result may be misleading, because what we want to reduce is the performance output z, not the sensor output y. We have to find the loop transfer function that gives the information about the closed-loop performance in terms of z, since the loop transfer function $G_{yu}(s)T(s)K_T(s)$ doesn't provide that information. Using the block diagram in Figure 6-69, we can see that the loop transfer

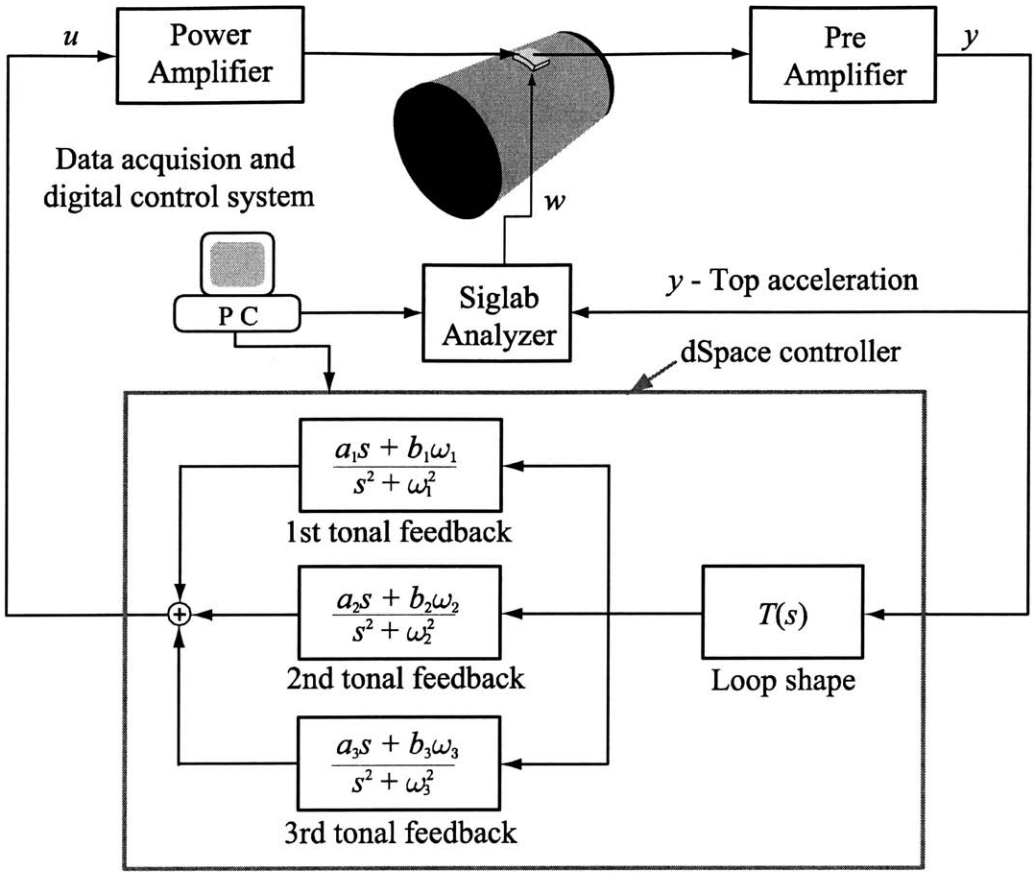

Figure 6-60: Block diagram of the digital tonal feedback control approach.

function related with z is written as $[G_{yu}(s) + C(s)]\,T(s)K'_T(s)$, where $K'_T(s)$ is given by

$$K'_T(s) = \frac{K_T(s)}{1 + C(s)T(s)K_T(s)}\,. \tag{6.51}$$

The frequency response of the loop transfer function $[G_{yu}(s) + C(s)]\,T(s)K'_T(s)$ is shown in Figure 6-70. Surprisingly, the loop gain is always less than 0 dB, even at the target frequency 300 Hz. The resulting closed-loop autospectrum $S_{zz}(s)$, which is what we want to reduce, is shown in Figure 6-71. As expected from the loop transfer function, the attenuation achieved using this controller is less than 5 dB at 300 Hz. This result is significantly different from $S_{yy}(s)$ in Figure 6-68, and cannot be predicted from the loop transfer function $G_{yu}(s)T(s)K_T(s)$.

One solution for this problem may be to design the tonal feedback controller $K'_T(s)$ based on $G_{yu}(s) + C(s)$, not on $G_{yu}(s)$, and implement the equivalent controller $K_T(s)$, given as

$$K_T(s) = \frac{K'_T(s)}{1 - C(s)T(s)K'_T(s)}\,. \tag{6.52}$$

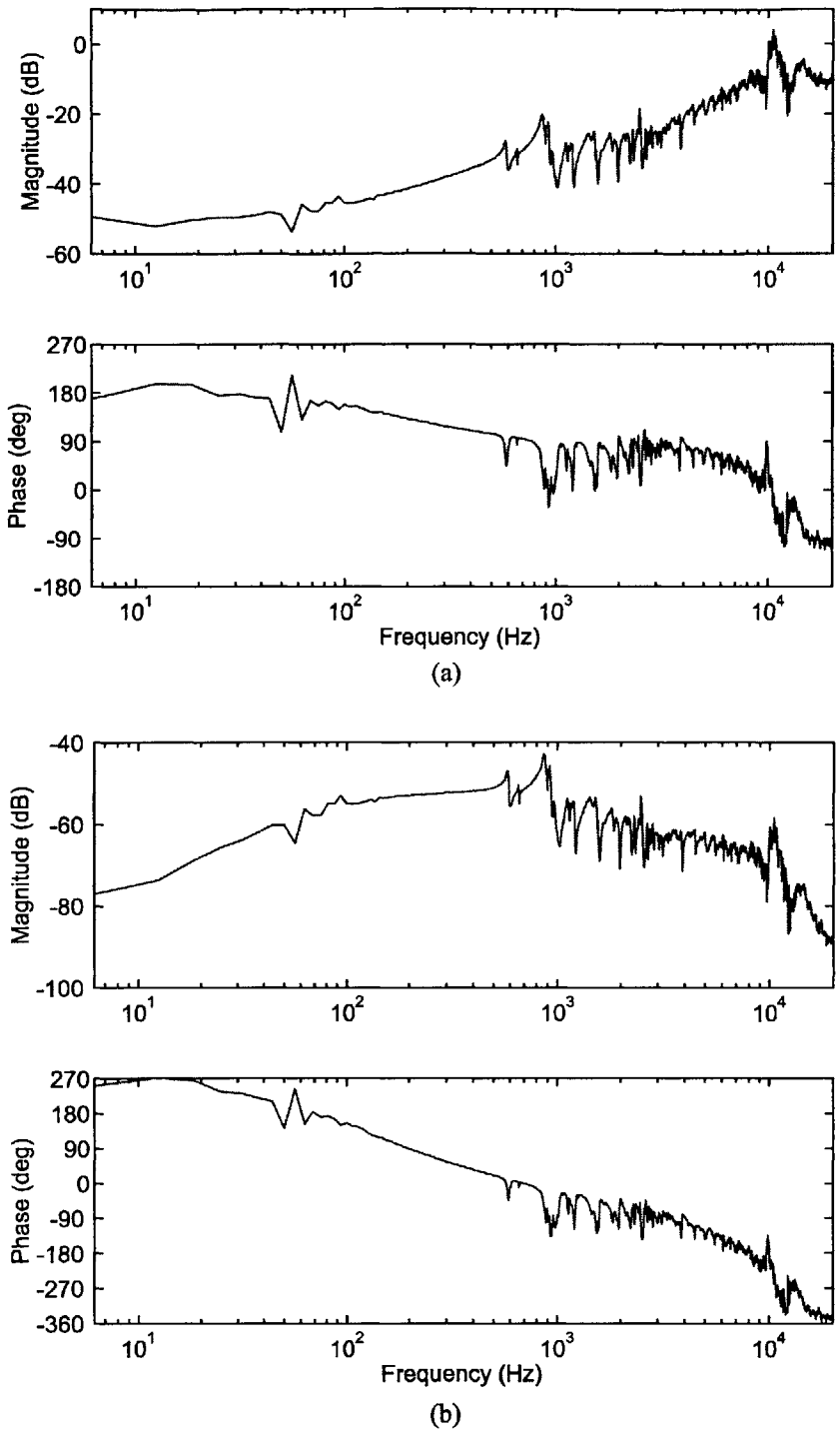

Figure 6-61: Frequency response of (a) $G_{yu}(s)$, and (b) $G_{yu}(s)T(s)$.

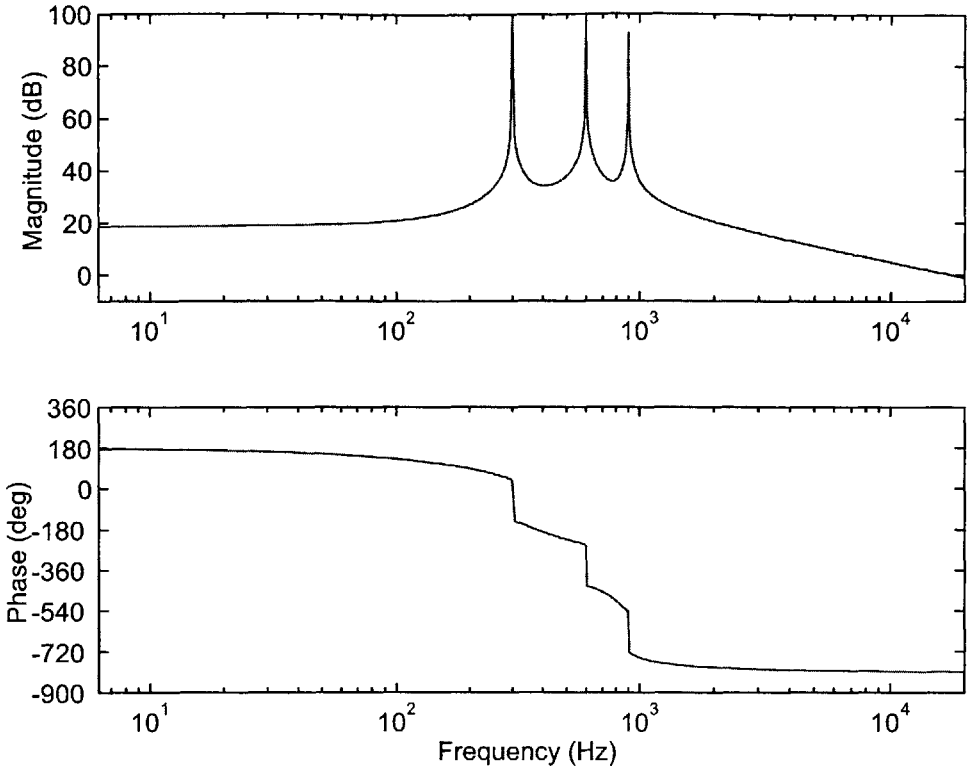

Figure 6-62: Frequency response of the tonal feedback controller. The target frequencies are 300, 600, and 900 Hz.

Unfortunately, this approach will significantly increase the order of the controller $K_T(s)$, especially if other controllers are also implemented, such as feedback or feedforward control, simultaneously with the tonal feedback control. It may not be feasible to implement 55 tonal feedback controllers with this structure for 55 panels that will cover the cylindrical shell. However, $K_T(s)$ can be simplified using the fact that two complex poles are dominant in $K_T(s)$, given as

$$K_T(s) \approx \frac{c}{s+p} + \frac{c^*}{s+p^*} = \frac{(c+c^*)\,s + (cp^* + c^*p)}{s^2 + (p+p^*)\,s + pp^*}, \tag{6.53}$$

where p and p^* are the dominant complex conjugate poles of $K_T(s)$, and c and c^* are the corresponding residues of those poles. Frequently, $p + p^*$ is less than 0, which means that the simplified $K_T(s)$ is unstable. However, this instability will not cause any problem, or destabilize the closed-loop system, if $K_T'(s)$ is well-designed such that the closed-loop system is stable.

Figure 6-72 shows the loop transfer function $[G_{yu}(s) + C(s)]\,T(s)\,K_T'(s)$, where $K_T'(s)$ is the tonal feedback controller designed based on $[G_{yu}(s) + C(s)]$. Since $[G_{yu}(s) + C(s)]\,T(s)\,K_T'(s)$ is the loop transfer function related with the performance output z, it can help predict the closed-loop performance. It has a gain of about 30 dB at 300 Hz, and a phase margin of 90°, which implies that about 30 dB of attenuation will be achieved at 300 Hz in the closed-loop

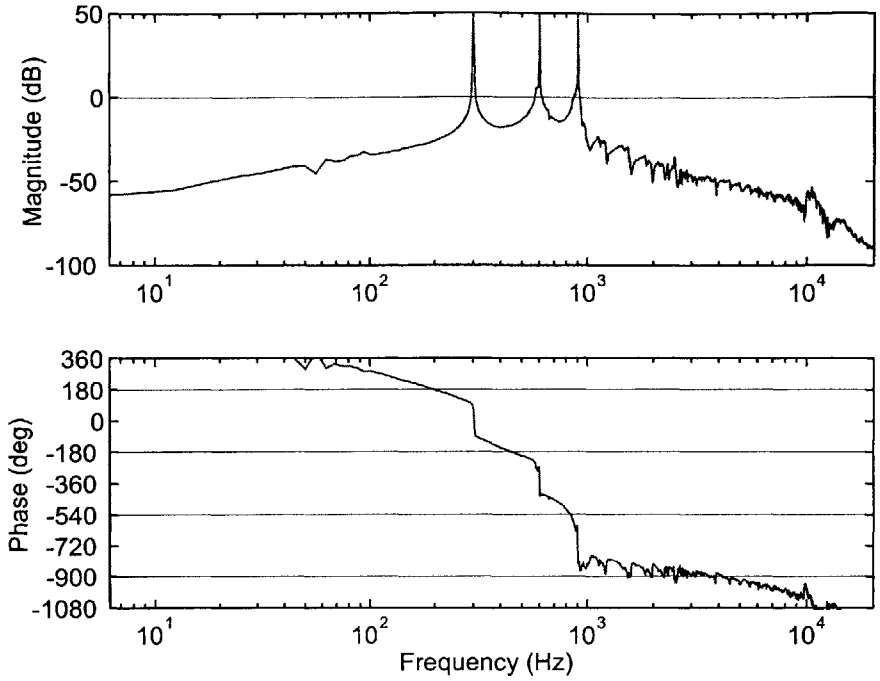

Figure 6-63: Frequency response of loop transfer function using the digital tonal feedback controller.

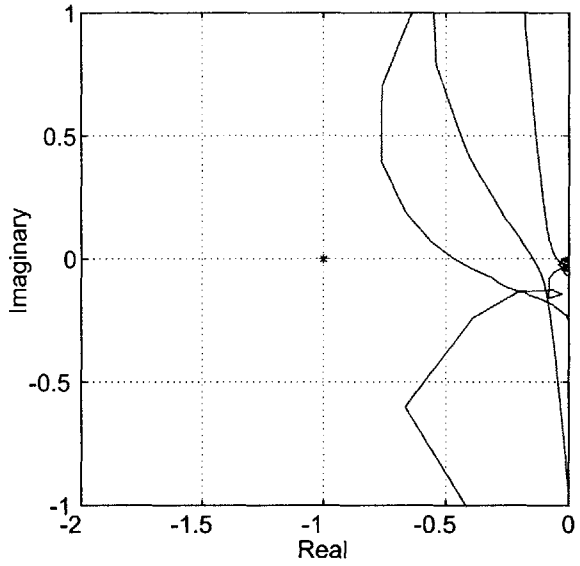

Figure 6-64: Nyquist plot of the loop transfer function using the digital tonal feedback controller.

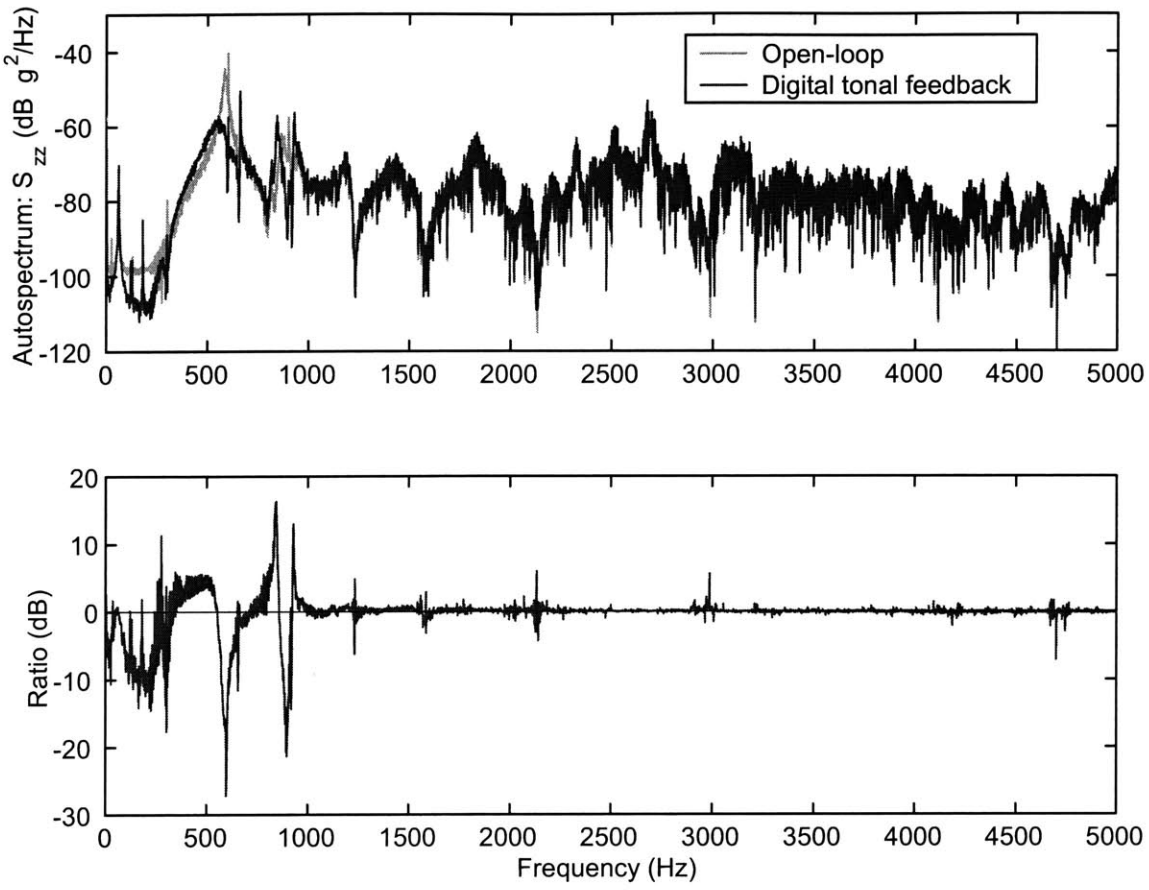

Figure 6-65: Closed-loop performance obtained with the digital tonal feedback controller. "Ratio" represents the ratio of the open-loop response to the closed-loop response. Negative ratios indicate attenuation; positive ratios indicate amplification.

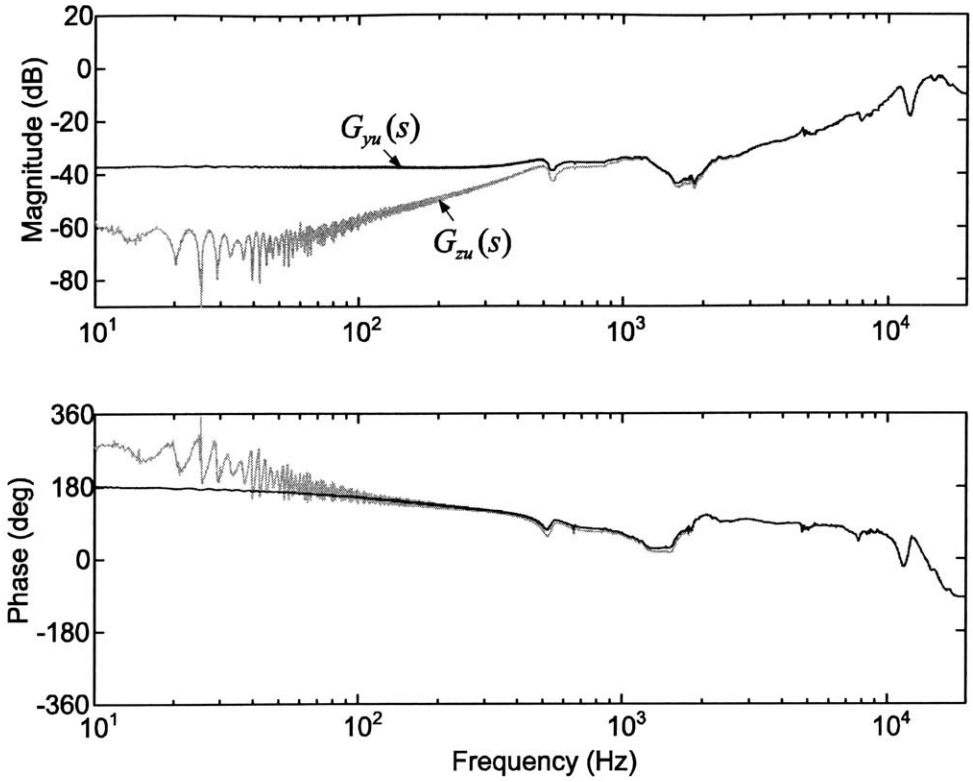

Figure 6-66: Frequency response of plant transfer functions $G_{zu}(s)$ and $G_{yu}(s)$.

response. The result is as expected. The closed-loop autospectrum S_{zz} in Figure 6-73 shows that S_{zz} is reduced by more than 30 dB at 300 Hz. Once $K'_T(s)$ is determined, the equivalent tonal feedback controller $K_T(s)$ that considers $C(s)$ can be obtained using Equation 6.52. Also, $K_T(s)$ can be simplified by retaining only the dominant complex poles, as in Equation 6.53. Both of exact and simplified $K_T(s)$ are simulated, plotted and compared in Figure 6-74. It can be seen that they are unstable transfer functions, because the phase goes up by 180° above the resonant frequency at 300 Hz. Therefore, they cannot be measured experimentally. The result of the simulation in Figure 6-74 implies that the exact and the simplified $K_T(s)$ are very similar to each other, at least above 10 Hz. Furthermore, it is much easier to implement the simplified $K_T(s)$ than the exact one, because the exact $K_T(s)$ in Equation 6.52 needs nine states, while the simplified one in Equation 6.53 needs only two states to implement. This is a very important advantage of simplifying $K_T(s)$, considering the fact that we need to implement $K_T(s)$ for each panel.

The Nyquist plot of the loop transfer function $G_{yu}(s)T(s)K_T(s)$ is shown in Figure 6-75. Here, $K_T(s)$ is the simplified one defined in Equation 6.53. We can see that the closed-loop system is stable, because there are two encirclements about the critical point -1, and the loop transfer function has two unstable complex conjugate poles. The resulting closed-loop performance is shown in Figure 6-76. It can be seen that better than 30 dB of attenuation is

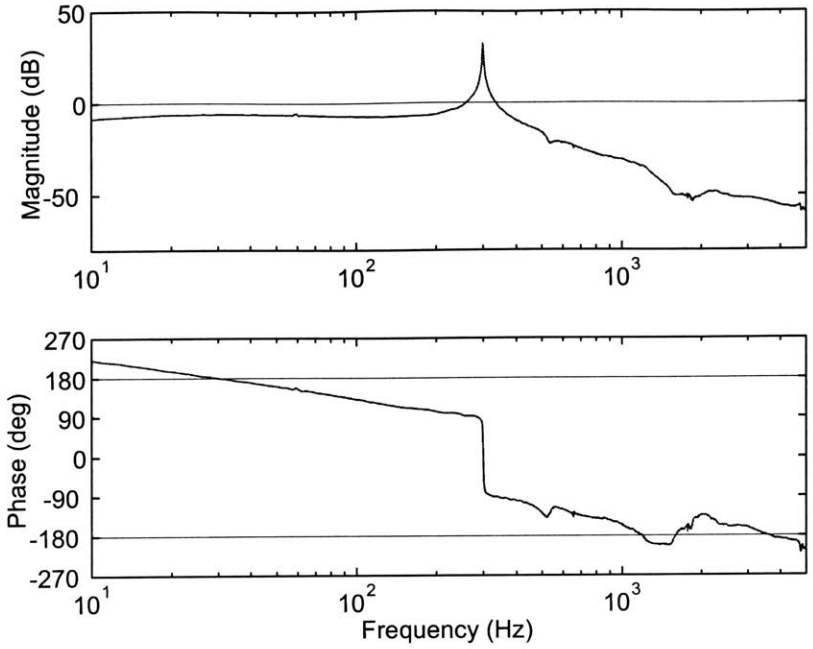

Figure 6-67: Frequency response of loop transfer function $G_{yu}(s)T(s)K_T(s)$.

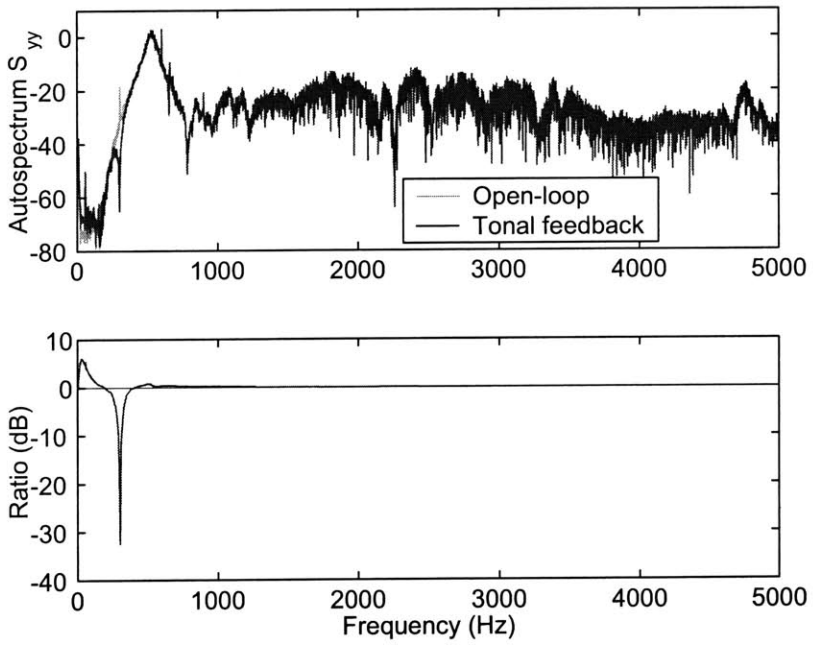

Figure 6-68: Closed-loop autospectrum S_{yy}.

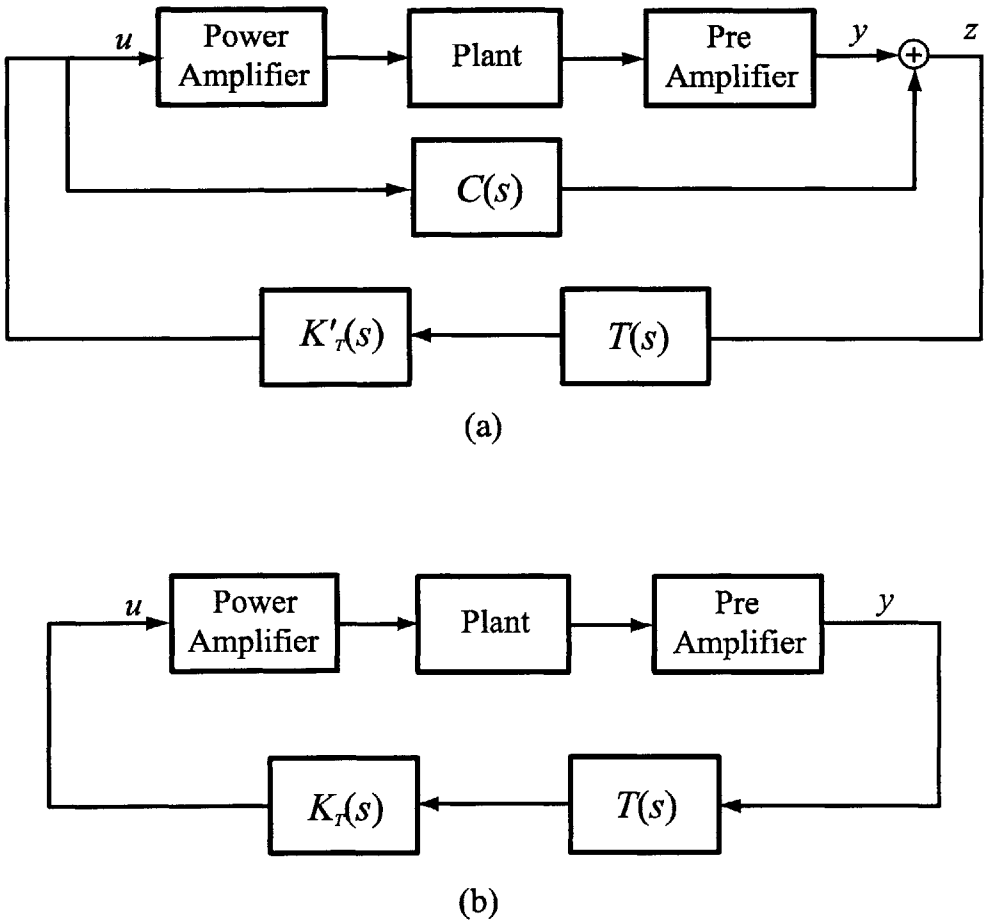

Figure 6-69: Equivalent block diagram of the closed-loop system using the tonal feedback controller. (a) $C(s)$ is considered as a part of the plant. (b) $C(s)$ is incorporated into the controller.

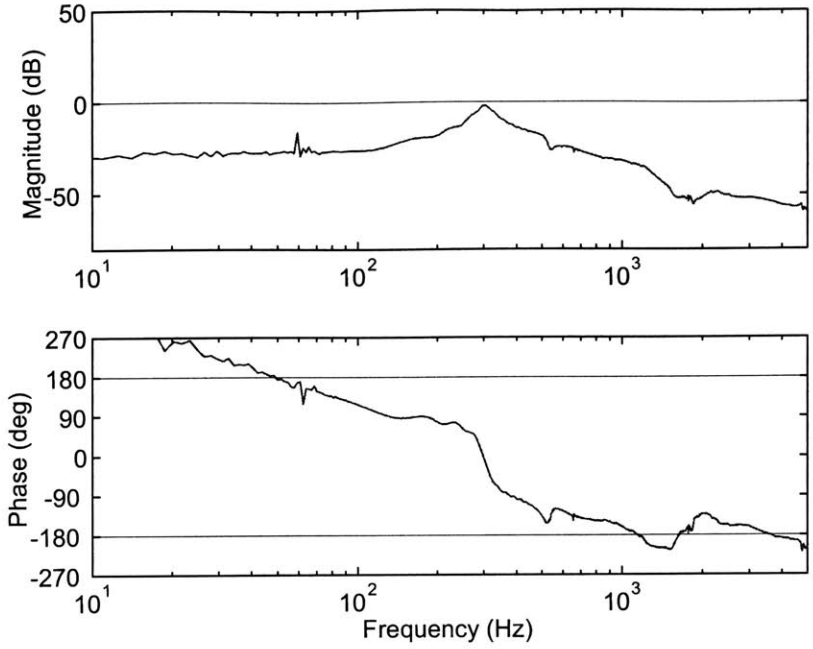

Figure 6-70: Frequency response of the loop transfer function $[G_{yu}(s) + C(s)]\,T(s)K_T'(s)$.

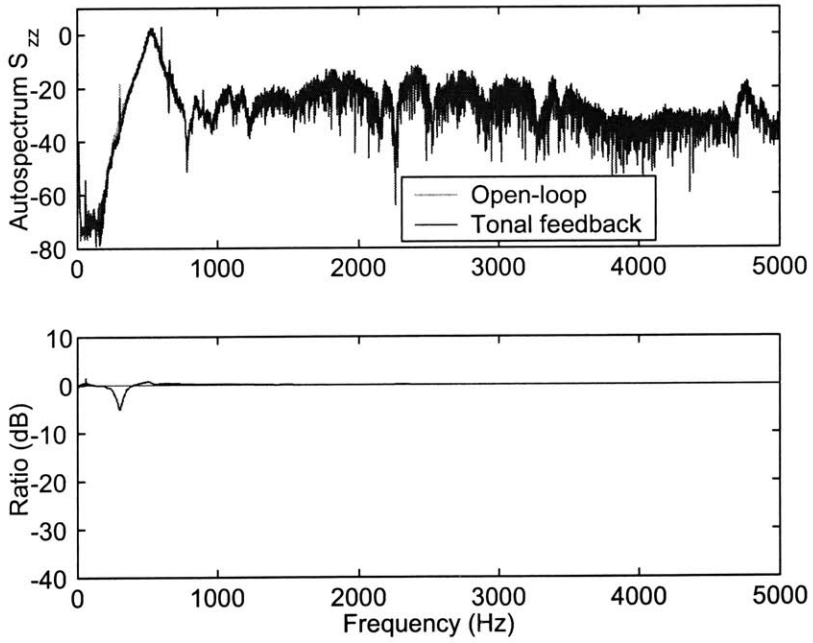

Figure 6-71: Closed-loop autospectrum $S_{zz}(s)$.

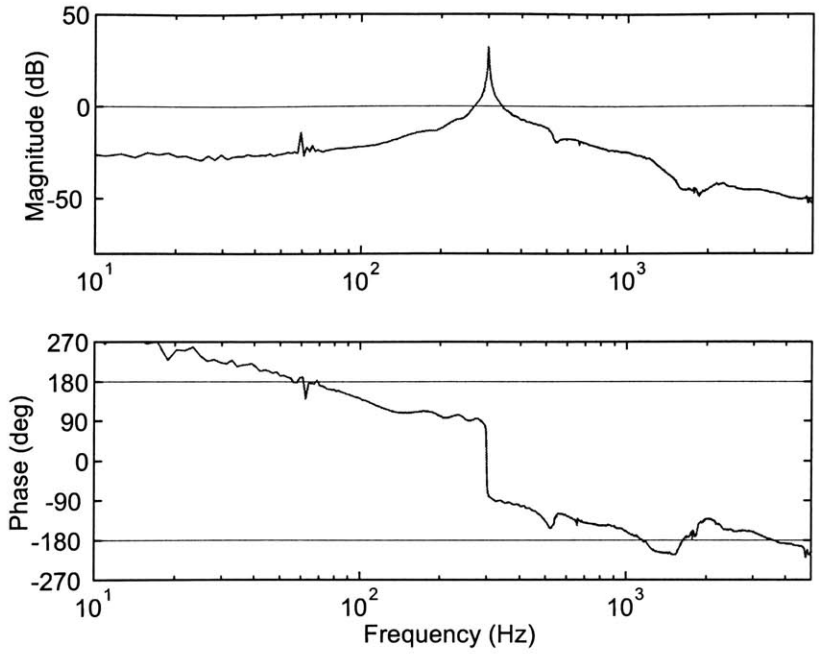

Figure 6-72: Frequency response of loop transfer function $[G_{yu}(s) + C(s)]\,T(s)K'_T(s)$.

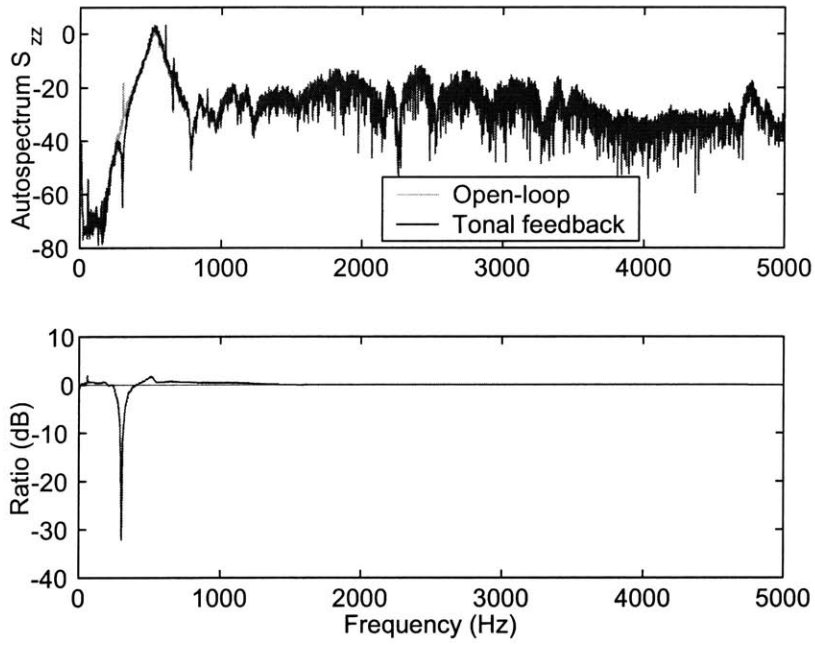

Figure 6-73: Closed-loop autospectrum S_{zz} obtained with the tonal feedback controller $K'_T(s)$.

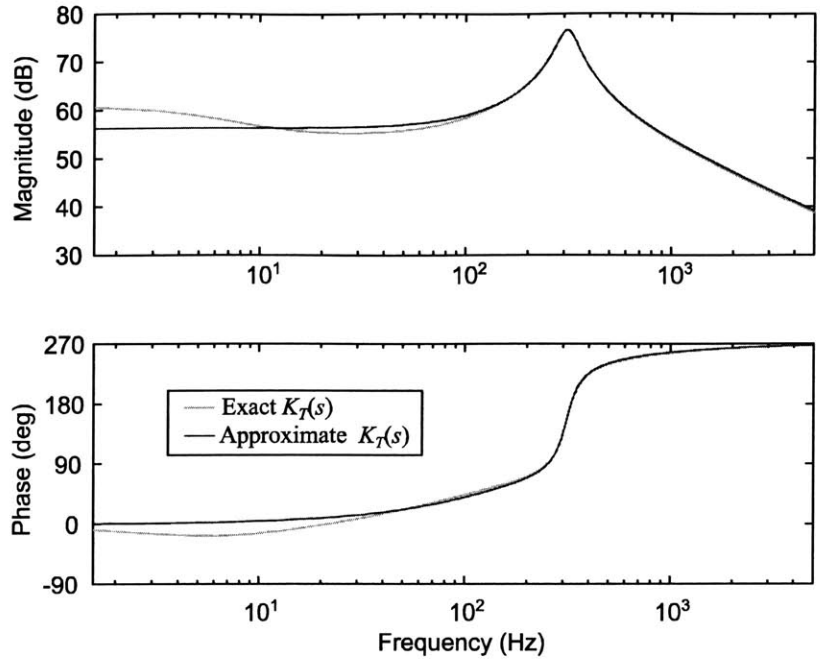

Figure 6-74: Frequency reponse of tonal feedback controller $K_T(s)$: the exact one in Equation 6.52, and the approximate one in Equation 6.53.

achieved at 300 Hz in the closed-loop autospectrum $S_{zz}(s)$.

6.10 Digital Feedback, Feedforward, and Tonal Feedback Controller

In this section, the digital feedback controller, the digital feedforward controller, and the digital tonal feedback controller are implemented simultaneously on the cylindrical shell with one active composite panel mounted. The block diagram for this control approach is shown in Figure 6-77. This control configuration is the most complicated and complete one considered as local control architecture for each panel in this study. The design procedure for this control configuration can be summarized as follows:

1. Measure the plant transfer functions $G_{y_t w}(s)$, $G_{y_b w}(s)$, $G_{y_t u}(s)$, $G_{y_b u}(s)$.

2. Measure the performance transfer function $G_{zu}(s)$ using an external accelerometer.

3. Estimate the low-frequency feedthrough compensator $C(s)$. It is a low-pass filter that best fits $G_{zu}(s) - G_{y_t u}(s)$.

4. Design the digital feedback controller. First, design the controller based on $[G_{y_t u}(s) + C(s)]$, and then find the equivalent controller that has $C(s)$. (See Section 6.8.)

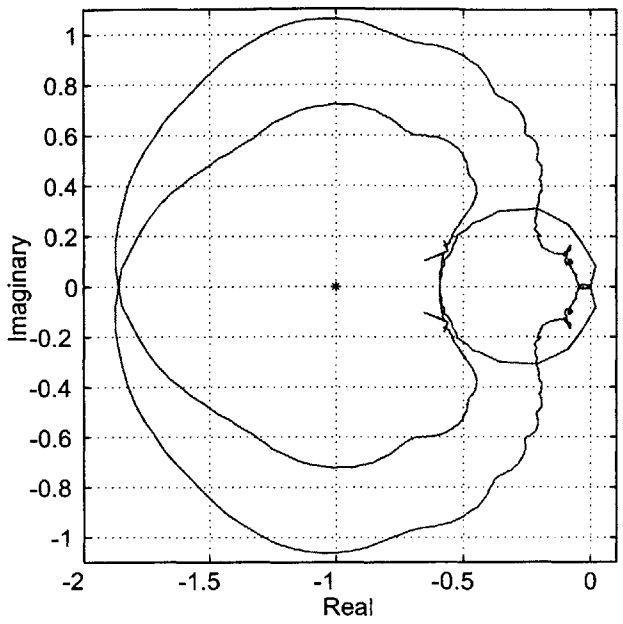

Figure 6-75: Nyquist plot of the loop transfer function $G_{yu}(s)T(s)K_T(s)$, where $K_T(s)$ is the simplified one.

5. Design the digital feedforward controller. First, find a stabilizing controller such that it fits the frequency response that cancels the performance output. Then, find the equivalent controller that considers the effect of $C(s)$. (See Section 6.8.)

6. Estimate or measure the closed-loop plant transfer function $T_{y_t u}(s)$, with both digital feedback and feedforward controllers acting.

7. Determine $T(s)$ that modifies the plant transfer function $T_{y_t u}(s)$, such that it becomes easier to design the tonal feedback controller by yielding a good loop shape.

8. Design the digital tonal feedback controller based on $[T_{y_t u}(s) + C(s)]T(s)$. Then, simplify the controller using the method in Section 6.9.3.

These control algorithms are implemented in dSpace controller with a sampling frequency of 25 kHz. The sampling frequency has to be reduced, compared with the case of hybrid feedback and analog feedforward control or digital feedback and feedforward control approach, due to the increased amount of calculation in the DSP system. The sampling frequency is another design constraint on the digital controller design and implementation, because it produces a time delay of roughly one and half times the sampling time (Equation 6.18). It should be selected as high as possible, which is limited by the amount of the computation required in the DSP system. Therefore, the control algorithms should be as simple as possible, so that they can be performed in the DSP system with a small sampling time, while at the same time they

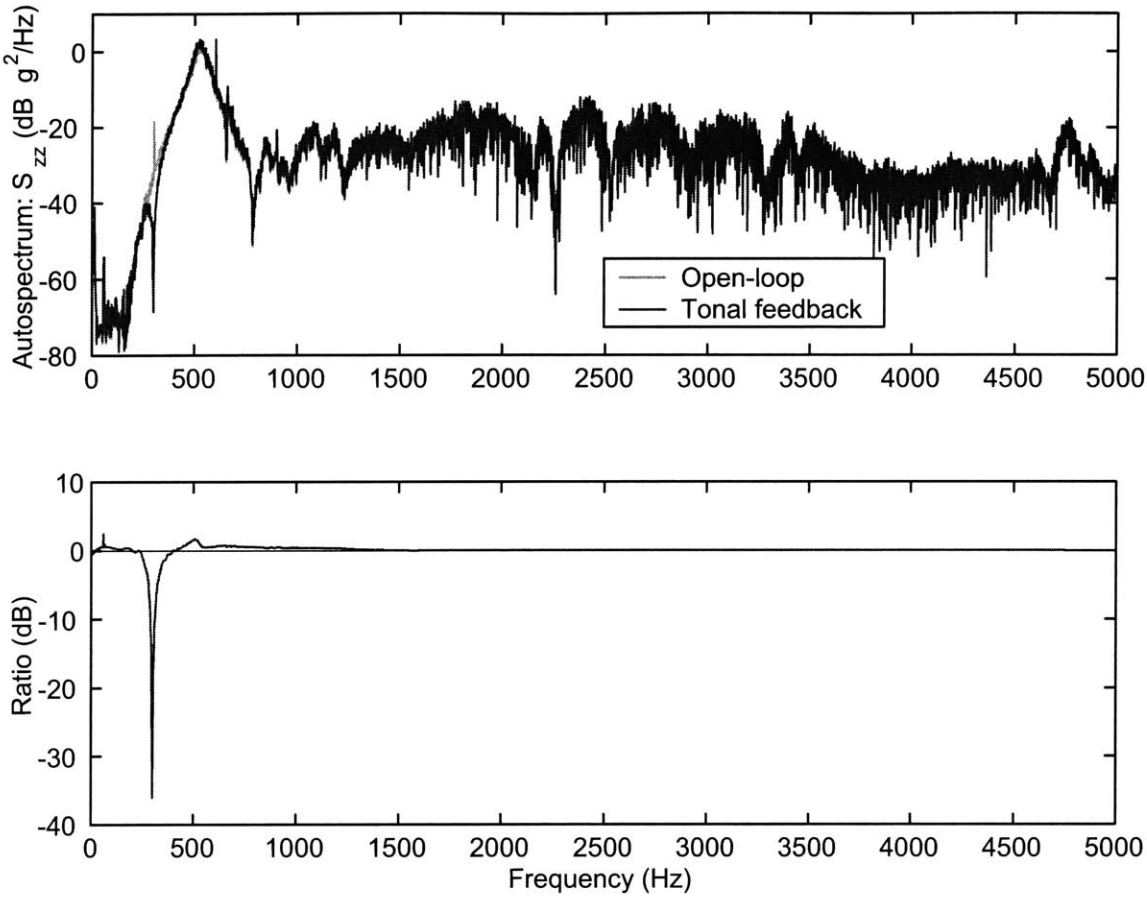

Figure 6-76: Closed-loop autospectrum S_{zz} obtained with the simplified tonal feedback controller $K_T(s)$. "Ratio" represents the ratio of the open-loop response to the closed-loop response. Negative ratios indicate attenuation; positive ratios indicate amplification.

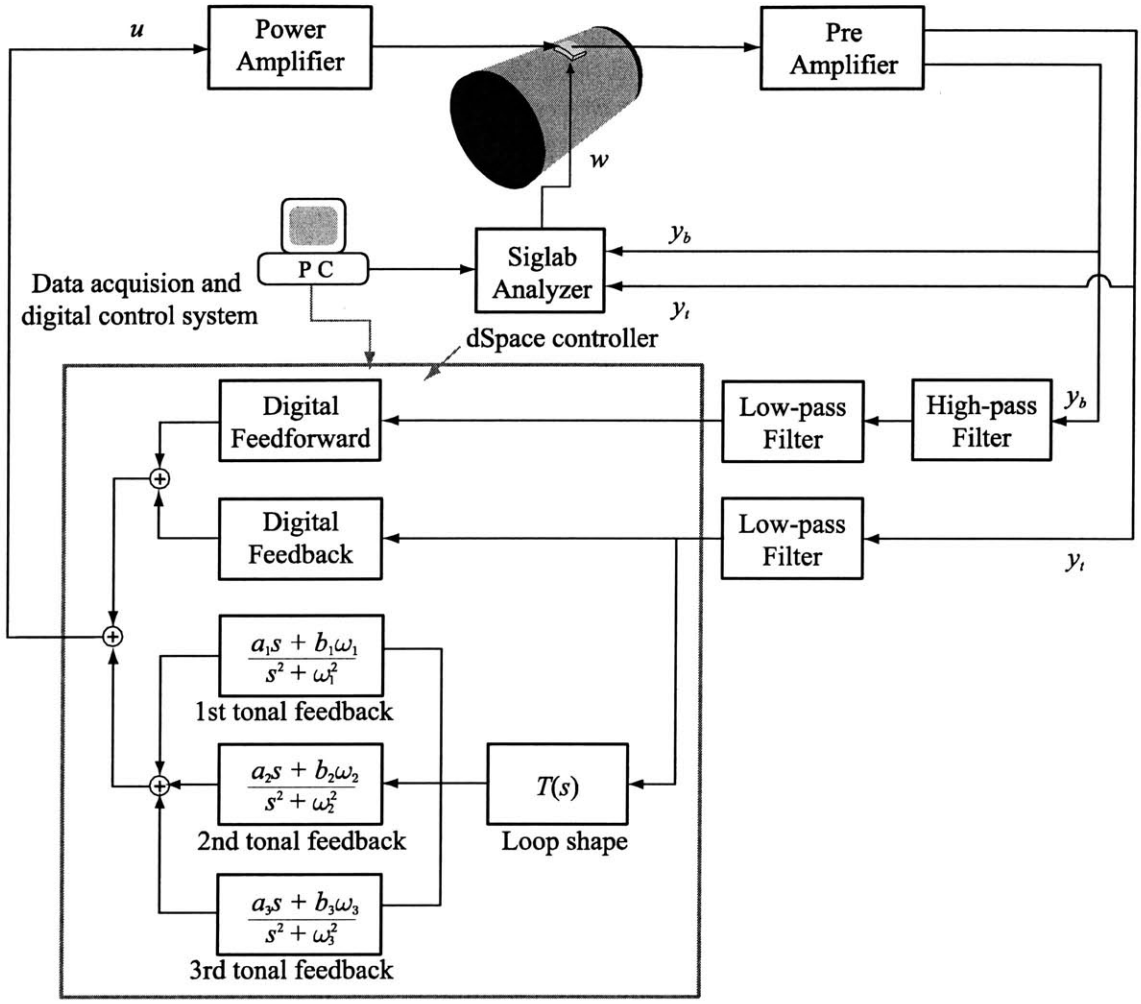

Figure 6-77: Block diagram of the digital feedback, digital feedforward, and tonal feedback control.

can have the desired frequency response. It explains why we have been trying to reduce the order of the controller by approximating it throughout this chapter.

The resulting closed-loop performance using this control architecture is shown in Figure 6-78. The disturbance spectrum in Figure 6-57 is used to compare the open-loop and the closed-loop autospectrum. With only feedback control, 10 dB of attenuation is achieved between 300 and 1300 Hz. With feedforward control added, an additional 10 dB of reduction is achieved between 500 and 1000 Hz. Finally, tonal feedback control, which has been designed to reduce three discrete harmonics at 300, 600, and 900 Hz, behaves as expected, and reduces the disturbance at those discrete frequencies by more than 10 dB. The disturbance is amplified, *i.e.*, the performance is degraded, between 1500 and 2500 Hz. This effect may not be serious, because the disturbance doesn't have enough energy above 1 kHz anyway. As mentioned in Section 6.8, if we want better performance below 1.5 kHz, we have to accept the some amplification above 1.5 kHz. Also, the degraded performance is inevitable, because the effect of the phase delay in the digital component becomes severe above that frequency. The effect can be negligible at higher frequencies (above 3 kHz), because the control gain is low there. Considering all these facts, it can be concluded that this control configuration is a good solution as a local control architecture for each panel, since the controller variables can be adjusted in software, and more than 20 dB of attenuation is achieved between 400 and 1400 Hz, and more than 30 dB of reduction is achieved at the target discrete frequencies.

6.11 Hybrid Analog/Digital Feedback and Digital LQG Controller

Throughout this chapter, several control algorithms have been designed and implemented on the cylindrical shell with one active composite panel. These algorithms are distinguished by which signal is taken as input (feedback vs. feedforward control), and how they are implemented (analog vs. digital vs. analog-digital hybrid approach). However, there is one thing that is the same for all of those control algorithms— none of them are model-based controllers. The control design is based on the measured frequency responses of the plant transfer functions, and the closed-loop stability and performance are predicted by using the measured loop transfer function.

In this section, the results of closed-loop experiments obtained with a model-based controller are presented. In particular, a linear quadratic gaussian (LQG) controller is designed and implemented on the cylindrical shell with one panel mounted. The motivation for this section is to test the concept of the model-based controller in a single-input single-output (SISO) configuration using one panel, before designing multi-input multi-output (MIMO) LQG controllers using several panels, and eventually 55 panels. The block diagram of the setup for SISO LQG controller, showing the disturbances w, inputs u', and outputs y is shown in Figure 6-79. In this section, the disturbance w represents the input to a shaker installed inside the shell. The performance z is the acceleration of the outer surface of the composite panel mounted directly above the shaker (not shown in the figure), and the control input u' is the voltage input to the panel actuator layer. The sensor output y (or controller input) is the measurement from the complementary low-pass filter. The SISO LQG controller will be designed and implemented on the plant with the hybrid analog/digital controllers closed.

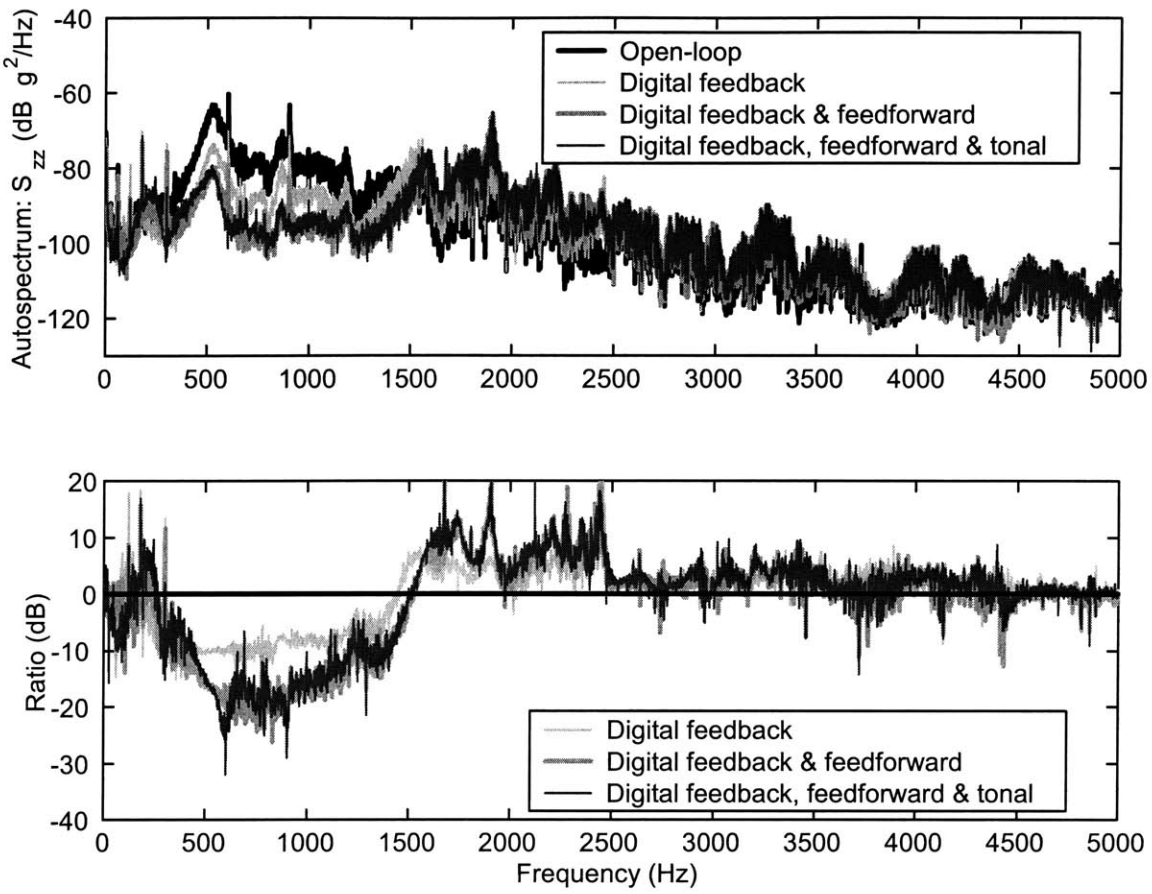

Figure 6-78: Closed-loop performance obtained with the digital feedback, feedforward, and tonal feedback controller. "Ratio" represents the ratio of the open-loop response to the closed-loop response. Negative ratios indicate attenuation; positive ratios indicate amplification.

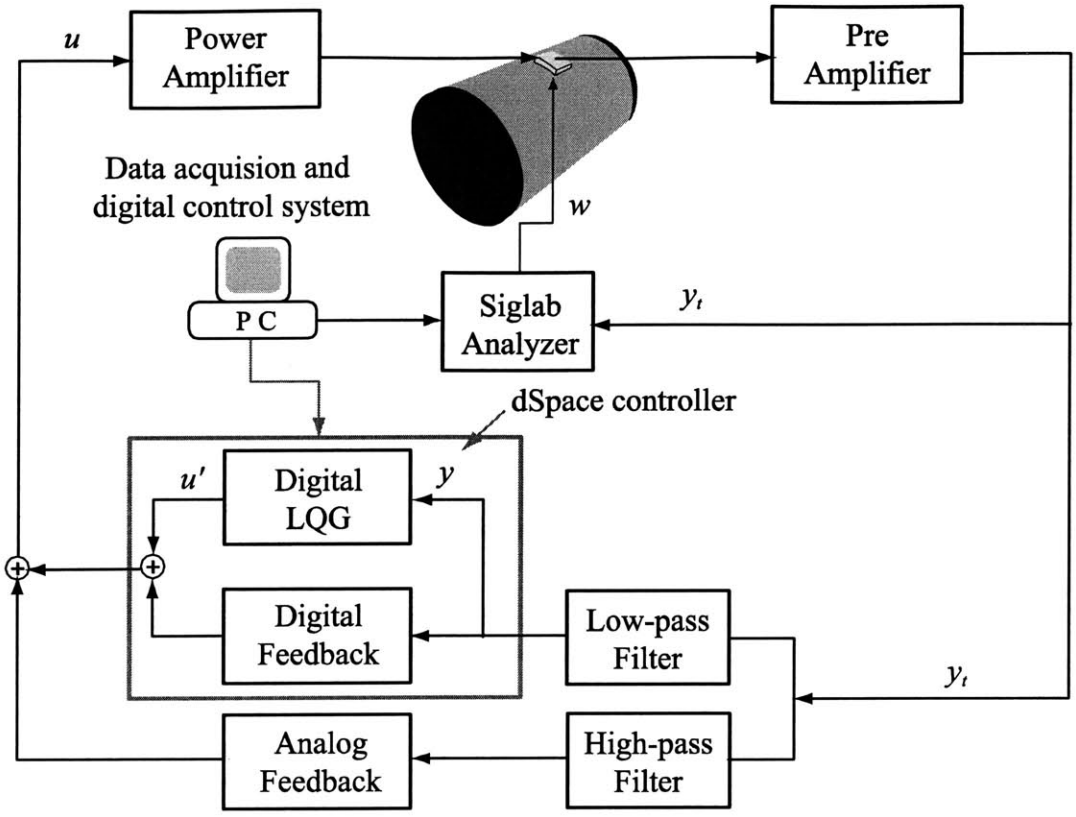

Figure 6-79: Block diagram of the SISO LQG controller design.

In order to synthesize the LQG controller, a state-space model that accurately captures the dynamic behavior of the system (at least below controller bandwidth) is necessary. The model is obtained by identifying the measured transfer functions from (w, u') to (z, y). The system identification method used here is Frequency domain Observability Range Space Extraction (FORSE) method [Jacques, 1994]. The resulting state-space model has thirty states, and the state-space representation is given by

$$\begin{aligned} \frac{d\mathbf{x}}{dt} &= \mathbf{A}\mathbf{x} + \mathbf{B}_1 w + \mathbf{B}_2 u' \\ z &= \mathbf{C}_1 x + \mathbf{D}_{11} w + \mathbf{D}_{12} u' \\ y &= \mathbf{C}_2 x + \mathbf{D}_{21} w + \mathbf{D}_{22} u' \,. \end{aligned} \tag{6.54}$$

The results of the system identification are shown in Figures 6-80 and 6-81. The identified transfer function $G_{zw}(s)$ matches quite well with the measured transfer function $G_{zw}(s)$ below 2 kHz in both magnitude and phase. The good match is critical for the closed-loop performance using model-based controllers, such as LQG controller. Above 2 kHz, the two transfer functions show some discrepancies. However, the discrepancies are not serious, because the expected bandwidth of LQG controller is around 1 kHz, reflecting the fact that the input to the LQG

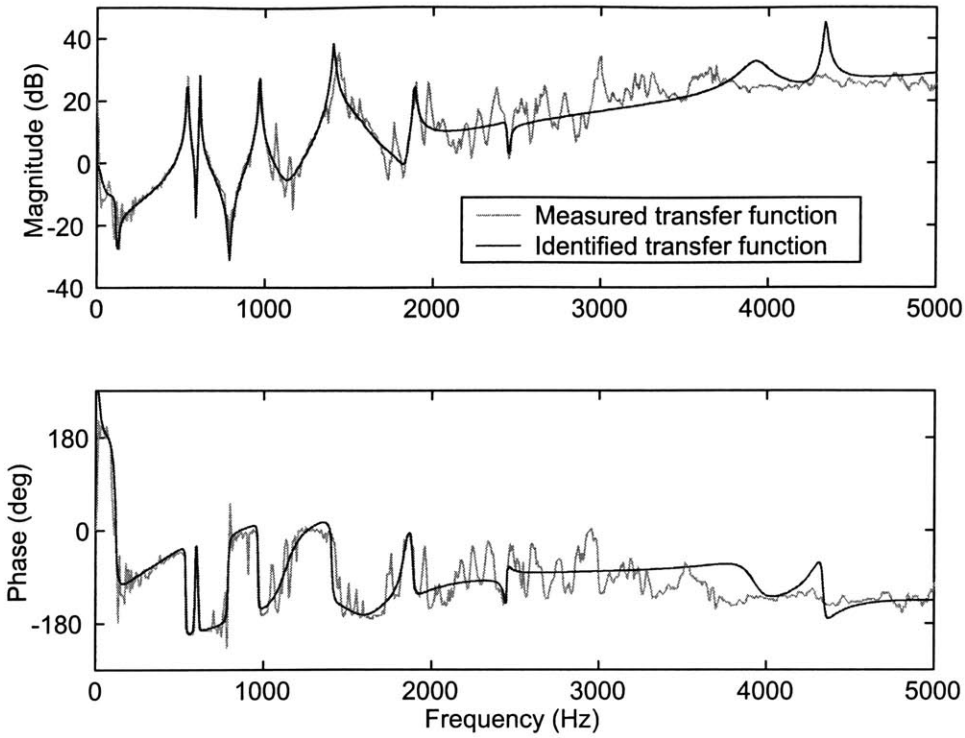

Figure 6-80: Frequency response of measured and identified transfer function $G_{zw}(s)$.

controller is filtered by the complementary second order Butterworth low-pass filter at 1 kHz. Figure 6-81 shows that the identified transfer function $G_{yu'}(s)$ is also almost identical to the measured transfer function up to 5 kHz.

Two different approaches are possible in LQG controller design in order to account for the low-frequency feedthrough. The first approach is to use the state-space equation in Equation 6.54 directly, which means that z is defined as the performance output to be minimized, and y is defined as the sensor output (or input to the controller) in LQG design. Then, we don't need to consider the low-frequency feedthrough effect, because it is already reflected in z. The second approach is to consider z as both performance output and sensor output, and design the LQG controller based on the modified plant model. Then, using the same techniques introduced in Section 3.3.3, the low-frequency feedthrough compensator $C(s)$ can be incorporated into the LQG controller. This approach is the same one as used throughout this chapter, which is first to design the feedback controller based on the modified plant transfer function by adding $C(s)$ to it, and then to combine $C(s)$ into the designed controller. In this section, the second approach will be used.

Although the identified state-space model is accurate enough in the bandwidth interest, frequency weighting functions should be used to get satisfactory performance. Otherwise, the controller might try to minimize the H_2 norm of the system by reducing $G_{zw}(s)$ in the high frequency region, because the performance z is an acceleration measurement, making $G_{zw}(s)$ roll

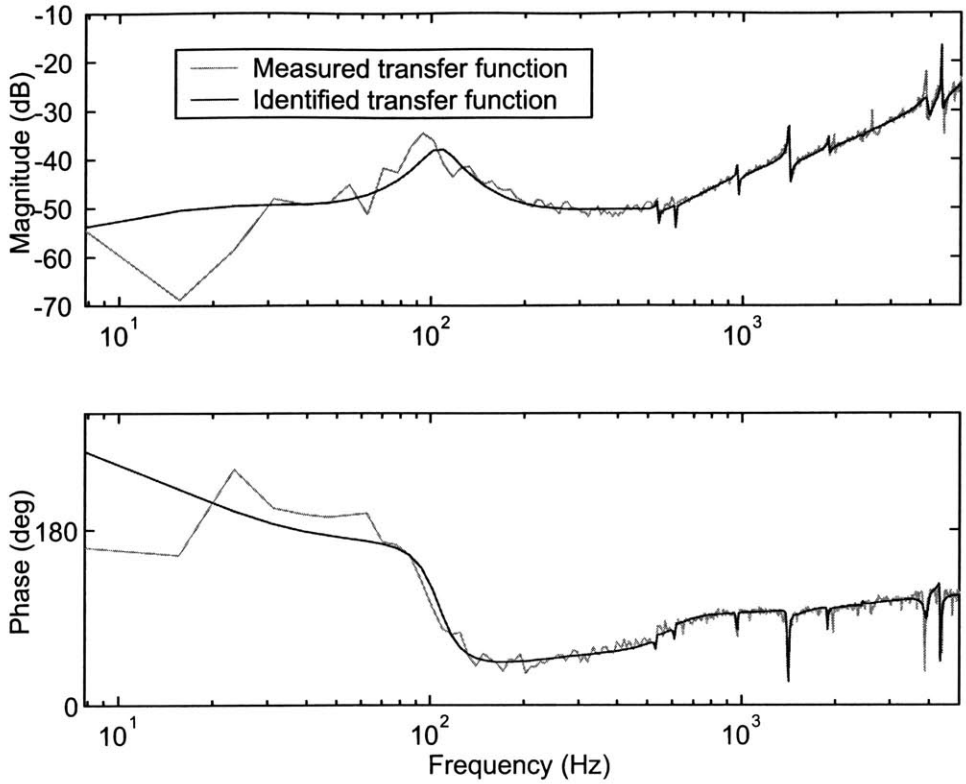

Figure 6-81: Frequency response of measured and identified transfer function $G_{yu'}(s)$.

up with a slope of 40 dB/decade. The frequency weighting function used for the performance (z) and sensor output (y) is a second order Butterworth low-pass filter at 1 kHz, while that for the disturbance (w) is a first order low-pass filter at 1 kHz. Ideally, the given disturbance spectrum (Figure 6-57) should be used as a frequency weighting function for the disturbance. However, the size of the state-space model for the spectrum turned out to be quite large. Since the order of the LQG controller is that of the plant model, plus the order of frequency weighting functions, the model for frequency weighting should be as simple as possible. Therefore, this model was discarded and a simple first order low-pass filter was selected as a frequency weighting function for the disturbance.

The identified plant model, combined with the frequency weighting functions, results in LQG controller with 37 states. However, the order of the original LQG controller had to be reduced, because it was found that the DSP system used in this study cannot implement this size in a real-time. Balanced model-order reduction was used to reduce the order of the LQG controller into 26 states [Zhou, 1995].

The resulting closed-loop performance using this controller configuration is shown in Figure 6-82. The result is very promising— nearly 40 dB of attenuation is achieved at resonant frequencies up to 1.5 kHz. The few spots where the attenuation is less than 0 dB (*i.e.* the disturbance is amplified) occur at frequencies where there is a zero in the disturbance to perfor-

mance transfer function, so that the performance there is less critical. Because the attenuation at resonant frequencies is most important for the reduction of broadband disturbance, we can conclude that the closed-loop performance using this controller configuration is satisfactory.

6.12 Summary

In this chapter, the control algorithms proposed in Chapter 3 were validated on the model of the testbed developed in Chapter 2, and several controller architecture with different configurations were designed and experimentally implemented on the cylindrical shell with one active composite panel. First, a completely analog controller (both feedback and feedforward) was implemented to evaluate the proposed feedback and feedforward control approaches on the real system, and to establish a benchmark against which the other controllers can be compared. This controller gave the best performance, nearly 15–30 dB of attenuation in the bandwidth interest (250 – 2000 Hz), although the other controllers showed very similar results. After verifying that the proposed control algorithms work well, some parts of the controller were discretized. The first part to be discretized was a notch filter. The result of closed-loop performance using a digital notch filter was almost indistinguishable from that obtained with the analog controller. Furthermore, this controller configuration enables us to change the frequency to be notched out easily in software, not in hardware as in the analog notch filter. Then, the feedback controller was decomposed into analog and digital sections in parallel using complementary high-pass and low-pass filters. This configuration was denoted as a hybrid approach, and its result was also very similar to that obtained using the analog controller. The feedforward controller was also implemented digitally. (strictly speaking, the feedforward controller was decomposed into analog and digital sections in series.) The performance of the digital feedforward controller was slightly worse than, but very similar to, that obtained using analog feedforward controller. Also, both feedback and feedforward controllers were implemented digitally. The result showed that this configuration may be a good solution if the disturbance doesn't have much energy at high frequencies, although the performance was worse than the analog controller or hybrid controller. To reduce the discrete harmonics in the disturbance spectrum, a tonal feedback control approach was introduced, and more than 20 dB of attenuation was achieved at the target frequencies. Finally, an LQG controller, which is model-based, was designed and implemented on the testbed on which hybrid feedback controller is acting.

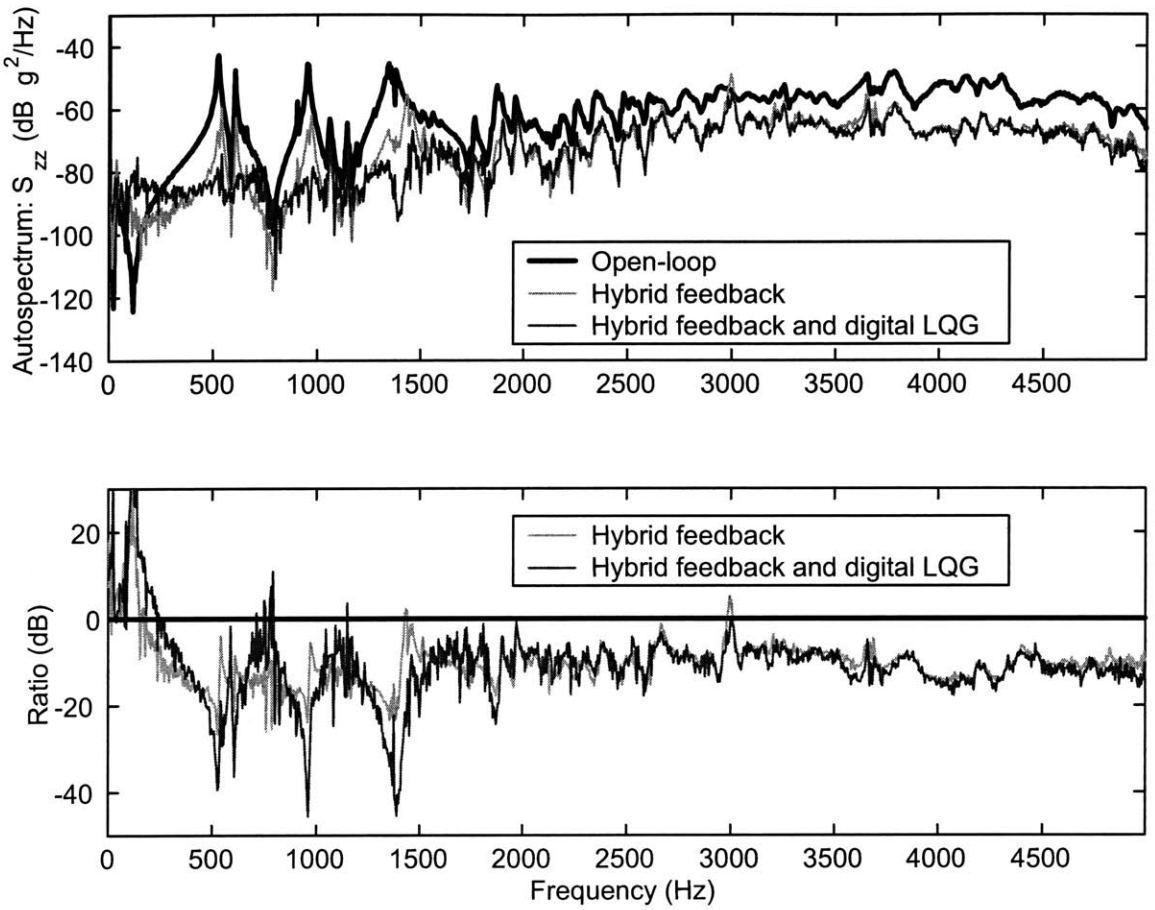

Figure 6-82: Closed-loop performance obtained with the hybrid feedback and digital LQG controller. "Ratio" represents the ratio of the open-loop response to the closed-loop response. Negative ratios indicate attenuation; positive ratios indicate amplification.

Table 6.1: Summary of the controller configuration implemented in this chapter

Controller configuration	Features	Achievable closed-loop performance
Analog-only controller	· Everything in analog · Best performance · Unfeasible to implement	· 15–30 dB between 200 and 2500 Hz
Analog controller with digital notch filter	· Notch filter is implemented digitally · Notch frequency can be adjusted in software	· 15–30 dB between 200 and 2500 Hz
Hybrid feedback and analog feedforward	· Feedback controller is decomposed as analog and digital part in parallel · Complementary filters are used	· 15–25 dB between 200 and 2500 Hz
Hybrid feedback and digital notch filter	· Combines hybrid feedback and digital notch filter approach	· 10–15 dB between 200 and 2500 Hz
Hybrid feedback and digital feedforward	· Feedback is implemented in hybrid · Feedforward is implemented digitally	· 15–25 dB between 200 and 2500 Hz
Digital feedback and digital feedforward	· Feedback is implemented digitally · Feedforward is implemented digitally	· 10–20 dB between 200 and 1500 Hz · Amplification above 2 kHz
Digital tonal feedback	· Reduces discrete harmonics in the disturbance spectrum	· 20–30 dB at target frequencies
Hybrid feedback and digital LQG	· Feedback is implemented in hybrid · LQG is implemented digitally	· 15–20 dB between 200 and 2500 Hz · 40 dB at resonant frequencies

Chapter 7

Closed-loop Experimental Results for Testbed

7.1 Introduction and Objective

In this chapter, the results of closed-loop experiments obtained with multiple panel-level controllers are reported. The panel-level local controllers were designed and implemented on the cylindrical shell with 55 active composite panels mounted. The experimental setup for testing the controllers, including the cylindrical shell with panels, a water tank, and the signal conditioners are described. The results of identification and analysis of plant transfer functions are explained, and their implications for controller design are discussed. Then, the design process for local controllers and the corresponding closed-loop performance are reported. Finally, the results of investigating panel dynamics are presented and their effects on the closed-loop performance are addressed.

7.2 Experimental Setup

Figure 7-1 shows the cylindrical shell on the surface of which 55 active composite panels are mounted. As shown in the figure, each panel is labeled from "1" to "5" in the axial direction, while from "A" to "K" in the circumferential direction. A shaker, which is used as a disturbance source, is mounted inside the shell below panel F3. The cylindrical shell was installed in a water tank (Northrop Grumman Corp., Annapolis, MD) to measure open-loop transfer functions, design controllers, and evaluate their closed-loop performance. Figure 7-2 shows a schematic view of the water tank with a diameter of 50 ft, which contains the cylindrical shell and six hydrophones. The depth of the water is about 28 ft, and the cylindrical shell and hydrophones are located at mid-depth. The shell is 12.5 ft from the tank wall, and hydrophones 1–5 are 10 ft from the shell, while hydrophone 6 is located at 12.5 ft from the far wall.

As mentioned in Chapter 2, the PZT actuator layer and accelerometers in each panel need signal conditioners to process their input and output signals. Each panel has a power amplifier for the actuator layer, and a pre-amplifier with a receiver board for the accelerometers. The pre-amplifiers are installed inside the shell, while the power amplifiers and receiver boards are installed outside the shell. Each pre-amplifier has a constant gain of 40 dB, while each power

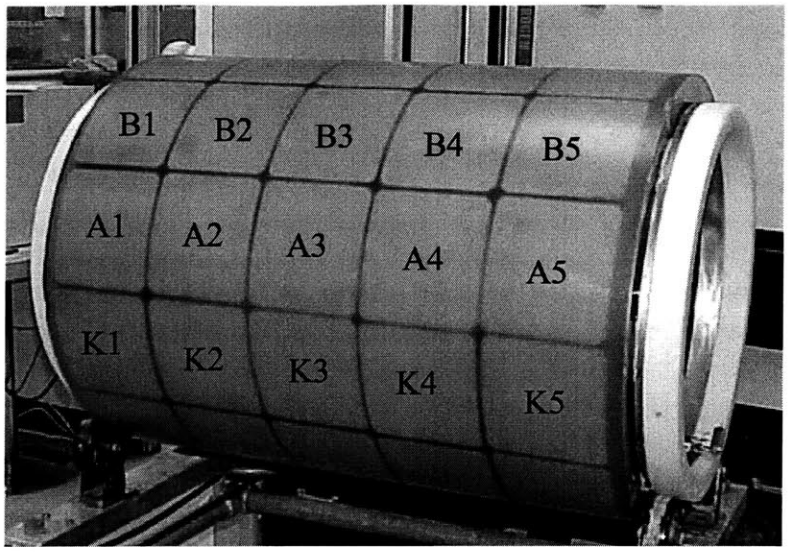

Figure 7-1: The cylindrical shell with 55 active composite panels mounted. (Photo courtesy of NGC)

amplifier has a low-pass filter at 190 Hz with a DC gain of 34 dB, and each receiver board has a high-pass filter at 14 Hz and low-pass filter at 2200 Hz, with five selectable gains (26, 30, 32, 34, or 36 dB). Their frequency responses are shown in Figure 7-3 and 7-4, respectively. The block diagram of the plant, analog electronics for signal conditioners, and digital control system is shown in Figure 7-5.

We expect that the plant transfer function matrix from 55 panel actuator layer inputs to 55 panel accelerometer outputs will be *diagonally dominant*, although it is a structural modal system. In other words, when driving the actuator layer in panel A2, the signal output from the embedded accelerometers in panel A2 should be much higher than those from other panels, because the weight of the panel is supposed to be much smaller than that of the shell. Therefore, the effect of panel motion on the shell would be negligible, which would make off-diagonal terms in the plant transfer function matrix much smaller than the diagonal terms.

7.3 Identification and Analysis of Plant Transfer Functions

Before designing controllers for each panel, all the open-loop transfer functions from the disturbance input (w) and 55 panel actuator inputs (u) to 55 panel accelerometer outputs (y) and six hydrophone outputs (z) were measured and analyzed. Specifically, in order to design feedback controllers that will be implemented digitally, transfer functions from D/A input (u) to A/D output (y) are required (Figure 7-6). All the transfer functions were measured by injecting a swept sine signal into the proper D/A input channel, and measuring the corresponding A/D output channel. The sampling frequency for the digital system is 20 kHz.

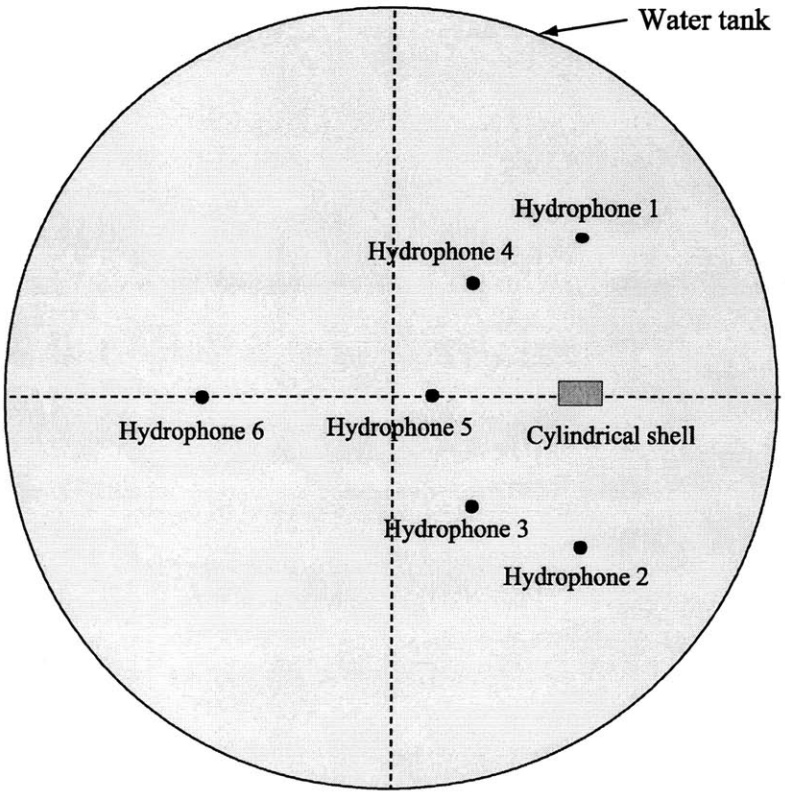

Figure 7-2: Schematic view of the water tank with the cylindrical shell and six hydrophones. (Figure courtesy of NGC)

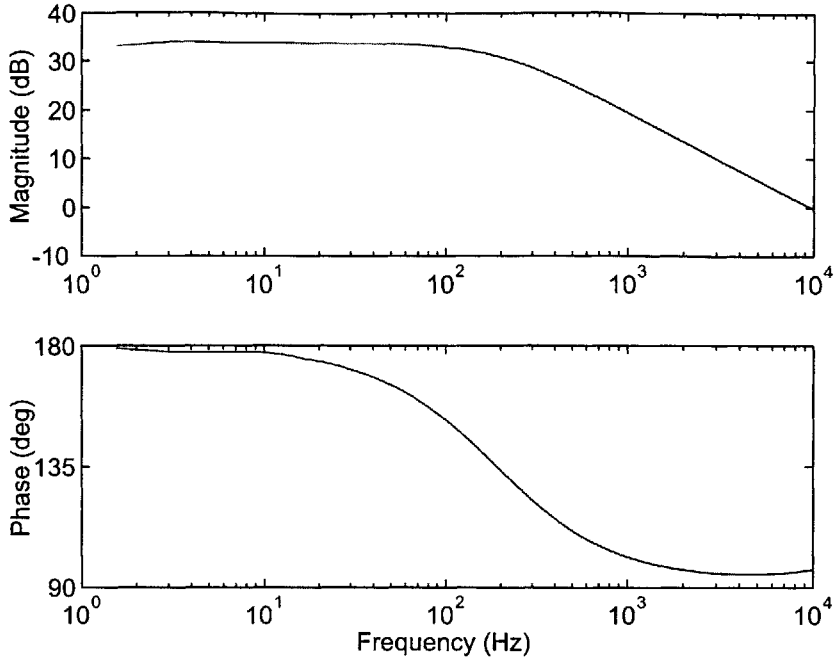

Figure 7-3: Frequency response of the power amplifiers.

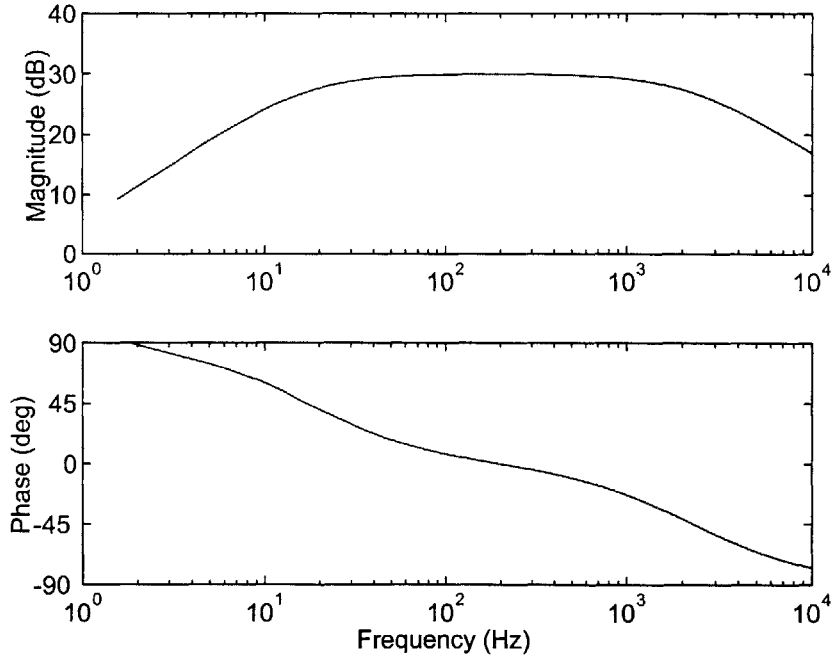

Figure 7-4: Frequency response of the receiver boards.

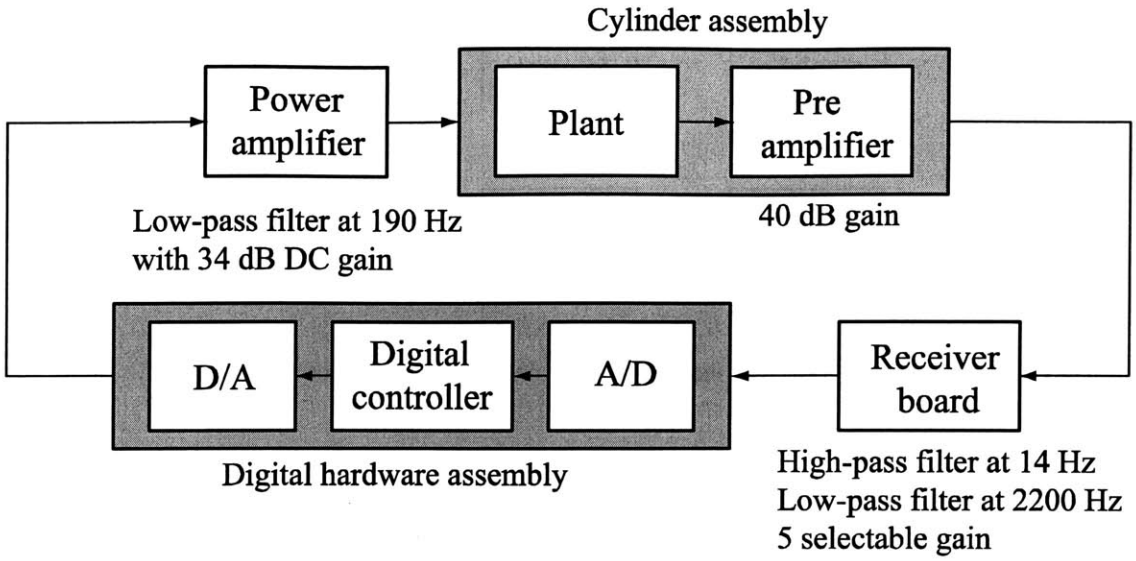

Figure 7-5: Block diagram of the experimental setup, including plant, analog electronics, and digital control system.

7.3.1 Transfer Functions of Multiple Panels

As mentioned earlier, we expect that the plant transfer function matrix will be *diagonally dominant*. In order to see whether it is true, diagonal and off-diagonal transfer functions are compared. Figure 7-7 shows the transfer functions of panels in a row in the axial direction obtained by driving a panel in that row (panel A3), while Figure 7-8 shows the transfer functions of panels in a circumferential ring obtained by driving a panel in that ring (panel A2). We can see that diagonal transfer functions (from panel A3 to panel A3 in Figure 7-7, and from panel A2 to panel A2 in Figure 7-8) have much higher magnitudes than those of the other panels, *i.e.*, the off-diagonal transfer functions, below 100 Hz, by more than 30 dB. Above 100 Hz, the magnitudes of the diagonal transfer functions are still higher than those of the off-diagonal transfer functions, but the differences are not as great. In some frequency ranges, the off-diagonal transfer functions have the same order of magnitude as that of the diagonal transfer functions. Considering that the bandwidth of interest for controller design is between 150–1000 Hz, the observations indicate that the plant is *weakly diagonally dominant*, in contrast to the initial expectation.

There are two possible explanations for the weak diagonal dominance in the plant. The first one is that the weight of each panel has been increased significantly since its first prototype design. As mentioned in Chapters 3 and 6, the panels show resonant peaks around 10 kHz, primarily due to participation of the embedded accelerometers in the modal behavior of the panel. In order to suppress the undesirable dynamics in the panel, its manufacturer (Materials Systems Inc., Littleton, MA) mounted an aluminum plate on the upper surface of the panel. This and other modifications increased the weight of the panels, although they helped reduce the resonant peak of the accelerometer dynamics. Therefore, the effect of panel motion on the

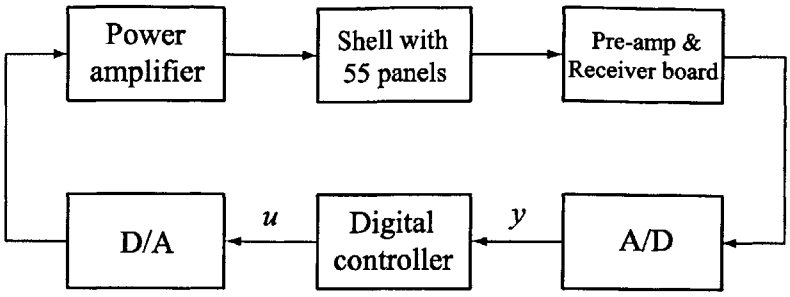

Figure 7-6: Block diagram of the plant and digital control system.

shell dynamics is no longer negligible, as was initially expected. The second reason is related to the cavity in the panel where the accelerometers are embedded, which will be addressed later in this chapter.

7.3.2 Transfer Function of a Single Panel

One of 55 panels was selected and its transfer function was analyzed in detail to investigate the characteristics of the plant and determine which controller configurations can be implemented. Figure 7-9 shows four frequency responses related with the dynamics of panel G3. The light thin transfer function corresponds to the measured transfer function of panel G3, while the light thick transfer function corresponds to the simplified transfer function that the light thin transfer function is supposed to follow, neglecting shell modes, which is $ks^2G_{\text{power}}(s)G_{\text{pre}}(s)$. Here, $G_{\text{power}}(s)$ and $G_{\text{pre}}(s)$ represent the transfer functions of a power amplifier and a pre-amplifier with a receiver board, respectively, and k is a constant gain. Note that the light thick transfer function has the same magnitude as the dark thick transfer function, which is obtained by multiplying the light thick transfer function by $e^{-(3.5sT)}$, which represents a time delay of $3.5T$. Here, T is a sampling period, which is set to be 50 μs.

As can be seen from the figure, the light thin transfer function and the light thick transfer function show a significant difference below 500 Hz, due to the low-frequency feedthrough effect in the panel. As mentioned in Chapter 3, a compensator should be designed and included in the controller such that this effect can be minimized. The dark thin transfer function in Figure 7-9 represents the compensated transfer function, which was obtained by subtracting a low-frequency feedthrough compensator from the measured transfer function. In contrast to the measured transfer function, the compensated transfer function matches well with the light thick transfer function above 100 Hz.

Another important observation is that the transfer function has a phase delay of 3.5 times the sampling period. We can see that the phase of the light thin transfer function, *i.e.*, the measured transfer function, follows that of the dark thick transfer function, *i.e.*, the simplified transfer function with an apparent time delay of $3.5T$. In order to figure out where the phase delay comes from, several transfer functions were measured and analyzed. First, transfer functions of a power amplifier and a pre-amplifier with a receiver board were measured, and they showed the expected behavior, as shown in Figure 7-3 and 7-4. Then, an external frequency analyzer

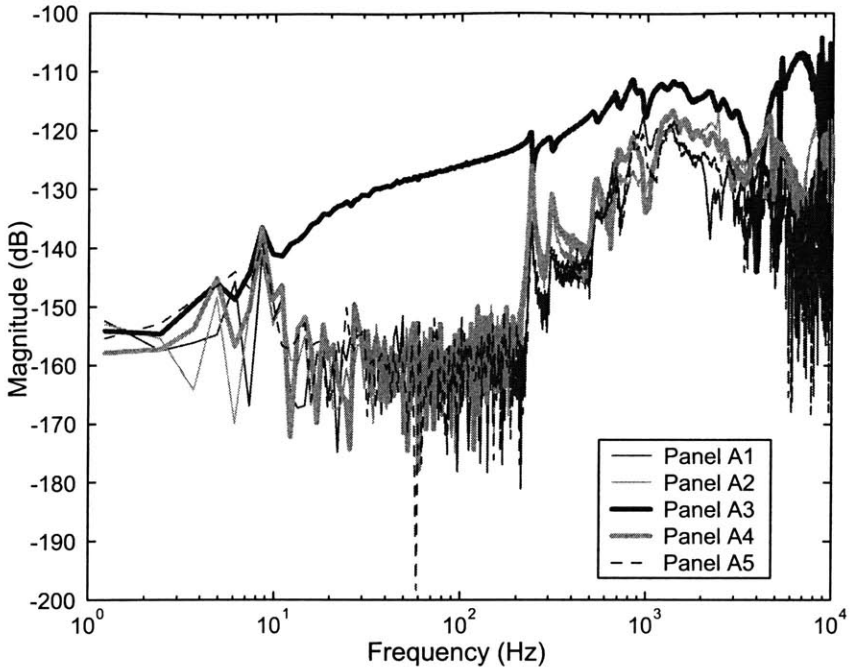

Figure 7-7: Transfer functions from panel A3 to panels A1–A5.

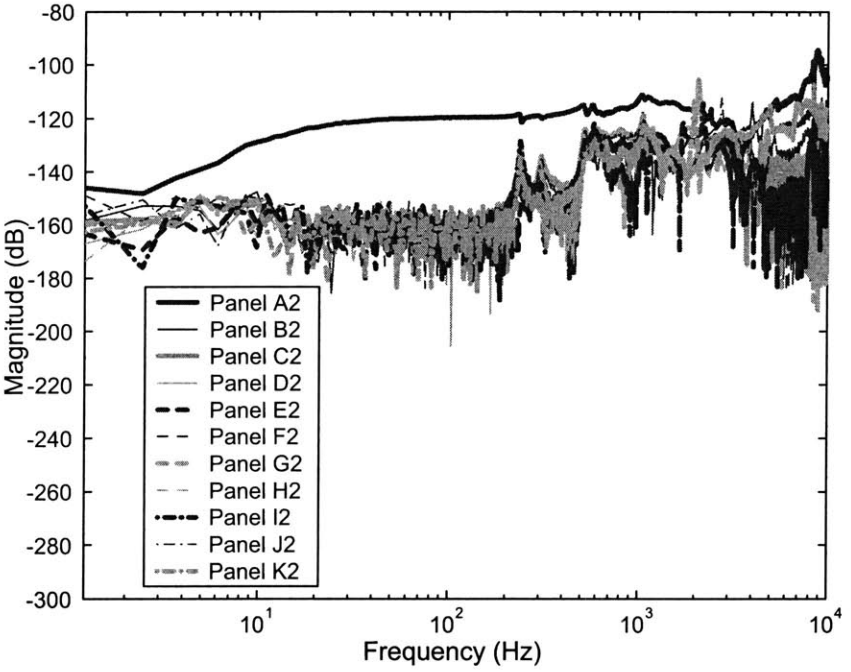

Figure 7-8: Transfer functions from panel A2 to panels A2–K2.

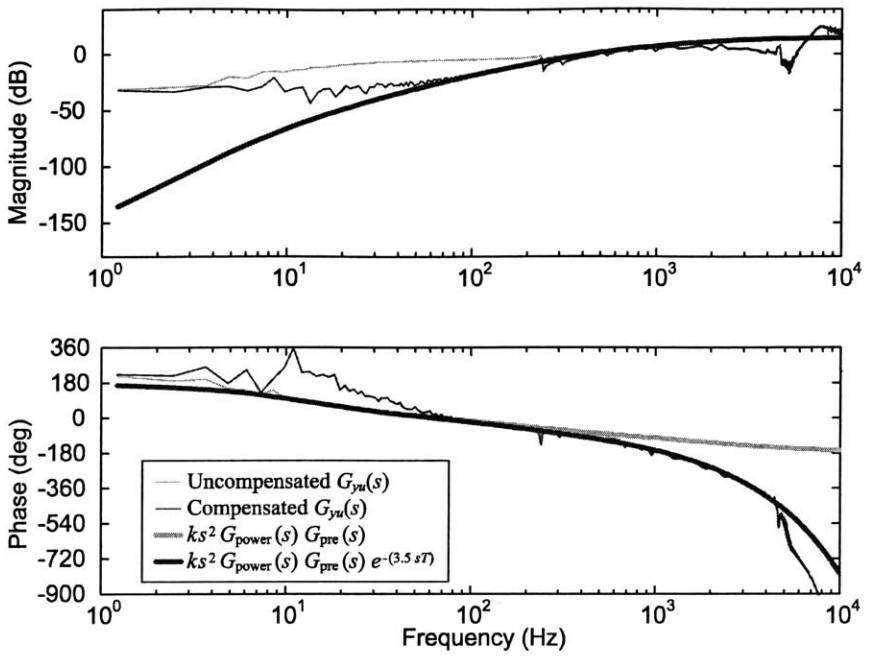

Figure 7-9: Uncompensated and compensated transfer function of panel G3.

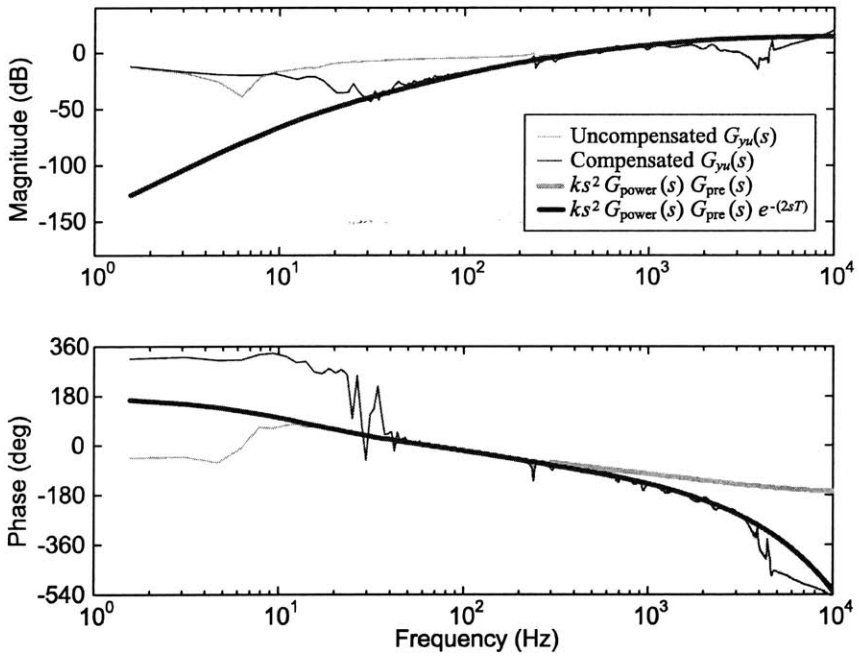

Figure 7-10: Transfer function of panel G3 measured using an external frequency analyzer.

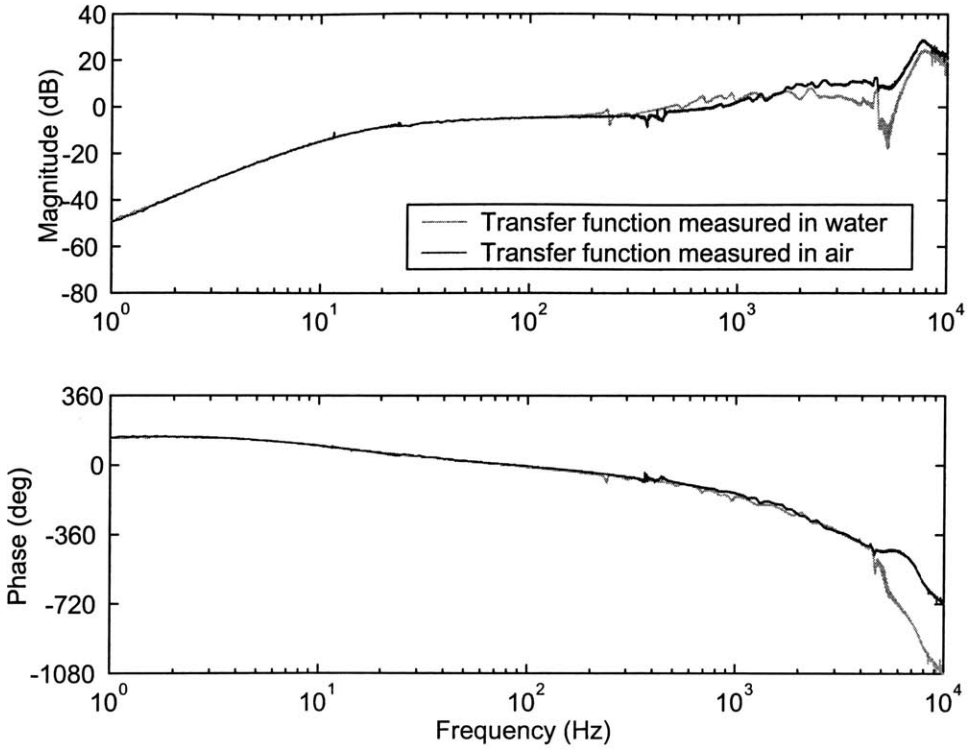

Figure 7-11: Comparison in time delay between transfer functions measured in air and in water.

was used to take transfer functions from D/A output to A/D input in Figure 7-6, *i.e.*, including the shell with 55 panels (plant) and analog electronics only, to see if the phase delay is caused by the plant or by the digital control system. The results are shown in Figure 7-10, where the same methods are used as in Figure 7-9 to represent each transfer function. Figure 7-10 indicates that the transfer function measured using an external frequency analyzer has a phase delay of 100 μs (=$2T$). Since the effective time delay in a digital control system is generally $1.5T$, assuming that the computation takes a full cycle, the result implies that the phase delay comes from the plant with analog electronics, not from the digital control system.

Once we determined that the phase delay does not originate from the DSP system, the transfer function of the panel was measured in air and compared with that measured in water, to see if the phase delay comes from the effect of water. Both transfer functions measured in air and in water are given in Figure 7-11. It is observed that they have very similar phase delay, which means that the effect of water does not cause the phase delay.

Finally, the transfer function of panel G3 was measured in air using an external accelerometer attached on the surface of the panel, to see if the phase delay is still there. In this case, the same power amplifier was used as the previous cases for the panel actuator layer. However, a different signal conditioner, not a pre-amplifier with a receiver board, was used for the external accelerometer in order to condition the output signal. The result is given in Figure 7-12, which shows that the phase delay still exists, but its amount is $2.5T$, not $3.5T$. Considering the time

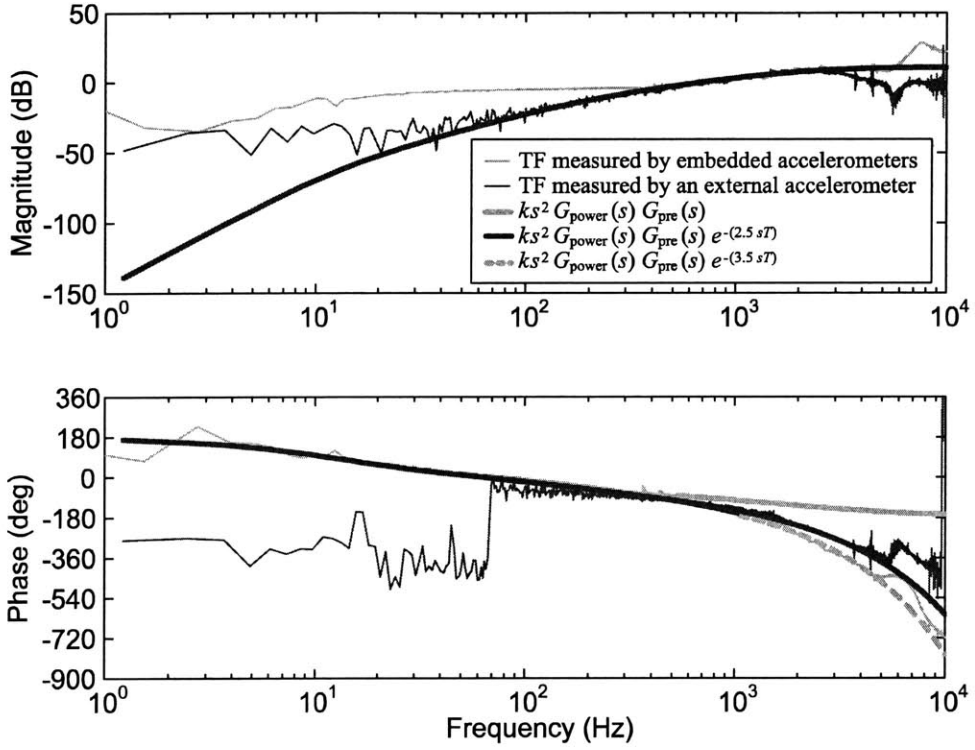

Figure 7-12: Frequency responses measured by embedded accelerometers and an external accelerometer.

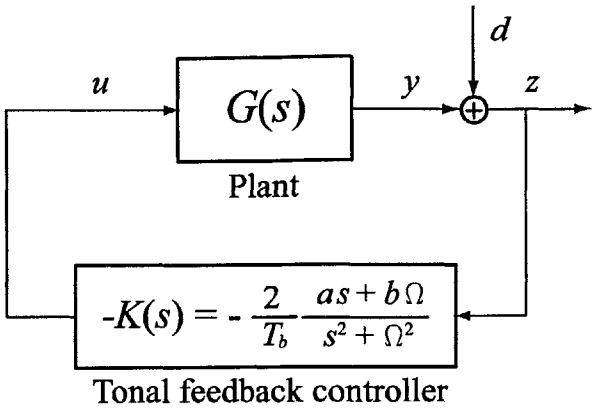

Figure 7-13: Block diagram of the tonal feedback controller.

delay of $1.5T$ in the digital system, we can conclude that the phase delay of 50 μs (=T) occurs in the power amplifier and the plant, while another 50 μs phase delay occurs in the plant and the pre-amplifier with a receiver board, due to unexplained reason.

7.4 Design and Implementation of Tonal Feedback Controllers

Based on the observations so far, it turned out that the implementation of 55 broadband feedback controllers was unfeasible. It is difficult to design multiple single-input single-output (SISO) controllers for a weakly diagonally dominant plant, even using sequential loop closure. Furthermore, a phase delay in the plant makes it almost impossible to design 55 SISO broadband feedback controllers. For example, the time delay of $2T$ in the plant causes an additional phase delay of 36° at 1 kHz, so the resulting phase margin would be unacceptable. Therefore, instead of broadband feedback controllers, multiple tonal feedback controllers were designed and implemented to reduce the vibration level of each panel at a selected target frequency.

A tonal feedback controller rejects a disturbance at selected target frequencies using high controller gains at those frequencies. A block diagram for the tonal feedback controller is shown in Figure 7-13. The constants in the controller are determined such that the control system has enough stability margins and controller bandwidth of ω_b at the target frequency $s = j\Omega$. The controller parameters are given as [Hall, 1989]

$$\begin{aligned} a &= \mathrm{Re}\left\{\frac{1}{G(j\Omega)}\right\} \\ b &= -\mathrm{Im}\left\{\frac{1}{G(j\Omega)}\right\} \\ T_b &\approx \frac{1}{\omega_b}. \end{aligned} \tag{7.1}$$

The amplification or attenuation of the disturbance by the closed-loop system is determined by

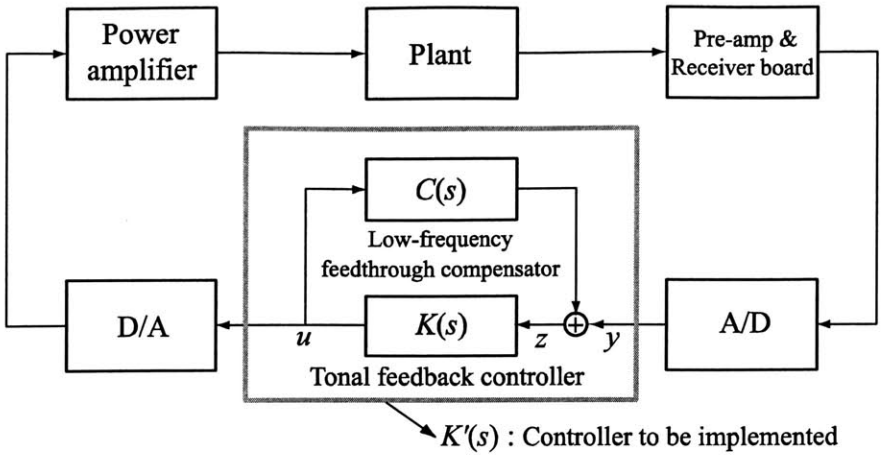

Figure 7-14: Design setup for the tonal feedback controller.

the sensitivity transfer function $S(s)$, given as

$$S(s) = \frac{z}{d} = \frac{1}{1 + G(s)K(s)} . \tag{7.2}$$

Since the controller $K(s)$ in Figure 7-13 has an infinite gain at the frequency $s = j\Omega$, $S(s)$ has a zero magnitude at that frequency. Therefore, the controller should completely eliminate vibration at the frequency $s = j\Omega$.

In order to apply the tonal feedback controller, the sensor used in the control system should be able to measure the performance variable z, which is what we want to reduce. The signal from the embedded accelerometers in the panel, however, is corrupted by the low-frequency feedthrough. If the target frequency is away from the range corrupted by the low-frequency feedthrough, its effect can be neglected, and we can design the tonal feedback controller as described above. However, if the bandwidth of interest is inside the range affected by the low-frequency feedthrough, it should be compensated before the controller is designed. Considering this fact, the design setup for the tonal feedback controller used in this chapter is given in Figure 7-14. Before designing the controller, a low-frequency feedthrough compensator $C(s)$ is designed and subtracted from the measured transfer function $G_{yu}(s)$, so that we can get the compensated transfer function $G_{zu}(s)$. Based on $G_{zu}(s)$, the tonal feedback controller $K(s)$ is designed such that the performance variable z is significantly reduced at the target frequency. However, since what we can measure directly is y, not z, the actual controller that should be implemented is not $K(s)$, but $K'(s)$, given as

$$K'(s) = \frac{K(s)}{1 - C(s)K(s)} . \tag{7.3}$$

Note that the low-frequency feedthrough effect not only complicates the controller design, but also makes the actual controller $K'(s)$ *unstable*. This can be explained using the simplified model for the plant in Figure 7-15. The actual transfer function $G_{yu}(s)$ can be modeled as

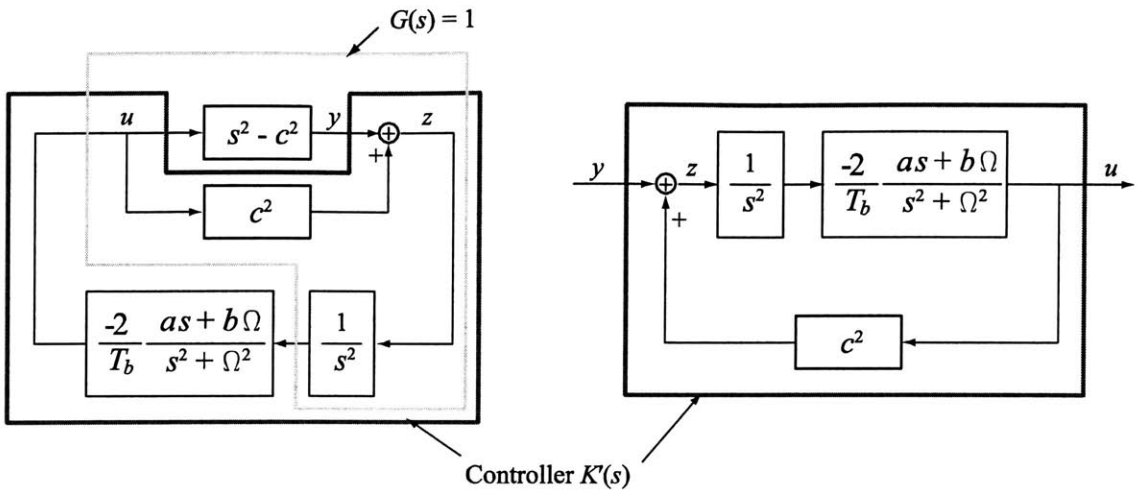

Figure 7-15: Simplified model for the plant showing that the actual controller $K'(s)$ is always unstable.

$s^2 - c^2$, where s^2 and c^2 correspond to the double differentiation (*i.e.*, acceleration) and the low-frequency feedthrough, respectively. We can compensate the plant by adding c^2 to $G_{yu}(s)$, so that we get pure acceleration s^2. After integrating twice to get displacement, we design a tonal feedback controller based on the plant $G(s) = 1$. Using Equation 7.1, we can compute a and b as

$$\begin{aligned} a &= \mathrm{Re}\left\{\frac{1}{G(j\Omega)}\right\} = 1\,, \\ b &= -\mathrm{Im}\left\{\frac{1}{G(j\Omega)}\right\} = 0\,. \end{aligned} \tag{7.4}$$

So, the tonal feedback controller $K(s)$ for $G_{zu}(s)$, including double integrators, can be written as

$$K(s) = \frac{2}{T_b} \cdot \frac{1}{s^2} \cdot \frac{s}{s^2 + \Omega^2}\,. \tag{7.5}$$

The actual controller $K'(s)$ to be implemented for the plant $G_{yu}(s) = s^2 - c^2$ is given as

$$\begin{aligned} K'(s) &= \frac{-K(s)}{1 + c^2 K(s)} \\ &= -\frac{2}{T_b} \frac{1}{s^3 + \Omega^2 s + \frac{2}{T_b} c^2}\,. \end{aligned} \tag{7.6}$$

We can easily check that $K'(s)$ is unstable. Although an unstable controller is used, the closed-loop system should be stabilized by the plant dynamics, if the controller is properly designed.

Now, the design process for tonal feedback controllers implemented on the shell with 55 panels is presented. The target frequency of the controllers was set to be 400 Hz. As mentioned

earlier, a low-frequency feedthrough compensator was designed for each panel, so that we can get the compensated transfer function and design the controller for each panel. Before using directly Equation 7.1 to design tonal feedback controllers, the plant transfer function was augmented by a high-pass filter at 200 Hz and two low-pass filters at 250 and 350 Hz, to make controller design easier by yielding a good loop shape. Figure 7-16 shows the effect of adding those filters on the resulting plant transfer function. Note that the transfer function in Figure 7-16(a) is $G_{zu}(s)$, not $G_{yu}(s)$. Before adding filters, the transfer function rolls up in the high frequency and shows a peak resonance around 9 kHz, which will consequently limit the achievable closed-loop performance by limiting the gain of the controller. However, by adding those filters to the plant, the transfer function will have a better loop shape, so that the tonal feedback controller at 400 Hz will yield better closed-loop performance. It should be noted that "$G(s)$" in Equation 7.1 represents the plant augmented with filters (Figure 7-16(b)), not the plant itself (Figure 7-16(a)).

The design procedure described above was iterated for 52 out of 55 panels, since the embedded accelerometers in three panels were faulty. Instead of designing a controller for each panel independently and closing all the loops simultaneously, controllers were designed by closing the loop sequentially to improve the stability and performance of the control system. In other words, after the first controller was implemented, the second controller was designed on the plant with the first controller closed. This procedure was iterated until the last controller was designed, so that the effect of closing the other loops on the plant could be considered when designing each controller.

In order to check the stability margin of the system before its implementation, the loop transfer function is examined in the frequency domain. Figures 7-17 and 7-18 show a Bode plot and a Nichols plot, respectively, of the loop transfer function for panel E3. Note that the loop transfer function in both figures is $G_{zu}(s)K(s)$, not $G_{yu}(s)K'(s)$. Also, the loop transfer function was obtained by closing the other 51 loops, and multiplying the resulting transfer function from u_{E3} to z_{E3} $[G_{z_{E3}u_{E3}}(s)]$ by $K(s)$ designed on $G_{z_{E3}u_{E3}}(s)$.

Although Bode plots and Nichols plots contain the same information about the control system, stability margins, such as gain margin and phase margin, can be more easily identified from Nichols plots. For example, the gain margin can be identified by measuring the distance of the contour to the critical point (-180°, 0 dB) when the phase is -180°, while the phase margin is the distance of the contour to the critical point when the magnitude is unity. As shown in Figures 7-17 and 7-18, the magnitude of the loop transfer function crosses the 0 dB line twice, which results in two different phase margins. Since the controller should assume the worst case, smaller phase margin should be considered as a proper stability margin. In this section, "the phase margin" represents the smaller phase margin among two different values. The gain margin and phase margin for the controller in Figure 7-18 are 30 dB and 90°, respectively. These stability margins may look too high, and we may want to increase the controller gain to improve the performance. However, these margins were selected considering the stability margins of other loops. Actually, increasing the gain for this controller may reduce the stability margins significantly for the other 51 loops. So, we should consider the stability margins for all the loops in the control system, not just one loop there. Gain and phase margins of the tonal feedback controllers for other panels are given in Table 7.1. We can see that the other 51 loops show the same order of gain margin and phase margin.

In addition to the stability margin, Nichols plot gives information about the level of atten-

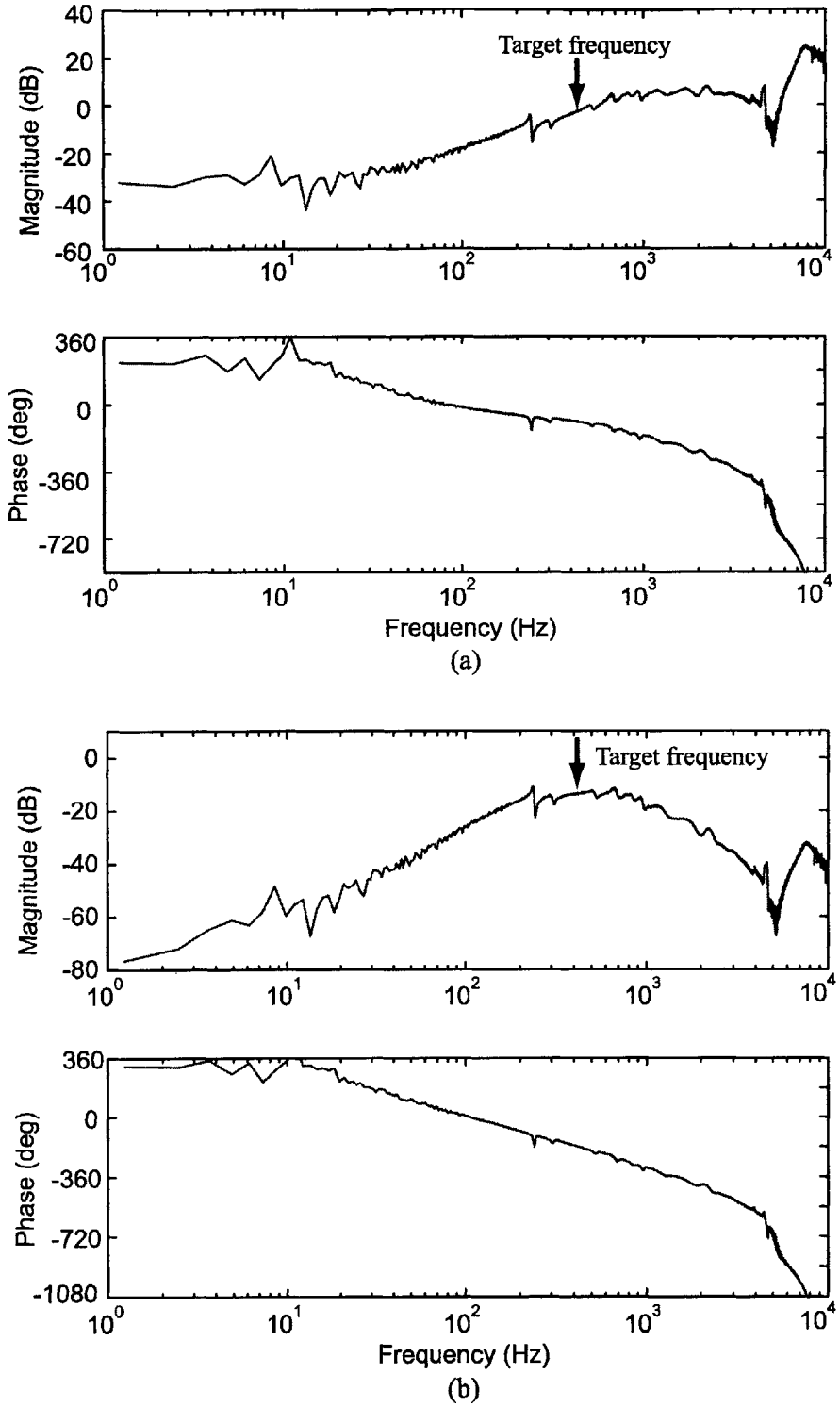

Figure 7-16: Effect of adding high and low-pass filters on the plant transfer function. (a) before adding filters, (b) after adding filters.

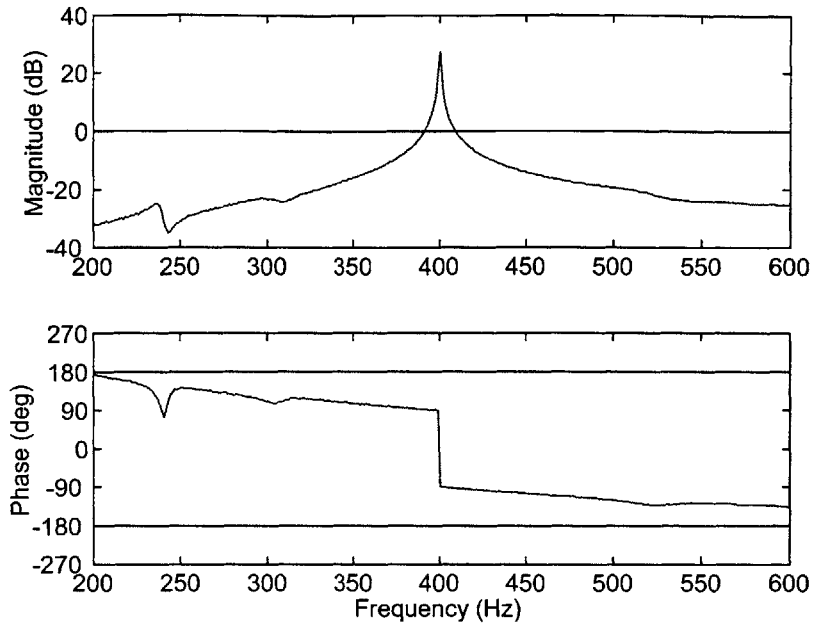

Figure 7-17: Bode plot of the loop transfer function of panel E3 for the tonal feedback controller.

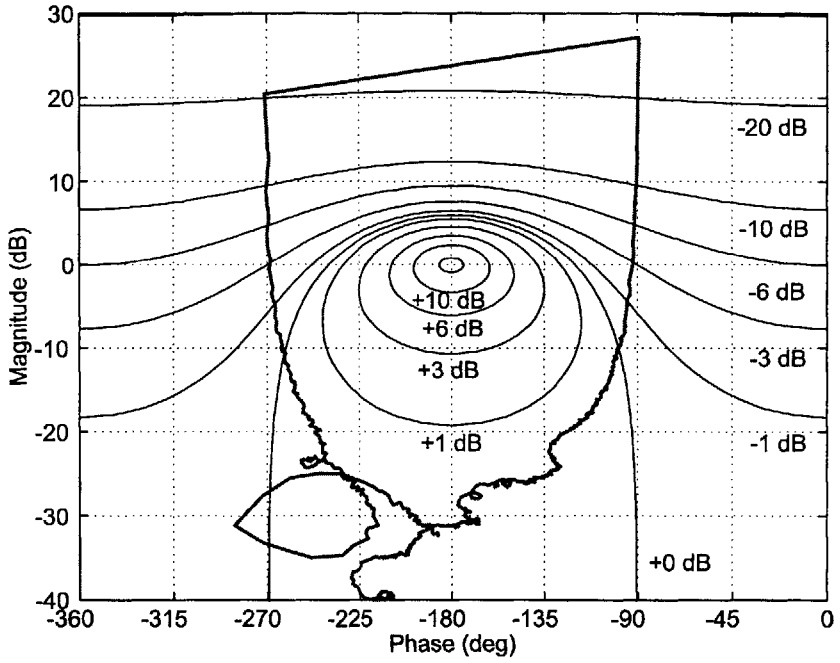

Figure 7-18: Nichols plot of the loop transfer function of panel E3 for the tonal feedback controller.

Table 7.1: Gain and phase margins of the tonal feedback controllers at each panel. The phase margin in this table represents the smaller phase margin among two different values. "×" represents the faulty accelerometers.

Panel	GM (dB)	PM (deg)	Panel	GM (dB)	PM (deg)	Panel	GM (dB)	PM (deg)
A1	29	81	E1	29	83	I1	29	80
A2	29	78	E2	29	78	I2	30	79
A3	29	87	E3	30	88	I3	28	87
A4	28	77	E4	28	76	I4	28	77
A5	30	80	E5	30	82	I5	29	85
B1	29	80	F1	29	80	J1	30	82
B2	30	73	F2	29	77	J2	29	79
B3	29	88	F3	×	×	J3	29	86
B4	28	76	F4	25	74	J4	29	80
B5	28	82	F5	30	85	J5	30	87
C1	30	82	G1	25	75	K1	29	85
C2	30	78	G2	28	70	K2	29	78
C3	28	87	G3	27	86	K3	28	87
C4	28	75	G4	29	85	K4	23	83
C5	30	85	G5	29	80	K5	×	×
D1	30	78	H1	29	82			
D2	30	79	H2	24	78			
D3	29	87	H3	29	87			
D4	30	83	H4	22	77			
D5	30	80	H5	×	×			

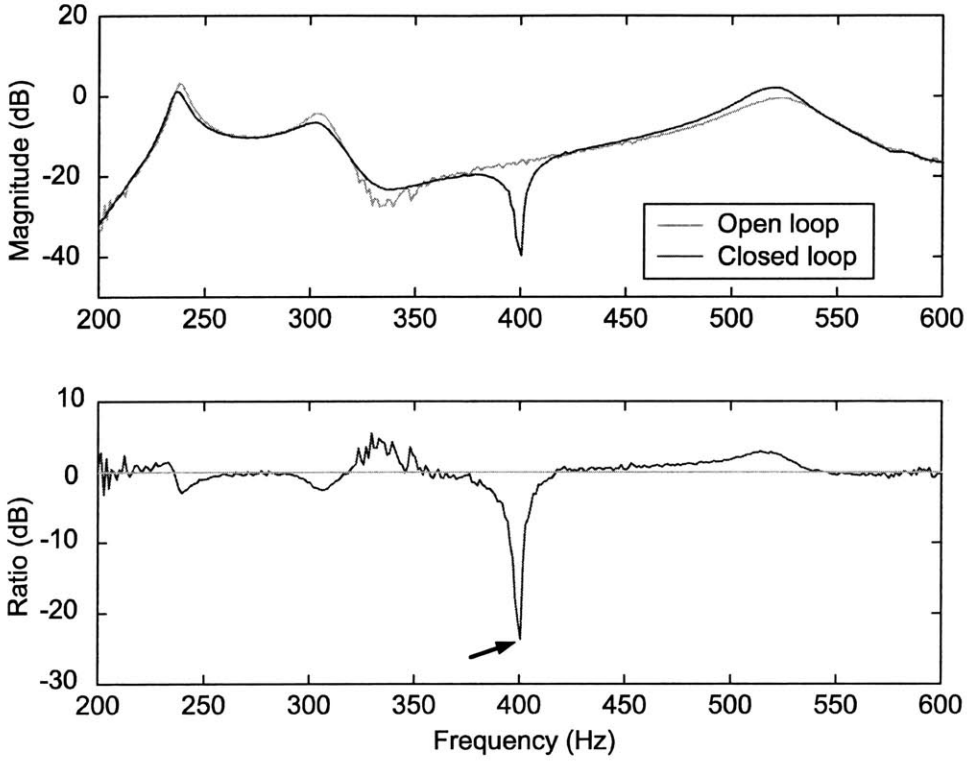

Figure 7-19: Open and closed-loop responses of compensated acceleration of panel E3 for the tonal feedback controller at 400 Hz. "Ratio" represents the ratio of the open-loop response to the closed-loop response. Negative ratios indicate attenuation; positive ratios indicate amplification.

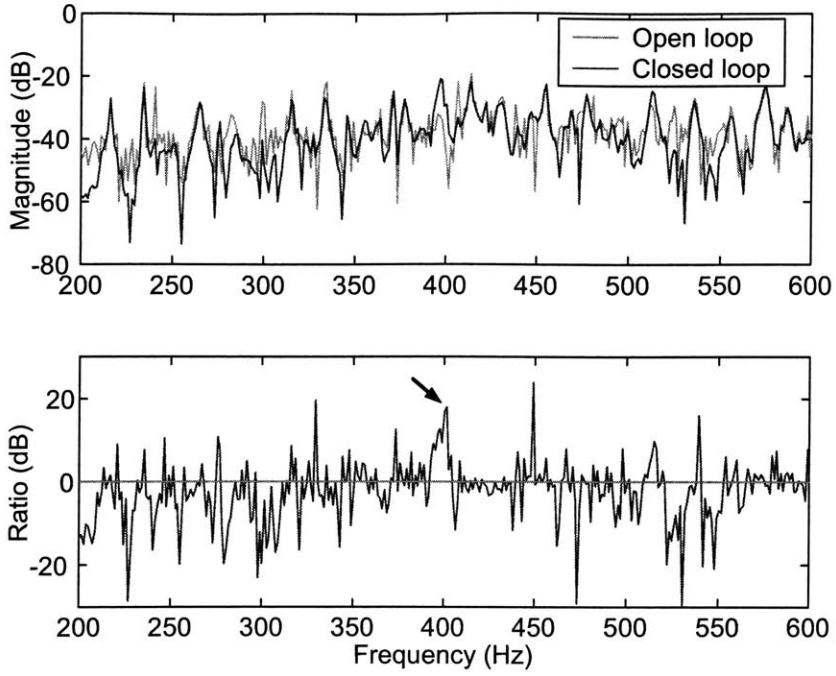

Figure 7-20: Open and closed-loop response of hydrophone 4 for the tonal feedback controller at 400 Hz. Negative ratios indicate attenuation; positive ratios indicate amplification.

uation or amplification of the disturbance. In Figure 7-18, contours of constant disturbance attenuation or amplification, which is the sensitivity transfer function $S(s)$ in Equation 7.2, are also plotted. Positive and negative values in the contours represent the amplification and attenuation of disturbance, respectively. Figure 7-18 indicates that the system also has a good closed-loop performance at the target frequency 400 Hz, with at least 20 dB of reduction. The actual closed-loop response, which was obtained using the controller in Figure 7-17 and 7-18, was measured, and is shown in Figure 7-19. The upper plot in Figure 7-19 shows both open-loop and closed-loop compensated acceleration for panel E3, and the lower one shows their ratio. Note that the negative and positive ratio mean the attenuation and the amplification of the disturbance, respectively. Figure 7-19 demonstrates that an attenuation of more than 20 dB is achieved at 400 Hz. The level of performance achieved using the tonal feedback controllers for other panels is given in Table 7.2. Controllers for other panels show the similar closed-loop performance, *i.e.*, about 20 dB of reduction at 400 Hz. Considering that all the 52 controllers implemented are unstable, the implementation of control systems and its performance is a remarkable success.

Since the compensated acceleration is reduced by 20 dB for most panels (52 out of 55) at 400 Hz, it is natural that we can expect the similar level of reduction for the hydrophone signal. Figure 7-20 shows both open-loop and closed-loop responses measured by the hydrophone 4. In contrast to the expectations, the actual closed-loop signal for hydrophone 4 was amplified by 15 dB at 400 Hz. The level of amplification for other hydrophones is given in Table 7.3.

Table 7.2: The level of performance achieved using the tonal feedback controllers at 400 Hz. "×" represents the faulty accelerometers. Note that positive performance ratios indicate attenuation.

Panel	Performance (dB)	Panel	Performance (dB)	Panel	Performance (dB)
A1	28.5	E1	25.9	I1	15.5
A2	23.8	E2	21.2	I2	17.8
A3	22.9	E3	23.7	I3	14.6
A4	24.6	E4	22.9	I4	19.0
A5	32.7	E5	30.9	I5	20.8
B1	18.4	F1	26.6	J1	21.7
B2	21.5	F2	16.6	J2	22.6
B3	21.5	F3	×	J3	22.9
B4	22.2	F4	17.3	J4	21.6
B5	20.5	F5	20.3	J5	21.2
C1	19.5	G1	28.9	K1	27.8
C2	17.1	G2	20.2	K2	20.5
C3	17.6	G3	20.2	K3	20.1
C4	17.5	G4	21.7	K4	17.3
C5	14.0	G5	21.8	K5	×
D1	20.6	H1	18.5		
D2	18.4	H2	26.8		
D3	18.1	H3	22.3		
D4	19.7	H4	19.8		
D5	19.0	H5	×		

Table 7.3: The level of amplification for each hydrophone.

Hydrophone No.	Amplification level (dB)
1	12.9
2	10.5
3	8.9
4	18.4
5	6.2
6	14.8

The other five hydrophones show similar amplification level (6–20 dB). Obviously, this result is unexpected, and unacceptable. In the next section, we investigate the cause for this result.

7.5 Investigation of Panel Dynamics

Using the tonal feedback controllers implemented in the previous section, we could reduce the compensated acceleration over the surface of the shell by 20 dB at 400 Hz. However, the comparison between open-loop and closed-loop hydrophone signal indicates that the actual noise is increased at that frequency. Several tests were performed to figure out what causes the unexpected result. In this section, the results of testing and investigating panel dynamics are reported. As will be shown, the main problem is that the internal accelerometers do not accurately measure the motion of the panel's outer surface, which is what they are supposed to measure.

7.5.1 Acceleration Survey of a Panel Using Four External Accelerometers

As discussed in Chapter 2, there are four internal accelerometers embedded on the top surface of each active composite panel, and the output from each accelerometer is summed to yield the averaged acceleration of the panel's outer surface. In order to investigate whether the internal accelerometers measure the surface motion, four external accelerometers were attached on top of the internal accelerometers, and the output of the two different accelerometers were compared (Figure 7-21). Signals from four external accelerometers were averaged, as in the case for internal accelerometers. The results are shown in Figure 7-22. First, the shaker inside the shell was driven to take transfer functions for internal and external accelerometers, and their sensitivities were adjusted such that they could be overplotted (Figure 7-22(a)). Then, the actuator layer in the panel was driven and transfer functions for both accelerometers were compared (Figure 7-22(b)).

Figure 7-22(a) shows that the internal accelerometers yield very similar transfer functions as the external accelerometers when the shaker was driven. In this case, the panel moves as a rigid body, so both accelerometers would yield the same measurement below the resonant frequency for the internal accelerometer mode. However, Figure 7-22(b) indicates that there is about 10 dB difference between transfer functions measured by internal and external accelerometers for panel excitation, although the same sensitivities are used for both accelerometers as in the case of shaker excitation. What this result implies is that the internal accelerometers measure

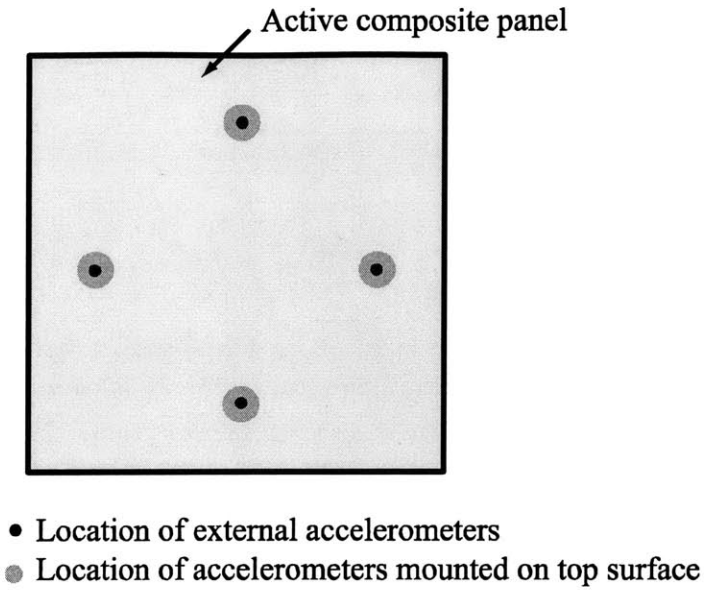

Figure 7-21: Acceleration survey using four external accelerometers.

only about 30% of the actual motion of the panel's outer surface when the panel excitation causes the motion. What causes this problem, and how it affects the closed-loop performance, will be addressed in the following sections.

7.5.2 Laser Scanning Vibrometer Test of a Suspended Panel

In order to investigate the panel dynamics in detail, a laser scanning vibrometer was used to measure a panel's deformed shape due to self-excitation. The experimental setup is shown in Figure 7-23. An active composite panel is suspended from two sticks and the velocity field on both top and bottom surfaces of the panel is measured by driving the actuator layer in the panel and scanning the velocity over its surfaces. The results of laser scanning vibrometer test of a panel are shown in Figure 7-24. Note that the velocity field measured by the laser scanning vibrometer is different on the top and bottom surfaces, because an aluminum plate was mounted only on the top surface.

Figure 7-24 indicates that the panel is deformed irregularly when its actuator layer is driven. This could be partly because the piezoelectric constant in the actuator layer is not uniform over the surface. Also, the bending that occurred during panel's self-excitation could be another reason for its irregular deformed shape. Although it would be best if the panel moves in a piston-mode for self-excitation, it would still be feasible to design control system for reducing radiated noise with this panel if the internal accelerometers would provide information about the panel's net volume change. However, Figure 7-24 shows that there are dimples inside the panel where the internal accelerometers are mounted. The dimples can be seen more easily from the bottom surface than from the top surface, because those on the top surface are hidden by the aluminum plate. The dimples may explain why the internal accelerometers measure only

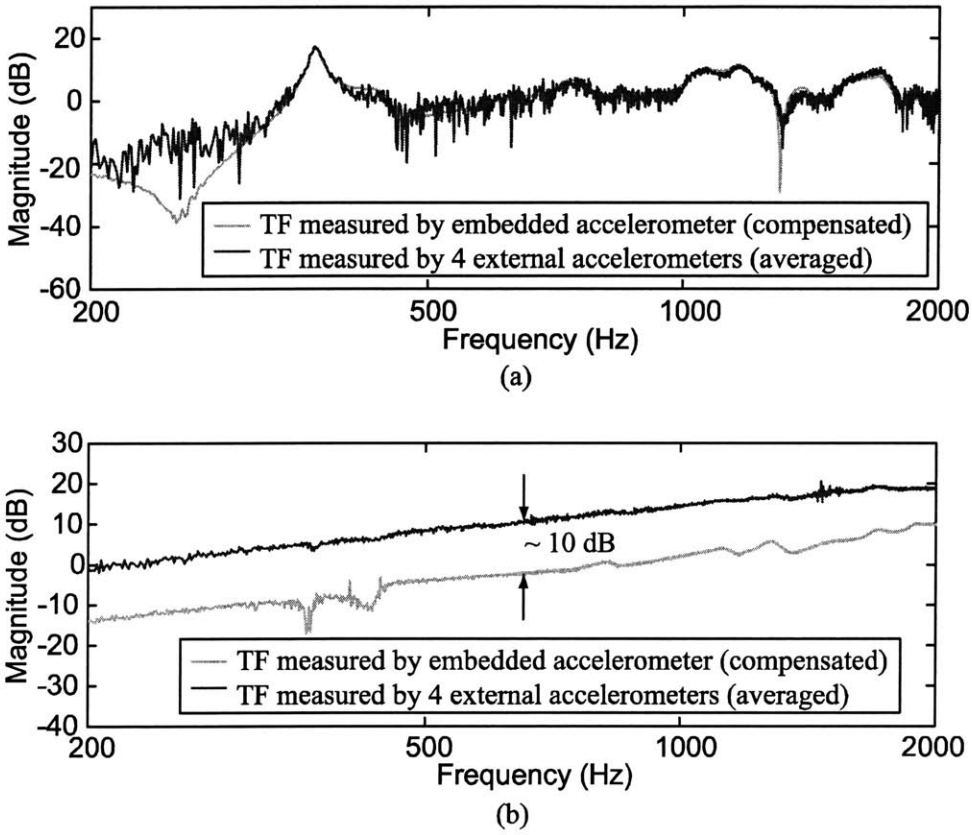

Figure 7-22: Transfer functions measured by embedded and external accelerometers. (a) shaker excitation, (b) panel excitation.

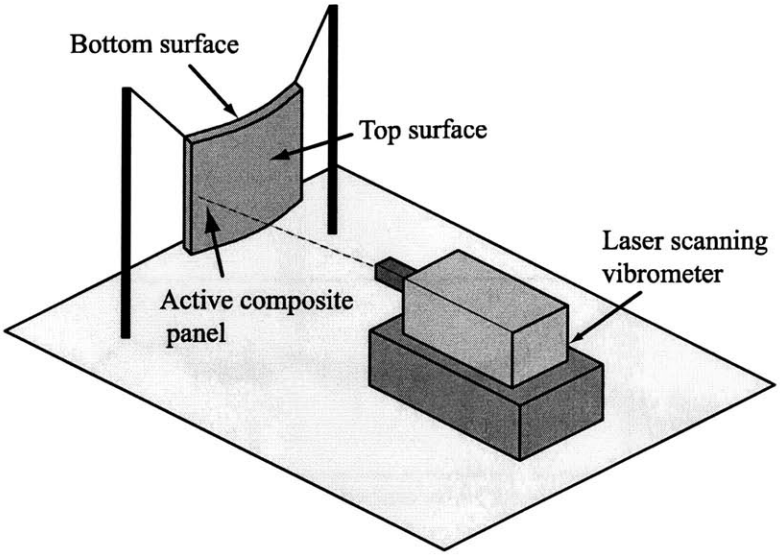

Figure 7-23: Experimental setup for testing a suspended panel using a laser scanning vibrometer.

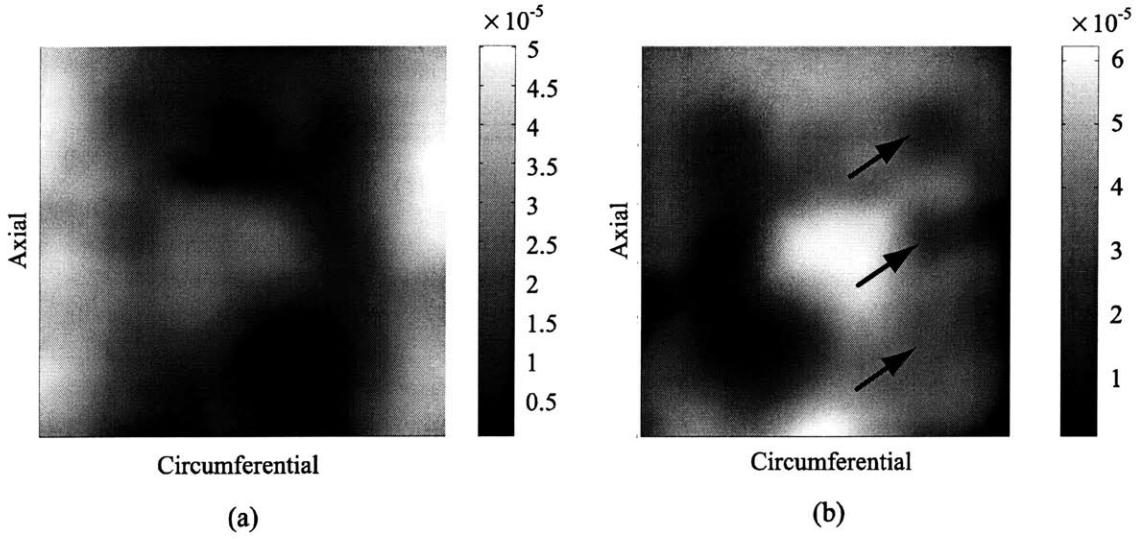

Figure 7-24: Panel deformed shape at 400 Hz. (a) top surface, (b) bottom surface.

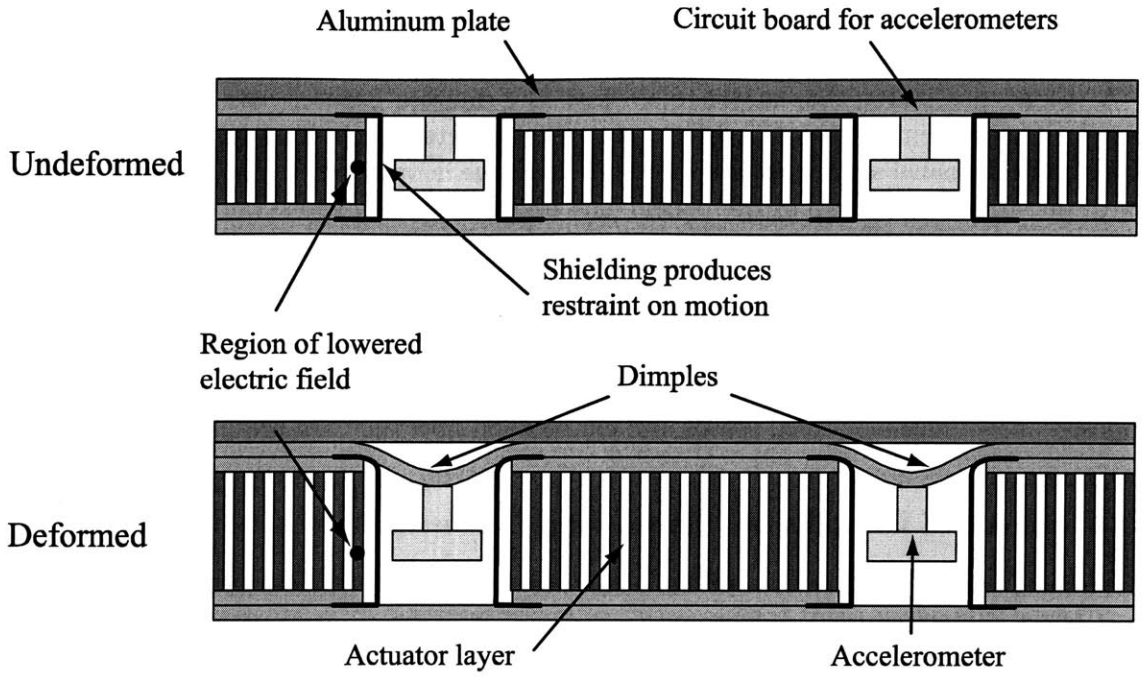

Figure 7-25: Possible panel deformed shape.

about 30% of the actual motion of the panel's outer surface for panel excitation. The dimples don't appear for external excitation, *i.e.*, shaker excitation, because the whole panel moves as a rigid body. However, for panel excitation, the panel is deformed due to the actuator layer and the dimples prevent the internal accelerometers from measuring the panel's outer surface motion.

The dimples also explain why the measured plant transfer function matrix is weakly diagonally dominant. As mentioned in Section 7.3.1, increased panel weight makes the interaction between panels significant, which is one reason for weakly diagonally dominant plant. However, if the internal accelerometers could measure panel's outer surface motion accurately, the diagonal terms in the plant transfer function matrix would be increased by 10 dB, which would make design of multiple SISO feedback controllers much easier.

7.5.3 Hypotheses to Explain the Panel Dynamics

Although we found that there are dimples inside the panel where the internal accelerometers are mounted and they cause the measured acceleration different from the actual acceleration by 10 dB for self-excitation, it still remains to explain why they occur. There is no decisive way to answer that question without further investigation. However, two hypotheses are proposed here that can explain physically how they occur for self-excitation. The basic concept of the first hypothesis is shown in Figure 7-25. As shown in the figure, copper shielding was inserted between internal accelerometers and PZT actuator layer to reduce the electric coupling between them. The hypothesis is that the copper shielding would be stiff enough to produce restraint

on motion near the internal accelerometers for self-excitation. Also, when PZT actuator layer is driven for self-excitation, the electric field could be lowered by the shielding near internal accelerometers compared with other regions, which would reduce the displacement near them.

A second possibility that may explain how the dimples occur is the hoop stress. When the actuator layer in the panel is driven, the panel is extended in its thickness direction. The extension in the panel's thickness direction produces the hoop stress in the accelerometer circuit board, due to the curvature of the panel. The hoop stress may cause the dimples around the cavity near the internal accelerometers, which are mounted on the circuit board, because the circuit board is more compliant than the aluminum plate. The effect of the hoop stress becomes significant if the panel is rigidly mounted on the surface of the shell.

As mentioned earlier, there is no clear answer to explain why the dimples occur before the panel is taken apart and examined in detail. However, it is believed that the hypothesis proposed above makes physical senses and can explain how they are produced.

7.5.4 Effect of Dimples on Closed-loop Performance

A simplified model of the shell with the panel was proposed to explain how the dimples in the panel affect the closed-loop performance. Figure 7-26 shows a shell with mass of M_s and a panel with mass of M_p, which are excited by a disturbance force f. The acceleration of the shell's outer surface and the panel's outer surface are denoted as a and z, respectively, while the relative acceleration due to the panel actuation is denoted by u.

Before the control input is applied, *i.e.*, $u = 0$, z and a can be written as

$$\begin{aligned} z &= \frac{f}{M_s + M_p}\,, \\ a &= \frac{f}{M_s + M_p}\,. \end{aligned} \tag{7.7}$$

After the controller is turned on ($u \neq 0$), the system equation can be expressed as

$$\begin{aligned} f &= (M_s + M_p)\, a + \frac{1}{2} M_p\, u \\ z &= a + u\,. \end{aligned} \tag{7.8}$$

Now, we assume that the internal accelerometer embedded in the panel gives an output y as

$$y = a + \alpha u\,. \tag{7.9}$$

Here, α is a factor that accounts for the difference between the measured acceleration y and the actual acceleration z. If $\alpha = 1$, the internal accelerometers measure the actual acceleration for self-excitation. On the other hand, if there are dimples inside the panel, α would be less than 1. Specifically, if there is about a 10 dB difference between the measured and actual acceleration for self-excitation as in Figure 7-22, α would be about $\frac{1}{3}$.

If the controller is designed such that the measured acceleration y is *exactly* cancelled, *i.e.*, u is chosen as

$$u = -\frac{a}{\alpha}\,, \tag{7.10}$$

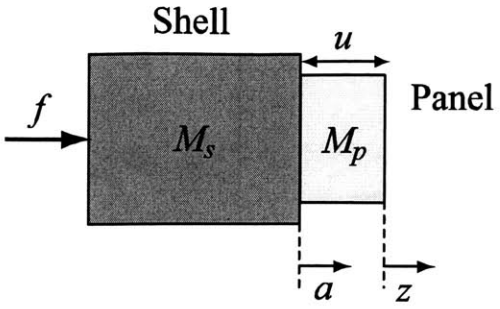

Figure 7-26: Simplified model for the shell with the panel.

then the closed-loop responses a and z can be computed using Equation 7.8, which yields

$$\begin{aligned} a &= \frac{f}{M_s + \left(1 - \frac{1}{2\alpha}\right) M_p}, \\ z &= \left(1 - \frac{1}{\alpha}\right) a \\ &= \frac{f}{M_s + M_p} \cdot \frac{\left(1 - \frac{1}{\alpha}\right)(M_s + M_p)}{M_s + \left(1 - \frac{1}{2\alpha}\right) M_p}. \end{aligned} \tag{7.11}$$

Comparing Equation 7.7 with Equation 7.11, we can find the ratio of open-loop (OL) and closed-loop (CL) a and z as

$$\begin{aligned} \frac{a_{\mathrm{CL}}}{a_{\mathrm{OL}}} &= \frac{1 + \frac{M_p}{M_s}}{1 + \left(1 - \frac{1}{2\alpha}\right) \frac{M_p}{M_s}}, \\ \frac{z_{\mathrm{CL}}}{z_{\mathrm{OL}}} &= \frac{\left(1 - \frac{1}{\alpha}\right)\left(1 + \frac{M_p}{M_s}\right)}{1 + \left(1 - \frac{1}{2\alpha}\right) \frac{M_p}{M_s}}. \end{aligned} \tag{7.12}$$

Figure 7-27 shows the magnitude of ratio $\frac{a_{\mathrm{CL}}}{a_{\mathrm{OL}}}$ and $\frac{z_{\mathrm{CL}}}{z_{\mathrm{OL}}}$ as α varies from 0 to 1 for $\frac{M_p}{M_s} = 1$. Note that M_p represents the total mass of 55 panels mounted on the shell, which is similar to the mass of the shell. For $\alpha = 1$, the closed-loop z is exactly cancelled as expected, while the closed-loop a is increased by $\frac{4}{3}$ (= 2.5 dB). However, for $\alpha = \frac{1}{3}$, *i.e.*, the internal accelerometers measure only 30% of the actual acceleration for self-excitation, the closed-loop z is *increased* by 18 dB, and the closed-loop a is increased by 12 dB. What this result implies is that the actual

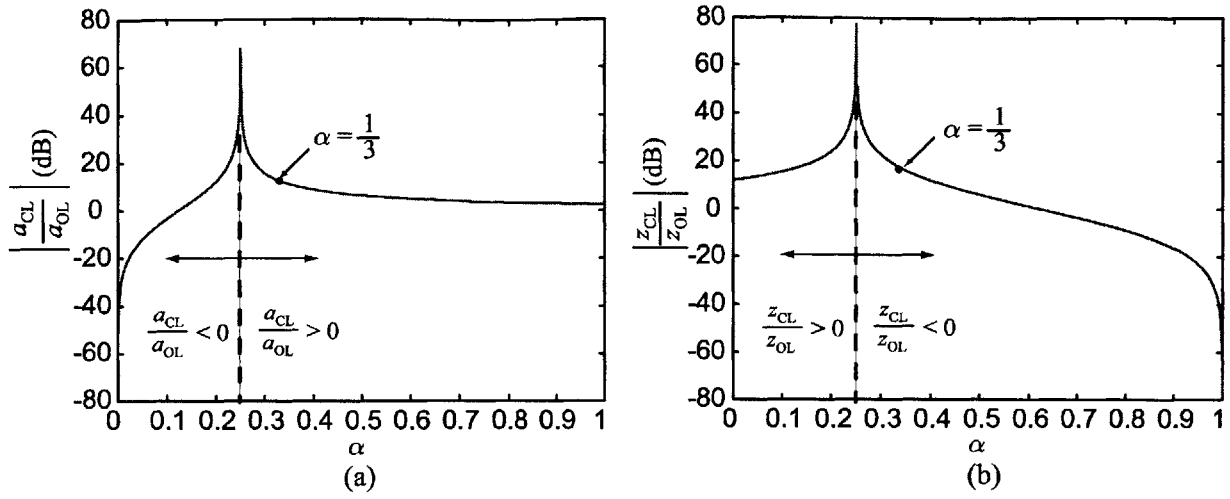

Figure 7-27: Ratio of open-loop and closed-loop a and z. (a) $\left|\frac{a_{CL}}{a_{OL}}\right|$, (b) $\left|\frac{z_{CL}}{z_{OL}}\right|$.

acceleration may be increased if there are dimples inside the panel and we design controllers reducing the measured acceleration with an objective of attenuating the actual acceleration. Also, note that the closed-loop response z_{CL} becomes out of phase with the open-loop response z_{OL}, if α is greater than $\frac{1}{2}\left(\frac{M_p}{M_p+M_s}\right)$, which is 0.25 in this case ($\frac{M_p}{M_s}=1$).

In order to see whether the bottom acceleration level was increased due to controllers, which should be true if there are dimples in the panel, the open-loop and closed-loop bottom acceleration was compared. Figure 7-28 shows both open-loop and closed-loop bottom acceleration (upper plot) and their ratio (lower plot) for panel H3. It demonstrates that the closed-loop bottom acceleration is amplified by 15 dB at 400 Hz, which is similar to the results in Figure 7-27. The level of amplification using the tonal feedback controllers for other panels are given in Table 7.4. Most panels show the level of amplification 10–20 dB, except for panels E2 and E3. This implies that the internal accelerometers in most panels do not measure the actual acceleration over their surfaces for self-excitation.

7.5.5 Simulated Closed-loop Responses Using Tonal Feedback Controller

The closed-loop acceleration was simulated using eight external accelerometers attached on a panel, to see how the actual acceleration over the surface of the panel behaves when the controller is operating. Figure 7-29 shows the location and number of eight external accelerometers mounted on the surface of the panel. The tonal feedback controller was designed in the same way as in Section 7.4, such that the closed-loop response measured by internal accelerometer was reduced by more than 20 dB at 400 Hz. Then, the closed-loop responses measured by eight external accelerometers on the top surface of the panel were simulated. Figure 7-30(a) and (b) show open-loop and closed-loop responses over the surface of the panel at 400 Hz, respectively, while Figure 7-30(c) shows their ratio in dB scale. Note that the positive ratio represents the amplification of the disturbance. As expected from the results in Section 7.5.4, the actual accel-

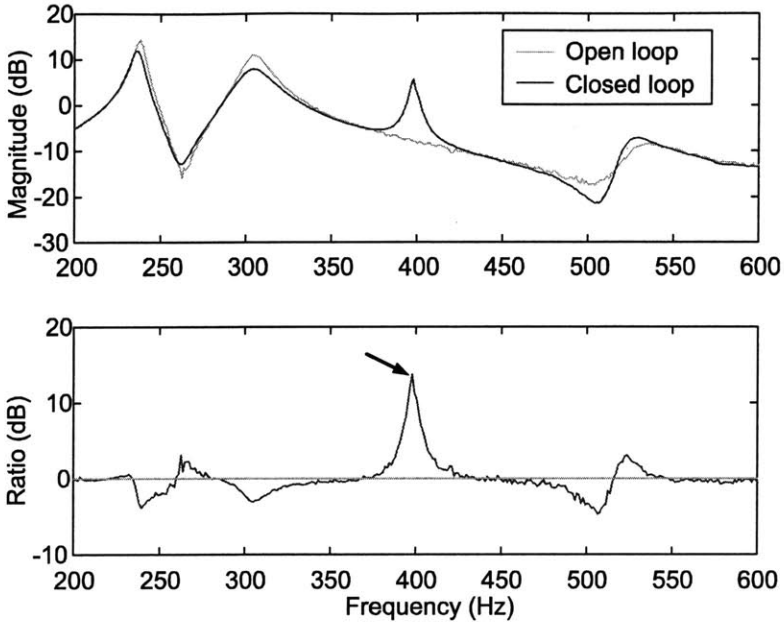

Figure 7-28: Open and closed-loop responses of bottom acceleration of panel E3 for the tonal feedback controller at 400 Hz.

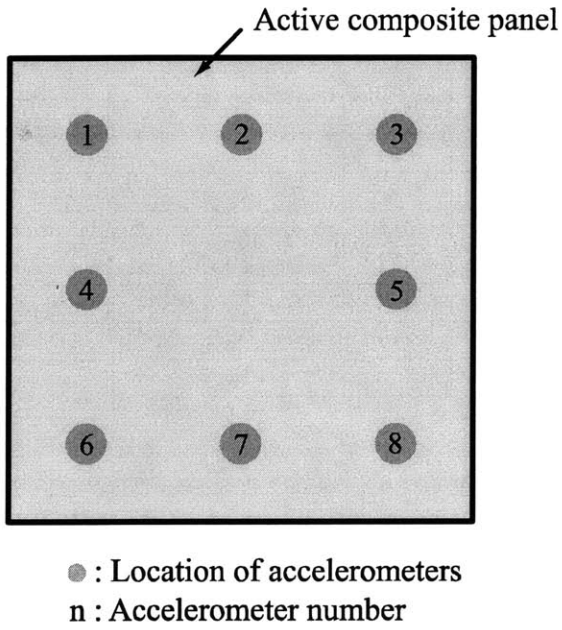

Figure 7-29: Acceleration survey using eight external accelerometers.

Table 7.4: The level of amplification for bottom accelerations using the tonal feedback controllers at 400 Hz.

Panel	Amplification level(dB)	Panel	Amplification level(dB)	Panel	Amplification level(dB)
A1	9.9	E1	5.4	I1	10.4
A2	12.0	E2	1.9	I2	12.0
A3	14.5	E3	1.4	I3	11.4
A4	11.6	E4	4.4	I4	9.1
A5	10.4	E5	6.6	I5	15.6
B1	12.8	F1	8.3	J1	13.7
B2	12.2	F2	12.2	J2	8.5
B3	9.2	F3	24.0	J3	9.0
B4	11.5	F4	11.0	J4	9.9
B5	14.6	F5	7.4	J5	10.9
C1	10.9	G1	6.2	K1	13.6
C2	12.7	G2	8.7	K2	17.3
C3	11.6	G3	10.4	K3	20.4
C4	11.8	G4	7.1	K4	16.1
C5	17.0	G5	12.3	K5	11.1
D1	12.0	H1	10.7		
D2	11.3	H2	10.0		
D3	10.0	H3	11.3		
D4	12.9	H4	8.5		
D5	9.7	H5	11.4		

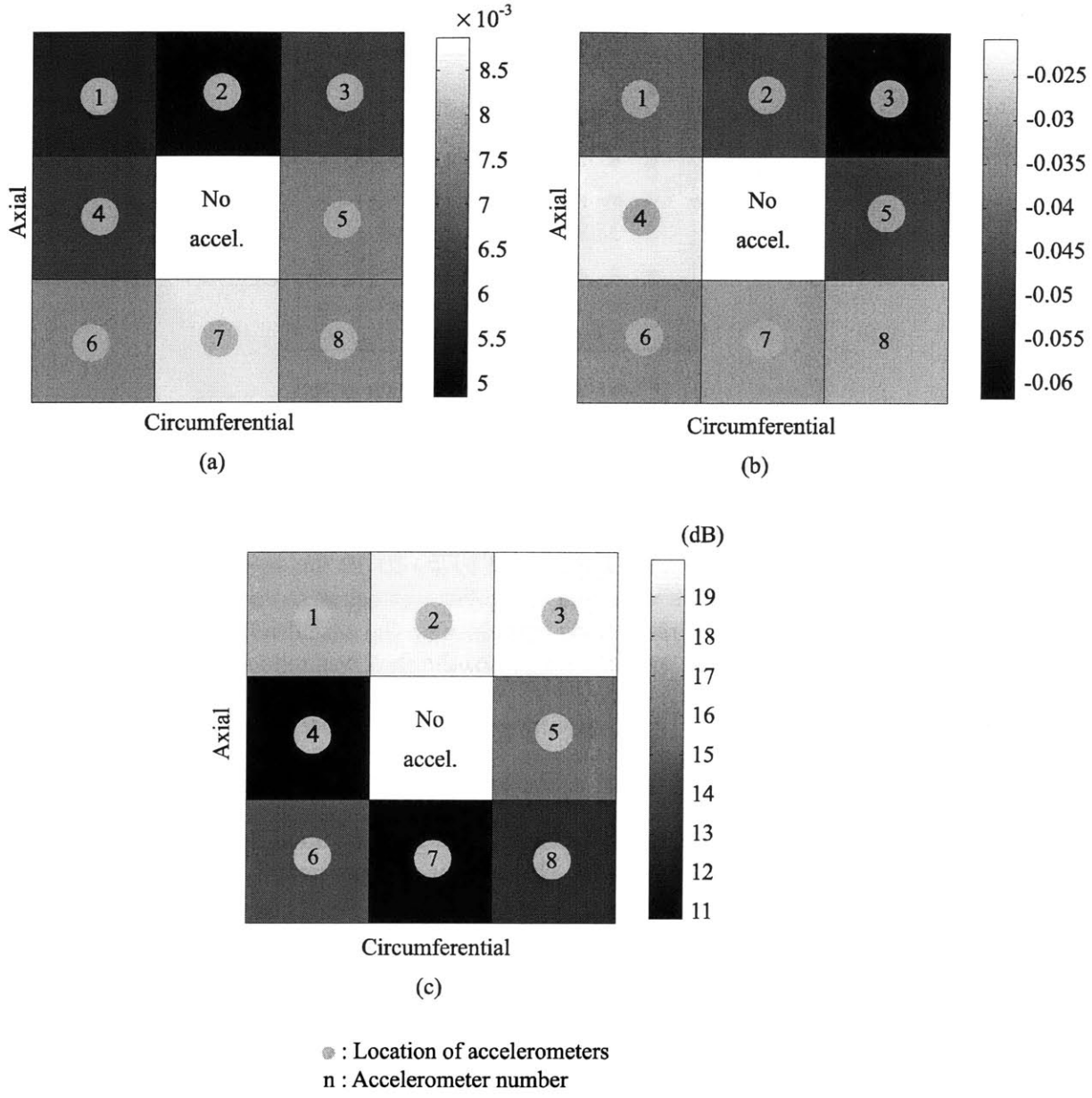

Figure 7-30: Simulated closed-loop acceleration over the surface of panel G3 using the tonal feedback controller at 400 Hz. (a) open-loop response, (b) closed-loop response, and (c) level of amplification in dB scale.

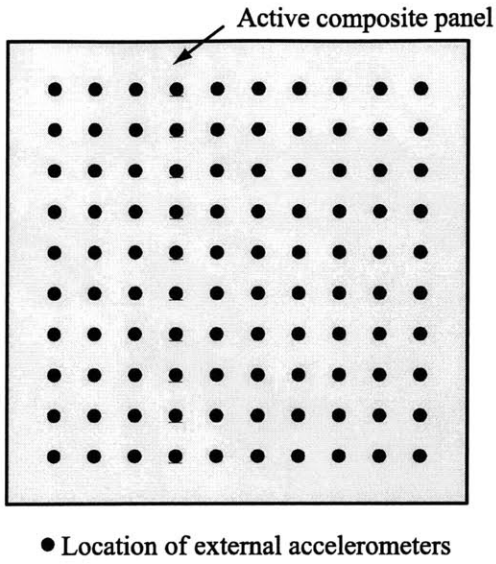

Figure 7-31: Acceleration survey using 100 external accelerometers.

eration over the surface of panel was increased by 10–20 dB due to the controller, although the internal acceleration, which is what the controller was asked to reduce, was reduced by more than 20 dB. This simulation result may explain why the actual noise was amplified, although the compensated acceleration over the surface of the shell was reduced using the tonal feedback controllers.

7.5.6 Acceleration Survey of a Panel Using 100 External Accelerometers

In Section 7.5.2, a laser scanning vibrometer was used to measure the deformed shape of a suspended panel due to self-excitation. However, it was necessary to investigate the dynamics of panels mounted on the shell in order to see how panels behave for self-excitation on the shell. Unfortunately, the laser scanning vibrometer couldn't be used in this case, because it could not be transported to the NGC facility. Instead, 100 external accelerometers were attached on the top surface of panel E3 on the shell (Figure 7-31), and its deformed shape was measured by driving the actuator layer in the panel. The result is shown in Figure 7-32. As mentioned in Section 7.5.2, the dimples are not clear, due to the aluminum plate on the panel. However, Figure 7-32 indicates that there is another serious problem in the panels. For self-excitation, the upper-left part and upper-middle part of panel E3 move *out of phase* with other parts in the panel. The result implies that some bristle blocks in the panel actuator layer were poled backwards. The effect of the incorrectly-poled bristle blocks in the panels on the closed-loop performance has not been explored in this study; it would depend on how many panels have those bristle blocks and how many backward bristle blocks those panels have. However, it is clear that they would make the closed-loop performance worse in terms of the hydrophone signal.

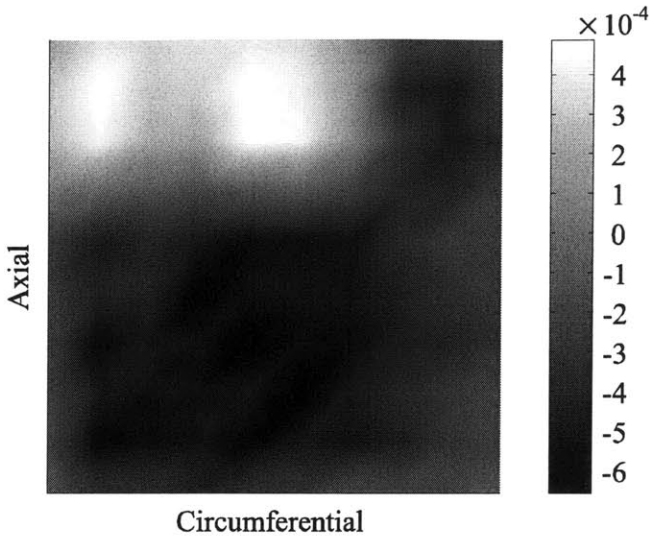

Figure 7-32: Deformed shape of Panel E3 at 400 Hz.

7.6 Summary

In this chapter, the results of closed-loop experiments obtained with multiple SISO controllers were reported. Tonal feedback controllers were chosen as SISO controller scheme, rather than broadband feedback controllers, due to the excessive time delay and significant interaction between panels. The low-frequency feedthrough effect was compensated for during the controller design, resulting in unstable controllers. 52 tonal feedback controllers, all of which were unstable themselves, were successfully designed and implemented. The compensated acceleration measured by internal accelerometers was reduced by 20 dB at 400 Hz over the surface of the shell. However, the actual noise level measured by six hydrophones was found to be increased. After performing several tests to figure out why, it turned out that there are several serious problems in the panels, including irregular deformed shape for self-excitation and backwards bristle blocks. The main problem, however, is that the internal accelerometers embedded in the panel cannot measure the actual acceleration, primarily due to the dimples that occur during self-excitation. The effect on the closed-loop performance was explored, and the result is that it seriously deteriorates the closed-loop performance. For example, when the internal accelerometer measures 30% of the actual acceleration for self-excitation and controllers are designed to cancel the measured acceleration, the simple model indicates that the actual acceleration is increased by 18 dB. This result was verified by the control simulation on a panel on which eight external accelerometers were attached. Through the investigation, it is believed that the main reason for the increased noise level is the dimpling that occur during self-excitation, which prevents the internal accelerometers from measuring the actual acceleration. However, it still remains to determine definitively why the dimpling occurs.

Chapter 8

Conclusions and Recommendations

8.1 Summary and Conclusions

This thesis presents the development of control architectures and methodologies for reducing noise radiated from a thick-walled cylindrical shell. One of the challenges in this problem is that directly controlling the shell dynamics is unfeasible because the shell is very stiff due to its large thickness. Also, feedback control schemes should be adopted as a control architecture, rather than feedforward control, because the source of disturbance is not available during the control action. In contrast to feedforward control, feedback control has had much less attention in the area of active structural acoustic control, primarily due to its difficulty of implementation for acoustic control system. Finally, the large number of sensor-actuator pairs mounted on the shell should be handled efficiently in order to achieve the goal of reducing the radiated noise. Design and implementation of controllers with large number of sensors and actuators is a challenging problem.

In order to overcome the first difficulty, which is to reduce the radiated noise from stiff structures, the use of external piezoelectric panels was proposed in this thesis. The approach is to cover the shell's outer surface with those panels and to control the motion of the panel's outer surface, not the motion of the shell. The piezoelectric panel contains several embedded accelerometers mounted to its outer and inner surfaces, which can sense both the motion of the panel base (*i.e.*, outer motion of the shell) and the motion of the panel's outer surface (*i.e.*, the radiating surface). Also, the panel contains PZT rods embedded in a stiff polymer matrix. This configuration results in an almost collocated sensor-actuator pair, which is desirable for controlling modally-dense systems, such as structural systems.

The use of external piezoelectric panels proposed in this thesis has significant advantages for stiff structures over the conventional way of directly controlling the structure. One of the important advantages is that the former needs much less control authority than the latter, because controlling panels requires less actuation power than controlling the stiff shell. Furthermore, the approach allows the control system to be significantly less dependent on the dynamics and characteristics of the structure than directly controlling the structure. The rationale is that the controller is designed on the transfer function of the panel, which can be simply approximated as a double differentiation (s^2), not the transfer function of the shell, which is a complex modal system. Therefore, we can expect that the approach will result in *robust* control systems.

Two different feedback control architectures have been proposed in this thesis to efficiently

reduce the radiated noise, which are denoted as "local" and "global" controllers, respectively. The local controllers are designed and implemented for each panel, with an objective of reducing the motion of panel's outer surface, *i.e.*, the radiating surface. Since the length of each panel is much less than the acoustic wavelength of interest, the noise radiated from each panel will be reduced if the averaged motion of panel's outer surface is reduced. Because internal accelerometers in each panel can measure both the motion of the shell and the radiating surface, two different feedback control configurations have been proposed for panel-level local controllers. The first one takes as its input the output of the accelerometers mounted to the outer surface of the panel and aims at reducing the output signal, which provides information about the averaged motion of each panel's outer surface. On the other hand, the second feedback loop, which is denoted as "feedforward" loop in this thesis due to its strong dependence on the disturbance source, measures the motion of the surface of the shell and feeds it back to the panel actuator layer.

Two undesirable panel dynamics, which are low-frequency feedthrough due to electromechanical coupling and high-frequency resonance due to accelerometer dynamics, were identified and found to limit the achievable closed-loop performance significantly. Low-frequency feedthrough compensator and high-frequency notch filter have been devised to compensate for those undesirable panel dynamics during the controller design procedure. Several control algorithms were investigated, including analog-only, hybrid analog-digital, and digital-only controllers, in order to find the control configuration that satisfies good performance and stability, low cost, and easy implementation. Each configuration has its own advantages and disadvantages, *e.g.*, those which yield good performance and stability require high cost and vice versa. Experimental results show that 15–30 dB of attenuation can be achieved between 200 and 2000 Hz in most local control configurations. However, among the configurations considered in this thesis, the hybrid analog-digital control scheme, with its digital and analog sub-controller used to control the low and high frequency behavior of the system, respectively, is believed to be the best control configuration given the constraint of the problem. The rationale is that the hybrid control scheme contains the advantages of both analog and digital controllers, and yields excellent performance similar to the analog-only controller, which produces the best closed-loop performance.

In contrast to the local controller, the "global" controller considers the dynamics of all the panels simultaneously and aims at making the shell a weak radiator. Since 55 panels are mounted on the shell, the global controller should be able to coordinate those large number of sensors and actuators efficiently. In order to satisfy these requirements, a new wavenumber domain sensing method has been developed and applied to feedback control design for reducing the radiated noise. The proposed approach is to minimize the total acoustic power radiated from vibrating structures using a formulation based on the wavenumber domain. The target wavenumbers in the supersonic domain (*i.e.*, the radiating wavenumbers) can be determined when the bandwidth of the disturbance spectrum is known, and a state-space model can be found to estimate the magnitude of these supersonic wavenumber components. Once a state-space model of the structure that can be used for active structural acoustic control is developed, a modern control design paradigm, such as H_2 or H_∞ controllers, can be applied to minimize the acoustic power radiated from vibrating structures.

One of the significant advantages of the new wavenumber domain sensing method is that it greatly reduces the effort to model the acoustic radiation from the structure. The discrete

wavenumber transform matrix, where sensor measurements are processed, is obtained from the definition of wavenumber transform, not from the structural acoustic models. Furthermore, the performance weights, which are required for model-based controller design, can be selected such that the difference between the actual and estimated acoustic power is minimized, if we have enough information on the actual acoustic power. If we cannot get the actual acoustic power due to the insufficient measurements or complexity of the plant, we can still use the performance weights as design knobs for optimal controller design. The new wavenumber domain sensing method enables the closed-loop performance to be insensitive to the availability of the actual acoustic power.

Another significant advantage of the new sensing method is that it simplifies the design of MIMO LQG controllers for active structural acoustic control by reducing the number of transfer functions that need to be identified. The method reduces the size of transfer function matrix to be identified from (the number of sensors)^2 to the order of (the number of wavenumber components to be considered)^2. These advantages are critical when the structure is complex enough that we may not be able to get an accurate model for the plant and, therefore, we need to perform the system identification to get a plant model.

The new sensing method has been numerically validated on a beam structure with 10 active composite panels, and a thick-walled cylindrical shell with 55 active composite panels mounted on its surface. Finite element method and analytic expressions were used to model the structural and acoustic responses, respectively, and to compute the open-loop and closed-loop behavior of the system. Once frequency responses were computed for the structural system from the model, the plant model needed to design LQG controller was obtained by doing system identification on those computed frequency responses. No acoustic model was included in the LQG controller designed to reduce the acoustic power from vibrating structures. The results of computer simulation show that the method greatly simplifies the design of MIMO LQG controllers for active structural acoustic control, by reducing the effort to model the acoustic radiation from the structure and allowing the systematic development of state-space models for wavenumber components in the supersonic region. Also, the numerical examples demonstrate that the closed-loop performance is still satisfactory in spite of the unavailability of the acoustic power for the controller design. In other words, the weights selected in an *ad-hoc* way, not using the actual acoustic power, yielded the closed-loop performance similar to the weights selected optimally using the actual acoustic power. This has a critical implication in the control system design for active structural acoustic control, because it is not easy to compute or measure the acoustic power for most engineering systems, and therefore use it in the controller design. In addition to making the acoustic modeling unnecessary to design controllers, the new wavenumber domain sensing method significantly simplifies the controller design by reducing the transfer functions to be considered from 100 to 25 in the case of beam structures, and from 3025 to 25 in the case of cylindrical shells. This advantage again makes the method a useful tool to design feedback controllers for reducing the radiated noise from structures.

After mounting 55 active composite panels on the cylindrical shell, panel-level local controllers were designed and experimentally implemented on the shell vibrating in water. Due to the unexplained excessive time delay and significant interaction between panels, tonal feedback controllers were chosen using a SISO controller scheme, rather than broadband feedback controllers. 52 tonal feedback controllers, all of which ended up with open-loop unstable controllers due to the compensation for low-frequency feedthrough, were successfully designed and

implemented. More than 20 dB of attenuation in the compensated acceleration, which was measured by internal accelerometers, was achieved over the radiating surface at 400 Hz using the tonal feedback controllers. However, the actual noise level measured by six hydrophones turned out to be increased despite the reduced acceleration over the radiating surface, so several tests were performed to investigate what causes this contradictory-looking results. The test results indicate that there are several serious problems in the panels, which prevent the internal accelerometers embedded in the panel from measuring the actual acceleration. Specifically, a laser scanning vibrometer test verified that dimples occur during self-excitation on the locations where internal accelerometers are mounted. Simulation results using eight external accelerometers showed that the actual acceleration over the radiating surface can be significantly increased if the internal accelerometers cannot measure the actual acceleration and controllers are designed to cancel those inaccurate measurements. Although it still remains to figure out why dimples occur during self-excitation, it is believed that the main reason for the increased noise level, despite the attenuation of measured acceleration, is the dimpling that occurs during self-excitation, which prevents the internal accelerometers from measuring the actual acceleration.

8.2 Contributions

The principle contributions from this thesis are in the development of control design techniques to reduce the radiated noise from stiff structures. These contributions are:

1. The use of external piezoelectric panels has been proposed to develop active acoustic control systems for stiff structures. Its main philosophy is to *minimize* the coupling between the structure and the control system. It is the opposite of the conventional method of directly controlling the structure, which tries to *maximize* that coupling. The approach proposed in this thesis ends up with robust control systems, by making the controllers insensitive to the shell dynamics.

2. A method of compensating for undesirable dynamics in active composite panels has been developed. The low-frequency feedthrough, which occurs due to mechanical coupling between internal accelerometers and the shell, and electrical coupling between panel actuator layer and accelerometers, could be compensated efficiently by designing the low-frequency feedthrough compensator and subtracting it from the plant transfer function. On the other hand, the high-frequency resonance, which occurs due to the participation of accelerometer dynamics into the system bandwidth, could be cancelled using notch filters.

3. Several panel-level local controllers have been designed, implemented, and compared, with an objective of finding the local control configuration that will be eventually incorporated in the shell in order to reduce the motion of panel's outer surface. They include analog-only controller, hybrid analog-digital controller, digital-only controller, and tonal feedback controller, *etc.* Most configurations yielded 15–30 dB of attenuation between 200 and 2000 Hz, although the analog-only controller showed the best closed-loop performance.

4. The concept of digital notch filters has been proposed. Digital filters may be preferred to analog filters due to their easiness in tuning the frequency to be notched out. However, the digital notch filters cannot be implemented directly in this problem because the target frequency is relatively high, compared with the sampling frequency. A novel method of designing digital notch filters resolved this difficulty, and the notch filters were successfully implemented to cancel out the high-frequency resonance due to accelerometers dynamics.

5. A new wavenumber domain sensing method has been developed and used to design active control systems for reducing the radiated noise from vibrating structures. The method aims at minimizing the acoustic power using the formulation in the wavenumber domain. The method allows the design of active acoustic control systems to be much easier, because it doesn't require the acoustic modeling process to design active structural acoustic control systems, and reduces the number of inputs and outputs of controllers from (the number of sensors)^2 to the order of (the number of wavenumber components to be considered)^2.

6. Three dimensional finite element model has been developed to simulate the structural responses of a finite cylindrical shell with active composite panels. The motivation for the modeling is not to correlate the simulation result with the experimental result, nor to generate the plant model needed for the synthesis of the model-based controller. The main objective of the modeling performed in this study is to generate the mathematical model that captures the important dynamics of the real test-bed, with the same order of the complexity, such that the proposed control algorithms can be tested on the model before they are experimentally implemented.

7. The wavenumber domain feedback control method developed in this thesis was numerically validated on the 3D finite element model. In order to mimic the controller design and implementation procedure for the real systems, the model was used only to obtain open-loop and closed-loop responses, and not used to get a plant model for controller synthesis. The results of numerical studies showed that the method greatly simplifies the design of MIMO LQG controllers for active structural acoustic control, by mitigating the effort to model the acoustic radiation from the structure, allowing the systematic development of state-space models for radiating wavenumber components, and reducing significantly the number of transfer functions to be identified. Furthermore, it was found that the closed-loop performance is not very sensitive to whether we have enough information about the acoustic power in advance.

8. The wavenumber domain feedback control method has been extended to reduce the radiated noise from general three-dimensional structures. It was shown that only first a few wavenumber components are enough to estimate and reduce the acoustic power in the reasonable bandwidth of interest.

9. Fifty-two tonal feedback controllers, which had to be unstable to compensate for the low-frequency feedthrough, were successfully implemented on the cylindrical shell with 55 panels mounted. More than 20 dB of attenuation was achieved at the target frequency in terms of compensated acceleration measured by the internal accelerometers.

10. Several tests were performed to investigate the problems in panels, and showed that the dimples that occur during self-excitation are the main reasons for the increased noise level

under closed-loop control. This information is important for any future redesign of the panels.

8.3 Recommendations

Based on the results described in this thesis, the following recommendations for further research are made:

1. The active composite panels should be redesigned. In particular, it is necessary for the internal accelerometers to be redesigned, considering the problems that originate from them, such as low-frequency feedthrough, high-frequency resonance, dimples, *etc.* Furthermore, an aluminum plate mounted on the panel to reduce the high-frequency accelerometer dynamics increased its weight, which made interaction between panels significant. One possible way of redesigning panels is to use two layers of panels as a single sensor-actuator pair. In other words, the lower panel, which is mounted on the shell, contains only actuator layer without any holes, while the upper panel, which is mounted on top of lower panels, contains internal accelerometers. By doing that, the electrical coupling between actuator layer and internal accelerometers can be avoided and the dimples will not appear.

2. The current panel contains injection-molded piezoceramic accelerometers, which are big and have large mass. As a result, they can yield output signals with high signal-to-noise ratio, but may cause a significant resonance near the bandwidth of interest. Therefore, in the future, other type of accelerometers should be considered, such as small MEMS-type accelerometers. Furthermore, simultaneous use of large and small accelerometers may be considered so that the advantages of each accelerometer can be preserved.

3. The PZT actuator layer in the current panels works as expected, in the sense that the displacement of panels is proportional to the voltage input to the actuator layer. However, it turned out that the PZT actuator layer in the current panels is unnecessarily thick, given the displacement required to cancel the shell motion. Considering this fact, future panels should be thinner than the current ones, which will reduce the mass of the panels, and allow the use of two layers of panels as a single set.

4. Although it turned out that the hybrid analog-digital control scheme has many of the advantages of both analog and digital controllers, it couldn't be implemented for 55 panels mounted on the shell due to the cost of building analog electronics. However, it should be pursued in the future in order to improve the closed-loop performance. The difficulty of tuning the target frequency for notch filters, which was proposed to cancel the high-frequency resonance due to accelerometer dynamics, may be lessened by using analog-programmable filters or digital notch filters proposed in this thesis.

5. The concept of the wavenumber domain feedback control was validated numerically in this thesis. However, the controller should be implemented experimentally in the future to verify that it works for real systems.

6. The active acoustic control systems for the cylindrical shell should be able to work as well, even when the shell's characteristics are changing. This can happen when the shell's speed or depth in water is changing. Therefore, the control systems should be developed in the future that are robust enough to deal with the uncertainty in the plant, or adaptive enough to modify their functions to maintain the control performance for time-varying plants. Although the use of external piezoelectric panels enables the control systems to be insensitive to the shell's characteristics to some extent, it would be better if the control systems can be robust and adaptive enough to handle the unexpected change in the environment.

Bibliography

[Ashwell, 1972] Ashwell, D. G., and A. B. Sabir, "A New Cylindrical Shell Finite Element Based on Simple Independent Strain Functions," *International Journal of Mechanical Sciences*, Vol. 14, pp. 171–183, 1972.

[Atalla, 1996] Atalla, N., J. Nicolas, and C. Gauthier, "Acoustic Radiation of an Unbaffled Vibrating Plate with General Elastic Boundary Conditions," *The Journal of the Acoustical Society of America*, Vol. 99, No. 3, pp. 1484–1494, 1996.

[Bathe, 1996] Bathe, K. J., *Finite Element Procedures*, Prentice-Hall, 1996.

[Baumann, 1991] Baumann, W. T., W. R. Saunders, and H. H. Robertshaw, "Active Suppression of Acoustic Radiation from Impulsively Excited Structures," *The Journal of the Acoustical Society of America*, Vol. 90, No. 6, pp. 3202–3208, 1991.

[Baumann, 1992] Baumann, W. T., F. S. Ho, and H. H. Robertshaw, "Active Structural Acoustic Control of Broadband Disturbances," *The Journal of the Acoustical Society of America*, Vol. 92, No. 4, pp. 1998–2005, 1992.

[Bingham, 1998] Bingham, B. S., and N. W. Hagood, *Structural-Acoustic Design and Control of an Integrally Actuated Composite Panel*, AMSL Report 98-5, Massachusetts Institute of Technology, 1998.

[Blevins, 1979] Blevins, R. D., *Formulas for Natural Frequency and Mode Shape*, Krieger Publishing Company, 1979.

[Burdisso, 1992] Burdisso, R. A., and C. R. Fuller, "Theory of Feedforward Controlled System Eigenproperties," *Journal of Sound and Vibration*, Vol. 153, No. 3, pp. 437–451, 1992.

[Cazzolato, 1998] Cazzolato, B. S., and C. H. Hansen, "Active Control of Sound Transmission Using Structural Error Sensing," *The Journal of the Acoustical Society of America*, Vol. 105, No. 5, pp. 2878–2889, 1998.

[Clark, 1992A] Clark, R. L., and C. R. Fuller, "Active Structural Acoustic Control with Adaptive Structures Including Wavenumber Considerations," *Journal of Intelligent Material Systems and Structures*, Vol. 3, pp. 296–315, 1992.

[Clark, 1992B] Clark, R. L., and C. R. Fuller, "Experiments on Active Control of Structurally Radiated Sound Using Multiple Piezoceramic Actuators," *The Journal of the Acoustical Society of America*, Vol. 91, No. 6, pp. 3313–3320, 1992.

[Clark, 1992C] Clark, R. L., and C. R. Fuller, "Modal Sensing of Efficient Acoustic Radiators with Polyvinylidene Fluoride Distributed Sensors in Active Structural Acoustic Control Approaches," *The Journal of the Acoustical Society of America*, Vol. 91, No. 6, pp. 3321–3329, 1992.

[Clark, 1992D] Clark, R. L., and C. R. Fuller, "Optimal Placement of Piezoelectric Actuators and Polyvinylidene Fluoride Error Sensors in Active Structural Acoustic Control Approaches," *The Journal of the Acoustical Society of America*, Vol. 92, No. 3, pp. 1521–1533, 1992.

[Clark, 1994] Clark, R. L., and C. R. Fuller, "Active Control of Structurally Radiated Sound from an Enclosed Finite Cylinder," *Journal of Intelligent Material Systems and Structures*, Vol. 5, pp. 379–391, 1994.

[Coughlin, 1991] Coughlin, R. F., and F. F. Driscoll, *Operational Amplifiers and Linear Integrated Circuits*, Prentice-Hall, 1991.

[Crawley, 1987] Crawley, E. F., and J. de Luis, "Use of Piezoelectric Actuators as Elements of Intelligent Structures," *AIAA Journal*, Vol. 25, No. 10, pp. 1373–1385, 1987.

[Crawley, 1991] Crawley, E. F., and S. R. Hall, "Dynamics of Controlled Structure: Lecture notes," Department of Aeronautics and Astronautics, Massachusetts Institute of Technology, 1991.

[Dimitriadis, 1991] Dimitriadis, E. K., and C. R. Fuller, "Active Control of Sound Transmission Through Elastic Plates Using Piezoelectric Actuators," *AIAA Journal*, Vol. 29, No. 11, pp. 1771–1777, 1991.

[Elliott, 1987] Elliott, S. J., I. M. Stothers, and P. A. Nelson, "A Multiple Error LMS Algorithm and Its Application to the Active Control of Sound and Vibration," *IEEE Transactions on Acoustics, Speech, and Signal Processing*, Vol. 35, No. 10, pp. 1423–1434, 1987.

[Elliott, 1993] Elliott, S. J., and M. E. Johnson, "Radiation Modes and the Active Control of Sound Power," *The Journal of the Acoustical Society of America*, Vol. 94, No. 4, pp. 2194–2204, 1993.

[Fahy, 1985] Fahy, F. J., *Sound and Structural Vibration: Radiation, Transmission and Response*, (Academic: London), 1985.

[Francis, 1986] Francis, B., *A Course in H_∞ Control Theory*, Springer-Verlag, New York, 1986.

[Franklin, 1998] Franklin, G. F., J. D. Powell, and M. L. Workman, *Digital Control of Dynamic System*, Addison-Wesley, 1998.

[Fuller, 1990] Fuller, C. R., "Active Control of Sound Transmission/Radiation from Elastic Plates by Vibration Inputs: I. Analysis," *Journal of Sound and Vibration*, Vol. 136, No. 1, pp. 1–15, 1990.

[Fuller, 1991A] Fuller, C. R., and R. A. Burdisso, "A Wavenumber Domain Approach to the Active Control of Structure-borne Sound," *Journal of Sound and Vibration*, Vol. 148, No. 2, pp. 355–360, 1991.

[Fuller, 1991B] Fuller, C. R., C. H. Hansen, and S. D. Snyder, "Experiments on Active Control of Sound Radiation from a Panel Using a Piezoelectric Actuator," *Journal of Sound and Vibration*, Vol. 150, No. 2, pp. 179–190, 1991.

[Fuller, 1992] Fuller, C. R., C. A. Rogers, and H. H. Robertshaw, "Control of Sound Radiation with Active/adaptive Structures," *Journal of Sound and Vibration*, Vol. 157, No. 1, pp. 19–39, 1992.

[Ghausi, 1981] Ghausi, M. S., and K. R. Laker, *Modern Filter Design*, Prentice-Hall, 1981.

[Gibbs, 2000] Gibbs, G. P., R. L. Clark, D. E. Cox, and J. S. Vipperman, "Radiation Model Expansion: Application to Active Structural Acoustic Control," *The Journal of the Acoustical Society of America*, Vol. 107, No. 1, pp. 332–339, 2000.

[Griffin, 1999] Griffin, S., C. Hansen, and B. Cazzolato, "Feedback Control of Structurally Radiated Sound into Enclosed Spaces Using Structural Sensing," *The Journal of the Acoustical Society of America*, Vol. 106, No. 5, pp. 2621–2628, 1999.

[Hall, 1989] Hall, S. R. and N. M. Wereley, "Linear Control Issue in the Higher Harmonic Control of Helicopter Vibration," *Proceedings of the 45th Annual Forum of the American Helicopter Society*, pp. 955–972, 1989.

[Jacques, 1994] Jacques, R. N., *On-Line System Identification and Control Design for Flexible Structures*, Ph.D. thesis, Department of Aeronautics and Astronautics, Massachusetts Institute of Technology, 1994.

[Johnson, 1995] Johnson, M. E., and S. J. Elliott, "Active Control of Sound Radiation Using Volume Velocity Cancellation," *The Journal of the Acoustical Society of America*, Vol. 98, No. 4, pp. 2174–2186, 1995.

[Johnson, 1997] Johnson, M. E., and S. J. Elliott, "Active Control of Sound Radiation from Vibrating Surfaces Using Arrays of Discrete Actuators," *Journal of Sound and Vibration*, Vol. 207, No. 5, pp. 743–759, 1997.

[Johnson, 2000] Johnson, B. D., and C. R. Fuller, "Broadband Control of Plate Radiation Using a Piezoelectric, Double-amplifier Active Skin and Structural Acoustic

Sensing," *The Journal of the Acoustical Society of America*, Vol. 107, No. 2, pp. 876–884, 2000.

[Junger, 1986] Junger, M. C., and D. Feit, *Sound, Structures, and Their Interaction*, MIT Press, 1986.

[Kim, 1999] Kim, S. J., and K. Song, "Active Control of Sound Field from Plates in Flow by Piezoelectric Sensor/Actuator," *AIAA Journal*, Vol. 37, No. 10, pp. 1180–1186, 1999.

[Koopmann, 1989] Koopmann, G. H., L. Song, and J. B. Fahnline, "A Method for Computing Acoustic Fields Based on the Principle of Wave Superposition," *The Journal of the Acoustical Society of America*, Vol. 86, No. 6, pp. 2433–2438, 1989.

[Lane, 1998] Lane, S. A., and R. L. Clark, "Dissipative Feedback Control of a Reverberant Enclosure Using a Constant Volume Velocity Source," *Journal of Vibration and Acoustics*, Vol. 120, pp. 987–993, 1998.

[Lane, 2000] Lane, S. A., R. L. Clark, and S. C. Southward, "Active Control of Low Frequency Modes in an Aircraft Fuselage Using Spatially Weighted Arrays," *Journal of Vibration and Acoustics*, Vol. 122, pp. 227–234, 2000.

[Lee, 1990] Lee, C. K., and F. C. Moon, "Modal Sensors/Actuators," *Journal of Applied Mechanics*, Transactions of the ASME, Vol. 57, pp. 434–441, 1990.

[Lewis, 1992] Lewis, F. L., *Applied Optimal Control and Estimation*, Prentice-Hall, 1992.

[Maciejowski, 1989] Maciejowski, J. M., *Multivariable Feedback Design*, Addison Wisley, 1989.

[Maillard, 1994A] Maillard, J. P., and C. R. Fuller, "Advanced Time Domain Wavenumber Sensing for Structural Acoustic System: I. Theory and Design," *The Journal of the Acoustical Society of America*, Vol. 95, No. 6, pp. 3252–3261, 1994.

[Maillard, 1994B] Maillard, J. P., and C. R. Fuller, "Advanced Time Domain Wavenumber Sensing for Structural Acoustic System: II. Active Radiation Control of a Simply Supported Beam," *The Journal of the Acoustical Society of America*, Vol. 95, No. 6, pp. 3262–3272, 1994.

[Maillard, 1995] Maillard, J. P., and C. R. Fuller, "Advanced Time Domain Wavenumber Sensing for Structural Acoustic System: III. Experiments on Active Broadband Radiation Control of a Simply Supported Plate," *The Journal of the Acoustical Society of America*, Vol. 98, No. 5, pp. 2613–2621, 1995.

[Maillard, 1997] Maillard, J. P., *Advanced Time Domain Sensing for Structural Acoustical Control*, Ph.D. thesis, Virginia Polytechnic Institute & State University, 1997.

[Mandic, 1991] Mandic, D. S., and J. D. Jones, "Adaptive Active Control of Sound Fields in Elastic Cylinders via Vibrational Inputs," *AIAA Journal*, Vol. 29, No. 10, pp. 1552–1561, 1991.

[Metcalf, 1992] Metcalf, V. L., C. R. Fuller, R. J. Silcox, and D. E. Brown, "Active Control of Sound Transmission/Radiation from Elastic Plates by Vibration Inputs: II. Experiments," *Journal of Sound and Vibration*, Vol. 153, No. 3, pp. 387–402, 1992.

[Naghshineh, 1993] Naghshineh, K., and G. H. Koopmann, "Active Control of Sound Power Using Acoustic Basis Functions as Surface Velocity Filters," *The Journal of the Acoustical Society of America*, Vol. 93, No. 5, pp. 2740–2752, 1993.

[Oppenheim, 1997] Oppenheim, A. V., and A. S. Willsky, *Signals and Systems*, Prentice-Hall, 1997.

[Pan, 1998] Pan, X., T. J. Sutton, and S. J. Elliott, "Active Control of Sound Transmission through a Double-leaf Partition by Volume Velocity Cancellation," *The Journal of the Acoustical Society of America*, Vol. 104, No. 5, pp. 2828–2835, 1998.

[Pierce, 1981] Pierce, A. D., *Acoustics: An Introduction to Its Physical Principles and Applications*, McGraw-Hill, 1981.

[Savran, 2000] Savran, C. A., M. J. Atalla, and S. R. Hall, "Broadband Active Structural Acoustic Control of a Fuselage Test-bed Using Collocated Piezoelectric Sensors and Actuators," *Proceedings of SPIE conference on Mathematics and Control in Smart Structures*, Vol. 3984, pp. 137–147, 2000.

[Scott, 1997] Scott, B. L., and S. D. Sommerfeldt, "Estimating Acoustic Radiation from a Bernoulli-Euler Beam Using Shaped Polyvinylidene Flouride Film," *The Journal of the Acoustical Society of America*, Vol. 101, No. 6, pp. 3475–3485, 1997.

[Song, 2000] Song, K., M. J. Atalla, and S. R. Hall, "Active Structural Acoustic Control of a Thick-walled Cylindrical Shell," *Proceedings of SPIE conference on Mathematics and Control in Smart Structures*, Vol. 3984, pp. 112–124, 2000.

[Song, 2001] Song, K., M. J. Atalla, and S. R. Hall, "A New Wavenumber Domain Sensing Method for Active Structural Acoustic Control," *Proceedings of SPIE conference*, Vol. 4326, pp. 46–57, 2001.

[Strang, 1986] Strang, G., *Introduction to Applied Mathematics*, Wellesley-Cambridge press, 1986.

[Timoshenko, 1959] Timoshenko, S. P., and S. Woinowsky-Krieger, *Theory of Plates and Shells*, McGraw-Hill, New York, 1959.

[Vipperman, 1993] Vipperman, J. S., R. A. Burdisso, and C. R. Fuller, "Active Control of Broadband Structural Vibration Using the LMS Adaptive Algorithm," *Journal of Sound and Vibration*, Vol. 166, No. 2, pp. 283–299, 1993.

[Vipperman, 1999] Vipperman, J. S., and R. L. Clark, "Multivariable Feedback Active Structural Acoustic Control Using Adaptive Piezoelectric Sensoriactuators," *The Journal of the Acoustical Society of America*, Vol. 105, No. 1, pp. 219–225, 1999.

[Wang, 1991] Wang, B. T., C. R. Fuller, and E. K. Dimitriadis, "Active Control of Structurally Radiated Noise Using Multiple Piezoelectric Actuators," *AIAA Journal*, Vol. 29, No. 11, pp. 1802–1809, 1991.

[Wang, 1998] Wang, B. T., "The PVDF-based Wavenumber Domain Sensing Techniques for Active Sound Radiation Control from a Simply Supported Beam," *The Journal of the Acoustical Society of America*, Vol. 103, No. 4, pp. 1904–1915, 1998.

[Zhou, 1995] Zhou, K., J. C. Doyle, and K. Glove, *Robust and Optimal Control*, Prentice-Hall, 1995.

Appendix A

Finite Element Formulation of the Cylindrical Shell

In Chapter 2, the finite element formulation for the cylindrical shell was presented. This appendix presents the expressions for the matrices used in Chapter 2. Recall that the displacement at the mid-surface of the cylindrical shell can be written as [Ashwell, 1972]

$$\begin{aligned} u_0 &= ac_2\cos\varphi + ac_4\sin\varphi + c_5 + c_7x + \left(ac_{11} + a^3c_{19} - a^2c_{20}\right)\varphi \\ &\quad - \frac{1}{2}a^3c_{17}\varphi^2 + c_8x\varphi - \frac{1}{6}a^3c_{19}\varphi^3 \\ v_0 &= (c_1 + c_2x)\sin\varphi - (c_3 + c_4x)\cos\varphi + c_6 + \left(-a^2c_{19} + ac_{20}\right)x \\ &\quad + a^2c_{16}\varphi + a^2c_{17}x\varphi + \frac{1}{2}a^2c_{18}\varphi^2 + \frac{1}{2}a^2c_{19}x\varphi^2 \\ w_0 &= -(c_1 + c_2x)\cos\varphi - (c_3 + c_4x)\sin\varphi + \left(ac_9 - a^2c_{16}\right) + \left(ac_{10} - a^2c_{17}\right)x \\ &\quad - a^2c_{18}\varphi - a^2c_{19}x\varphi - \frac{1}{2}c_{12}x^2 - \frac{1}{6}c_{13}x^3 - \frac{1}{2}c_{14}x^2\varphi - \frac{1}{6}c_{15}x^3\varphi\,, \end{aligned} \tag{A.1}$$

where (u_0, v_0, w_0) is the displacement at the mid-surface in the axial, circumferential, and radial directions, respectively, a is the radius of the cylindrical shell, (x,φ) is the coordinate of the shell element (Figure A-1), and $c_1, c_2, ..., c_{20}$ are constants used to define the displacement field, which should be determined by the nodal displacements. Equation A.1 can also be written in matrix form as

$$\mathbf{u_0} = \mathbf{N_c c} = \begin{bmatrix} \mathbf{N}_u \\ \mathbf{N}_v \\ \mathbf{N}_w \end{bmatrix} \mathbf{c}\,, \tag{A.2}$$

where $\mathbf{u}_0 = [u_0\ v_0\ w_0]^T$, $\mathbf{c} = [c_1\ c_2\ ...\ c_{20}]^T$, and $\mathbf{N}_u$, $\mathbf{N}_v$ and $\mathbf{N}_w$ are 1×20 row vectors that represent the relationships between $\mathbf{c}$ and u_0, v_0, and w_0, respectively. They are written as

$$\begin{aligned}
\mathbf{N}_u(x,\varphi) &= \Big[\ 0\ \ a\cos\varphi\ \ 0\ \ a\sin\varphi\ \ 1\ \ 0\ \ x\ \ x\varphi\ \ 0\ \ 0\ \ a\varphi\ \ 0\ \ 0\ \ 0\ \ 0\ \ 0 \\
&\quad -\tfrac{1}{2}a^3\varphi^2\ \ 0\ \ \left(a^3\varphi - \tfrac{1}{6}a^3\varphi^3\right)\ \ -a^2\varphi\ \Big] \\
\mathbf{N}_v(x,\varphi) &= \Big[\ \sin\varphi\ \ x\sin\varphi\ \ -\cos\varphi\ \ -x\cos\varphi\ \ 0\ \ 1\ \ 0\ \ 0\ \ 0\ \ 0\ \ 0\ \ 0\ \ 0\ \ 0 \\
&\quad 0\ \ a^2\varphi\ \ a^2x\varphi\ \ \tfrac{1}{2}a^2\varphi^2\ \ \left(\tfrac{1}{2}a^2x\varphi^2 - a^2x\right)\ \ ax\ \Big] \\
\mathbf{N}_w(x,\varphi) &= \Big[\ -\cos\varphi\ \ -x\cos\varphi\ \ -\sin\varphi\ \ -x\sin\varphi\ \ 0\ \ 0\ \ 0\ \ 0\ \ a\ \ ax\ \ 0 \\
&\quad -\tfrac{1}{2}x^2\ \ -\tfrac{1}{6}x^3\ \ -\tfrac{1}{2}x^2\varphi\ \ -\tfrac{1}{6}x^3\varphi\ \ -a^2\ \ -a^2x\ \ -a^2\varphi\ \ -a^2x\varphi\ \ 0\ \Big]\ .
\end{aligned} \tag{A.3}$$

The next step is to express $\mathbf{c}$ in terms of the nodal displacements. Let $(u_k, v_k, w_k, \phi_{x,k}, \phi_{y,k})$ $(k = 1,2,3,4)$ be the nodal displacements at the kth node in the element. The nodal numbers are defined in Figure A-1. Using the definition of ϕ_x and ϕ_y in Equation 2.2, the nodal displacements at the kth node can be written as $(k = 1,2,3,4)$

$$\begin{aligned}
u_k &= \mathbf{N}_u(x_k,\varphi_k)\,\mathbf{c} \\
v_k &= \mathbf{N}_v(x_k,\varphi_k)\,\mathbf{c} \\
w_k &= \mathbf{N}_w(x_k,\varphi_k)\,\mathbf{c} \\
\phi_{x,k} &= -\frac{\partial \mathbf{N}_w(x_k,\varphi_k)}{\partial x}\,\mathbf{c} \\
\phi_{y,k} &= \frac{1}{a}\left[\mathbf{N}_v(x_k,\varphi_k) - \frac{\partial \mathbf{N}_w(x_k,\varphi_k)}{\partial \varphi}\right]\mathbf{c}\ ,
\end{aligned} \tag{A.4}$$

where (x_k, φ_k) is the coordinate at the kth nodal point, defined as

$$x_k = \begin{cases} \dfrac{d}{2}\ ,\ k = 1,4 \\ -\dfrac{d}{2}\ ,\ k = 2,3 \end{cases}\ ,\quad \varphi_k = \begin{cases} \dfrac{b}{2a}\ ,\ k = 1,2 \\ -\dfrac{b}{2a}\ ,\ k = 3,4 \end{cases}\ . \tag{A.5}$$

Therefore, the nodal displacement $\widehat{\mathbf{U}} = \left[u_1\, v_1\, w_1\, \phi_{x,1}\, \phi_{y,1} \cdots u_4\, v_4\, w_4\, \phi_{x,4}\, \phi_{y,4}\right]^T$ can be written as

$$\widehat{\mathbf{U}} = \mathbf{T}_{\widehat{u}c}\,\mathbf{c}\ , \tag{A.6}$$

where the matrix of transformation from $\mathbf{c}$ to $\widehat{\mathbf{U}}$, $\mathbf{T}_{\widehat{u}c}$, is expressed as

$$\mathbf{T}_{\widehat{u}c} = \begin{bmatrix} \vdots \\ \mathbf{N}_u(x_k,\varphi_k) \\ \mathbf{N}_v(x_k,\varphi_k) \\ \mathbf{N}_w(x_k,\varphi_k) \\ -\dfrac{\partial \mathbf{N}_w(x_k,\varphi_k)}{\partial x} \\ \dfrac{1}{a}\left[\mathbf{N}_v(x_k,\varphi_k) - \dfrac{\partial \mathbf{N}_w(x_k,\varphi_k)}{\partial \varphi}\right] \\ \vdots \end{bmatrix}\ ,\ k = 1,2,3,4\ . \tag{A.7}$$

Using $\mathbf{T}_{\widehat{uc}}$, the displacement field at the mid-surface, $\mathbf{u}_0$, can be represented in terms of the nodal displacements, $\widehat{\mathbf{U}}$, as

$$\mathbf{u}_0 = \mathbf{N}_c\mathbf{c} = \mathbf{N}_c\mathbf{T}_{\widehat{uc}}^{-1}\widehat{\mathbf{U}} . \tag{A.8}$$

Also, using Equation 2.3 and 2.4, the displacement and strain field at (x, y, z) can be written in terms of the nodal displacements, $\widehat{\mathbf{U}}$, as

$$\begin{aligned} \mathbf{u} &= \mathbf{H}\widehat{\mathbf{U}} \\ \varepsilon &= \mathbf{B}\widehat{\mathbf{U}} , \end{aligned} \tag{A.9}$$

where $\mathbf{H}$ and $\mathbf{B}$ are the displacement interpolation matrix, and the strain-displacement matrix [Bathe, 1996], respectively, defined as (note that $y = a\varphi$)

$$\mathbf{H} = \begin{bmatrix} \mathbf{N}_u(x,\varphi) - z\dfrac{\partial \mathbf{N}_w(x,\varphi)}{\partial x} \\ \mathbf{N}_v(x,\varphi) - \dfrac{z}{a}\left[\dfrac{\partial \mathbf{N}_w(x,\varphi)}{\partial \varphi} - \mathbf{N}_v(x,\varphi)\right] \\ \mathbf{N}_w(x,\varphi) \end{bmatrix} \mathbf{T}_{\widehat{uc}}^{-1} \tag{A.10}$$

$$\begin{aligned} \mathbf{B} &= \left\{ \begin{bmatrix} \dfrac{\partial \mathbf{N}_u(x,\varphi)}{\partial x} \\ \dfrac{1}{a}\dfrac{\partial \mathbf{N}_v(x,\varphi)}{\partial \varphi} + \dfrac{\mathbf{N}_w(x,\varphi)}{a} \\ \dfrac{1}{a}\dfrac{\partial \mathbf{N}_u(x,\varphi)}{\partial \varphi} + \dfrac{\partial \mathbf{N}_v(x,\varphi)}{\partial x} \end{bmatrix} - z \begin{bmatrix} \dfrac{\partial^2 \mathbf{N}_w(x,\varphi)}{\partial x^2} \\ \dfrac{1}{a^2}\dfrac{\partial^2 \mathbf{N}_w(x,\varphi)}{\partial \varphi^2} - \dfrac{1}{a^2}\dfrac{\partial \mathbf{N}_v(x,\varphi)}{\partial \varphi} \\ \dfrac{2}{a}\dfrac{\partial^2 \mathbf{N}_w(x,\varphi)}{\partial x \partial \varphi} - \dfrac{2}{a}\dfrac{\partial \mathbf{N}_v(x,\varphi)}{\partial x} \end{bmatrix} \right\} \mathbf{T}_{\widehat{uc}}^{-1} \\ &= \{\varepsilon_0 - z\boldsymbol{\chi}\}\,\mathbf{T}_{\widehat{uc}}^{-1} . \end{aligned}$$

Here, ε_0 and $\boldsymbol{\chi}$ are the strains and the change of curvature defined in Equation 2.4 and 2.5, evaluated at the mid-surface. They are written as

$$\varepsilon_0 = \begin{bmatrix} \dfrac{\partial \mathbf{N}_u(x,\varphi)}{\partial x} \\ \dfrac{1}{a}\dfrac{\partial \mathbf{N}_v(x,\varphi)}{\partial \varphi} + \dfrac{\mathbf{N}_w(x,\varphi)}{a} \\ \dfrac{1}{a}\dfrac{\partial \mathbf{N}_u(x,\varphi)}{\partial \varphi} + \dfrac{\partial \mathbf{N}_v(x,\varphi)}{\partial x} \end{bmatrix}, \boldsymbol{\chi} = \begin{bmatrix} \dfrac{\partial^2 \mathbf{N}_w(x,\varphi)}{\partial x^2} \\ \dfrac{1}{a^2}\dfrac{\partial^2 \mathbf{N}_w(x,\varphi)}{\partial \varphi^2} - \dfrac{1}{a^2}\dfrac{\partial \mathbf{N}_v(x,\varphi)}{\partial \varphi} \\ \dfrac{2}{a}\dfrac{\partial^2 \mathbf{N}_w(x,\varphi)}{\partial x \partial \varphi} - \dfrac{2}{a}\dfrac{\partial \mathbf{N}_v(x,\varphi)}{\partial x} \end{bmatrix} . \tag{A.11}$$

Substituting Equation A.9 into Equation 2.13, and assembling all the elements, we obtain the equation of motion for the cylindrical shell.

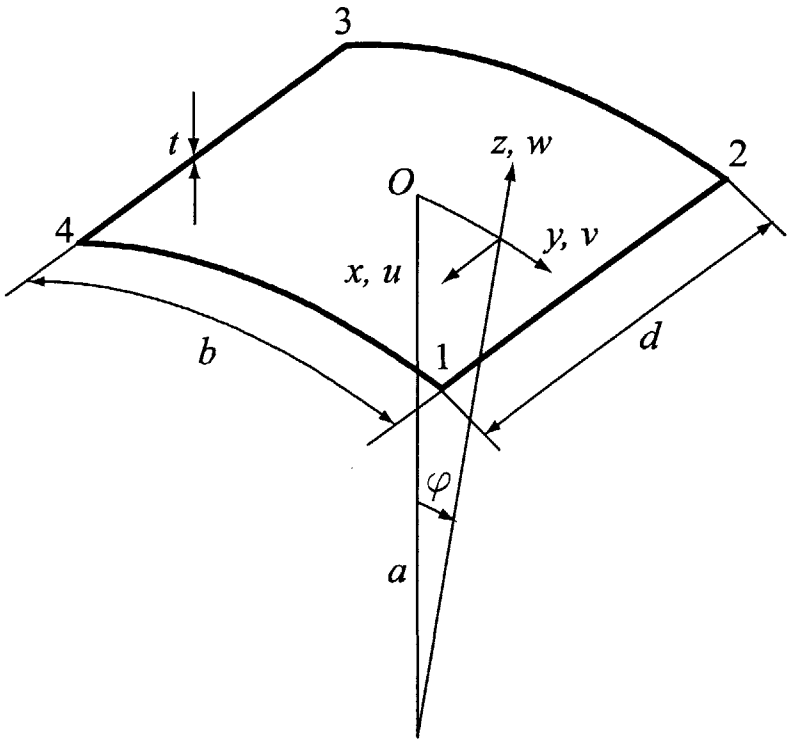

Figure A-1: An element of the cylindrical shell.

Appendix B

Basic Op-Amp Circuits for Controller Implementation

This appendix presents basic analog circuits consisting of operational amplifiers (Op-amp) for the feedback and feedforward controllers implemented in Chapter 6. The circuits introduced in this appendix will be extensively used to build the circuits for analog feedback, analog feedforward, hybrid analog/digital feedback controllers, *etc.*, as shown in the following appendices. Only the circuit diagram and its transfer function are shown here for brevity. More information on the detailed derivation of the transfer function and the characteristics of the circuit can be found in [Ghausi, 1981] and [Coughlin, 1991]. It should also be noted that the transfer functions given here are derived for the ideal infinite gain op-amps.

An Inverting Amplifier

Figure B-1 shows a schematic of the inverting amplifier, which is one of the most widely used op-amp circuits. It consists of two resistors, R_1 and R_2. The transfer function of the circuit

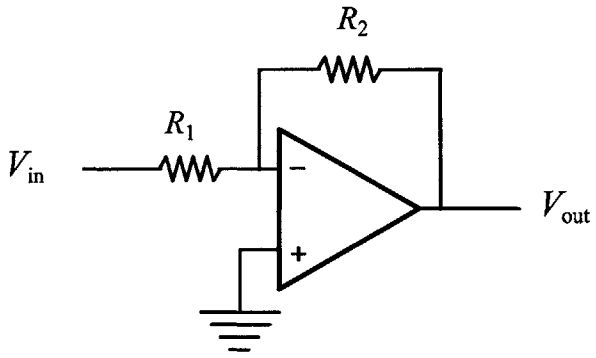

Figure B-1: An inverting amplifier.

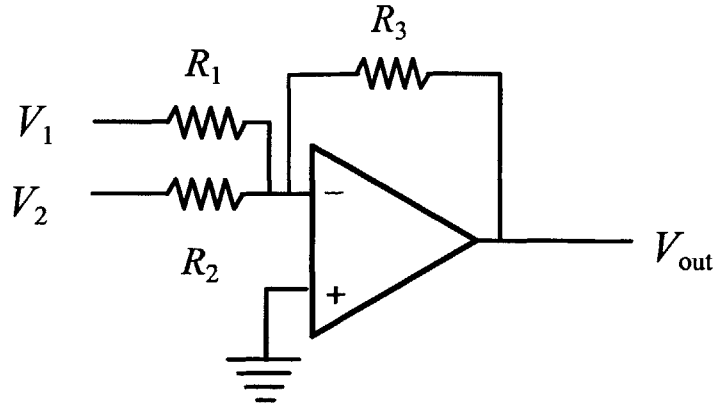

Figure B-2: An inverting adder.

can be written as

$$\frac{V_{\text{out}}(s)}{V_{\text{in}}(s)} = -\frac{R_2}{R_1} . \tag{B.1}$$

Ideally, the circuit should not show any phase delay, because its transfer function is just a constant gain. However, the actual circuit *has* a phase delay, although it is not significant in low-frequency range, because an op-amp has a gain-bandwidth product that limits its performance. The phase delay may become significant in high-frequency range, especially when the gain of the circuit, $\frac{R_2}{R_1}$, is very high. Since the controllers designed in this study generally need high-gain amplifiers, it is better to build several inverting amplifiers with reasonable gains in series, rather than one amplifier with a high gain.

An Inverting Adder

The circuit of an inverting adder is shown in Figure B-2 . Its basic characteristics are the same as the inverting amplifier shown in Figure B-1. The relationship between input and output voltages can be written as

$$V_{\text{out}}(s) = -\left[\frac{R_3}{R_1} V_1(s) + \frac{R_3}{R_2} V_2(s)\right] . \tag{B.2}$$

If the same resistor is used for three resistors in the figure, *i.e.*, $R_1 = R_2 = R_3$, the relationship in Equation B.2 is simplified to

$$V_{\text{out}}(s) = -[V_1(s) + V_2(s)] . \tag{B.3}$$

In this thesis, this circuit is generally used to add two signals from feedback and feedforward controllers, in order to produce the control input to the power amplifier, which is connected to the embedded actuator in the active composite panel.

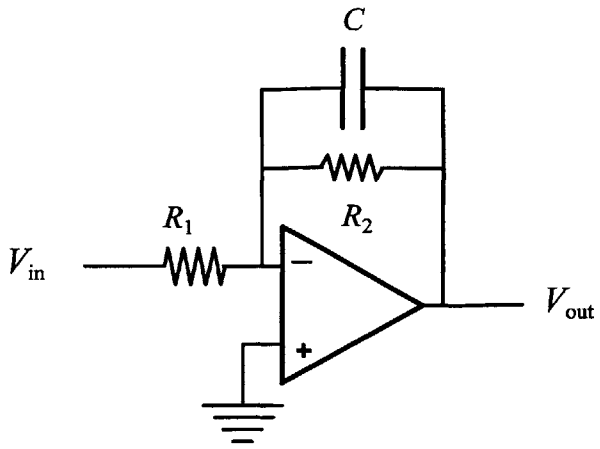

Figure B-3: An inverting low-pass filter.

The Inverting Low-pass Filter

Figure B-3 shows the circuit of an inverting low-pass filter with two resistors R_1, R_2 and one capacitor C. Its transfer function is given by

$$\frac{V_{\text{out}}(s)}{V_{\text{in}}(s)} = -\frac{R_2}{R_1}\frac{1}{1 + R_2 C s}. \tag{B.4}$$

Equation B.4 indicates that the DC gain and the cut-off frequency, ω_c (rad/sec), are given by

$$\text{DC gain} = \frac{R_2}{R_1}, \ \omega_c = \frac{1}{R_2 C}. \tag{B.5}$$

This circuit has two applications in this thesis. The first usage of this circuit is to approximate an integrator. Since we measure the accelerations using the embedded accelerometers in the active composite panels, we need integrators to get velocity or displacement from acceleration. However, a pure integrator with an infinite DC gain cannot be implemented in practice, because a small DC offset in the input voltage will saturate the circuit. An alternative to the pure integrator is a low-pass filter with a low cut-off frequency, as shown in Figure B-3. The frequency responses of a pure integrator and a low-pass filter are compared in Figure B-4. The low-pass filter has a cut-off frequency of 5 Hz. As shown in the figure, the low-pass filter converges to the pure integrator above 10 Hz. If the bandwidth of interest is well above 10 Hz, the low-pass filter shown in the figure is a good approximation to the pure integrator.

The other application of the circuit in the thesis is to add a roll-off to loop-transfer functions. Since the active composite panel has its own significant dynamics in high frequency range, the closed-loop system may be destabilized if those effects are not considered in the controller design. Therefore, in addition to the low-pass filters for integrating accelerations, we need additional low-pass filters to add a roll-off at high frequency, such that the instability can be avoided. A notch filter, which will be introduced later in this appendix, can also be used to

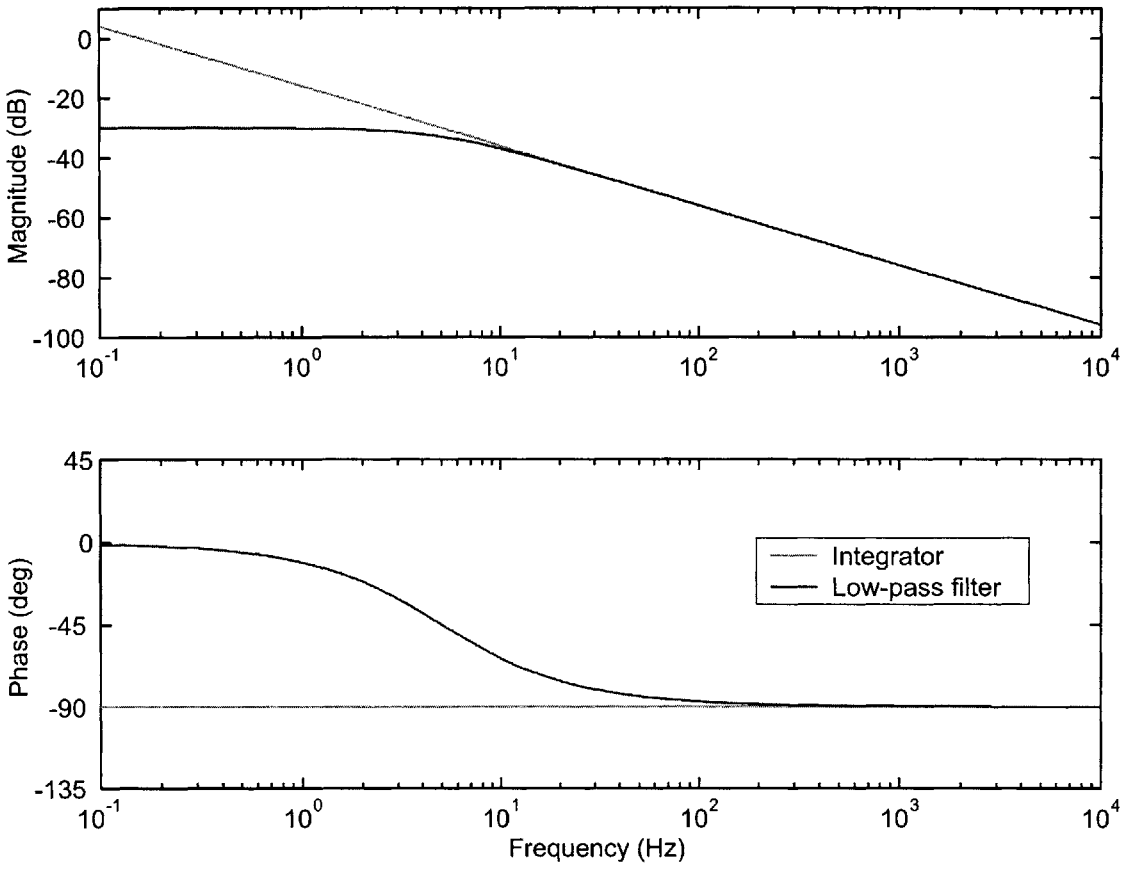

Figure B-4: Comparison between a pure integrator and a low-pass filter.

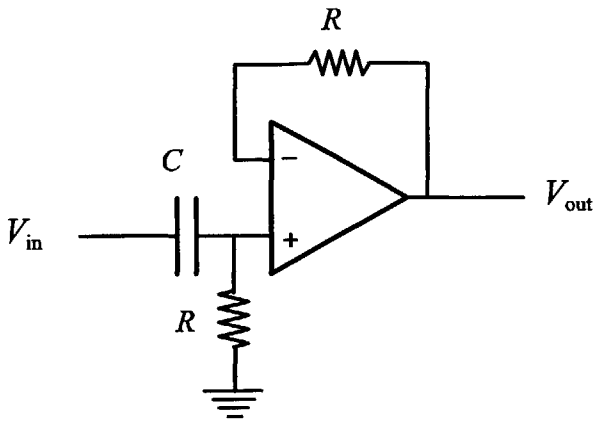

Figure B-5: A high-pass filter.

reduce the effect of the panel's undesirable dynamics.

A High-Pass Filter

Figure B-5 shows a circuit of a high-pass filter used in this study. Its transfer function is given as

$$\frac{V_{\text{out}}(s)}{V_{\text{in}}(s)} = \frac{RCs}{1 + RCs}. \tag{B.6}$$

The cut-off frequency ω_c of the filter is expressed as

$$\omega_c = \frac{1}{RC}. \tag{B.7}$$

In this study, the high-pass filter is generally used with a high-gain amplifier to eliminate the DC saturation, which happens when there is a small DC offset at the input to the amplifier.

A Notch Filter

The analog or hybrid analog/digital feedback controller designed in this study needs a notch filter to cancel the undesirable dynamics of the active composite panel at high frequency. A notch filter can be implemented as a biquadratic filter (second-order numerator and second-order denominator), given as

$$G(s) = \frac{b_1 s^2 + b_2 s + b_3}{a_1 s^2 + a_2 s + a_3}. \tag{B.8}$$

Figure B-6 shows a circuit of a notch filter used in this study. It is a universal building block for the general biquad circuit proposed by Akerbeg and Mossberg [Ghausi, 1981]. The transfer

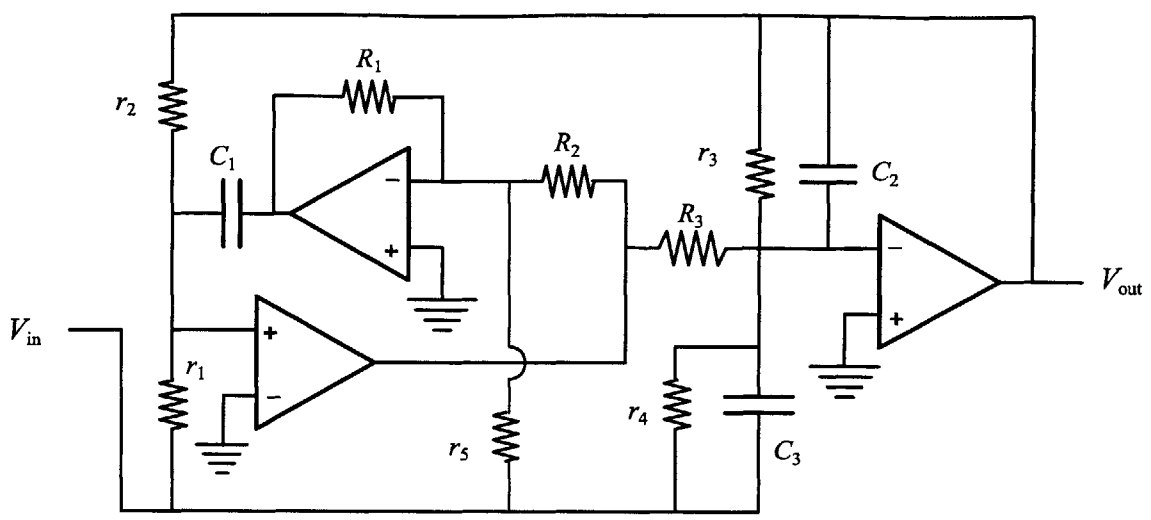

Figure B-6: A notch filter.

function for the circuit is given by

$$\frac{V_{\text{out}}(s)}{V_{\text{in}}(s)} = -\frac{C_3}{C_2}\frac{s^2 + \frac{1}{C_3}\left(\frac{1}{r_4} - \frac{R_2}{r_5 R_3}\right)s + \frac{R_2}{r_1 R_1 R_3 C_1 C_3}}{s^2 + \frac{1}{r_3 C_2}s + \frac{R_2}{r_2 R_1 R_3 C_1 C_2}} . \tag{B.9}$$

Typically, one chooses

$$\begin{aligned} R_1 &= R_2 = R_3 = r_1 = r_2 = R \\ C_1 &= C_2 = C . \end{aligned} \tag{B.10}$$

Under these conditions, the transfer function given in Equation B.9 is simplified to

$$\frac{V_{\text{out}}(s)}{V_{\text{in}}(s)} = -\frac{C_3}{C}\frac{s^2 + \frac{1}{C_3}\left(\frac{1}{r_4} - \frac{1}{r_5}\right)s + \frac{1}{R^2 C C_3}}{s^2 + \frac{1}{r_3 C}s + \frac{1}{R^2 C^2}} . \tag{B.11}$$

After determining the constants $a_1 - a_3$, and $b_1 - b_3$ in Equation B.8 based on the controller design requirement, and matching them with those in Equation B.11, we can determine the values for resistors and capacitors in the circuit.

This concludes the introduction of basic op-amp circuits needed for controller implementation. In the following appendices, it will be shown how those circuits introduced in this appendix will be used to build analog circuits for feedback and feedforward controllers designed in Chapter 6.

Appendix C

Analog Circuit for Analog Control Approach

This appendix presents the analog circuit for analog control approach, *i.e.*, analog feedback and analog feedforward controller, which was introduced in Chapter 6. Both controllers include the low-frequency feedthrough compensator. As mentioned in Chapter 6, the motivation for the analog-only approach is to evaluate the proposed feedback and feedforward control approaches on the real system, and to provide a benchmark against which the other controllers can be compared.

Figure C-1 shows the block diagram of the analog-only control approach. Before the signals from the accelerometers mounted on the top and bottom surface of the active composite panel enter the feedback and feedforward controller, they are processed at the pre-amplifier, which is a pure gain amplifier. Also, the control input is further amplified at the power amplifier, so that high voltage input can be applied to the panel actuator layer. The power amplifier consists of a low-pass filter at 188 Hz.

The analog circuits corresponding to the blocks "Analog feedforward" and "Analog feedback" in Figure C-1 are shown in Figure C-2. In the figure are also shown the signals from the top and bottom accelerometers mounted on the panel that are processed at the pre-amplifier (y_t and y_b, respectively), and the control input u to the power amplifier. The circuit for the analog feedback controller contain several gain amplifiers, a high-pass filter, a notch filter, and the low-frequency feedthrough compensator. On the other hand, the circuit for the analog feedforward controller has several low-pass filters, a gain amplifier, and the low-frequency feedthrough compensator. As mentioned in Chapter 6, a notch filter is not needed in the feedforward control loop, because its effect is negligible well above the control bandwidth in the feedforward loop. The circuits for both controllers consist of the basic op-amp circuits introduced in Appendix B. The values for resistors and capacitors used in the circuit are shown in Table C.1. Since the dynamic characteristics of the active composite panels, such as the low-frequency feedthrough and high-frequency resonance, are different from panel to panel, those values in Table C.1 may be subject to change, depending on which panel is used.

Table C.1: The values of resistors and capacitors used in the circuit for analog control approach.

Resistor	Value ($k\Omega$)	Capacitor	Value (nF)
R_1	15	C_1	34
R_2	33	C_2	24
R_3	82	C_3	0.1
R_4	330	C_4	1000
R_5	330	C_5	3.9
R_6	8.5	C_6	0.2
R_7	1000	C_7	470
R_8	400	C_8	0.49
R_9	4.1	C_9	0.8
R_{10}	22	C_{10}	54
R_{11}	330		
R_{12}	22		
R_{13}	1000		
R_{14}	12		
R_{15}	22		
R_{16}	13.5		
R_{17}	270		
R_{18}	18		
R_{19}	180		
R_{20}	33		

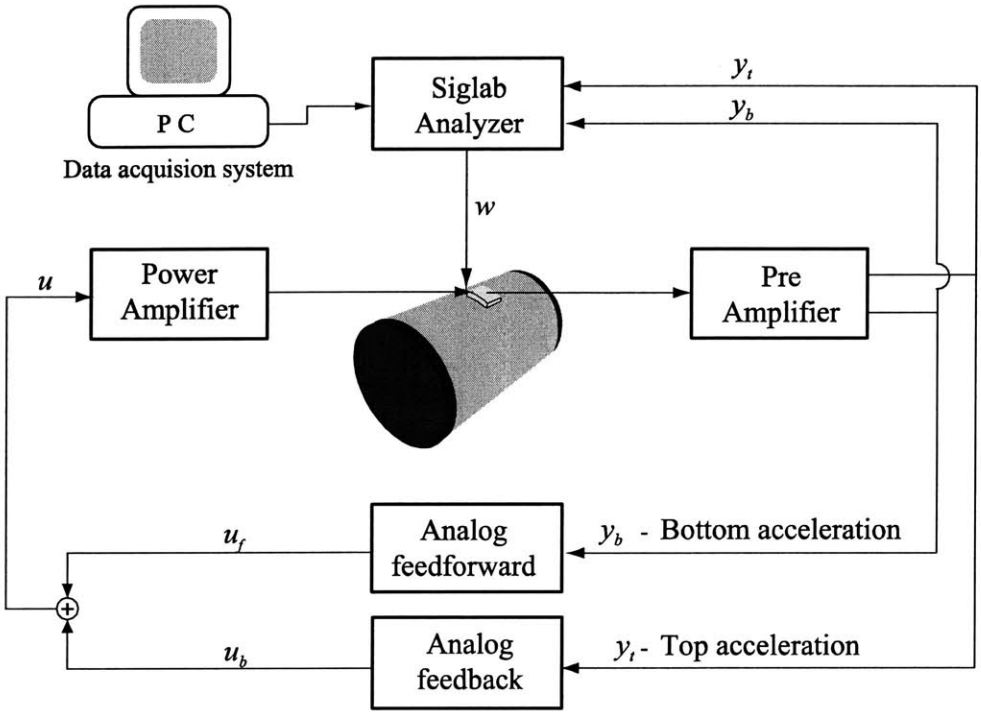

Figure C-1: The block diagram of the analog-only control approach.

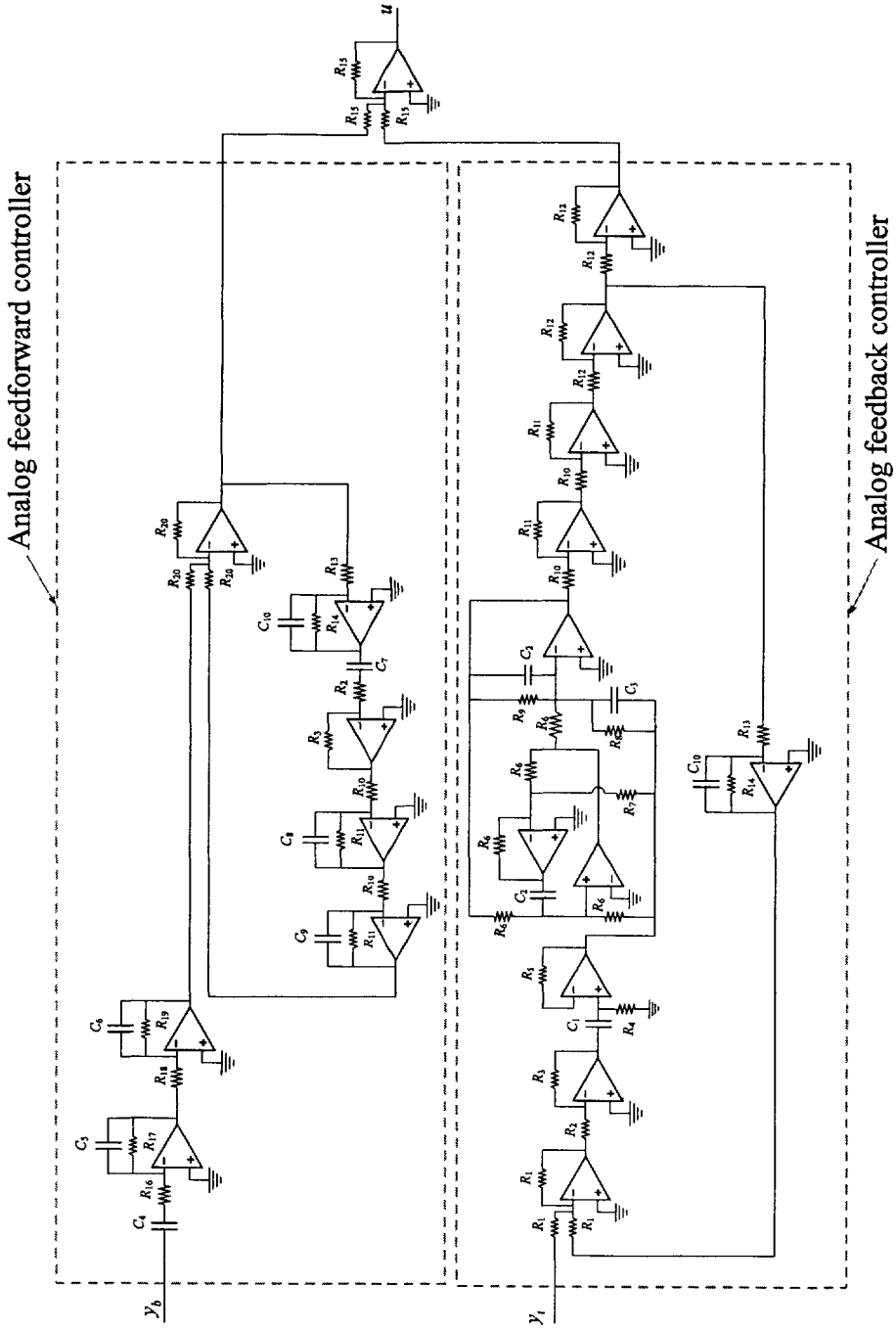

Figure C-2: Analog circuit for analog control approach.

Appendix D

Analog Circuits for the Analog Controller with Digital Notch Filter

This appendix presents the analog circuit for the analog controller with digital notch filter that was introduced in Chapter 6. As mentioned in the chapter, the implementation of the notch filters is critical to the closed-loop performance of the system, because the loop gain or controller bandwidth must be reduced considerably to guarantee stability without the notch. The success of using the notch significantly depends on whether the notch is tuned to the resonance of the panel with enough accuracy. However, as shown in Chapter 2, each panel has different resonant frequency, which makes it impractical to design and implement different analog notch filters with different target frequencies for all the panels. The implementation of the digital notch filter enables us to modify the frequency to be notched out in software, rather in hardware, so that it becomes much easier to implement notch filters with different target frequencies for each panel.

Figure D-1 shows the block diagram of the analog feedback/feedforward controller with digital notch filter. The analog circuits corresponding to the blocks "Analog feedforward" and "Analog feedback" in Figure D-1 are shown in Figure D-2. Both controllers include the low-frequency feedthrough compensator. The circuit for the analog feedforward controller in the figure is the same as that given in Appendix C. On the other hand, the circuit for the analog feedback controller in Figure D-1 is different from its counterpart in the previous appendix in that it doesn't have an analog notch filter. It is replaced by a digital notch filter, in which the analog feedthrough term ("1") and the digital bandpass filter $\widehat{K}_2(s)$ are connected in parallel. The way to design $\widehat{K}_2(s)$ is described in Chapter 6. The values for resistors and capacitors used in the circuit are given in Table D.1.

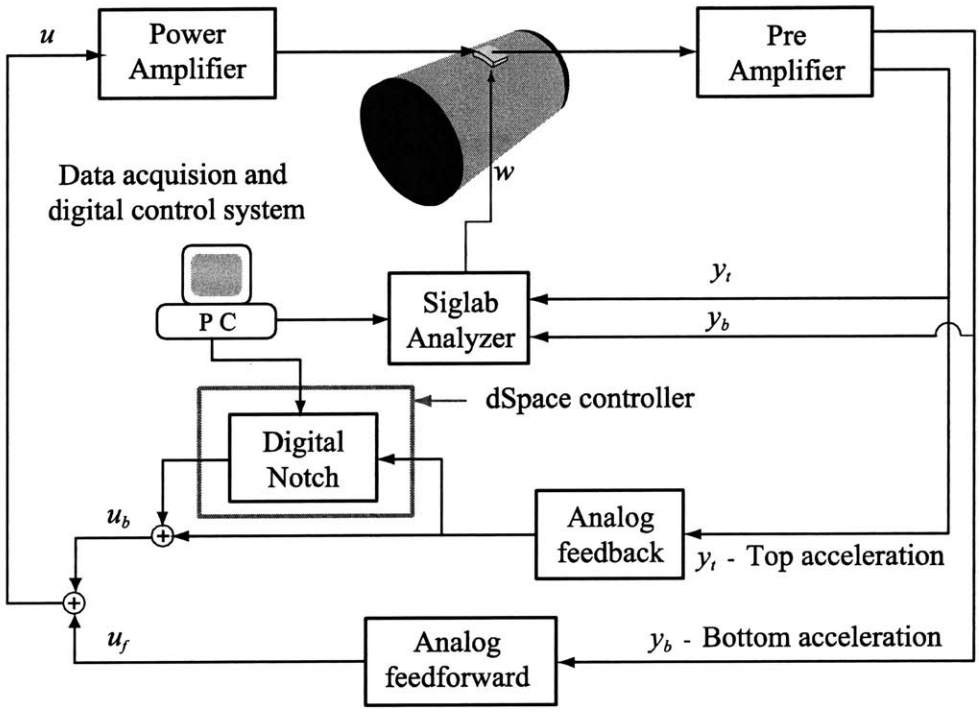

Figure D-1: Block diagram of the analog controller with digital notch filter.

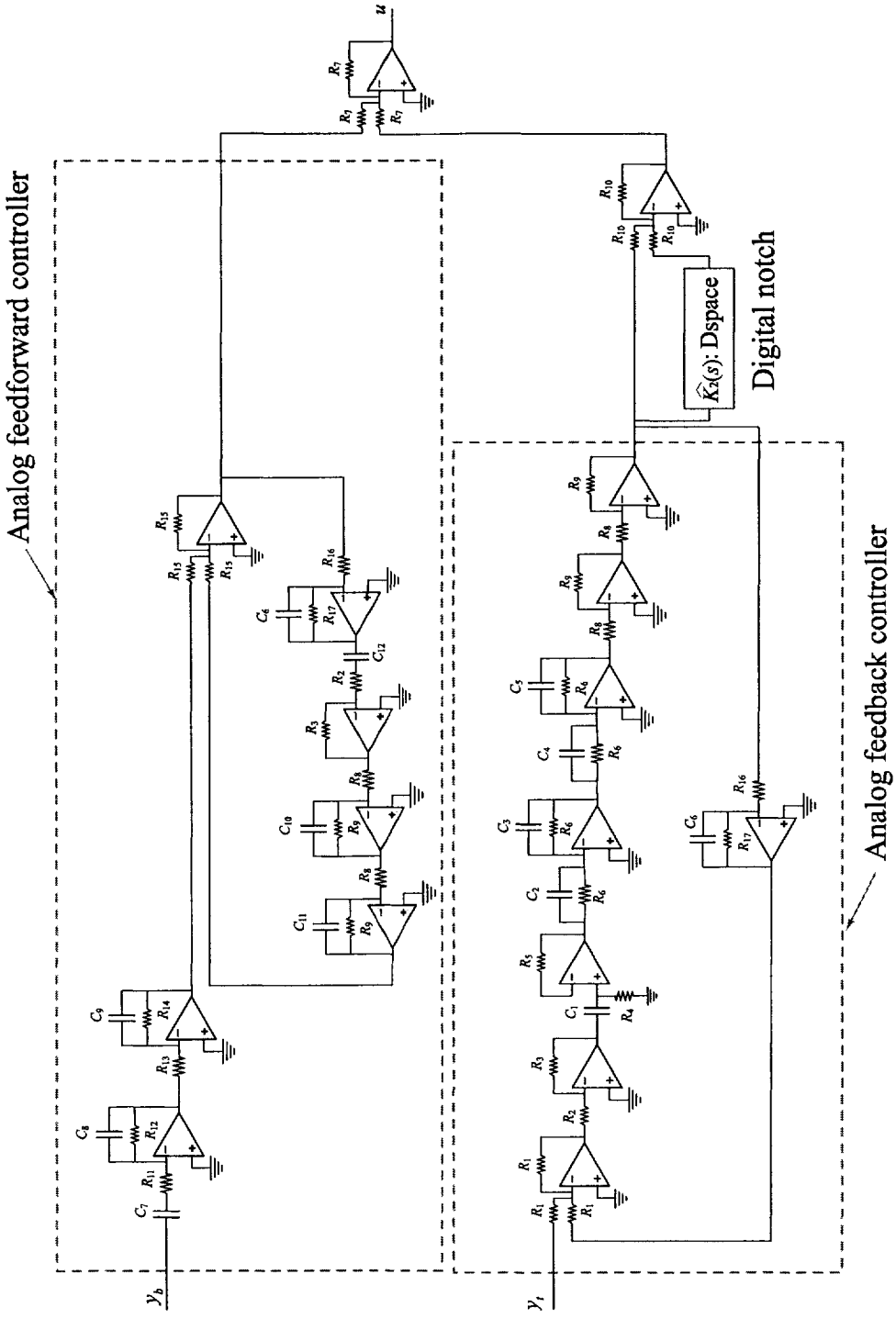

Figure D-2: The circuit for analog feedback/feedforward and digital notch filter.

Table D.1: The values of resistors and capacitors used in the circuit for analog controller with digital notch filter.

Resistor	Value ($k\Omega$)	Capacitor	Value (nF)
R_1	15	C_1	22
R_2	33	C_2	1
R_3	82	C_3	20
R_4	330	C_4	1
R_5	330	C_5	12.2
R_6	13.2	C_6	54
R_7	22	C_7	1000
R_8	22	C_8	3.9
R_9	330	C_9	0.2
R_{10}	22	C_{10}	0.49
R_{11}	13.5	C_{11}	0.8
R_{12}	270	C_{12}	470
R_{13}	18		
R_{14}	180		
R_{15}	33		
R_{16}	1000		
R_{17}	12		

Appendix E

Analog Circuits for Hybrid Feedback and Analog Feedforward Control Approach

This appendix presents the analog circuits used for a hybrid analog/digital feedback and analog feedforward control approach. Figure E-1 shows the block diagram of the hybrid feedback and analog feedforward controller. As mentioned in Chapter 6, the main new features of this configuration are the complementary high-pass and low-pass filters, which control the bands in which the analog and digital control laws act. The low-pass filter consists of a second-order Butterworth low-pass filter with a corner frequency of 1 kHz [Ghausi, 1981]. The analog circuit for the low-pass filter is shown in Figure E-2. Its transfer function is given by

$$\frac{V_{\text{out}}(s)}{V_{\text{in}}(s)} = \frac{\omega_c^2}{s^2 + 2\zeta_c\omega_c s + \omega_c^2}, \tag{E.1}$$

where the corner frequency ω_c and the damping ratio ζ_c are expressed in terms of the values of resistors and capacitors in the circuit as

$$\begin{aligned} \omega_c &= \sqrt{\frac{1}{R_1 R_2 C_1 C_2}}, \\ \zeta_c &= \sqrt{\frac{C_2 (R_1 + R_2)^2}{4 R_1 R_2 C_1}}. \end{aligned} \tag{E.2}$$

Typically, one chooses $R_1 = R_2$ and $C_1 = 2C_2$ to build a second-order Butterworth low-pass filter, so that the damping ratio ζ_c becomes $\zeta_c = 1/\sqrt{2}$. Figure E-3 shows the frequency response of the low-pass filter for $R_1 = R_2 = 100\ k\Omega$ and $C_1 = 2C_2 = 2.2\ n\text{F}$, which results in the second-order Butterworth low-pass filter at 1 kHz.

On the other hand, the high-pass filter is implemented such that it is *complementary* to the low-pass filter, so that its sum with the low-pass filter becomes unity. The analog circuit for the complementary high-pass filter is shown in Figure E-4. As shown in the figure, it consists of two op-amp circuits. The first one is the second-order Butterworth low-pass filter, which is the same one as shown in Figure E-2, and the other one is the differential amplifier. The transfer

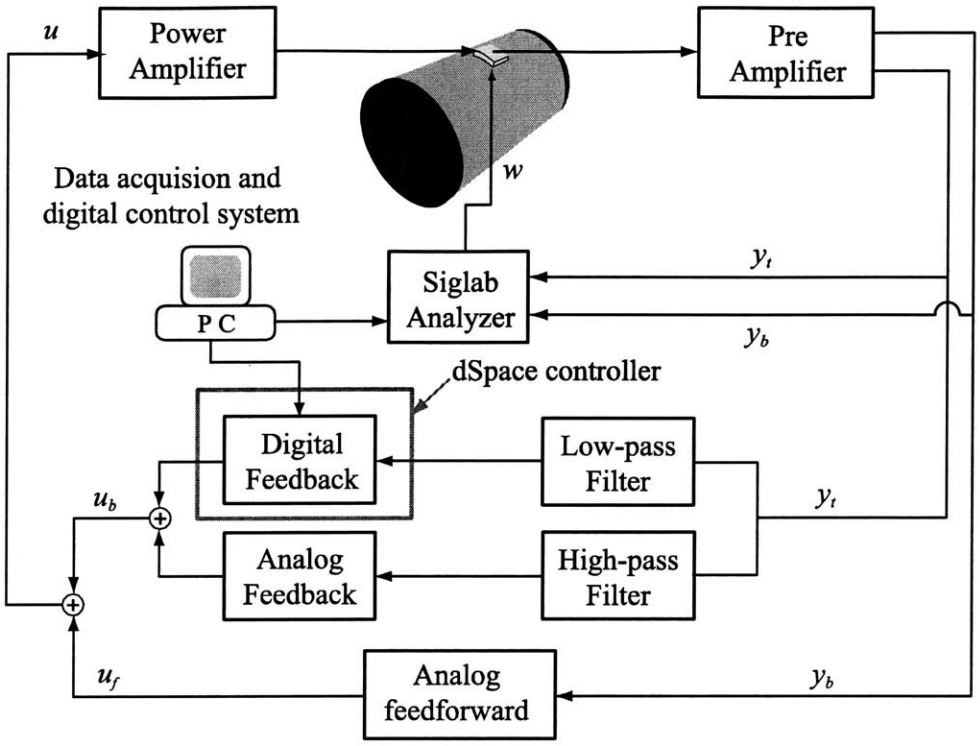

Figure E-1: Block diagram of the hybrid feedback and analog feedforward controller.

function of the circuit is given by

$$\begin{aligned} \frac{V_{\text{out}}(s)}{V_{\text{in}}(s)} &= 1 - \frac{\omega_c^2}{s^2 + 2\zeta_c\omega_c s + \omega_c^2} \\ &= \frac{s^2 + 2\zeta_c\omega_c s}{s^2 + 2\zeta_c\omega_c s + \omega_c^2}. \end{aligned} \tag{E.3}$$

The same expressions for the corner frequency ω_c and the damping ratio ζ_c are used as in Equation E.2. The resulting frequency response of the circuit for $R_1 = R_2 = 100\ k\Omega$, $C_1 = 2C_2 = 2.2\ n\text{F}$ and $R_3 = 10\ k\Omega$ is shown in Figure E-5.

The analog circuit for the hybrid feedback and analog feedforward control approach is shown in Figure E-6. The circuit for the analog feedforward controller in the figure is the same as that given in Appendix C. Also, the same notch filter as in Appendix C is used for the analog feedback control in the hybrid feedback controller. The way to design $K_b'^D(s)$ in the digital feedback control is described in Chapter 6. The values for resistors and capacitors used in the circuit are given in Table E.1.

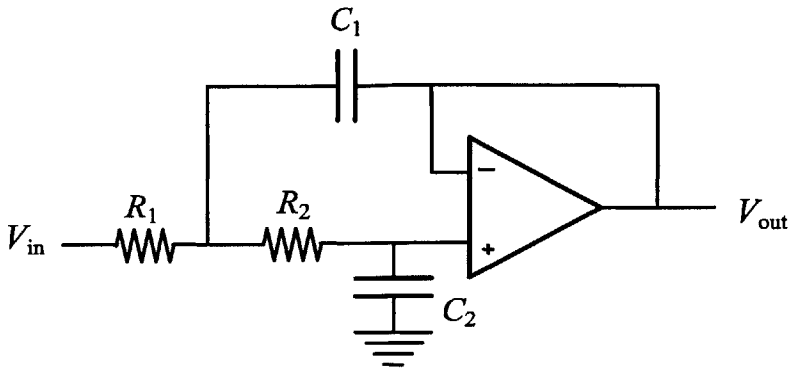

Figure E-2: Analog circuit for the complementary low-pass filter.

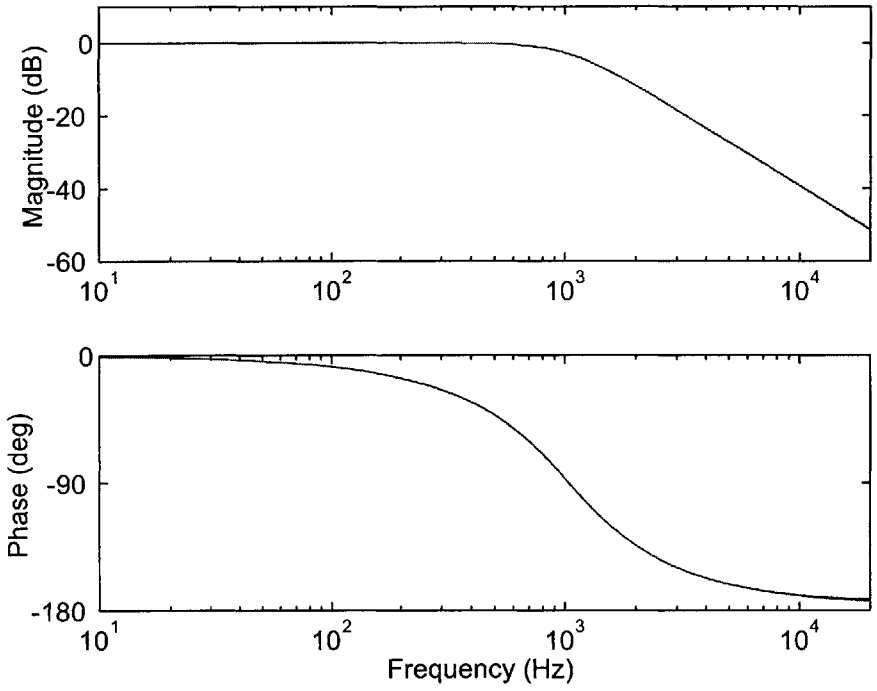

Figure E-3: Frequency response of a second order Butterworth low-pass filter at 1 kHz.

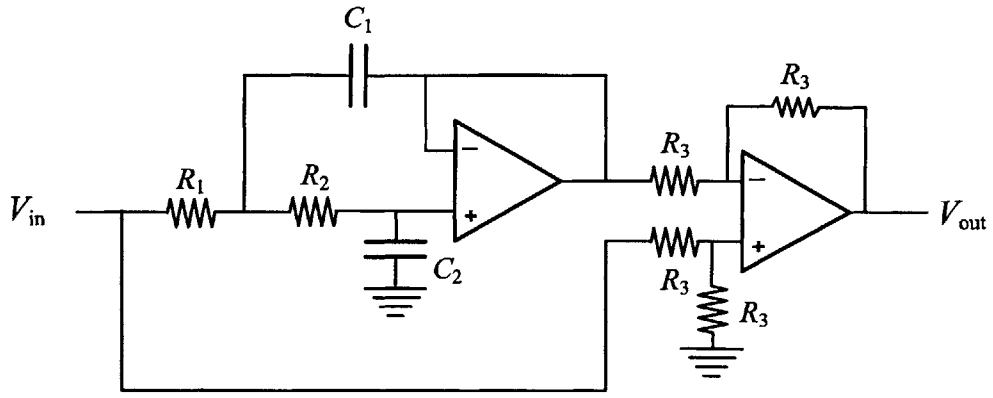

Figure E-4: Analog circuit for the complementary high-pass filter.

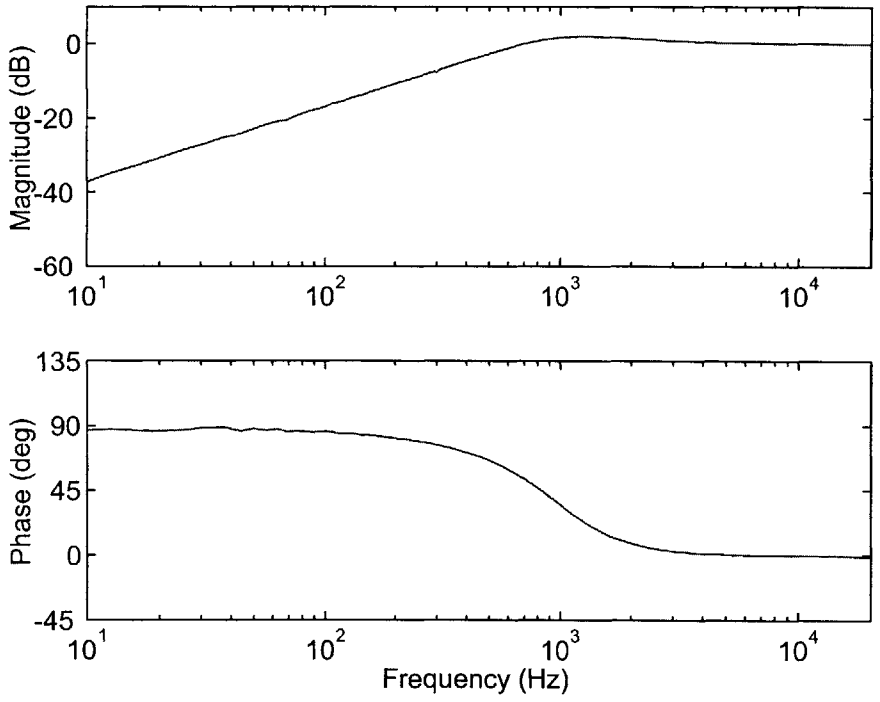

Figure E-5: Frequency response of the complementary high-pass filter.

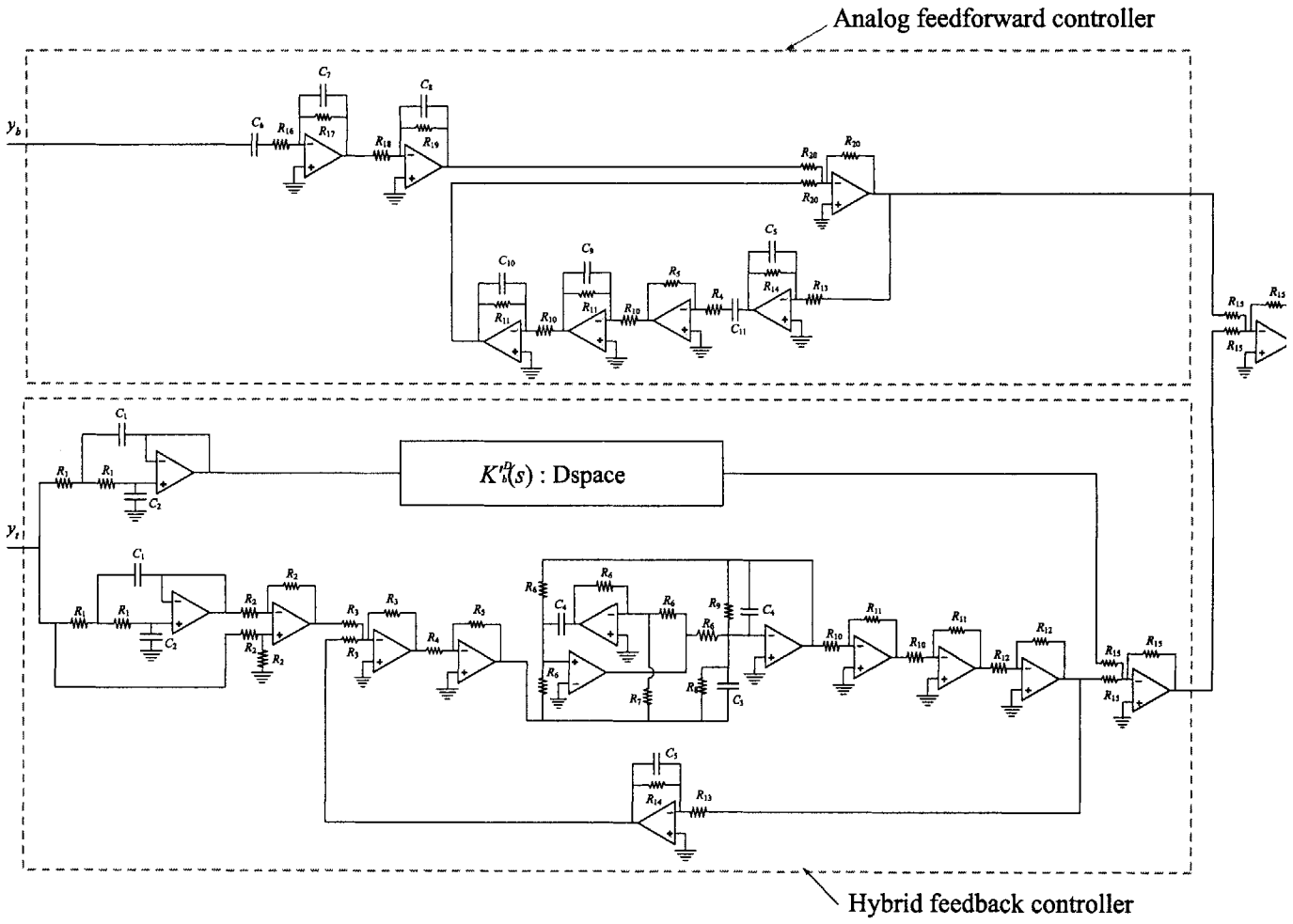

Figure E-6: Analog circuit for hybrid feedback and analog feedforward approach.

Table E.1: The values of resistors and capacitors used in the circuit for hybrid feedback and analog feedforward control.

Resistor	Value ($k\Omega$)	Capacitor	Value (nF)
R_1	100	C_1	2.2
R_2	10	C_2	1.1
R_3	15	C_3	0.1
R_4	33	C_4	24
R_5	56	C_5	54
R_6	8.5	C_6	1000
R_7	1000	C_7	3.9
R_8	400	C_8	0.2
R_9	4.1	C_9	0.49
R_{10}	22	C_{10}	0.8
R_{11}	330	C_{11}	470
R_{12}	22		
R_{13}	1000		
R_{14}	12		
R_{15}	22		
R_{16}	13.5		
R_{17}	270		
R_{18}	18		
R_{19}	180		
R_{20}	33		

3794 - 601